Molecular response to perturbed translation in Gram-positive bacteria

Dissertation zur Erlangung der Würde des Doktors der Naturwissenschaften der Fakultät für Mathematik, Informatik und Naturwissenschaften, Fachbereich Chemie der Universität Hamburg vorgelegt von Caillan Crowe-McAuliffe aus Dunedin, Neuseeland.

Hamburg 2021

Gutachter: Prof. Dr. Daniel N. Wilson, Universität Hamburg, Dr. Yaser Hashem, Université de Bordeaux.
Drittgutachter: Prof. Alexander Mankin, University of Illinois Chicago.
Prüfungskommission: Prof. Dr. Daniel N. Wilson, Prof. Dr. Michael Kolbe, Prof. Dr. Henning Tidow.

Die Disputation fand am 11.02.2022 statt.

Die für diese Dissertation erforderlichen Arbeiten wurden zwischen September 2017 und September 2021 an der Universität Hamburg, Deutschland, durchgeführt.

I List of publications

Crowe-McAuliffe C., Graf M., Huter P., Takada H., Abdelshahid M., Nováček J., Murina V., Atkinson G.C., Hauryliuk V., and Wilson D.N. Structural basis for antibiotic resistance mediated by the *Bacillus subtilis* ABCF ATPase VmlR. *Proc. Natl. Acad. Sci. U.S.A.* (2018) 115, 8978–8983.

Crowe-McAuliffe C.*, Murina V.*, Turnbull K.J., Kasari M., Mohamad M., Polte C., Takada H., Vaitkevicius K., Johansson J., Ignatova Z., Atkinson G.C., O'Neill A.J., Hauryliuk V., Wilson D.N. *First author equal
Structural basis of ABCF-mediated resistance to pleuromutilin, lincosamide, and streptogramin A antibiotics in Gram-positive pathogens. *Nat Commun.* (2021) 12, 3577.

Crowe-McAuliffe C.*, Murina V.*, Kasari, M., Takada H., Turnbull K.J., Polikanov, Y.S., Sundsfjord, A., Hegstad, K., Atkinson G.C., Wilson D.N., Hauryliuk V. *First author equal
Structural basis for PoxtA-mediated resistance to Phenicol and Oxazolidinone antibiotics. *bioRxiv* (2021) doi 10.1101/2021.06.18.448924.

Crowe-McAuliffe C.*, Takada H.*, Murina V., Polte C., Kasvandik S., Tenson T., Ignatova Z., Atkinson G.C., Wilson D.N., Hauryliuk V. *First author equal
Structural basis for bacterial ribosome-associated quality control by RqcH and RqcP. *Mol. Cell* (2021) 81, 115–126.

Takada H., Crowe-McAuliffe C., Polte C., Sidorova Z.Y., Murina V., Atkinson G.C., Konevega A.L., Ignatova Z., Wilson D.N., Hauryliuk V.
RqcH and RqcP catalyze processive poly-alanine synthesis in a reconstituted ribosome-associated quality control system. *Nucleic Acids Res.* 2021 49, 8355–8369.

Müller C., Crowe-McAuliffe C., Wilson D.N.
Ribosome rescue pathways in bacteria. (Literature review) *Front. Microbiol.* 2021 18, 652980.

Zhao W., Cross A.R., Crowe-McAuliffe C., Weigert-Munoz A., Csatary E.E., Solinski A.E., Krysiak J., Goldberg J.B., Wilson D.N., Medina E., Wuest W.M., Sieber S.A.
The natural product elegaphenone potentiates antibiotic effects against *Pseudomonas aeruginosa*. *Angew. Chem. Int. Ed. Engl.* 2019 17, 8581–8584.

Contents

III List of abbreviations

Å	Ångstrom
A-(site)	Aminoacyl
ABC	ATP-binding cassette
ABCF	ATP-binding cassette F family
ADP	Adenosine diphosphate
ADPNP	Adenosine diphosphate-imidophosphate
ARE	Antibiotic resistance element
Arf	Alternative rescue system
ATP	Adenosine triphosphate
CP	Central protuberance
C-terminus	Carboxyl terminus (of a protein)
DNA	Deoxyribonucleic acid
E-(site)	Exit
EF	Elongation factor
EM	Electron microscopy
fMet	Formylmethionine
Gcn	General control nonderepressible
GDP	Guanosine diphosphate
GTP	Guanosine triphosphate
IF	Initiation factor
LsaA	Lincosamide and streptogramin A resistance
LSU	Large subunit
mRNA	Messenger RNA
Msr	MS (macrolide and streptogramin B) resistance
N-terminus	Amino terminus (of a protein)
NBD	Nucleotide-binding domain
NEMF	Nuclear export mediating factor
P-(site)	Peptidyl
P_i	Inorganic phosphate
PLS_A	Pleuromutilin, lincosamide, and streptogramin A
PTC	Peptidyltransferase center
Pth	Peptidyl-tRNA hydrolase
RF	Release factor
RNA	Ribonucleic acid
RNP	Ribonucleoprotein
RQC	Ribosome quality control
rRNA	Ribosomal RNA
S	Svedbergs
SD	Shine–Dalgarno
smFRET	Single-molecule Förster resonance energy transfer
SRL	Sarcin–ricin loop
SRP	signal recognition particle
SSU	Small subunit
tRNA	Transfer ribonucleic acid

tmRNA	Transfer–messenger RNA
UTR	Untranslated region
Vga	Virginiamycin A-like resistance protein
VmlR	Virginiamycin M and lincomycin resistance

Amino acid residues and nucleotides are referred to using the standard single-letter nomenclature. ϕ refers to a hydrophobic amino acid.

1 Zusammenfassung

Die Proteinsynthese auf der Grundlage der mRNA, die so genannte Translation, ist ein entscheidender Prozess, der in allen sich teilenden Zellen stattfindet. Im Allgemeinen ist der Prozess der Translation, der auf dem Ribosom stattfindet, im Laufe der Evolution konserviert worden. Verschiedene Störungen können die Translation beeinträchtigen, so dass die Zellen Strategien entwickelt haben, um mit den daraus resultierenden fehlerhaften Zwischenstufen umzugehen. In dieser Dissertation werden zwei solcher Prozesse in Gram-positiven Bakterien untersucht: die Antibiotikaresistenz, die durch die ABCF-Proteinfamilie vermittelt wird, und das Alanin-Tailing von blockierten Translationsintermediaten, das durch Proteine der NEMF-Familie vermittelt wird. Es wird über die Strukturen von Vertretern beider Proteinfamilien im Komplex mit dem Ribosom berichtet. Die ABCF-Proteine, die Antibiotikaresistenz vermitteln, wirken offenbar über einen indirekten Mechanismus, indem sie die Antibiotika-Bindungsstelle modulieren, um die Freisetzung des Wirkstoffs auszulösen. Das Protein der NEMF-Familie, RqcH, vermittelt im Zusammenspiel mit einem neu beschriebenen Protein das Alanin-Tailing durch Zwischenstufen, die denen der kanonischen Translation verblüffend ähnlich sind. Anhand der gezeigten Strukturen wird ein allgemeines Modell für jeden Prozess vorgeschlagen.

2 Abstract

Protein synthesis templated by mRNA, termed translation, is a critical process that occurs in all dividing cells. In general, the process of translation, which occurs on the ribosome, has been conserved throughout evolution. Various insults may perturb translation, and cells have consequently evolved strategies to address the resulting defective intermediates. This dissertation examines two such processes found in Gram-positive bacteria: antibiotic resistance mediated by the ABCF family of proteins, and alanine tailing of stalled translation intermediates mediated by NEMF-family proteins. Structures of representatives of both protein families in complex with the ribosome are reported. The ABCF antibiotic-resistance proteins apparently act through an indirect mechanism, modulating the antibiotic binding site to trigger drug release. The NEMF-family protein RqcH, in concert with a newly described protein, mediates alanine tailing through intermediates that strikingly resemble those observed in canonical translation. Through the reported structures, a general model of each process is proposed.

3 Introduction

Ribosomes are dense particles found in the cytoplasm and associated with membranes and which are the site of cellular protein synthesis (Palade, 1955).[1] All living cells, as well as some large viruses, contain ribosomes. Although somewhat divergent between organisms, all ribosomes share some common features. Bacterial ribosomes are approximately 2.5 MDa and have three tRNA-binding sites, termed the aminoacyl (A), peptidyl (P), and exit (E) sites (Kurland, 1960; Rheinberger et al., 1981). Ribosomes consist of two subunits: a small subunit (SSU), which sediments at 30S and checks base pairing between the incoming tRNA and mRNA to determine which amino acid is added to the nascent protein chain, and a large subunit (LSU), which sediments at 50S and catalyses the polymerisation of amino acids (Figure 1; Huxley and Zubay (1960); Kurland (1960); Takanami and Okamoto (1963); Monro (1967)). The SSU can be divided into further domains, with the path of the mRNA running between the head and body (Figure 1). In the act of coded protein synthesis, called translation, proteins are synthesised sequentially from N-terminus to C-terminus (Dintzis, 1961; Bishop et al., 1960), with the identity of each the amino acid specified by a three-base codon of the mRNA (Crick et al., 1961).

Various stresses and insults may perturb translation. For example, the bacterial ribosome is a common target for antibiotics which disrupt protein synthesis, and bacteria have correspondingly evolved mechanisms to overcome such inhibition (Wilson, 2014). Damaged or truncated mRNA and various physicochemical insults may also disrupt translation, resulting in the deployment of various cellular responses. This introduction first briefly discusses bacterial translation in general, followed by bacterial response to perturbed translation, then finally addresses a family of antibiotic-resistance proteins that belong to the ABCF family.

3.1 Overview of bacterial translation

Translation can be loosely divided into three phases. The first is initiation, in which a start site is selected on the mRNA. This is followed by elongation, in which amino acids are incorporated into the nascent peptide chain according to the sequence of the mRNA. Finally, the process ends with termination, in which the reaction is terminated and the ribosomal subunits recycled for further rounds of translation. Protein translation factors, many of which are G-protein GTPases that share a common origin, are required to mediate various steps of translation (Leipe et al., 2002). Only bacterial translation is addressed in this document.

3.1.1 Initiation

Translation begins with the recruitment of the ribosome to the mRNA, with translation beginning at a start codon (usually AUG). Three protein initiation factors (IFs) mediate this process. Ultimately, these IFs orchestrate the positioning of the SSU on the mRNA at the start codon with a charged fMet-tRNA in the P-site. IF1 is a small protein that occupies the A-site of the SSU and makes contacts with IF2 and IF3 (Carter et al., 2001). IF2 is a large GTPase that contacts the CCA-fMet moiety of the initiator tRNA. IF3 is dumbbell-shaped, with two domains separated by an α-helical linker and which is highly mobile during bacterial translation initiation (Hussain et al., 2016). The first events in bacterial translation initiation—that is, the binding of the three IFs and the mRNA to the SSU—can likely occur in any order (Milón et al., 2012). Subsequently, the initiator tRNA binds and accommodates, which induces a conformation of the SSU conducive to LSU binding.

[1] Rare exceptions include non-ribosomal peptide synthetases

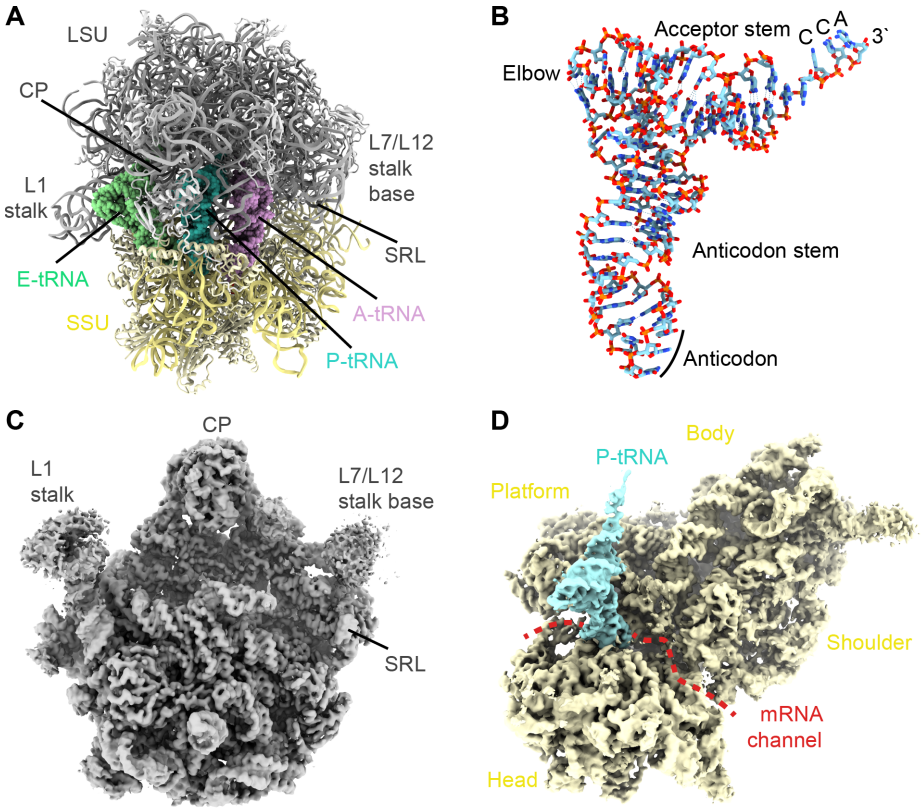

Figure 1: (A) Molecular model of a *Thermus thermophilus* ribosome (PDB ID 6CFJ) (Tereshchenkov et al., 2018). A-, P-, and E-site tRNAs are indicated. CP, central protuberance; SRL, sarcin–ricin loop. (B) Molecular model of a tRNA from PDB 6CFJ with regions of interest labelled. (C) The LSU from a cryo-electron microscopy (cryo-EM) reconstruction of a 70S ribosome from *Staphylococcus aureus* (EMDB-12333), viewed from the intersubunit interface. CP, central protuberance, SRL, sarcin–ricin loop. (D) The SSU and P-tRNA from the map shown in panel C. The path of the mRNA is indicated with a dotted red line. The shoulder and platform regions together make up the SSU body. Figure assembled with UCSF ChimeraX (Pettersen et al., 2021).

The initiation factors induce an 'open' conformation of the SSU head, in which the mRNA channel is widened in the A- and P-sites, potentially allowing mRNA loading without scanning from the 5′-UTR. Initiator tRNA at first binds to the SSU head in a conformation that is tilted away from the SSU body, and proceeds to the standard conformation as the SSU head closes, accompanied by large-scale movements of IF3 and the formation of the codon–anticodon interaction (Hussain et al., 2016). This conformation likely facilitates 50S subunit joining (Hussain et al., 2016; Sprink et al., 2016).

The presence of the LSU induces the compaction and dissociation of IF3 (Nakamoto et al., 2021), as well as GTP hydrolysis by IF2, perhaps through back-rotation of the SSU (Grigoriadou et al., 2007; Sprink et al., 2016). This ultimately results in IF1 and IF2 dissociation and the formation of an elongation-competent complex (Grigoriadou et al., 2007; Sprink et al., 2016).

The Shine–Dalgarno (SD) sequence is a purine-rich element in the 5′-UTR that can base-pair with a motif at the 3′ end of 16S rRNA to help position the SSU at the start codon of an mRNA (Shine and Dalgarno, 1974; Shultzaberger et al., 2001; Korostelev et al., 2007). However, the presence of SD sequences in mRNAs varies widely among prokaryotes (Nakagawa et al., 2010), and some clades, such as the Flavobacteriia, only rarely utilise an SD sequence (Jha et al., 2021).

3.1.2 Elongation

Translation elongation involves the delivery of a charged tRNA to the ribosome, decoding and accommodation of the tRNA, peptidyl transfer, and finally translocation of the mRNA and tRNAs through the ribosome. The translational GTPases elongation factors (EF) -Tu and -G mediate some steps of these processes. Such translational elongation factors can be bound non-specifically by the multi-copy, highly flexible bL12 protein of the L7/L12 stalk, which increases the local concentration of factors around the factor binding site in the ribosome (Imai et al., 2020; Mustafi and Weisshaar, 2018). *In vitro*, translation can occur in the absence of elongation factors, albeit slowly (Pestka, 1968; Gavrilova et al., 1976).

3.1.2.1 Delivery of tRNA to the ribosome, decoding, and accommodation In the cytosol, EF-Tu binds to aminoacylated tRNA with GTP to form a ternary complex in which the EF-Tu binds to one face of the tRNA acceptor stem (Nissen et al., 1995). Such a ternary complex can bind to a translating ribosome to deliver the correct tRNA needed for decoding.

In the ribosomal A-site, the universally conserved 16S rRNA bases A1492, A1493, and G530 monitor the minor groove of the interaction between the tRNA anticodon and the mRNA codon at the first two positions of the codon, and allow for some non-canonical pairing at the third position (Ogle et al., 2001). Decoding triggers movement of the SSU to a closed conformation, facilitated by a G530·A1492 interaction, in which the SSU shoulder moves closer to the SSU platform, which in turn brings EF-Tu into contact with the sarcin–ricin loop of the 23S rRNA (Loveland et al., 2017). This process is much less efficient for near-cognate ternary complexes (Loveland et al., 2020). The sarcin–ricin loop positions His84 of switch II to facilitate GTP hydrolysis (Voorhees et al., 2010).

A recent time-resolved cryo-EM study has elucidated the steps following decoding and preceding peptidyl transfer (Loveland et al., 2020). After GTP hydrolysis EF-Tu dissociates from the tRNA, which allows the tRNA to 'accommodate' into the PTC—a movement of more than 80 Å for the acceptor stem. This process involves both a small rotation of the SSU and movement of the A-site finger on the LSU. At this stage, ribosomal proofreading can still occur, perhaps due to spontaneous SSU opening as the G530·A1492 interaction is disrupted, and EF-Tu may re-associate in the case of failed accommodation (Morse et al., 2020). Reversal of the minor SSU rotation positions the A-tRNA for peptidyl transfer (Loveland et al., 2020).

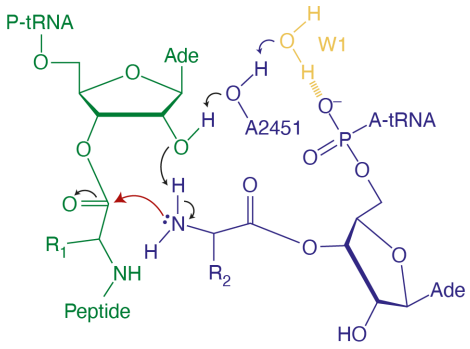

Figure 2: The proton wire model of peptidyl transfer. The carbonyl carbon of the ester bond between the P-tRNA and peptide is attacked by the incoming amino acid (red arrow). This is facilitated by a 'proton wire' running through the P-tRNA 2′ OH, the 23S rRNA A2451 2′ OH, and a water molecule. Peptidyl tRNA, green; A-tRNA, blue; A2451, dark red; Modified from (Rodnina, 2018).

After EF-Tu dissociation, the guanine nucleotide exchange factor EF-Ts forms a complex with EF-Tu·GDP, disrupting the nucleotide binding site and resulting in dissociation of GDP, thus allowing the formation of another ternary complex (Kawashima et al., 1996).

3.1.2.2 Peptidyl transfer During peptidyl transfer, the nascent chain on the P-tRNA is transferred to the amino acid on the A-tRNA, as suggested by Watson (1963). This process occurs on the LSU, in a site termed the peptidyltransferase center (PTC) which is formed entirely from RNA, leading to the suggestion that the ribosome is a ribozyme (Monro, 1967; Ban et al., 2000; Noller et al., 1992; Cech, 2000). The CCA ends of the P- and A-tRNAs bind to the P- and A-loops of the 23S rRNA, respectively (Moazed and Noller, 1989; Nissen et al., 2000), helping to position the nascent chain and aminoacyl moiety for catalysis. Positioning of an A-tRNA induces a conformation of nucleotides in the PTC that is conducive to peptidyl transfer: U2585 forms an H-bond with A76 of the A-site tRNA, and G2583 and U2584 shift to facilitate positioning of the A-tRNA (Schmeing et al., 2005). Additionally, A2602 is positioned between the CCA ends of each tRNA, A2451 shifts moderately, and the N-terminus of bL27 becomes ordered (Nissen et al., 2000; Selmer et al., 2006).

Peptidyl transfer is rather insensitive to changes in pH, which is not consistent with acid-base catalysis (Bieling et al., 2006). Rather, it has been proposed that the ribosome acts as an entropic catalyst, positioning the substrates in a conformation conducive to peptidyl transfer (Sievers et al., 2004). In the most current model of peptide bond formation, the 2′ OH of the P-tRNA A76 abstracts a proton from the amide group of the aminoacyl-tRNA, facilitated by a 'proton wire' involving the 2′ OH of A2451, the 2′ OH of the P-tRNA A76, and a water molecule (Figure 2). This in turn allows attack of the carbonyl carbon of the P-tRNA–nascent peptide ester bond by the amino acid attached to the A-tRNA. The resulting tetrahedral intermediate is resolved via nucleophilic attack of another water molecule, and as a result, the nascent chain is transferred to the A-tRNA and extended by one amino acid (Polikanov et al., 2014).

It is important to note that this model involves the N-terminus of bL27, a protein found only in bacteria, coordinating a critical water molecule that forms part of the proton wire. However, truncation of the bL27 N-terminus reduced but did not eliminate bacterial growth and peptide bond formation (Maguire et al., 2005). Although the proton wire model is a parsimonious model given current information, its generalisability requires further scrutiny.

3.1.2.3 Translocation After peptidyl transfer, a peptidyl-tRNA occupies the A-site and a deacylated tRNA occupies the P-site. These tRNAs must move to the P- and E-sites, respectively, while maintaining base pairing with the mRNA which travels three nucleotides through the ribosome in the 5′ direction, before the next round of elongation can occur. This process, termed

translocation, is mediated by EF-G and a ratchet-like motion of the SSU relative to the LSU (Conway and Lipmann, 1964; Frank and Agrawal, 2000). The E-tRNA must leave the E-site prior to EF-G binding (Choi and Puglisi, 2017).

Capturing and validating authentic translocation intermediates proved difficult by traditional crystallographic methods (reviewed in Ling and Ermolenko (2016)), and an early cryo-EM reconstruction resulted only in a modest resolution (Brilot et al., 2013). Three recent structural studies have analysed translocation with cryo-EM, utilising either antibiotics to trap states validated as authentic translocation intermediates by smFRET (Rundlet et al., 2021), time-resolved cryo-EM in which grids are prepared rapidly after mixing the complex (Carbone et al., 2021), or a hybrid approach (Petrychenko et al., 2021).

Each study observed a population of spontaneously rotated ribosomes, indicating that EF-G binds to, rather than induces, the rotated state, as previously suggested by smFRET (Cornish et al., 2008; Blanchard et al., 2004). After EF-G binding, the tRNA-like domain 4 of EF-G reaches into the A-site and interacts with the codon–anticodon mini-helix, displacing the probing nucleotides A1492 and A1493 of the 16S rRNA and partially displacing the mRNA–tRNA complex from the A-site (Rundlet et al., 2021; Petrychenko et al., 2021). Similarly to EF-Tu, the SRL activates GTPase activity of EF-G by positioning a catalytic histidine. This process appears to happen quickly after binding of EF-G to the ribosome, although the switch regions of the G-domain remain ordered, preventing P_i release (Rundlet et al., 2021; Carbone et al., 2021).

In two studies, EF-G remained essentially rigid throughout the translocation process, with few domain-level rearrangements—albeit with some states in which portions of EF-G were poorly resolved (Carbone et al., 2021; Petrychenko et al., 2021)—while in the third a 17°hinge-like motion between domains 4 and 5 was observed (Rundlet et al., 2021). Nonetheless, all three studies identified a large-scale repositioning of EF-G on the ribosome, namely a pivot around the SRL, after P_i release. This was coincident with reverse rotation of the SSU and movement of the tRNAs from hybrid to chimeric positions. Ultimately, the mRNA and tRNAs move relative to the SSU body. After EF-G dissociation, reverse head swivel completes translocation, with the P-tRNA now occupying the P-site. Late translocation intermediates, for example the details of reverse head swivel, remain to be analysed structurally.

3.1.3 Other processes during elongation

In most genomes, 20–30% of coded proteins are targeted to the membrane (Krogh et al., 2001). In the major pathway for protein membrane insertion or secretion, an N-terminal signal sequence is bound by the signal recognition particle (SRP) during translation elongation, as it emerges from the nascent peptide exit tunnel (Bernstein et al., 1989; Akopian et al., 2013). SRP then binds with FtsY to target the translating ribosome–SRP complex to the SecYEG complex, a translocon that spans the cytoplasmic membrane (Miller et al., 1994; Angelini et al., 2005). The translocon contains a lateral gate that allows transmembrane regions to shift into the membrane during passage through the channel (Berg et al., 2004; Kater et al., 2019).

Translation is generally an accurate process, with miscoding rates 10^{-5}–10^{-3} (Wohlgemuth et al., 2011). However, in cells the genetic code can occasionally be bypassed in a regulated manner, a process termed translational recoding (Atkins et al., 2016; Rodnina et al., 2020). For example, the ribosome may change reading frames, decode a stop codon as the non-canonical amino acid selenocysteine, or bypass in-frame portions of an mRNA entirely (Craigen et al., 1985; Huang et al., 1988; Forchhammer et al., 1989; Fischer et al., 2016)

3.1.4 Termination

In contrast to the amino-acid-specifying codons which are bound in the A-site by tRNAs, stop codons are instead recognised by class-I protein release factors (Capecchi, 1967). These release factors emerged independently in bacteria and archaea/eukaryotes, although they convergently developed some shared features such as the GGQ motif which mediates peptide release (Burroughs and Aravind, 2019). In bacteria, there are two class-I release factors: RF1 recognises the stop codons UAG and UAA, while RF2 recognises UGA and UAA (Scolnick et al., 1968; Brown and Tate, 1994). The mRNA nucleotide immediately downstream of the stop codon additionally affects the efficiency of translation termination (Poole et al., 1995).

Bacterial class I release factors bind to the ribosome in a compact conformation, first assessing the stop codon in the decoding centre with a combination of domains II and IV before converting to an 'open' conformation in which the GGQ motif of domain III is positioned in the PTC (James et al., 2016; Fu et al., 2019). Peptide release proceeds through a water (or hydroxyl) molecule (Shaw and Green, 2007; Indrisiunaite et al., 2015; Trobro and Åqvist, 2007; Laurberg et al., 2008). In the case of RF2, a rearrangement of the GGQ loop to a β sheet forms a plug through the PTC to the nascent peptide exit channel, perhaps facilitating directional release of the completed polypeptide (Svidritskiy et al., 2019).

A class-II release factor, the translational GTPase RF3, also contributes to translation termination in some bacteria (Capecchi and Klein, 1969; Milman et al., 1969; Mikuni et al., 1994; Grentzmann et al., 1994). The distribution of RF3 is sporadic in bacteria (it is absent, for example, in *B. subtilis*; Margus et al. (2007)), and the factor is not essential in *E. coli* (Mikuni et al., 1994), implying that this protein is not essential for peptide release. RF3 appears to function in increasing the rate of release of the class-I release factors by inducing SSU rotation (Koutmou et al., 2014; Graf et al., 2018). Additionally, RF3 has been reported to function in ribosome-associated quality control (Vivanco-Domínguez et al., 2012; Heurgué-Hamard et al., 1998; Gong et al., 2007; Watanabe et al., 2010; Zaher and Green, 2011).

3.1.5 Recycling

After dissociation of the translated protein and release factors, the 70S–mRNA–tRNA complex is reduced to its constitutive components for further translational passages. A specialised factor found only in bacteria, termed the ribosome recycling factor (RRF), cooperates with EF-G to mediate this process (Hirashima and Kaji, 1973). RRF consists of a small α/β domain and the three-helix bundle and is essential for growth in *E. coli* (Selmer, 1999; Kim et al., 2000; Janosi et al., 1994).

On the ribosome, RRF binds in the intersubunit space near the A-site, with its three-helix bundle overlapping with the position of A- and P-tRNA acceptor stems to contact the P-loop, while the α/β domain contacts the SSU (Lancaster et al., 2002; Agrawal et al., 2004; Wilson et al., 2005). RRF binding favours SSU rotation and entry of the deacylated tRNA to the P/E-site (Dunkle et al., 2011; Prabhakar et al., 2017). EF-G binds the RRF-bound 70S complex, with domain 4 contacting the RRF α/β domain, and mediates subunit splitting in a GTP-dependent manner (Gao et al., 2005; Zavialov et al., 2005; Fu et al., 2016; Prabhakar et al., 2017). IF3 may contribute to recycling, particularly in the dissociation of mRNA and tRNA from the SSU, although its role is controversial (Hirokawa et al., 2002; Fu et al., 2016; Karimi et al., 1999; Peske et al., 2005; Prabhakar et al., 2017). The order of events during recycling remains disputed, with some studies supporting a model in which mRNA and tRNA are released prior to subunit splitting (Chen et al., 2017; Iwakura et al., 2017).

3.2 Response to abnormalities during translation in bacteria

Between 2 and 4% of translational passages in *E. coli* fail to finish normally in the absence of specialised systems to address stalled translational products (Ito et al., 2011). Ribosome stalling can be caused by truncated mRNAs, ribosome-targeting antibiotics, chemical damage to the mRNA, stretches of rare codons, certain nascent polypeptides in combination with a ligand, combinations of certain codons immediately after initiation, and perturbed translation termination (Sunohara et al., 2004; Li et al., 2006; Jacinto-Loeza et al., 2008; Garza-Sánchez et al., 2009; Wurtmann and Wolin, 2009; Wilson et al., 2016; Verma et al., 2019; Su et al., 2019; Thomas et al., 2020). Chemically damaged ribosomes can presumably also stall and require rescue through unknown mechanisms. Cells have evolved numerous systems to resolve such stalled translation intermediates (reviewed in Müller et al. (2021)), which are briefly reviewed below.

3.2.1 Peptidyl-tRNA drop-off

In response to stalled translation, peptidyl tRNA may 'drop off' the ribosome. This occurs most efficiently for nascent polypeptides $\leq$6 amino acids, also can also occur in response to macrolides and for some stalling peptides (Heurgué-Hamard et al., 2000; Tenson et al., 2003; Gong et al., 2007). Presumably, for long nascent polypeptides any folded domain outside of the nascent peptide exit channel would form a steric block as well as contribute entropic pulling force to prevent dissociation of the peptidyl-tRNA from the LSU. Drop-off can be facilitated by EF-G, RRF, and RF3 (Heurgué-Hamard et al., 1998; Rao and Varshney, 2001; Gong et al., 2007; Singh et al., 2008; Watanabe et al., 2010; Vivanco-Domínguez et al., 2012).

Free peptidyl-tRNA can be hydrolysed to peptide and tRNA by peptidyl-tRNA hydrolase (Pth) (Cuzin et al., 1967; Kössel and RajBhandary, 1968; García-Villegas et al., 1991). Free peptidyl-tRNA naturally accumulates in *E. coli* with deficient Pth activity, and is toxic to the cell (Menninger, 1976, 1979). One well-known example of peptidyl-tRNA drop-off is caused by the *bar* so-called minigenes of *E. coli* λ page, which encode only the dipeptide fMet-Ile before a stop codon (Ontiveros et al., 1997). Expression of minigenes can cause growth arrest through sequestration of free tRNA (Tenson et al., 1999).

3.2.2 The transfer–message RNA system

Transfer–messenger RNA (tmRNA) is a ribonucleoprotein particle consisting of an RNA, encoded by *ssrA*, and the smpB protein (Tu et al., 1995; Keiler et al., 1996; Karzai et al., 1999). Together, these factors form an RNP with the functional characteristics of both a tRNA (which can be aminoacylated with alanine) and an mRNA (which encodes a short degradation-inducing peptide with a regular stop codon) (Komine et al., 1994; Ushida et al., 1994). Nearly all bacteria, and some eukaryotic organelles, contain the tmRNA system (Keiler et al., 2000; Hudson et al., 2014).

When the ribosome encounters the end of an mRNA during elongation, which may be induced by cleavage with a nuclease after stalling, the tmRNA molecule can bind to the stalled translation complex (Hayes and Sauer, 2003; Thomas et al., 2020). Initially, the tRNA component of the tmRNA binds in complex with EF-Tu similarly to regular elongation but with the C-terminus of SmpB in the mRNA entrance channel (Neubauer et al., 2012). SmpB additionally contacts the tip of helix 5 of the tmRNA, thus circularising the RNP (Fu et al., 2010; Weis et al., 2010). After the nascent chain is transferred to the tmRNA, translocation of the tRNA-like component from the A to the P-site is mediated by EF-G (Ramrath et al., 2012). The C-terminal tail of smpB then changes position to occupy the mRNA channel in the P- and E-sites, and the mRNA-like portion of the tmRNA is pulled into the A-site, allowing translation of the mRNA-like component

to proceed as normal (Rae et al., 2019; Guyomar et al., 2021). During this process the helical region of the tmRNA sweeps over the solvent-exposed side of the SSU head, with smpB finally occupying a site close to the mRNA exit channel (Rae et al., 2019).

After translation termination, the original truncated polypeptide encoded by the damaged mRNA has been extended by a short C-terminal stretch of amino acids, encoded by the tmRNA, and released from the ribosome. The C-terminal peptide extension then targets the truncated protein for degradation (Gottesman et al., 1998). Approximately 0.4% of translational passages in *E. coli* end with tmRNA tagging under normal conditions (Moore and Sauer, 2005).

3.2.3 Alternative rescue factors

In addition to the tmRNA system, bacteria may contain protein-based alternative rescue factors (Arfs). *ArfA*, which is found in some clades of proteobacteria, encodes a small protein and is essential in *E. coli* when *ssrA* is deleted (Chadani et al., 2010; Schaub et al., 2012). Once a ribosome with truncated mRNA is bound by ArfA, RF2 is recruited to mediate release of the polypeptide (Chadani et al., 2012; Shimizu, 2012). ArfA specifically binds stalled translation complexes by occupying the empty mRNA entrance channel and complements a β-sheet of RF2, thus stabilising binding and facilitation the transition of RF2 from a closed to an open form on the ribosome (James et al., 2016; Huter et al., 2017b; Demo et al., 2017; Zeng et al., 2017; Ma et al., 2017).

An unrelated protein with a similar function to ArfA, termed BrfA, has been described in *Bacillus* (Shimokawa-Chiba et al., 2019). Like ArfA, BrfA also binds in the mRNA entry channel and complements a β-sheet of RF2 to mediate peptide release on non-stop mRNAs (Shimokawa-Chiba et al., 2019).

A second class of alternative rescue factor, termed ArfB, has also been described (Chadani et al., 2011; Handa et al., 2011). Unlike ArfA and BrfA, ArfB has intrinsic peptidyl hydrolase activity and does not require a class-I release factor to terminate stalled translation reactions (Chadani et al., 2011; Handa et al., 2011). ArfB partially occupies the mRNA entry channel, and, like a class-I release factor, has a GGQ-containing loop positioned for peptide hydrolysis (Gagnon et al., 2012; Carbone et al., 2020; Chan et al., 2020). ArfB is active on ribosomal complexes with mRNA extending 9 nt beyond the A-site, hinting at a yet-unknown specialisation of ArfB function and consistent with the synthetic lethality of *ssrA* and *arfA* while *arfB* remains intact (Chan et al., 2020).

In contrast to *ArfA*, which is limited to some clades of proteobacteria, *ArfB* is widely distributed but not universal among bacteria (Feaga et al., 2014; Keiler and Feaga, 2014; Schaub et al., 2012). An orthologue of ArfB, ICT1, is present in human mitochondria and is both a structural constituent of the mitoribosome and an alternative release factor, binding similarly to ArfB on bacterial ribosomes (Kummer et al., 2021; Richter et al., 2010; Brown et al., 2014; Greber et al., 2014).

3.2.4 Target protection as a response to translation-targeting antibiotics

Target protection is a form of antibiotic resistance in which a protein binds to the antibiotic target to mediate resistance (Wilson et al., 2020). One family of target protection proteins consists of EF-G homologues, such as TetM and TetO, which confer resistance to tetracyclines (Burdett, 1991, 1986; Manavathu et al., 1990), a class of antibiotics that bind to the A-site of the SSU (Brodersen et al., 2000). This family of antibiotic-resistance proteins is found throughout Gram-positive and Gram-negative pathogens (Roberts, 2005). These proteins bind similarly to EF-G on the ribosome (Spahn et al., 2001) and require GTP binding, but not hydrolysis, for drug release (Trieber et al., 1998). Structures of TetM and TetO on the ribosome indicate that

a direct overlap between domain IV of the protein and the antibiotic binding site mediates drug egress from the ribosome (Dönhöfer et al., 2012; Li et al., 2013; Arenz et al., 2015).

Fusidic acid inhibits EF-G, trapping it on the ribosome (Tanaka et al., 1968; Bodley et al., 1969). FusB-family proteins are approximately 25 kDa and found throughout Staphylococci, especially *S. aureus* (O'Neill et al., 2007; Cox et al., 2012; Guo et al., 2012). This family counteracts the inhibitory effect of fusidic acid by binding EF-G (O'Neill and Chopra, 2006). Curiously, resistance is conferred not through displacement of fusidic acid, as these proteins likely bind EF-G at a site distinct from the fusidic-acid-binding site (Cox et al., 2012; Tomlinson et al., 2016).

3.2.5 Ribosome-associated heat-shock proteins

HflX is a GTPase, related to ribosome biogenesis factors, that is widely but not universally conserved among all domains of life (Leipe et al., 2002; Dutta et al., 2009). *E. coli* HflX is a heat-shock protein that can bind to ribosomes and trigger splitting of ribosomes that have a deacylated P-site tRNA in a process that requires binding, but not hydrolysis of GTP (Zhang et al., 2015). After splitting, HflX remains bound to the LSU at the translation-factor-binding site, with an N-terminal domain extending towards the PTC (Zhang et al., 2015). Homologues of HflX with extended N-terminal domains have been reported to mediate low-level resistance to some LSU-binding antibiotics (Duval et al., 2018; Rudra et al., 2020). The mechanism of such resistance remains to be elucidated, although modelling indicates that the extended N-terminal domain may overlap with the binding site of relevant antibiotics (Wilson et al., 2020).

Hsp15 is a heat-shock protein found in *E. coli* (Korber et al., 2000). It binds with nanomolar affinity to a complex of the LSU with peptidyl-tRNA, which may occur when ribosomal subunits dissociate during elongation (Korber et al., 2000). Hsp15 is a relatively small protein with an S4 RNA-binding fold (Staker et al., 2000). Using a low-resolution cryo-EM structure of Hsp15 bound to a LSU–peptidyl-tRNA complex, Hsp15 was proposed to bind to the central protuberance of the LSU (Jiang et al., 2009).

3.2.6 Alternative translation factors

Ribosomes naturally stall while translating three or more consecutive proline residues, a process alleviated by a protein called EF-P (IF5A in eukaryotes and archaea) (Glick and Ganoza, 1975; Ude et al., 2013; Doerfel et al., 2013). EF-P binds in the E site of the ribosome and contacts the 3′ CCA end of the P-site tRNA (Blaha et al., 2009). In particular, a modified lysine of *E. coli* EF-P forms a hydrogen bond with the phosphate group between C765 and A76, helping to stabilise the P-site tRNA and nascent chain in a conformation conducive to peptide bond formation (Huter et al., 2017a).

LepA, also called EF-4, is an EF-G paralogue that lacks an equivalent to EF-G domain IV but contains an additional C-terminal domain (Qin et al., 2006). It is highly conserved, nearly universal in bacteria and also present in some eukaryotic organelles (Qin et al., 2006; Margus et al., 2007). Despite its high conservation, deletion of LepA has no or only a mild phenotype (Dibb and Wolfe, 1986), while overexpression causes substantial growth defects (Qin et al., 2006).

LepA has been shown to catalyse 'back-translocation' *in vitro*, catalysing the movement from a post-transfer to pre-transfer state as shown by puromycin reactivity, chemical protection, and toeprinting assays (Qin et al., 2006; Liu et al., 2010). However, it has also been implicated in ribosome biogenesis and its function remains controversial (Gibbs and Fredrick, 2018). A crystal structure showed that LepA binds similarly to EF-G on the ribosome, with its unique C-terminal domain contacting the P-tRNA 3′ CCA, displacing the A-tRNA from its normal position in the process (Gagnon et al., 2016). However, the sample used for this structure was reconstituted

and contained a fusion between bL9 and LepA, and therefore might not represent the complex to which LepA binds in the cell (Gagnon et al., 2016).

3.2.7 The stringent response

When starved of a particular amino acid, *E. coli* halts RNA synthesis (Sands and Roberts, 1952). In 1969 it was shown that in response to such starvation *E. coli* produces the second messengers guanosine tetraphosphate and guanosine pentaphosphate (ppGpp and pppGpp, respectively, and collectively referred to referred to as (p)ppGpp) (Cashel and Gallant, 1969). These second messengers bind to RNA polymerase to modulate transcription (Artsimovitch et al., 2004) and additionally have profound and varied effects on physiology throughout the bacterial kingdom, generally halting growth (reviewed in Potrykus and Cashel (2008); Hauryliuk et al. (2015)).

The signal to trigger synthesis of (p)ppGpp is a ribosome with a non-acylated tRNA in the A-site (Haseltine and Block, 1973; Pedersen et al., 1973). This process is mediated by a family of proteins called RelA/SpoT homologues, many of which contain domains that mediate both the synthesis and hydrolysis of (p)ppGpp (Stent and Brenner, 1961; Atkinson et al., 2011). The *E. coli* synthetase RelA binds the ribosome with an extended conformation, making contact with the uL11 stalk base and the A-site finger as well as a deacylated tRNA, a conformation which may relieve autoinhibition to stimulate (p)ppGpp production (Brown et al., 2016; Arenz et al., 2016; Loveland et al., 2016).

3.2.8 Bacterial ribosome-associated quality control

In eukaryotes, truncated mRNA can result in dissociation of the ribosomal subunits without resolution of the peptidyl-tRNA, which remains threaded through the LSU. Such complexes can be bound by NEMF-family proteins, which extend the nascent chain with alanines (and sometimes other amino acids) in the absence of mRNA or the SSU in a process termed ribosome-associated quality control (RQC; Brandman et al. (2012); Shen et al. (2015); Udagawa et al. (2021)). Recently, NEMF homologues in bacteria, which are widely dispersed but absent in a few lineages, including *E. coli*, have been reported to mediate alanine tailing on truncated mRNAs (Lytvynenko et al., 2019). Ala-tailed proteins are degraded by the ClpXP protease (Lytvynenko et al., 2019). Mechanistic details of the alanine-tailing process, as well as the identity of the native substrates and release factor, remain elusive.

3.3 ATP-binding cassettes

ATP-binding cassette (ABC) proteins are an ancient and widespread class of proteins, best characterised as transporters but with examples of proteins contributing to diverse cellular functions (Davidson et al., 2008; Ogasawara et al., 2020). Individual ABCs are also referred to as nucleotide-binding domains (NBDs). A typical ABC transport system consists, at minimum, of at least two NBDs and two transmembrane domains, which may be spread over multiple polypeptides (Higgins et al., 1982; Gilson et al., 1982; Higgins et al., 1986; Davidson and Nikaido, 1990). Like the translational GTPases, ABC proteins belong to the P-loop protein superfamily, so-named for a loop with a conserved sequence—also termed the Walker A motif, with the consensus motif GXXXXGK[TS], where X is any amino acid—that binds the β and γ phosphate of the bound trinucleotide (Walker et al., 1982; Saraste et al., 1990).

In addition to the P-loop/Walker A motif, the Walker B motif (ϕϕϕϕD, where ϕ is a hydrophobic amino acid) and a helix-rich signature domain, containing the signature sequence (also known as the C-loop, consensus sequence LSGGQ) are necessary for catalysis. The Walker B motif, which is immediately followed by a catalytic glutamate, consists of a β-sheet with the

terminal aspartate coordinating a magnesium ion (Oldham and Chen, 2011). ABC proteins with mutated catalytic glutamines, so-called EQ_2 mutants which can bind but not hydrolyse ATP, have been used as tools to to trap ABC proteins in otherwise-unstable intermediate states (Oldham et al., 2007; Moody et al., 2002; Johnson and Chen, 2018). The signature sequence resides at the end of an α-helix and is involved in NBD dimerisation. NBDs dimerise with the Walker A and B motifs of one monomer interacting with the signature sequence of the other monomer, forming two ATP binding sites, each of which contains components of both NBDs. Binding of ATP brings the two monomers together, acting as a 'molecular glue' which reverses after nucleotide hydrolysis and product dissociation (Karpowich et al., 2001; Johnson and Chen, 2018). In the context of membrane transporters, NBD dimerisation and its reversal after nucleotide hydrolysis can result in a tweezer-like motion to facilitate transport of a substrate across a membrane (Chen et al., 2003) Structural aspects of ABC proteins have been recently reviewed in Orelle et al. (2019) and Thomas and Tampé (2020).

3.3.1 The ABCF subfamily

ABCF proteins are a subfamily of ABCs, classified as containing two NBDs but no transmembrane regions (Kerr, 2004). These proteins are found in bacteria and eukaryotes and many have been shown to be involved in translation (Murina et al., 2019). A defining characteristic of the ABCF proteins is an interdomain linker, consisting of two α helices, residing between the NBDs. Although the broad structure of the linker element is maintained throughout ABCFs, it varies considerably by length and is not characterised by any particular sequence motif other than an enrichment in positively charged amino acids (Kerr, 2004; Murina et al., 2019).

A number of bacterial ABCF genes have been characterised as antibiotic-resistance elements (AREs). Initially thought to be part of an efflux system, in 2016 these proteins were conclusively shown instead to bind directly to the ribosome to mediate antibiotic resistance (Ross et al., 1989, 1990; Reynolds et al., 2003; Sharkey et al., 2016). ABCF AREs tend to have relatively long interdomain linkers (Kerr, 2004). Characterised ABCF AREs can be roughly grouped into three classes: those conferring resistance to pleuromutilin, lincosamides, and streptogramin A (PLS_A) antibiotics, those conferring resistance to macrolides and streptogramin B antibiotics, and those conferring resistance to phenicols and oxazolidinones (Figure 3; Sharkey et al. (2016); Sharkey and O'Neill (2018); Ero et al. (2019); Ousalem et al. (2019)). A fourth class consists largely of predicted ARE-ABCFs in antibiotic producers, which are largely uncharacterised (Sharkey and O'Neill, 2018; Olano et al., 1995; Peschke et al., 1995; Aparicio et al., 1996; Karray et al., 2007; Kitani et al., 2010; Rosteck et al., 1991). These groups are not monophyletic, implying that specificity of resistance has emerged multiple times during evolution (Murina et al., 2019).

Among ABCF AREs, the length of the interdomain linker is related to the spectrum of antibiotic resistance: long linkers correlate with resistance to macrolides and streptogramin Bs, which bind in the nascent peptide exit tunnel; medium-length linkers correlate with resistance to PLS_A antibiotics; and short linkers correlate with resistance to oxazolidinones and phenicols (usefully reviewed in Fostier et al. (2021)).

3.3.1.1 EttA Energy-dependent translational throttle A (EttA) is an ABCF protein that is broadly distributed in bacteria (Murina et al., 2019). On the basis of ABCF involvement in eukaryotic translation, two papers identified and characterised EttA, one of four endogenous ABCF proteins in *E. coli* (Boël et al., 2014; Chen et al., 2014)

In a biochemical assay, EttA-EQ_2 prevented translocation after formation of the first peptide bond, in competition with EF-G (Boël et al., 2014). By contrast, native EttA had no or a mild stimulatory effect in the elongation assay in the presence of ATP, but prevented peptide bond

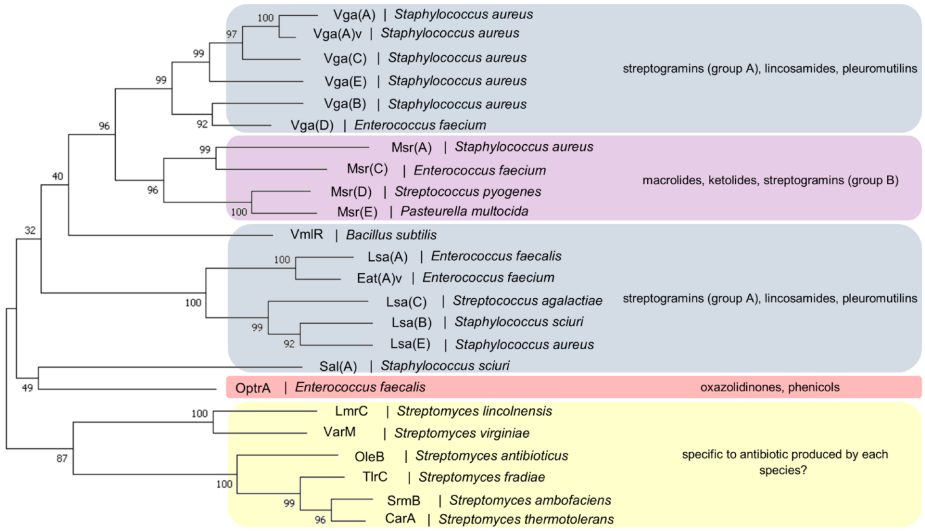

Figure 3: Phylogenetic tree of ARE-ABCF proteins, with antibiotic resistance profile indicated on the right. Modified from Sharkey and O'Neill (2018).

formation in the presence of high ADP. This led to the conclusion that EttA may act as a sensor of the ATP/ADP ratio in the cell and decrease protein synthesis under conditions of energy depletion. Consistent with this hypothesis, although EttA is not essential in *E. coli*, it supports regrowth after stationary phase (Boël et al., 2014).

A 70S–EttA-EQ$_2$ complex was analysed by cryo-EM (Chen et al., 2014). EttA binds the ribosome with dimerised NBDs positioned in the E site and the interdomain linker contacting the P-tRNA, which is in the canonical position (Chen et al., 2014). The 'Arm', an α-helical insertion in NBD1 which interacts with the L1 stalk, was required for EttA binding to the ribosome (Boël et al., 2014). The 70S–EttA-EQ$_2$ complex was in a non-rotated state (Chen et al., 2014).

A clinical *S. aureus* isolate with a defective *ettA* gene had very few differences in grown across various conditions and antibiotic susceptibility compared to an isogenic wild-type strain, implying that EttA is not essential in *S. aureus* (Meir et al., 2020). Although widespread and the best-studied bacterial ABCF, more work is required to understand the role of EttA *in vivo*, as well as the relationship between nucleotide levels and NBD conformation.

3.3.1.2 Macrolide- and streptogramin B-resistance ABCFs *MsrA*, the first ABCF ARE gene to be characterised, was isolated from a plasmid in *Staphylococcus epidermidis* and characterised as conferring resistance to both macrolides and streptogramins B (Ross et al., 1989). Homologues were subsequently described in numerous Gram-positive bacteria, particularly *Enterococcus* sp., as well as one Gram-negative genus (*Pseudomonas*) (Portillo et al., 2000; Singh et al., 2001; Werner et al., 2001; Ojo et al., 2006). MsrA confers erythromycin resistance when expressed heterologously in *Staphylococcus aureus* but not *E. coli* (Ross et al., 1990). An apparent efflux phenotype was observed using a [^{14}C]-erythromycin uptake assay, and uptake/retention was inhibited by arsenate and dinitrophenol, indicating that this effect was ATP-dependent. This observation was corroborated by a separate group using a different electron transport uncoupler (Matsuoka et al., 1999). The authors concluded that MsrA likely acts as part of a typical ABC transport system, although later noted that disruption of ribosome binding would be expected

to produce similar results in the uptake assay, because free erythromycin can diffuse out of bacterial cells (Reynolds et al., 2003). *Msr* genes are atypical among AREs in that some confer macrolide resistance when expressed heterologously in Gram-negative *E. coli* (Nunez-Samudio and Chesneau, 2013).

3.3.1.3 PLS_A-resistance ABCFs The *vga* class of ABCFs was first described in *Staphylococcus* as a virginiamycin M-resistance protein (Allignet et al., 1992). The specificity and distribution of this class was later expanded to PLS_A antibiotics and *Enterococcus* (Allignet and El Solh, 1997; Haroche et al., 2000; Kadlec and Schwarz, 2009; Lozano et al., 2012; Hauschild et al., 2012; Li et al., 2014; Chesneau et al., 2005; Novotna and Janata, 2006; Jung et al., 2010; Lenart et al., 2015). The interdomain linker is crucial for antibiotic resistance in VgaA, and mutagenesis of this region can shift antibiotic specificity among the PLS_A class (Lenart et al., 2015).

An ARE in *Listeria monocytogenes*, provisionally termed Lmo0919, is homologous to VgaA and confers resistance to streptogramin A and lincosamide when expressed heterologously in Staphylococcus (Chesneau et al., 2005). This observation was corroborated by Dar et al. (2016) as part of a genome-wide study of lincomycin-inducible transcripts.

Lsa proteins, which have been described in *Enterococcus* and *Streptococcus*, are another family of ABCF AREs that confer resistance to PLS_A antibiotics (Singh et al., 2002; Malbruny et al., 2011; Wendlandt et al., 2013). Additionally, SalA is a PLS_A resistance ABCF found in staphylococci (Hot et al., 2014; Deng et al., 2017). Finally, VmlR (formerly called ExpZ) is a chromosomal PLS_A-resistance ABCF found in *B. subtilis* (Quentin et al., 1999; Ohki et al., 2003, 2005).

PLS_A-resistance ARE-ABCFs have been shown to interact with the PTC, either inhibiting peptidyl transfer (as EQ_2 variants) or reversing antibiotic-mediated inhibition of peptidyl transfer in the presence of ATP using a puromycin release assay (Murina et al., 2018). Surprisingly, there was little preference for ATP over other NTPs in this assay (Murina et al., 2018).

3.3.1.4 Phenicol and oxazolidinone-resistance ABCFs In 2015, OptrA was reported as a novel phenicol and oxazolidinone resistance protein in *Enterococcus* in humans and livestock (Wang et al., 2015). Although the degree of resistance conferred is rather mild, this gene is particularly concerning because it confers resistance to linezolid, a drug used to treat multidrug-resistant Gram-positive pathogens such as methicillin-resistant *S. aureus* and vancomycin-resistant enterococci (FDA/Pfizer, 2010). Since 2015 dozens of reports of OptrA have been published, indicating that this element is widely dispersed, spread through plasmids and transposons (reviewed in Schwarz et al. (2021)). An additional phenicol and oxazolidinone-resistance ARE-ABCF, PoxtA, has also been reported (Antonelli et al., 2018). Similarly to OptrA, subsequent reports of PoxtA have been numerous (Schwarz et al., 2021). Unusually, poxtA was reported to confer a mild resistance to tetracycline, although this was not observed with a close homologue (Antonelli et al., 2018; Baccani et al., 2021) OptrA and PoxtA are distinguished by having short interdomain linkers in comparison to other ARE-ABCFs (Fostier et al., 2021).

3.3.1.5 ARE-like genes in antibiotic producers Several ARE-like genes have been described in antibiotic-producing *Streptomyces* sp., although compared to ARE proteins from pathogenic Firmicutes they remain poorly characterised (Murina et al., 2019).

In *Streptococcus lincolnensis*, *lmrC* is part of an operon responsible for lincomycin biogenesis and encodes an apparent ARE protein. LmrC, when expressed heterologously in *Streptococcus lividans*, confers resistance to lincomycin (Peschke et al., 1995).

Streptococcus antibioticus produces and secretes oleandomycin, a macrolide. The *OleB* gene encodes for an ABCF protein which is expressed coincidently with oleandomycin production (Olano et al., 1995). *OleB* confers oleandomycin resistance when expressed heterologously in *Streptococcus albus*, and, curiously, a construct encoding only either the N-terminal or C-terminal NBD was reported to be competent in conferring such resistance if the central linker region is intact (Olano et al., 1995).

3.3.1.6 Regulation of ARE expression In *B. subtilis* in the absence of antibiotics, transcription of the nascent *vmlR* transcript terminates prior to the main ORF. Addition of a sub-inhibitory concentration of virginiamycin M results in a long transcript containing the *vmlR* ORF, perhaps through bypassing of a ρ-independent transcription terminator (Ohki et al., 2005). Interestingly, it was later found that in cells lacking the ribosome-associated endonuclease Rae1, the *vmlR* transcript is nearly 5-fold more abundant compared to wild-type cells (Leroy et al., 2017). Overexpression of Rae1, however, does not result in decreased vmlR transcript, perhaps because of the presumed low level of full-length vmlR in the absence of antibiotics.

A genome-wide screen of premature transcriptional termination in *Listeria monocytogenes* identified short *lmo0919* transcripts, truncated prior to the main ORF. Addition of a low level of lincomycin to *L. monocytogenes* cultures caused an increase in full-length transcript, which was proposed to be mediated by ribosome stalling at an upstream tri-peptide ORF, exposing an anti-termination arm which in turn disrupts the RNA polymerase terminator hairpin. The position, although not the sequence, of the tripeptide was found to be conserved among homologous related proteins. The same study noted apparent readthrough in the transcripts of other AREs, including *vmlR* (in *B. subtilis*, with lincomycin) and *msrC* (in *E. faecalis*, by erythromycin; Dar et al. (2016)).

3.3.2 Eukaryotic ABCF proteins

A number of ABCF proteins have been reported in eukaryotes (Murina et al., 2019; Krishnan et al., 2020). Aside from a few well-studied examples, the function of most eukaryotic ABCFs remains poorly understood.

3.3.2.1 The EF3-like ABC subfamily eEF3 was first identified as an additional elongation factor required for reconstitution of protein synthesis in yeast (Skogerson and Wakatama, 1976). eEF3 is found only in fungi and some non-fungi single-celled eukaryotes and represents an early branch of the ABCF family (Mateyak et al., 2018; Murina et al., 2019). In contrast to the majority of core translation factors, eEF3 is an ATPase (Dasmahapatra and Chakraburtty, 1981; Uritani and Miyazaki, 1988). In addition to eEF3, the New1p and EF3L paralogues have been described which may be partially redundant with eEF3 (Murina et al., 2019; Kasari et al., 2019).

eEF3 is a long protein that contains HEAT repeats, a unique C-terminal domain, and a chromodomain in addition to two NBDs (Murina et al., 2019). It binds the ribosome distinctly from the prokaryotic ABCFs such as EttA, spanning the large and small ribosomal subunits through the central protuberance and the SSU head (Andersen et al., 2006; Ranjan et al., 2021). eEF3 binds stably to non-rotated ribosomes with various tRNA states, but appeared rather disordered on rotated ribosomes (Ranjan et al., 2021). The chromodomain of eEF3 can interact with the ribosomal L1 stalk, favouring an open conformation and thereby facilitating E-tRNA release, rationalising a crucial role for this protein in the yeast translation elongation cycle (Andersen et al., 2006; Ranjan et al., 2021).

3.3.2.2 ABCF1 ABCF1 (also known as ABC50) is an ABCF protein found in mammals which is conserved among vertebrates. ABCF1 co-purifies with eIF2α from human cell lines and rabbit reticulocyte lysate, an interaction that is stable at high salt but sensitive to detergent (Tyzack et al., 2000). Binding of methionyl-tRNA to eIF2α is significantly greater in complexes with ABCF1. ABCF1 sediments at 40S or 60S depending on the presence of ADP or ATP in the sample; sedimentation in the presence of non-hydrolysable ATP analogues was not determined (Tyzack et al., 2000). ABCF1 is a crucial factor in cryptic cap- and IRES-independent translation initiation that is dependent upon m^6A in the 5′ UTR (Coots et al., 2017). It remains unknown whether ABCF1 interacts with the ribosome analogously to other ABCF proteins.

3.3.2.3 Arb1 Arb1, also known as ABCF2, is an ABCF that has been proposed to function at multiple steps in ribosome biogenesis in yeast (Dong et al., 2005). It is closely related to Gcn20 and is found in most eukaryotes but has a patchy distribution among bacteria (Krishnan et al., 2020).

In the course of the termination stage of ribosome-associated quality control, Su et al. (2019) used an *ex vivo* immunoprecipitation of tagged Vms1, a release factor homologue, to prepare complexes for analysis by cryo-EM. The resulting reconstruction consisted of a 60S LSU with peptidyl-tRNA and Vms1, as well as a sub-class that unexpectedly contained Arb1. Arb1 was bound in the E site of the LSU, broadly analogously to EttA but with the NBDs in an open conformation and the interdomain linker contacting the peptidyl-tRNA. Arb1 enhanced release activity of Vms1 (Su et al., 2019).

3.3.2.4 Gcn20 In vertebrates there are four kinases that phosphorylate eIF2α in response to a wide range of known stresses (Taniuchi et al., 2016). One such kinase, General control nonderepressible 2 (Gcn2), is activated by uncharged tRNA and thus senses amino acid depletion. Several binding partners of Gcn2 have been described in yeast, among them the Gcn1–Gcn20 complex (Vazquez de Aldana et al., 1995). Gcn20 is an ABCF protein, consisting of an N-terminal domain and two C-terminal ABCs, which cosediments with polysomes. The ABCs of Gcn20 are required for ribosome association but are dispensable for Gcn2 stimulation upon amino acid starvation, while the N-terminal domain is required for complex formation with Gcn1 and Gcn2 stimulation but not ribosome association (Marton et al., 1997). These results imply that binding of Gcn20 to the ribosome is dispensable for stimulation of Gcn2 activity upon amino acid starvation. Interestingly, a portion of Gcn1 contains HEAT repeats, so that the Gcn1–Gcn20 complex partially recapitulates the domain structure of EF3, albeit without the chromodomain insertion. It has been suggested that Gcn2, perhaps in concert with the Gcn1–Gcn20 complex, acts analogously to the bacterial RelA which senses deacylated tRNA bound to the ribosome to activate the stringent response (Castilho et al., 2014). Gcn20 appeared to bind at the interface between stalled ribosomes in an *in vivo* pullout; however, the density was not sufficient to build a molecular model of Gcn20 in this complex (Pochopien et al., 2021). Thus, despite the paralogous relationship between Arb1 and Gcn20, these proteins bind to different positions on the ribosome (Krishnan et al., 2020; Su et al., 2019; Pochopien et al., 2021).

3.3.3 ABCE1

ABCE1 (Rli1 in yeast) is a human protein belonging to ABC subfamily E, which is highly conserved in eukaryotes and archaea. It contains two N-terminal FeS clusters and, like ABCF proteins, two tandem ABCs (Kerr, 2004; Barthelme et al., 2007). ABCE1/Rli1 is a recycling factor which causes dissociation of ribosomal subunits after translation termination, when the class-I

release factor is still bound to the ribosome (Pisarev et al., 2010; Barthelme et al., 2011; Shoemaker and Green, 2011). Additionally, this protein functions subsequent to ribosome-associated quality control mediated by Hbs1/Pelota (Pisareva et al., 2011).

On the 80S ribosome, ABCE1/Rli1 binds in the GTPase factor site, with the FeS cluster contacting the release factor (Becker et al., 2012; Preis et al., 2014; Brown et al., 2015). The two ATP-binding sites (labelled according the NBD housing the Walker motifs of each site) have different dynamics and can cycle through three states: open, intermediate, and closed (Karcher et al., 2008; Barthelme et al., 2011; Becker et al., 2012; Heuer et al., 2017; Nürenberg-Goloub et al., 2018; Gouridis et al., 2019; Nürenberg-Goloub et al., 2020). Broadly, in the 80S pre-splitting state, the ABCE1 NBDs adopt an intermediate conformation, which proceeds to a closed conformation in the post-splitting state (when ABCE1 remains bound to the SSU; Becker et al. (2012); Heuer et al. (2017)). This transition is concomitant with a large rearrangement of the FeS domain, which moves from a cleft formed by the two NBDs into the intersubunit space and which is likely to directly cause splitting (Heuer et al., 2017; Nürenberg-Goloub et al., 2020). Site II must be closed to allow formation of the pre-splitting complex, and this allosterically activates the ATPase activity of site I which in turn drives rearrangements necessary for splitting (Nürenberg-Goloub et al., 2018). ATP hydrolysis in site II is necessary for release of ABCE1 from the 40S SSU (Gouridis et al., 2019; Kratzat et al., 2021).

After splitting, ABCE1 remains bound to the 40S SSU, remaining bound to 43S pre-initiation and 48S initiation complexes with ADP bound in site I and ATP in site II (Kratzat et al., 2021). Interestingly, in the context of initiation, the N-terminus of eIF3j extends across the SSU into the cleft formed between the NBDs of ABCE1 in the post-splitting state (Kratzat et al., 2021). Although absent in bacteria, ABCE1 represents the best-characterised translation-associated ABC ATPase.

3.4 Summary

Bacterial translation has been the object of intensive study for more than six decades, with many details of ribosome structure and function elucidated, mostly through work in the model organism *E. coli*. Although the initiation, elongation, and termination and recycling stages of bacterial translation are generally well-characterised, our understanding of the cellular response to perturbed translational events remains lacking. For example, only recently have the ARE-ABCF proteins conclusively been demonstrated to act directly on the ribosome (Sharkey et al., 2016). Additionally, our understanding of the bacterial response to stalled translation products has been dominated by the tmRNA system, but more alternative rescue factors continue to be discovered (Goralski et al., 2018; Shimokawa-Chiba et al., 2019). Indeed, only recently was an equivalent of the eukaryotic RQC system shown to operate in bacteria (Lytvynenko et al., 2019).

4 Aims

The work presented in this dissertation had two major goals:

1. Understand how ARE-ABCF proteins cause antibiotic dissociation from the ribosome. In particular, how these proteins presumably access the PTC while the P-tRNA would act as a barrier was to be addressed.

2. Understand the alanine tailing reaction mediated by RqcH. As relatively little is known about this process, the work began without particular hypotheses to test but rather the broad goal of learning more about the alanine tailing process, in which protein synthesis occurs in the absence of mRNA or the SSU.

5 Results

Summary of presented manuscripts

Five manuscripts are presented in this section, each describing at least one molecular structure determined by single-particle cryo-EM. The first three examine ARE-ABCFs, and the final two examine RqcH. A brief description of the structure(s) presented in each manuscript is listed below.

1. The ARE-ABCF VmlR in complex with 70S–P-tRNA. Additionally, the structure of the *B. subtilis* 70S–P-tRNA complex.
2. Three ARE-ABCFs LsaA, VgaA_{LC}, and VgaL, in complex with 70S–P-tRNA. Each ribosome comes from a difference species of Gram-positive bacteria. Additionally, the *S. aureus* 70S–P-tRNA complex.
3. The ARE-ABCF PoxtA in complex with 70S–P-tRNA. Additionally, the *E. faecalis* 70S–P-tRNA complex.
4. RqcH in complex with LSU–P-tRNA. Many sub-states, some containing additional protein factors, were observed, as described below.
5. The RqcH^{DR} variant in complex with LSU–P-tRNA.

Summary of contributions

Each manuscript was created in collaboration with other laboratories. For the first manuscript, I performed laboratory work to help prepare the complex for analysis, while for the other manuscripts my contribution was mostly processing and interpretation of the cryo-EM data and assembly of the manuscript. A detailed breakdown of my contributions is provided below for each manuscript.

5.1 Structure of the VmlR ABCF protein in complex with the 70S ribosome

5.1.1 Summary

This manuscript describes the structure of VmlR in complex with the *B. subtilis* 70S ribosome and a distorted P-site tRNA. The globular domains of VmlR are positioned in the ribosomal E-site, while the helical interdomain linker extends towards the ribosomal PTC. The P-tRNA has a highly distorted acceptor stem, particularly the CCA 3′ end. One phenylalanine of VmlR overlaps with the binding site of relevant antibiotics. Surprisingly, mutagenesis of this phenylalanine to alanine, which is predicted to not overlap with the antibiotic binding site, had only a minor effect on the antibiotic resistance profile of VmlR. An alternative model of antibiotic resistance, involving modulation of the rRNA to perturb the antibiotic binding site, is presented.

5.1.2 Contributions

Purification of VmlR for sample preparation, processing of the cryo-EM data, creation of the molecular models, and generation of the figures. Data for Fig. 4E came from our collaborators Prof. V. Hauryliuk and Dr G. Atkinson (Umeå University). Writing of the manuscript with help from Prof. Daniel N. Wilson.

Structural basis for antibiotic resistance mediated by the *Bacillus subtilis* ABCF ATPase VmlR

Caillan Crowe-McAuliffe[a], Michael Graf[a], Paul Huter[a], Hiraku Takada[b,c], Maha Abdelshahid[a], Jiří Nováček[d], Victoriia Murina[b], Gemma C. Atkinson[b], Vasili Hauryliuk (Василий Гаврилюк)[b,c,e], and Daniel N. Wilson[a,1]

[a]Institute for Biochemistry and Molecular Biology, University of Hamburg, 20146 Hamburg, Germany; [b]Department of Molecular Biology, Umeå University, 90187 Umeå, Sweden; [c]Laboratory for Molecular Infection Medicine Sweden, Umeå University, 90187 Umeå, Sweden; [d]Central European Institute of Technology, Masaryk University, 62500 Brno, Czech Republic; and [e]Institute of Technology, University of Tartu, 50411 Tartu, Estonia

Edited by Peter B. Moore, Yale University, New Haven, CT, and approved July 23, 2018 (received for review May 17, 2018)

Many Gram-positive pathogenic bacteria employ ribosomal protection proteins (RPPs) to confer resistance to clinically important antibiotics. In *Bacillus subtilis*, the RPP VmlR confers resistance to lincomycin (Lnc) and the streptogramin A (S_A) antibiotic virginiamycin M (VgM). VmlR is an ATP-binding cassette (ABC) protein of the F type, which, like other antibiotic resistance (ARE) ABCF proteins, is thought to bind to antibiotic-stalled ribosomes and promote dissociation of the drug from its binding site. To investigate the molecular mechanism by which VmlR confers antibiotic resistance, we have determined a cryo-electron microscopy (cryo-EM) structure of an ATPase-deficient *B. subtilis* VmlR-EQ_2 mutant in complex with a *B. subtilis* ErmDL-stalled ribosomal complex (SRC). The structure reveals that VmlR binds within the E site of the ribosome, with the antibiotic resistance domain (ARD) reaching into the peptidyltransferase center (PTC) of the ribosome and a C-terminal extension (CTE) making contact with the small subunit (SSU). To access the PTC, VmlR induces a conformational change in the P-site tRNA, shifting the acceptor arm out of the PTC and relocating the CCA end of the P-site tRNA toward the A site. Together with microbiological analyses, our study indicates that VmlR allosterically dissociates the drug from its ribosomal binding site and exhibits specificity to dislodge VgM, Lnc, and the pleuromutilin tiamulin (Tia), but not chloramphenicol (Cam), linezolid (Lnz), nor the macrolide erythromycin (Ery).

ABC ATPase | cryo-EM | ribosome | antibiotic resistance | VmlR

The ribosome is one of the major targets in the cell for antibiotics, including many clinically important antibiotic classes, for example the streptogramins, lincosamides, pleuromutilins, and macrolides (reviewed in refs. 1 and 2). However, the ever-increasing emergence of multidrug resistant bacteria is rendering our current antibiotic arsenal obsolete. Therefore, it is important to understand the mechanisms that bacteria employ to obtain antibiotic resistance to develop improved antimicrobial agents to overcome these mechanisms. Two important antibiotic resistance strategies employed by bacteria include antibiotic efflux and ribosome protection, both of which can be mediated by members of the large family of ATP-binding cassette (ABC) proteins. ABC proteins involved in drug efflux include membrane-bound transporters that use energy to pump the antibiotic out of the cell. By contrast, ABC proteins of the subclass F (ABCF) do not contain transmembrane domains to anchor them to the membrane and instead confer resistance by binding to the ribosome and chasing the antibiotic from its binding site (reviewed in ref. 3).

Antibiotic resistance (ARE) ABCF proteins are widespread in Gram-positive bacteria but also found in some Gram-negative bacteria (3, 4). ARE-ABCF proteins can be chromosomally and/or plasmid-encoded and are found in many clinically relevant pathogenic bacteria, including *Staphylococcus aureus*, *Enterococcus faecalis*, *Listeria monocytogenes*, and *Escherichia coli* (3, 4). To date, all ARE-ABCF proteins confer resistance to antibiotics that bind to the large ribosomal subunit (LSU), either at the peptidyl-transferase center (PTC) or adjacent to the PTC in the ribosomal exit tunnel. ARE-ABCF proteins can be divided into distinct classes on the basis of their resistance profiles (3, 4). For example, the Vga/Lsa/Sal/Vml class confers resistance to streptogramin A (S_A) antibiotics, lincosamides, and sometimes pleuromutilins, whereas the Msr class confers resistance to streptogramin B (S_B) antibiotics, macrolides, and sometimes ketolides. In *Enterococci*, the ARE-ABCF OptrA has been reported to confer resistance to oxazolidinones and chloramphenicols (5). Several studies have demonstrated that ARE-ABCFs are RPPs that confer resistance by displacing the drug from its binding site on the ribosome (6, 7), analogous to the displacement of tetracycline from the ribosome mediated by the RPPs TetM/TetO (8).

ARE-ABCF proteins comprise two ABC nucleotide-binding domains (NBD1 and NBD2) that are separated by a helical linker and, depending on the species, may have an additional "Arm" subdomain inserted within NBD1 as well as a C-terminal extension (CTE) (4). The ATPase activity of ARE-ABCF proteins is essential for their function since mutations of the catalytic glutamate in NBD1 or NBD2 lead to a loss of the ability of VgaA to confer resistance to VgM (6, 9). Consistently, the inhibition of ribosomal transpeptidation (transfer of fMet from the P-site tRNA to puromycin) that results from the presence of Lnc

Significance

The recent increase in multidrug-resistant pathogenic bacteria is limiting the utility of our current arsenal of clinically important antibiotics. The development of improved antibiotics would therefore benefit from a better understanding of the current resistance mechanisms employed by bacteria. Many Gram-positive bacteria, including pathogenic *Staphylococcus aureus* and *Enterococcus faecalis*, utilize ribosome protection proteins to confer resistance to medically relevant antibiotics, such as streptogramins A, lincosamides, and pleuromutilins. We have employed cryo-electron microscopy to reveal the structural basis for how the *Bacillus subtilis* VmlR protein binds to the ribosome to confer resistance to the streptogramin A antibiotic virginiamycin M, the lincosamide lincomycin, and the pleuromutilin tiamulin.

Author contributions: G.C.A., V.H., and D.N.W. designed research; C.C.-M., H.T., J.N., and G.C.A. performed research; M.A. and V.M. contributed new reagents/analytic tools; C.C.-M., M.G., P.H., H.T., V.H., and D.N.W. analyzed data; and C.C.-M. and D.N.W. wrote the paper.

The authors declare no conflict of interest.

This article is a PNAS Direct Submission.

Data deposition: The atomic coordinates have been deposited in the Protein Data Bank, www.wwpdb.org (PDB ID codes 6HA1 and 6HA8). The cryo-EM maps have been deposited in the Electron Microscopy Data Bank (EMDB ID codes EMD-0176 and EMD-0177).

[1]To whom correspondence should be addressed. Email: daniel.wilson@chemie.uni-hamburg.de.

This article contains supporting information online at www.pnas.org/lookup/suppl/doi:10.1073/pnas.1808535115/-/DCSupplemental.

Published online August 20, 2018.

is relieved by VgaA, but not the catalytically inactive VgaA-EQ_2 mutant (4). Similarly, transpeptidation was restored by VgaA in the presence of ATP, but not ADP or nonhydrolysable ATP analogs (4).

ARE-ABCFs are closely related to energy-dependent translational throttle A (EttA), an ABCF protein that binds within the ribosomal E site to regulate translation in response to energy levels in the cell (10, 11). A recent cryo-electron microscopy (cryo-EM) structure of the *Pseudomonas aeruginosa* ARE-ABCF MsrE bound to the *Thermus thermophilus* 70S ribosome revealed that MsrE, like EttA, binds in the E site and has an extended interdomain linker that reaches toward the PTC of the ribosome (7). Large variations in sequence and length are observed within the interdomain linker between different classes of ARE-ABCFs (*SI Appendix*, Fig. S1), and mutations within a loop at the tip of the interdomain linker can alter the antibiotic specificity of the ARE-ABCF proteins (6, 7, 12, 13). Furthermore, VgaA variants where the interdomain linker is truncated cannot restore the ribosomal transpeptidation in the presence of lincomycin (4). While the MsrE-70S structure provides insight into how the Msr class confers resistance to macrolide antibiotics (7), structural insight into how the Vga/Lsa/Sal/Vml class confers resistance to PTC-targeting antibiotics has been lacking.

Here, we have determined a cryo-EM structure of *Bacillus subtilis* VmlR bound to a stalled ribosome complex (SRC) at 3.5-Å resolution, revealing that VmlR, like EttA and MsrE, binds within the E site of the ribosome. The interdomain linker of VmlR accesses the PTC of the ribosome by inducing a noncanonical conformation of the P-site tRNA where the acceptor arm is disengaged from the PTC and the CCA end is shifted toward the A site. While the interdomain linker of VmlR directly encroaches the binding site of PTC-targeting antibiotics, we observe specificity in the VmlR resistance profile, such that VmlR confers resistance to VgM, Lnc, and Tia, but not to Cam, Lnz, or Ery. We also identify a VmlR-F237A variant that exhibits altered specificity, conferring resistance to Lnc and Tia, but not to VgM. Our combined structural and mutagenesis analyses suggest that VmlR dislodges VgM, Lnc, and Tia using an indirect allosteric, rather than a direct steric, mechanism of action.

Results

Generation of a *B. subtilis* VmlR–70S Ribosome Complex. Initially, we in vitro-reconstituted complexes between wild-type VmlR (previously called ExpZ) and tight-coupled *B. subtilis* 70S ribosomes in the presence of the nonhydrolysable ATP analog ADPNP. Despite observing binding in pelleting assays, no density for VmlR was observed in low-resolution cryo-EM reconstructions, suggesting that the VmlR–ribosome interaction was not stable. A previous study employed an ATPase-deficient form of EttA (EttA-EQ_2) to trap and visualize the factor in the ATP form on the ribosome using cryo-EM (11). Therefore, we generated an equivalent ATPase-deficient VmlR-EQ_2 variant where Glu129 in NBD1 and Glu432 in NBD2 were mutated to Gln129 and Gln432, respectively. A low-resolution cryo-EM reconstruction of the VmlR–EQ_2–70S complex revealed density for VmlR in the E site of the 70S ribosomes bearing a tRNA in the P site. Unfortunately, this represented a small percentage of the population, as the P-site tRNAs were only present as contaminants that remained bound to the tight-coupled ribosomes despite the purification process. To increase the ribosomal occupancy of the P-site tRNAs, and thus promote binding of VmlR, we replaced 70S ribosomes with stalled ribosome complexes (SRCs), as used previously to visualize RelA (14) and TetM (15) on the ribosome. To generate the SRCs, translation of an ErmDL stalling peptide in the presence of the ketolide telithromycin was carried out, leading to ribosomes stalled with a short seven-amino acid peptidyl-tRNA decoding the seventh codon of the mRNA (16). In contrast to our previous studies, we performed translation in the *E. coli* PURE system using *B. subtilis* rather than *E. coli* 70S ribosomes (17), thus enabling a homogeneous *B. subtilis* VmlR-EQ_2-SRC to be generated. Since VmlR does not confer resistance to the macrolide class of antibiotics (18), we rationalized that using the ErmDL-SRC may also contribute to trapping VmlR on the ribosome. We did not attempt to generate Lnc or VgM SRCs as substrates for VmlR binding, since our past experience in forming TetM-SRC revealed that the presence of the drug (in this case, tetracycline) only generated additional sample heterogeneity due to competition for binding between TetM and tetracycline (19).

Cryo-EM Structure of a *B. subtilis* VmlR-EQ_2-SRC. Cryo-EM data for the *B. subtilis* VmlR-EQ_2-SRC was collected on a Titan Krios transmission electron microscope (TEM) with a Falcon III direct electron detector (DED) and processed with RELION 2.1 (20). After 2D classification, a total of 159,722 ribosomal particles were sorted into two major populations, both of which contained a P-site tRNA but differed with respect to the presence (18–21%, 28,972–33,392) or absence (43%, 68,652 particles) of VmlR-EQ_2 (Fig. 1 and *SI Appendix*, Fig. S2*A*). The cryo-EM maps of the VmlR-EQ_2-SRC (Fig. 1*A*) and P-tRNA-SRC could be refined to yield final average resolutions of 3.5 Å and 3.1 Å, respectively (*SI Appendix*, Fig. S2 *B–D*). Molecular models for the *B. subtilis* 70S ribosome were based on a previous model of a *B. subtilis* MifM-SRC (21), which could be improved to include side chains for the proteins of the SSU due to the better resolution (*SI Appendix*, Table S1). The VmlR model was initially based on a homology model generated using the crystal structure of EttA (10) as a template (Fig. 1*B*). The density for the C-terminal extension (CTE) that is absent in EttA and MsrE was modeled as two α-helices connected by a short linker to the NBD2 (Fig. 1*B*), which is consistent with secondary structure predictions; however, the quality of the density map only permitted the backbone to be traced. By contrast, the interdomain linker between NBD1 and NBD2, which we refer to as the antibiotic resistance domain (ARD), was well-resolved and could be modeled de novo (*SI Appendix*, Fig. S2*E*), presumably because the ARD is sandwiched between the 23S rRNA of the LSU and the acceptor arm of the P-site tRNA (Fig. 1*A*). Clear density was observed for two molecules of ATP bound within the active sites formed by NBD1 and NBD2 (Fig. 1*C*), in agreement with the ability of the VmlR-EQ_2 to bind, but not hydrolyze, ATP. Consistently, previous studies have shown that EQ mutations in either NBD lead to a loss in the ability of VgaA to confer resistance to VgM (9). NBD1 and NBD2 of VmlR-EQ_2 adopt a closed conformation on the ribosome, similar to that observed for the ABC multidrug resistance protein 1 (MRP1) (22) as well as the modeled ATP conformation of EttA (10, 11), but distinct from the open conformation observed for the free state of ABCE1 (23) (*SI Appendix*, Fig. S3 *A–C*).

Binding Site of VmlR on the 70S Ribosome. VmlR binds within the E site of the 70S ribosome (Fig. 1*A*), analogously to EttA (11) (*SI Appendix*, Fig. S3 *D–F*). The NBD1 of VmlR directly contacts and stabilizes an open conformation of the L1 stalk (Fig. 2*A*), which is similar but distinct from that observed in the presence of EttA due to the EttA "Arm" being absent in VmlR (*SI Appendix*, Fig. S2 *D–F*). NBD1 of VmlR also establishes interactions with H68 of the 23S rRNA as well as ribosomal protein bL33 (Fig. 2 *A* and *B*). The ARD, linking NBD1 and NBD2, comprises two long α-helices that span from the E site across the interface of the LSU inserting the ARD loop into the PTC (Fig. 2 *A* and *B*). Helix α2 of the ARD runs parallel to H74-H75 and forms multiple contacts with the backbone of nucleotides within these helices, whereas helix α1 interacts predominantly with the acceptor arm of the P-site tRNA (Fig. 2*A*). The elbow region of the P-site tRNA is contacted by NBD2, which establishes additional interactions with ribosomal protein uL5 of the LSU (Fig. 2 *A* and *B*) and h41-42 of the 16S rRNA located within the head of the SSU (Fig. 2*C*). The CTE of VmlR, which has no equivalent in EttA, extends from NBD2 where a short linker guides the CTE between a cleft created by ribosomal proteins uS7 and uS11 on the SSU head and positions the two CTE α-helices into the

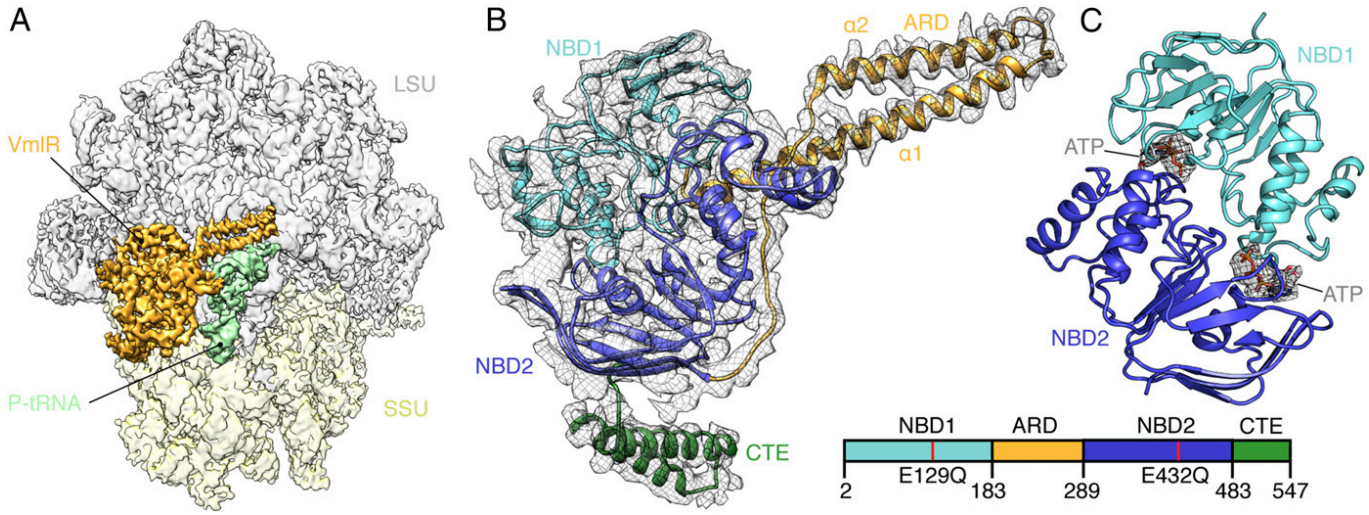

Fig. 1. Structure of VmlR–ribosome complex. (*A*) Cryo-EM map with isolated densities for VmlR (orange), P/V-tRNA (pale green), small subunit (SSU, yellow), and large subunit (LSU, gray). (*B*) Electron density (gray mesh) with molecular model for VmlR, colored according to domains as represented in the schematic (*Bottom Right*): nucleotide binding domain 1 (NBD1, cyan), antibiotic-resistance domain (ARD, orange), nucleotide binding domain 2 (NBD2, blue), and C-terminal extension (CTE, green). (*C*) Molecular model for NBD1 (cyan) and NBD2 (blue) of VmlR with isolated electron density (gray mesh) for the modeled ATP nucleotides (sticks).

Shine–Dalgarno (SD)–anti-SD cavity located on the SSU platform (Fig. 2*C*). This interaction is likely to be important for VmlR function since a VmlR variant lacking the CTE loses its ability to confer antibiotic resistance (*SI Appendix*, Fig. S4 *A–D*), as observed previously for VgaA (9).

VmlR Stabilizes a Noncanonical P/V-tRNA Conformation. Binding of VmlR to the ribosome and accommodation of the ARD at the PTC of the LSU requires the P-site tRNA to be displaced from its canonical position and adopt a noncanonical state, which we term the P/V-tRNA (Fig. 3*A*). The ARD of VmlR is 27 amino acids longer than the equivalent region in EttA (Fig. 3 *A–C*), explaining why binding of EttA does not affect the conformation of the P-site tRNA, nor encroach on the PTC (Fig. 3*B*). Compared with the canonical P-site tRNA position, the elbow region of the P/V-tRNA is shifted by ∼10 Å away from the PTC toward the E site and is likely to be stabilized via interactions with the NBD2 of VmlR (Fig. 3*C*). As a consequence, the CCA end of the P/V-tRNA is redirected by 37 Å into the A site, where it overlaps with the binding site of the acceptor arm of a canonical A-site tRNA, but not with an A/T-tRNA state (Fig. 3*D*). This suggests that the VmlR-stabilized P/V-tRNA would allow delivery of aminoacyl-tRNA to the ribosome by EF-Tu but prevent the subsequent accommodation at the A site of the PTC. It should be noted that the density for the CCA end of the P/V-tRNA was poorly resolved and the nascent chain was not observed (*SI Appendix*, Fig. S5*A*), indicative of high flexibility and consistent with local resolution calculations (*SI Appendix*, Fig. S5*B*). Although we cannot exclude that the nascent chain was hydrolyzed by VmlR, we do not believe this is likely since the

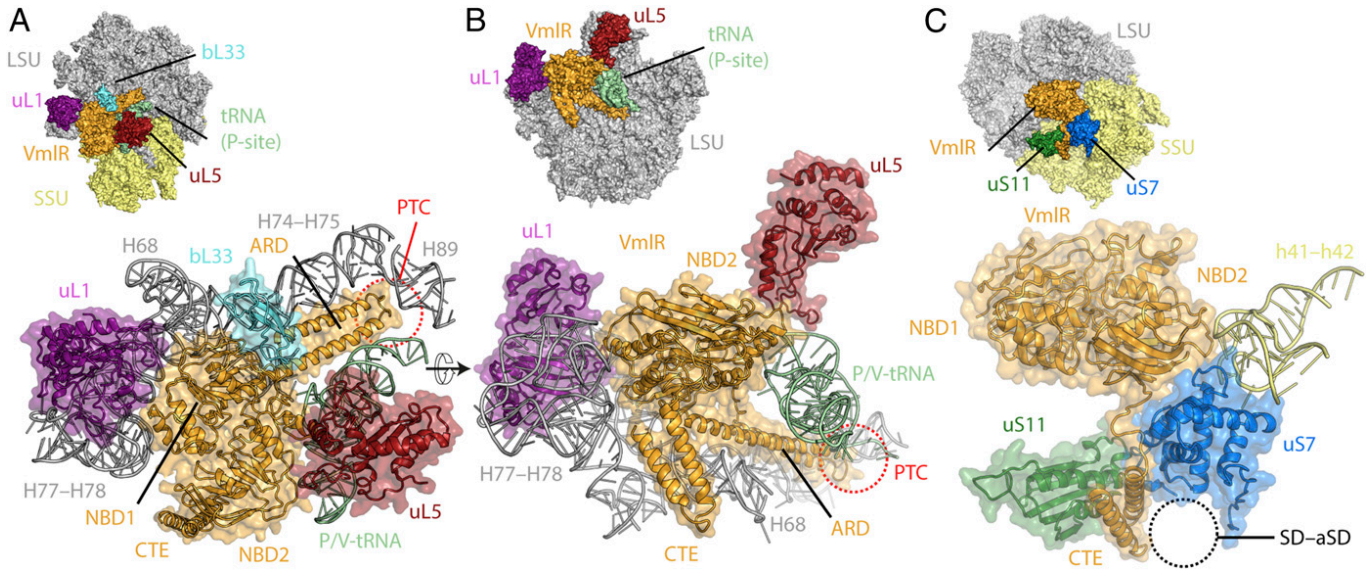

Fig. 2. Interaction of VmlR with the ribosome. (*A–C*) *Inset* and zoom showing VmlR (orange) interaction P/V-tRNA (green) and components of the large subunit (LSU, gray); 23S rRNA helices H68, H74-H75; and H89 (gray) and ribosomal proteins uL1 (magenta), uL5 (red), and bL33 (cyan) (*A* and *B*) and components of the small subunit (SSU, yellow), including 16S rRNA helices h41-42 and ribosomal proteins uS7 (blue) and uS11 (green) (*C*).

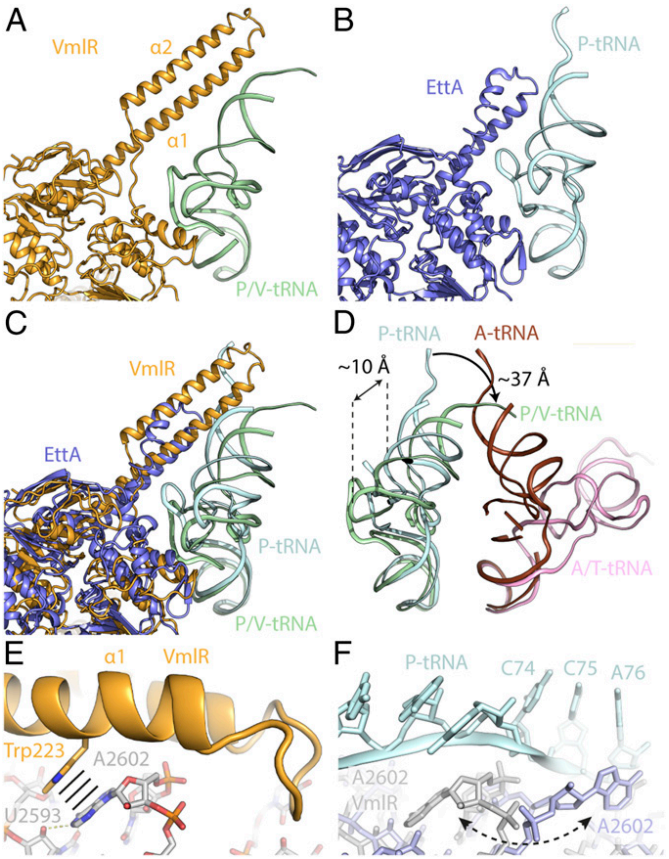

Fig. 3. Comparison of VmlR and EttA on the ribosome. (*A–C*) Relative position of VmlR (orange) and P/V-tRNA (green) (*A*), EttA (blue, PDB ID code 3J5S) (11) and P-tRNA (cyan) (*B*), and superimposition of *A* and *B* (*C*). (*D*) Comparison of P/V-tRNA (green), P-tRNA (cyan), A-tRNA (brown) (39), and A/T-tRNA (pink, PDB ID code 4V5G) (40). (*E*) Stacking interaction (indicated by black lines) of Trp223 of VmlR (orange) with 23S rRNA nucleotide A2602 (gray), which forms hydrogen bonds (dashed lines) with U2593. (*F*) Conformation of VmlR bound conformation of A2602 (gray) compared with the A2602 (slate) conformation in the pretranslocation state conformation (39) with P-tRNA (cyan) and A-tRNA (data not shown).

related VgaA has no detectable peptidyl-tRNA hydrolysis activity (4).

By contrast, the canonical P-site tRNA was well-resolved in the cryo-EM map of the P-tRNA-SRC and the nascent chain could be visualized extending down the ribosomal tunnel toward the telithromycin-binding site (*SI Appendix*, Fig. S5 *E* and *F*). Therefore, binding of VmlR to the ribosome can disengage the P-site tRNA from the PTC despite the presence of the oligopeptidyl-tRNA. Compared with the P-tRNA-SRC, binding of VmlR induces a 3.4° rotation of the SSU body and 4.1° swivel of the SSU head (*SI Appendix*, Fig. S5 *G* and *H*), which may also contribute to destabilizing the P-site tRNA. Displacement of the P-site tRNA from the PTC by the ARD of VmlR leads to a rearrangement in 23S rRNA nucleotide A2602 (*E. coli* numbering is used for rRNA nucleotides) (Fig. 3 *E* and *F*). In the VmlR-SRC, the nucleobase of A2602 stacks upon Trp223 within helix α1 of the ARD of VmlR and forms potential hydrogen bond interactions with U2593 (Fig. 3*E*). By contrast, the VmlR position of A2602 is flipped by 180° compared with the canonical A2602 that interacts with the CCA end of the P-site tRNA (Fig. 3*F*). Therefore, in addition to stabilizing VmlR on the ribosome, flipping of A2602 may also be necessary to clear the way for the transition from the P to the P/V-tRNA state.

VmlR and Resistance to PTC-Targeting Antibiotics. At the PTC, the binding position of helix α1 of the ARD of VmlR overlaps that of the CCA end of a P-site tRNA, whereas the ARD loop and specifically Phe237 extends into the A-site pocket where the aminoacyl moiety of the A-site tRNA normally resides (Fig. 4 *A* and *B*). The A-site pocket is also the binding site of PTC-targeting antibiotics, such as VgM, Lnc, Tia, Cam, and Lnz, whereas S_B antibiotics, such as VgS, and macrolides, such as Ery, bind deeper within the ribosomal tunnel (Fig. 4 *B–D*). While VmlR has been shown to confer resistance to VgM and Lnc, but not to VgS or the macrolides Ery, oleandomycin, and spiramycin (18), the effect on other PTC-targeting antibiotics remains unknown. To test this, we monitored growth of a wild-type (WT) *B. subtilis* strain containing VmlR as well as a *B. subtilis* strain where the *vmlR* gene was inactivated (Δ*vmlR*), in the presence of increasing concentrations of the relevant antibiotics. Growth was also monitored for a Δ*vmlR* strain that was complemented by inserting the *vmlR* gene into the *thrC* locus under the control of an IPTG-inducible promoter. In agreement with previous findings (18), VmlR conferred resistance to VgM and Lnc, but not to Ery (Fig. 4*E* and *SI Appendix*, Fig. S4 *A–C*). In addition, we could also demonstrate that VmlR conferred resistance to Tia, as expected based on the steric overlap between Phe237 of VmlR and the drug, but surprisingly not to Cam or Lnz, which also sterically overlap with VmlR (Fig. 4*E* and *SI Appendix*, Fig. S4 *C–E*).

This observation, coupled with the incomplete conservation of Phe237 (*SI Appendix*, Fig. S1), led us to generate VmlR variants where Phe237 was mutated to Ala (VmlR-F237A) or Val (VmlR-F237V). Growth experiments revealed that the VmlR-F237V retained a WT-like activity profile, conferring resistance to VgM, Lnc, and Tia, but not Ery, Cam, and Lnz (Fig. 4*E* and *SI Appendix*, Fig. S6). By contrast, the VmlR-F237A variant displayed altered specificity, conferring resistance to Lnc and Tia, but not to VgM (Fig. 4*E* and *SI Appendix*, Fig. S6). The retention of resistance activity of the VmlR-F237V variant suggested that VmlR does not employ direct steric interference to dislodge the drug from the binding site at the PTC, but rather an indirect allosteric mechanism. This prompted us to analyze whether the binding of VmlR induced any specific conformational changes within PTC nucleotides that could mediate dissociation of antibiotics from the ribosome. Comparing the PTC conformation in the VmlR-SRC with structures of ribosomes bound with VgM (24), Lnc (25), and Tia (26) revealed the most significant difference for U2585, which is stacked upon by Tyr240 of VmlR, thereby preventing other conformations being adopted that interact with the drugs (Fig. 4 *F–H* and *SI Appendix*, Fig. S7 *F–I*). In addition, shifted conformations were also observed for U2506 and A2062 that may be influenced indirectly by VmlR binding (Fig. 4 *F–H* and *SI Appendix*, Fig. S7 *F–K*).

Discussion

Together with the available literature and the insights gained from the VmlR-EQ_2-SRC structure, we present a model for the mechanism of action of VmlR (Fig. 5) and discuss how it relates to other ARE-ABCF proteins. First, our structure revealed that VmlR recognizes and binds to antibiotic-stalled ribosomes with vacant E sites (Fig. 5 *A* and *B*). We envisage two main scenarios when this can occur during translation, namely, directly following initiation when the E site is free and only an initiator fMet-tRNA is bound in the P site, or subsequent to E-tRNA release from a posttranslocation state during elongation (27). Although a pretranslocational state also has a free E site, we do not believe this is a substrate for VmlR since the relevant PTC-targeting antibiotics prevent A-site tRNA binding and, thereby, block the pretranslocation state from forming. The VmlR-EQ_2-SRC structure suggests that VmlR binds to antibiotic-stalled ribosomes in the ATP conformation with the NBDs adopting a closed conformation (Fig. 5*B*). Binding of VmlR, which is facilitated by important CTE–30S interactions, induces a slight rotation of the SSU relative to the LSU and disengages the P-site tRNA from the PTC, leading to stabilization of a noncanonical P/V-tRNA state (Fig. 5*B*). The VmlR-EQ_2-SRC structure

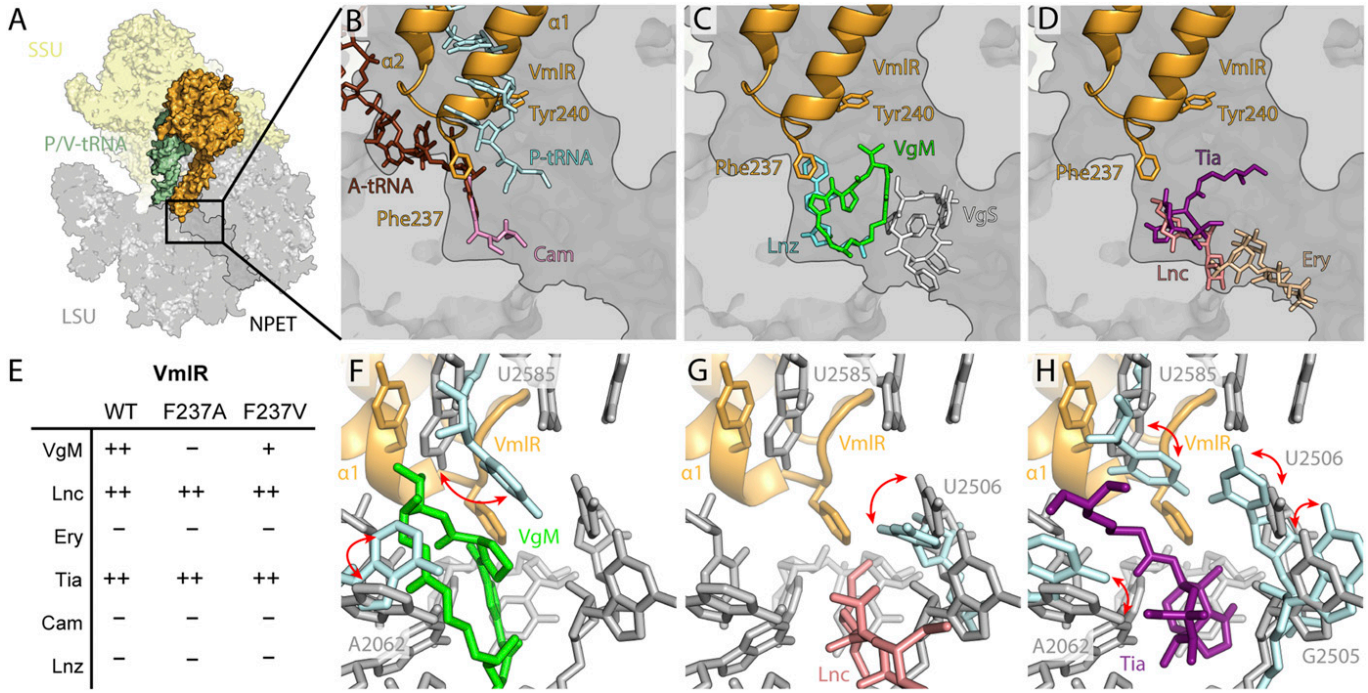

Fig. 4. Interaction of VmlR at the peptidyltransferase center. Overview of VmlR (orange) and P/V-tRNA (green) on the ribosome (SSU, yellow; LSU, gray) (*A*) with transverse section of the LSU to reveal the nascent polypeptide exit tunnel (NPET) with VmlR (orange) superimposed (*B–D*) against A-site tRNA (brown) and P-site tRNA (cyan) from a pretranslocation state (39) and chloramphenicol (Cam, pink, PDB ID code 4V7U) (41) (*B*); virginiamycin M (VgM, green) and S (VgS, white) (PDB ID code 1YIT) (24) and linezolid (Lnz, cyan, PDB ID code 3DLL) (42) (*C*); lincomycin (Lnc, salmon, PDB ID code 5HKV) (25), tiamulin (Tia, purple, PDB ID code 1XBP) (26), and erythromycin (Ery, tan, PDB ID code 4V7U) (41) (*D*). (*E*) Summary of antibiotic resistance conferred by WT VmlR as well as VmlR variants F237A and F237V complementing a Δ*vmlR* strain of *B. subtilis* (see also *SI Appendix*, Fig. S6 *A–F*). (*F–H*) The conformation of selected 23S rRNA nucleotides (gray sticks) at the PTC in the presence of VmlR (orange) superimposed with with different nucleotide (cyan) conformations (indicated by red arrows) when virginiamycin M (VgM, green, PDB ID code 1YIT) (24) (*F*), lincomycin (Lnc, pink, PDB ID code 5HKV) (25) (*G*), and tiamulin (Tia, purple, PDB ID code 1XBP) (26) (*H*) are bound to the ribosome.

revealed that VmlR could even disengage short oligopeptidyl-tRNAs from the PTC, although it remains unclear whether longer peptidyl-tRNA will be refractory to the action of VmlR or other ARE-ABCFs. By inducing a P/V-tRNA state, the ARD of VmlR can access the PTC of the ribosome where it indirectly dislodges the PTC-targeting antibiotics from their binding sites (Fig. 5*B*). This presumably occurs because VmlR induces allosteric conformational changes within PTC nucleotides that comprise the drug-binding site; however, the transition of the P-tRNA to the P/V-tRNA may also contribute to drug dissociation. Surprisingly, our results suggest that VmlR can promote dissociation of some PTC inhibitors, such as VgM, Lnc, and Tia, but not others, such as Cam and Lnz. While we also observe some conformational differences between the PTC bond with VmlR or Cam/Lnz (*SI Appendix*, Fig. S7 *J* and *K*), we note that Cam and Lnz display strong nascent chain-dependent stalling (28), which may preclude VmlR from acting on these stalled complexes, but this needs to be investigated further.

Transpeptidation experiments in the presence and absence of VgaA/Lsa and Lnc indicate that ATP hydrolysis is critical for recycling of ARE-ABCFs (4), suggesting that VmlR-ADP is the low-affinity form that dissociates from the ribosome following drug release (Fig. 5*B*). Moreover, since processive transpeptidation reactions require VmlR-ADP release, the observed

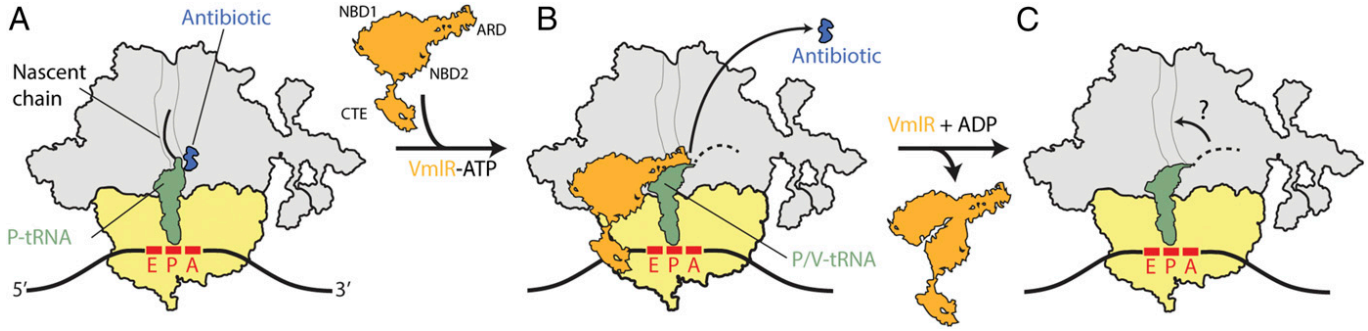

Fig. 5. Model for ribosome protection by VmlR. (*A*) Antibiotic-stalled ribosomes with a peptidyl-tRNA in the P site are recognized by the ABCF ATPase VmlR, which binds to the E site of the ribosome with a closed ATP-bound conformation. (*B*) Binding of VmlR induces a shifted P/V-tRNA conformation in the ribosome allowing the ARD of VmlR to access the peptidyl-transferase center (PTC) and dislodge the drug from its binding. (*C*) Hydrolysis of ATP to ADP leads to dissociation of VmlR from the ribosome, which may allow the peptidyl-tRNA to accommodate back on the ribosome with the nascent chain inserting into the NPET and translation to continue. In *B* and *C*, the dashes line extending from the P/V-tRNA represents a flexible nascent chain.

transpeptidation in the presence of ATP (4) indicates that the P/V-tRNA can reaccommodate at the P site of the PTC (Fig. 5*C*). The transpeptidation experiments were performed with fMet-tRNA (4), thus it is still unclear whether reaccommodation at the PTC can occur with longer peptidyl-tRNAs.

Before submission of this manuscript, a cryo-EM structure was reported of *P. aeruginosa* MsrE in complex with a *T. thermophilus* 70S ribosome bearing a deacylated $tRNA^{fMet}$ in the P site (7). At the time of revision, the cryo-EM map and model were still unavailable, therefore a comparison can only be made based on the publication figures, which are in good overall agreement with the structure and interpretation of the *B. subtilis* VmlR-EQ_2-SRC reported here. The two main differences appear to be that (*i*) MsrE lacks the CTE and therefore also lacks the associated SSU interactions that are available for VmlR, and (*ii*) the ARD loop differs in sequence and length between MsrE and VmlR (*SI Appendix*, Fig. S1) and therefore the interactions at the PTC are likewise distinct. While the ARD loop of MsrE is longer and reaches to the macrolide binding site (7), the VmlR loop is shorter and approaches only the PTC-targeting antibiotics, which is consistent with the respective antibiotic resistance profiles of these proteins.

Materials and Methods

The *B. subtilis* VmlR-EQ_2-SRC was generated by incubating recombinant *B. subtilis* VmlR-EQ_2 protein in the presence of ATP with *B. subtilis* ErmDL-SRC, which were essentially prepared as described (29, 30). Cryo-EM data collection was performed on a Titan Krios 300 kV TEM equipped with a Falcon III DED (FEI). Images of individual ribosome particles were aligned using MotionCor2 (31) and then particles were selected automatically using Gautomatch (https://www.mrc-lmb.cam.ac.uk/kzhang/). All images were processed using RELION 2.1 (20). Final reconstructions were corrected for the modulation transfer function and sharpened by applying a negative B factor estimated by RELION 2.1 (20). The average resolution of reconstructions was determined using the "gold-standard" criterion ($FSC_{0.143}$) (32). ResMap was used for local resolution estimation (33), and the final volumes were locally filtered using SPHIRE (34). Molecular models were fitted and adjusted using Coot (35) and refined in Phenix (36). Model validation was carried out using the MolProbity server (37), and the final model statistics are presented in *SI Appendix*, Table S1. All figures were generated using PyMOL (Schrödinger, LLC) and/or Chimera (38). Further details can be found in the *SI Appendix, Material and Methods*. The cryo-EM maps and models for the VmlR- and P-tRNA-SRC are deposited in the EMDatabank (EMD-0177 and EMD-0176) and RCSB Protein Data Bank (6HA8 and 6HA1), respectively.

ACKNOWLEDGMENTS. We thank Susanne Rieder for expert technical assistance and Seki Takahiro for generating the Δ*vmlR* strain. This research was supported by Deutsche Forschungsgemeinschaft Grants FOR1805 and WI3285/8-1 (to D.N.W.), Swedish Research Council Grants 2013-4680 (to V.H.) and 2015-04746 (to G.C.A.), the Ragnar Söderberg Foundation (V.H.), Carl Tryggers stiftelse CTS 34 (G.C.A.), Jeanssons stiftelse (G.C.A.), and from the Umeå Centre for Microbial Research (UCMR): postdoctoral grant 2017 (to H.T.) and Gender Policy Support 2017 (to G.C.A.). iNEXT, project number 5966, was funded by the Horizon 2020 program of the European Union. Czech Infrastructure for Integrative Structural Biology research infrastructure project LM2015043 funded by Ministry of Education, Youth, and Sports of the Czech Republic is gratefully acknowledged for the financial support of the measurements at the CF Cryo-electron Microscopy and Tomography Central European Institute of Technology, Masaryk University. This article reflects only the author's view, and the European Commission is not responsible for any use that may be made of the information it contains.

1. Wilson DN (2014) Ribosome-targeting antibiotics and bacterial resistance mechanisms. *Nat Rev Microbiol* 12:35–48.
2. Lin J, Zhou D, Steitz TA, Polikanov YS, Gagnon MG (2018) Ribosome-targeting antibiotics: Modes of action, mechanisms of resistance, and implications for drug design. *Annu Rev Biochem* 87:451–478.
3. Sharkey LKR, O'Neill AJ (2018) Antibiotic resistance ABC-F proteins: Bringing target protection into the limelight. *ACS Infect Dis* 4:239–246.
4. Murina V, Kasari M, Hauryliuk V, Atkinson GC (2018) Antibiotic resistance ABCF proteins reset the peptidyl transferase centre of the ribosome to counter translational arrest. *Nucleic Acids Res* 46:3753–3763.
5. Wang Y, et al. (2015) A novel gene, *optrA*, that confers transferable resistance to oxazolidinones and phenicols and its presence in *Enterococcus faecalis* and *Enterococcus faecium* of human and animal origin. *J Antimicrob Chemother* 70:2182–2190.
6. Sharkey LK, Edwards TA, O'Neill AJ (2016) ABC-F proteins mediate antibiotic resistance through ribosomal protection. *MBio* 7:e01975.
7. Su W, et al. (2018) Ribosome protection by antibiotic resistance ATP-binding cassette protein. *Proc Natl Acad Sci USA* 115:5157–5162.
8. Nguyen F, et al. (2014) Tetracycline antibiotics and resistance mechanisms. *Biol Chem* 395:559–575.
9. Jacquet E, et al. (2008) ATP hydrolysis and pristinamycin IIA inhibition of the Staphylococcus aureus Vga(A), a dual ABC protein involved in streptogramin A resistance. *J Biol Chem* 283:25332–25339.
10. Boël G, et al. (2014) The ABC-F protein EttA gates ribosome entry into the translation elongation cycle. *Nat Struct Mol Biol* 21:143–151.
11. Chen B, et al. (2014) EttA regulates translation by binding the ribosomal E site and restricting ribosome-tRNA dynamics. *Nat Struct Mol Biol* 21:152–159.
12. Novotna G, Janata J (2006) A new evolutionary variant of the streptogramin A resistance protein, $Vga(A)_{LC}$, from *Staphylococcus haemolyticus* with shifted substrate specificity towards lincosamides. *Antimicrob Agents Chemother* 50:4070–4076.
13. Lenart J, Vimberg V, Vesela L, Janata J, Balikova Novotna G (2015) Detailed mutational analysis of Vga(A) interdomain linker: Implication for antibiotic resistance specificity and mechanism. *Antimicrob Agents Chemother* 59:1360–1364.
14. Arenz S, et al. (2016) The stringent factor RelA adopts an open conformation on the ribosome to stimulate ppGpp synthesis. *Nucleic Acids Res* 44:6471–6481.
15. Arenz S, Nguyen F, Beckmann R, Wilson DN (2015) Cryo-EM structure of the tetracycline resistance protein TetM in complex with a translating ribosome at 3.9-Å resolution. *Proc Natl Acad Sci USA* 112:5401–5406.
16. Sothiselvam S, et al. (2014) Macrolide antibiotics allosterically predispose the ribosome for translation arrest. *Proc Natl Acad Sci USA* 111:9804–9809.
17. Chiba S, et al. (2011) Recruitment of a species-specific translational arrest module to monitor different cellular processes. *Proc Natl Acad Sci USA* 108:6073–6078.
18. Ohki R, Tateno K, Takizawa T, Aiso T, Murata M (2005) Transcriptional termination control of a novel ABC transporter gene involved in antibiotic resistance in *Bacillus subtilis*. *J Bacteriol* 187:5946–5954.
19. Dönhöfer A, et al. (2012) Structural basis for TetM-mediated tetracycline resistance. *Proc Natl Acad Sci USA* 109:16900–16905.
20. Kimanius D, Forsberg BO, Scheres SH, Lindahl E (2016) Accelerated cryo-EM structure determination with parallelisation using GPUs in RELION-2. *eLife* 5:e18722.
21. Sohmen D, et al. (2015) Structure of the *Bacillus subtilis* 70S ribosome reveals the basis for species-specific stalling. *Nat Commun* 6:6941.
22. Johnson ZL, Chen J (2018) ATP binding enables substrate release from multidrug resistance protein 1. *Cell* 172:81–89.e10.
23. Barthelme D, et al. (2011) Ribosome recycling depends on a mechanistic link between the FeS cluster domain and a conformational switch of the twin-ATPase ABCE1. *Proc Natl Acad Sci USA* 108:3228–3233.
24. Tu D, Blaha G, Moore PB, Steitz TA (2005) Structures of MLS_BK antibiotics bound to mutated large ribosomal subunits provide a structural explanation for resistance. *Cell* 121:257–270.
25. Matzov D, et al. (2017) Structural insights of lincosamides targeting the ribosome of *Staphylococcus aureus*. *Nucleic Acids Res* 45:10284–10292.
26. Schlünzen F, Pyetan E, Fucini P, Yonath A, Harms JM (2004) Inhibition of peptide bond formation by pleuromutilins: The structure of the 50S ribosomal subunit from *Deinococcus radiodurans* in complex with tiamulin. *Mol Microbiol* 54:1287–1294.
27. Choi J, Puglisi JD (2017) Three tRNAs on the ribosome slow translation elongation. *Proc Natl Acad Sci USA* 114:13691–13696.
28. Marks J, et al. (2016) Context-specific inhibition of translation by ribosomal antibiotics targeting the peptidyl transferase center. *Proc Natl Acad Sci USA* 113:12150–12155.
29. Arenz S, et al. (2014) Drug sensing by the ribosome induces translational arrest via active site perturbation. *Mol Cell* 56:446–452.
30. Arenz S, et al. (2014) Molecular basis for erythromycin-dependent ribosome stalling during translation of the ErmBL leader peptide. *Nat Commun* 5:3501.
31. Zheng SQ, et al. (2017) MotionCor2: Anisotropic correction of beam-induced motion for improved cryo-electron microscopy. *Nat Methods* 14:331–332.
32. Scheres SH, Chen S (2012) Prevention of overfitting in cryo-EM structure determination. *Nat Methods* 9:853–854.
33. Kucukelbir A, Sigworth FJ, Tagare HD (2014) Quantifying the local resolution of cryo-EM density maps. *Nat Methods* 11:63–65.
34. Moriya T, et al. (2017) High-resolution single particle analysis from electron cryomicroscopy images using SPHIRE. *J Vis Exp* e55448.
35. Emsley P, Cowtan K (2004) Coot: Model-building tools for molecular graphics. *Acta Crystallogr D Biol Crystallogr* 60:2126–2132.
36. Adams PD, et al. (2010) PHENIX: A comprehensive Python-based system for macromolecular structure solution. *Acta Crystallogr D Biol Crystallogr* 66:213–221.
37. Chen VB, et al. (2010) MolProbity: All-atom structure validation for macromolecular crystallography. *Acta Crystallogr D Biol Crystallogr* 66:12–21.
38. Pettersen EF, et al. (2004) UCSF Chimera–A visualization system for exploratory research and analysis. *J Comput Chem* 25:1605–1612.
39. Polikanov YS, Steitz TA, Innis CA (2014) A proton wire to couple aminoacyl-tRNA accommodation and peptide-bond formation on the ribosome. *Nat Struct Mol Biol* 21:787–793.
40. Schmeing TM, et al. (2009) The crystal structure of the ribosome bound to EF-Tu and aminoacyl-tRNA. *Science* 326:688–694.
41. Dunkle JA, Xiong L, Mankin AS, Cate JH (2010) Structures of the *Escherichia coli* ribosome with antibiotics bound near the peptidyl transferase center explain spectra of drug action. *Proc Natl Acad Sci USA* 107:17152–17157.
42. Wilson DN, et al. (2008) The oxazolidinone antibiotics perturb the ribosomal peptidyl-transferase center and effect tRNA positioning. *Proc Natl Acad Sci USA* 105:13339–13344.

5.2 Structures of the LsaA, $VgaA_{LC}$, and VgaL ABCF protein in complex with 70S ribosomes

5.2.1 Summary

This manuscript describes three structures of ARE-ABCF proteins bound to 70S ribosomes with distorted P-tRNAs. The complexes were prepared by *ex vivo* immunoprecipitation from relevant Gram-positive bacteria, and represent post-initiation 70S ribosomes which are the native substrate for the ARE-ABCFs studied. The complexes are broadly similar to each other, with the ARE-ABCF NBDs bound in the E-site and distorted P-tRNAs, as observed for the VmlR–70S structure. Each structure differed in modulation of the antibiotic binding site, with only one region of 23S rRNA, which we termed PL2, distorted similarly among structures. This led to the proposal of a general model of PLS_A-resistance ARE-ABCF action.

5.2.2 Contributions

Processing of the cryo-EM data, creation of the molecular models, and generation of the figures. The tRNA microarray data in Fig. 2e came from Prof. Z. Ignatova (University of Hamburg). Writing of the manuscript with help from Prof. Daniel N. Wilson.

nature COMMUNICATIONS

ARTICLE

https://doi.org/10.1038/s41467-021-23753-1 OPEN

Structural basis of ABCF-mediated resistance to pleuromutilin, lincosamide, and streptogramin A antibiotics in Gram-positive pathogens

Caillan Crowe-McAuliffe[1,7], Victoriia Murina[2,3,7], Kathryn Jane Turnbull[2,3], Marje Kasari[4], Merianne Mohamad[5], Christine Polte[1], Hiraku Takada[2,3], Karolis Vaitkevicius[2,3], Jörgen Johansson[2,3], Zoya Ignatova[1], Gemma C. Atkinson[2], Alex J. O'Neill[5], Vasili Hauryliuk[2,3,4,6]✉ & Daniel N. Wilson[1]✉

Target protection proteins confer resistance to the host organism by directly binding to the antibiotic target. One class of such proteins are the antibiotic resistance (ARE) ATP-binding cassette (ABC) proteins of the F-subtype (ARE-ABCFs), which are widely distributed throughout Gram-positive bacteria and bind the ribosome to alleviate translational inhibition from antibiotics that target the large ribosomal subunit. Here, we present single-particle cryo-EM structures of ARE-ABCF-ribosome complexes from three Gram-positive pathogens: *Enterococcus faecalis* LsaA, *Staphylococcus haemolyticus* $VgaA_{LC}$ and *Listeria monocytogenes* VgaL. Supported by extensive mutagenesis analysis, these structures enable a general model for antibiotic resistance mediated by these ARE-ABCFs to be proposed. In this model, ABCF binding to the antibiotic-stalled ribosome mediates antibiotic release via mechanistically diverse long-range conformational relays that converge on a few conserved ribosomal RNA nucleotides located at the peptidyltransferase center. These insights are important for the future development of antibiotics that overcome such target protection resistance mechanisms.

[1] Institute for Biochemistry and Molecular Biology, University of Hamburg, Hamburg, Germany. [2] Department of Molecular Biology, Umeå University, Umeå, Sweden. [3] Laboratory for Molecular Infection Medicine Sweden (MIMS), Umeå University, Umeå, Sweden. [4] University of Tartu, Institute of Technology, Tartu, Estonia. [5] Astbury Centre for Structural Molecular Biology, School of Molecular & Cellular Biology, Faculty of Biological Sciences, University of Leeds, Leeds, UK. [6] Department of Experimental Medical Science, Lund University, Lund, Sweden. [7] These authors contributed equally: Caillan Crowe-McAuliffe, Victoriia Murina. ✉email: vasili.hauryliuk@med.lu.se; Daniel.Wilson@chemie.uni-hamburg.de

The bacterial ribosome is a major antibiotic target[1]. Despite the large size of the ribosome, and the chemical diversity of ribosome-targeting small compounds, only a few sites on the ribosome are known to be bound by clinically used antibiotics. On the 50S large ribosomal subunit, two of the major antibiotic-binding sites are the peptidyl transferase centre (PTC) and the nascent peptide exit tunnel. The PTC is targeted by pleuromutilin, lincosamide and streptogramin A (PLS_A) antibiotics, as well as phenicols and oxazolidinones[2–6]. Representatives of macrolide and streptogramin B classes bind at adjacent sites at the beginning of the nascent peptide exit tunnel[3,5]. In contrast to the macrolides and streptogramin B antibiotics that predominantly inhibit translation during elongation[7], the PLS_A antibiotics overlap with the amino acids attached to the CCA-ends of the A- and/or P-site of tRNAs and trap ribosomes during or directly after initiation[8–10]. This is highlighted by the recent usage of the pleuromutilin retapamulin to identify translation initiation sites in Ribo-Seq experiments[8].

Many mechanisms have evolved to overcome growth inhibition by such antibiotics in bacteria, among them target protection mediated by a subset of ABC family of proteins[11]. ATP-binding cassette (ABC) ATPases are a ubiquitous superfamily of proteins found in all domains of life, best-known as components of membrane transporters[12,13]. A typical ABC transporter contains two nucleotide-binding domains (NBDs), each of which contribute one of two faces to an ATP-binding pocket, as well as transmembrane domains[14]. Some sub-groups of ABC proteins, however, lack membrane-spanning regions and have alternative cytoplasmic functions, such as being involved in translation[15–17]. For example, in eukaryotes Rli1/ABCE1 is a ribosome splitting factor involved in recycling after translation termination, and the fungal eEF3 proteins bind the ribosome to facilitate late steps of translocation and E-site tRNA release[18,19]. The F-type subfamily of ABC proteins, which are present in bacteria and eukaryotes, contain at least two NBDs separated by an α-helical interdomain linker and notably lack transmembrane regions[20–22].

One group of bacterial ABCFs, which are termed antibiotic resistance (ARE) ABCFs[23], confer resistance to antibiotics that bind to the 50S subunit of the bacterial ribosome[11,21,24,25]. Characterized ARE-ABCFs are found predominantly in Gram-positive bacteria, including human and animal pathogens, typically have a restricted host specificity, and can be further divided into eight subfamilies[11,20,26]. Although initially thought to act as part of efflux systems[27,28], these proteins were subsequently shown instead to bind the ribosome, oppose antibiotic binding, and to reverse antibiotic-mediated inhibition of translation in vitro[29].

Phylogenetic analyses indicate that ARE-ABCFs may have arisen multiple times through convergent evolution, and that antibiotic specificity can be divergent within a related subgroup[20]. Classified by the spectrum of conferred antibiotic resistance, ARE-ABCFs can be categorized into eight subfamilies with three different resistance spectra[20,25]:

1. A highly polyphyletic group of ARE-ABCFs that confer resistance to the PTC-binding PLS_A antibiotics (ARE1, ARE2, ARE3, ARE5 and ARE6 subfamilies). The most well-studied representatives are VmlR, VgaA, SalA, LmrC and LsaA[26,30–33]. Additionally, a lincomycin-resistance ABCF that belongs to this group, termed Lmo0919, has been reported in *Listeria monocytogenes*[34–36].
2. ARE-ABCFs that confer resistance to antibiotics that bind within the nascent peptide exit channel (a subset of the ARE1 subfamily, and ARE4). The most well-studied representatives are Macrolide and streptogramin B resistance (Msr) proteins[28,37,38].
3. Poorly experimentally characterized ARE-ABCF proteins belonging to subfamilies ARE7 (such as OptrA) and ARE8 (PoxtA). These resistance factors confer resistance to phenicols and oxazolidinones that bind in the PTC overlapping with the PLS_A-binding site[11,39,40] and are spreading rapidly throughout bacteria in humans and livestock by horizontal gene transfer[41–44].

Additionally, several largely unexplored groups of predicted novel ARE-ABCFs are found in high-GC Gram-positive bacteria associated with antibiotic production[20].

So far, two structures of ARE-ABCFs bound to the 70S ribosome have been determined[24,38,45]. In each instance, the ARE-ABCF interdomain linker extends from the E-site-bound NBDs into the relevant antibiotic-binding site in the ribosome, distorting the P-site tRNA into a non-canonical state located between the P and E sites. The tip of the interdomain linker—termed the antibiotic resistance determinant (ARD) in ARE-ABCFs—is not well conserved among (and sometimes not even within) subfamilies, and mutations in this region can abolish activity as well as change antibiotic specificity. Mutagenesis indicates that both steric overlap between the ARD and the antibiotic, as well as indirect reconfiguration of the rRNA and the antibiotic-binding site, may contribute to antibiotic resistance[24,38,45,46]. Non-ARE ribosome-associated ABCFs that do not confer resistance to antibiotics—such as EttA—tend to have relatively short interdomain linkers that contact and stabilize the P-site tRNA[22,47]. ARE-ABCFs that confer resistance to PLS_A antibiotics (such as VmlR) have extensions in the interdomain linker that allow them to reach into the antibiotic-binding site in the PTC[45]. The longest interdomain linkers belong to ARE-ABCFs that confer resistance to macrolides and streptogramin B antibiotics (e.g. MsrE), and such linkers can extend past the PTC into the nascent peptide exit tunnel[38]. The length of the bacterial ABCF ARD generally correlates with the spectrum of conferred antibiotic resistance. Notable exceptions to this pattern are OptrA and PoxtA ARE-ABCF which have short interdomain linkers, yet still confer resistance to some PTC-binding antibiotics[39,40], while typically PTC-protecting ARE-ABCFs such as VmlR, LsaA and VgaA typically have comparatively long interdomain linkers[46,48].

The available ARE-ABCF-ribosome structures were generated by in vitro reconstitution. *Pseudomonas aeruginosa* MsrE, which confers resistance to tunnel-binding macrolides and streptogramin B antibiotics (that inhibit translation elongation) was analysed bound to a heterologous *Thermus thermophilus* initiation complex[38]. *Bacillus subtilis* VmlR, which confers resistance to PLS_A antibiotics that bind in the PTC (which stall translation at initiation), was analysed in complex with a *B. subtilis* 70S ribosome arrested during elongation by the presence of a macrolide antibiotic[33,45]. Structures of native physiological complexes (such as those generated using pull-down approaches from the native host) are currently lacking.

In this work, we systematically characterize the antibiotic resistance specificity and determine the structure of three in vivo formed ARE-ABCF-70S ribosome complexes using affinity chromatography and cryo-electron microscopy (cryo-EM). Our study focusses on ARE-ABCFs that confer resistance to PLS_A antibiotics in clinically relevant Gram-positive pathogens, namely, the ARE3 representative *Enterococcus faecalis* LsaA[30], as well as the ARE1 representatives *Listeria monocytogenes* Lmo0919 (refs. [34–36])—which we have termed VgaL—and the well-characterized $VgaA_{LC}$ protein, initially isolated from *Staphylococcus haemolyticus*[26,36,46,49,50]. *Staphylococcus* and *Enterococcus* are commensal organisms that are prevalent in diverse healthcare-associated infections, and antibiotic resistance is

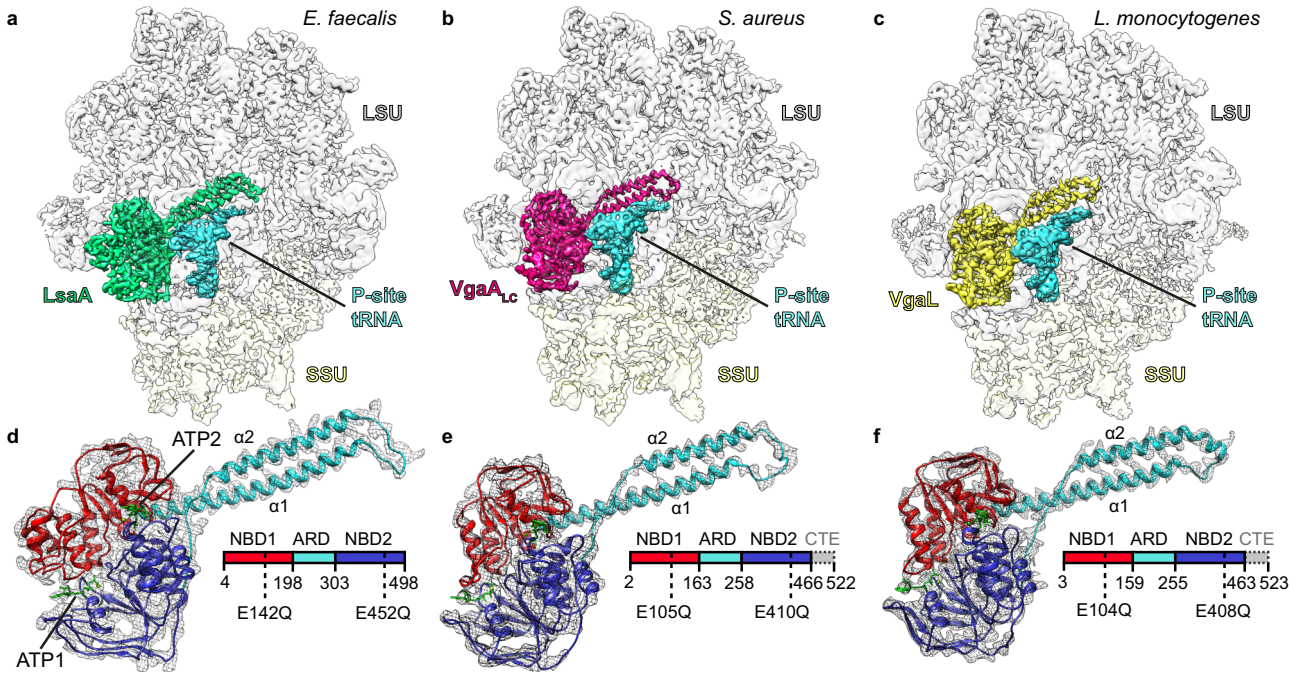

Fig. 1 Cryo-EM structures of ARE-ABCF–ribosome complexes. a–c Cryo-EM maps with isolated densities for **a** *E. faecalis* LsaA (green), **b** *S. aureus* $VgaA_{LC}$ (magenta), **c** *L. monocytogenes* VgaL (yellow) as well as P-site tRNA (cyan), small subunit (SSU, yellow) and large subunit (LSU, grey). **d–f** Density (grey mesh) with molecular model for **d** LsaA, **e** $VgaA_{LC}$ and **f** VgaL, coloured according to domain as represented in the associated schematics: nucleotide-binding domain 1 (NBD1, red), antibiotic-resistance domain (ARD, cyan), nucleotide-binding domain 2 (NBD2, blue) and C-terminal extension (CTE, grey, not modelled). α1 and α2 indicate the two α-helices of the ARD interdomain linker. In **d–f**, the ATP nucleotides are coloured green.

spreading through these species[51–54]. *L. monocytogenes* is a foodborne pathogen that poses a particular risk to pregnant women and immunocompromised patients[55]. Our structures, supported by extensive mutagenesis experiments, provide insight into the mechanism by which these distinct ARE-ABCFs displace antibiotics from their binding site on the ribosome to confer antibiotic resistance.

Results

Cryo-EM structures of in vivo formed ARE-ABCF-70S complexes. To obtain in vivo formed ARE-ABCF-70S complexes, we expressed C-terminally $FLAG_3$-tagged ATPase-deficient EQ_2 variants of *E. faecalis* LsaA, *S. aureus* $VgaA_{LC}$ and *L. monocytogenes* VgaL in their corresponding native host bacterial species. The $FLAG_3$ tag was used for affinity purification of each protein locked onto their respective ribosomal target. The ARE-ABCFs co-migrated with the 70S fraction through sucrose gradients—with the complex further stabilized in the presence of ATP in the case of LsaA and $VgaA_{LC}$—and co-eluted with ribosomal proteins after affinity purification (Supplementary Figs. 1–3).

The resulting in vivo formed complexes were characterized by single-particle cryo-EM (see 'Methods'), yielding ARE-70S complexes with average resolutions of 2.9 Å for *E. faecalis* LsaA, 3.1 Å for *S. aureus* $VgaA_{LC}$ and 2.9 Å for *L. monocytogenes* VgaL (Fig. 1a–c, Supplementary Table 4 and Supplementary Figs. 4–6). In each instance, the globular NBDs of the ARE-ABCF were bound in the E-site, and the α-helical interdomain linker, consisting of two α-helices (α1 and α2) and the ARD loop, extended towards the PTC (Fig. 1a–c). Additionally, a distorted tRNA occupied the P-site (Fig. 1a–c), similarly to what was observed previously for *P. aeruginosa* MsrE and *B. subtilis* VmlR[38,45]. For the LsaA and VgaL samples, occupancy of the factor on the ribosome was high, with >95% and ~70% of picked ribosomal particles containing LsaA and VgaL, respectively (Supplementary Figs. 4 and 6). By contrast, $VgaA_{LC}$ had lower occupancy (~60%), implying that the factor dissociated after purification and/or during grid preparation (Supplementary Fig. 5). In silico 3D classification revealed that the major class not containing $VgaA_{LC}$ in the dataset was a 70S ribosome with P-tRNA, which could also be refined to an average resolution of 3.1 Å (Supplementary Fig. 5). Generally, the 50S ribosomal subunit and ARE-ABCF interdomain linkers were well-resolved (Fig. 1d–f and Supplementary Figs. 4–6). While ARE-ABCF NBDs, occupying the E-site, had a lower resolution—especially in the regions that contact the ribosomal L1 stalk and the 30S subunit—the density was nonetheless sufficient to dock and adjust homology models in each instance (Fig. 1d–f and Supplementary Figs. 4–6). Densities corresponding to the 30S subunits were of lower quality, indicating flexibility in this region, but, with multibody refinement, were nonetheless sufficient to build near-complete models of each ribosome. Density between NBD1 and NBD2 of each ARE was most consistent with the presence of two molecules of ATP (or another NTP) and a cation, which we tentatively assigned as ATP-1, ATP-2 and magnesium, respectively. Nonetheless, the density in this region was not sufficiently detailed to model this region de novo and caution is warranted in interpreting exact geometries from the model (Fig. 1d–f and Supplementary Fig. 7). Interestingly, the density for the nucleobase of ATP-1 bound in the peripheral nucleotide-binding site of each ARE-ABCF was particularly poor (Supplementary Fig. 7), consistent with the relaxed nucleotide specificity of these proteins, i.e., the ability of ARE-ABCFs to hydrolyze other nucleotides, such as CTP, UTP and GTP[56].

By comparison to structures of other ABC proteins, the NBDs adopted a closed conformation bound tightly to each nucleotide (Supplementary Fig. 8). In each ARE-bound 70S structure, the ribosomal small subunit was in a semi-rotated state, although this varied between AREs, with the LsaA- and VgaL-bound ribosomes more rotated than $VgaA_{LC}$-bound 70S (Supplementary Fig. 9a–d).

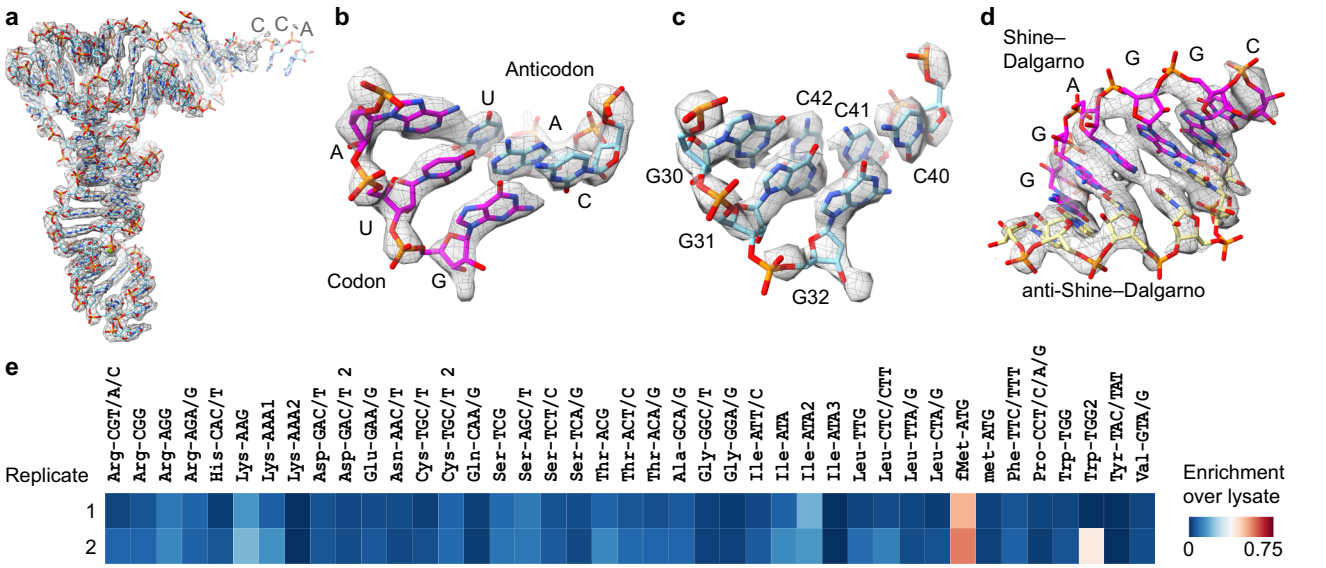

Fig. 2 The LsaA-70S complex contains an initiator tRNA and SD-helix. a–d Isolated density (grey mesh) with molecular models (sticks) for **a** initiator $tRNA^{fMet}$ (cyan), **b** interaction between AUG start codon of the mRNA (magenta) and anticodon of initiator $tRNA^{fMet}$ (cyan) in the P-site, **c** three G-C base pairs specific to the initiator $tRNA^{fMet}$ (cyan) and **d** helix formed between Shine-Dalgarno (SD) sequence of the mRNA (magenta) and anti-SD of the 16S rRNA (yellow). **e** Replicate tRNA microarray analysis of the LsaA-70S complex, illustrating the enrichment of initiator $tRNA^{fMet}$ in the LsaA-70S complex over the lysate. Confidence intervals between replicates were 92%.

In each ARE-ABCF-70S map, the P-site tRNA was distorted compared to a classic P-site tRNA, resulting in a substantial shift of the acceptor stem away from the PTC (Supplementary Fig. 9e–h), as observed previously for MsrE and VmlR[38,45]. In each case, the distorted P-site tRNA was rotated compared to a classic P-site tRNA (21–29°), possibly due to a defined interaction of the tRNA elbow with the NBD2 of the ARE (Supplementary Fig. 9i–k). The CCA 3′ end was particularly disordered, precluding any additional density corresponding to an amino acid or nascent chain from being modelled, although the approximate path could be traced in low-pass-filtered maps (Fig. 1a–c and Supplementary Figs. 4–6). We have used our high-resolution maps to present a model of the ribosome from the Gram-positive pathogen *L. monocytogenes* and update the model of the *S. aureus* ribosome[57]. Our models of the *E. faecalis* and *S. aureus* ribosomes are in good agreement with those recently described[58,59].

LsaA, $VgaA_{LC}$ and VgaL bind to translation initiation states. In each cryo-EM map, the P-site tRNA body was sufficiently well-resolved to unambiguously assign the density to initiator $tRNA^{fMet}$ on the basis of (i) general fit between sequence and density, (ii) the well-resolved codon–anticodon interaction and (iii) a characteristic stretch of G:C base pairs found in the anticodon stem loop of $tRNA^{fMet}$ (Fig. 2a–c). Additionally, in the small subunit mRNA exit tunnel, density corresponding to a putative Shine-Dalgarno–anti-Shine-Dalgarno helix was observed, consistent with the ARE-ABCF binding to an initiation complex containing $tRNA^{fMet}$ (Fig. 2d). LsaA–*E. faecalis* 70S samples were further analysed with a custom tRNA microarray, which confirmed $tRNA^{fMet}$ was the dominant species found in the sample (Fig. 2e). Collectively, these observations indicate that in our structures the majority of the ARE-ABCFs are bound to 70S translation initiation complexes. While the initiation state is also the state that would result from PLS_A inhibition, we note that our complexes were formed in the absence of an antibiotic. Thus, in our experimental set-up it is likely that the use of the EQ_2 mutants traps the ARE-ABCFs on initiation complexes due to the availability of the E-site.

Further examination of the LsaA-70S volume revealed weak density in the ribosomal A-site (Supplementary Fig. 4f), suggesting that some complexes had entered the elongation cycle. This was unexpected, as the distorted P-site tRNA is predicted to overlap with an accommodated A-site tRNA, although as noted would be compatible with a pre-accommodated A/T-tRNA[45]. A mask around the A-site was used for partial signal subtraction, and focused 3D classification was used to further sub-sort the LsaA-70S volume. One class, containing approximately one-third of the particles, was shown to indeed contain a tRNA in the A-site (Supplementary Figs. 4 and 10a). This tRNA was poorly resolved, suggesting flexibility, and was slightly rotated compared to a canonical, fully accommodated A-site tRNA, and, as for the P-site tRNA, the acceptor stem was significantly disordered and displaced (Supplementary Fig. 10b, c). This state likely reflects an incomplete or late-intermediate accommodation event, as observed previously when translation is inhibited by PTC-binding antibiotics hygromycin A or A201A, both of which were shown to sterically exclude the acceptor stem of a canonical A-site tRNA[60]. A very weak density corresponding to an A-site tRNA was also observed in $VgaA_{LC}$ and VgaL volumes, but sub-classification was unsuccessful for these datasets.

$VgaA_{LC}$ and VgaL, both of which belong to the ARE1 subfamily—although not LsaA, which belongs to the ARE3 subfamily—contain a short C-terminal extension (CTE) predicted to form two α-helices[20,45]. Although not conserved among all AREs, deletion of the CTE abolished antibiotic resistance in VmlR and reduced antibiotic resistance in VgaA, implying that this extension is necessary for function in some ARE-ABCFs[45,49]. Density for this region, which emanates from NBD2 and was located between ribosomal proteins uS7 and uS11, was present in the $VgaA_{LC}$-70S and VgaL-70S maps and was essentially consistent with the position of the VmlR CTE, although was not sufficiently resolved to create a model for this region. Although bound close to the mRNA exit channel, the CTEs of $VgaA_{LC}$ and VgaL did not contact the Shine-Dalgarno–anti-Shine-Dalgarno helix of the initiation complexes, indicating they are not critical for substrate recognition in these ARE-ABCFs (Supplementary Fig. 10d–f).

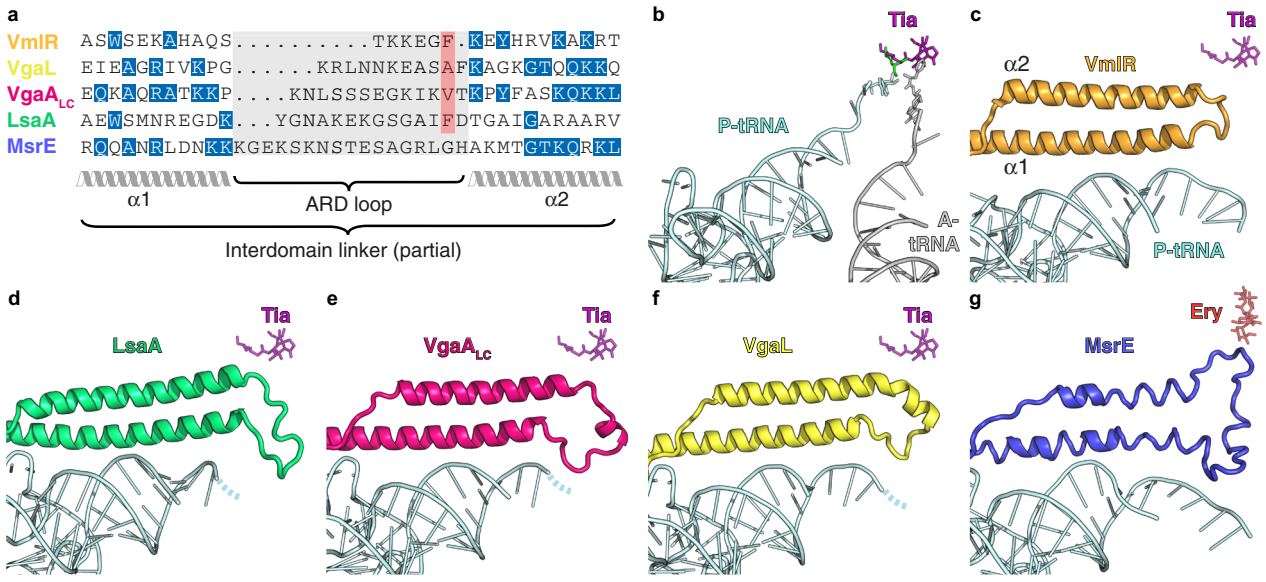

Fig. 3 Comparison of the ARD loops of different ARE-ABCFs. a The sequence length of the ARD loops differs significantly for VmlR, VgaL, VgaA$_{LC}$, LsaA and MsrE. Although the lack of sequence homology precludes accurate sequence alignment of the ARD loops, the red highlighted residues can be aligned structurally. Sequences were aligned with Clustal Omega and edited by hand to match the structures. **b**–**g** Comparison of the positions of **b** A-site tRNA (grey) and P-site tRNA (cyan) from pre-attack state (PDB 1VY4)[103], with shifted P-site tRNA (cyan) and ABCF ARD from ribosome complexes containing **c** VmlR (orange, PDB 6HA8)[45], **d** LsaA (green), **e** VgaA$_{LC}$ (magenta), **f** VgaL (yellow) and **g** MsrE (blue, PDB 5ZLU)[38]. In **b**–**g**, the relative position of either tiamulin (Tia, magenta, PDB 1XBP)[2] or erythromycin (Ery, red, PDB 4V7U)[5] has been superimposed. Dashed lines in **d**–**f** represent the likely path of the CCA end of the tRNA.

The location and conformation of short and long ARDs on the ribosome. The ARD loop, positioned between the two long α-helices that link the NBDs, is a critical determinant of antibiotic resistance[29,38,45,46,56]. Despite sharing a similar antibiotic specificity profile, the ARDs of LsaA, VgaA$_{LC}$, VgaL and VmlR are divergent in both amino acid composition and length, which is consistent with the polyphyletic nature of this group but precludes confident sequence alignment of this region (Fig. 3a). Despite such sequence divergence, the position of the ARDs on the ribosome is broadly similar in each instance (Fig. 3b–g). By comparison to tiamulin, which overlaps with the aminoacyl moieties of A- and P-tRNAs in the PTC[2,60], VmlR, LsaA, VgaA$_{LC}$ and VgaL are all positioned similarly on the ribosome, with the ARD backbone adjacent to the antibiotic-binding site (Fig. 3b–f). Compared to VmlR[45], the additional residues in the ARDs of LsaA, VgaA$_{LC}$ and VgaL extend away from the antibiotic-binding site, towards the CCA 3′ end of the distorted P-tRNA (Fig. 3c–f). By contrast, MsrE, which confers resistance to tunnel-binding antibiotics deeper in the ribosome, has a longer ARD that extends both past the PTC to approach the macrolide/streptogramin A-binding site, as well as towards the distorted P-tRNA (Fig. 3a, g)[38]. Thus, the length of the ARD does not necessarily provide insights into the extent to which the ARD will penetrate into the ribosomal tunnel and thus one cannot easily predict whether long ARDs will confer resistance to macrolide antibiotics.

Position of the ARDs with respect to PLS$_A$ antibiotic-binding site. We next made a careful comparison of the LsaA, VgaA$_{LC}$ and VgaL ARDs with the binding sites of relevant antibiotics within the PTC (Fig. 4a, b)[2,5,6,61]. For LsaA, the side chain of Phe257 overlapped with the binding sites of tiamulin, virginiamycin M and lincomycin, but was not close to erythromycin (Fig. 4a–c), consistent with the spectrum of antibiotic resistance conferred by this protein (Supplementary Table 1). In the VgaA$_{LC}$ ARD, Val219 was situated close to tiamulin and virginiamycin M, and had a modest predicted overlap with lincomycin (Fig. 4d). Notably, in the closely related variant VgaA, which has a similar specificity with modestly higher resistance to tiamulin and virginiamycin M, residue 219 is a glycine, which we predict would not overlap with the PLS$_A$-binding site[46]. Thus, VgaA$_{LC}$ confers resistance to virginiamycin M and tiamulin despite the lack of overlap between the ARE-ABCF and the antibiotic-binding site (Supplementary Table 2). For VgaL, the closest residue to the PLS$_A$-binding site was Ala216, which had no predicted overlap with tiamulin, virginiamycin M or lincomycin (Fig. 4e). VgaL therefore confers resistance to lincomycin, virginiamycin M and tiamulin without directly overlapping the binding sites of these antibiotics. In summary, there was no general pattern of overlap or non-overlap with the PLS$_A$ binding sites among LsaA, VgaA$_{LC}$ and VgaL, and our structural evidence is not consistent with a steric overlap model of antibiotic egress.

Mutational analysis of LsaA and VgaA$_{LC}$ ARDs. Our models of the ARD loops allowed us to design and test mutants for capacity to confer antibiotic resistance. Because genetic manipulation in *Enterococcus faecalis* is difficult, and LsaA complements the *B. subtilis* Δ*vmlR* strain (Supplementary Fig. 11), we performed the mutational analysis of LsaA in the *B. subtilis* Δ*vmlR* background. When LsaA Phe257, which directly overlaps the PLS$_A$-binding site (Fig. 4c), was mutated to alanine, no change in resistance was observed (Supplementary Fig. 11). By contrast, mutation of Lys244, which is not situated close to the PLS$_A$-binding sites but forms a hydrogen bond with 23S rRNA G2251 and G2252 (*Escherichia coli* numbering is used for 23S rRNA nucleotides) of the P-loop (Supplementary Fig. 11), nearly abolished antibiotic resistance activity (Supplementary Fig. 12). Taken together, these observations indicate that LsaA does not confer resistance via simple steric occlusion, and that interactions with the P-loop may be required for positioning the LsaA ARD.

For VgaA$_{LC}$, extensive alanine mutations within the ARD were explored (Supplementary Table 2). As expected from the above analyses and natural variants, mutating Val219—the only residue in VgaA$_{LC}$ that sterically overlaps the PLS$_A$-binding site—did not

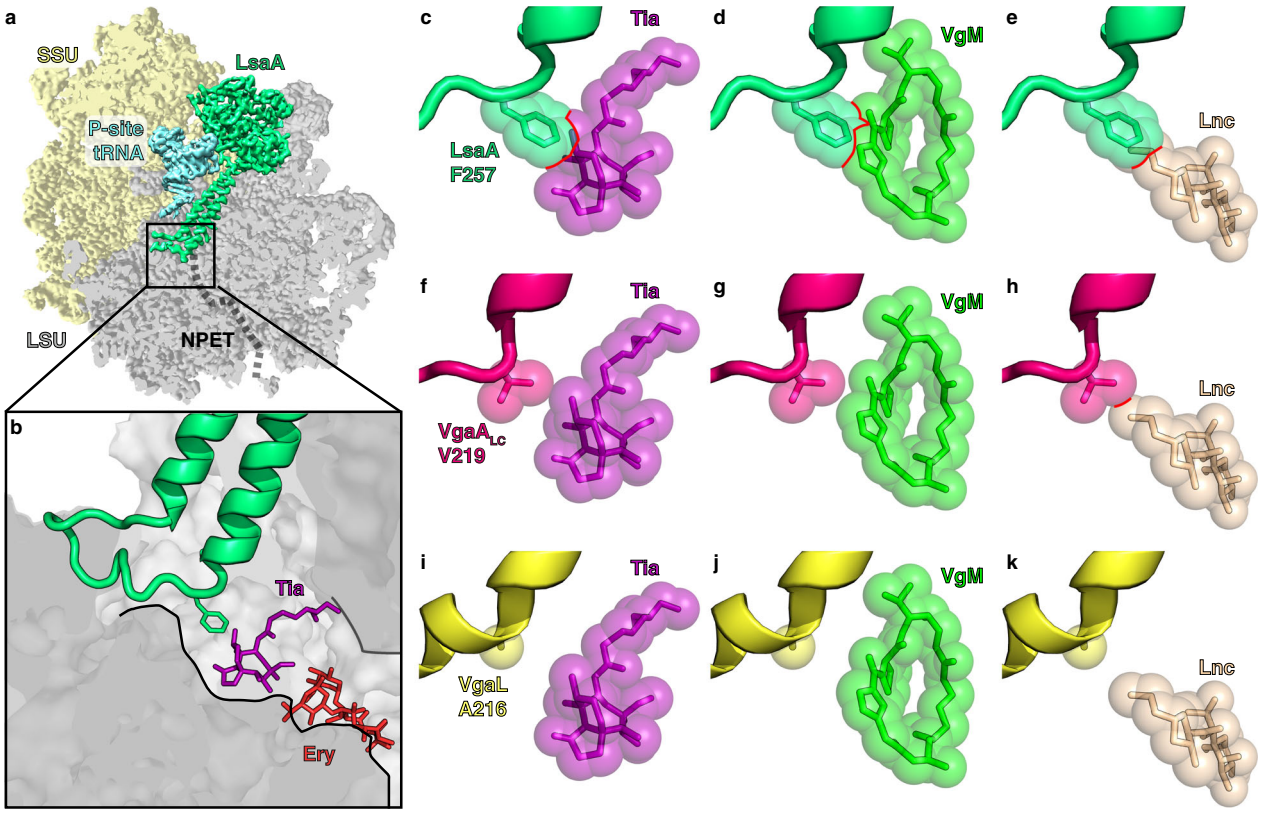

Fig. 4 Interaction of LsaA, VgaA$_{LC}$ and VgaL at the peptidyl transferase centre. a–b LsaA and distorted P-site tRNA superimposed on a transverse section of the large subunit (LSU, grey) to reveal **a** the ARD of LsaA extending into the nascent polypeptide exit tunnel (NPET) and **b** the relative position of Phe257 of LsaA to tiamulin (Tia, purple, PDB 1XBP)[2] and erythromycin (Ery, red, PDB 4V7U)[5]. **c–k** Relative position of LsaA (green, top row, **c–e**), VgaA$_{LC}$ (pink, middle row, **f–h**) and VgaL (yellow, bottom row, **i–k**) to tiamulin (Tia, purple, PDB 1XBP), virginiamycin M (VgM, lime, PDB 4U25)[61] and lincomycin (Lnc, tan, PDB 5HKV)[6]. When present, clashes in **c–k** are shown with red outlines.

affect the antibiotic resistance profile. Three residues at the beginning of α2, directly after the ARD loop, were required for resistance: Tyr223, which stacks with U2585 (part of the pleuromutilin-binding site); Phe224, which stacks with A2602 held in the centre of the ARD; and Lys227, which forms a hydrogen bond with the 5′ phosphate of C2601 (Supplementary Table 2). These residues do not overlap with the PLS$_A$-binding site, but may be required to position the ARD in the PTC to impede antibiotic binding, or for the folding of the ARD itself (Supplementary Fig. S12d–f). In the naturally variable VgaA$_{LC}$ ARD loop, mutation of Ser213, which sits adjacent to U2506 and C2507 (Supplementary Fig. S12e), to alanine similarly reduced antibiotic resistance (Supplementary Table 2). Of note, mutating the most conserved residue among VgaA variants in this region, Lys218, did not substantially affect resistance (Supplementary Table 2)[62]. Extensive alanine substitutions in the surrounding residues that contact the 23S rRNA (Supplementary Fig. 12d–f) either did not affect, or had only a mild influence on, the antibiotic resistance conferred by this protein (Supplementary Table 2). In summary, mutation of VgaA$_{LC}$ residues that interact with 23S rRNA nucleotides that form part of the PLS$_A$-binding pocket affected antibiotic-resistance activity.

Modulation of the ribosomal antibiotic-binding site by ARE-ABCFs. We next sought to explore how the ARDs of LsaA, VgaA$_{LC}$ and VgaL affect the conformation of the ribosomal PTC. The 23S rRNA A2602, which is flexible in the absence of tRNAs and positioned between the P- and A-tRNAs during peptidyl transfer, is bound and stabilized by all structurally characterized ARE-ABCFs. In LsaA and VmlR, a tryptophan stacks and stabilizes A2602 in a flipped position (Supplementary Fig. 13)[45], reminiscent of the stacking interaction between the equivalent rRNA nucleotide and Tyr346 of the yeast ABCF protein Arb1 observed in a structure of a ribosome-associated quality control complex[63]. In VgaA$_{LC}$, VgaL, and MsrE, A2602 is instead positioned within the ARD loop, interacting with multiple residues from the ARE (Supplementary Fig. 13)[38].

We have designated four regions within domain V of the 23S rRNA (Fig. 5a) as PTC loops 1–4 (PL1–4) that comprise the binding site for the A- and P-site tRNA (Fig. 5b), are close to the ARD of the ARE-ABCFs (Fig. 5c) and form the binding pocket for the PLS$_A$ antibiotics (Fig. 5d–f). There is a significant overlap between nucleotides that form the PLS$_A$-binding pockets and nucleotides that are shifted when LsaA, VgaA$_{LC}$ or VgaL are bound to the ribosome (Fig. 5a). While the ARE-ABCFs come close to PL1, they do not interact directly and the conformation of nucleotides within PL1 do not appear to be altered when comparing the ARE-ABCF and PLS$_A$ conformations (Fig. 5g–i and Supplementary Fig. 14). An exception was a slight rotation of the A2062 nucleobase (Supplementary Fig. 14), which is most likely a consequence of drug binding rather than ARE engagement. By contrast, multiple rearrangements were evident in PL2 that appear to arise due to direct contact between the ARD loop of the ARE-ABCF and the backbone of 23S rRNA nucleotides A2451–A2452 within PL2 (Fig. 6a–d and Supplementary Fig. 15). Displacement of the backbone was largest (3.3–4.4 Å) upon LsaA binding, intermediate (3.1 Å) for VgaA$_{LC}$, and smallest (1.0 Å) for VgaL, and resulted in corresponding shifts in the position of the nucleobases that comprise the PLS$_A$-binding pocket (Fig. 6a–d and Supplementary Fig. 15).

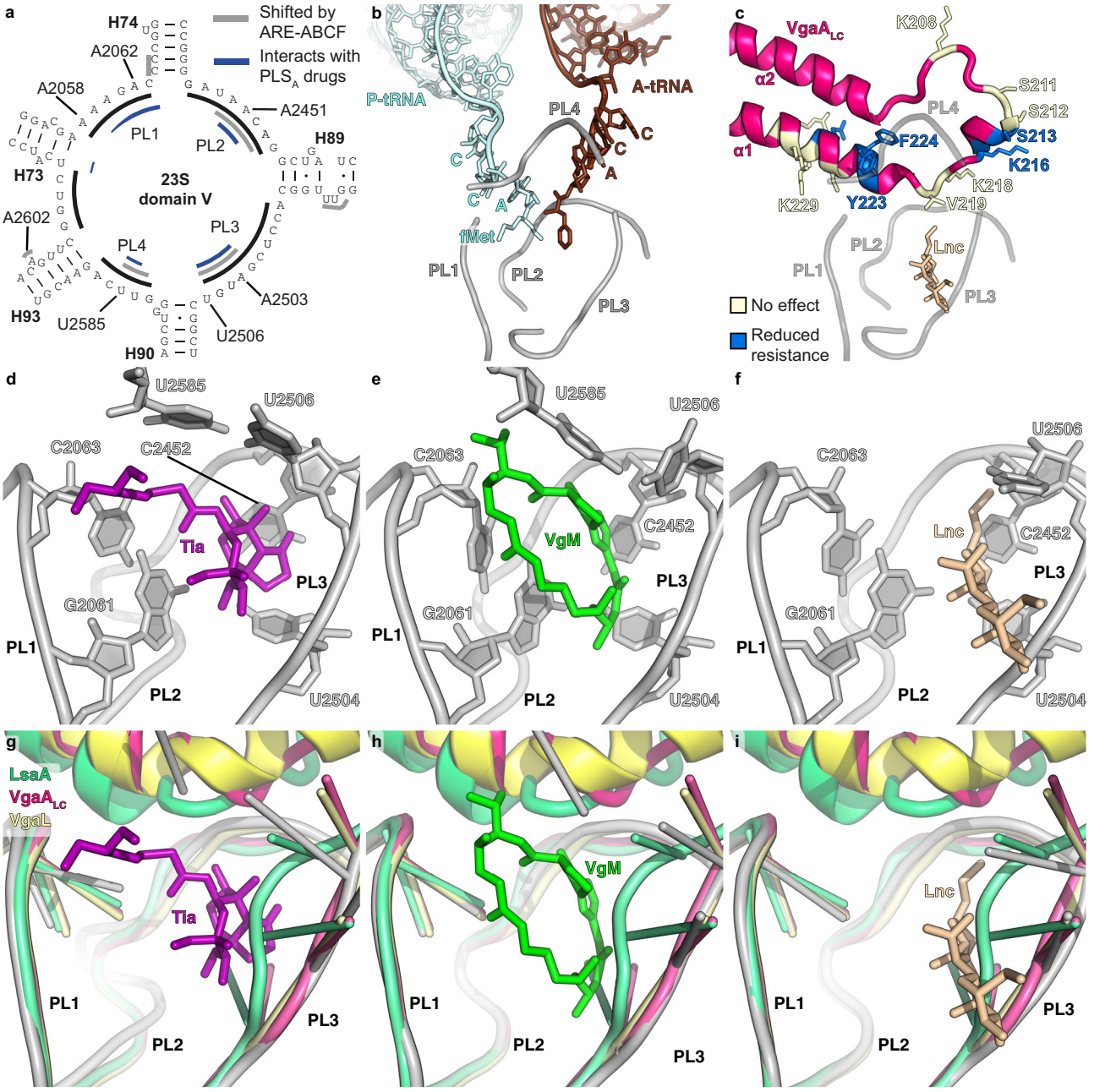

Fig. 5 ARE-ABCF binding induces conformational changes at the PTC. a Secondary structure of peptidyl transferase ring within domain V of the 23S rRNA, highlighting residues within PTC loops 1–4 (PL1–4) that comprise the binding site of PLS$_A$ antibiotics (blue) and/or undergo conformational changes upon ARE-ABCF binding (grey). **b** View of the PTC in the pre-peptidyl transfer state (PDB 1VY4)[103] with tRNAs and PLs 1–4 from **a** labelled. **c** Same view as **b**, except with the VgaA$_{LC}$ structure shown. For reference, lincomycin is also included (PDB 5HKV)[6]. Residues coloured yellow had no effect on resistance when mutated to alanine. For residues coloured blue, antibiotic resistance was significantly affected when mutated to alanine. **d**–**f** Binding site of **d** tiamulin (Tia, magenta, PDB 1XBP, 3.5 Å)[2], **e** virginiamycin M (VgM, green, PDB 4U25, 2.9 Å)[61] and **f** lincomycin (Lnc, tan, PDB 5HKV, 3.7 Å)[6] on the ribosome. **g**–**i** Comparison of conformations of rRNA nucleotides comprising the **g** Tia, **h** VgM and **i** Lnc binding site (shown as grey cartoon ladder representation), with rRNA conformations when LsaA (green), VgaA$_{LC}$ (magenta) or VgaL (yellow) are bound.

Unexpectedly, large changes were also observed in PL3, around nucleotides U2504–U2506, in the ARE-bound structures, despite the lack of contact between this region and the ARDs (Fig. 6e–h and Supplementary Fig. 16). Such shifts are likely a consequence of disturbances in PL2 since nucleotides within PL2 are in direct contact with nucleotides in PL3 (Fig. 6i). Specifically, the 23S rRNA nucleotides G2505 and U2506 in PL2 were shifted by 2.8-3.0 Å when comparing each ARE-bound 70S to the drug-bound states (Fig. 6e–h and Supplementary Fig. 17). Additionally, in the LsaA-bound 70S, U2504 was shifted such that it directly overlaps with the PLS$_A$-binding site (Fig. 6f). The rearrangement of U2504 appears to arise because of a cascade of changes in PL2 due to LsaA binding, namely, A2453 of PL2 is shifted slightly away from the PTC and pairs with G2499 (instead of U2500), allowing C2452 (which normally pairs with U2504 and forms part of the PLS$_A$-binding pocket) to instead hydrogen bond with U2500. The relocation of C2452 frees U2504, and PL3 more generally, allowing it to reposition into the PLS$_A$-binding pocket upon LsaA binding (Fig. 6i, j).

U2585, which is part of PL4, forms part of the tiamulin (Fig. 6k) and virginiamycin M-binding site, but not that of

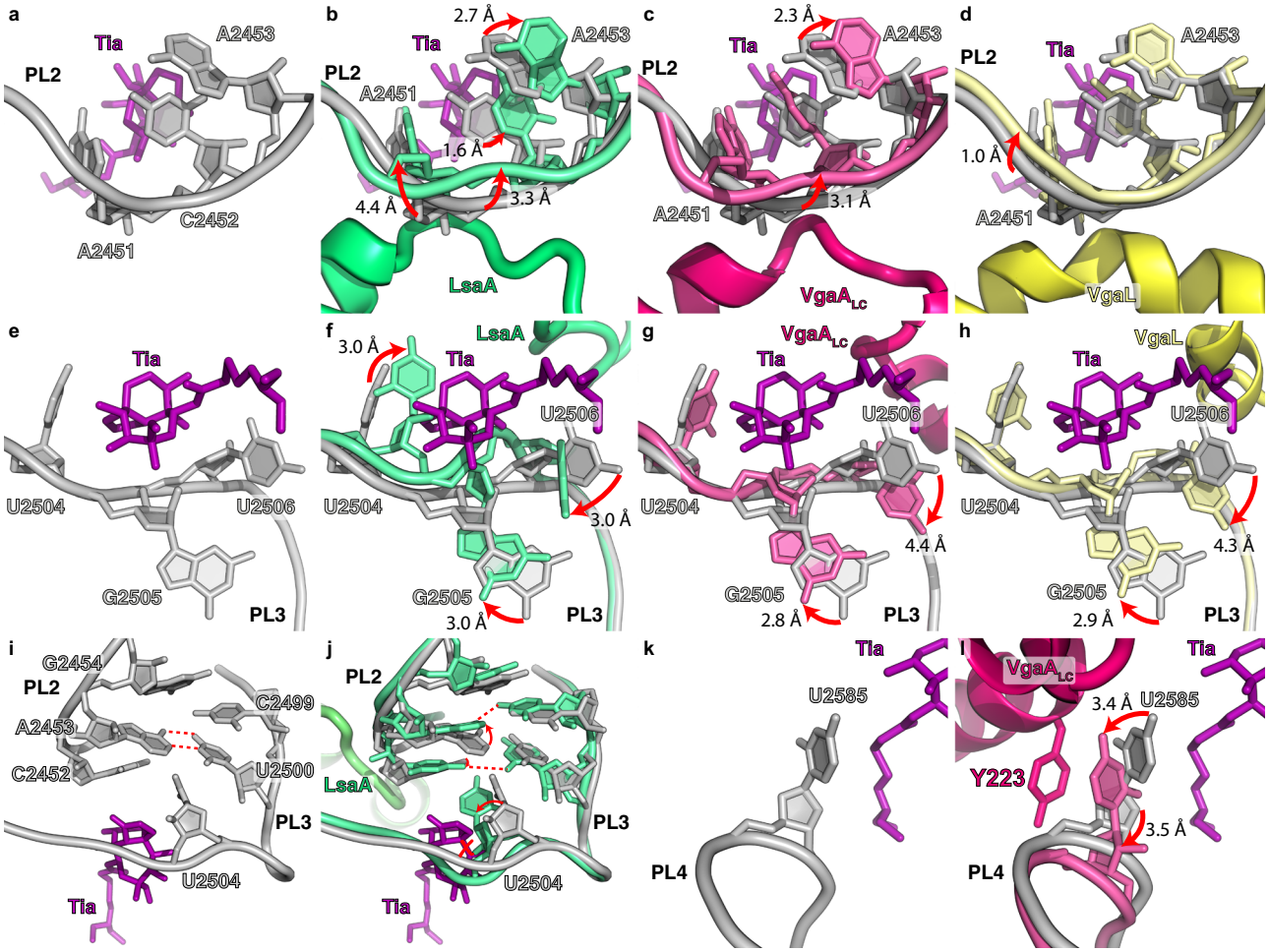

Fig. 6 Changes in the PTC induced by ARE-ABCF binding. a–d Effects of ARE binding on PL2 with respect to the tiamulin-binding site (PDB 1XBP)[2]. **a** The tiamulin-binding site only. **b–d** Same as **a** but with the LsaA- (**b**), $VgaA_{LC}$- (**c**), or VgaL-bound structure (**d**) superimposed. **e–h** Same as **a–d** but focused on PL3. **i**, **j** U2585 in the tiamulin site without (**i**) or with (**j**) $VgaA_{LC}$ superimposed. Tyrosine223 of $VgaA_{LC}$ is indicated. **k**, **l** Interaction between PL2 and PL3 contributing to the tiamulin-binding site, either without (**k**) or with (**l**) LsaA superimposed.

lincomycin (Supplementary Fig. 17). While the density for U2585 is not well-resolved in the LsaA- and VgaL-bound 70S structures, it appears nevertheless to adopt distinct conformations in the ARE-ABCFs compared to the drug-bound structures (Supplementary Fig. 17). By contrast, U2585 is clearly ordered in the $VgaA_{LC}$-70S structure where it stacks upon Tyr223 of $VgaA_{LC}$ (Fig. 6l) in a position that precludes interaction with tiamulin (Fig. 6k, l) or virginiamycin M (Supplementary Fig. 17). Substituting Tyr223 of $VgaA_{LC}$ to alanine diminished antibiotic resistance (Supplementary Table 2), indicating that the repositioning of U2585 is likely to contribute to antibiotic resistance conferred by this ARE-ABCF.

Discussion

Model of antibiotic resistance mediated by LsaA, $VgaA_{LC}$, and VgaL. Based on our findings and the available literature on ARE-ABCFs, we propose a model for how the ARE-ABCFs LsaA, $VgaA_{LC}$ and VgaL confer antibiotic resistance to their respective host organism (Fig. 7). PLS_A antibiotics have binding sites overlapping with the nascent polypeptide chain, and inhibit translation at, or soon after, initiation (Fig. 7a)[8–10]. As observed in our and previously reported structures[38,45], the incoming ARE-ABCFs bind in the E-site, triggering closure of the L1 stalk and inducing a distorted conformation of the P-tRNA. The ARD extends into the antibiotic-binding pocket at the PTC causing drug release. In LsaA and $VgaA_{LC}$, the changes to the drug-binding site are substantial, while for VgaL the changes are rather subtle, as observed in other instances of antibiotic resistance[64,65] (Fig. 7b). We observed subpopulations of ARE-ABCF-bound complexes containing A-tRNA, suggesting that an incoming ternary complex can still be delivered to the A-site, despite the distortion of the P-tRNA (Fig. 7c). However, we note that our complexes were stalled with EQ_2-variant AREs, and in a natural context the ARE may bind and dissociate prior to an A-tRNA accommodation attempt. We propose that upon dissociation of the ARE-ABCF from the ribosome, the 3′ end of the A- and P-tRNAs can re-accommodate at the PTC (Fig. 7d). The trigger for nucleotide hydrolysis and exit of the ARE-ABCF from the E-site is unknown. In our model, rapid peptidyl transfer then creates a short nascent chain that overlaps with the antibiotic-binding site, thus preventing re-binding of the PLS_A drug until the next round of translation (Fig. 7d). We cannot exclude the possibility that an A-tRNA may also partially accommodate on the stalled initiation complex prior to ARE-ABCF binding, and become distorted as part of a ‘knock-on’ effect of P-tRNA disruption, consistent with the ability of ARE-ABCFs to ‘reset’ the P-tRNA independently of additional accommodation events[56]. In this model, potentially only one round of ATP hydrolysis per translation cycle is

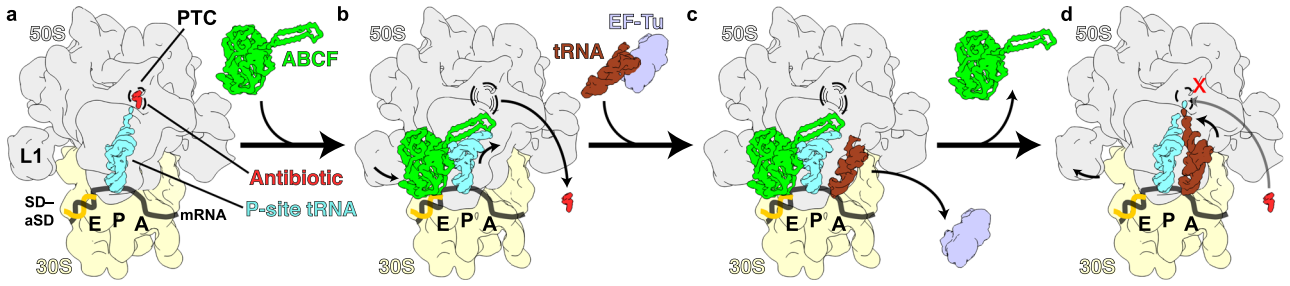

Fig. 7 Model for ribosome protection by ARE-ABCFs VmlR, LsaA, VgaA$_{LC}$ and VgaL. a PLS$_A$-stalled ribosomes containing an initiator tRNA in the P-site are recognized by the ARE-ABCFs such as VmlR, LsaA, VgaA$_{LC}$ and VgaL, which bind to the E-site of the ribosome with a closed ATP-bound conformation. **b** Binding of the ARE-ABCF induces a shifted P-site tRNA conformation in the ribosome allowing the ARD of the ARE-ABCF to access the peptidyl transferase centre (PTC). The ARD induces conformational changes within the 23S rRNA at the PTC that promotes dissociation of the drug from its binding site (shown as dashed lines). **c** Aminoacyl-tRNAs can still bind to the ARE-ABCF-bound ribosomal complex, but cannot accommodate at the PTC due to the presence of the ABCF and shifted P-site tRNA conformation. **d** Hydrolysis of ATP to ADP leads to dissociation of ARE-ABCF from the ribosome, which may allow the peptidyl-tRNA as well as the incoming aminoacyl-tRNA to simultaneously accommodate at the PTC. Peptide bond formation can then ensue, converting the ribosome from an initiation to an elongation (pre-translocation) state, which is resistant to the action of initiation inhibitors, such as PLS$_A$ antibiotics.

necessary to confer resistance. We can also not exclude that the P-tRNA dissociates following release of the ARE-ABCF and/or that other factors are involved in recycling of the post-antibiotic release complexes.

ARE-ABCFs such as LsaA, VgaA$_{LC}$, VgaL and VmlR confer resistance to PLS$_A$ antibiotics but not phenicols or oxazolidinones[25]. This observation has been puzzling, as both groups of antibiotics have overlapping binding sites[2–6]. However, phenicols and oxazolidinones inhibit translation during elongation at specific motifs[9,66], while PLS$_A$ antibiotics instead inhibit translation at the initiation stage[8–10]. This suggests that ARE-ABCFs such as LsaA, VgaA$_{LC}$, VgaL and VmlR are likely to be specific for initiation complexes, whereas ARE-ABCFs such as OptrA and PoxtA may have an additional specificity for drug-stalled elongation complexes. It will be interesting in the future to see how OptrA and PoxtA remove phenicols and oxazolidinones from the ribosome given the short ARD is not predicted to be able to reach into the PTC.

Another question is whether the EQ$_2$-substituted ATPase-deficient variants of ARE-ABCF, like the ones used in this study, bind the ribosome in the pre- or post-antibiotic-release state (Fig. 7b). Although direct evidence is lacking, three reasons lead us to propose that these proteins are bound in the post-antibiotic-release state:

1. In the case of LsaA, VgaA$_{LC}$ and VmlR the position of the ARD directly overlaps with the antibiotic-binding site. Although the side chain of the overlapping amino acid is not critical for antibiotic resistance in most instances, the overlap nonetheless implies mutually exclusive binding.
2. MsrE-EQ$_2$ stimulates dissociation of azithromycin from the ribosome[38].
3. Our attempts to form complexes containing both antibiotic and ARE-ABCF have been unsuccessful, resulting in exclusive binding of either the ARE-ABCF or the antibiotic, similarly to what we observed for TetM, a tetracycline-resistance ribosome protection protein[67].

How does the ARE-ABCF ARD mediate antibiotic resistance (Fig. 7b, c)? In one model, by analogy to the TetM tetracycline-resistance protein[11,68], the ARD may induce antibiotic dissociation by a direct steric overlap with the antibiotic. In the case of VmlR, substitutions of the Phe237 residue that overlaps the binding site of PLS$_A$ antibiotics affect resistance to one of three relevant antibiotics, indicating that both direct steric overlap and an indirect mechanism—for example, modulation of the antibiotic-binding site—can contribute to resistance[45]. In the case of MsrE substitution of Leu242, which overlaps with the erythromycin binding site, as well as adjacent residues abolished or severely reduced the antibiotic resistance activity of this protein[38]. In both cases, a mixture of direct steric overlap and indirect long-distance effects is consistent with the available data[24]. The ARDs of LsaA, VgaA$_{LC}$ and VgaL either do not directly overlap with the PLS$_A$-binding site, or where there is an overlap, as with LsaA Phe257 and VgaA$_{LC}$ Val219, the side chains are not essential for resistance, implicating an indirect mechanism for these proteins (Figs. 4–6, Supplementary Figs. 14–16 and Supplementary Table 2). Alanine mutagenesis instead indicates that the side chains of residues surrounding the amino acid closest to the antibiotic-binding pocket, as well as those that contact the 23S rRNA, are necessary for resistance (Fig. 5c, Supplementary Figs. 11 and 12 and Supplementary Table 2). These residues may position the ARD in the PTC. No single set of 23S rRNA rearrangements was identical among LsaA, VgaA$_{LC}$ and VgaL, although displacement of PTC loops PL2 and PL3, especially residue U2504, was ultimately observed in each ARE-ABCF-70S structure (Fig. 6). Broadly, changes to the PTC were similar between the VgaA$_{LC}$- and VgaL-bound 70S structures (Fig. 5g–i and Supplementary Figs. 14–16), consistent with the grouping of these proteins together in the ARE1 subfamily[20]. While structures of the same or similar antibiotic bound to ribosomes from different species are generally similar, we cannot completely exclude that some differences in nucleotide conformations arise because of comparing our ARE-ABCF-bound PTC conformations with antibiotic-ribosome structures from different species, for example, *E. coli* for VgM[61] and *D. radiodurans* for tiamulin[2]. Similarly, some conformational variability can also arise due to limitations in resolution of some of the antibiotic structures, such as the tiamulin-50S structure that was reported at 3.5 Å[2] and the *S. aureus* lincomycin-50S structure at 3.7 Å[6]. A future goal could be to determine higher resolution structures of the antibiotic-stalled ribosomal complexes prior to ARE-ABCF binding and from the same organisms as the ARE-ABCF.

In summary, we present three structures of ARE-ABCFs bound to 70S ribosomes from relevant Gram-positive pathogenic bacteria and present the model of the ribosome from *Listeria monocytogenes*. Our structures and mutagenesis experiments support an indirect mechanism of ARE-ABCF action, in which a conformational selection in the PTC, elicited by ARE binding to the ribosome, leads to antibiotic egress, and hint at a

rationalization for the specificity of LsaA, $VgaA_{LC}$ and VgaL for PLS_A antibiotics. Each ARE-ABCF binds the 70S similarly as observed for other bacterial ABCF proteins, but alters the geometry of the PTC distinctively, consistent with the convergent evolution—and divergent sequences—of this class of ABCF proteins.

Methods

Strains and plasmids. All strains and plasmids used in this work are listed in Table S5. Primers are listed in Table S6.

E. faecalis. OG1RF and TX5332, a LsaA disruption mutant of OG1RF[30], were kindly provided by Dr. Barbara E. Murray (Health Science Center, University of Texas). All cloning was performed by Protein Expertise Platform at Umeå University. *E. faecalis* LsaA ORF was PCR amplified from pTEX5333 plasmid and cloned into pCIE vector[69] for cCF10-induced expression. The LsaA ORF was supplemented with C-terminal His_6-TEV-$FLAG_3$-tag (HTF tag) and the ribosome-binding site was optimized for high expression yield. Point mutations $E_{142}Q$ and $E_{452}Q$ were introduced to LsaA resulting in pCIE_LsaA-EQ_2-HTF.

S. haemolyticus. *vga(A)$_{LC}$* gene was PCR-amplified from a *S. haemolyticus* isolate held in the O'Neill strain collection at the University of Leeds, using oligonucleotide primers $vgaA_{LC}$-F (5′-GGTGGTGGTACCAGGATGAGGAAATATGA AAA-3′) and $vgaA_{LC}$-R (5′-GGTGGTGAATTCGGTAATTTATTTATCTAAA TTTCTT-3′) (engineered restriction sites shown underlined). The protein encoded by this gene is identical to that previously reported[50] (accession number DQ823382). The fragment was digested with *Kpn*I and *Eco*RI and ligated into the tetracycline-inducible expression vector pRMC2 (ref. [70]). Constructs encoding the $VgaA_{LC}$ protein fused with a C-terminal $FLAG_3$ tag were obtained by synthesis (Genewiz), with $E_{105}Q$, $E_{410}Q$ and EQ_2 mutants subsequently created by site-directed mutagenesis. Generation of other point mutants of untagged $Vga(A)_{LC}$ was performed by NBS Biologicals, again using chemical synthesis to generate the original *vga(A)$_{LC}$* template, followed by site-directed mutagenesis.

L. monocytogenes. VgaL (Lmo0919). In order to construct *L. monocytogenes* EGDe::Δ*lmo0919*, regions corresponding to the upstream and downstream flanking regions of *lmo0919*, present on the EGDe genome were amplified with primer pairs VKT35 (5′-GGGGGGATCCATCACTAGCCGAATCCAAAC-3′), VKT36 (5′-ggg ggaattcaaaaaataacctcctgaatattttcagag-3′) and VHKT37 (5′-GGGGGAATTCAAAA AATAACCTCCTGAATATTTTCAGAG-3′), VHKT38 (5′-GGGGCCATGGCG TGCTGTACGGTATGC-3′), respectively. Fragments were then cloned in tandem into the pMAD vector using *Bam*HI, *Eco*RI and *Nco*RI restriction sites. The resulting vector, VHp689, was then sequenced to ensure wild-type sequences of clones. Gene deletion was then performed as per Arnaud et al.[71].

lmo0919 was amplified from EGDe genomic DNA using primers VHKT12 (5′-CCCCCCATGGCATCTACAATCGAAATAAATC-3′) and VHKT39 (5′-GGGGCTGCAGTTAACTAAATTGCTGTCTTTTTG-3′), and cloned into pIMK3 using *Nco*I and *Pst*I restriction sites, resulting in plasmid VHp690.

Overlap extension PCR was used in order to introduce a HTF tag at the C-terminus of *lmo0919* (ref. [72]). The *lmo0919* locus and HTF tag were amplified with primer pairs VHKT12, VHKT15 (5′-ATGATGATGGCCGCCACTAAATTGCT GTCTTTTTG-3′) and VHKT14 (5′-AGACAGCAATTTAGTGGCGGCCATC ATCATCATC-3′), VHKT13 (5′-GGGGCTGCAGTTAGCCTTTGTCATCGTC-3′) using EGDe genomic DNA and VHp100 template DNA, respectively, producing fragments with overlapping ends. VHKT12 and VHKT13 were then used to fuse the fragments and the resulting PCR product was cloned into pIMK3 using *Nco*I and *Pst*I sites resulting in VHp692.

To introduce two EQ mutations (E104Q and E408Q) simultaneously into the VHp692 plasmid, primers VHT266 (5′-TCTTGATCAACCAACCAACTATTTGG ATATCTACGCAATGGAA-3′) and VHT267 (5′-TTGTTGGTTGGTCTGCTAG GAGAACACTTGGATTTTGGCGCA-3′) containing both mutations were used to extend out from *lmo0919^{HTF}* to amplify the VHp692 backbone. Primers VHT264 (5′-AGCAGACCAACCAACAAGCAATCTTGATGTCG-3′) and VHT265 (5′-TG GTTGGTTGATCAAGAATCAAGAAATTGGCGT-3′) also containing *lmo0919^{EQ2}* mutations were used to amplify a fragment with overlapping sequence to the backbone fragment. Both PCR products were then assembled using NEBuilder® HiFi DNA Assembly Master Mix (NEB), resulting in VHp693.

B. subtilis. To construct the VHB109 [*trpC2 ΔvmlR* thrC::$P_{hy\text{-}spnak}$-*lsaA kmR*] strain untagged LsaA under the control of an IPTG-inducible $P_{hy\text{-}spank}$ promotor, a PCR product encoding lsa(A) was PCR-amplified from pTEX5333 using the primers VHT127 (5′-CGACGAAGGAGAGAGCGATAATGTCGAAAATTGAACTAA AACAACTATC-3′) and VHT128 (5′-CACCGAATTAGCTTGCATGCTTATGA TTTCAAGACAATTTTTTTATCTGTTA-3′). The second PCR fragment encoding a kanamycin-resistance marker, a polylinker downstream of the Phy-spank promoter and the lac repressor ORF—all inserted in the middle of the thrC gene—was PCR-amplified from pHT009 plasmid using primers VHT123 (5′-CATTATC GCTCTCTCCTTCGTCGACTAAGCTAATTG-3′) and VHT125 (5′-TAAGCA TGCAAGCTAATTCGGTGGAAACGAGG-3′). The two fragments were ligated using the NEBuilder HiFi DNA Assembly master mix (New England BioLabs, Ipswich, MA) yielding the pHT009-lsaA plasmid (VHp369) which was used to transform the VHB5 [*trpC2 ΔvmlR*] strain. Selection for kanamycin resistance yielded the desired VHB109 strain. To construct the VHB168 [*trpC2 ΔvmlR* thrC::$P_{hy\text{-}spnak}$-*lsaAK244A kmR*] strain, VHp369 plasmid was subjected to site-directed mutagenesis using primer VHP303 (5′-GCATCACCTTCACGGTTCATCGACC ATTCCGCT-3′) and VHP304 (5′-GTACGGCAACGCTAAGGAAAAAGGGA GCGGGGCGA-3′), according to the directions of Phusion Site-Directed Mutagenesis Kit (Thermo Fisher Scientific), yielding VHp526 (pHT009-*lsaAK244A*) plasmid which was used to transform the VHB5 [*trpC2 ΔvmlR*] strain. Selection for kanamycin resistance yielded the desired VHB168 strain. To construct the VHB169 [*trpC2 ΔvmlR thrC*::$P_{hy\text{-}spnak}$-*lsaAF257A kmR*] strain, VHp369 plasmid was subjected to site-directed mutagenesis using primer VHP305 (5′-CAATCGCCCCGC TCCCTTTTTCCTTAGCGT-3′) and VHP306 (5′-CGGATACAGGAGCCATT GGTGCCCGGGCA-3′), according to the directions of Phusion Site-Directed Mutagenesis Kit (Thermo Fisher Scientific), yielding, yielding VHp527 (pHT009-*lsaAF257A*) plasmid which was used to transform the VHB5 [*trpC2 ΔvmlR*] strain. Selection for kanamycin resistance yielded the desired VHB169 strain.

Bacterial transformation

E. faecalis. Electrocompetent cells were prepared as per Bhardwaj et al.[73]. In short, an overnight culture grown in the presence of appropriate antibiotics was diluted to OD_{600} of 0.05 in 50 mL of BHI media (supplemented with 2 mg/mL kanamycin in case of TX5332), grown to OD_{600} of 0.6–0.7 at 37 °C with moderate shaking (160 r.p.m.). Cells were collected by centrifugation at 3200 × *g* at 4 °C for 10 min. Cells were resuspended in 0.5 mL of sterile lysozyme buffer (10 mM Tris-HCl pH 8; 50 mM NaCl, 10 mM EDTA, 35 μg/mL lysozyme), transferred to 1.5 mL Eppendorf tube and incubated at 37 °C for 30 min. Cells were pelleted at 8700 × *g* at 4 °C for 10 min and washed three times with 1.5 mL of ice-cold electroporation buffer (0.5 M sucrose, 10% glycerol(w/v)). After last wash the cells were resuspended in 500 μL of ice-cold electroporation buffer and aliquoted and stored at −80 °C. For electroporation 35 μL of electrocompetent cells were supplemented with 1 μg of plasmid DNA, transferred to ice-cold 1 mm electroporation cuvette and electroporated at 1.8 keV. Immediately after electroporation 1 mL of ice-cold BHI was added to the cells, the content of the cuvette was transferred to 1.5 mL Eppendorf tubes and the cells were recovered at 37 °C for 2.5 h and plated onto BHI plates containing appropriate antibiotics (10 μg/mL chloramphenicol and 2 mg/mL kanamycin).

S. aureus. Preparation and transformation of *S. aureus* electrocompetent cells followed the method of Schenk and Laddaga[74], though used TSBY (Tryptone soya broth [Oxoid] containing 2.5% yeast extract) in place of B2 medium. Briefly, bacteria were grown with vigorous aeration in TSBY to an OD_{600} of 0.6, harvested by centrifugation, and washed three times in an equal volume of sterile, deionized water. Subsequent wash steps used decreasing volumes of 10% glycerol; first 1/5 the original culture volume, then 1/10, finally resuspending in ~1/32 volume and storing the resultant electrocompetent cells at −80 °C. For electroporation, 60 μL of electrocompetent cells were mixed with ≧1 μg of plasmid DNA in a 1 mm electroporation cuvette at room temperature and pulsed at 2.3 kV, 100 Ω, 25 μFD. Immediately after electroporation, 390 μL room temperature TSBY was added to the cells and incubated with aeration at 37 °C for 1–2 h, before plating onto tryptone soya agar with appropriate antibiotic selection. Using this method, sequence-verified constructs established in *E. coli* were first transferred into the restriction deficient *S. aureus* RN4220 strain[75], before recovery and introduction into *S. aureus* SH1000 (refs. [76,77]).

L. monocytogenes. *L. monocytogenes* EGD-e was transformed with pIMK3 integrative plasmids via conjugation. *E. coli* S17.1 harbouring pIMK3 and its derivatives was grown at 37 °C overnight in LB media supplemented with 50 μg/mL kanamycin; 1 mL of culture was washed three times with sterile BHI media to remove antibiotics. Two hundred microliters of washed *E. coli* culture was mixed with an equal volume of *L. monocytogenes* overnight culture grown at 37 °C in BHI media. Two hundred microliters of mixed bacterial suspension was then dropped onto a conjugation filter (Millipore #HAEP047S0) placed onto a BHI agar plate containing 0.2 μg/mL penicillin-G. After overnight incubation at 37 °C, bacterial growth from the filter was resuspended in 1 mL of BHI and 100–300 μL plated onto BHI agar plates supplemented with 50 μg/mL kanamycin (to select for pIMK3), 50 μg/mL nalidixic acid and 10 μg/mL colistin sulfate (Sigma-Aldrich C4461-100MG). Resulting colonies were checked for correct integration via PCR and subsequent sequencing using primers VHKT42 and VHKT43.

Antibiotic susceptibility testing. Minimum inhibitory concentrations (MIC) were determined based on guidelines from the European Committee on Antimicrobial Susceptibility Testing (EUCAST) (http://www.eucast.org/ast_of_bacteria/mic_determination).

E. faecalis. Bacteria were grown in BHI media supplemented with 2 mg/mL kanamycin (to prevent *lsa* revertants), 0.1 mg/mL spectinomycin (to maintain the $pCIE_{spec}$ plasmid), 100 ng/mL of cCF10 peptide (to induce expression of LsaA

protein) as well as increasing concentrations of antibiotics was inoculated with 5×10^5 CFU/mL (OD_{600} of approximately 0.0005) of *E. faecalis* Δ*lsaA* (*lsa*::*Kan*) strain TX5332 transformed either with empty $pCIE_{spec}$ plasmid or with $pCIE_{spec}$ encoding LsaA. After 16–20 h at 37 °C without shaking, the presence or absence of bacterial growth was scored by eye.

S. aureus. Bacteria were grown in cation-adjusted Mueller-Hinton Broth (MHB) at 37 °C with vigorous aeration, supplemented with 10 mg/L chloramphenicol to maintain the pRMC2 plasmid. Upon reaching an absorbance of OD_{625} of 0.6, anhydrotetracycline (ATC) (Sigma-Aldrich, UK) was added at a final concentration of 100 ng/mL to induce expression from pRMC2, and incubated for a further 3 h. Cultures were then diluted to 5×10^5 CFU/mL using MHB supplemented with ATC (100 ng/mL) and used in MIC determinations essentially as described above (though cultures were shaken).

L. monocytogenes. Bacteria were grown in BHI media supplemented with 50 µg/mL kanamycin (to prevent loss of the integrated pIMK3 plasmid), 1 mM of IPTG (to induce expression of VgaL protein) as well as increasing concentrations of antibiotics was inoculated with 5×10^5 CFU/mL (OD_{600} of approximately 0.0003) of *L. monocytogenes* EGD-e wild-type strain or EGD-e::Δ*lmo0919* strain transformed either with empty pIMK3 plasmid or with pIMK3 encoding VgaL variants. After 16–20 h at 37 °C without shaking, the presence or absence of bacterial growth was scored by eye.

B. subtilis (for LsaA mutants). *B. subtilis* strains were pre-grown on LB plates supplemented with 1 mM IPTG overnight at 30 °C. Fresh individual colonies were used to inoculate filtered LB medium in the presence of 1 mM IPTG, and OD_{600} adjusted to 0.01. The cultures were seeded on a 100-well honeycomb plate (Oy Growth Curves AB Ltd, Helsinki, Finland), and plates incubated in a Bioscreen C (Labsystems, Helsinki, Finland) at 37 °C with continuous medium shaking. After 90 min ($OD_{600} \approx 0.1$), antibiotics were added and growth was followed for an additional 6 h.

Preparation of bacterial lysates

Preparation of bacterial biomass. *E. faecalis*: *E. faecalis* TX5332 transformed with pCIE plasmids (either empty vector and expressing either wild type or EQ_2 variants of C-terminally HTF-tagged LsaA) were grown overnight from single colony in BHI supplemented with 2 mg/mL kanamycin and 10 µg/mL of chloramphenicol. Next day overnight cultures were diluted to starting OD_{600} of 0.05 in 160 mL BHI supplemented with 0.5 mg/mL kanamycin and 10 µg/mL of chloramphenicol. Cells were grown with intensive shaking at 37 °C till OD_{600} of 0.6 and were induced with 300 ng/mL of cCF10 peptide for 30 min prior harvesting by centrifugation at 10,000 × *g* for 15 min at 4 °C.

S. aureus: *S. aureus* SH1000 transformed with pRMC2 plasmids (empty vector, wild type and EQ_2 $VgaA_{LC}$-$FLAG_3$) were grown in LB supplemented with 25 µg/mL of chloramphenicol. Saturated cultures were diluted to an OD_{600} of 0.1 in 400 mL LB supplemented with 20 µg/mL of chloramphenicol and grown at 37 °C with vigorous aeration to an OD_{600} of 0.6. Protein expression was induced with 100 ng/mL of anhydrotetracycline for 30 min prior to harvesting by centrifugation at 10 000 × *g* for 15 min at 4 °C.

L. monocytogenes: *L. monocytogenes* EGD-e was transformed with pIMK3 plasmids (empty vector, wild type and EQ_2 VgaL-HTF) were grown overnight from single colony in LB supplemented with 50 µg/mL of kanamycin. Next day overnight cultures were diluted till starting OD_{600} of 0.005 in 200 mL BHI supplemented with 50 µg/mL of kanamycin. Cells were grown at 37 °C with shaking at 160 r.p.m. till OD_{600} of 0.6 and were induced with 1 mM IPTG for 60 min prior harvesting by centrifugation at 10,000 × *g* for 15 min at 4 °C.

Preparation of clarified lysates. Cell pellets were resuspended in 1.5 mL of cell lysis buffer (95 mM KCl, 5 mM NH_4Cl, 20 mM HEPES pH 7.5, 1 mM DTT, 5 mM Mg $(OAc)_2$, 0.5 mM $CaCl_2$, 8 mM putrescine, 1 mM spermidine, 1 tablet of cOmplete™ EDTA-free Protease Inhibitor Cocktail (Roche) per 10 mL of buffer and in the absence or presence of either 0.5 or 0.75 mM ATP), resuspended cells were opened by a FastPrep homogeniser (MP Biomedicals) with 0.1 mm zirconium beads (Techtum) in four cycles by 20 s with 1 min chill on ice. Cell debris was removed after centrifugation at 14,800 × *g* for 15 min at 4 °C. Total protein concentration in supernatant was measured by Bradford assay (Bio-Rad), supernatant was aliquoted and frozen in liquid nitrogen.

Polysome fractionation and immunoblotting

Sucrose density gradient centrifugation. After melting the frozen lysates on ice, 2 A_{260} units of each extract was aliquoted into three tubes and supplemented with or without 0.5–0.75 mM ATP and was loaded onto 5–25 or 7–35% (w/v) sucrose density gradients in HEPES:Polymix buffer[78], 5 mM $Mg(OAc)_2$ and supplemented or not with 0.5–0.75 mM ATP. Gradients were resolved at 245,000 × *g* for 2.5 h at 4 °C in an SW41 rotor (Beckman) and analysed and fractionated using Biocomp Gradient Station (BioComp Instruments) with A_{280} as a readout.

Immunoblotting. LsaA and $VgaA_{LC}$: Schleicher & Schuell Minifold II Slot Blot System SRC072/0 44-27570 manifold was used for transferring samples from sucrose gradient fractions to PVDF membranes (Immobilon PSQ, Merck Millipore). Shortly, 15–100 µL of each sucrose gradient fraction was added to 200 µL of slot-blotting buffer (20 mM HEPES:KOH pH 7.5, 95 mM KCl, 5 mM NH_4Cl, 5 mM $Mg(OAc)_2$) in slots and blotted onto PVDF membrane that had been activated with methanol for 1 min, wetted in MilliQ water and equilibrated with Slot-blotting Buffer (1c PM 5 mM Mg^{2+} without putrescine and spermidine) for 10 min. After blotting of the samples each slot was washed twice with 200 µL of Slot-blotting Buffer. The membrane was removed from the blotter, transferred to hybridization bottle, equilibrated for 10 min in PBS-T (1× PBS supplemented with 0.05% Tween-20) and blocked in PBS-T supplemented with 5% w/v nonfat dry milk for 1 h. Antibody incubations were performed for 1 h in 1% nonfat dry milk in PBS-T with five 5-min washes in fresh PBS-T between and after antibody incubations. HTF-tagged LsaA and $FLAG_3$-tagged $VgaA_{LC}$ proteins were detected using anti-Flag M2 primary (Sigma-Aldrich, F1804; 1:10,000 dilution) antibodies combined with anti-mouse-HRP secondary (Rockland; 610-103-040; 1:10,000 dilution) antibodies. An ECL detection was performed on ImageQuant LAS 4000 (GE Healthcare) imaging system using Pierce® ECL western blotting substrate (Thermo Scientific). The blotting and all incubations were performed at room temperature in a hybridization oven.

VgaL (Lmo0919): Western blotting of lysates on sucrose gradient fractionation was performed as previously described[78]. In all, 1.5 mL of 99.5% ethanol was added to each 0.5 mL sucrose fraction and precipitated at −20 °C overnight. Samples were then pelleted via centrifugation for 30 min at 14,800 × *g*, air dried and resuspended in 2× SDS loading buffer (100 mM Tris-HCl pH 6.8, 4% SDS w/v, 0.02% bromophenol blue, 20% glycerol (w/v), 4% β-mercaptoethanol). Samples were resolved on a 12% SDS-PAGE gel and transferred to a nitrocellulose membrane (pore size 0.2 µM, BioTrace™ NT) using the Bio-Rad Trans-Blot Turbo Transfer apparatus (30 min, 1 A, 25 V). The membrane was then blocked for 1 h at room temperature in PBS-T (1× PBS, 0.05% Tween-20) with 5% (w/v) nonfat dry milk. VgaL-HTF was then detected using anti-Flag M2 primary antibodies as described above for Lsa and $VgaA_{LC}$. VgaL-HTF was detected using anti-Flag M2 primary (Sigma-Aldrich, F1804; 1:10,000 dilution) antibodies combined with anti-mouse-HRP secondary (Rockland; 610-103-040; 1:10,000 dilution) antibodies.

Affinity purification on anti-FLAG M2 affinity gel. One hundred microlitres of well mixed anti-FLAG M2 Affinity Gel aliquots were loaded on columns (Micro Bio-Spin Columns, Bio-Rad) and washed two times with 1 mL of cell lysis buffer by gravity flow. All incubations, washings and elutions were done at 4 °C.

The total protein concentration of each lysate was adjusted to 2 mg/mL with cell lysis buffer and 1 mL of each lysate was loaded on columns and incubated for 2 h with end-over-end mixing for binding. The columns were washed five times by 1 mL of cell lysis buffer by gravity flow. For elution of FLAG-tagged proteins and their complexes 100–300 µL of 0.1 mg/mL $FLAG_3$ peptide (Sigma) was added to samples, the solutions were incubated at 4 °C for 20 min with end-over-end mixing. Elutions were collected by centrifugation at 2000 × *g* for 2 min at 4 °C.

Twenty microlitre-aliquots of collected samples (flow-through, washes and elutions) were mixed with 5 µL of 5× SDS loading buffer and heated up at 95 °C for 15 min. The beads remaining in the column were washed twice with 1 mL of cell lysis buffer and resuspended in 100 µL of 1× SDS loading buffer. Denatured samples were resolved on 12–15% SDS-PAGE. SDS-gels were stained by Blue-Silver Coomassie Staining[79] and washed with water for 6 h or overnight before imaging with LAS 4000 (GE Healthcare).

tRNA microarrays. To fully deacylate tRNAs, eluates and input lysate samples from two biological replicates were mixed with 80 µL 250 mM Tris-HCl, pH 9.0, 10 µL 0.2 M EDTA, 10 µL 1% SDS, and incubated for 45 min, and neutralized with 200 µL 1 M NaOAc, pH 5.5, before mixing 1:1 with acidic phenol:chloroform alcohol 5:1. The supernatant was precipitated with ethanol and dissolved in ddH_2O.

tRNA microarrays were performed as described[80]. Briefly, using the unique invariant single-stranded 3′-NCCA-ends of intact tRNA a Cy3-labelled or Atto647-labelled RNA/DNA hybrid oligonucleotide was ligated to the tRNA extracted from the ARE-immunoprecipitated samples and total *E. faecalis* tRNA (from the lysate), respectively. Labelled tRNA was purified by phenol:chloroform extraction and loaded on a microarray containing 24 replicates of full-length tDNA probes recognizing *E. faecalis* tRNA isoacceptors. Fluorescence signals were normalized to four in vitro-transcribed human tRNAs, spiked into each sample. Microarrays were statistically analysed with in-house scripts written in Python 3.7.0. Data are available at the Gene Expression Omnibus under accession GSE 162168.

Grid preparation, cryo-electron microscopy and single-particle reconstruction

Preparation of cryo-EM grids and data collection. Elutions from LsaA and VgaL pull-downs were loaded on grids within 2 h after obtaining them without freezing, samples were kept on ice. The $VgaA_{LC}$ sample was frozen in liquid nitrogen after pull-down, defrosted and loaded later. After glow-discharging of grids, 3.5 µL of sample was loaded on grids in Vitrobot (FEI) in conditions of 100% humidity at 4 °C, blotted for 5 s and vitrified by plunge-freezing in liquid ethane. Samples were

imaged on a Titan Krios (FEI) operated at 300 kV at a nominal magnification of ×130k (LsaA) or ×165k ($VgaA_{LC}$ and VgaL, 1.09 Å/pixel and 0.86 Å/pixel, respectively, later estimated to be 1.041 and 0.82 Å/pixel, respectively, by comparing refined maps to structures with known magnification) with a Gatan K2 Summit camera at an exposure rate of 5.80 electrons/pixel/s with a 4 s exposure and 40 frames (LsaA), or 20 frames ($VgaA_{LC}$ and VgaL) using the EPU software. Quantifoil 1.2/1.3 Cu_{200} grids were used for LsaA and $VgaA_{LC}$ and Quantifoil 2/2 Cu_{200} grids were used for VgaL.

Single-particle reconstruction. Motion correction was performed with MotionCor2 with 5 × 5 patches[81]. Relion 3.0 or 3.1 was used for further processing unless otherwise stated and resolutions are reported according to the so-called 'gold standard' criteria[82–84]. CTFFIND4 (LsaA dataset) or Gctf v1.06 ($VgaA_{LC}$ and VgaL datasets) was used for CTF estimation[85,86]. Particles were picked with Gautomatch (https://www2.mrc-lmb.cam.ac.uk/research/locally-developed-software/zhang-software/#gauto, developed by K. Zhang) without supplying a reference, and in the case of LsaA, re-picked using RELION autopicker after templates were generated by 2D classification. Particles were initially extracted at three times the original pixel size and subjected to 2D classification. Classes that resembled ribosomes were used for 3D refinement, with a 60 Å low-pass filter applied to initial references. For 3D refinement of LsaA-70S, the initial reference was EMDB-0176, a *B. subtilis* 70S ribosome with no factor bound in the E-site[45]; for $VgaA_{LC}$-70S and VgaL-70S 3D refinements the RELION initial model job type was used to create a reference from particles selected after 2D classification. 3D classification was performed without angular sampling, and classes of interest were re-extracted at 1.041 Å/pixel (LsaA) or 0.82 Å/pixel ($VgaA_{LC}$ and VgaL) for further refinement.

In the case of LsaA, after initial 3D classification, a soft mask around the A-site was used for partial signal subtraction followed by focussed classification. The classes with the strongest and weakest A-site density were selected for signal restoration and refinement. In the case of the $VgaA_{LC}$ dataset, initial 3D classification yielded a class with apparent sub-stoichiometric density in the E-site corresponding to $VgaA_{LC}$. Micrographs with poor values from CTF estimation were discarded, particles were re-extracted, subjected to an additional 2D classification and 3D refinement, followed by Bayesian polishing and CTF refinement. An additional 3D classification yielded a class with strong E-site density corresponding to the factor. Refer to Supplementary Figs. 4–6 for details.

For multibody refinements, soft masks around the small subunit body, small subunit head, and large subunit/ARD were applied. In the case of the $VgaA_{LC}$ dataset, particles were first re-extracted in a smaller box (360 × 360 pixels) and subjected to 3D refinement prior to multibody refinement.

ResMap was used to estimate local resolution[87]. Maps were locally filtered using SPHIRE[88].

Molecular modelling. For the *E. faecalis* and *L. monocytogenes* ribosomes, homology models were generated with SWISS-MODEL[89], mostly from PDB 6HA1/6HA8 (ref. [45]). PDBs 4YBB[90] 5MDV[91] were used as additional templates and references where necessary, 4V9O[92] was used for bS21, 7K00 (ref. [93]) for bL31, 5ML7 (ref. [94]) and 3U4M[95] were used for the L1 stalk region, 5AFI[96] and 5UYQ[97] were used for tRNAs, and 6QNQ was used to help tentatively place metal ions[98]. PDB 5LI0 (ref. [57]) was used as a starting model for the *S. aureus* ribosome. Where appropriate, individual components of multibody refinements were fitted into density from the corresponding locally filtered map to help modelling. Models were adjusted with Coot[99] and refined using locally filtered maps in Phenix version dev-2947-000 (ref. [100]).

Figures were created with PyMOL 2.0 (Schrödinger, LLC), UCSF Chimera[101], UCSF ChimeraX[102], RELION[82], and Igor Pro (WaveMetrics, Inc.). Structures were aligned in PyMOL using the 23S rRNA unless otherwise noted. Subunit rotation was visualized in PyMOL using the modevectors script, which was initially developed by Sean Law and modified by others, and the rotation angle measured using the draw_axis script, made by Pablo Guardado Calvo.

Figures were assembled with Adobe Illustrator (Adobe Inc.).

Reporting summary. Further information on research design is available in the Nature Research Reporting Summary linked to this article.

Data availability

Micrographs have been deposited as uncorrected frames in the Electron Microscopy Public Image Archive (EMPIAR) with the accession codes EMPIAR-10682 (LsaA immunoprecipitation), EMPIAR-10683 ($VgaA_{LC}$ immunoprecipitation), and EMPIAR-10684 (VgaL immunoprecipitation). Cryo-EM maps have been deposited in the Electron Microscopy Data Bank (EMDB) with accession codes EMD-12331 (LsaA-70S), EMD-12332 ($VgaA_{LC}$-70S), EMD-12333 (*S. aureus* 70S with P-tRNA from $VgaA_{LC}$ immunoprecipitation) and EMD-12334 (VgaL-70S). Molecular models have been deposited in the Protein Data Bank with accession codes 7NHK (LsaA-70S), 7NHL ($VgaA_{LC}$-70S), 7NHM (*S. aureus* 70S with P-tRNA from $VgaA_{LC}$ immunoprecipitation) and 7NHN (VgaL-70S). Microarray data have been deposited in Gene Expression Omnibus under accession GSE 162168. Scripts for analysing microarray data are available upon request to C.P. and Z.I. Source data are provided with this paper.

Received: 4 February 2021; Accepted: 11 May 2021;
Published online: 11 June 2021

References

1. Wilson, D. N. Ribosome-targeting antibiotics and mechanisms of bacterial resistance. *Nat. Rev. Microbiol.* **12**, 35–48 (2014).
2. Schlünzen, F., Pyetan, E., Fucini, P., Yonath, A. & Harms, J. M. Inhibition of peptide bond formation by pleuromutilins: the structure of the 50S ribosomal subunit from *Deinococcus radiodurans* in complex with tiamulin. *Mol. Microbiol.* **54**, 1287–1294 (2004).
3. Tu, D., Blaha, G., Moore, P. B. & Steitz, T. A. Structures of MLS_BK antibiotics bound to mutated large ribosomal subunits provide a structural explanation for resistance. *Cell* **121**, 257–270 (2005).
4. Wilson, D. N. et al. The oxazolidinone antibiotics perturb the ribosomal peptidyl-transferase center and effect tRNA positioning. *Proc. Natl Acad. Sci. USA* **105**, 13339–13344 (2008).
5. Dunkle, J. A., Xiong, L., Mankin, A. S. & Cate, J. H. Structures of the *Escherichia coli* ribosome with antibiotics bound near the peptidyl transferase center explain spectra of drug action. *Proc. Natl Acad. Sci. USA* **107**, 17152–17157 (2010).
6. Matzov, D. et al. Structural insights of lincosamides targeting the ribosome of *Staphylococcus aureus*. *Nucleic Acids Res.* **45**, 10284–10292 (2017).
7. Vázquez-Laslop, N. & Mankin, A. S. How macrolide antibiotics work. *Trends Biochem. Sci.* **43**, 668–684 (2018).
8. Meydan, S. et al. Retapamulin-assisted ribosome profiling reveals the alternative bacterial proteome. *Mol. Cell* **74**, 481–493 (2019).
9. Orelle, C. et al. Tools for characterizing bacterial protein synthesis inhibitors. *Antimicrob. Agent Chemother.* **57**, 5994–6004 (2013).
10. Dornhelm, P. & Högenauer, G. The effects of tiamulin, a semisynthetic pleuromutilin derivative, on bacterial polypeptide chain initiation. *Eur. J. Biochem.* **91**, 465–473 (1978).
11. Wilson, D. N., Hauryliuk, V., Atkinson, G. C. & O'Neill, A. J. Target protection as a key antibiotic resistance mechanism. *Nat. Rev. Microbiol.* **18**, 637–648 (2020).
12. Rees, D. C., Johnson, E. & Lewinson, O. ABC transporters: the power to change. *Nat. Rev. Mol. Cell Biol.* **10**, 218–227 (2009).
13. Krishnan, A., Burroughs, A. M., Iyer, L. M. & Aravind, L. Comprehensive classification of ABC ATPases and their functional radiation in nucleoprotein dynamics and biological conflict systems. *Nucleic Acids Res.* **48**, 10045–10075 (2020).
14. Thomas, C. & Tampé, R. Structural and mechanistic principles of ABC transporters. *Ann. Rev. Biochem.* **89**, 605–636 (2020).
15. Fostier, C. R. et al. ABC-F translation factors: from antibiotic resistance to immune response. *FEBS Lett.* **595**, 675–706 (2021).
16. Gerovac, M. & Tampé, R. Control of mRNA translation by versatile ATP-driven machines. *Trends Biochem. Sci.* **44**, 167–180 (2019).
17. Davidson, A. L., Dassa, E., Orelle, C. & Chen, J. Structure, function, and evolution of bacterial ATP-binding cassette systems. *Microbiol. Mol. Biol. Rev.* **72**, 317–364 (2008).
18. Andersen, C. B. F. et al. Structure of eEF3 and the mechanism of transfer RNA release from the E-site. *Nature* **443**, 663–668 (2006).
19. Ranjan, N. et al. Yeast translation elongation factor eEF3 promotes late stages of tRNA translocation. *EMBO J.* **40**, e106449 (2021).
20. Murina, V. et al. ABCF ATPases involved in protein synthesis, ribosome assembly and antibiotic resistance: structural and functional diversification across the tree of life. *J. Mol. Biol.* **431**, 3568–3590 (2019).
21. Ousalem, F., Singh, S., Chesneau, O., Hunt, J. F. & Boël, G. ABC-F proteins in mRNA translation and antibiotic resistance. *Res. Microbiol.* **170**, 435–447 (2019).
22. Boël, G. et al. The ABC-F protein EttA gates ribosome entry into the translation elongation cycle. *Nat. Struct. Mol. Biol.* **21**, 143–151 (2014).
23. Dorrian, J. & Kerr, I. *Can ABC Proteins Confer Drug Resistance in Micro-organisms Without Being Export Pumps?* (Caister Academic Press, 2009).
24. Ero, R., Kumar, V., Su, W. & Gao, Y. G. Ribosome protection by ABC-F proteins—molecular mechanism and potential drug design. *Protein Sci.* **28**, 684–693 (2019).
25. Sharkey, L. K. & O'Neill, A. J. Antibiotic resistance ABC-F proteins: bringing target protection into the limelight. *ACS Infect. Dis.* **4**, 239–246 (2018).
26. Allignet, J., Loncle, V., El & Solh, N. Sequence of a staphylococcal plasmid gene, *vga*, encoding a putative ATP-binding protein involved in resistance to virginiamycin A-like antibiotics. *Gene* **117**, 45–51 (1992).
27. Ross, J. I., Farrell, A. M., Eady, E. A., Cove, J. H. & Cunliffe, W. J. Characterisation and molecular cloning of the novel macrolide-streptogramin B resistance determinant from *Staphylococcus epidermidis*. *J. Antimicrob. Chemother.* **24**, 851–862 (1989).

28. Ross, J. I. et al. Inducible erythromycin resistance in staphlyococci is encoded by a member of the ATP-binding transport super-gene family. *Mol. Microbiol.* **4**, 1207–1214 (1990).
29. Sharkey, L. K., Edwards, T. A. & O'Neill, A. J. ABC-F proteins mediate antibiotic resistance through ribosomal protection. *MBio* **7**, e01975 (2016).
30. Singh, K. V., Weinstock, G. M. & Murray, B. E. An Enterococcus faecalis ABC homologue (Lsa) is required for the resistance of this species to clindamycin and quinupristin-dalfopristin. *Antimicrob. Agents Chemother.* **46**, 1845–1850 (2002).
31. Hot, C., Berthet, N. & Chesneau, O. Characterization of *sal*(A), a novel gene responsible for lincosamide and streptogramin A resistance in *Staphylococcus sciuri*. *Antimicrob. Agents Chemother.* **58**, 3335–3341 (2014).
32. Koberska, M. et al. Beyond self-resistance: ABCF ATPase LmrC is a signal-transducing component of an antibiotic-driven signaling cascade hastening the onset of lincomycin biosynthesis. Preprint https://www.biorxiv.org/content/10.1101/2020.10.16.343517v1 (2020).
33. Ohki, R., Tateno, K., Takizawa, T., Aiso, T. & Murata, M. Transcriptional termination control of a novel ABC transporter gene involved in antibiotic resistance in *Bacillus subtilis*. *J. Bacteriol.* **187**, 5946–5954 (2005).
34. Dar, D. et al. Term-seq reveals abundant ribo-regulation of antibiotics resistance in bacteria. *Science* **352**, 9822–9822 (2016).
35. Duval, M. et al. HflXr, a homolog of a ribosome-splitting factor, mediates antibiotic resistance. *Proc. Natl Acad. Sci. USA* **115**, 13359–13364 (2018).
36. Chesneau, O., Ligeret, H., Hosan-Aghaie, N., Morvan, A. & Dassa, E. Molecular analysis of resistance to streptogramin A compounds conferred by the Vga proteins of Staphylococci. *Antimicrob. Agents Chemother.* **49**, 973–980 (2005).
37. Reynolds, E. D. & Cove, J. H. Resistance to telithromycin is conferred by *msr* (A), *msrC* and *msr*(D) in *Staphylococcus aureus*. *J. Antimicrob. Chemother.* **56**, 1179–1180 (2005).
38. Su, W. et al. Ribosome protection by antibiotic resistance ATP-binding cassette protein. *Proc. Natl Acad. Sci. USA* **115**, 5157–5162 (2018).
39. Antonelli, A. et al. Characterization of poxtA, a novel phenicol–oxazolidinone–tetracycline resistance gene from an MRSA of clinical origin. *J. Antimicrob. Chemother.* **73**, 1763–1769 (2018).
40. Wang, Y. et al. A novel gene, *optrA*, that confers transferable resistance to oxazolidinones and phenicols and its presence in *Enterococcus faecalis* and *Enterococcus faecium* of human and animal origin. *J. Antimicrob. Chemother.* **70**, 2182–2190 (2015).
41. Zhang, C. et al. Capsular serotypes, antimicrobial susceptibility, and the presence of transferable oxazolidinone resistance genes in *Streptococcus suis* isolated from healthy pigs in China. *Vet. Microbiol.* **247**, 108750 (2020).
42. Iimura, M. et al. Identification of a multiresistant mosaic plasmid carrying a new segment of *IS1216E*-flanked *optrA* with integrated Tn551-*ermB* element in linezolid-resistant *Enterococcus faecalis* human isolate. *J. Glob. Antimicrob. Res.* **22**, 679–699 (2020).
43. Freitas, A. R. et al. Detection of *optrA* in the African continent (Tunisia) within a mosaic *Enterococcus faecalis* plasmid from urban wastewaters. *J. Antimicrob. Chemother.* **72**, 3245–3251 (2017).
44. Sadowy, E. Linezolid resistance genes and genetic elements enhancing their dissemination in enterococci and streptococci. *Plasmid* **99**, 89–98 (2018).
45. Crowe-McAuliffe, C. et al. Structural basis for antibiotic resistance mediated by the *Bacillus subtilis* ABCF ATPase VmlR. *Proc. Natl Acad. Sci. USA* **115**, 8978–8983 (2018).
46. Lenart, J., Vimberg, V., Vesela, L., Janata, J. & Novotna, G. B. Detailed mutational analysis of Vga(A) interdomain linker: implication for antibiotic resistance specificity and mechanism. *Antimicrob. Agents Chemother.* **59**, 1360–1364 (2015).
47. Chen, B. et al. EttA regulates translation by binding the ribosomal E site and restricting ribosome-tRNA dynamics. *Nat. Struct. Mol. Biol.* **21**, 152–159 (2014).
48. Singh, K. V., Malathum, K. & Murray, B. E. Disruption of an *Enterococcus faecium* species-specific gene, a homologue of acquired macrolide resistance genes of staphylococci, is associated with an increase in macrolide susceptibility. *Antimicrob. Agent Chemother.* **45**, 263–266 (2001).
49. Jacquet, E. et al. ATP hydrolysis and pristinamycin IIA inhibition of the *Staphylococcus aureus* Vga(A), a dual ABC protein involved in streptogramin A resistance. *J. Biol. Chem.* **283**, 25332–25339 (2008).
50. Novotna, G. & Janata, J. A new evolutionary variant of the streptogramin A resistance protein, $Vga(A)_{LC}$, from *Staphylococcus haemolyticus* with shifted substrate specificity towards lincosamides. *Antimicrob. Agent Chemother.* **50**, 4070–4076 (2006).
51. Mendes, R. E. et al. Low prevalence of Gram-positive isolates showing elevated lefamulin MIC results during the SENTRY Surveillance Program for 2015–2016 and characterization of resistance mechanisms. *Antimicrob. Agents Chemother.* **63**, e02158–02118 (2019).
52. Mamtora, D., Saseedharan, S., Bhalekar, P. & Katakdhond, S. Microbiological profile and antibiotic susceptibility pattern of Gram-positive isolates at a tertiary care hospital. *J. Lab Physicians* **11**, 144–148 (2019).
53. Magill, S. S. et al. Multistate point-prevalence survey of health care-associated infections. *N. Engl. J. Med.* **370**, 1198–1208 (2014).
54. Pfaller, M. A., Cormican, M., Flamm, R. K., Mendes, R. E. & Jones, R. N. Temporal and geographic variation in antimicrobial susceptibility and resistance patterns of enterococci: results from the SENTRY Antimicrobial Surveillance Program, 1997-2016. In: *Open Forum Infect Dis.* (Oxford University Press US, 2019).
55. Camargo, A. C., Woodward, J. J. & Nero, L. A. The continuous challenge of characterizing the foodborne pathogen *Listeria monocytogenes*. *Foodborne Pathog. Dis.* **13**, 405–416 (2016).
56. Murina, V., Kasari, M., Hauryliuk, V. & Atkinson, G. C. Antibiotic resistance ABCF proteins reset the peptidyl transferase centre of the ribosome to counter translational arrest. *Nucleic Acids Res.* **46**, 1–11 (2018).
57. Khusainov, I. et al. Structure of the 70S ribosome from human pathogen *Staphylococcus aureus*. *Nucleic Acids Res.* **44**, 10491–10504 (2016).
58. Golubev, A. et al. Cryo-EM structure of the ribosome functional complex of the human pathogen *Staphylococcus aureus* at 3.2 Å resolution. *FEBS Lett.* **594**, 3551–3567 (2020).
59. Murphy, E. L. et al. Cryo-electron microscopy structure of the 70S ribosome from *Enterococcus faecalis*. *Sci. Rep.* **10**, 16301 (2020).
60. Polikanov, Y. S. et al. Distinct tRNA accommodation intermediates observed on the ribosome with the antibiotics Hygromycin A and A201A. *Mol. Cell* **58**, 832–844 (2015).
61. Noeske, J. et al. Synergy of streptogramin antibiotics occurs independently of their effects on translation. *Antimicrob. Agent Chemother.* **58**, 5269–5279 (2014).
62. Vimberg, V. et al. Ribosome-mediated attenuation of *vga*(A) expression is shaped by the antibiotic resistance specificity of Vga(A) protein variants. *Antimicrob. Agent Chemother.* **64**, e00666–00620 (2020).
63. Su, T. et al. Structure and function of Vms1 and Arb1 in RQC and mitochondrial proteome homeostasis. *Nature* **570**, 538–542 (2019).
64. Blaha, G., Gürel, G., Schroeder, S. J., Moore, P. B. & Steitz, T. A. Mutations outside the anisomycin-binding site can make ribosomes drug-resistant. *J. Mol. Biol.* **379**, 505–519 (2008).
65. Belousoff, M. J. et al. Structural basis for linezolid binding site rearrangement in the Staphylococcus aureus ribosome. *MBio* **8**, e00395-17 (2017).
66. Marks, J. et al. Context-specific inhibition of translation by ribosomal antibiotics targeting the peptidyl transferase center. *Proc. Natl Acad. Sci. USA* **113**, 12150–12155 (2016).
67. Dönhöfer, A. et al. Structural basis for TetM-mediated tetracycline resistance. *Proc. Natl Acad. Sci. USA* **109**, 16900–16905 (2012).
68. Arenz, S., Nguyen, F., Beckmann, R. & Wilson, D. N. Cryo-EM structure of the tetracycline resistance protein TetM in complex with a translating ribosome at 3.9-Å resolution. *Proc. Natl Acad. Sci. USA* **112**, 5401–5406 (2015).
69. Weaver, K. E. et al. Examination of *Enterococcus faecalis* toxin-antitoxin system toxin Fst function utilizing a pheromone-inducible expression vector with tight repression and broad dynamic range. *J. Bacteriol.* **199**, e00065-00017 (2017).
70. Corrigan, R. M. & Foster, T. J. An improved tetracycline-inducible expression vector for *Staphylococcus aureus*. *Plasmid* **61**, 126–129 (2009).
71. Arnaud, M., Chastanet, A. & Débarbouillé, M. New vector for efficient allelic replacement in naturally nontransformable, low-GC-content, gram-positive bacteria. *Appl Environ. Microbiol.* **70**, 6887–6891 (2004).
72. Ho, S. N., Hunt, H. D., Horton, R. M., Pullen, J. K. & Pease, L. R. Site-directed mutagenesis by overlap extension using the polymerase chain reaction. *Gene* **77**, 51–59 (1989).
73. Bhardwaj, P., Ziegler, E. & Palmer, K. L. Chlorhexidine induces VanA-type vancomycin resistance genes in enterococci. *Antimicrob. Agent Chemother.* **60**, 2209–2221 (2016).
74. Schenk, S. & Laddaga, R. A. Improved method for electroporation of *Staphylococcus aureus*. *FEMS Microbiol. Lett.* **94**, 133–138 (1992).
75. Fairweather, N., Kennedy, S., Foster, T., Kehoe, M. & Dougan, G. Expression of a cloned *Staphylococcus aureus* α-hemolysin determinant in *Bacillus subtilis* and *Staphylococcus aureus*. *Infect. Immun.* **41**, 1112–1117 (1983).
76. O'Neill, A. *Staphylococcus aureus* SH1000 and 8325-4: comparative genome sequences of key laboratory strains in staphylococcal research. *Lett. Appl. Microbiol.* **51**, 358–361 (2010).
77. Horsburgh, M. J. et al. σB modulates virulence determinant expression and stress resistance: characterization of a functional *rsbU* strain derived from *Staphylococcus aureus* 8325-4. *J. Bacteriol.* **184**, 5457–5467 (2002).
78. Takada, H. et al. The C-terminal RRM/ACT domain is crucial for fine-tuning the activation of 'long' RelA-SpoT Homolog enzymes by ribosomal complexes. *Front. Microbiol.* **11**, 277 (2020).
79. Candiano, G. et al. Blue silver: a very sensitive colloidal Coomassie G-250 staining for proteome analysis. *Electrophoresis* **25**, 1327–1333 (2004).
80. Kirchner, S., Rauscher, R., Czech, A. & Ignatova Z. Microarray-based quantification of cellular tRNAs. *Protocols* https://doi.org/10.17504/protocols.io.hfcb3iw (2017).

81. Zheng, S. Q. et al. MotionCor2: anisotropic correction of beam-induced motion for improved cryo-electron microscopy. *Nat. Methods* **14**, 331–332 (2017).
82. Zivanov, J. et al. New tools for automated high-resolution cryo-EM structure determination in RELION-3. *Elife* **7**, e42166 (2018).
83. Henderson, R. et al. Outcome of the first electron microscopy validation task force meeting. *Structure* **20**, 205–214 (2012).
84. Scheres, S. H. & Chen, S. Prevention of overfitting in cryo-EM structure determination. *Nat. Methods* **9**, 853–854 (2012).
85. Rohou, A. & Grigorieff, N. CTFFIND4: fast and accurate defocus estimation from electron micrographs. *J. Struct. Biol.* **192**, 216–221 (2015).
86. Zhang, K. Gctf: Real-time CTF determination and correction. *J. Struct. Biol.* **193**, 1–12 (2016).
87. Kucukelbir, A., Sigworth, F. J. & Tagare, H. D. Quantifying the local resolution of cryo-EM density maps. *Nat. Methods* **11**, 63–65 (2014).
88. Moriya, T. et al. High-resolution single particle analysis from electron cryo-microscopy images using SPHIRE. *J. Vis. Exp.* https://doi.org/10.3791/55448 (2017).
89. Waterhouse, A. et al. SWISS-MODEL: homology modelling of protein structures and complexes. *Nucleic Acids Res.* **46**, W296–W303 (2018).
90. Noeske, J. et al. High-resolution structure of the *Escherichia coli* ribosome. *Nat. Struct. Mol. Biol.* **22**, 336–341 (2015).
91. James, N. R., Brown, A., Gordiyenko, Y. & Ramakrishnan, V. Translational termination without a stop codon. *Science* **354**, 1437–1440 (2016).
92. Pulk, A. & Cate, J. H. Control of ribosomal subunit rotation by elongation factor G. *Science* **340**, 1–7 (2013).
93. Watson, Z. L. et al. Structure of the bacterial ribosome at 2 Å resolution. *Elife* **9**, e60482 (2020).
94. Gabdulkhakov, A. et al. Crystal structure of the 23S rRNA fragment specific to r-protein L1 and designed model of the ribosomal L1 stalk from *Haloarcula marismortui*. *Crystals* **7**, 37 (2017).
95. Tishchenko, S. et al. High-resolution crystal structure of the isolated ribosomal L1 stalk. *Acta Crystallogr. D Biol. Crystallogr.* **68**, 1051–1057 (2012).
96. Fischer, N. et al. Structure of the *E. coli* ribosome–EF-Tu complex at <3Å resolution by Cs-corrected cryo-EM. *Nature* **520**, 567–570 (2015).
97. Loveland, A. B., Demo, G., Grigorieff, N. & Korostelev, A. A. Ensemble cryo-EM elucidates the mechanism of translation fidelity. *Nature* **546**, 113–117 (2017).
98. Rozov, A. et al. Importance of potassium ions for ribosome structure and function revealed by long-wavelength X-ray diffraction. *Nat. Commun.* **10**, 1–12 (2019).
99. Casañal, A., Lohkamp, B. & Emsley, P. Current developments in *Coot* for macromolecular model building of electron cryo-microscopy and crystallographic data. *Protein Sci.* **29**, 1069–1078 (2020).
100. Liebschner, D. et al. Macromolecular structure determination using X-rays, neutrons and electrons: recent developments in Phenix. *Acta Crystallogr. D Struct. Biol.* **75**, 861–877 (2019).
101. Pettersen, E. F. et al. UCSF Chimera—a visualization system for exploratory research and analysis. *J. Comp. Chem.* **25**, 1605–1612 (2004).
102. Pettersen, E. F. et al. UCSF ChimeraX: structure visualization for researchers, educators, and developers. *Protein Sci.* **30**, 70–82 (2021).
103. Polikanov, Y. S., Steitz, T. A. & Innis, C. A. A proton wire to couple aminoacyl-tRNA accommodation and peptide-bond formation on the ribosome. *Nat. Struct. Mol. Biol.* **21**, 787–793 (2014).

Acknowledgements

We are grateful to Barbara E. Murray for sharing *E. faecalis* Δ*lsaA* (*lsa*::Kan) strain TX5332 (ref. [30]) and Jose A. Lemos for sharing the pCIE plasmid vector[69]. We thank Michael Hall for help with cryo-EM data collection. We would also like to thank the reviewers for their comments that improved the manuscript. The electron microscopy data were collected at the Umeå Core Facility for Electron Microscopy, a node of the Cryo-EM Swedish National Facility, funded by the Knut and Alice Wallenberg, Family Erling Persson and Kempe Foundations, SciLifeLab, Stockholm University and Umeå University. This work was supported by the Deutsche Forschungsgemeinschaft (DFG) (grant WI3285/8-1 to D.N.W.), the Swedish Research Council (Vetenskapsrådet) grants (2017-03783 to V.H. and 2019-01085 to G.C.A.), Ragnar Söderbergs Stiftelse (to V.H.), postdoctoral grant from the Umeå Centre for Microbial Research, UCMR (to H.T.), the European Union from the European Regional Development Fund through the Centre of Excellence in Molecular Cell Engineering (2014-2020.4.01.15-0013 to V.H.), and the Estonian Research Council (PRG335 to V.H.). D.N.W. and V.H. groups are also supported by the Deutsche Zentrum für Luft- und Raumfahrt (DLR01Kl1820 to D.N.W.) and the Swedish Research Council (2018-00956 to V.H.) within the RIBOTARGET consortium under the framework of JPIAMR.

Author contributions

C.C.-M. processed the microscopy data, generated and refined the molecular models and made the structure figures. V.M., K.J.T. and M.K. cloned the ARE constructs, performed genetic manipulations of *E. faecalis* and *L. monocytogenes*, performed polysome fractionations and immunoblotting as well as performed MICs and immunoprecipitations. K.J.T. and V.M. prepared cryo-EM grids. K.V. and J.J. assisted genetic manipulations of *L. monocytogenes*. V.M. collected cryo-EM datasets. H.T. performed genetic manipulations of *B. subtilis* as well as MICs for LsaA variants in *B. subtilis*. M.M. and A.J.O. performed genetic manipulation of *S. aureus* and the generation/characterization of $VgaA_{LC}$ variants. G.C.A. performed sequence conservation analyses. C.P. and Z.I. performed microarray experiments. C.C.-M. and D.N.W. wrote the manuscript with input from all authors. D.N.W. and V.H. conceived and supervised the project.

Funding

Open Access funding enabled and organized by Projekt DEAL.

Competing interests

The authors declare no competing interests.

Additional information

Supplementary information The online version contains supplementary material available at https://doi.org/10.1038/s41467-021-23753-1.

Correspondence and requests for materials should be addressed to V.H. or D.N.W.

Peer review information *Nature Communications* thanks the anonymous reviewers for their contributions to the peer review of this work. Peer review reports are available.

Reprints and permission information is available at http://www.nature.com/reprints

Publisher's note Springer Nature remains neutral with regard to jurisdictional claims in published maps and institutional affiliations.

5.3 Structure of the PoxtA ABCF protein in complex with the 70S ribosome

5.3.1 Summary

This manuscript describes the structure of the ARE-ABCF PoxtA in complex with the 70S ribosome and moderately distorted P-tRNA. As expected, the PoxtA NBDs were bound in the E-site. In contrast to other ARE-ABCFs, however, the relatively short interdomain linker of PoxtA did not extend into the PTC, instead triggering a defined, relatively mild distortion of the P-tRNA. By integrating knowledge from recent studies of stalling by chloramphenicol and oxazolidinones, we could propose a novel mechanism for antibiotic resistance, in which displacement of the nascent polypeptide chain is responsible for dissociation of the drug.

5.3.2 Contributions

Processing of the cryo-EM data, creation of the molecular models, and generation of the figures. Writing of the manuscript with help from Prof. Daniel N. Wilson.

Structural basis for PoxtA-mediated resistance to Phenicol and Oxazolidinone antibiotics

Caillan Crowe-McAuliffe[1,#], Victoriia Murina[2,3,4,#], Marje Kasari[2,3,5], Hiraku Takada[2,3,6], Kathryn Jane Turnbull[2,7], Yury S. Polikanov[8], Arnfinn Sundsfjord[9,10], Kristin Hegstad[9,10], Gemma C. Atkinson[3,11], Daniel N. Wilson[1,*], Vasili Hauryliuk[2,3,4,5,11,*]

[1] Institute for Biochemistry and Molecular Biology, University of Hamburg, Martin-Luther-King-Platz 6, 20146 Hamburg, Germany.

[2] Laboratory for Molecular Infection Medicine Sweden (MIMS), Umeå University, 90187 Umeå, Sweden.

[3] Umeå Centre for Microbial Research (UCMR), Umeå University, 901 87 Umeå, Sweden

[4] Department of Molecular Biology, Umeå University, 90187 Umeå, Sweden.

[5] University of Tartu, Institute of Technology, 50411 Tartu, Estonia.

[6] Faculty of Life Sciences, Kyoto Sangyo University, Kamigamo, Motoyama, Kita-ku, Kyoto 603-8555, Japan.

[7] Department of Clinical Microbiology, Rigshospitalet, 2200, Copenhagen, Denmark.

[8] Department of Biological Sciences, College of Liberal Arts and Sciences, University of Illinois at Chicago, Chicago, IL 60607, USA.

[9] Department of Microbiology and Infection Control, Norwegian National Advisory Unit on Detection of Antimicrobial Resistance, University Hospital of North Norway, Tromsø, Norway.

[10] Research Group for Host-Microbe Interaction, Department of Medical Biology, Faculty of Health Sciences, UiT Arctic University of Norway, NO-9037 Tromsø, Norway.

[11] Department of Experimental Medical Science, Lund University, 221 00 Lund, Sweden.

[#] These authors contributed equally.

*Correspondence to:

Daniel Wilson (Daniel.Wilson@chemie.uni-hamburg.de) and Vasili Hauryliuk (vasili.hauryliuk@med.lu.se)

Abstract

PoxtA and OptrA are ATP binding cassette (ABC) proteins of the F subtype (ABCF) that confer resistance to oxazolidinone, such as linezolid, and phenicol antibiotics, such as chloramphenicol. PoxtA/OptrA are often encoded on mobile genetic elements, facilitating their rapid spread amongst Gram-positive bacteria. These target protection proteins are thought to confer resistance by binding to the ribosome and dislodging the antibiotics from their binding sites. However, a structural basis for their mechanism of action has been lacking. Here we present cryo-electron microscopy structures of PoxtA in complex with the *Enterococcus faecalis* 70S ribosome at 2.9–3.1 Å, as well as the complete *E. faecalis* 70S ribosome at 2.2–2.5 Å. The structures reveal that PoxtA binds within the ribosomal E-site with its antibiotic resistance domain (ARD) extending towards the peptidyltransferase center (PTC) on the large ribosomal subunit. At its closest point, the ARD of PoxtA is still located >15 Å from the linezolid and chloramphenicol binding sites, suggesting that drug release is elicited indirectly. Instead, we observe that the ARD of PoxtA perturbs the CCA-end of the P-site tRNA causing it to shift by ~4 Å out of the PTC, which correlates with a register shift of one amino acid for the attached nascent polypeptide chain. Given that linezolid and chloramphenicol are context-specific translation elongation inhibitors, we postulate that PoxtA/OptrA confer resistance to oxazolidinones and phenicols indirectly by perturbing the P-site tRNA and thereby altering the conformation of the attached nascent chain to disrupt the drug binding site.

Introduction

Antibiotic resistance (ARE) is a growing threat to the efficacy of our current arsenal of clinically approved antimicrobial agents. The ATP-binding cassette (ABC) family of proteins are well-known for their role as multidrug resistance transporters, which use the energy of ATP hydrolysis to drive the efflux of antibiotics from the bacterial cytoplasm (Lubelski et al., 2007; Orelle et al., 2019). In recent years, it has become clear that a subfamily of ARE ABC proteins that belong to the subfamily F of the ABC family (ABCF) are not transporters – and thus do not confer resistance via efflux – but rather act via a direct target protection mechanism (Ero et al., 2021; Fostier et al., 2021; Murina et al., 2018; Murina et al., 2019; Ousalem et al., 2019; Sharkey et al., 2016; Sharkey and O'Neill, 2018; Wilson et al., 2020).

ARE-ABCF proteins confer resistance to a diverse range of antibiotics that inhibit protein synthesis by targeting the large subunit (LSU) of the ribosome. Based on the spectrum of antibiotic resistance that they confer ARE-ABCF proteins fall into three functional groups: (i) those that protect from pleuromutilins, lincosamides and streptogramins A (PLS_A), (ii) those that protect from macrolides and streptogramin B (MS_B), and, finally, (iii) those that protect from phenicols and oxazolidinones (PhO) (Ero et al., 2021; Fostier et al., 2021; Ousalem et al., 2019; Sharkey et al., 2016; Sharkey and O'Neill, 2018; Wilson et al., 2020). These functional groups do not map exactly to the phylogenetic tree of ARE-ABCFs, in which seven subclasses (ARE1-7) were originally distinguished, but are rather scattered amongst non-ARE ABCFs, implying that these resistance factors have arisen multiple times by convergent evolution (Murina et al., 2019). Despite the divergence in the spectrum of antibiotic resistance, the ARE-ABCFs share a common architecture and are comprised of two ABC nucleotide-binding domains (NBD1 and NBD2) that are separated by a helical linker, termed an ARD (antibiotic resistance domain), and, depending on the species, may have an additional “Arm” subdomain inserted within NBD1 as well as a C-terminal extension (CTE) (Murina et al., 2018). In fact, this architecture is similar to many non-ARE ABCFs, such as the *E. coli* housekeeping ABCF ATPase EttA, in which the ARD equivalent is shorter and referred to as a P-site tRNA-interaction motif (PtIM) (Boel et al., 2014; Chen et al., 2014), thus making it difficult to judge whether many ABCF proteins are actually resistance determinants or endogenous proteins of mostly unknown function (Murina et al., 2018).

Cryo-EM structures of ribosomes in complex with ARE-ABCFs that confer resistance to PLS_A (ARE1 $VgaA_{LC}$ and VgaL, ARE2 VmlR, ARE3 LsaA) and MS_B (ARE1 MsrE) classes of antibiotics have revealed that these proteins bind within the E-site (Crowe-McAuliffe et

al., 2018; Crowe-McAuliffe et al., 2021; Su et al., 2018), similar to that reported previously for the housekeeping non-ARE ABCF EttA (Chen et al., 2014). However, in contrast to EttA (Boel et al., 2014; Chen et al., 2014), the longer ARD of the ARE-ABCF proteins distorts the P-site tRNA, allowing the factor to access the peptidyl transferase center (PTC) on the LSU of the ribosome and dislodge the relevant antibiotics from their binding sites (Crowe-McAuliffe et al., 2018; Crowe-McAuliffe et al., 2021; Su et al., 2018). These structures revealed that there is often no steric overlap between the ARD of the ARE-ABCF and the drugs and even when there is a steric overlap, mutational analysis indicated that it is not strictly required for resistance (Crowe-McAuliffe et al., 2018; Crowe-McAuliffe et al., 2021; Su et al., 2018). Collectively, these results support a model where the ARE-ABCFs dislodge the drugs from the PTC by inducing a cascade of conformational changes within the 23S rRNA nucleotides that comprise the drug binding site (Crowe-McAuliffe et al., 2021). For MsrE, drug release was reported to occur in the presence of a non-hydrolysable ATP analog (Su et al., 2018), suggesting that ATP hydrolysis is not essential for drug release, but rather is needed for recycling of the factor from the ribosome.

In contrast to the relatively well-understood PLS_A- and MS_B-protecting ARE-ABCFs, mechanistic insights into how ARE7 OptrA and ARE8 PoxtA confer resistance to PhO antibiotics are lacking. The first ARE-ABCF from this group to be discovered is OptrA. This factor confers resistance to the phenicols, such as chloramphenicol and florfenicol, as well as the oxazolidinones linezolid and, to a lesser extent, tedizolid (Wang et al., 2015). OptrA was originally found on the conjugative plasmid pE349 from *Enterococcus faecalis* (Wang et al., 2015), but has subsequently been detected, both plasmid and chromosomal-encoded, across many Gram-positive enterococci, staphylococci and streptococci of human and animal origin (Cai et al., 2015; Fan et al., 2017; Lazaris et al., 2017; Li et al., 2016; Schwarz et al., 2021; Vorobieva et al., 2017; Wang et al., 2015). At least 69 variants of the *optrA* gene have been reported to date, differing by 1–20 aa substitutions, which corresponds to an amino acid identity of 97.1–99.8% compared to the first reported OptrA sequence (Schwarz et al., 2021). Moreover, evidence for horizontal transfer of OptrA to Gram-negative bacteria, such as *Campylobacter coli*, has also been recently described (Liu et al., 2020; Tang et al., 2020). While oxazolidinones are not clinically efficient against Gram-negative pathogens, this raises the concern of possible co-selection of antibiotic co-resistance, i.e. selection for simultaneous transfer and spread of several antibiotic resistance genes encoded by one mobile genetic element. In addition to OptrA, a second ARE-ABCF from this group was detected by bioinformatic analysis of the genome of a methicillin-resistant *Staphylococcus*

aureus (MRSA) strain AOUC-0915 isolated from a cystic fibrosis patient at the Florence Careggi University Hospital in Florence, Italy (Antonelli et al., 2018). Expression of the resistance determinant in *S. aureus*, *E. faecalis* and *E. coli* was reported to confer resistance to phenicol-oxazolidinone-tetracycline antibiotics, and was therefore termed PoxtA (Antonelli et al., 2018). To date, PoxtA has been found exclusively in *Enterococcus* and *Staphylococcus* species, most frequently in *E. faecium* isolates of both human and animal origin (Schwarz et al., 2021).

In the absence of structures of OptrA and PoxtA on the ribosome, it has remained unclear how these ARE-ABCFs confer antibiotic resistance. Both chloramphenicol and linezolid bind at the PTC and inhibit the elongation phase of protein synthesis (Wilson, 2014). However, their activity is context-specific such that translation arrest is most efficient when the nascent polypeptide chain on the ribosome carries an alanine residue and, to a lesser extent, serine or threonine in its penultimate position (Choi et al., 2020; Marks et al., 2016; Vazquez-Laslop and Mankin, 2018). Although the ARDs of OptrA and PoxtA are slightly longer (4–5 aa) than the PtIM of non-ARE ABCFs such as EttA, they are considerably shorter than the ARDs of ARE-ABCFs from other groups, and at least 20 amino acids shorter than other ARE-ABCFs for which structures have been reported (**Fig. 1**). Thus, assuming OptrA and PoxtA bind similarly to the ribosome as other ARE-ABCFs, the ARDs are unlikely to be able to reach into the PTC to dislodge the drugs from their binding site (Wilson et al., 2020). Moreover, it is hard to rationalize how PoxtA also confers resistance to tetracycline antibiotics, which bind near the decoding site on the small subunit (SSU), which is located far from the PTC on the LSU (Antonelli et al., 2018).

Here we have systematically characterized the PoxtA and OptrA resistance determinants, revealing that both increase the minimum inhibitory concentrations (MICs) to phenicols, such as chloramphenicol, thiamphenicol and florfenicol, as well as to the oxazolidinone linezolid, but not to macrolides, pleuromutilins, lincomycins, streptogramins that also bind at the PTC. Morever, we find no evidence for either PoxtA or OptrA confering resistance to non-PTC binding antibiotics, such as tetracycline. Cryo-EM structures of PoxtA on the ribosome reveal that it binds in the E site and, despite the short ARD, still induces a distortion of the P-site tRNA, leading to retraction of its CCA-end from the PTC. Unlike for other ARE-ABCFs, we observe no conformational rearrangements within the 23S rRNA around the drug binding sites within the A site of the PTC upon binding of PoxtA to the ribosome. This leads us to propose a model whereby the distortion of the P-site tRNA by PoxtA (and OptrA) reduces

the affinity of the drugs for their binding site by altering the context and therefore interaction of the nascent polypeptide chain with respect to the drugs.

Results

PoxtA and OptrA confer resistance to phenicols and oxazolidinones, but not tetracyclines

To systematically characterise the antibiotic resistance profiles of PoxtA and OptrA, representatives of these ARE-ABCF groups were expressed in an *E. faecalis* TX5332 strain where the *lsaA* gene had been disrupted (Δ*lsaA*), and MICs were determined for phenicol (chloramphenicol, thiamphenicol and florfenicol), oxazolidinone (linezolid), macrolide (erythromycin, azithromycin and leucomycin), lincosamide (lincomycin and clindamycin), pleuromutilin (tiamulin, retapamulin), streptogramin A and B (Virginiamycin M1 and S1, respectively) and tetracycline antibiotics (**Table 1**). We have characterised OptrA E35048 from *E. faecium* (Morroni et al., 2018), OptrA ST16 from the clinical *E. faecalis* ST16 isolate (Vorobieva et al., 2017), PoxtA AOUC-0915 from MRSA (Antonelli et al., 2018) and, finally, PoxtA E9F6 from a multidrug-resistant ST872 *E. faecium* clinical isolate 9-F-6 (Sivertsen et al., 2018). As controls, we determined MICs for the *E. faecalis* Δ*lsaA* strain transformed with the empty vector plasmid $pCIE_{spec}$, as well as expressing LsaA, the native genome-encoded ARE-ABCF from *E. faecalis*.

In agreement with earlier reports, expression of LsaA confers resistance to PLS_A antibiotics, but not PhO, MS_B or tetracycline (Crowe-McAuliffe et al., 2021; Singh et al., 2002). By contrast, cCF10-inducible expression of either OptrA or PoxtA results in from 2- to 16-fold MIC increase for PhO antibiotics, and does not, as expected, result in resistance against either PLS_A or MS_B, as observed in earlier reports (Antonelli et al., 2018; Wang et al., 2015). While the earlier study (Antonelli et al., 2018) reported a minor protective effect of PoxtA against tetracycline (a two-fold increase in MIC for *E. faecalis* and *S. aureus*), in our hands expression of neither of the PoxtA variants resulted in any increase in MIC for this antibiotic. Notably, the lack of effect of PoxtA AOUC-0915 expression on the MIC for the tetracycline antibiotic tigecycline in either *E. faecalis* or *S. aureus* (Antonelli et al., 2018) is consistent with the original *E. faecium* 9-F-6 strain from which we have isolated PoxtA E9F6 also being susceptible to tigecycline (**Table S1**). Therefore, we concluded that the antibiotic resistance spectrum of PoxtA is similar, if not identical, to that of OptrA. This similarity appears to be a case of convergent evolution, as there is no phylogenetic support for PoxtA and OptrA being

more closely related to each other than to any other ABCF subfamily (**Fig. S1**). Indeed, OptrA is more closely related to the vertically inherited and probable housekeeping ABCF YdiF of Firmicutes (84% bootstrap support, **Fig. S1**), while the relationship of PoxtA to other subfamilies is unresolved (bootstrap support below 50%). On these grounds we conclude that PoxtA-like proteins constitute a separate ARE subfamily which we call ARE8.

Cryo-EM structures of PoxtA-70S complexes

Our attempts to reconstitute OptrA- and PoxtA-70S ribosome complexes *in vitro* were unsuccessful due to problems obtaining soluble homogenous OptrA and PoxtA proteins. Therefore, we employed an *in vivo* pull-out approach with strains overexpressing C-terminally $FLAG_3$-tagged OptrA and PoxtA proteins, as used recently to generate other ARE-ABCF–ribosome complexes (Crowe-McAuliffe et al., 2021). We note that the inclusion of chloramphenicol or linezolid blocks OptrA/PoxtA overexpression and therefore complex formation and purification was performed in the absence of the antibiotic. We expressed both the wild-type ATPase-competent OptrA- and PoxtA and the ATPase-deficient variants bearing Glu-to-Gln substitutions in both NBD cassettes (EQ_2). Such EQ_2 variants have been successfully employed to trap other ABCF proteins on the ribosome because they allow binding but prevent hydrolysis of ATP (Chen et al., 2014; Crowe-McAuliffe et al., 2018; Crowe-McAuliffe et al., 2021; Kasari et al., 2019). The OptrA-EQ_2 variant was earlier shown to have a compromised *in vitro* ATPase activity and be incompetent in promoting antibotic resistance *in vivo* (Zhong et al., 2018). Affinity purification via the $FLAG_3$ tag was performed in the presence of 0.5 mM ATP from clarified lysates prepared from the *E. faecalis* Δ*lsaA* strain expressing the $FLAG_3$-tagged ARE-ABCF, either wildtype or EQ_2-variant. Analysis of the elution fractions from the purifications indicated that only the *E. faecium* PoxtA(E9F6)-EQ_2 factor was bound stably to the ribosome (**Fig. S2**). Furthermore, our attempts with OptrA carrying a single individual EQ substitution (E470Q) were equally unsuccessful. Therefore, we focused on the PotxA(E9F6)-EQ_2–70S sample and subjected it to structural analysis using single-particle cryo-EM.

Using a Titan Krios transmission electron microscope with a K2 direct electron detector, we collected 3,640 micrographs which, after 2D classification, yielded 140,310 ribosomal particles (**Fig. S3**). *In silico* sorting revealed that 80% of these particles contained an additional density for PoxtA and/or tRNAs, which after 3D refinement resulted in a cryo-EM map of *E. faecalis* 70S ribosome with an average resolution of 2.4 Å (**Figure S4A**). Subsequent mutibody refinement yielded average resolutions of 2.2 Å and 2.5 Å for the LSU

and SSU, respectively (**Fig. S4B–E**). The increase in resolution compared to the previous *E. faecalis* 70S ribosome models at 2.8–2.9 Å (Crowe-McAuliffe et al., 2021; Murphy et al., 2020) is evident from improved quality and features of the cryo-EM density, including visualization of some rRNA modifications (e.g. N2-methylguanosine), water molecules and hydrated magnesium ions (**Fig. S5A–F, Table S2**).

Further subsorting of ribosomal particles using a mask focused on the intersubunit space yielded four defined classes, which we refer to as states I–IV (**Fig. S3**). States I and II contained density for PoxtA bound in the E site and tRNA in the P site, and had average resolutions of 2.9 Å and 3.0 Å, respectively (**Fig. 2A** and **Fig. S6A–B, Table S2**). State II differed from state I by only a slight rotation of the SSU relative to the LSU. State III was similar to state II, but additionally contained an A-site tRNA (**Fig. 2B**), whereas state IV contained P-site tRNA only (**Fig. 2C**), presumably because PoxtA dissociated during sample preparation. States III and IV were also refined, resulting in final reconstructions with average resolutions of 2.9 Å and 3.1 Å, respectively (**Fig. S6A–B, Table S2**). The cryo-EM density for PoxtA in states I–III was generally well-resolved (**Fig. S6C**), enabling a reliable model to be built for NBD1, NBD2 and the ARD (**Fig. 2D**). By contrast, the Arm domain, which interacts with uL1, appeared flexible (**Fig. S6C**) and could only be modeled as a rigid body fit of the two α-helices (**Fig. 2D**). The best-resolved region of PoxtA was the ARD, consisting of two α-helices (α1 and α2) and the ARD loop (**Fig. 2D** and **Fig. S6C**), where the majority of sidechains could be modeled unambiguously (**Fig. 2E**). Additional density located between NBD1 and NBD2 of PoxtA was attributed to two ATP molecules (ATP-1 and ATP-2) and a magnesium ion (**Fig. 2F**), as expected from the use of the ATPase-deficient PoxtA-EQ_2 variant. As observed for other ribosome-bound ARE-ABCF structures (Crowe-McAuliffe et al., 2018; Crowe-McAuliffe et al., 2021; Su et al., 2018), the NBDs of PoxtA adopt a closed conformation, which is also consistent with the inability to hydrolyze ATP. In all states, the anticodon stem loop (ASL) and acceptor arm, including the CCA-end, are well-resolved, whereas the elbow region of the tRNAs exhibit some flexibility (**Fig. S6D**). The density for the P-site tRNA is consistent with initiator $tRNA^{fMet}$, indicating that in the absence of chloramphenicol- or linezolid-stalled ribosomes, the PoxtA-EQ_2 variants bind to the vacant E site of initiation complexes, as observed previously for other ARE-ABCF-ribosome complexes (Crowe-McAuliffe et al., 2021). In state IV, clear density for the fMet moiety attached to the P-site tRNA is evident, whereas state III appears to be a post-peptide bond formation state with a deacylated P-site tRNA and A-site tRNA bearing a dipeptide. In

states I and II, which contain PoxtA but lack A-site tRNA, some density for the fMet moiety on the distorted P-site tRNA is evident but is poorly resolved.

Interaction of PoxtA with the ribosome and P-site tRNA

In states I–III, PoxtA is located within the ribosomal E site (**Fig. 3A**) and generally binds similarly to that observed for other ARE-ABCF proteins, such as VmlR, MsrE, LsaA, VgaL and $VgaA_{LC}$ (Crowe-McAuliffe et al., 2018; Crowe-McAuliffe et al., 2021; Su et al., 2018), as well as the non-ARE-ABCF protein EttA (Chen et al., 2014). Unlike these ARE-ABCFs that lack an Arm subdomain (or have a short Arm in the case of LsaA) (Murina et al., 2018), the Arm subdomain of PoxtA (and OptrA (Murina et al., 2018)) is prominent, like that of EttA (Boel et al., 2014; Chen et al., 2014), and stabilises an open conformation of the L1 stalk via direct interaction with domain II of uL1 (**Fig. 3A**). Additional contacts to the 23S rRNA helices H77/H78 of the L1 stalk are evident from the NBD1 of PoxtA, as are interactions for NBD1 with H68 and bL33 on the LSU (**Fig. 3A**). By contrast, NBD2 of PoxtA spans across the intersubunit interface, establishing interactions with uL5 on the LSU as well as uS7 and h41 on the SSU (**Fig. 3A**). NBD2 also interacts directly with the elbow region of the P-site tRNA, namely, with the G19-C56 basepair that links the D- and T-loops (**Fig. 3A,B**). Here, Ser430 of PoxtA is within hydrogen bonding distance of the N7 of G19 and the sidechain of Arg426 of PoxtA stacks upon the nucleobase of C56 of the T-loop (**Fig. 3B**). However, it is the ARD that makes the most extensive interactions with the P-site tRNA, establishing a complex network of hydrogen bonding interactions with the acceptor arm and CCA-end (**Fig. 3A**). In particular, two glutamine residues, Gln275 and Gln279, located at the distal end of the α-helix α1 of the ARD insert into the minor groove of the acceptor arm where hydrogen bond interactions can form with the C3-G70 base-pair (**Fig. 3C**). Hydrogen bonding is also possible from the ε-amino group of Lys278 and the backbone carbonyl of Gln275 of PoxtA with the phosphate-oxygen of G4 and the ribose-oxygen of C71 of the P-tRNA, respectively. The loop region of the ARD of PoxtA interacts predominantly with the single-stranded CCA-3' end of the P-site tRNA (**Fig. 3D**). Ser281 is within H-bonding distance to the phosphate-oxygen of A73, whereas the sidechain of Gln282 stacks upon the base of C74 and can interact with the ribose-hydroxyl of A72 (**Fig. 3D**). C75 of the P-site tRNA is also stabilized by indirect contacts with the backbone carbonyl of Thr283 via a water molecule, as well as a direct H-bond with the sidechain of His285, the first residue of α-helix α2 of the ARD of PoxtA (**Fig. 3E**). The ARD is stabilized by multiple contacts between residues within α-helix α2 and rRNA nucleotides located in H74 and H93. For example, the sidechains of Arg294

and Arg297 contact nucleotides A2595–G2598 (*E. coli* numbering used throughout) located within the loop of H93 of the 23S rRNA, and Glu293 interacts with G2597 directly as well as G2598 via a putative water molecule (**Fig. 3F**).

PoxtA perturbs the position of the CCA-end of the P-site tRNA at the PTC

Despite the short ARD, binding of PoxtA to the E site nevertheless causes a distortion of the P-site tRNA when compared to the canonical P-site tRNA binding position such as that observed in state IV (**Fig. 4A, B**). While the ASL remains fixed in position on the SSU where it decodes the P-site codon of the mRNA, the elbow region shifts towards the E site by ~6-7 Å, thus bringing it into contact with NBD2 of PoxtA (**Fig. 4B**). The shift of the elbow region is very similar to that observed for the distorted P-site tRNAs observed on the ribosome in the presence of the other ARE-ABCFs (Crowe-McAuliffe et al., 2018; Crowe-McAuliffe et al., 2021; Cue et al., 2009; Su et al., 2018), such as LsaA (**Fig. 4C**). However, in the PoxtA-70S complex, the distortion is accompanied by a smaller ~4 Å shift of the acceptor arm of the P-site tRNA away from the PTC (**Fig. 4D**), whereas for other ARE-ABCF complexes, the CCA-end of the P-site tRNA completely vacates the PTC due to the presence of the longer ARD (as illustrated here for LsaA in **Fig. 4C**). Although PoxtA contains a shorter ARD than other ARE-ABCFs, the loop of the ARD still contacts the acceptor stem of the P-tRNA, precluding canonical interactions between the tRNA and the ribosome (**Fig. 4D**). As a consequence, the single-stranded CCA-3' end of the P-site tRNA becomes contorted in the presence of PoxtA and the canonical interactions of the C75 and C74 of a P-site tRNA with 23S nucleotides G2251 and G2252, respectively, of the P-loop (H80) are disrupted (**Fig. 4E, F**). This results in a shift in register such that C75 basepairs with G2252 and C74 stacks upon Gln282 of PoxtA and interacts with G2253 and C2254 (**Fig. 4F**). The register shift is reminiscent of, but distinct to, that observed for the P_{int}-tRNA in *E. coli* 70S ribosome complexes formed in the presence of the antimicrobial peptide apidaecin and the termination release factor RF3 (Graf et al., 2018).

A comparison of the binding position of the ARD of PoxtA with that of the phenicol (chloramphenicol) and oxazolidinone (linezolid) antibiotics reveals that there is no steric overlap between PoxtA and either drug (**Fig. 4B**). Indeed, His285 of PoxtA, which comes closest to the drugs, is still located >16 Å away, and furthermore the ARD of PoxtA is partitioned from the drugs by the CCA-3' end of the P-site tRNA (**Fig. 4B**). This raises the question as to whether PoxtA dislodges these drugs from the ribosome using an indirect mechanism, such as by inducing conformational changes within the 23S rRNA nucleotides

comprising the drug binding site(s), as proposed for other ARE-ABCFs (Crowe-McAuliffe et al., 2018; Crowe-McAuliffe et al., 2021; Su et al., 2018). To examine this, we compared the conformation of the PTC nucleotides comprising the drug binding sites in our structures with those in the presence of chloramphenicol and linezolid. We could find no evidence that the presence of PoxtA induces any conformational changes within the drug binding sites that would lead to dissociation of the drugs (**Fig. S7–S8**). In fact, we note that the conformation of the A-site pocket where the drugs bind is very similar, if not identical, for states I–IV, regardless of whether PoxtA is present (state I–III) or absent (state IV), or whether the A-site is vacant (state I–II, IV) or occupied (state III) (**Fig. S7–S8**). Although this suggests that PoxtA does not dislodge the drugs from the ribosome by altering the 23S rRNA in the binding site, we cannot exclude that such conformational changes occur upon ATP hydrolysis or upon dissociation of PoxtA from the ribosome.

An alternative scenario is that the distortion of the P-site tRNA induced by PoxtA binding indirectly reduces the affinity of the drugs for their A-site binding pocket. Both chloramphenicol and linezolid are context-specific inhibitors of translation elongation, such that the highest translation arrest activity occurs when the penultimate amino acid (−1 position) attached to the CCA-end of the P-site tRNA is alanine, and to a lesser extent, serine or threonine (Choi et al., 2020; Marks et al., 2016; Vazquez-Laslop and Mankin, 2018). Structures of chloramphenicol with peptidyl-tRNA mimics reveal an intimate interaction between the drug and the nascent polypeptide chain, illustrating how alanine in the −1 position stabilizes drug binding via a CH-π interaction (**Fig. 4G**) (Syroegin et al., 2021). Since the distortion of the P-site tRNA by PoxtA involves a shift out of the PTC by 4 Å, effectively altering the nascent chain register by one amino acid, this would also result in a shift of the alanine away from chloramphenicol (**Fig. 4H**) and thereby perturb the interactions and reduce the affinity of the drug for the ribosome.

Discussion

Model of antibiotic resistance mediated by PoxtA and OptrA

Based on the structures of the PoxtA-ribosome complexes determined here, as well as the available literature on the mechanism of action of oxazolidinones and phenicols, we propose a model for how PoxtA can confer antibiotic resistance to these antibiotic classes (**Fig. 5**). As mentioned, linezolid and chloramphenicol are context-specific inhibitors that stall the ribosome during translation elongation with the peptidyl-tRNA in the P site and the drug

bound within the A-site pocket of the PTC (**Fig. 5A**) (Choi et al., 2020; Marks et al., 2016; Vazquez-Laslop and Mankin, 2018). The amino acid in the −1 position of the nascent polypeptide chain influences the strength of the arrest. Specifically, alanine – and, to a lesser extent, serine and threonine – elicit the strongest arrest (Choi et al., 2020; Marks et al., 2016; Vazquez-Laslop and Mankin, 2018), apparently due to direct interaction with the ribosome-bound drug (**Fig. 5A**) (Syroegin et al., 2021).

We propose that PoxtA recognizes these drug-arrested ribosomes and binds to the vacant E site (**Fig. 5B**). In contrast to other ARE-ABCFs where the CCA end is completely removed from the PTC (Crowe-McAuliffe et al., 2018; Crowe-McAuliffe et al., 2021; Su et al., 2018), the binding of PoxtA causes the CCA-end to shift by only ~4 Å. Although modest, such a shift would be sufficient to change the register of the nascent polypeptide chain with respect to the drug, such that the drug can no longer interact with the amino acid in the −1 position, thereby decreasing its affinity for the ribosome and leading to its dissociation (**Fig. 5B**). It is possible that the shift of the nascent chain upon distortion of the P-site tRNA by PoxtA also contributes to “brushing” the drug from the ribosome (Ousalem et al., 2019), analogous to the mechanism proposed for leader peptides that confer resistance to macrolides (Tenson and Mankin, 2001). We also cannot exclude the possibility that conformational changes in PoxtA upon ATP hydrolysis play a role in drug release, in addition to facilitating dissociation of PoxtA from the ribosome (**Fig. 5C**).

What prevents PhO antibiotics from rebinding following their dissociation by PoxtA? As suggested previously for other ARE-ABCFs (Crowe-McAuliffe et al., 2018; Crowe-McAuliffe et al., 2021), we favour a model where, following PoxtA dissociation, the peptidyl-tRNA can reaccommodate in the P site, thus allowing accommodation of a tRNA in the A site, which, in turn, would occlude the PhO binding site (**Fig. 5D**). In this respect, we note that in contrast to previous ARE-ABCF structures (Crowe-McAuliffe et al., 2018; Crowe-McAuliffe et al., 2021), we observe here a subpopulation of PoxtA-70S complexes where the A-site tRNA is fully accommodated at the PTC despite the presence of PoxtA and the distorted P-site tRNA. Thus, once the drug has been released, the A-site tRNA could accommodate at the PTC and following peptide bond formation and translocation, the context of the nascent chain would be shifted by one amino acid i.e. alanine in the −1 position would now be located at the −2 position and therefore disfavour drug rebinding (**Fig. 5D**). PoxtA and OptrA are often found on the same mobile genetic element as drug efflux pumps (Schwarz et al., 2021),

which may also contribute to preventing drug rebinding by transporting the dissociated drug directly out of the cell.

Our insights into the mechanism of action of PoxtA also provide a possible explanation for why these ARE-ABCFs do not confer resistance to MS_B or PLS_A antibiotics. Firstly, the ARD of PoxtA is too short to sterically overlap with these drugs and directly displace them from the ribosome, and secondly, binding of PoxtA does not perturb the rRNA portion of the drug binding sites and therefore could not induce their dissociation by conformational relays in the 23S rRNA. For PLS_A antibiotics, which stall translation after initiation, there is no nascent chain that forms part of the drug-binding site. In the case of MS_B antibiotics, which stall translation elongation but bind deeper in the nascent peptide exit channel, perhaps the "pulling" effect of PoxtA on the nascent chain is mitigated by conformation elasticity of the several amino acids between the P-tRNA and the drug-binding site. Interestingly, ARE-ABCF antibiotics, such as MsrE or LsaA that confer resistance to MS_B and PLS_A antibiotics, respectively, do not confer resistance to PhO antibiotics, despite direct overlap between the ARDs and the drug binding sites. We speculate that in these cases, the peptidyl-tRNA of the PhO-stalled ribosomes are refractory to the action of these ARE-ABCFs to distort the P-site tRNA; however, further investigations will be needed to validate this.

Given the similarity in ARD length and antibiotic spectrum, we believe that the findings and model presented here for PoxtA are likely to also be applicable for OptrA. Indeed, like OptrA, our MIC analysis provides no evidence for PoxtA conferring resistance to tetracycline antibiotics, consistent with the binding site of PoxtA in the E site being far from the tetracycline binding site located in the decoding A-site of the small subunit. We also see no evidence for conformational differences in the 16S rRNA nucleotides that comprise the tetracycline binding site in the absence or presence of PoxtA. For this reason, we suggest reassigning letters from the PoxtA acronym from phenicol oxazolidinone tetracycline A to phenicol oxazolidinone transmissible A, analogous to OptrA.

Methods

Identification of poxtA *EF9F6 and characterisation of* E. faecium *9-F-6 antibiotic susceptibility*

The *poxtA* EF9F6 gene was identified in the multidrug-resistant ST872 *E. faecium* 9-F-6 isolated in 2012 from faeces of a patient in a Norwegian hospital which had recently also been hospitalized in India (Sivertsen et al., 2018). ST872 is a single locus variant of ST80 which is a pandemic hospital-adapted genetic lineage. Transferable linezolid resistance (*optrA* and *cfr(D)* has recently been described in blood culture *E. faecium* ST872 strain from Australia (Pang et al., 2020). Species identification was performed by MALDI-TOF (Bruker, Billerica, US) according to the manufacturer's instructions and later confirmed by whole genome sequencing (Sivertsen et al., 2018). Antimicrobial susceptibility testing was performed by broth microdilution using the EUENCF Sensititre plate (Thermo Fisher Scientific, Waltham, Massachusetts, USA), and further by gradient tests for vancomycin, teicoplanin, ampicillin, clindamycin, chloramphenicol and gentamicin (MIC Test strip, Liofilchem, Roseto Degli Abruzzi, Italy). The results (MICs) were interpreted according to EUCAST clinical breakpoints v. 10.0 2020 and MICs were within the accepted range for quality control strain *E. faecalis* ATCC 29212. The *E. faecium* 9-F-6 is resistant to linezolid (MIC = 8 mg/L), ampicillin (>256 mg/L), ciprofloxacin (> 16 mg/L), high-level gentamicin (HLGR >256 mg/L), high-level streptomycin (HLSR >1024 mg/L) and high-level glycopeptides (vancomycin >256 mg/L and teicoplanin 128 mg/L), but susceptible to quinupristin/dalfopristin (MIC 4 mg/L) and tigecycline (MIC 0,12 mg/L) (**Table S1**). Whole-genome sequences confirmed *vanA* and the *aac(6')-Ie-aph(2'')-Ia* genes conferring high-level glycopeptide and gentamicin resistance, respectively, as well as a defunct, functionally inactive *cfr* pseudogene.

Strains and plasmids

All bacterial strains and plasmids used in the study are listed in **Table S3**. *E. faecalis* TX5332 (Rif^r Fus^r Kan^r; *lsa* gene disruption mutant (OG1RF *lsa*::pTEX4577)) is a *lsa* knockout strain that was received from Barbara Murray (Singh et al., 2002). pCIE$_{spec}$ plasmid was constructed on the basis of the pCIE$_{cam}$ plasmid, where the chloramphenicol resistance gene was substituted with spectinomycin, due to intrinsic resistance of PoxtA to phenicol antibiotics. All cloning was performed by the PEP facility (Umeå University). Plasmids encoding OptrA-ST16 (Vorobieva et al., 2017) and OptrA-E35048 (Morroni et al., 2018) were kindly provided by Anette M. Hammerum and Alberto Antonelli, respectively. In each case,

the *optrA* gene was amplified with ribosome binding sequence (RBS) (TAAGAGGAGGAGATAAAC) and inserted into $pCIE_{spec}$ plasmid, resulting in $pCIE_{spec}$:*optrA-ST16* and $pCIE_{spec}$:*optrA-E35048*, respectively. The *poxtA AOUC-0915* gene (Antonelli et al., 2018) was PCR amplified from genomic DNA of *S. aureus* AOUC 0915 (kindly provided by Alberto Antonelli) and inserted in $pCIE_{spec}$ plasmid using the BamHI and HindIII restriction sites. The RBS (TAAGAGGAGGAGATAAAC) was inserted directly in front of the ATG to improve expression levels. Genetic material encoding PoxtA-E9F6 (OZN12776.1) was obtained from an *E. faecium* (9-F-6) isolated from a Norwegian patient in 2012, the genome of which has been sequenced (GCA_002263195.1) (Sivertsen et al., 2018). The *poxtA-E9F6* gene with added RBS was inserted in the $pCIE_{spec}$ plasmid resulting in $pCIE_{spec}$:*poxtA-EF9F6*. These plasmids were used for MIC determinations. For use in pull-out experiments we introduced His_6-TEV-$FLAG_3$ tags at the C-terminus of either OptrA or PoxtA protein, with and without EQ mutations (E184Q and E471Q for PoxtA EQ_2, E190Q and E470Q for OptrA EQ_2, E470Q for OptrA EQ_1) expressed from $pCIE_{cam}$ plasmid.

Bacterial transformation

E. faecalis electrocompetent cells were prepared as described previously (Bhardwaj et al., 2016). Briefly, an over-night culture *E. faecalis* TX5332 grown in the presence of 2 mg/mL of kanamycin was diluted to OD_{600} of 0.05 in 50 mL of Brain Heart Infusion (BHI) media and grown further to an OD_{600} of 0.6-0.7 at 37 °C with moderate shaking (160 rpm). Cells were collected by centrifugation at 4,000 rpm at 4 °C for 10 min. Cells were resuspended in 0.5 mL of sterile lysozyme buffer (10 mM Tris-HCl pH 8; 50 mM NaCl, 10 mM EDTA, 35 µg/mL lysozyme), transferred to 0.5 mL Eppendorf tube and incubated at 37 °C for 30 minutes. Cells were pelleted at 10000 rpm at 4 °C for 10 min and washed three times with 1.5 mL of ice-cold electroporation buffer (0.5 M sucrose, 10% (w/v) glycerol). After last wash the cells were resuspended in 500 µL of ice-cold electroporation buffer and aliquoted and stored at –80°C. For electroporation, 35 µL of electrocompetent cells were supplemented with 0.5–1 µg of plasmid DNA, transferred to ice-cold 1 mm electroporation cuvette and electroporated at 1.8 keV. Immediately after electroporation 1 mL of ice-cold BHI media was added to the cells, the content of the cuvette was transferred to 1.5 mL Eppendorf tubes and the cells were recovered at 37 °C for 2.5 hours and plated to BHI plates containing appropriate antibiotics.

Antibiotic susceptibility testing

E. faecalis cells were grown in BHI media supplemented with 2 mg/mL kanamycin (to prevent *lsa* revertants), 0.1 mg/mL spectinomycin (to maintain the $pCIE_{spec}$ plasmid), 100 ng/mL of cCF10 peptide (to induce expression of proteins of interest) as well as increasing concentrations of antibiotics. The media was inoculated with 5×10^5 CFU/mL (OD_{600} of approximately 0.0005) of *E. faecalis* Δ*lsaA* (*lsa::Kan*) strain TX5332 transformed either with empty $pCIE_{spec}$ plasmid or with $pCIE_{spec}$ encoding indicated protein of interest. After 16-20 h at 37 °C without shaking, the presence or absence of bacterial growth was scored by eye.

Preparation of bacterial biomass

E. faecalis TX5332 transformed with $pCIE_{spec}$ / $pCIE_{cam}$-based expression constructs (either empty vector or expressing wild type/EQ_2 variants of both PoxtA-HTF and OptrA-HTF as well as EQ_1 variant of OptrA-HTF) were grown overnight from single colony in BHI media supplemented with appropriate antibiotics (100 µg/mL of spectinomycin for $pCIE_{spec}$-based constructs, 10 µg/mL chloramphenicol for $pCIE_{cam}$-based constructs). Overnight cultures were then diluted to a starting OD_{600} of 0.05 in 200 mL of the same media. Cells were grown with intensive shaking at 37 °C till OD_{600} of 0.6 and were induced with 100 ng/mL of cCF10 peptide for 30 minutes prior harvesting by centrifugation at 10,000 x g for 15 min at 4 °C.

Preparation of clarified lysates

Cell pellets were resuspended in 1.5 mL of cell opening buffer (95 mM KCl, 5 mM NH_4Cl, 20 mM HEPES pH 7.5, 1 mM DTT, 5 mM $Mg(OAc)_2$, 0.5 mM $CaCl_2$, 8 mM putrescine, 0.5-0.75 mM ATP, 1 mM spermidine, 1 tablet of cOmplete™ EDTA-free Protease Inhibitor Cocktail (Roche) per 10 mL of buffer). Resuspended cells were opened by FastPrep homogeniser (MP Biomedicals) with 0.1 mm Zirconium beads (Techtum) in 4 cycles by 20 seconds with a 1 min chill on ice. Cell debris was removed after centrifugation at 14,800 x g for 15 min at 4 °C. Total protein concentration in supernatant was measured by Bradford assay (BioRad), supernatant was aliquoted and frozen in liquid nitrogen.

Affinity purification on anti-FLAG M2 affinity gel

100 µL of well-mixed anti-FLAG M2 Affinity Gel aliquots (Sigma) were loaded on columns (Micro Bio-Spin Columns, Bio-Rad) and washed two times with 1 mL of cell opening buffer by gravity flow. All incubations, washings and elutions were done at 4 °C. The total protein concentration of each lysate was adjusted to 2 mg/mL with cell opening buffer with HEPES pH 7.5 to glycine pH 9.0. 1 mL of each lysate was loaded on columns and incubated for 2 h

with end-over-end mixing for binding. The columns were washed 5 times with 1 mL of cell opening buffer by gravity flow. For elution of FLAG-tagged proteins and their complexes 100 µL of 0.2 mg/mL $FLAG_3$ peptide (Sigma) was added to samples, the solutions were incubated at 4 °C for 20 minutes with end-over-end mixing. Elutions were collected by centrifugation at 2,000 x g for 2 min at 4 °C. 20 µL aliquots of collected samples (flow-through, washes and elutions) were mixed with 5 µL of 5 x SDS loading buffer and heated up at 95 °C for 15 min. The beads remaining in the column were resuspended in 100 µL of 1x SDS loading buffer. Denatured samples were loaded on 15% SDS-PAGE. SDS-gels were stained by "Blue-Silver" Coomassie Staining (Candiano et al., 2004) and destained in water overnight hours or overnight before imaging with LAS4000 (GE Healthcare).

Preparation of cryo-EM grids

Elutions from pull-downs were kept on ice until being applied within two hours to glow discharged cryo-grids (Quantifoil 2/2 Cu_{300} coated with 2 nm continuous carbon). 3.5 µL of sample was loaded on grids 3 times manually at room temperature conditions and a fourth time in Vitrobot (FEI) under conditions of 100% humidity at 4 °C, blotted for 5 seconds and vitrified by plunge-freezing in liquid ethane. Samples were imaged on a Titan Krios (FEI) operated at 300 kV at a nominal magnification of 165,000 x (0.86 Å/pixel) with a Gatan K2 Summit camera at an exposure rate of 5.85 electrons/pixel/s with a 4 seconds exposure and 20 frames using the EPU software.

Single-particle reconstruction

Processing was performed in RELION 3.1 unless otherwise specified (Zivanov et al., 2018). MotionCor2 with 5×5 patches and CTFFIND4 (using power spectra) were used for motion correction and initial CTF estimation (Rohou and Grigorieff, 2015; Zheng et al., 2017). Micrographs with estimated CTF fits beyond 4.5 Å and CTF figure of merits > 0.04 were selected for further processing. Particles were picked with crYOLO using the general model (Wagner et al., 2019). After 2D classification, all ribosome-like classes were selected, particles extracted with a 3× reduced pixel size (2.46 Å), and an initial model created *ab initio*. After 3D refinement using the *ab initio* model as a reference (Scheres and Chen, 2012), 3D classification with eight classes and without angular searching was performed. The majority of particles (~80%) clustered into two classes that contained protein-like density in the E site, and which were selected for further processing. Particles were re-extracted at the original pixel size, and serial 3D refinements with CTF refinement and Bayesian polishing (Zivanov et al., 2019) were performed until the resolution did not improve further,

resulting in the 'combined 70S volume'. A mask around the A, P, and E sites was created and used for partial signal subtraction with re-extraction at a pixel size of 2.46 Å. These particles were used for 3D classification with six classes, T = 40 and the resolution of the expectation step limited to 12 Å. Four of the six resulting classes, labelled states I–IV, were chosen for refinement with the original pixel size. For the multibody refinement of the combined 70S class (Nakane et al., 2018), volumes corresponding to the LSU core, CP, SSU body, SSU head, and E-site were isolated using the volume eraser tool in UCSF ChimeraX (Pettersen et al., 2021), and masks created from the densities low-pass-filtered to 30 Å. Bsoft was used to estimate local resolution (Heymann, 2018).

Molecular modelling

Molecular models were created/adjusted with Coot (Casanal et al., 2020) and ISOLDE (Croll, 2018), and refined with Phenix (Liebschner et al., 2019) against unsharpened maps. A previous structure of the *E. faecalis* 70S ribosome in complex with the ABCF-ARE LsaA (PDB 7NHK) (Crowe-McAuliffe et al., 2021) was used as the starting model for the ribosome, initially into multibody-refined maps from the combined 70S volume. PDB IDs 7K00 (Watson et al., 2020) and 6O90 (Murphy et al., 2020) were also used as templates in parts of the 70S, and PDB ID 3U4M (Tishchenko et al., 2012) was used as a template for the L1 stalk region. Likely metal ions were assigned by the presence of typical coordination shapes, as well as strength of density and estimated coordination distances. However, we caution that these assignments could not always be made unambiguously. Phenix.douse was used to place water molecules. A recent structure of the *S. aureus* ribosome with modified nucleotides (PDB ID 6YEF (Golubev et al., 2020)) was compared to the density to check for RNA modifications, and where the density matched the modification with high confidence, that modification was inserted into the *E. faecalis* 70S model. For PoxtA, homology models were generated by SWISS-MODEL (Waterhouse et al., 2018) using the crystal structure of EttA (PDB ID 4FIN (Boel et al., 2014)) and the previous cryo-EM structure of LsaA (PDB 7NHK) (Crowe-McAuliffe et al., 2021). The ARD was sufficiently well-resolved that it could be built manually. The Arm insertion in NBD1 was built manually with low confidence (especially in the loop connecting the two α-helices). PSI-PRED secondary structure predictions were used to help define secondary structure boundaries (Buchan and Jones, 2019). The models for states I–IV were assembled using the model from the combined 70S as a template. For the A-tRNA in state III, tRNA-Lys from PDB ID 5E7K (Rozov et al., 2016)

was used as a template for *E. faecalis* tRNA-Lys-UUU-1-1 (gtRNAdb nomenclature (Chan and Lowe, 2016)) based on density.

Sequence analysis methods

Representative ABCF sequences were aligned with Mafft L-INS-i 7.453 (Katoh and Standley, 2013) and visualised with Jalview 2.11.1.4 (Waterhouse et al., 2009) and Aliview 1.26 (Larsson, 2014). Phylogenetic analysis was carried out with IQTree version 2.1.2 on the CIPRES server with 1000 rapid bootstrap replicates and automatic model detection (Miller et al., 2010; Minh et al., 2020). Positions with more than 50% gaps were removed with TrimAL v1.4.rev6 before phylogenetic analysis (Capella-Gutierrez et al., 2009).

Figures

Figures were created using UCSF ChimeraX, PyMol v2.4, and assembled with Adobe Illustrator (Adobe Inc.).

Data availability

Micrographs have been deposited as uncorrected frames in the Electron Microscopy Public Image Archive (EMPIAR) with the accession codes EMPIAR-10XXX [https://www.ebi.ac.uk/pdbe/emdb/empiar/entry/10XXX/]. Cryo-EM maps have been deposited in the Electron Microscopy Data Bank (EMDB) with accession codes EMD-12XXX [https://www.ebi.ac.uk/pdbe/entry/emdb/EMD-12XXX] (PoxtA-70S state I), EMD- 12XXX [https://www.ebi.ac.uk/pdbe/entry/emdb/EMD-12XXX] (PoxtA-70S state II), EMD-12XXX [https://www.ebi.ac.uk/pdbe/entry/emdb/EMD-12XXX] (PoxtA-70S state III with A-site tRNA) and EMD-12XXX [https://www.ebi.ac.uk/pdbe/entry/emdb/EMD-12XXX] (*E. faecalis* 70S with P-tRNA state IV). Molecular models have been deposited in the Protein Data Bank with accession codes 7XXX [https://doi.org/10.2210/pdb7XXX/pdb] (PoxtA-70S state I), 7XXX [https://doi.org/10.2210/pdb7XXX/pdb] (PoxtA-70S state II), 7XXX [https://doi.org/10.2210/pdb7XXX/pdb] (PoxtA-70S state III with A-site tRNA) and 7XXX [https://doi.org/10.2210/pdb7XXX/pdb] (*E. faecalis* 70S with P-tRNA, state IV). Source data are provided with this paper.

References

Antonelli, A., D'Andrea, M.M., Brenciani, A., Galeotti, C.L., Morroni, G., Pollini, S., Varaldo, P.E., and Rossolini, G.M. (2018). Characterization of *poxtA*, a novel phenicol-oxazolidinone-tetracycline resistance gene from an MRSA of clinical origin. J Antimicrob Chemother *73*, 1763-1769.

Bhardwaj, P., Ziegler, E., and Palmer, K.L. (2016). Chlorhexidine induces VanA-type vancomycin resistance genes in enterococci. Antimicrobial agents and chemotherapy *60*, 2209-2221.

Boel, G., Smith, P.C., Ning, W., Englander, M.T., Chen, B., Hashem, Y., Testa, A.J., Fischer, J.J., Wieden, H.J., Frank, J.*, et al.* (2014). The ABC-F protein EttA gates ribosome entry into the translation elongation cycle. Nature structural & molecular biology *21*, 143-151.

Buchan, D.W.A., and Jones, D.T. (2019). The PSIPRED Protein Analysis Workbench: 20 years on. Nucleic Acids Res. *47*, W402-W407.

Cai, J., Wang, Y., Schwarz, S., Lv, H., Li, Y., Liao, K., Yu, S., Zhao, K., Gu, D., Wang, X.*, et al.* (2015). Enterococcal isolates carrying the novel oxazolidinone resistance gene optrA from hospitals in Zhejiang, Guangdong, and Henan, China, 2010-2014. Clin Microbiol Infect *21*, 1095 e1091-1094.

Candiano, G., Bruschi, M., Musante, L., Santucci, L., Ghiggeri, G.M., Carnemolla, B., Orecchia, P., Zardi, L., and Righetti, P.G. (2004). Blue silver: a very sensitive colloidal Coomassie G-250 staining for proteome analysis. Electrophoresis *25*, 1327-1333.

Capella-Gutierrez, S., Silla-Martinez, J.M., and Gabaldon, T. (2009). trimAl: a tool for automated alignment trimming in large-scale phylogenetic analyses. Bioinformatics *25*, 1972-1973.

Casanal, A., Lohkamp, B., and Emsley, P. (2020). Current developments in Coot for macromolecular model building of Electron Cryo-microscopy and Crystallographic Data. Protein Sci *29*, 1069-1078.

Chan, P.P., and Lowe, T.M. (2016). GtRNAdb 2.0: an expanded database of transfer RNA genes identified in complete and draft genomes. Nucleic Acids Res. *44*, D184-189.

Chen, B., Boel, G., Hashem, Y., Ning, W., Fei, J., Wang, C., Gonzalez, R.L., Jr., Hunt, J.F., and Frank, J. (2014). EttA regulates translation by binding the ribosomal E site and restricting ribosome-tRNA dynamics. Nature structural & molecular biology *21*, 152-159.

Choi, J., Marks, J., Zhang, J., Chen, D.H., Wang, J., Vazquez-Laslop, N., Mankin, A.S., and Puglisi, J.D. (2020). Dynamics of the context-specific translation arrest by chloramphenicol and linezolid. Nat Chem Biol *16*, 310-317.

Croll, T.I. (2018). ISOLDE: a physically realistic environment for model building into low-resolution electron-density maps. Acta Crystallogr D Struct Biol *74*, 519-530.

Crowe-McAuliffe, C., Graf, M., Huter, P., Takada, H., Abdelshahid, M., Novacek, J., Murina, V., Atkinson, G.C., Hauryliuk, V., and Wilson, D.N. (2018). Structural basis for antibiotic resistance mediated by the Bacillus subtilis ABCF ATPase VmlR. Proc Natl Acad Sci U S A *115*, 8978-8983.

Crowe-McAuliffe, C., Murina, V., Turnbull, K.J., Kasari, M., Mohamad, M., Polte, C., Takada, H., Vaitkevicius, K., Johansson, J., Ignatova, Z.*, et al.* (2021). Structural basis of ABCF-mediated resistance to pleuromutilin, lincosamide, and streptogramin A antibiotics in Gram-positive pathogens. Nat Commun *12*, 3577.

Cue, D., Lei, M.G., Luong, T.T., Kuechenmeister, L., Dunman, P.M., O'Donnell, S., Rowe, S., O'Gara, J.P., and Lee, C.Y. (2009). Rbf promotes biofilm formation by Staphylococcus aureus via repression of icaR, a negative regulator of icaADBC. J Bacteriol *191*, 6363-6373.

Ero, R., Yan, X.F., and Gao, Y.G. (2021). Ribosome Protection Proteins-"New" Players in the Global Arms Race with Antibiotic-Resistant Pathogens. Int J Mol Sci *22*.

Fan, R., Li, D., Fessler, A.T., Wu, C., Schwarz, S., and Wang, Y. (2017). Distribution of *optrA* and cfr in florfenicol-resistant *Staphylococcus sciuri* of pig origin. Vet Microbiol *210*, 43-48.

Fostier, C.R., Monlezun, L., Ousalem, F., Singh, S., Hunt, J.F., and Boel, G. (2021). ABC-F translation factors: from antibiotic resistance to immune response. FEBS Lett *595*, 675-706.

Golubev, A., Fatkhullin, B., Khusainov, I., Jenner, L., Gabdulkhakov, A., Validov, S., Yusupova, G., Yusupov, M., and Usachev, K. (2020). Cryo-EM structure of the ribosome functional complex of the human pathogen *Staphylococcus aureus* at 3.2 A resolution. FEBS Lett *594*, 3551-3567.

Graf, M., Huter, P., Maracci, C., Peterek, M., Rodnina, M.V., and Wilson, D.N. (2018). Visualization of translation termination intermediates trapped by the Apidaecin 137 peptide during RF3-mediated recycling of RF1. Nat Commun *9*, 3053.

Heymann, J.B. (2018). Guidelines for using Bsoft for high resolution reconstruction and validation of biomolecular structures from electron micrographs. Protein Sci *27*, 159-171.

Kasari, V., Pochopien, A.A., Margus, T., Murina, V., Turnbull, K., Zhou, Y., Nissan, T., Graf, M., Novacek, J., Atkinson, G.C.*, et al.* (2019). A role for the *Saccharomyces cerevisiae* ABCF protein New1 in translation termination/recycling. Nucleic Acids Res. *47*, 8807-8820.

Katoh, K., and Standley, D.M. (2013). MAFFT multiple sequence alignment software version 7: improvements in performance and usability. Mol Biol Evol *30*, 772-780.

Larsson, A. (2014). AliView: a fast and lightweight alignment viewer and editor for large datasets. Bioinformatics *30*, 3276-3278.

Lazaris, A., Coleman, D.C., Kearns, A.M., Pichon, B., Kinnevey, P.M., Earls, M.R., Boyle, B., O'Connell, B., Brennan, G.I., and Shore, A.C. (2017). Novel multiresistance cfr plasmids in linezolid-resistant methicillin-resistant *Staphylococcus epidermidis* and vancomycin-resistant *Enterococcus faecium* (VRE) from a hospital outbreak: co-location of *cfr* and *optrA* in VRE. J Antimicrob Chemother *72*, 3252-3257.

Li, D., Wang, Y., Schwarz, S., Cai, J., Fan, R., Li, J., Fessler, A.T., Zhang, R., Wu, C., and Shen, J. (2016). Co-location of the oxazolidinone resistance genes *optrA* and *cfr* on a multiresistance plasmid from *Staphylococcus sciuri*. J Antimicrob Chemother *71*, 1474-1478.

Liebschner, D., Afonine, P.V., Baker, M.L., Bunkóczi, G., Chen, V.B., Croll, T.I., Hintze, B., Hung, L.-W., Jain, S., and McCoy, A.J. (2019). Macromolecular structure determination using X-rays, neutrons and electrons: recent developments in Phenix. Acta Crystallogr D Struct Biol *75*, 861-877.

Liu, D., Yang, D., Liu, X., Li, X., Fessler, A.T., Shen, Z., Shen, J., Schwarz, S., and Wang, Y. (2020). Detection of the enterococcal oxazolidinone/phenicol resistance gene *optrA* in *Campylobacter coli*. Vet Microbiol *246*, 108731.

Lubelski, J., Konings, W.N., and Driessen, A.J. (2007). Distribution and physiology of ABC-type transporters contributing to multidrug resistance in bacteria. Microbiol Mol Biol Rev *71*, 463-476.

Marks, J., Kannan, K., Roncase, E.J., Klepacki, D., Kefi, A., Orelle, C., Vazquez-Laslop, N., and Mankin, A.S. (2016). Context-specific inhibition of translation by ribosomal antibiotics targeting the peptidyl transferase center. Proc Natl Acad Sci U S A *113*, 12150-12155.

Matzov, D., Eyal, Z., Benhamou, R.I., Shalev-Benami, M., Halfon, Y., Krupkin, M., Zimmerman, E., Rozenberg, H., Bashan, A., Fridman, M.*, et al.* (2017). Structural insights of lincosamides targeting the ribosome of *Staphylococcus aureus*. Nucleic Acids Res. *45*, 10284-10292.

Miller, M.A., Pfeiffer, W., and Schwartz, T. (2010). Creating the CIPRES Science Gateway for Inference of Large Phylogenetic Trees. In Gateway Computing Environments Workshop (GCE) (New Orleans, LA), pp. 1-8.

Minh, B.Q., Schmidt, H.A., Chernomor, O., Schrempf, D., Woodhams, M.D., von Haeseler, A., and Lanfear, R. (2020). IQ-TREE 2: New Models and Efficient Methods for Phylogenetic Inference in the Genomic Era. Mol Biol Evol *37*, 1530-1534.

Morroni, G., Brenciani, A., Antonelli, A., D'Andrea, M.M., Di Pilato, V., Fioriti, S., Mingoia, M., Vignaroli, C., Cirioni, O., Biavasco, F*., et al.* (2018). Characterization of a Multiresistance Plasmid Carrying the *optrA* and *cfr* Resistance Genes From an *Enterococcus faecium* Clinical Isolate. Front Microbiol *9*, 2189.

Murina, V., Kasari, M., Hauryliuk, V., and Atkinson, G.C. (2018). Antibiotic resistance ABCF proteins reset the peptidyl transferase centre of the ribosome to counter translational arrest. Nucleic Acids Res. *46*, 3753-3763.

Murina, V., Kasari, M., Takada, H., Hinnu, M., Saha, C.K., Grimshaw, J.W., Seki, T., Reith, M., Putrins, M., Tenson, T*., et al.* (2019). ABCF ATPases Involved in Protein Synthesis, Ribosome Assembly and Antibiotic Resistance: Structural and Functional Diversification across the Tree of Life. J. Mol. Biol.

Murphy, E.L., Singh, K.V., Avila, B., Kleffmann, T., Gregory, S.T., Murray, B.E., Krause, K.L., Khayat, R., and Jogl, G. (2020). Cryo-electron microscopy structure of the 70S ribosome from *Enterococcus faecalis*. Sci Rep *10*, 16301.

Nakane, T., Kimanius, D., Lindahl, E., and Scheres, S.H. (2018). Characterisation of molecular motions in cryo-EM single-particle data by multi-body refinement in RELION. Elife *7*.

Orelle, C., Mathieu, K., and Jault, J.M. (2019). Multidrug ABC transporters in bacteria. Res Microbiol *170*, 381-391.

Ousalem, F., Singh, S., Chesneau, O., Hunt, J.F., and Boel, G. (2019). ABC-F proteins in mRNA translation and antibiotic resistance. Res Microbiol *170*, 435-447.

Pang, S., Boan, P., Lee, T., Gangatharan, S., Tan, S.J., Daley, D., Lee, Y.T., and Coombs, G.W. (2020). Linezolid-resistant ST872 *Enterococcus faecium* harbouring *optrA* and *cfr (D)* oxazolidinone resistance genes. Int J Antimicrob Agents *55*, 105831.

Pettersen, E.F., Goddard, T.D., Huang, C.C., Meng, E.C., Couch, G.S., Croll, T.I., Morris, J.H., and Ferrin, T.E. (2021). UCSF ChimeraX: Structure visualization for researchers, educators, and developers. Protein Science *30*, 70-82.

Rohou, A., and Grigorieff, N. (2015). CTFFIND4: Fast and accurate defocus estimation from electron micrographs. J Struct Biol *192*, 216-221.

Rozov, A., Demeshkina, N., Khusainov, I., Westhof, E., Yusupov, M., and Yusupova, G. (2016). Novel base-pairing interactions at the tRNA wobble position crucial for accurate reading of the genetic code. Nat Commun *7*, 10457.

Scheres, S.H., and Chen, S. (2012). Prevention of overfitting in cryo-EM structure determination. Nat Methods *9*, 853-854.

Schwarz, S., Zhang, W., Du, X.D., Kruger, H., Fessler, A.T., Ma, S., Zhu, Y., Wu, C., Shen, J., and Wang, Y. (2021). Mobile Oxazolidinone Resistance Genes in Gram-Positive and Gram-Negative Bacteria. Clin Microbiol Rev, e0018820.

Sharkey, L.K., Edwards, T.A., and O'Neill, A.J. (2016). ABC-F Proteins Mediate Antibiotic Resistance through Ribosomal Protection. MBio *7*, e01975.

Sharkey, L.K.R., and O'Neill, A.J. (2018). Antibiotic Resistance ABC-F Proteins: Bringing Target Protection into the Limelight. ACS Infect Dis *4*, 239-246.

Singh, K.V., Weinstock, G.M., and Murray, B.E. (2002). An *Enterococcus faecalis* ABC homologue (Lsa) is required for the resistance of this species to clindamycin and quinupristin-dalfopristin. Antimicrob Agents Chemother *46*, 1845-1850.

Sivertsen, A., Janice, J., Pedersen, T., Wagner, T.M., Hegstad, J., and Hegstad, K. (2018). The Enterococcus Cassette Chromosome, a Genomic Variation Enabler in Enterococci. mSphere *3*.

Su, W., Kumar, V., Ding, Y., Ero, R., Serra, A., Lee, B.S.T., Wong, A.S.W., Shi, J., Sze, S.K., Yang, L.*, et al.* (2018). Ribosome protection by antibiotic resistance ATP-binding cassette protein. Proc Natl Acad Sci U S A *115*, 5157-5162.

Svetlov, M.S., Plessa, E., Chen, C.W., Bougas, A., Krokidis, M.G., Dinos, G.P., and Polikanov, Y.S. (2019). High-resolution crystal structures of ribosome-bound chloramphenicol and erythromycin provide the ultimate basis for their competition. RNA *25*, 600-606.

Syroegin, E.A., Flemmich, L., Klepacki, D., Vazquez-Laslop, N., Mankin, A.S., Micura, R., and Polikanov, Y.S. (2021). Structural basis for the context-specific action of a classic peptidyl transferase inhibitor. Biorxiv.

Tang, Y., Lai, Y., Wang, X., Lei, C., Li, C., Kong, L., Wang, Y., and Wang, H. (2020). Novel insertion sequence ISChh1-like mediating acquisition of *optrA* gene in foodborne pathogen *Campylobacter coli* of swine origin. Vet Microbiol *252*, 108934.

Tenson, T., and Mankin, A. (2001). Short peptides conferring resistance to macrolide antibiotics. Peptides *22*, 1661-1668.

Tishchenko, S., Gabdulkhakov, A., Nevskaya, N., Sarskikh, A., Kostareva, O., Nikonova, E., Sycheva, A., Moshkovskii, S., Garber, M., and Nikonov, S. (2012). High-resolution crystal structure of the isolated ribosomal L1 stalk. Acta Crystallogr D Biol Crystallogr *68*, 1051-1057.

Vazquez-Laslop, N., and Mankin, A.S. (2018). Context-Specific Action of Ribosomal Antibiotics. Annu Rev Microbiol *72*, 185-207.

Vorobieva, V., Roer, L., Justesen, U.S., Hansen, F., Frimodt-Moller, N., Hasman, H., and Hammerum, A.M. (2017). Detection of the *optrA* gene in a clinical ST16 *Enterococcus faecalis* isolate in Denmark. J Glob Antimicrob Resist *10*, 12-13.

Wagner, T., Merino, F., Stabrin, M., Moriya, T., Antoni, C., Apelbaum, A., Hagel, P., Sitsel, O., Raisch, T., Prumbaum, D.*, et al.* (2019). SPHIRE-crYOLO is a fast and accurate fully automated particle picker for cryo-EM. Commun Biol *2*, 218.

Wang, Y., Lv, Y., Cai, J., Schwarz, S., Cui, L., Hu, Z., Zhang, R., Li, J., Zhao, Q., He, T.*, et al.* (2015). A novel gene, optrA, that confers transferable resistance to oxazolidinones and phenicols and its presence in *Enterococcus faecalis* and *Enterococcus faecium* of human and animal origin. J Antimicrob Chemother *70*, 2182-2190.

Waterhouse, A., Bertoni, M., Bienert, S., Studer, G., Tauriello, G., Gumienny, R., Heer, F.T., de Beer, T.A.P., Rempfer, C., Bordoli, L.*, et al.* (2018). SWISS-MODEL: homology modelling of protein structures and complexes. Nucleic Acids Res. *46*, W296-W303.

Waterhouse, A.M., Procter, J.B., Martin, D.M., Clamp, M., and Barton, G.J. (2009). Jalview Version 2--a multiple sequence alignment editor and analysis workbench. Bioinformatics *25*, 1189-1191.

Watson, Z.L., Ward, F.R., Meheust, R., Ad, O., Schepartz, A., Banfield, J.F., and Cate, J.H. (2020). Structure of the bacterial ribosome at 2 A resolution. Elife *9*.

Weaver, K.E., Chen, Y., Miiller, E.M., Johnson, J.N., Dangler, A.A., Manias, D.A., Clem, A.M., Schjodt, D.J., and Dunny, G.M. (2017). Examination of *Enterococcus faecalis* Toxin-Antitoxin System Toxin Fst Function Utilizing a Pheromone-Inducible Expression Vector with Tight Repression and Broad Dynamic Range. J Bacteriol *199*.

Wilson, D.N. (2014). Ribosome-targeting antibiotics and bacterial resistance mechanisms. Nat. Rev. Microbiol. *12*, 35-48.

Wilson, D.N., Hauryliuk, V., Atkinson, G.C., and O'Neill, A.J. (2020). Target protection as a key antibiotic resistance mechanism. Nat Rev Microbiol *18*, 637-648.

Wilson, D.N., Schluenzen, F., Harms, J.M., Starosta, A.L., Connell, S.R., and Fucini, P. (2008). The oxazolidinone antibiotics perturb the ribosomal peptidyl-transferase center and effect tRNA positioning. Proc Natl Acad Sci U S A *105*, 13339-13344.

Zheng, S.Q., Palovcak, E., Armache, J.-P., Verba, K.A., Cheng, Y., and Agard, D.A. (2017). MotionCor2: anisotropic correction of beam-induced motion for improved cryo-electron microscopy. Nat Methods *14*, 331-332.

Zhong, X., Xiang, H., Wang, T., Zhong, L., Ming, D., Nie, L., Cao, F., Li, B., Cao, J., Mu, D., *et al.* (2018). A novel inhibitor of the new antibiotic resistance protein OptrA. Chem Biol Drug Des *92*, 1458-1467.

Zivanov, J., Nakane, T., Forsberg, B.O., Kimanius, D., Hagen, W.J., Lindahl, E., and Scheres, S.H. (2018). New tools for automated high-resolution cryo-EM structure determination in RELION-3. Elife *7*, e42166.

Zivanov, J., Nakane, T., and Scheres, S.H.W. (2019). A Bayesian approach to beam-induced motion correction in cryo-EM single-particle analysis. IUCrJ *6*, 5-17.

Acknowledgments

We are grateful to Barbara E. Murray for sharing *E. faecalis* Δ*lsaA* (*lsa*::Kan) strain TX5332 (Singh et al., 2002), Jose A. Lemos for sharing pCIE plasmid (Weaver et al., 2017), Alberto Antonelli for sharing genetic material containing *poxtA* AOUC-0915 and *optrA* E35048 and Anette M. Hammerum for sharing the plasmid containing *optrA* ST16 (Vorobieva et al., 2017). We thank Michael Hall for help with cryo-EM data collection. The electron microscopy data was collected at the Umeå Core Facility for Electron Microscopy, a node of the Cryo-EM Swedish National Facility, funded by the Knut and Alice Wallenberg, Family Erling Persson and Kempe Foundations, SciLifeLab, Stockholm University and Umeå University. This work was supported by the Deutsche Forschungsgemeinschaft (DFG) (grant WI3285/8-1 to D.N.W), Swedish Research Council (Vetenskapsrådet) grants (2017-03783 to V.H. and 2019-01085 to G.C.A.), Ragnar Söderbergs Stiftelse (to V.H.), postdoctoral grant from the Umeå Centre for Microbial Research, UCMR (to H.T.), the European Union from the European Regional Development Fund through the Centre of Excellence in Molecular Cell Engineering (2014-2020.4.01.15-0013 to V.H.); and the Estonian Research Council (PRG335 to V.H.). D.N.W. and V.H. groups are also supported by the Deutsche Zentrum für Luft- und Raumfahrt (DLR01KI1820 to D.N.W.) and the Swedish Research Council (2018-00956 to V.H.) within the RIBOTARGET consortium under the framework of JPIAMR. GCA and VH were also supported by a project grant from the Knut and Alice Wallenberg Foundation (2020-0037 to GCA). Y.S.P. group is supported by the National Institutes of Health (R01-GM132302 to Y.S.P).

Author contributions

C.C.M. processed the microscopy data, generated and refined the molecular models and made the structure figures. V.M, H.T. and M.K. cloned the ARE constructs, performed genetic manipulations of *E. faecalis*, performed polysome fractionations and immunoblotting as well as performed MICs. V.M, K.J.T. and M.K. performed immunoprecipitations. V.M. prepared cryo-EM grids and collected cryo-EM datasets. A.S. and K.H. provided research materials and performed MICs. G.C.A. performed sequence conservation analyses. Y.S.P. provided structural insights into the mechanism of chloramphenicol action. C.C.M. and D.N.W. wrote the manuscript with input from all authors. D.N.W and V.H. conceived and supervised the project.

Competing interest statement

The authors declare no competing interests.

Table 1. Antibiotic resistance spectra LsaA, OptrA and PoxtA ARE-ABCFs.

	Minimum Inhibitory Concentration (MIC, μg/mL)					
	pCIE$_{spec}$ vector	**LsaA**	**OptrA ST16**	**OptrA 35048**	**PoxtA EF9F6**	**PoxtA AOUC 0915**
Chloramphenicol	2-4	2-4	**8-16**	**4-8**	**4-8**	**4-8**
Thiamphenicol	4	4	**32-64**	**16-32**	**8-16**	**32-64**
Florfenicol	1-2	1-2	**16-32**	**8**	**2-4**	**16-32**
Linezolid	1	1	**8**	**2-4**	**2-4**	**4-8**
Erythromycin	0.5-1	0.5	0.5	0.5	0.5	0.5
Azithromycin	0.5	0.5	0.5	0.5	0.5	0.5
Leucomycin	0.5	0.5	0.5	0.5	0.5	0.5
Lincomycin	0.125	**16-32**	0.125	0.125	0.125	0.125
Clindamycin	0.0156	**16**	0.0156	0.0156	0.0156	0.0156
Tiamulin	0.0625	**128**	0.0156	0.0156	0.031	0.031
Retapamulin	0.0156	**>64**	0.0156	0.0156	0.0156	0.0156
Virginiamycin M1	4	**>128**	4	4	4	4
Virginiamycin S1	8	8	8	8	8	8
Tetracycline	0.25	0.25	0.25	0.25	0.25	0.25

BHI media supplemented with 2 mg/mL kanamycin (to prevent *lsa* revertants), 0.1 mg/mL spectinomycin (to maintain the pCIE$_{spec}$ plasmid), 100 ng/mL of cCF10 peptide (to induce expression of ABCF proteins) as well as increasing concentrations of antibiotics was inoculated with 5 x 10^5 CFU/mL (≈OD_{600} 0.0005) of *E. faecalis* Δ*lsaA* (*lsa*::Kan) strain TX5332 transformed either with empty pCIE$_{spec}$ plasmid, or with pCIE$_{spec}$ derivatives for expression of ARE-ABCF proteins. After 16-20 hours at 37 °C without shaking, the presence or absence of bacterial growth was scored by eye. The MIC values that are higher than the empty vector control are shown in bold. The experiments were performed in triplicates.

Figures

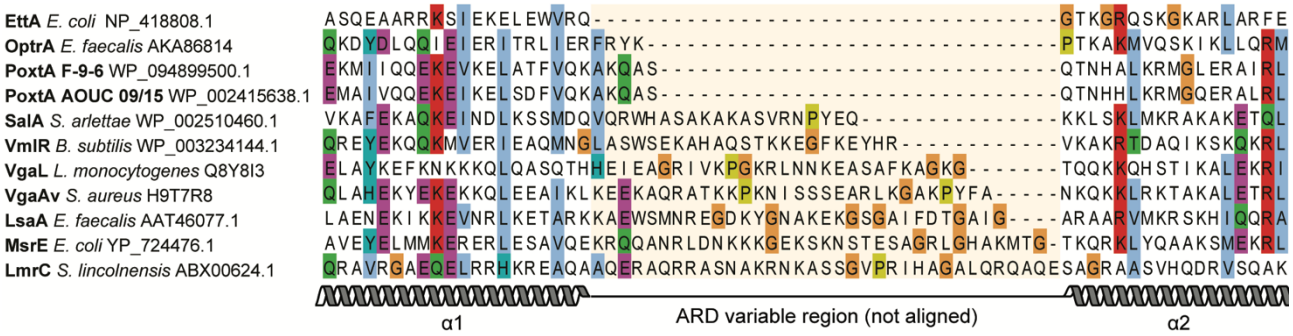

Fig. 1 Alignment of the ARDs from diverse bacterial ABCFs. The PoxtA and OptrA ARDs are slightly longer (4–5 amino acids) than the equivalent region in EttA, but significantly shorter than for other ARE-ABCFs. The central region with orange highlight, which includes the ARD loop and some of the adjacent helices in some proteins, was not aligned but simply ordered by length. Sequences were aligned with MAFFT (Katoh and Standley, 2013) and edited by hand to reduce gap placement.

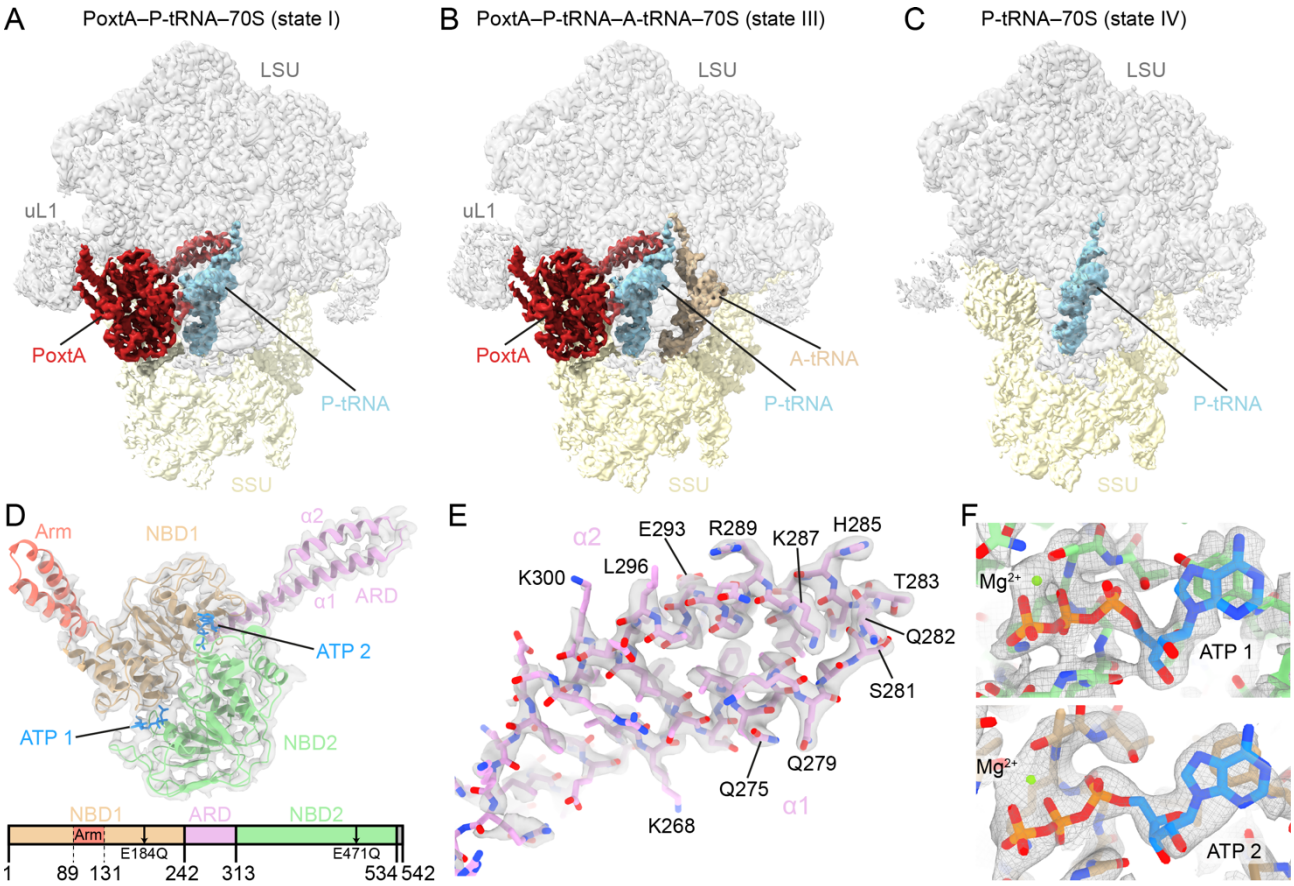

Fig. 2 Cryo-EM structures of PoxtA–70S complexes. (*A*–*C*) Cryo-EM maps with isolated densities for (*A*, *B*) *E. faecium* PoxtA (red) in complex with the *E. faecalis* 70S ribosome and (*A*) P-tRNA (cyan) or (*B*) P-tRNA (cyan) and A-tRNA (tan), (*C*) P-tRNA (cyan) only, with small subunit (SSU, yellow) and large subunit (LSU, grey). (*D*) Density (grey mesh) with molecular model of PoxtA from (*A*) coloured according to domain as represented in the associated schematics: nucleotide binding domain 1 (NBD1, tan), antibiotic-resistance domain (ARD, pink), nucleotide binding domain 2 (NBD2, green) and C-terminal extension (CTE, grey, not modelled). α1 and α2 indicate the two α-helices of the ARD interdomain linker. In (*D*), the ATP nucleotides are coloured blue. (*E*) Close view of the ARD tip from state I with sharpened map. (*F*) Close view of ATPs bound by PoxtA (state I).

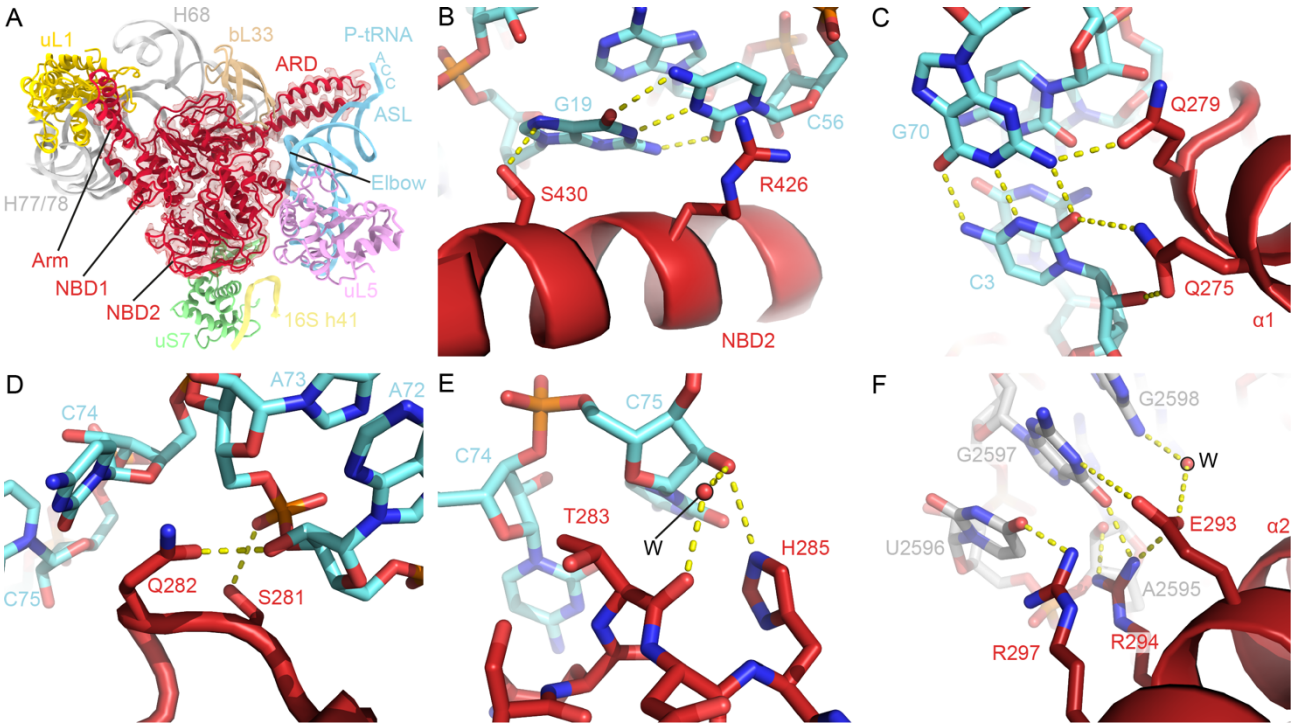

Fig. 3. Interactions between PoxtA and the ribosome-P-tRNA complex. (*A*) Overview of PoxtA interactions with the 23S rRNA (grey), 16S rRNA h41 (yellow), uL1 (gold), uS7 (green), uL5 (pink), bL33 (tan) and the P-tRNA (light blue). (*B*–*E*) Interactions between the P-tRNA elbow (light blue) and the PoxtA NBD2 (*B*), the P-tRNA acceptor stem (light blue) and the PoxtA ARD (*C*), the ARD and the CCA end (*D*, *E*). (*F*) An interaction between the PoxtA ARD α2 and the 23S rRNA. The high-resolution model from the combined 70S volume was used.

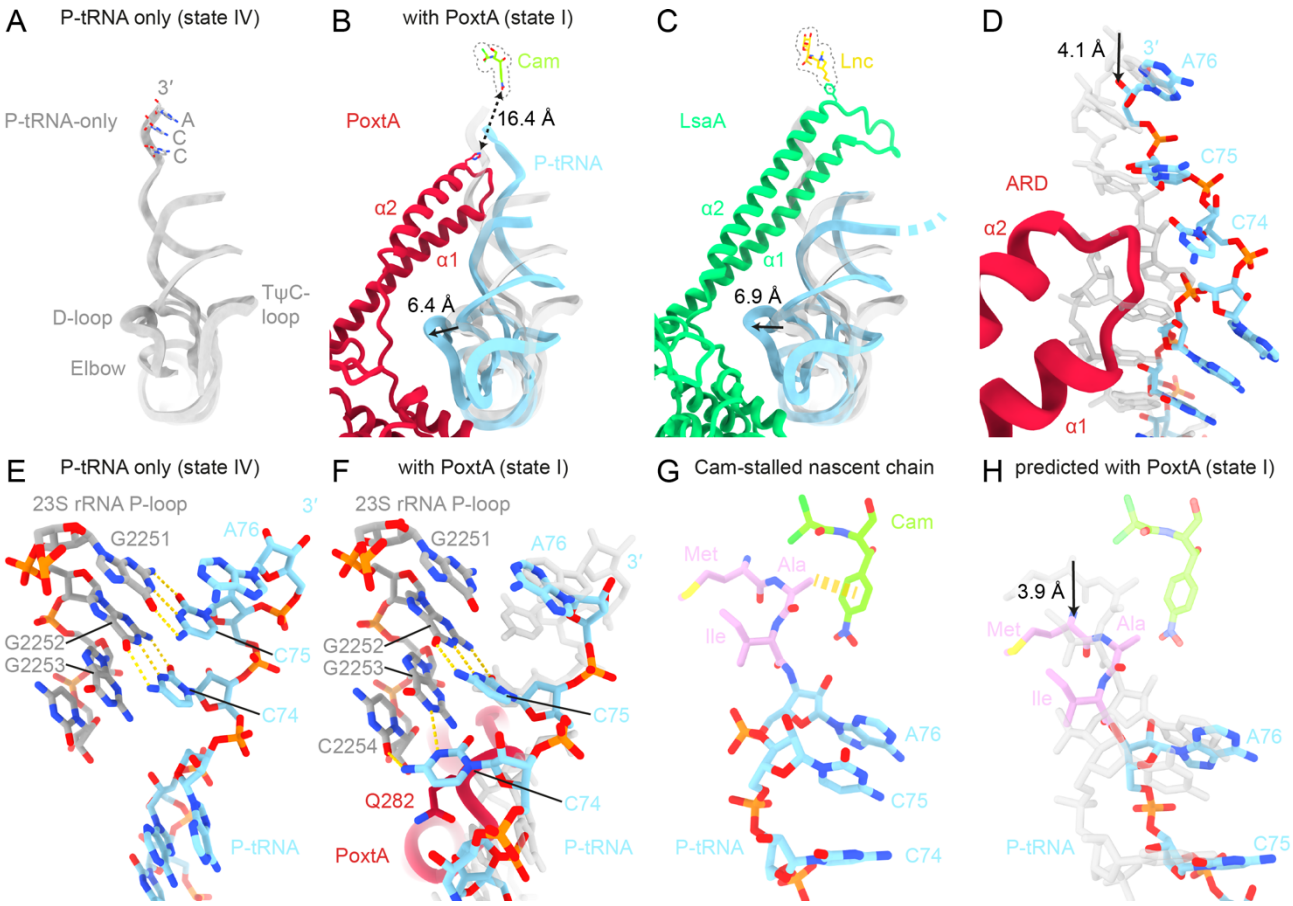

Fig. 4 Conformational changes at the peptidyltransferase centre. (*A*, *B*) Comparison of position of CCA-end of the P-site tRNA at PTC from the (*A*) *E. faecalis* 70S-P-tRNA only complex (grey), (*B*) PoxtA-70S complex (state I, PoxtA in red and P-tRNA in light blue), and (*C*) LsaA-70S complex (PDB ID 7NHK, (Crowe-McAuliffe et al., 2021), LsaA in green and P-tRNA in light blue). Models of chloramphenicol for PoxtA (PDB ID 6ND5, (Svetlov et al., 2019)) and lincomycin for LsaA (PDB ID 5HKV) (Matzov et al., 2017) are superimposed for referece (*D*) Close-up of (*B*) showing P-tRNA acceptor stem distortion induced by PoxtA binding. (*E*, *F*) Interaction between the 23S rRNA P-loop (grey) and P-tRNA (light blue) for (*E*) the P-tRNA-only complex (state IV) and (*F*) with bound PoxtA (state IV P-tRNA is overlayed in transparent grey for comparison). (*G*, *H*) Indirect modulation of the chloramphenicol binding site by PoxtA. (*G*) The structure of chloramphenicol (cam) stabilised by a nascent peptide chain with alanine in the −1 position (Syroegin et al., 2021). (*H*) modelled shift of the nascent chain shown in (*G*) induced by PoxtA displacement of the P-tRNA CCA end. The P-tRNA from (*G*) is overlayed in transparent grey for comparison.

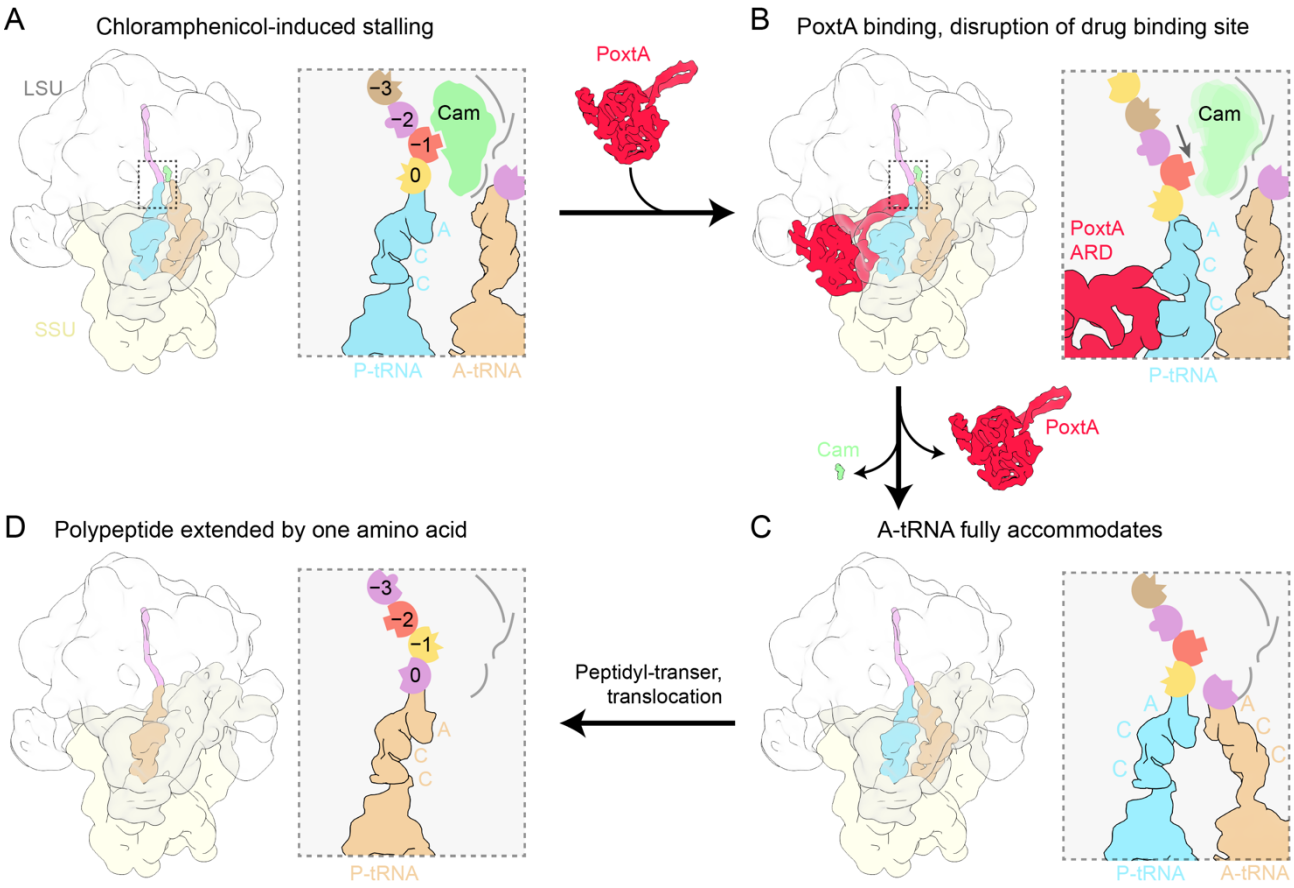

Fig. 5 Model for ribosome protection by PoxtA. (*A*) Elongating ribosomes are stalled by PhO antibiotics with a peptidyl-tRNA in the P-site. The side chain of the amino acid at position −1 contributes to the PhO binding site. (*B*) Stalled ribosomes are recognized by PoxtA, which induces a shifted P-site tRNA and nascent chain, thereby disrupting the PhO binding site. (*C*) After dissociation of the PhO drug and PoxtA, the P-tRNA and nascent chain return to the regular conformation. (*D*) Accommodation of an A-tRNA occludes the drug binding site. After peptidyl transfer and translocation, amino acid at position −1 would change, thereby resetting the PhO binding site.

5.4 Structures of bacterial RQC elongation complexes

5.4.1 Summary

This manuscript describes structures of bacterial RQC alanine tailing intermediates. Extensive classification revealed a suite of states, consisting minimally of an LSU and peptidyl-tRNA. RqcH was bound to some states, and an uncharacterised protein, which we renamed RqcP, was found in all states that contained the peptidyl-tRNA in the LSU P-site. Combined, these states allowed us to propose a model of elongation for the non-canonical alanine tailing reaction.

5.4.2 Contributions

Processing of all cryo-EM data, creation of the molecular models, some processing of the samples for tRNA microarrays, and generation of figures. Data for Fig. 2E, 2J and 3D–F and 4E came from our collaborators Prof. V. Hauryliuk and Dr G. Atkinson (Umeå University), and tRNA microarray data in Fig. 5A came from Prof. Z. Ignatova (University of Hamburg). Writing of the manuscript with help from Prof. Daniel N. Wilson.

Please cite this article in press as: Crowe-McAuliffe et al., Structural Basis for Bacterial Ribosome-Associated Quality Control by RqcH and RqcP, Molecular Cell (2020), https://doi.org/10.1016/j.molcel.2020.11.002

Molecular Cell

CellPress

Article

Structural Basis for Bacterial Ribosome-Associated Quality Control by RqcH and RqcP

Caillan Crowe-McAuliffe,[1,5] Hiraku Takada,[2,3,5] Victoriia Murina,[2,3] Christine Polte,[1] Sergo Kasvandik,[4] Tanel Tenson,[4] Zoya Ignatova,[1] Gemma C. Atkinson,[2] Daniel N. Wilson,[1,6,*] and Vasili Hauryliuk[2,3,4,*]

[1]Institute for Biochemistry and Molecular Biology, University of Hamburg, Martin-Luther-King-Pl. 6, 20146 Hamburg, Germany
[2]Department of Molecular Biology, Umeå University, 90187 Umeå, Sweden
[3]Laboratory for Molecular Infection Medicine Sweden (MIMS), Umeå University, 90187 Umeå, Sweden
[4]University of Tartu, Institute of Technology, 50411 Tartu, Estonia
[5]These authors contributed equally
[6]Lead Contact
*Correspondence: daniel.wilson@chemie.uni-hamburg.de (D.N.W.), vasili.hauryliuk@umu.se (V.H.)
https://doi.org/10.1016/j.molcel.2020.11.002

SUMMARY

In all branches of life, stalled translation intermediates are recognized and processed by ribosome-associated quality control (RQC) pathways. RQC begins with the splitting of stalled ribosomes, leaving an unfinished polypeptide still attached to the large subunit. Ancient and conserved NEMF family RQC proteins target these incomplete proteins for degradation by the addition of C-terminal "tails." How such tailing can occur without the regular suite of translational components is, however, unclear. Using single-particle cryo-electron microscopy (EM) of native complexes, we show that C-terminal tailing in *Bacillus subtilis* is mediated by NEMF protein RqcH in concert with RqcP, an Hsp15 family protein. Our structures reveal how these factors mediate tRNA movement across the ribosomal 50S subunit to synthesize polypeptides in the absence of mRNA or the small subunit.

INTRODUCTION

In all cells, translational stalling on truncated or damaged mRNAs is harmful because it sequesters ribosomes from active protein production and can result in the synthesis of cytotoxic truncated proteins. Therefore, ribosome-associated quality control (RQC) pathways have evolved in all domains of life to disassemble such stalled complexes (Inada, 2020; Joazeiro, 2019). In eukaryotes, stalled 80S ribosomes are recognized and split into small 40S and large 60S subunits by Pelota/Dom34 and ABCE1/Rli1 (Franckenberg et al., 2012). The resulting 60S-peptidyl-tRNA complexes are then processed by the RQC pathway, where conserved NEMF-family proteins—Rqc2p in yeast and NEMF in humans—facilitate the addition of C-terminal alanine and threonine (CAT) tails to the nascent polypeptide chains (Brandman et al., 2012; Defenouillère and Fromont-Racine, 2017; Inada, 2020; Joazeiro, 2019; Kostova et al., 2017; Shen et al., 2015; Sitron and Brandman, 2019; Yan and Zaher, 2019). The nascent polypeptides are ubiquitinated by Listerin/Ltn1 (Bengtson and Joazeiro, 2010; Lyumkis et al., 2014) and are extracted by p97/Cdc48 prior to proteasomal degradation (Defenouillère et al., 2013; Verma et al., 2013).

Bacterial NEMF-family homologs are members of the FbpA (fibronectin binding protein A) family of virulence factors. FbpA proteins from a number of Gram-positive bacterial species—including *Enterococcus faecalis* (Singh et al., 2015), *Listeria monocytogenes* (Osanai et al., 2013), *Streptococcus pneumoniae* (Pracht et al., 2005), and *Bacillus subtilis* (Rodriguez Ayala et al., 2017)—were proposed to directly mediate bacterial adhesion to the extracellular matrix, although a direct experimental demonstration of this function has been lacking. A recent study demonstrated that the *B. subtilis* NEMF homolog, RqcH ("bacterial Rqc2 homolog"), is a bona fide bacterial RQC factor (Lytvynenko et al., 2019). *B. subtilis* RqcH is recruited to 50S-peptidyl-tRNA complexes to promote the addition of C-terminal polyalanine tails to stalled aberrant polypeptides, targeting incomplete proteins for degradation by the ClpXP machinery (Lytvynenko et al., 2019). Although *rqcH* is absent in a number of bacterial lineages, this discovery, along with the broad distribution of this factor in archaea, implies that the NEMF proteins were present in the last universal common ancestor (LUCA) and that C-terminal tailing is, therefore, integral to RQC in all three domains of life (Burroughs and Aravind, 2014; Lytvynenko et al., 2019).

NEMF-family proteins are widely distributed in all three kingdoms of life and typically contain, from N terminus to C terminus, (1) an NFACT-N domain followed by (2) two helix-hairpin-helix (HhH) motifs, which have homology to DNA glycosylases but have no known enzymatic activity; (3) a coiled-coil motif, consisting of two long α helices separated by a small "middle" domain, termed CC-M; (4) an NFACT-R domain, which is predicted to bind RNA; and (5) an NFACT-C domain of unknown function

Please cite this article in press as: Crowe-McAuliffe et al., Structural Basis for Bacterial Ribosome-Associated Quality Control by RqcH and RqcP, Molecular Cell (2020), https://doi.org/10.1016/j.molcel.2020.11.002

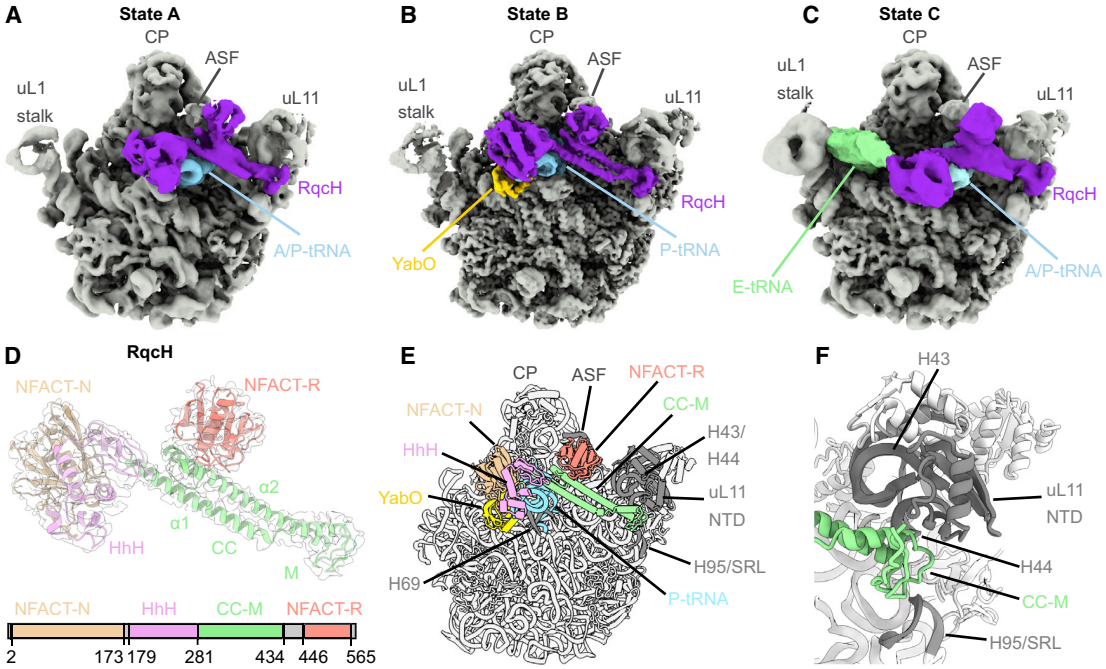

Figure 1. Cryo-EM Structures of *B. subtilis* RqcH-50S Complexes

(A–C) Cryo-EM maps of RqcH-50S complexes with (A) A/P-site tRNA (state A), (B) P-site tRNA and YabO (state B), and (C) A/P-site and E-site tRNAs (state C). 50S, gray; RqcH, purple; A/P-site and P-site tRNAs, light blue; YabO, yellow; and E-site tRNA, green.

(D) Cryo-EM map of RqcH from state B multibody refinement with RqcH model indicated by domain according to the color key.

(E) Model of state B with RqcH domains labeled as in (D). SRL, sarcin-ricin loop.

(F) Highlight of the interaction between the CC-M domain of RqcH (green) and the uL11 stalk base and SRL.

See also Figures S1 and S2 and Table S1.

that is absent from bacterial NEMF homologs (Burroughs and Aravind, 2014; Shao et al., 2015). An early structural study proposed that yeast Rqc2p is bound to the 60S subunit around the P site, likely recognizing the peptidyl-tRNA (Lyumkis et al., 2014). Subsequently, two more structures of NEMF proteins bound to the large ribosomal subunit were reported: a yeast Rqc2p-60S complex with tRNAs bound in the aminoacyl site (A site) and peptidyl site (P site) (Shen et al., 2015) and an *in vitro* reconstituted mammalian 60S-Listerin-NEMF complex with a P-site peptidyl-tRNA (Shao et al., 2015). In both structures, the NFACT-N and HhH domains bound the stalled 60S complex close to the P-site tRNA, and the coiled coil spanned the A site to contact the stalk base with the middle CC-M domain. Although these structures revealed the global binding mode of NEMF factors to the 60S ribosome and associated P-site tRNA, due to the low resolution of the NEMF-family proteins, at most only a partial molecular model could be built (Lyumkis et al., 2014; Shao et al., 2015; Shen et al., 2015). A detailed understanding of how NEMF-family proteins interact with RQC complexes, mechanistic insight into how NEMF homologs catalyze C-terminal tailing, and the identity of other factors involved in the bacterial RQC pathway have so far remained elusive.

Here, we present cryo-electron microscopy (EM) structures of native complexes obtained by affinity purification of *B. subtilis* RqcH bound to a 50S-peptidyl-tRNA complex and discover an additional factor, RqcP (formerly YabO), which was previously not known to be associated with RQC and which is co-distributed with RqcH across many bacterial lineages. Surprisingly, our series of RQC structures mimic distinct pre- and post-translocational states observed during canonical translation elongation. This provides the structural and mechanistic basis for how RqcH and RqcP cooperate to mediate tRNA movement, and thereby processive alanine tailing, through an RQC translation cycle that is independent of mRNA, the small ribosomal subunit, and the translocase EF-G.

RESULTS

Cryo-EM Structures of Native RqcH-50S Complexes

To investigate how RqcH mediates C-terminal tailing in *B. subtilis*, we have determined cryo-EM structures of native RqcH-50S complexes isolated by affinity purification. The RqcH-50S complexes were purified by affinity chromatography from *B. subtilis* cells expressing RqcH C-terminally tagged with a $FLAG_3$ epitope (Figure S1A). Single-particle cryo-EM analysis of the RqcH-50S complexes, with extensive *in silico* sorting, yielded four distinct 50S functional states: states A–D (Figure S1B). State A contained RqcH and a peptidyl-tRNA in an A/P-like configuration (Figure 1A), whereas state B contained RqcH, a peptidyl-tRNA in a classical P-site-like conformation, as well as an additional protein factor that we identified as YabO (Figures 1B and S1B)—a homolog of *E. coli* Hsp15. State

Please cite this article in press as: Crowe-McAuliffe et al., Structural Basis for Bacterial Ribosome-Associated Quality Control by RqcH and RqcP, Molecular Cell (2020), https://doi.org/10.1016/j.molcel.2020.11.002

CellPress

Table 1. Cryo-EM Data Collection, Model Refinement, and Validation Statistics

Collection Details	RqcH state A	RqcH state B	RqcH state B multibody
Number of micrograph movies	3,032/4,145	3,032/4,145	3,032/4,145
Electron fluence ($e^-/Å^2$)	28.3/29.7	28.3/29.7	28.3/29.7
Defocus range (μm)	−0.7 to −1.9	−0.7 to −1.9	−0.7 to −1.9
Accession numbers	EMDB: 11890, PDB: 7AS9	EMDB: 11889, PDB: 7AS8	EMDB: 11891, PDB: 7ASA
Average map resolution (Å)	3.5	2.9	4.0
Number of particles	10,703	74,210	74,210
Number of non-hydrogen atoms	93,142	93,805	8,110
Number of protein residues	3,720	3,810	750
Number of RNA bases	2,999	2,997	116
Refinement			
Map CC around atoms	0.84	0.90	0.75
Map CC whole volume	0.82	0.90	0.74
Map sharpening B factor ($Å^2$)	−66.07	−71.99	−98.32
Root-Mean-Square Deviation			
Bond length (Å)	0.007	0.011	0.013
Bond angle (°)	1.050	1.010	2.026
Validation			
MolProbity score	2.08	1.70	0.98
Clash score	8.30	4.05	0.66
% Poor rotamers	0.00	0.03	0.18
Ramachandran plot			
% Favored	86.78	91.27	96.19
% Allowed	13.00	8.65	3.54
% Disallowed	0.22	0.08	0.27

C was similar to state A, but with the additional presence of a tRNA in the exit site (E site) (Figure 1C). State D contained YabO and P-site tRNA, but no RqcH, implying that RqcH had dissociated during sample preparation (Figure S1B). States A, B, C, and D were refined to average resolutions of 3.5 Å, 2.9 Å, 3.1 Å, and 2.6 Å, respectively (Figures S2A–S2D); however, while the 50S subunit was well resolved, the quality of the density for the ligands varied (Figures S2E–S2H). RqcH exhibited high flexibility in states A and C, where the peptidyl-tRNA was in the A/P site, but was better ordered in state B, where YabO was present and the peptidyl-tRNA was in a classical P-site conformation (Figures 1A–1C and S2E–S2G). We further improved the cryo-EM map density for RqcH using multibody refinement (Figure S1B). The resulting map was sufficient for unambiguous fitting of individual domains of a homology model for *B. subtilis* RqcH based on the X-ray structures of RqcH homologs from related Gram-positive bacteria (Manne et al., 2019; Musyoki et al., 2016) (Figure 1D; Table 1; Video S1). The NFACT-N and CC-M domains were relatively well resolved (Figures S2I–S2K), consistent with the presence of density for many bulky and aromatic side chains, with the exception of the minimal M domain, which was small and resembled a hairpin (Figures S3L–S3O). The NFACT-R and HhH domains appeared more flexible and less well resolved (Figures S3I and S3J). Nonetheless, and with the exception of three short loops, we were able to model residues 2 to 565 of RqcH and use this model to fit and refine structures of RqcH in states A and B (Table 1).

Interaction of RqcH on the 50S Subunit

In the best resolved state, state B, the RqcH N-terminal NFACT-N and HhH domains are located near the central protuberance (CP) between the P and E sites, while the coiled coils of the CC-M domain span the interface of the 50S subunit to the uL11 stalk base and then back to the A-site finger (ASF; H38), where the NFACT-R domain is positioned (Figure 1E; Video S1). The overall binding site of *B. subtilis* RqcH on the 50S subunit is similar to that of the eukaryotic homologs, yeast Rqc2p (Shen et al., 2015) and human NEMF (Shao et al., 2015), on the 60S subunit (Figures S3A–S3H); however, the higher resolution of RqcH-50S complexes reveals many additional details not observed before. The NFACT-N and HhH domains of RqcH interact predominantly with the anticodon-stem loop (ASL) of P-site tRNA (Figures 1E and S2O) and do not appear to establish any contact with the 50S subunit. This rationalizes how the previously reported D97A/R98A (DR) and E121A/I122A/M123A (EIM) mutations in the NFACT-N domain specifically abrogate tRNA binding (Lytvynenko et al., 2019), since these motifs are located within loops that approach the anticodon of the tRNA (Figures 2A–2C). In

Please cite this article in press as: Crowe-McAuliffe et al., Structural Basis for Bacterial Ribosome-Associated Quality Control by RqcH and RqcP, Molecular Cell (2020), https://doi.org/10.1016/j.molcel.2020.11.002

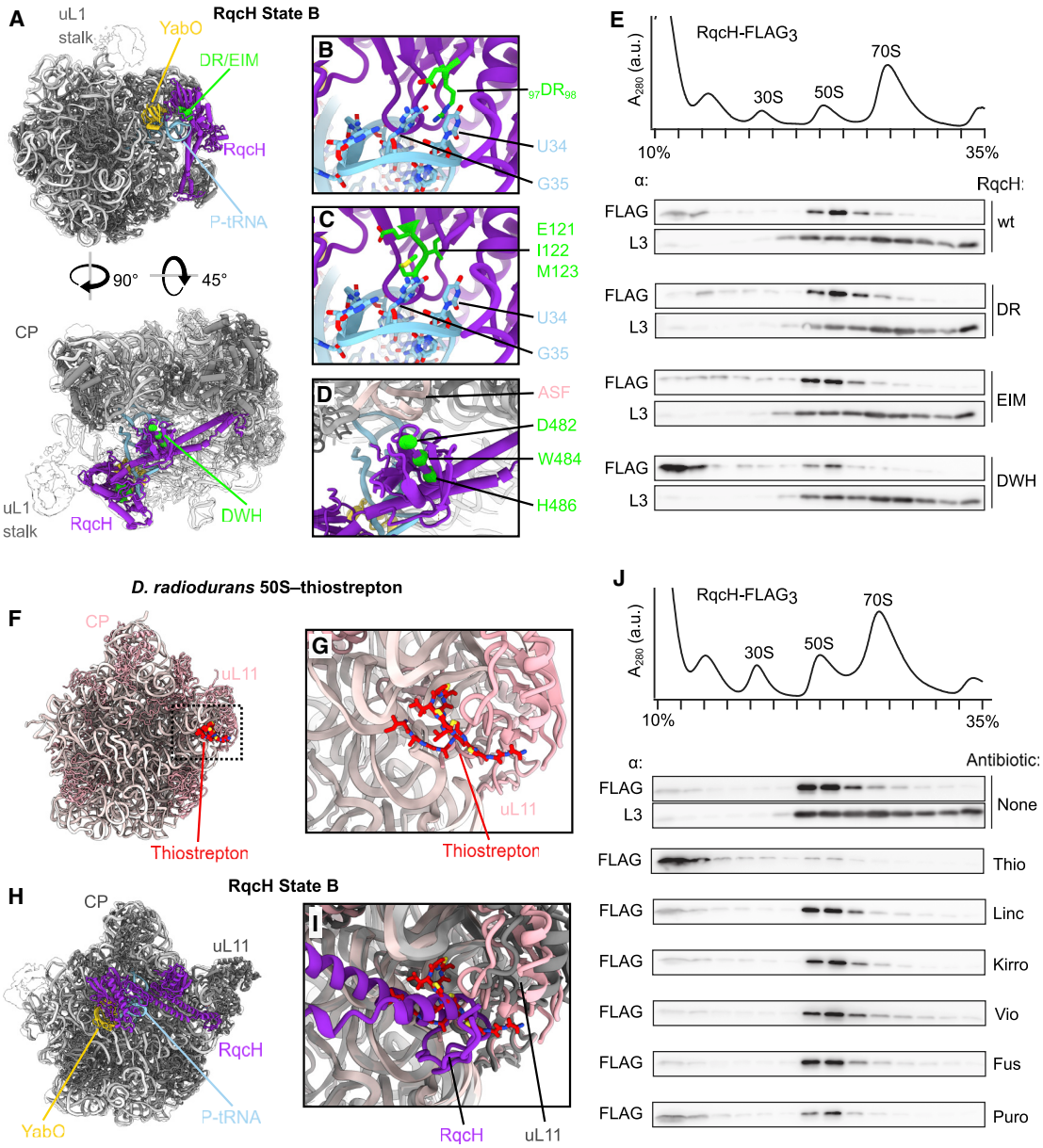

Figure 2. The Interaction of RqcH with the 50S Probed with Mutagenesis and Antibiotics

(A–D) Overview of RqcH mutants on the ribosome (A) and structural details of RqcH mutants (B) DR, D97A/R98A; (C) EIM, E121A/I122A/M123A; and (D) DWH, D482A/W484A/H486A. Mutated residues are indicated in green.

(E) Sucrose gradient sedimentation of RqcH-FLAG$_3$ variants expressed in a wild-type background. Immunoblots were probed with either α-FLAG, to detect RqcH wild-type and mutant RqcH variants, or α-L3.

(F) The thiostrepton-bound 50S from *D. radiodurans* (PDB: 3CF5) (Harms et al., 2008).

(G) Close view of thiostrepton interacting with the ribosome close to uL11.

(H) RqcH State B shown from the same perspective as (F).

(I) Overlay of thiostrepton-bound 50S and RqcH state B from the same view as (G).

(J) Sucrose gradient sedimentation of RqcH-FLAG$_3$ in the presence or absence of translation-targeting antibiotics added after cell lysis: Thio, thiostrepton (50 μM); Kirro, kirromycin (50 μM); Linc, lincomycin, (1 μM); Vio, viomycin (100 μM); Fus, fusidic acid (100 μM); Puro, puromycin (1 mM).

good agreement with a previous report (Lytvynenko et al., 2019), introduction of the DR and EIM mutations did not destabilize the interaction of RqcH with the 50S subunit (Figure 2E). Indeed, one volume obtained from *in silico* sorting resembled state B (termed hereinafter as state B*) but with little density for the NFACT-N and HhH domains, indicating that these domains can be flexible on the 50S subunit and are not required for RqcH binding (Figure S1B). There are only two direct contacts between RqcH

Please cite this article in press as: Crowe-McAuliffe et al., Structural Basis for Bacterial Ribosome-Associated Quality Control by RqcH and RqcP, Molecular Cell (2020), https://doi.org/10.1016/j.molcel.2020.11.002

and components of the 50S subunit, namely, between the RqcH NFACT-R domain and the ASF (Figure 1E) and between the distal portion of the RqcH CC-M domain and uL11/H44 at the stalk base (Figure 1F). Both interactions are necessary for RqcH function because (1) mutations in the conserved DWH motif of the NFACT-R domain, which is in close proximity to the ASF, leads to a loss in interaction with the 50S subunit as assessed by sucrose gradient centrifugation of cellular lysates (Figures 2D and 2E); and (2) treatment of *B. subtilis* lysates with thiostrepton, an antibiotic that has an overlapping binding site with the CC-M domain (Figures 2F–2I), abrogated the association of RqcH with the 50S subunit (Figure 2J). In good agreement with a recent study of yeast Rqc2p (Osuna et al., 2017), antibiotics targeting the peptidyl-transferase center (lincomycin), the small ribosomal subunit (viomycin), or canonical GTPase translation factors EF-Tu (kirromycin) and EF-G (fusidic acid) did not perturb RqcH association with the 50S subunit (Figure 2J). Puromycin, which releases the nascent chain if the A site is accessible, had only a mild effect, if any (Figure 2J).

Discovery of a Role for YabO during Bacterial RQC

State B contained additional density—positioned between the RqcH NFACT-N domain, P-site tRNA, and 23S rRNA helices 68 and 69—that did not correspond to RqcH or any ribosomal component (Figures 3A and 3B). This density was assigned to YabO based on mass spectrometry (Table S1) and the excellent agreement between the density features and a fitted homology model for *B. subtilis* YabO using the crystal structure of *E. coli* Hsp15 as the template (Staker et al., 2000) (Figure 3C). *E. coli* Hsp15 binds 50S-peptidyl-tRNA complexes (Korber et al., 2000) and can translocate the peptidyl-tRNA from the A to the P site (Jiang et al., 2009). While *E. coli* Hsp15 was reported to bind at the CP of the 50S (Jiang et al., 2009), YabO instead binds the 50S at a distinct site adjacent to H69 (Figures S3I–S3K). *E. coli* and other Gammaproteobacteria do not contain RqcH homologs, suggesting that *E. coli* Hsp15 may function differently than *B. subtilis* YabO. Additionally, *E. coli* Hsp15 has a C-terminal extension (CTE) that is absent in YabO (Figures 3D and S3L). YabO/Hsp15 homologs across diverse bacterial clades divide into either those having the CTE, such as *E. coli* Hsp15, or those that do not, such as YabO (Figure 3D); strikingly, this division is strongly associated with the presence or absence of RqcH. Presence of the Hsp15 CTE is entirely mutually exclusive with the presence of RqcH, and, with few exceptions, bacteria with YabO/Hsp15 homologs lacking the CTE contain RqcH (Figure 3D; Table S2). Together with the presence of Proteobacteria in both clades of YabO/Hsp15, this suggests that these proteins are not functionally equivalent orthologs but are rather functionally divergent paralogs. This is further supported by the observation that, unlike that of Hsp15, expression of YabO is not induced by heat shock (Nicolas et al., 2012). Collectively, these findings suggest that YabO homologs are likely to be involved in RQC in bacteria containing RqcH, but they raise the question as to the role of Hsp15 and its CTE in bacteria lacking RqcH.

We used a genetic approach to assess the role of *B. subtilis* YabO in RQC. As was shown earlier, the loss of RqcH does not result in a strong phenotype in *B. subtilis* grown in laboratory conditions on rich medium (Lytvynenko et al., 2019). However, when this mutation is combined with the loss of tmRNA, the resultant Δ*ssrA* Δ*rqcH* strain is particularly sensitive to translation inhibitors such as tetracycline and displays a growth defect at elevated temperatures (Figure 3E). Consistent with the role of YabO in RQC, while a Δ*yabO* strain has no growth defect, the simultaneous loss of YabO and tmRNA phenocopies the Δ*ssrA* Δ*rqcH* double deletion. Importantly, heterologous expression of *E. coli* Hsp15—either a full-length (Figure 3F) or a truncated version lacking either the N-terminal extension alone or both the N-terminal extension and CTE (Figure S3M)—does not counter the growth defect and heat sensitivity of the Δ*ssrA* Δ*yabO* strain. This is consistent with YabO being a specialized RQC factor that is functionally distinct from *E. coli* Hsp15.

To further dissect the role of YabO in RQC, we affinity-purified YabO with a C-terminal $FLAG_3$ tag, yielding YabO-50S complexes (Figure S4A). RqcH co-purified with these complexes, as confirmed by mass spectrometry (Table S1). Single-particle cryo-EM analysis and *in silico* sorting yielded state B with RqcH and P-site tRNA as well as state D with P-site tRNA, but no RqcH (Figure S4B), both of which were also observed for the RqcH pull-outs (Figures 1B and S1B). We observed an additional novel state E, containing YabO with P- and E-site tRNAs, but no RqcH (Figure S4B). States B, D, and E in the YabO pull-out dataset were refined to average resolutions of 3.2 Å, 2.6 Å, and 3.2 Å, respectively (Figures S5A–S5C). In most states, YabO was well resolved (Figures S5D–S5F) and established defined contacts with H69 of the 50S and the ASL of the P-site tRNA (Figures 4A–4D). The interaction between YabO and RqcH was less well resolved and does not appear to be essential for recruitment of these factors to the 50S, since RqcH migrated with the 50S in the absence of YabO and vice versa (Figure 4E). By contrast, interaction with 23S rRNA H69 is critical for YabO function, since mutation of the conserved Arg16 to Ala (R16A) completely abolished YabO association with the 50S subunit (Figures 3D, 4E, and S4A; Table S1). Consistent with this result, substitution of native *yabO* with *yabO R16A* in the Δ*ssrA* background phenocopies the Δ*ssrA* Δ*yabO* double deletion (Figure 3E), thus reinforcing the crucial role of the Arg16 residue in YabO functionality. Comparison of state A (RqcH and A/P-site tRNA but no YabO; Figure 4F) with state B (RqcH with YabO and a P-site tRNA instead of an A/P-site tRNA; Figure 4G) shows that YabO is associated with the translocation-like movement of the peptidyl-tRNA from the A site (Figure 4H) into the P site (Figure 4I), consistent with previous proposals (Jiang et al., 2009). YabO may selectively bind and stabilize a P-like conformation of the tRNA that results from RqcH-induced tRNA movement, itself perhaps ultimately driven by thermal motion of the L7/L12 stalk relative to the large subunit 50S body. The entire RqcH protein shifted with the tRNA during the translocation-like event, with large-scale movements in the range of 15–20 Å (Figure 4J; Video S2). The shift in RqcH is also accompanied by a corresponding movement in the uL11 stalk base to which RqcH is tethered via the CC-M domain (Figure 4J).

Identification of Additional Factors in the YabO- and RqcH-P-tRNA-50S Complexes

During 3D classification of the 50S subunits, we also noticed a substoichiometric extra density in the vicinity of uL14. This

Please cite this article in press as: Crowe-McAuliffe et al., Structural Basis for Bacterial Ribosome-Associated Quality Control by RqcH and RqcP, Molecular Cell (2020), https://doi.org/10.1016/j.molcel.2020.11.002

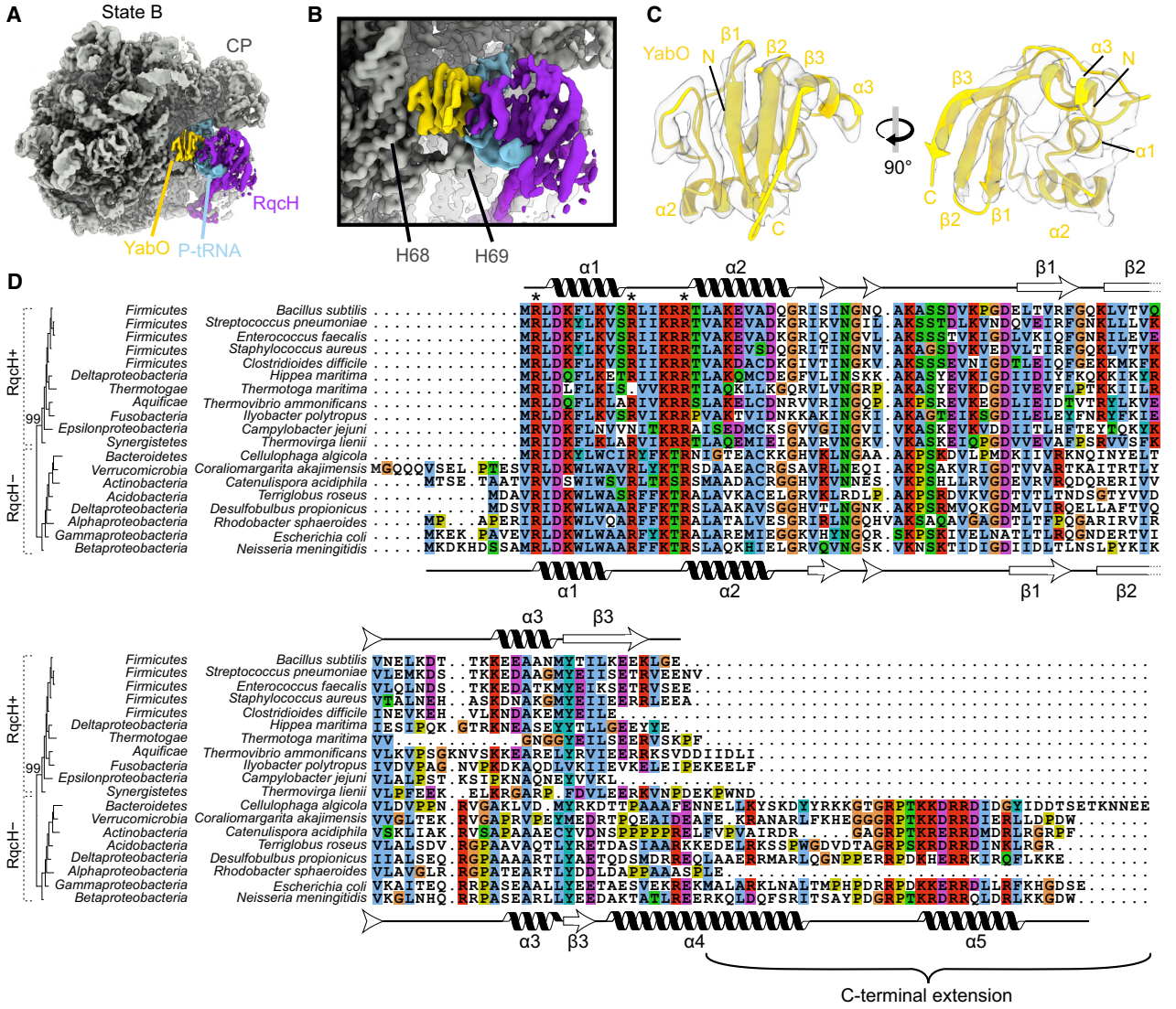

Figure 3. YabO Binds the 50S Adjacent to RqcH, and Lack of the CTE in YabO/Hsp15 Is Associated with the Presence of RqcH

(A and B) View of YabO in RqcH state B showing global position on the 50S (A) or zoomed view (B).

(C) Views of YabO model fitted into density from state B.

(D) Phylogenetic tree and sequence alignment of YabO/Hsp15 homologs from diverse bacteria. The RqcH+/RqcH− phylogenetic split is supported with 99% bootstrap support. Secondary structure, calculated with DSSP or predicted by PSIPRED where no structure was available, is indicated above (YabO, present study) or below (*E. coli* Hsp15, from PDB: 1DM9).

(E) Simultaneous deletion of *yabO* and *ssrA* genes results in a synthetic growth defect in *B. subtilis*. 10-fold serial dilutions were spotted onto LB agar plates and incubated for 18 h at 37°C (left), 49°C (middle), or 37°C with a low dose (0.5 μg/mL) of tetracycline (Tc).

(F) IPTG-inducible expression of *E. coli* Hsp15 does not rescue the growth defect of Δ*yabO* Δ*ssrA B. subtilis* strain.

See also Figures S3, S4, and S5 and Table S2.

Please cite this article in press as: Crowe-McAuliffe et al., Structural Basis for Bacterial Ribosome-Associated Quality Control by RqcH and RqcP, Molecular Cell (2020), https://doi.org/10.1016/j.molcel.2020.11.002

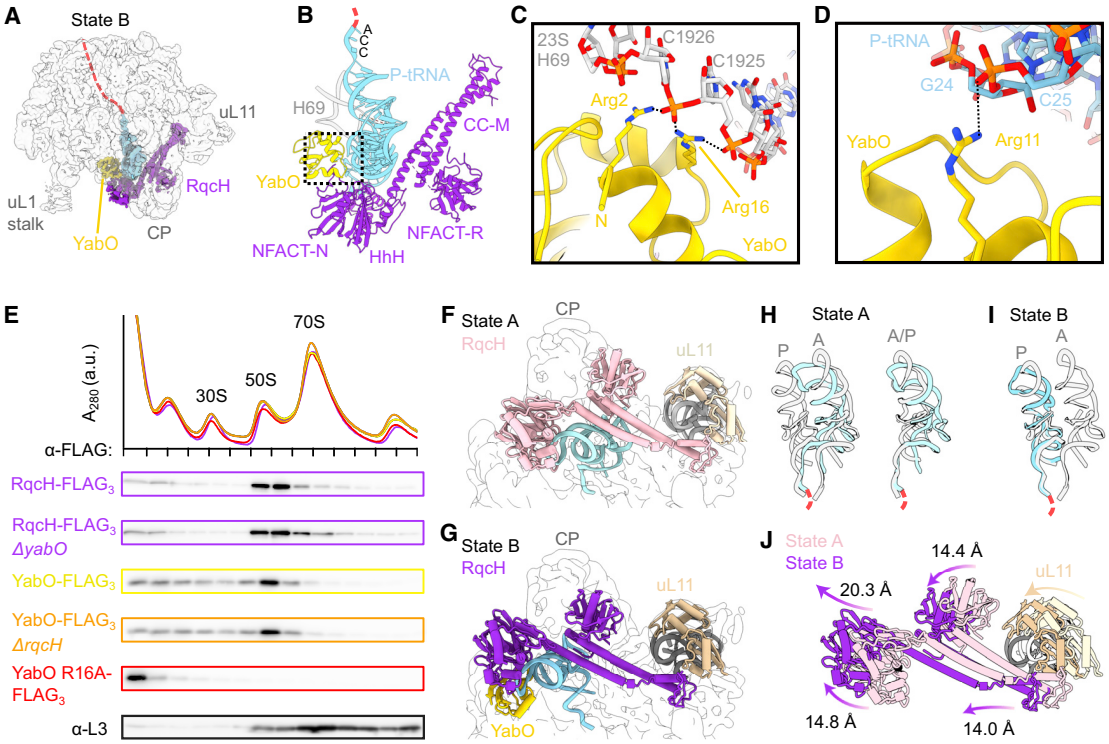

Figure 4. YabO Stabilizes a Classical P-Site tRNA Conformation

(A and B) Overview of YabO (yellow) interactions within state B.

(C and D) Selected interactions between YabO and 23S H69 (gray, C) or the P-site tRNA (light blue, D).

(E) Sucrose gradient analysis of *B. subtilis* strains expressing $FLAG_3$-tagged RqcH and YabO. Fractions were analyzed by immunoblot with α-FLAG or α-L3.

(F and G) Comparison of RqcH and tRNA within state A (F) and state B (G).

(H and I) Comparison of tRNAs (cyan) from state A (H) or state B (I) with classical A-site and P-site tRNAs (PDB: 6CFJ) (Tereshchenkov et al., 2018) or hybrid A/P-site tRNA (PDB: 6R6P) (Shanmuganathan et al., 2019).

(J) Superposition of RqcH from states A (pink) and B (purple), with degrees of movement indicated. uL11 and the stalk base are indicated for reference.

density was further improved by focused classification (Figure S4B) and identified as *B. subtilis* ribosomal silencing factor RsfS, bound in a position analogous to that observed previously on the 50S subunit (Brown et al., 2017; Khusainov et al., 2020; Li et al., 2015) (Figures S6A–S6E). This assignment is supported by mass spectrometry (Table S1) and retrospective inspection of the RqcH pull-out also revealed substoichiometric density for RsfS on the 50S subunit (Figure S6C). RsfS prevents association of 50S and 30S subunits (Häuser et al., 2012; Khusainov et al., 2020; Li et al., 2015); therefore, its presence in our datasets may indicate that RsfS also plays a similar role during RQC, analogous to that of Tif6/eIF6 in eukaryotic RQC (Su et al., 2019) (Figure S6F). Curiously, in the RqcH pull-out dataset, we observed the formation of 50S disomes (Figure S1B) containing RqcH, YabO, and P-site tRNA; i.e., the dimerization of state B (Figures S6G and S6H). While an overlay of the 50S-bound RsfS with the structure of the 50S disome reveals that RsfS would prevent 50S dimerization (Figures S6I and S6J), it remains to be determined whether this has any physiological relevance. The disruption of *rsfS* in the Δ*ssrA* background results in only a very mild increase, if any, in sensitivity to tetracycline or elevated temperatures (Figure S6K). This suggests that the role of RsfS in RQC is not as crucial as that of YabO, perhaps due to redundancy, as there are several bacterial factors with ribosome anti-association activity; e.g., the ribosome splitting factor HflX (Zhang et al., 2015) and initiation factor 3 (IF3) (Grunberg-Manago et al., 1975). Additional focused classification around the polypeptide exit tunnel revealed a minor class of particles (~4.0%) that contained YabO and the signal recognition particle (SRP) bound to the 50S-peptidyl-tRNA complex (Figure S4B). Although the significance of this finding is unclear, it is notable that *B. subtilis* contains a long SRP RNA with an Alu-like domain that contacts the L7/L12 stalk base (Figure S7A) (Beckert et al., 2015) in a position overlapping with the RqcH binding site, indicating that the binding of these two factors is mutually exclusive (Figure S7B). Consistently, no SRP was present in the sample obtained by affinity purification of RqcH (Table S1).

Interaction of RqcH with $tRNA^{Ala}$ on the Ribosome

Although the P-site tRNA in state B was relatively well resolved, the resolution was not sufficient to unambiguously distinguish the tRNA species. To test whether the sample contained *bona fide* RQC complexes containing $tRNA^{Ala}$, we performed tRNA microarray analysis on the RqcH pull-out sample. As expected,

Please cite this article in press as: Crowe-McAuliffe et al., Structural Basis for Bacterial Ribosome-Associated Quality Control by RqcH and RqcP, Molecular Cell (2020), https://doi.org/10.1016/j.molcel.2020.11.002

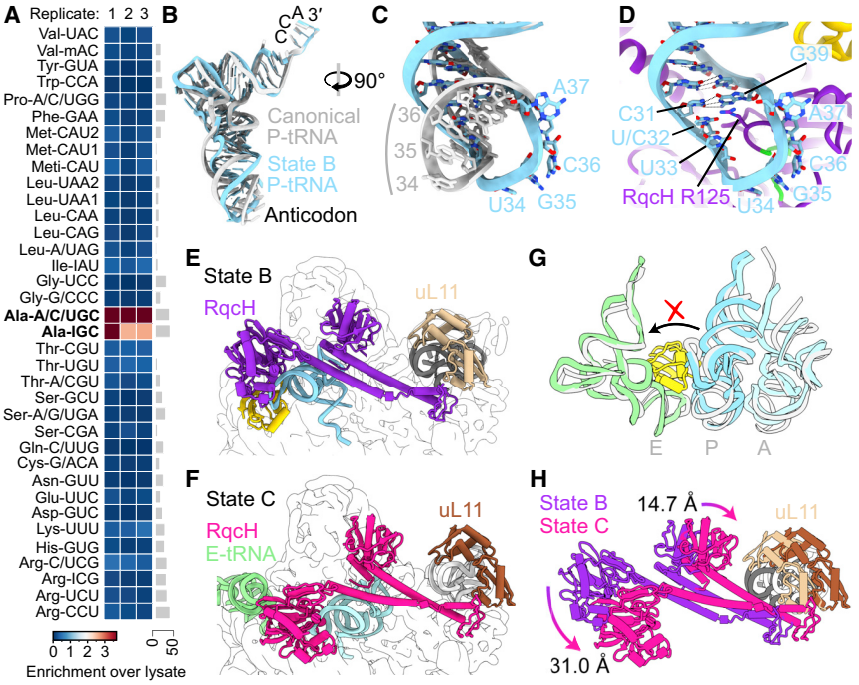

Figure 5. tRNA Composition and Dynamics within RqcH-50S Complexes

(A) tRNA microarray analysis of the RqcH-50S sample. Three replicates are shown with the gray bars on the right representing an example of covariance analysis between replicates 1 and 3. Confidence intervals between replicates 1 and 2, 2 and 3, and 1 and 3 were 94%, 93%, and 90%, respectively. Color key indicates the fold-enrichment over lysate.

(B) Comparison of RqcH-bound P-site tRNA from state B (blue) with canonical P-site tRNA from a 70S complex (gray, PDB: 6CFJ) (Tereshchenkov et al., 2018).

(C) Close-up of the anticodon region, rotated 90° relative to (B).

(D) Same view as (C) of the state B P-site tRNA but with RqcH (purple) and YabO (yellow) included. The RqcH $_{97}$DR$_{98}$ and $_{121}$EIM$_{123}$ motifs, which can be seen in the background, are indicated in green.

(E and F) Comparison of RqcH, tRNA, and YabO within (E) state B and (F) state C.

(G) Comparison of A/P-site (cyan), P-site (blue), and E-site (green) tRNAs from states B and C with canonical A-site, P-site, and E-site tRNAs (gray, (PDB: 6CFJ) (Tereshchenkov et al., 2018).

(H) Conformational changes of RqcH and the uL11 stalk base between states B and C.

we observed an enrichment for tRNA$^{Ala(UGC)}$ in our samples over the lysate. However, we also observed an enrichment of tRNA$^{Ala(IGC)}$ (Figure 5A) that was not detected previously in the bacterial RqcH complexes (Lytvynenko et al., 2019) but was observed in eukaryotic Rqc2p-60S complexes (Shen et al., 2015). Our findings suggest that *B. subtilis* RqcH can selectively recruit both Ala-tRNA^{Ala} isoacceptors to the ribosome to synthesize alanine tails. In state B, although the tRNA^{Ala} is bound to the 50S similarly to a P-site tRNA, the ASL element undergoes dramatic rearrangements (Figures 5B and 5C). Specifically, the ASL is unwound compared to a classical ASL-helix conformation, and the anticodon nucleotides 34–37 are splayed apart and poorly ordered, precluding confident modeling of this element (Figure 5C). Arg125 from the NFACT-N domain of RqcH inserts into the ASL, where it interacts with the nucleotide in position 32, which is U32 in tRNA$^{Ala(UGC)}$ and C32 in tRNA$^{Ala(IGC)}$ (Figure 5D). We doubt that the Arg125 interaction contributes to defining tRNA specificity of RqcH, since many *B. subtilis* tRNAs have either U or C at position 32. We note that, uniquely among tRNAs in *B. subtilis*, the anticodons of both tRNA^{Ala} isoacceptors end with $_{35}$GC$_{36}$ followed by an A at position 37, and RqcH residues close to these nucleotides, such as the $_{97}$DR$_{98}$ and $_{121}$EIM$_{123}$ motifs, may contribute to tRNA specificity (Figures 2B, 2C, and 5D).

No state contained both A- and P-site tRNAs, indicating that, as in regular translation, peptide bond formation is fast, and, following peptidyl transfer, the tRNAs move rapidly into A/P and E sites. Comparison of state B (RqcH, YabO, and P-site tRNA; Figure 5E) with state C (RqcH, A/P-site tRNA, and E-site tRNA; Figure 5F) shows that YabO binds in a position between the P and E sites, suggesting that YabO must dissociate from the 50S subunit to allow the uncharged P-site tRNA to move into the E site (Figure 5G; Video S3). Similarly, RqcH would also need to rearrange to accommodate uncharged tRNA at the E site, which involves a scissor-like separation of the coiled coils within the CC-M domain, so that the NFACT-N and HhH domains shift by an impressive 30 Å out of the E site (Figure 5H; Video S3).

DISCUSSION

Model of C-Terminal Alanine Tailing on the 50S Subunit Mediated by RqcH and YabO

Here, we show that C-terminal tailing in *Bacillus subtilis* is mediated by NEMF protein RqcH in concert with an additional factor, YabO, which we renamed as RqcP, for the RQC P-site tRNA stabilizing factor. Our ensemble of structures enables us to present a model for how polyalanine tailing of aborted 50S-peptidyl-tRNA complexes is catalyzed by RqcH and RqcP (Figure 6; Video S4). RsfS may play a role in preventing dissociated 50S with a peptidyl-tRNA from reassociation with the 30S subunits, although it is not necessary for this process. These 50S-peptidyl-tRNA complexes are recognized by RqcP, which binds and stabilizes the peptidyl-tRNA in the P site (state D; Figure 6B). Alternatively, the post-splitting complex may be directly recognized by RqcH (state A; Figure 6E). This frees the A site so that RqcH can deliver Ala-tRNA^{Ala}. Following peptide-bond formation, this results in a complex with uncharged tRNA at the P site and the peptidyl-tRNA at the A site (Figure 6C). To allow the uncharged tRNA to relocate to the E site, RqcP must dissociate from the 50S subunit, thus permitting the peptidyl-tRNA to adopt an A/P-like configuration (state C; Figure 6D). Dissociation of the uncharged tRNA from the E site of this complex then leaves a state with RqcH and A/P-site tRNA (state A; Figure 6E) which allows rebinding of RqcP, thus shifting the A/P-site tRNA

Please cite this article in press as: Crowe-McAuliffe et al., Structural Basis for Bacterial Ribosome-Associated Quality Control by RqcH and RqcP, Molecular Cell (2020), https://doi.org/10.1016/j.molcel.2020.11.002

CellPress

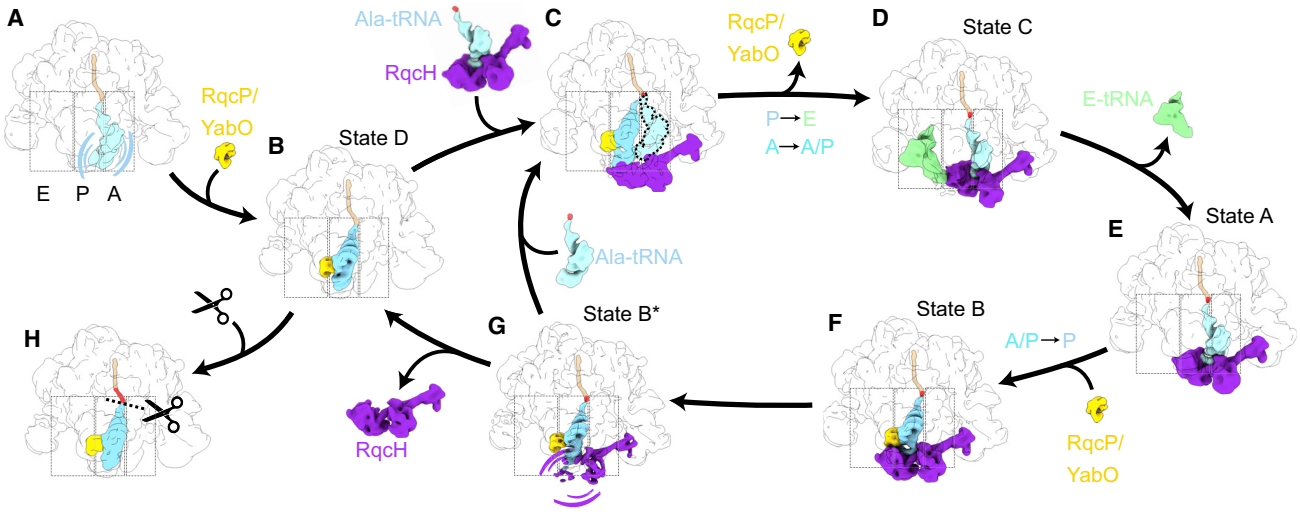

Figure 6. Model of C-Terminal Alanine Tailing on the 50S Mediated by RqcH and RqcP/YabO

(A) 50S with peptidyl-tRNA (nascent chain indicated in tan) serves an RQC substrate.

(B) Binding of RqcP/YabO to this 50S complex stabilizes the tRNA in the P site (state D).

(C) Hypothesized transient state in which Ala-tRNA^{Ala} is delivered to state D by RqcH. tRNA accommodates to the A site followed by rapid P transfer.

(D) RqcP/YabO dissociation facilitates translocation-type movement of the tRNAs from the P site to the E site and from the A site to the A/P site (state C).

(E) Dissociation of E-site tRNA results in a modest shift in the RqcH NFACT-N position (state A).

(F) Binding of RqcP/YabO stabilizes the tRNA in the classical P-site conformation, with concomitant movement of RqcH on the 50S (state B).

(G) Partial dissociation of RqcH, evidenced by classes in which only the RqcH CC-M domain was observed (state B*). This can lead to either full RqcH dissociation (state D) or delivery of the next Ala-tRNA^{Ala}, leading back to (C).

(H) Hypothesized termination state in which an unknown factor releases the alanine-tailed nascent polypeptide chain.

into the P site (state B; Figure 6F) and completing the translocation-like cycle. Successive binding-dissociation cycles of RqcP could act as a pawl of the RQC elongation ratchet, thus driving the processivity of alanine tailing. Our observation of state E with RqcP and P- and E-site tRNAs—but no RqcH—suggests that, if RqcP rebinds before E-site tRNA release, then RqcH would dissociate, thus providing an alternative pathway back to state D (Figure S5G). State B*, which contains a partially dissociated RqcH (Figure 4G), indicates that RqcH may processively recruit new Ala tRNAs while still tethered to the ribosome. Alternatively, RqcH could completely dissociate, leading back to state D (Figure 6B) and thereby requiring Ala tRNA^{Ala} to be delivered to the A site by another RqcH molecule.

Although our study provides structural insight into the mechanics of the bacterial RQC elongation cycle, a number of questions remain. Which cellular stresses and/or translational states lead to splitting of translating 70S ribosomes, and are there unknown factors that mediate this process? What is the functional state of the 50S-peptidyl-tRNA complex following splitting, and does it differ depending on the triggering conditions? How is polyalanine tail length regulated and eventually terminated? Is there a dedicated termination factor that mediates release of the tagged nascent polypeptide chain in bacteria, analogous to Vms1/ANKZF1 in eukaryotes? (Kuroha et al., 2018; Su et al., 2019; Verma et al., 2018; Yip et al., 2019; Zurita Rendón et al., 2018). In summary, we demonstrate the involvement of RqcP in RqcH-mediated bacterial RQC and propose an alternative model for protein synthesis on the ribosome that utilizes binding and rebinding of two non-GTPase protein factors to execute a whole elongation cycle without the small ribosomal subunit or mRNA.

Limitations of Study

Our work provides structural snapshots of the bacterial C-terminal alanine tailing mechanism. However, single-particle cryo-EM analysis of native complexes has some limitations. The method cannot directly establish the relationship between the visualized states or differentiate between complexes representing bona fide intermediates of the RQC tailing cycle from partially dissociated complexes generated during sample preparation. In particular, the order of events after ribosome splitting and the relationship between RqcH association with the 50S subunit and tRNA delivery remain unclear. Additionally, without a special intervention to stabilize them, short-lived or unstable intermediates in this unusual elongation cycle may be absent from our suite of structures. Therefore, an important next step is validation of the model through orthogonal approaches such as biochemical reconstitution.

STAR★METHODS

Detailed methods are provided in the online version of this paper and include the following:

- KEY RESOURCES TABLE
- RESOURCE AVAILABILITY
  - Lead Contact

SUPPLEMENTAL INFORMATION

Supplemental Information can be found online at https://doi.org/10.1016/j.molcel.2020.11.002.

ACKNOWLEDGMENTS

We thank Michael Hall for help with cryo-EM data collection. The EM data were collected at the Umeå Core Facility for Electron Microscopy, a node of the Cryo-EM Swedish National Facility, funded by the Knut and Alice Wallenberg, Family Erling Persson, and Kempe Foundations; SciLifeLab; Stockholm University; and Umeå University. This research was supported by grants from the Deutsche Forschungsgemeinschaft (WI3285/8-1 to D.N.W.), the Swedish Research Council (Vetenskapsrådet) (2017-03783 to V.H. and 2019-01085 to G.C.A.), and Ragnar Söderbergs stiftelse (to V.H.); a postdoctoral grant from the Umeå Centre for Microbial Research (UCMR; to H.T.); the European Union from the European Regional Development Fund through the Centre of Excellence in Molecular Cell Engineering (2014-2020.4.01.15-0013 to T.T. and V.H.); and the Estonian Research Council (PRG335 to T.T. and V.H.). The D.N.W. and V.H. groups are also supported by the Deutsche Zentrum für Luft- und Raumfahrt (DLR01KI1820 to D.N.W.) and the Swedish Research Council (2018-00956 to V.H.) within the RIBOTARGET consortium under the framework of JPIAMR.

AUTHOR CONTRIBUTIONS

D.N.W. and V.H. designed the study. H.T. and V.M. prepared the cryo-EM samples. H.T. performed biochemical and genetic studies. C.C.-M. processed the cryo-EM data and built and refined the molecular models. S.K. and T.T. performed the mass spectrometry analysis. G.C.A. performed sequence and phylogenetic analysis. C.P and Z.I. performed the tRNA microarray analysis. All authors interpreted the results and helped D.N.W. and C.C.-M. write the paper.

DECLARATION OF INTERESTS

The authors declare no competing interests.

Received: August 13, 2020
Revised: October 7, 2020
Accepted: October 29, 2020
Published: November 30, 2020

REFERENCES

Beckert, B., Kedrov, A., Sohmen, D., Kempf, G., Wild, K., Sinning, I., Stahlberg, H., Wilson, D.N., and Beckmann, R. (2015). Translational arrest by a prokaryotic signal recognition particle is mediated by RNA interactions. Nat. Struct. Mol. Biol. *22*, 767–773.

Beckert, B., Turk, M., Czech, A., Berninghausen, O., Beckmann, R., Ignatova, Z., Plitzko, J.M., and Wilson, D.N. (2018). Structure of a hibernating 100S ribosome reveals an inactive conformation of the ribosomal protein S1. Nat. Microbiol. *3*, 1115–1121.

Bengtson, M.H., and Joazeiro, C.A. (2010). Role of a ribosome-associated E3 ubiquitin ligase in protein quality control. Nature *467*, 470–473.

Brandman, O., Stewart-Ornstein, J., Wong, D., Larson, A., Williams, C.C., Li, G.W., Zhou, S., King, D., Shen, P.S., Weibezahn, J., et al. (2012). A ribosome-bound quality control complex triggers degradation of nascent peptides and signals translation stress. Cell *151*, 1042–1054.

Brown, A., Rathore, S., Kimanius, D., Aibara, S., Bai, X.C., Rorbach, J., Amunts, A., and Ramakrishnan, V. (2017). Structures of the human mitochondrial ribosome in native states of assembly. Nat. Struct. Mol. Biol. *24*, 866–869.

Buchan, D.W.A., and Jones, D.T. (2019). The PSIPRED Protein Analysis Workbench: 20 years on. Nucleic Acids Res. *47* (W1), W402–W407.

Burroughs, A.M., and Aravind, L. (2014). A highly conserved family of domains related to the DNA-glycosylase fold helps predict multiple novel pathways for RNA modifications. RNA Biol. *11*, 360–372.

Candiano, G., Bruschi, M., Musante, L., Santucci, L., Ghiggeri, G.M., Carnemolla, B., Orecchia, P., Zardi, L., and Righetti, P.G. (2004). Blue silver: a very sensitive colloidal Coomassie G-250 staining for proteome analysis. Electrophoresis *25*, 1327–1333.

Capella-Gutiérrez, S., Silla-Martínez, J.M., and Gabaldón, T. (2009). trimAl: a tool for automated alignment trimming in large-scale phylogenetic analyses. Bioinformatics *25*, 1972–1973.

Cox, J., Hein, M.Y., Luber, C.A., Paron, I., Nagaraj, N., and Mann, M. (2014). Accurate proteome-wide label-free quantification by delayed normalization and maximal peptide ratio extraction, termed MaxLFQ. Mol. Cell. Proteomics *13*, 2513–2526.

Croll, T.I. (2018). ISOLDE: a physically realistic environment for model building into low-resolution electron-density maps. Acta Crystallogr. D Struct. Biol. *74*, 519–530.

Crowe-McAuliffe, C., Graf, M., Huter, P., Takada, H., Abdelshahid, M., Nováček, J., Murina, V., Atkinson, G.C., Hauryliuk, V., and Wilson, D.N. (2018). Structural basis for antibiotic resistance mediated by the *Bacillus subtilis* ABCF ATPase VmlR. Proc. Natl. Acad. Sci. USA *115*, 8978–8983.

Defenouillère, Q., and Fromont-Racine, M. (2017). The ribosome-bound quality control complex: from aberrant peptide clearance to proteostasis maintenance. Curr. Genet. *63*, 997–1005.

Defenouillère, Q., Yao, Y., Mouaikel, J., Namane, A., Galopier, A., Decourty, L., Doyen, A., Malabat, C., Saveanu, C., Jacquier, A., and Fromont-Racine, M. (2013). Cdc48-associated complex bound to 60S particles is required for the clearance of aberrant translation products. Proc. Natl. Acad. Sci. USA *110*, 5046–5051.

Elias, J.E., and Gygi, S.P. (2007). Target-decoy search strategy for increased confidence in large-scale protein identifications by mass spectrometry. Nat. Methods *4*, 207–214.

Emsley, P., Lohkamp, B., Scott, W.G., and Cowtan, K. (2010). Features and development of Coot. Acta Crystallogr. D Biol. Crystallogr. *66*, 486–501.

Franckenberg, S., Becker, T., and Beckmann, R. (2012). Structural view on recycling of archaeal and eukaryotic ribosomes after canonical termination and ribosome rescue. Curr. Opin. Struct. Biol. *22*, 786–796.

Gabdulkhakov, A., Nikonov, S., and Garber, M. (2013). Revisiting the Haloarcula marismortui 50S ribosomal subunit model. Acta Crystallogr. D Biol. Crystallogr. *69*, 997–1004.

Galperin, M.Y., Makarova, K.S., Wolf, Y.I., and Koonin, E.V. (2015). Expanded microbial genome coverage and improved protein family annotation in the COG database. Nucleic Acids Res. *43*, D261–D269.

Goddard, T.D., Huang, C.C., Meng, E.C., Pettersen, E.F., Couch, G.S., Morris, J.H., and Ferrin, T.E. (2018). UCSF ChimeraX: Meeting modern challenges in visualization and analysis. Protein Sci. *27*, 14–25.

Grunberg-Manago, M., Dessen, P., Pantaloni, D., Godefroy-Colburn, T., Wolfe, A.D., and Dondon, J. (1975). Light-scattering studies showing the effect of initiation factors on the reversible dissociation of Escherichia coli ribosomes. J. Mol. Biol. *94*, 461–478.

Guérout-Fleury, A.M., Shazand, K., Frandsen, N., and Stragier, P. (1995). Antibiotic-resistance cassettes for Bacillus subtilis. Gene *167*, 335–336.

Guérout-Fleury, A.M., Frandsen, N., and Stragier, P. (1996). Plasmids for ectopic integration in Bacillus subtilis. Gene *180*, 57–61.

Harms, J.M., Wilson, D.N., Schluenzen, F., Connell, S.R., Stachelhaus, T., Zaborowska, Z., Spahn, C.M., and Fucini, P. (2008). Translational regulation via L11: molecular switches on the ribosome turned on and off by thiostrepton and micrococcin. Mol. Cell *30*, 26–38.

Häuser, R., Pech, M., Kijek, J., Yamamoto, H., Titz, B., Naeve, F., Tovchigrechko, A., Yamamoto, K., Szaflarski, W., Takeuchi, N., et al. (2012). RsfA (YbeB) proteins are conserved ribosomal silencing factors. PLoS Genet. *8*, e1002815.

Holm, L. (2019). Benchmarking fold detection by DaliLite v.5. Bioinformatics *35*, 5326–5327.

Horinouchi, S., and Weisblum, B. (1982). Nucleotide sequence and functional map of pC194, a plasmid that specifies inducible chloramphenicol resistance. J. Bacteriol. *150*, 815–825.

Inada, T. (2020). Quality controls induced by aberrant translation. Nucleic Acids Res. *48*, 1084–1096.

Jiang, L., Schaffitzel, C., Bingel-Erlenmeyer, R., Ban, N., Korber, P., Koning, R.I., de Geus, D.C., Plaisier, J.R., and Abrahams, J.P. (2009). Recycling of aborted ribosomal 50S subunit-nascent chain-tRNA complexes by the heat shock protein Hsp15. J. Mol. Biol. *386*, 1357–1367.

Joazeiro, C.A.P. (2019). Mechanisms and functions of ribosome-associated protein quality control. Nat. Rev. Mol. Cell Biol. *20*, 368–383.

Katoh, K., Kuma, K., Toh, H., and Miyata, T. (2005). MAFFT version 5: improvement in accuracy of multiple sequence alignment. Nucleic Acids Res. *33*, 511–518.

Khusainov, I., Fatkhullin, B., Pellegrino, S., Bikmullin, A., Liu, W.T., Gabdulkhakov, A., Shebel, A.A., Golubev, A., Zeyer, D., Trachtmann, N., et al. (2020). Mechanism of ribosome shutdown by RsfS in Staphylococcus aureus revealed by integrative structural biology approach. Nat. Commun. *11*, 1656.

Korber, P., Stahl, J.M., Nierhaus, K.H., and Bardwell, J.C. (2000). Hsp15: a ribosome-associated heat shock protein. EMBO J. *19*, 741–748.

Kostova, K.K., Hickey, K.L., Osuna, B.A., Hussmann, J.A., Frost, A., Weinberg, D.E., and Weissman, J.S. (2017). CAT-tailing as a fail-safe mechanism for efficient degradation of stalled nascent polypeptides. Science *357*, 414–417.

Kucukelbir, A., Sigworth, F.J., and Tagare, H.D. (2014). Quantifying the local resolution of cryo-EM density maps. Nat. Methods *11*, 63–65.

Kuroha, K., Zinoviev, A., Hellen, C.U.T., and Pestova, T.V. (2018). Release of Ubiquitinated and Non-ubiquitinated Nascent Chains from Stalled Mammalian Ribosomal Complexes by ANKZF1 and Ptrh1. Mol. Cell. *72*, 286–302.e8.

Li, X., Sun, Q., Jiang, C., Yang, K., Hung, L.W., Zhang, J., and Sacchettini, J.C. (2015). Structure of Ribosomal Silencing Factor Bound to Mycobacterium tuberculosis Ribosome. Structure *23*, 1858–1865.

Liebschner, D., Afonine, P.V., Baker, M.L., Bunkóczi, G., Chen, V.B., Croll, T.I., Hintze, B., Hung, L.W., Jain, S., McCoy, A.J., et al. (2019). Macromolecular structure determination using X-rays, neutrons and electrons: recent developments in Phenix. Acta Crystallogr. D Struct. Biol. *75*, 861–877.

Lytvynenko, I., Paternoga, H., Thrun, A., Balke, A., Muller, T.A., Chiang, C.H., Nagler, K., Tsaprailis, G., Anders, S., Bischofs, I., et al. (2019). Alanine Tails Signal Proteolysis in Bacterial Ribosome-Associated Quality Control. Cell *178*, 76–90.e22.

Lyumkis, D., Oliveira dos Passos, D., Tahara, E.B., Webb, K., Bennett, E.J., Vinterbo, S., Potter, C.S., Carragher, B., and Joazeiro, C.A. (2014). Structural basis for translational surveillance by the large ribosomal subunit-associated protein quality control complex. Proc. Natl. Acad. Sci. USA *111*, 15981–15986.

Manne, K., Narayana, S.V.L., and Chattopadhyay, D. (2019). Crystal structure of the N-terminal domain of the fibronectin-binding protein PavA from Streptococcus pneumoniae. Acta Crystallogr. F Struct. Biol. Commun. *75*, 657–662.

Miller, M.A., Schwartz, T., Pickett, B.E., He, S., Klem, E.B., Scheuermann, R.H., Passarotti, M., Kaufman, S., and O'Leary, M.A. (2015). A RESTful API for Access to Phylogenetic Tools via the CIPRES Science Gateway. Evol. Bioinform. Online *11*, 43–48.

Moriya, T., Saur, M., Stabrin, M., Merino, F., Voicu, H., Huang, Z., Penczek, P.A., Raunser, S., and Gatsogiannis, C. (2017). High-resolution Single Particle Analysis from Electron Cryo-microscopy Images Using SPHIRE. J. Vis. Exp. (123), 55448.

Murina, V., Kasari, M., Takada, H., Hinnu, M., Saha, C.K., Grimshaw, J.W., Seki, T., Reith, M., Putriņš, M., Tenson, T., et al. (2019). ABCF ATPases Involved in Protein Synthesis, Ribosome Assembly and Antibiotic Resistance: Structural and Functional Diversification across the Tree of Life. J. Mol. Biol. *431*, 3568–3590.

Musyoki, A.M., Shi, Z., Xuan, C., Lu, G., Qi, J., Gao, F., Zheng, B., Zhang, Q., Li, Y., Haywood, J., et al. (2016). Structural and functional analysis of an anchorless fibronectin-binding protein FBPS from Gram-positive bacterium Streptococcus suis. Proc. Natl. Acad. Sci. USA *113*, 13869–13874.

Nicolas, P., Mäder, U., Dervyn, E., Rochat, T., Leduc, A., Pigeonneau, N., Bidnenko, E., Marchadier, E., Hoebeke, M., Aymerich, S., et al. (2012). Condition-dependent transcriptome reveals high-level regulatory architecture in Bacillus subtilis. Science *335*, 1103–1106.

Osanai, A., Li, S.J., Asano, K., Sashinami, H., Hu, D.L., and Nakane, A. (2013). Fibronectin-binding protein, FbpA, is the adhesin responsible for pathogenesis of Listeria monocytogenes infection. Microbiol. Immunol. *57*, 253–262.

Osuna, B.A., Howard, C.J., Kc, S., Frost, A., and Weinberg, D.E. (2017). *In vitro* analysis of RQC activities provides insights into the mechanism and function of CAT tailing. eLife *6*, e27949.

Pettersen, E.F., Goddard, T.D., Huang, C.C., Couch, G.S., Greenblatt, D.M., Meng, E.C., and Ferrin, T.E. (2004). UCSF Chimera–a visualization system for exploratory research and analysis. J. Comput. Chem. *25*, 1605–1612.

Pracht, D., Elm, C., Gerber, J., Bergmann, S., Rohde, M., Seiler, M., Kim, K.S., Jenkinson, H.F., Nau, R., and Hammerschmidt, S. (2005). PavA of Streptococcus pneumoniae modulates adherence, invasion, and meningeal inflammation. Infect. Immun. *73*, 2680–2689.

Rodriguez Ayala, F., Bauman, C., Bartolini, M., Saball, E., Salvarrey, M., Leñini, C., Cogliati, S., Strauch, M., and Grau, R. (2017). Transcriptional regulation of adhesive properties of Bacillus subtilis to extracellular matrix proteins through the fibronectin-binding protein YloA. Mol. Microbiol. *104*, 804–821.

Scheres, S.H. (2012). RELION: implementation of a Bayesian approach to cryo-EM structure determination. J. Struct. Biol. *180*, 519–530.

Scheres, S.H., and Chen, S. (2012). Prevention of overfitting in cryo-EM structure determination. Nat. Methods *9*, 853–854.

Shanmuganathan, V., Schiller, N., Magoulopoulou, A., Cheng, J., Braunger, K., Cymer, F., Berninghausen, O., Beatrix, B., Kohno, K., von Heijne, G., and Beckmann, R. (2019). Structural and mutational analysis of the ribosome-arresting human XBP1u. eLife *8*, e46267.

Shao, S., Brown, A., Santhanam, B., and Hegde, R.S. (2015). Structure and assembly pathway of the ribosome quality control complex. Mol. Cell *57*, 433–444.

Shen, P.S., Park, J., Qin, Y., Li, X., Parsawar, K., Larson, M.H., Cox, J., Cheng, Y., Lambowitz, A.M., Weissman, J.S., et al. (2015). Protein synthesis. Rqc2p and 60S ribosomal subunits mediate mRNA-independent elongation of nascent chains. Science *347*, 75–78.

Shi, H., and Moore, P.B. (2000). The crystal structure of yeast phenylalanine tRNA at 1.93 A resolution: a classic structure revisited. RNA *6*, 1091–1105.

Singh, K.V., La Rosa, S.L., Somarajan, S.R., Roh, J.H., and Murray, B.E. (2015). The fibronectin-binding protein EfbA contributes to pathogenesis and protects against infective endocarditis caused by Enterococcus faecalis. Infect. Immun. *83*, 4487–4494.

Sitron, C.S., and Brandman, O. (2019). CAT tails drive degradation of stalled polypeptides on and off the ribosome. Nat. Struct. Mol. Biol. *26*, 450–459.

Staker, B.L., Korber, P., Bardwell, J.C., and Saper, M.A. (2000). Structure of Hsp15 reveals a novel RNA-binding motif. EMBO J. *19*, 749–757.

Stamatakis, A. (2014). RAxML version 8: a tool for phylogenetic analysis and post-analysis of large phylogenies. Bioinformatics *30*, 1312–1313.

Su, T., Izawa, T., Thoms, M., Yamashita, Y., Cheng, J., Berninghausen, O., Hartl, F.U., Inada, T., Neupert, W., and Beckmann, R. (2019). Structure and function of Vms1 and Arb1 in RQC and mitochondrial proteome homeostasis. Nature *570*, 538–542.

Takada, H., Fukushima-Tanaka, S., Morita, M., Kasahara, Y., Watanabe, S., Chibazakura, T., Hara, H., Matsumoto, K., and Yoshikawa, H. (2014). An essential enzyme for phospholipid synthesis associates with the Bacillus subtilis divisome. Mol. Microbiol. *91*, 242–255.

Takada, H., Roghanian, M., Murina, V., Dzhygyr, I., Murayama, R., Akanuma, G., Atkinson, G.C., Garcia-Pino, A., and Hauryliuk, V. (2020). The C-Terminal RRM/ACT Domain Is Crucial for Fine-Tuning the Activation of 'Long' RelA-SpoT Homolog Enzymes by Ribosomal Complexes. Front. Microbiol. *11*, 277.

Tereshchenkov, A.G., Dobosz-Bartoszek, M., Osterman, I.A., Marks, J., Sergeeva, V.A., Kasatsky, P., Komarova, E.S., Stavrianidi, A.N., Rodin, I.A., Konevega, A.L., et al. (2018). Binding and Action of Amino Acid Analogs of Chloramphenicol upon the Bacterial Ribosome. J. Mol. Biol. *430*, 842–852.

Tyanova, S., Temu, T., and Cox, J. (2016). The MaxQuant computational platform for mass spectrometry-based shotgun proteomics. Nat. Protoc. *11*, 2301–2319.

Verma, R., Oania, R.S., Kolawa, N.J., and Deshaies, R.J. (2013). Cdc48/p97 promotes degradation of aberrant nascent polypeptides bound to the ribosome. eLife *2*, e00308.

Verma, R., Reichermeier, K.M., Burroughs, A.M., Oania, R.S., Reitsma, J.M., Aravind, L., and Deshaies, R.J. (2018). Vms1 and ANKZF1 peptidyl-tRNA hydrolases release nascent chains from stalled ribosomes. Nature *557*, 446–451.

Vizcaíno, J.A., Deutsch, E.W., Wang, R., Csordas, A., Reisinger, F., Ríos, D., Dianes, J.A., Sun, Z., Farrah, T., Bandeira, N., et al. (2014). ProteomeXchange provides globally coordinated proteomics data submission and dissemination. Nat. Biotechnol. *32*, 223–226.

Wagner, T., Merino, F., Stabrin, M., Moriya, T., Antoni, C., Apelbaum, A., Hagel, P., Sitsel, O., Raisch, T., Prumbaum, D., et al. (2019). SPHIRE-crYOLO is a fast and accurate fully automated particle picker for cryo-EM. Commun. Biol. *2*, 218.

Waterhouse, A., Bertoni, M., Bienert, S., Studer, G., Tauriello, G., Gumienny, R., Heer, F.T., de Beer, T.A.P., Rempfer, C., Bordoli, L., et al. (2018). SWISS-MODEL: homology modelling of protein structures and complexes. Nucleic Acids Res. *46* (W1), W296–W303.

Williams, C.J., Headd, J.J., Moriarty, N.W., Prisant, M.G., Videau, L.L., Deis, L.N., Verma, V., Keedy, D.A., Hintze, B.J., Chen, V.B., et al. (2018). MolProbity: More and better reference data for improved all-atom structure validation. Protein Sci. *27*, 293–315.

Yan, L.L., and Zaher, H.S. (2019). How do cells cope with RNA damage and its consequences? J. Biol. Chem. *294*, 15158–15171.

Yip, M.C.J., Keszei, A.F.A., Feng, Q., Chu, V., McKenna, M.J., and Shao, S. (2019). Mechanism for recycling tRNAs on stalled ribosomes. Nat. Struct. Mol. Biol. *26*, 343–349.

Zhang, K. (2016). Gctf: Real-time CTF determination and correction. J. Struct. Biol. *193*, 1–12.

Zhang, Y., Mandava, C.S., Cao, W., Li, X., Zhang, D., Li, N., Zhang, Y., Zhang, X., Qin, Y., Mi, K., et al. (2015). HflX is a ribosome-splitting factor rescuing stalled ribosomes under stress conditions. Nat. Struct. Mol. Biol. *22*, 906–913.

Zheng, S.Q., Palovcak, E., Armache, J.P., Verba, K.A., Cheng, Y., and Agard, D.A. (2017). MotionCor2: anisotropic correction of beam-induced motion for improved cryo-electron microscopy. Nat. Methods *14*, 331–332.

Zivanov, J., Nakane, T., Forsberg, B.O., Kimanius, D., Hagen, W.J.H., Lindahl, E., and Scheres, S.H. (2018). New tools for automated high-resolution cryo-EM structure determination in RELION-3. eLife *7*, e42166.

Zurita Rendón, O., Fredrickson, E.K., Howard, C.J., Van Vranken, J., Fogarty, S., Tolley, N.D., Kalia, R., Osuna, B.A., Shen, P.S., Hill, C.P., et al. (2018). Vms1p is a release factor for the ribosome-associated quality control complex. Nat. Commun. *9*, 2197.

5.5 Structure of the RqcH^{DR}-variant complex

5.5.1 Summary

This manuscript describes further investigation into the mechanism of RqcH-mediated alanine tailing. The cryo-EM structure of the RqcH^{DR} variant in complex with 50S and peptidyl-tRNA was solved, revealing the role of the DR motif in interacting with the P-tRNA anticodon stem.

5.5.2 Contributions

Processing of the cryo-EM data, creation of the molecular models and generation of Figure 4, with some contribution to Figures 1, 5, and 6. Most data in this manuscript came from our collaborators Prof. V. Hauryliuk and Dr G. Atkinson (Umeå University), and Prof. Z. Ignatova (University of Hamburg).

Published online 13 July 2021

Nucleic Acids Research, 2021, Vol. 49, No. 14 ***8355–8369***
https://doi.org/10.1093/nar/gkab589

RqcH and RqcP catalyze processive poly-alanine synthesis in a reconstituted ribosome-associated quality control system

Hiraku Takada[1,2,3,*], Caillan Crowe-McAuliffe[4], Christine Polte[4], Zhanna Yu. Sidorova[5,6], Victoriia Murina[2,3], Gemma C. Atkinson[8], Andrey L. Konevega[5,7,8], Zoya Ignatova[4], Daniel N. Wilson[4,*] and Vasili Hauryliuk[2,3,9,10,*]

[1]Faculty of Life Sciences, Kyoto Sangyo University, Kamigamo, Motoyama, Kita-ku, Kyoto 603-8555, Japan, [2]Department of Molecular Biology, Umeå University, 90187 Umeå, Sweden, [3]Laboratory for Molecular Infection Medicine Sweden (MIMS), Umeå University, 90187 Umeå, Sweden, [4]Institute for Biochemistry and Molecular Biology, University of Hamburg, 20146 Hamburg, Germany, [5]Petersburg Nuclear Physics Institute named by B.P. Konstantinov of National Research Centre "Kurchatov Institute", 188300 Gatchina, Russia, [6]Russian Research Institute of Hematology and Transfusiology of FMBA, 191024 Saint Petersburg, Russia, [7]Peter the Great St. Petersburg Polytechnic University, 195251 Saint Petersburg, Russia, [8]National Research Centre "Kurchatov Institute", 123182 Moscow, Russia, [9]Department of Experimental Medical Science, Lund University, 221 00 Lund, Sweden and [10]University of Tartu, Institute of Technology, 50411 Tartu, Estonia

Received May 18, 2021; Revised June 21, 2021; Editorial Decision June 22, 2021; Accepted June 24, 2021

ABSTRACT

In the cell, stalled ribosomes are rescued through ribosome-associated protein quality-control (RQC) pathways. After splitting of the stalled ribosome, a C-terminal polyalanine 'tail' is added to the unfinished polypeptide attached to the tRNA on the 50S ribosomal subunit. In *Bacillus subtilis*, polyalanine tailing is catalyzed by the NEMF family protein RqcH, in cooperation with RqcP. However, the mechanistic details of this process remain unclear. Here we demonstrate that RqcH is responsible for $tRNA^{Ala}$ selection during RQC elongation, whereas RqcP lacks any tRNA specificity. The ribosomal protein uL11 is crucial for RqcH, but not RqcP, recruitment to the 50S subunit, and *B. subtilis* lacking uL11 are RQC-deficient. Through mutational mapping, we identify critical residues within RqcH and RqcP that are important for interaction with the P-site tRNA and/or the 50S subunit. Additionally, we have reconstituted polyalanine-tailing *in vitro* and can demonstrate that RqcH and RqcP are necessary and sufficient for processivity in a minimal system. Moreover, the *in vitro* reconstituted system recapitulates our *in vivo* findings by reproducing the importance of conserved residues of RqcH and RqcP for functionality. Collectively, our findings provide mechanistic insight into the role of RqcH and RqcP in the bacterial RQC pathway.

INTRODUCTION

In all cells, the process of synthesizing proteins by 'reading' the coded instructions in mRNA is called translation, and it is carried out by the molecular machine called the ribosome. Damaged or truncated mRNAs are harmful to cells because they sequester ribosomes from active protein production and can result in the synthesis of cytotoxic truncated proteins (1). Therefore, diverse ribosome rescue pathways have evolved in all domains of life to disassemble stalled ribosomal complexes (2–4). The first ribosome rescue pathway to be identified in bacteria was the trans-translation system (5). The system consists of transfer-messenger RNA (tmRNA; also referred to as small stable RNA A, *ssrA*) that serves both as an mRNA template (6) and a tRNA mimic (7). This RNA component of tmRNA is assisted by small protein B (SmpB) (8). Acting as a tRNA, alanyl-tmRNA mediates the addition of alanine to ribosome-stalled nascent polypeptide chains (7). Next, decoding of the ORF encoded within the tmRNA results in the addition of the short C-terminal ssrA peptide tag (6). This, in turn, marks the aberrant proteins for degradation by ClpA, ClpXP and FtsH proteases (9). In addition to the trans-translation system, *Escherichia coli* possess two alternative

*To whom correspondence should be addressed. Tel: +46 70 60 90 493; Email: vasili.hauryliuk@med.lu.se
Correspondence may also be addressed to Hiraku Takada. Tel: +81 80 7800 6466; Email: hiraku.takada@cc.kyoto-su.ac.jp
Correspondence may also be addressed to Daniel N. Wilson. Tel: +49 40 42838 2841; Email: daniel.wilson@chemie.uni-hamburg.de

rescue systems that are related to or rely on the canonical stop codon-dependent translation termination machinery involving class-1 release factors RF1 and RF2 (2,3). While alternative rescue factor A (ArfA) recruits RF2 to release the stalled polypeptide in the absence of the A-site stop codon (10), ArfB acts as a peptidyl hydrolase itself (11). Unlike the trans-translation system, which is universally conserved in bacteria (12,13), ArfA and ArfB have patchy evolutionary distributions, and are missing, for example, in the model firmicute bacterium *Bacillus subtilis* or the human pathogen *Francisella tularensis* (14). Instead, these species rely on release factor-dependent alternative rescue systems ArfT (*F. tularensis* (15)) and BrfA (*B. subtilis* (16)).

The translation apparatus of both archaea and the eukaryotic cytoplasm lack the trans-translation and Arf/Brf ribosome rescue systems. Instead, they rely on ribosome-associated protein quality control, RQC (17,18). RQC is executed by the concerted action of Ribosome quality control complex subunits 1 (Rqc1) and 2 (Rqc2, aka NEMF/SDCCAG1 in humans, Caliban in Drosophila and Tae2 in yeast), E3 ubiquitin ligase Ltn1/Listerin and the AAA ATPase Cdc48/p97 (19,20). Unlike the bacterial systems described above that operate on the 70S ribosomes, eukaryotic RQC operates on the large 60S subunit (19,20) which can be generated by splitting the stalled ribosome by Dom34/Pelota-Hbs1 and ABCE1/Rli1 (21–25) or, alternatively, the RQC-trigger/ASC-1 complex (26,27). In yeast, the resulting 60S-P-tRNA complex is a substrate for the mRNA-independent addition of C-terminal extensions of poly-alanine co-polymerised with threonine (CAT tails) (28). CAT tailing progresses the stalled nascent peptide through the exit tunnel, presenting lysine residues in the nascent peptide that are substrates for ubiquitinylation by Ltn1 (29). Off the ribosome, CAT tails promote protein aggregation (30,31) and serve as a degron tag promoting degradation by the proteasome (32). Recently, it has been shown that C-terminal tails mediated by the RQC machinery in mammalian cells and *Drosophila melanogaster* are composed predominantly of alanine, with minor contribution from other amino acids (33–35).

Diverse bacterial species of phyla across the bacterial tree of life encode NEMF-family fibronectin-binding protein A (FpbA) proteins homologous to eukaryotic Rqc2 proteins (36). For decades, the exact molecular function of these proteins was unclear. *Enterococcus faecalis* EfbA (37), *Listeria monocytogenes* FbpA (38,39) and *Streptococcus pneumoniae* PavA (40) were originally recognized as virulence factors. The situation changed in 2019 when *B. subtilis* FpbA homologue YloA was demonstrated to be a functional analogue as well as a homologue of eukaryotic Rqc2, which led to renaming of the protein to bacterial Rqc2 homolog, RqcH (41). RqcH, like other NEMF family proteins, contains a conserved core domain architecture of NFACT-N (NFACT means domain found in NEMF, FbpA, Caliban, and Tae2), helix-hairpin-helix (HhH), coiled coils (CC), a small β-hairpin-containing middle (M)-domain between the two helices of the CC, and an NFACT-R domain (28,36,41–43) (Figure 1A). RqcH recruits $tRNA^{Ala}$ to 50S-peptidyl-tRNA complexes generated by an as yet unknown molecular players that split stalled 70S ribosomes, and drives the addition of C-terminal poly-alanine tails that, in turn, act as degron tags recognized by the ClpP protease (41). The *rqcH* gene genetically interacts with *ssrA,* as the double deletion mutant *ssrA* and *rqcH* displays an increased sensitivity to antibiotics that inhibit translation and displays a synthetic growth defect at 45°C (41). This genetic interaction suggests that the two ribosome rescue systems have complementary functions in *B. subtilis*.

Cryo-EM structures of RqcH-50S complexes isolated using *in vivo* pull-down approaches have established that the NFACT-N domain of RqcH is the key structural element mediating $tRNA^{Ala}$ recognition (42,44), thus rationalizing the earlier report of D97A/R98A substitution ($RqcH^{DR}$) in the domain ablating RQC functionality (41). Indeed, RqcH appears to interact with both $tRNA^{Ala}$ isoacceptors, namely $tRNA^{Ala(UGC)}$ and $tRNA^{Ala(GGC)}$ (42) (note that the latter was annotated as $tRNA^{Ala(IGC)}$ in the original report due to the hybridization with the microarray probe designated as Ala-IGC, Supplementary Table S1)—and the conserved $_{97}DR_{98}$ residues have been suggested to contribute to this specificity by interacting with the anticodon–stem–loop of these tRNAs, in particular the G35 at the central position of the anticodon (42,44) (Figure 1B,C). A similar variant in yeast Rqc2 could bind to 50S-P-tRNA complexes, but not support CAT tailing (28). The structures also revealed that the M domain of RqcH is tethered to ribosomal protein uL11 located at the L7/L12 stalk base, suggesting that this interaction is critical for RqcH function. Furthermore, analysis of the RqcH-50S RQC pull-down complexes led to the discovery of RqcP, an Hsp15-family protein (42,44). By analysing the ensemble of generated cryo-EM structures, a putative mechanism of RqcH/RqcP-driven poly-alanine synthesis on the large 50S subunit was proposed (Figure 1D) (42). By associating with 50S-peptidyl-tRNA complexes, RqcP stabilizes the peptidyl-tRNA in the P-site, thus allowing efficient recruitment of RqcH:$tRNA^{Ala}$ to the A-site. Consequent spontaneous transpeptidation and RqcP dissociation allow the 50S-bound tRNAs to sample different ribosomal binding sites. This results in departure of the deacylated E-site tRNA and allows the peptidyl-tRNA extended with C-terminal alanine residue to adopt a hybrid A/P-like state. Rebinding of RqcP stabilizes the peptidyl-tRNA in the P-site, resulting in a complex with P-site tRNA, RqcH and RqcP. This latter complex was the best-resolved state observed in cryo-EM reconstructions, which we termed state B. An additional state, which was similar to state B, but with partially dissociated RqcH, was termed state B* and assumed to represent a transition towards RqcH dissociation.

Here, we employ biochemical and structural techniques to dissect the role of RqcH and RqcP during bacterial RQC. We show that RqcH can specifically select $tRNA^{Ala}$ in the absence of the 50S subunit and that RqcP does not contribute to this selection specificity. Indeed, we show that mutation of the conserved DR motif to AA leads to loss of this $tRNA^{Ala}$ specificity, supporting the importance of the motif for distinguishing $tRNA^{Ala}$ from other tRNA species. A cryo-EM structure of a $RqcH^{DR}$ mutant in complex with the peptidyl–tRNA–50S complex reveals that the NFACT-N domain of the $RqcH^{DR}$ mutant has disengaged from the anticodon stem loop of the P-site tRNA, thus providing a structural basis for the loss in specificity. In ad-

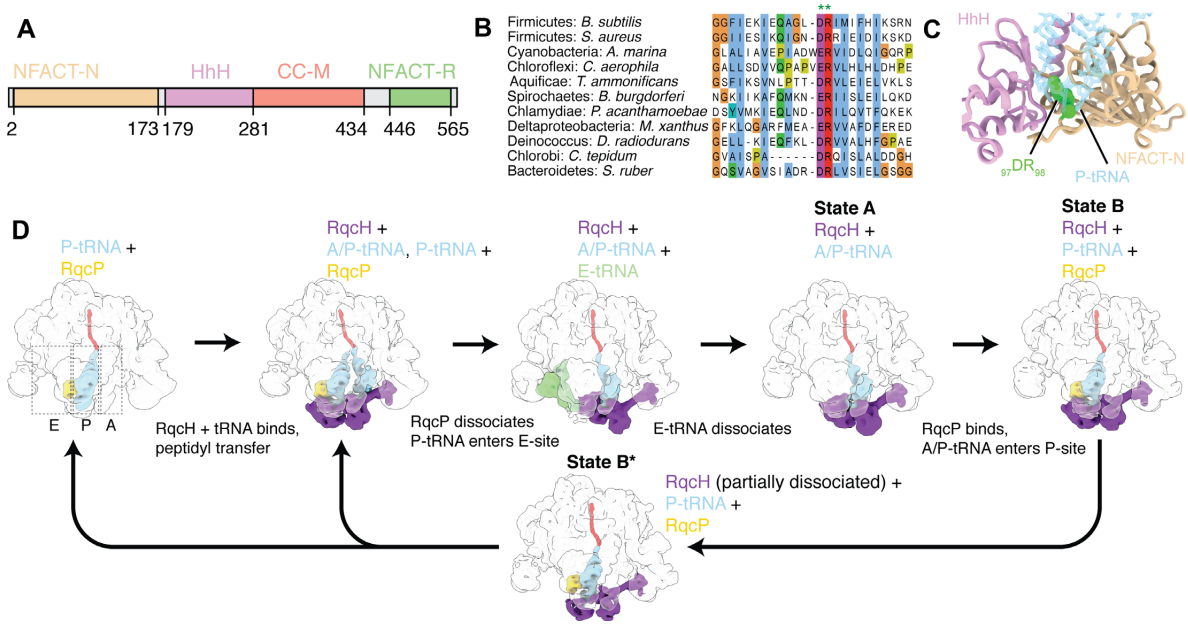

Figure 1. Bacterial ribosome-associated RQC is mediated by RqcH and RqcP. (**A**) RqcH domain composition. Amino acid positions are numbered as per *B. subtilis* RqcH. (**B**) Sequence alignment of RqcH homologs from diverse bacteria. (**C**) Interaction between RqcH (HhH domain in lilac, NFACT-N domain in tan, $_{97}$DR$_{98}$ motif in green) and P-tRNA (transparent cyan) in state B (PDB 7ASA (42)). (**D**) Overview of proposed RQC elongation cycle mediated by RqcH and RqcP (42). Beginning with a 50S with trapped P-tRNA, binding and dissociation cycles of RqcH and RqcP, accompanied by movement of tRNAs through the A-, P- and E-sites, results in mRNA- and 30S-independent elongation.

dition, we demonstrate that uL11 is critical for RqcH recruitment to the 50S subunit and *B. subtilis* lacking uL11 is RQC-deficient. We also identify critical residues within RqcH and RqcP that are important for recruitment to the peptidyl-tRNA 50S complexes. Furthermore, we establish an *in vitro*-reconstituted polyalanine-tailing assay, which we use to demonstrate that RqcH and RqcP are necessary and sufficient for processivity of polyalanine tailing. The *in vitro*-reconstituted polyalanine-tailing assay opens the way for further studies to dissect the role of other factors involved in bacterial RQC.

MATERIALS AND METHODS

Strains, plasmids (and details regarding the construction thereof) as well as oligonucleotides and synthetic DNA sequences used in this study are provided in Supplementary Table S2. Detailed description of protein and tRNA purification procedures is provided in the *Supplementary methods*.

Multiple sequence alignment

RqcH and RqcP sequences were extracted from the previously reported dataset (42), aligned with MAFFT v7.164b with the L-ins-i strategy (45) and alignments were visualized with Jalview (46).

Preparation of *B. subtilis* 50S ribosomal subunits

B. subtilis 70S was purified as described earlier (47), diluted with low-magnesium HEPES:Polymix buffer (1 mM MgOAc) and incubated on ice for 30 minutes to promote the dissociation of subunits. The sample was then resolved on a 10–40% sucrose gradient in overlay buffer (60 mM NH_4Cl, 1 mM $Mg(OAc)_2$, 0.25 mM EDTA, 3 mM β-mercaptoethanol, 20 mM Tris–HCl pH 7.5) in a zonal rotor (Ti 15, Beckman, 18 h at 21 000 rpm). The peak containing pure 50S subunits was pelleted by centrifugation (48 h at 35 000 rpm), and the final ribosomal preparation was dissolved in HEPES:Polymix buffer with 5 mM MgOAc.

Growth assays

B. subtilis 168 wild-type and deletion strains were pre-grown on LB plates overnight at 30°C. Fresh individual colonies were used to inoculate liquid LB medium cultures (OD_{600} adjusted to 0.01) at 37°C. Log phase cultures (OD_{600} of ≈0.4) diluted to OD_{600} of 0.1 were used to prepare 10- to 10^5-fold serial dilutions which were then spotted onto LB agar plates with or without 1 mM IPTG. The plates were scored after 18 hours incubation at either 37°C or 49°C.

Immunoprecipitation of $FLAG_3$-tagged proteins

The experiments were performed as described earlier (42). Strains expressing $FLAG_3$-tagged proteins were pre-grown on LB plates overnight at 30°C. Fresh individual colonies were used for inoculation and grown in LB medium. 3× 1 liter cultures were grown at 37°C to OD_{600} = 0.8. Cells were collected by centrifugation (8000 rpm for 10 min at 4°C, JLA-16.25 Beckman Coulter rotor), pellets frozen in liquid nitrogen and stored at –80°C. Cell pellets were re-suspended in 8 ml of cell opening buffer (95 mM KCl, 5 mM NH_4Cl, 20 mM HEPES (pH 7.5), 1 mM DTT, 15 mM $Mg(OAc)_2$, 0.5 mM $CaCl_2$, 8 mM putrescine, 1 mM spermidine, 1 tablet of cOmplete™ EDTA-free Protease Inhibitor Cocktail (Roche) per 50 ml of buffer) and disrupted using

FastPrep homogeniser (MP Biomedicals) with 0.1 mm Zirconium beads (Techtum) in 6 cycles by 20 s with 3 min chill on ice. Cell debris was removed by centrifugation at 14 800 rpm for 20 min 4°C in F241.5P rotor using a 149 Microfuge 22R centrifuge (Beckman Coulter). The supernatant was combined with 100 μl of ANTI-FLAG M2 Affinity Gel (Sigma) pre-equilibrated in cell opening buffer, and incubated for 1.5 h at 4°C on a turning wheel (Fisherbrand™ Multi-Purpose Tube Rotators). The samples were loaded on Micro Bio-Spin columns (Bio-Rad) pre-equilibrated in cell opening buffer, and washed 10 times with 1 ml of cell opening buffer by gravity flow. RqcH-FLAG$_3$ was eluted by addition of 200 μl opening buffer containing 0.1 mg/ml poly-FLAG peptide (Biotool, Bimake) for 45 min on a turning wheel. All incubations, washes and elutions were performed at 4°C. The eluted sample was collected by centrifugation at 2000 rpm for 1 min 4°C in a F241.5P rotor using a 149 Microfuge 22R centrifuge (Beckman Coulter). One aliquot of the eluted sample was resolved on SDS-PAGE, the other was blotted on cryo-EM grids, and the remaining sample was used for tRNA-array analyses. For SDS-PAGE analyses, 20 μl aliquots of samples were mixed with 5 μL of 5× SDS loading buffer and heated at 95°C for 15 min, and denatured samples were loaded on 12% SDS-PAGE. SDS-gels were stained by 'Blue-Silver' Coomassie Staining (48) and washed with water for 6 h or overnight before imaging with LAS4000 (GE Healthcare).

Preparation of cryo-EM grids

Eluted pull-down samples were kept on ice and loaded on grids within 2 h after preparation without freezing. The concentration of ribosomes in the samples was estimated from SDS-PAGE gels by comparison of ribosomal band intensities in eluted samples with the bands from loaded ribosomes with known concentration (Supplementary Figure S1). The concentration of ribosomes in elution of RqcH^{DR}-FLAG$_3$ was approximately 50 nM. Samples were loaded on Quantifoil 2/1 Cu300 grids three times with manual blotting followed by the final blotting using the Vitrobot (FEI). Vitrobot blotting was performed at 100% humidity, 4°C, 5 s blot time, 1 s wait time and 0 s drain time; the resultant sample was vitrified by plunge-freezing in liquid ethane. Grids were imaged on a Titan Krios (FEI) operated at 300 kV at a nominal magnification of 165 000× and a pixel size of 0.82 Å with a Gatan K2 Summit camera with a 4 s exposure and 20 frames using the EPU software.

Cryo-EM data analysis

Unless otherwise specified, all processing was performed in RELION 3.1 (49). 2510 raw micrograph stacks were motion-corrected with MotionCor2 (50) and the CTF was estimated with CTFFIND4 (51) (Supplementary Figure S2, Table S3). Micrographs with an estimated CTF fit that was significant beyond 4 Å were selected for further processing. crYOLO was used to pick particles (52), resulting in 145 631 initial particles which were extracted with 3× downsampling. After 2D classification, the remaining 125 573 particles were used to create an *ab initio* model, which was subsequently used as a reference for 3D refinement and 3D classification without angular sampling (53). The majority of particles were grouped into a single class containing a 50S ribosomal large subunit, P-tRNA, RqcP and weak surrounding density. This class was selected for another 3D refinement, followed by partial signal subtraction with a mask around the A, P and E sites (54). Another 3D classification was then performed without angular sampling, the regularization parameter T set to 50, and the resolution used in the expectation step limited to 7 Å. Classes of interest were re-extracted with the original pixel size, refined, and post-processed. FSCs were assessed using the 'gold-standard' approach (55). Local resolution was estimated with ResMap (56). For analysis, parts of an existing model of a bacterial RQC complex (PDB: 7AS8) were fitted, by domain, into density using ChimeraX (57).

Electrophoretic mobility shift assay (EMSA)

Experiments were performed as described earlier (58). Before performing the experiment, stock mRNA(MVF) (5′-GGC**AAGGAGGA**GAUAAGAAUGGUUUUCUAAUA-3′) was incubated for 2 min at 60°C to denature possible secondary structures. Reaction mixtures (10 μL) in HEPES:Polymix buffer (47) with 5 mM Mg^{2+} were assembled by adding either *E. coli* tRNA^{Val} or *B. subtilis* tRNA^{Ala} or tRNA^{Lys} (0.1 μM final concentration) as well as mRNA mRNA(MVF) competitor (1 μM final concentration), followed by the addition of RqcH-HTF (either wild-type or D97A R98A substituted). After incubation for 5 min at 37°C, 4 μL of 50% sucrose was added per sample, and the samples were electrophoretically resolved on a 12% Tris:borate:EDTA gel at 4°C (160–180 V) for 1–1.5 h. Gels were stained with SYBR Gold nucleic acid stain (Life Technologies) for 30 min, followed by visualization using a Typhoon Trio Variable Mode Imager (Amersham Biosciences). Bands were quantified using ImageJ (59). The efficiency of complex formation (effective concentration, EC_{50} ± standard deviation) was calculated using the 4PL model (Hill equation) as per Sebaugh (60) using eight data points; each experiment was performed at least two times.

Immunoprecipitation of purified His$_6$-TEV-FLAG$_3$-tagged RqcH variants with *B. subtilis* total tRNA

1 μM purified His$_6$-TEV-FLAG$_3$-tagged RqcH variants (wild-type and D97A/R98A) and 10 μM *B. subtilis* total tRNA were mixed on ice in IP buffer (HEPES:Polymix buffer pH 7.5, 1 mM DTT, 5 mM MgOAc; 200 μl total volume). The sample was mixed with 50 μl of ANTI-FLAG M2 Affinity Gel (Sigma) pre-equilibrated in IP buffer, and incubated for 0.5 h at 4°C on a turning wheel (Fisherbrand™ Multi-Purpose Tube Rotators). The samples were loaded on Micro Bio-Spin columns (Bio-Rad) pre-equilibrated in IP buffer, and washed 4 times with 0.5 ml of IP buffer by gravity flow. RqcH-His$_6$-TEV-FLAG$_3$ was eluted by addition of 200 μl IP buffer containing 0.1 mg/ml poly-FLAG peptide (Biotool, Bimake) for 30 min on a turning wheel. All incubations, washes and elutions were performed at 4°C. The eluted sample was collected by centrifugation at 2000 rpm for 1 min 4°C in a F241.5P rotor using a 149 Microfuge 22R centrifuge (Beckman Coulter). RNA was extracted

twice with 5:1 acidic phenol:chloroform, precipitated with ethanol, and resuspended in ddH_2O. Samples containing 150 ng of total RNA were separated on 8 M urea-containing 8% polyacrylamide gels. The gel was stained with SYBR Gold (Life technologies) for 30 min, followed by visualization using a Typhoon Trio Variable Mode Imager (Amersham Biosciences).

tRNA Northern blotting

For deacylation immunoprecipitated samples were incubated with 125 mM Tris–HCl, pH 9.0, 0.1 M EDTA, 0.5% (w/v) SDS at room temperature for 45 min, before neutralization with an equal volume of 1 M NaOAc, pH 5.5. RNA was extracted twice with 5:1 acidic phenol:chloroform, precipitated with ethanol, and resuspended in ddH_2O. Samples containing 150 ng of total RNA were separated on 8M urea-containing 8% polyacrylamide gels followed by electroblotting to Zeta-probe membranes (Bio-Rad). The blots were sequentially probed for *B. subtilis* $tRNA^{Ala}$, *B. subtilis* $tRNA^{Lys}$ and *E. coli* $tRNA^{Val}$ using ^{32}P-labeled oligonucleotides (Supplementary Table S2). The probes for *B. subtilis* $tRNA^{Ala}$ were designed to hybridize with the conserved TΨC-loop of both $tRNA^{Ala}$ isoacceptors. Signals were detected by phosphorimaging using a Typhoon FLA 9500 biomolecular imager. In parallel, a second gel was subjected to SYBR Gold (Life Technologies) nucleic acid staining for 30 min, followed by visualization using a Typhoon Trio Variable Mode Imager (Amersham Biosciences).

tRNA microarrays

tRNA microarrays were performed similarly to as previously described (42). A detailed protocol for the microarrays is published on protocols.io (dx.doi.org/10.17504/protocols.io.hfcb3iw). *In vivo* and *in vitro* co-immunoprecipitated tRNA samples as well as the corresponding total tRNA controls (tRNA from cell lysate for *in vivo* pulldown experiments or purified total *B. subtilis* tRNA for *in vitro* pulldown experiments, respectively) were incubated with 100 mM Tris-HCl pH = 9.0 at room temperature for 45 min, thereafter precipitated with one volume of 100 mM NaCl 100 mM NaOAc pH 4.8 as well as 2.7-volumes of absolute ethanol, resuspended in ddH_2O and tRNAs were subjected to labeling of the invariant 3′-NCCA-ends. The IP samples were labeled with Cy3-labeled RNA/DNA while the total tRNA control samples were labeled with Atto647-labeled RNA/DNA hybrid oligonucleotide. Labeled tRNA samples were loaded as pairs (i.e. Cy3-labeled IP and Atto647-labeled total tRNA) on the same microarray containing 24 replicates of full-length tDNA probes recognizing the 36 *B. subtilis* tRNA isoacceptors (see Supplementary Table S1) and hybridized for 16 h at 60°C. The fluorescence signals of microarrays were recorded with a GenePix 4200A scanner (Molecular Devices) and statistically analyzed with in-house scripts with Python version 3.7.0. Each fluorescent signal was normalised to intrinsic standards as described (61) and presented as ratios of the IP complexes against total tRNA (i.e. Cy3 vs Atto647 signals). Thereby, while equal amounts of IP samples and total tRNAs were analyzed on each array, the IP samples originated from larger cell amounts and this was also considered by calculating the final ratios. Enrichment of tRNA species in *in vivo* and *in vitro* IP samples was calculated over corresponding total tRNA pool, i.e. either tRNA from cellular lysates or purified total *B. subtilis* tRNA, respectively. To assess the spread of the data, covariance of the signal is calculated for each single isoacceptor (represented with grey bars on the corresponding figures) which is further used to compute the confidence intervals, i.e. the spread of the data for all isoacceptors. In the case of experiments with three replicates, the confidence intervals between replicates 1 and 2, 2 and 3, 1 and 3 were 98%, 99% and 99% (for Figure 2E), 95%, 97% and 92% (Figure 2F), 96%, 96% and 97% (Figure 3B), 95%, 97% and 92% (Figure 3C) and, finally, 94%, 98% and 97% (Figure 5F). In the case of experiments with two replicates, the confidence intervals between replicates 1 and 2 were 95% (Figures 3D and 3E).

Sucrose gradient fractionation and Western blotting

Experiments were performed as described earlier (42), with minor modifications. 50S ribosomal protein L3 was detected using anti-L3 primary antibodies provided by Fujio Kawamura (1:20,000 dilution) combined with goat anti-rabbit IgG-HRP secondary antibodies (Sigma-Aldrich, A0545; 1:10 000 dilution). ECL detection was performed using WesternBright™ Quantum (K-12042-D10, Advansta) western blotting substrate and ImageQuant LAS 4000 (GE Healthcare) imaging system.

Poly-Ala synthesis in a reconstituted *B. subtilis* RQC system

Initiation (2 μM *B. subtilis* 50S, 3 μM RqcH-HTF, 3 μM RqcP, 2 μM f[^{35}S]Met-$tRNA_i^{Met}$ in HEPES:Polymix buffer pH 7.0 1 mM DTT and 7.5 mM $MgCl_2$) and elongation (10 μM *B. subtilis* total tRNA (tBulk), 2 μM AlaRS, 1 mM ATP, 200 μM Alanine, 1 mM DTT and 7.5 mM $MgCl_2$ in HEPES:Polymix buffer pH 7.0) mixtures were separately prepared on ice. After 5 min incubation at 30°C, the two mixtures were combined and incubated at 30°C. 10 μl aliquots were taken (either after 15-min long incubation or throughout the time course), quenched with 10 μl of loading dye (7 M urea, 0.05% bromophenol blue and 100 mM NaOAc, pH 5) and resolved on acidic urea-PAGE in 1× TBE (8 M urea, 6.5% PAGE). The gel was exposed overnight, and the imaging plate was scanned on Typhoon FLA 9500 (GE Healthcare).

RESULTS AND DISCUSSION

RqcH specifically selects $tRNA^{Ala}$ from the tRNA pool in the absence of the 50S subunit

Previous studies indicated that *B. subtilis* RqcH appears to specifically interact with $tRNA^{Ala}$ and that this specificity may be mediated by the highly conserved $_{97}$DR$_{98}$ residues (41,42,44). To investigate this further, we used Electrophoretic Mobility Shift Assays (EMSAs) to study complex formation between *B. subtilis* RqcH – wild-type and D97A/R98A (DR) variant – and individual native deacylated tRNAs purified from *B. subtilis* bulk tRNA (Figure

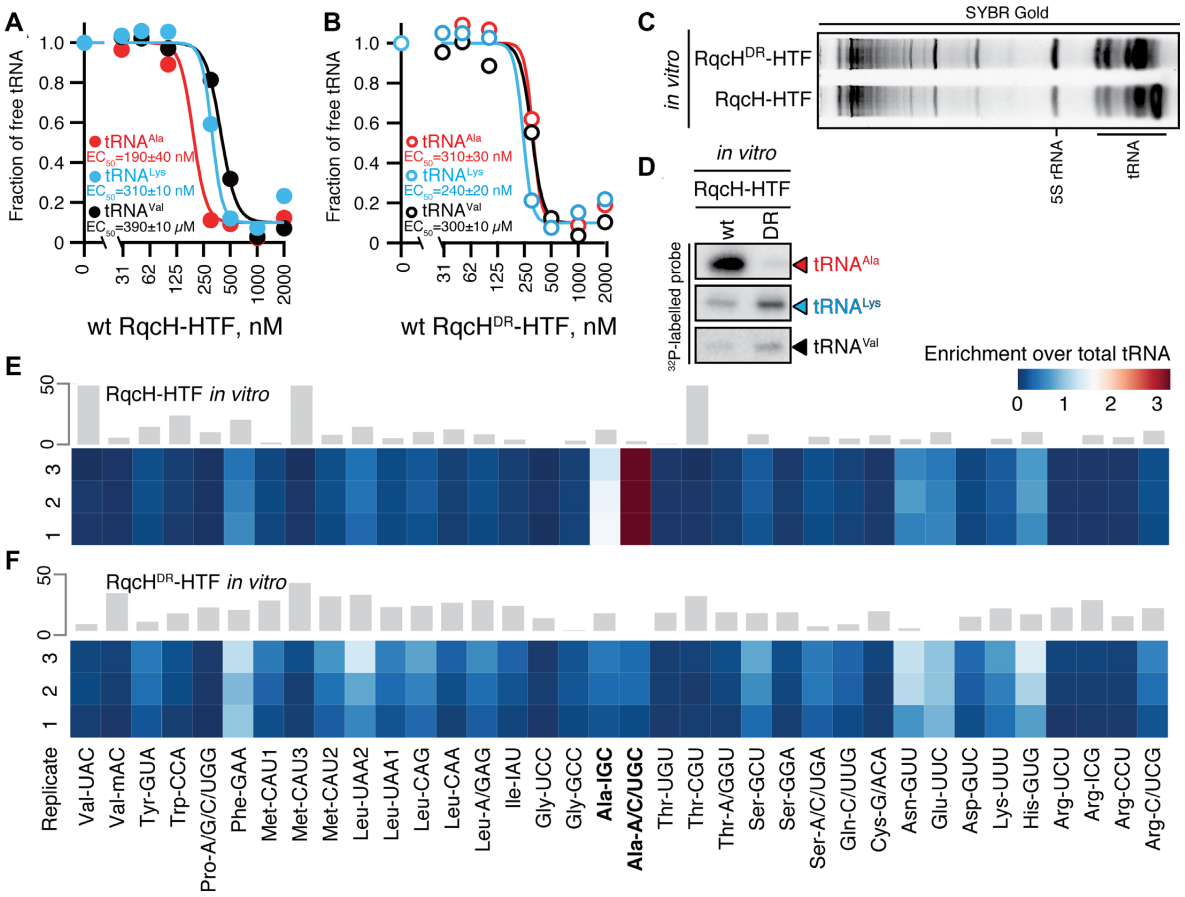

Figure 2. RqcH can specifically select tRNA^{Ala} from the tRNA pool off the 50S ribosome. (A, B) Complex formation between increasing concentrations of either wild-type (**A**) or DR variant (D97A R98A double substitution) (**B**) *B. subtilis* RqcH-HTF and 0.1 μM of either *B. subtilis* tRNA^{Val}, *B. subtilis* tRNA^{Ala} or *E. coli* tRNA^{Val} was monitored by EMSA. 1 μM of synthetic mRNA(MVF) RNA oligonucleotide was used as a nonspecific competitor. Representative full-size EMSA gels are provided as Supplementary Figure S3. (C, D) SYBR Gold staining (**C**) and Northern blotting (**D**) analyses of RqcH-HTF:tRNA complexes isolated through co-IP of either wild-type or DR variant of RqcH-HTF preincubated with total *B. subtilis* tRNA, tBulk. For validation of northern blot probe specificity see Supplementary Figure S4. (E, F) tRNA microarray analyses of tRNAs isolated through co-IP of either wild-type (**E**) or DR variant (**F**) of RqcH-HTF preincubated with *B. subtilis* total tRNA. Grey bars represent an example of covariance analysis between replicates 1 and 3 (E) and replicates 2 and 3 (F). The Ala-IGC tRNA array probe hybridizes with tRNA$^{Ala(GGC)}$, Ala-A/C/UGC probe hybridizes with tRNA$^{Ala(UGC)}$ and Lys-UUU hybridizes with tRNA$^{Lys(UUU)}$; the full reference table is provided as Supplementary Table S1. The colour key indicates the fold-enrichment of tRNAs in pulldown samples over total tRNA.

2A, B and Supplementary Figure S3). We tested *B. subtilis* tRNA^{Ala} as the native RQC tRNA substrate, and, as controls, *B. subtilis* tRNA^{Lys} and *E. coli* tRNA^{Val}; tRNA^{Ala} and tRNA^{Val} used for EMSA were not further purified into individual isoacceptors. While the wild-type RqcH displays a preference for tRNA^{Ala}, it also binds the control tRNAs, though with lower affinity: EC_{50} tRNA^{Ala} of 190 nM versus EC_{50} tRNA^{Lys} of 310 nM and EC_{50} tRNA^{Val} of 390 nM (Figure 2A). The preference for tRNA^{Ala} is lost in the RqcH^{DR} variant, which binds all the three tRNA species with the same (low) affinity, analogous to that observed for the wild-type protein binding to non-cognate tRNA (i.e. tRNA^{Val} and tRNA^{Lys}; EC_{50} 240–310 nM). The modest specificity of RqcH for tRNA^{Ala} observed in EMSAs is surprising given the pronounced selectivity for tRNA^{Ala} in *B. subtilis* RQC (41,42). The higher specificity for tRNA^{Ala} *in vivo* is only evident in kinetic competition with the other tRNA species. To assess this, time-resolved studies will be necessary; while our EMSA can quantify the equilibrium affinities (K_D/EC_{50}), the method is not suitable for measuring the on- and off-rates of RqcH:tRNA complex formation (k_{+1} and k_{-1}). Alternatively, it is also possible that the high selectivity is only evident when RqcH is recruited to the 50S subunit, and the preference for tRNA^{Ala} actually reflects the specificity of RqcH:50S RQC complex, rather than that of the RqcH itself.

To address the first of these possibilities, we performed a set of *in vitro* pulldown experiments using total *B. subtilis* tRNA preparation (total tRNA bulk, tBulk) and purified RqcH (C-terminally extended by the His_6-TEV-$FLAG_3$ (HTF) tag). The purified HTF-tagged wild-type RqcH or RqcH^{DR} were incubated with total tRNA, and the associated tRNA species were probed by (i) Northern blotting (Figure 2C, D; for validation of Northern blot probe specificity see Supplementary Figure S4), and (ii) tRNA microarray (Figure 2E, F). Both experiments were in agreement with each other, demonstrating strong preference of the wild-type RqcH for tRNA^{Ala}. In the microarrays, we de-

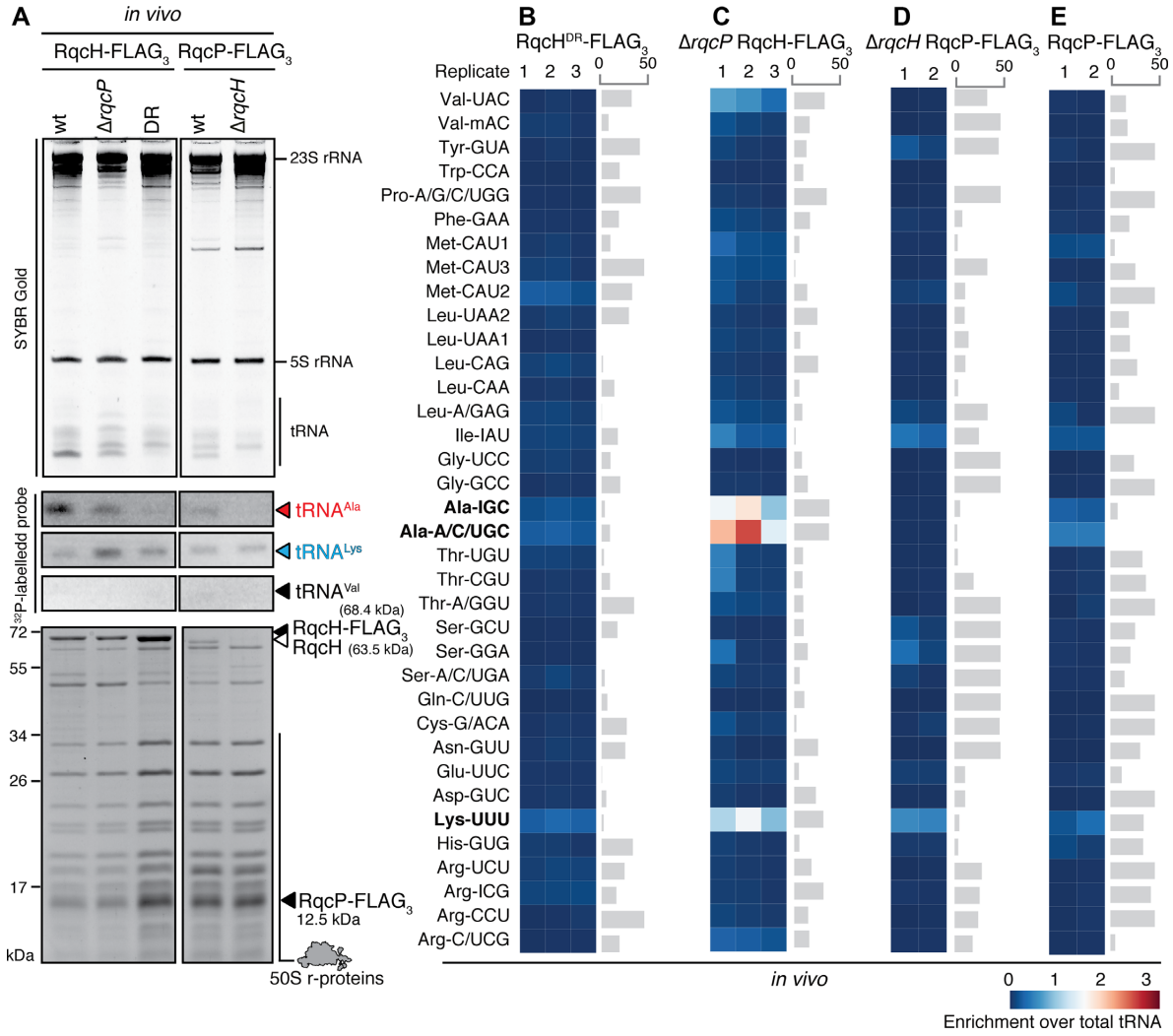

Figure 3. While RqcP itself does not have a specific preference for $tRNA^{Ala}$, loss of RqcP moderately compromises $tRNA^{Ala}$ selection by RqcH *in vivo*. (**A**) SYBR Gold staining (top), Northern blotting (middle) and SDS PAGE (bottom) analyses of 50S RQC complexes isolated through co-IP of either $RqcH\text{-}FLAG_3$ or $RqcP\text{-}FLAG_3$ from lysed *B. subtilis*. (B–E) tRNA microarray analyses of 50S RQC complexes isolated through co-IP of either $RqcH\text{-}FLAG_3$ (**B** and **C**, three independent biological replicates) or $RqcP\text{-}FLAG_3$ (**D** and **E**, two independent biological replicates) from lysed *B. subtilis*. Grey bars represent an example of covariance analysis between either replicates 1 and 3 (B), 2 and 3 (C), or 1 and 2 (D,E). The Ala-IGC tRNA array probe hybridizes with $tRNA^{Ala(GGC)}$, Ala-A/C/UGC probe hybridizes with $tRNA^{Ala(UGC)}$ and Lys-UUU hybridizes with $tRNA^{Lys(UUU)}$; the full reference table is provided as Supplementary Table S1. The colour key indicates the fold-enrichment of tRNAs in pulldown samples over total tRNA.

tected both $tRNA^{Ala(GGC)}$ and $tRNA^{Ala(UGC)}$ isoacceptors (hybridizing to the Ala-IGC and Ala-A/C/UGC probes, respectively, see Supplementary Table S1). The signal for $tRNA^{Ala}$ is abrogated in the $RqcH^{DR}$ variant. Notably, in the case of $RqcH^{DR}$, the $tRNA^{Lys}$ signal on the Northern blot (and to a lesser extent that of $tRNA^{Val}$) is stronger than that for the wild-type protein (Figure 2D). A possible explanation is that the RQC-cognate $tRNA^{Ala}$ efficiently out-competes $tRNA^{Lys}$ for binding to wild-type RqcH, but not to $RqcH^{DR}$. Finally, we validated the *in vitro* tRNA specificity results *in vivo*. Both northern blotting (Figure 3A) and tRNA microarray (Figure 3B) analyses of *in vivo* $FLAG_3$ pulldown RqcH:50S complexes demonstrate that, indeed, $tRNA^{Ala}$ specificity is lost in $RqcH^{DR}$. Note that $tRNA^{Ala}$ signal is clearly resolved from other RNA species on SYBR Gold gels, and the corresponding band is lacking in the $RqcH^{DR}$ sample (Figure 3A and Supplementary Figure S5). Collectively, our results demonstrate that RqcH recruitment to the 50S subunit is not necessary for the tRNA selection by RqcH.

We also probed the role of the second RQC elongation factor, RqcP, in tRNA selection using northern blotting, SYBR Gold staining (Figure 3A and Supplementary Figure S5) and tRNA microarrays (Figure 3C–E). Compared to the *rqcP*+ sample, in the $RqcH\text{-}FLAG_3$:50S pulldown from Δ*rqcP B. subtilis*, there is a moderate, but detectable decrease in abundance of both $tRNA^{Ala}$ isoacceptors, as well as an increase of the $tRNA^{Lys}$ signal (Figure 3C). This could be either a direct effect of intrinsic specificity of RqcP towards $tRNA^{Lys}$, or an indirect effect of the compromised RQC elongation through RqcP depletion leading to accumulation of 'initiation' RQC complexes con-

taining $tRNA^{Lys}$. Therefore, we next probed the intrinsic tRNA selectivity of RqcP by analysing RqcP-$FLAG_3$ pulldowns from both the RQC-incompetent Δ*rqcH* strain (Figure 3D) and RQC-competent *rqcH*+ strain (Figure 3E). While we see no tRNA specificity in the Δ*rqcH* pulldown samples, there is a weak signal for selection of $tRNA^{Lys}$ of a similar magnitude and preference $tRNA^{Ala}$ in *rqcH*+ pulldowns. This strictly-RqcH-dependent specificity signal in the *in vivo* RqcP-$FLAG_3$ pulldowns can be explained by the tRNA specificity of RqcH present in RqcP-$FLAG_3$-RqcH-50S (but not RqcP-$FLAG_3$-RqcH-50S) RQC complexes. Our RqcP pulldown results also suggest that the decrease in $tRNA^{Ala}$ abundance observed in the RqcH-$FLAG_3$:50S pulldown from the Δ*rqcP* strain is an indirect effect of compromised RQC elongation, with the increase of the $tRNA^{Lys}$ signal possibly reflecting the nature of the tRNA in the initial stalled 70S complexes.

Cryo-EM structures of an *in vivo* formed $RqcH^{DR}$-50S complex

To gain the structural insight into the specific role of D97/R98 residues in $tRNA^{Ala}$ recognition by RqcH, we determined the structure of a $RqcH^{DR}$-50S RQC complex by cryo-EM. Following an established affinity purification procedure (42), we generated 50S RQC complexes from *B. subtilis* expressing C-terminally $FLAG_3$-tagged $RqcH^{DR}$ (D97A/R98A double substitution in NFACT-N domain) (Supplementary Figure S2). As observed previously, RqcH apparently dissociated from many particles during sample preparation, but with focussed classification we nonetheless obtained a volume with RqcH stably bound (Supplementary Figure S2, Table S3). The main state observed is broadly similar to the previously defined state B, consisting of a 50S subunit with peptidyl-tRNA in approximately the P-site, nascent chain, RqcP, and RqcH (Figure 4A). Although the overall resolution of this complex was 3.2 Å, this mostly reflected the core of the 50S subunit, as RqcH and other bound factors were less well resolved (Supplementary Figure S6). Compared to the previously observed state B (42), the $RqcH^{DR}$ NFACT-N and HhH domains are swung away from the tRNA anticodon in the $RqcH^{DR}$-bound structure (Figure 4B). These domains are also especially poorly resolved, indicating flexibility (Figure 4A, Supplementary Figures S6 and S7). Such flexibility is likely due to the $_{97}DR_{98}$ motif interacting with the tRNA anticodon stem in the RqcH wild-type state B structure, possibly stabilizing the major conformation (Figure 4C). Nonetheless, we were able to fit the individual domains of $RqcH^{DR}$ into the map to create a model with sufficient confidence to examine domain-level movements. The $RqcH^{DR}$ complex is very similar to state B* that was also observed in the wild-type RqcH reconstructions (42) (Supplementary Figure S7). The P-tRNA in the $RqcH^{DR}$ complex had a poorly resolved anticodon (Figure 4D). Previously, wild-type RqcH has been shown to make close contact with the P-tRNA, unwinding the anticodon stem and forming interactions with the splayed anticodon (42,44). In comparison, the $RqcH^{DR}$-bound tRNA anticodon stem was not as distorted (Figure 4E). However, compared to a canonical P-tRNA or free crystallised tRNA (62), the $RqcH^{DR}$-bound P-tRNA was still somewhat distorted, perhaps as a result of other regions of RqcH, such as a N-terminus of the coiled-coil domain, that contact the tRNA (Figure 4F, G) (42,44). Collectively, the structure suggests that the mutation of $_{97}DR_{98}$ motif to $_{97}AA_{98}$ destabilizes the interaction of the NFACT-N domain of $RqcH^{DR}$ with the anticodon stem loop of the P-tRNA, thereby supporting the hypothesis that this interaction is critical for the specificity of RqcH for $tRNA^{Ala}$. In the available structures so far, RqcH $_{97}DR_{98}$ has been observed either to interact with G35 at the central position of the tRNA anticodon, which is common to several *B. subtilis* tRNAs, or not interact with the tRNA at all. It is therefore unlikely that these conformations alone can account for the tRNA specificity of RqcH. RqcH and $tRNA^{Ala}$ may form a complex with an alternative conformation when not bound in complex with the 50S subunit.

Ribosomal protein uL11 is important for RQC functionality

In the cryo-EM structure of the RqcH-50S RQC complex, we observed strong interaction between the M domain of RqcH and the uL11 stalk base (Figure 5A), as observed previously for the wild-type RqcH 50S complexes (42,44). This interaction appeared to be critical for RqcH function since treatment with the antibiotic thiostrepton that interacts with uL11 (63), and has an overlapping binding site with RqcH M domain (inset to Figure 5A), destabilised interaction of RqcH with the 50S RQC complex (42). To directly investigate the importance of uL11 for RQC function, we constructed a *B. subtilis* strain in which uL11 is expressed under the control of an IPTG-inducible $P_{hy-spank}$ promoter (64), while the genomic copy of *rplK* encoding uL11 is disrupted (Δ*rplK*). This allowed conditional depletion of uL11 in bacteria that are grown in the absence of an inducer. uL11 depletion results in a pronounced growth defect as seen in Figure 5B. When we combined the depletion of uL11 with *rqcH* disruption, we did not observe a further synthetic growth defect. This lack of genetic interaction is consistent with RQC functionality being already lost in the uL11-depleted strain. By contrast, simultaneous loss in functionality of both RQC and trans-translation ribosome rescue systems renders *B. subtilis* sensitive to elevated temperature and antibiotics targeting protein synthesis, such as tetracycline (41,42,44). This synergetic growth defect is commonly used for probing RQC functionality in an Δ*ssrA* background (41,42,44). Indeed, we observed a strong genetic interaction of *rplK* with *ssrA*: uL11 depletion in Δ*ssrA* Δ*rplK* genetic background results in the synthetic lethality of the strain (Figure 5B). This is likely due to the proteotoxic stress due to a defunct RQC and trans-translation, combined with the general translation defect due to loss of uL11.

Next, we assessed the effect of uL11 on the recruitment of RQC factors to the 50S RQC complex using sucrose gradient centrifugation and Western blotting against the FLAG-tagged RqcH or RqcP factors (Figure 5C). While RqcP remains associated with ΔuL11 50S, RqcH is lost from the 50S fractions in the Δ*rplK* strain (Figure 5C), strongly suggesting that uL11 plays a key role in RqcH recruitment to 50S, and, therefore, RQC function. In good agreement with decreased affinity of RqcH to 50S lacking uL11, character-

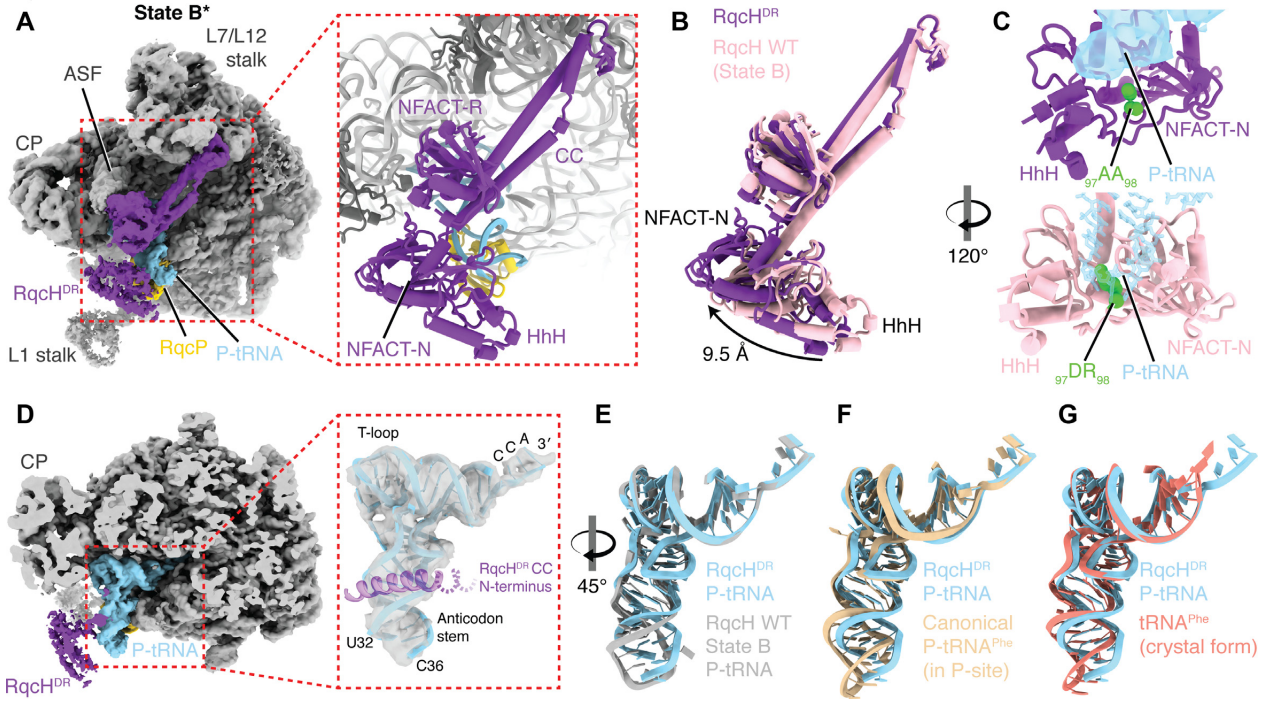

Figure 4. Cryo-EM structures of an *in vivo*-formed RqcH^{DR}-50S complex. (**A**) View of RqcH^{DR}-FLAG$_3$ bound to 50S with P-tRNA and RqcP. The state broadly resembles state B described in (42). (**B**) Comparison of RqcH^{DR} (purple) with wild-type RqcH (pink) state B. (**C**) Close views, rotated compared to C, showing the position of the mutated $_{97}$DR$_{98}$ residues. Transparent density (top panel) or model (bottom panel) is shown for the P-tRNA anticodon stem. (**D**) View of the P-tRNA on the RqcH^{DR}-bound 50S. The anticodon stem is poorly resolved, likely due to flexibility. Part of the RqcH CC N-terminus is shown. (**E**) Comparison of the P-tRNA in the RqcH^{DR} volume (light blue) with the P-tRNA in the RqcH WT-bound volume (state B, grey) (42). (**F**) As in E, except the RqcH^{DR}-FLAG$_3$ P-tRNA is compared to a canonical P-tRNA bound in the P-site of the ribosome (tan, PDB 6CFJ) (74). (**G**) As in E and F, except the RqcH^{DR}-FLAG$_3$ P-tRNA is compared to crystallised yeast tRNA^{Phe} (reddish, PDB 1EHZ) (62).

ization of RqcH-FLAG$_3$ pulldown samples revealed relatively low abundance of both rRNA and r-proteins in comparison to pulldowns from wild-type strain (Figure 5D, E, a side-by-side comparison is shown on Supplementary Figure S5). By contrast, the strong band consistent with tRNA remained (Figure 5D), in agreement with RqcH being able to specifically recruit tRNA^{Ala} in the absence of the 50S subunit. tRNA microarray analysis of the RqcH-FLAG$_3$ pulldown samples from *B. subtilis* Δ*rplK* revealed that indeed RqcH specifically interacts with both tRNA^{Ala} isoacceptors (Figure 5F), as seen previously for tRNA microarray analysis of RqcH 50S complexes (42).

Polypeptide release dissociates RqcP from RqcP-RqcH-50S RQC complexes

Our finding that uL11 is critical for RqcH, but not RqcP, interaction with the 50S subunit (Figure 5C) suggested that binding of RqcP to the 50S subunit is independent of RqcH. This is consistent with cryo-EM analysis where P-tRNA-50S complexes containing RqcP but lacking RqcH are observed (Supplementary Figure S2) (42). To pursue this further, we employed sucrose density gradient centrifugation and Western blotting to monitor the association of both RqcH and RqcP in the presence of the antibiotics thiostrepton and puromycin (Figure 6A,B). As before (42), we observed that thiostrepton abolished the interaction of RqcH with the 50S subunit (Figure 6A), whereas here we show that RqcP remains unaffected (Figure 6B). By contrast, the addition of puromycin, which mediates release of the polypeptide chain from the P-tRNA (65), led to a modest reduction in RqcH binding (Figure 6A), as observed previously (42), but more strikingly, resulted in a dramatic reduction of the RqcP band within the 50S fraction (Figure 6B). Since release of the nascent polypeptide chain by puromycin is likely to have a destabilizing effect on the binding of P-tRNA to the 50S subunit, these findings suggest that binding of RqcP, and to a lesser extent RqcH, is stabilized by the presence of the peptidyl-tRNA in the P-site.

Stable interaction of RqcP with 23S rRNA H69, but not with P-site tRNA^{Ala} is essential for RQC functionality

In the 50S RQC complex, RqcP forms a network of contacts with P-site tRNA, but also the 23S rRNA helix 69 (H69) (42,44). Interactions with H69 are mediated by conserved Arg2 and Arg16 of RqcP, whereas contacts with P-tRNA are formed by Arg11, Lys68 and Lys69 (Figure 6C–E). To date, only Arg16 of RqcP was assessed experimentally for its functional role, and the residue was shown to be crucial because Arg16Ala substitution abolished RqcP association with the 50S subunit and, when introduced in the Δ*ssrA* background, *rqcP R16A* phenocopies Δ*ssrA* Δ*rqcP* double deletion (42).

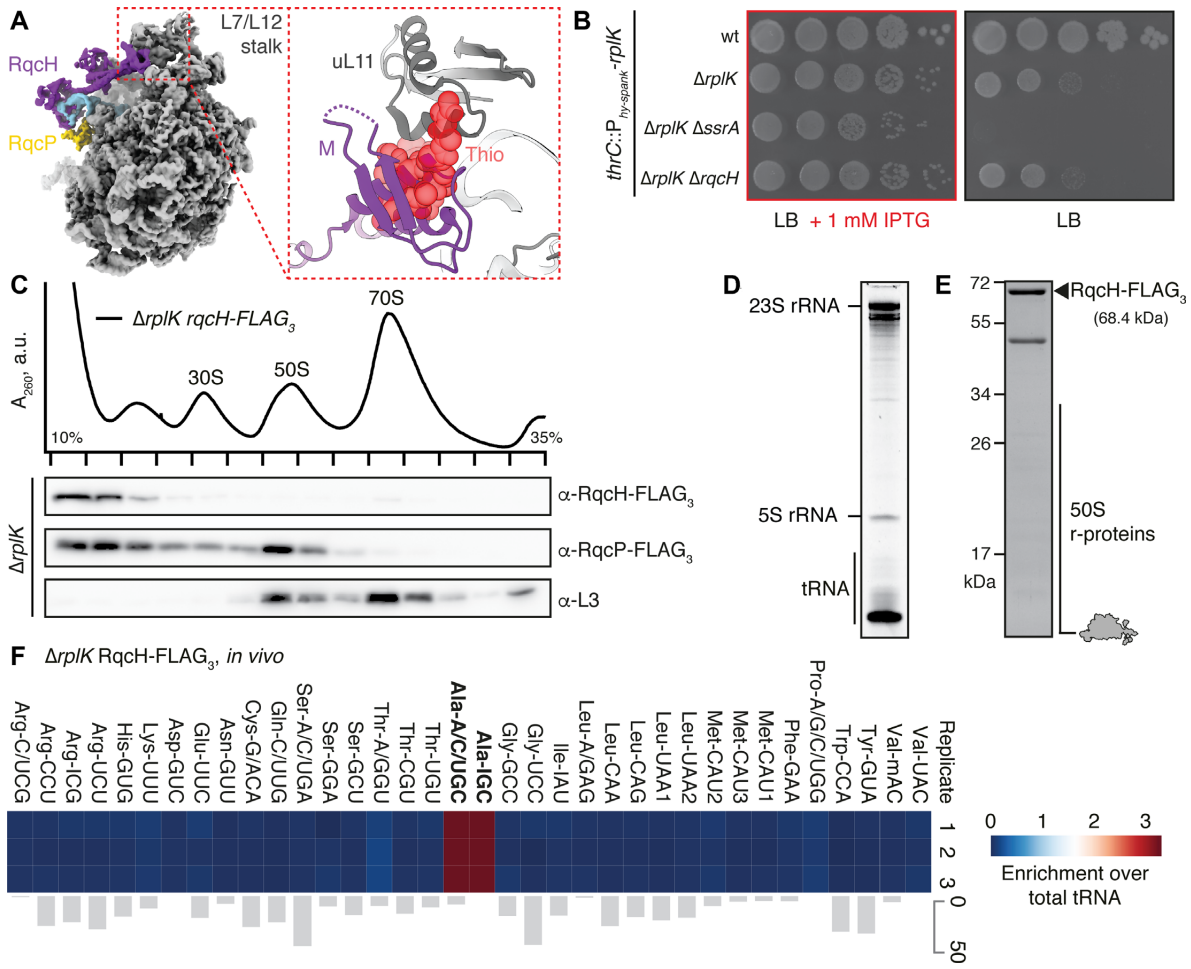

Figure 5. Ribosomal protein uL11 is important for RqcH recruitment to 50S and for RQC functionality. (**A**) Overview of wild-type RqcH (state B, PDB 7AS8, EMD-11889) bound to the 50S-P-tRNA complex with focus on the L7/L12 stalk base. Right, close view of the RqcH M hairpin interacting with uL11. Antibiotic thiostrepton (Thio, in red) is modeled based on PDB 3CF5 (63). (**B**) *B. subtilis* strains expressing ribosomal uL11 (*rplK*) under the control of IPTG-inducible $P_{hy-spank}$ promoter in wild-type, Δ*rplK*, Δ*rplK* Δ*ssrA* and Δ*rplK* Δ*rqcH* backgrounds were grown in either uL11-inducing (LB supplemented with 1 mM IPTG, left) or non-inducing (LB, right) conditions. Plates were scored after 18 hours at 37°C. (**C**) Sucrose gradient sedimentation and anti-$FLAG_3$ immunoblotting of either RqcH-$FLAG_3$ or RqcP-$FLAG_3$ expressed in Δ*rplK* background. (D–F) SYBR Gold staining (**D**), SDS PAGE (**E**) and tRNA microarray analyses (**F**) of 50S RQC complexes isolated through co-IP of RqcH-$FLAG_3$ from lysed Δ*rplK B. subtilis*. Three independent biological replicates of tRNA microarray analyses are shown. Grey bars represent an example of covariance analysis between replicates 1 and 3. The Ala-IGC tRNA array probe hybridizes with $tRNA^{Ala(GGC)}$, Ala-A/C/UGC probe hybridizes with $tRNA^{Ala(UGC)}$ and Lys-UUU hybridizes with $tRNA^{Lys(UUU)}$; the full reference table is provided as Supplementary Table S1. The colour key indicates the fold-enrichment of tRNAs in pulldown samples over the total tRNA.

We first probed the importance of Arg2, Arg11, Lys68 and Lys69 in RqcP association with the 50S through sucrose gradient sedimentation experiments. As seen in Figure 6B, the association with 50S was compromised for all of the tested RqcP variants, suggesting that the contacts of RqcP with both H69 and the P-site tRNA are both important for establishing a stable interaction with the large subunit. Next, we assessed the functional importance of Arg2, Arg11, Lys68 and Lys69 *in vivo* by following the growth of Δ*ssrA B. subtilis* strains expressing substituted RqcP variants. The cells were grown either in normal conditions (37°C), at elevated temperature (49°C), or in the presence of low concentrations of tetracycline (Figure 6F). Similar to R16A (42), the R2A substitution phenocopies the loss of RqcP (Δ*rqcP*), thereby re-emphasizing the importance of the interaction of RqcP with H69 of the 23S rRNA for RQC functionality. By contrast, there appears to be redundancy in the interactions between RqcP and the P-site tRNA: Δ*ssrA B. subtilis* strains expressing single R11A-substituted and the double K68A/K69A-substituted RqcP variants display wild-type-like phenotypes, only with the triple R11A/K68A/K69A substitution resulting in a growth defect (Figure 6F). The apparent discrepancy between the loss of interaction of the R11A and K68A/K69A variants with the 50S subunit (Figure 6B) and the lack of effect in the growth assays (Figure 6F) is likely due to the non-equilibrium nature of sucrose gradient sedimentation experiments, i.e. the lack of association does not indicate an

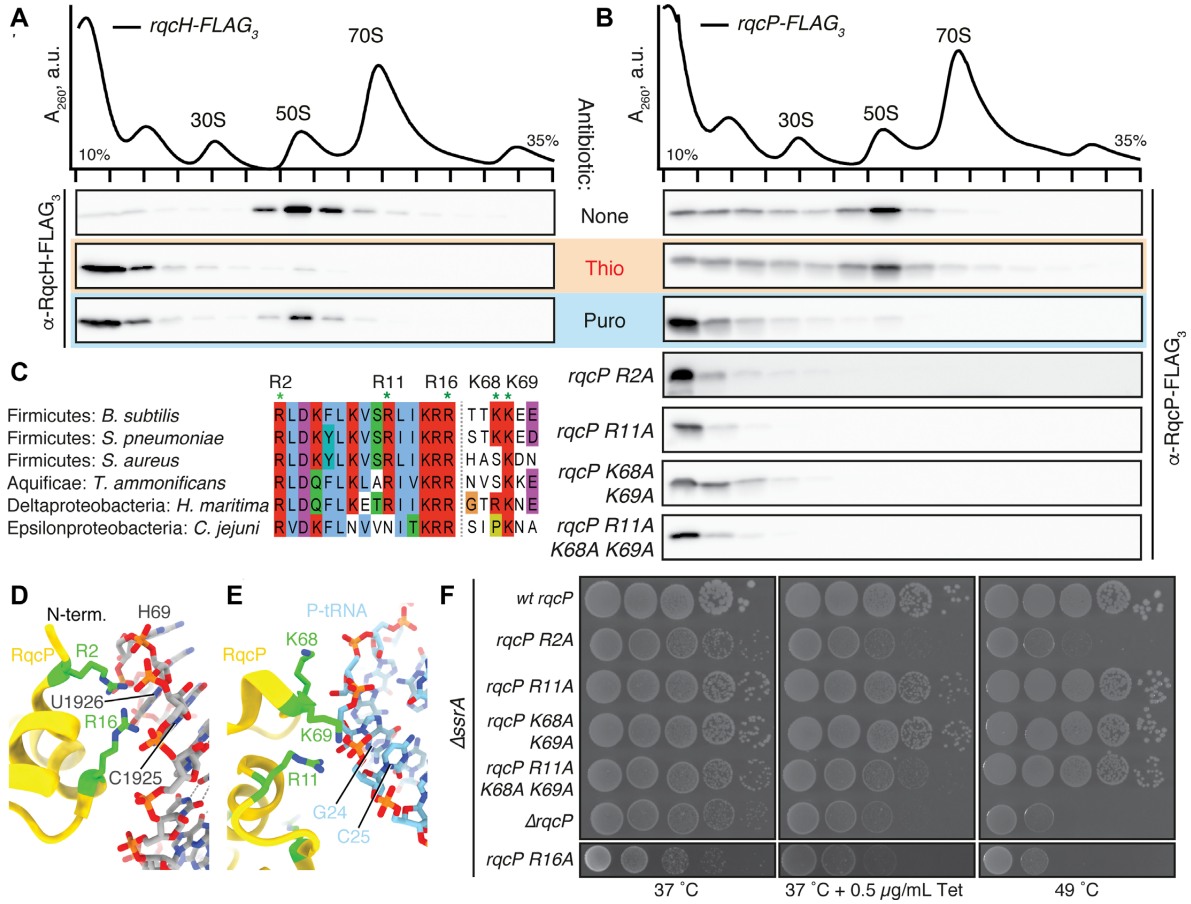

Figure 6. Interaction of RqcP with 23S rRNA H69, but not with P-site $tRNA^{Ala}$, is essential for RQC functionality. (A, B) Sucrose gradient sedimentation and anti-$FLAG_3$ immunoblotting analysis of *B. subtilis* strains expressing either wild-type RqcH-$FLAG_3$ (**A**) or RqcP-$FLAG_3$, wild-type and substituted variants (**B**). As indicated on the figure, the antibiotics were added after cell lysis: thiostrepton (Thio, 50 μM) and puromycin (Puro, 1 mM). (**C**) Sequence alignment of RqcP/Hsp15 homologs from diverse bacteria. (D, E) View of RqcP from state B interacting with (**D**) 23S rRNA H69 or (**E**) the P-tRNA (PDB 7AS8). Residues selected for mutation are coloured green. 23S rRNA nucleotides are numbered according to *E. coli* numbering. (**F**) Synthetic growth defects caused by amino acid substitutions in *rqcP*, or *rqcP* deletion in a Δ*ssrA* background. 10-fold serial dilutions were spotted onto LB agar plates and incubated for 18 hours at 37°C (left), 49°C (right) or 37°C in the presence 0.5 μg/ml tetracycline (Tet, middle).

absence of the interaction in the cell, but rather means that the complex is not retained during the 3-hour-long centrifugation.

RqcP is a processivity factor essential for poly-alanine synthesis during RQC elongation

Previous studies have shown using *in vivo* approaches that RqcP phenocopies RqcH in the Δ*ssrA* background (42,44) and that deletion of *rqcP* leads to a loss of poly-alanine tailing of a non-stop reporter construct (44), collectively indicating that RqcP has a critical role in bacterial RQC. However, it still remains unclear whether RqcH and RqcP are necessary and sufficient to mediate polyalanine tailing of 50S–peptidyl-tRNA complexes. To investigate this, we undertook to establish an *in vitro* polyalanine tailing system using only purified RQC factors, as has been previously performed for canonical translation (66,67). To initiate RQC, we loaded 50S subunits with radioactively labeled formylated initiator tRNA, ^{35}S-fMet-$tRNA_i^{Met}$, which has preferential affinity to the ribosomal P-site (68). We hypothesized that the fMet–tRNA–50S complex would mimic the peptidyl-tRNA 50S complexes that arise during RQC and thereby act as a substrate for RqcH and RqcP (Figure 7A). In parallel, we assembled a separate reaction containing Ala-$tRNA^{Ala}$ from *B. subtilis* total tRNA that had been incubated with *B. subtilis* alanyl-tRNA synthetase (AlaRS), ATP and L-alanine at 30°C. Since the Mg^{2+} concentration is a major determinant of tRNA affinity to the ribosome (69,70), we increased the concentration to 7.5 mM in our HEPES:Polymix-based buffer system (47) to find the optimal balance between tRNA affinity (for efficient Ala-$tRNA^{Ala}$ recruitment to 50S RQC complex) and dynamics (for efficient RQC elongation), and adjusted the pH to 7.0 in order to stabilise aminoacyl-tRNA. After preincubation the two mixtures were combined, the resultant reaction was further incubated for 30 minutes at 30°C, tRNA species were resolved in a bis-tris gel and then visualised by phosphoimaging.

In the reaction lacking RqcP, we only detect ^{35}S-labeled fMet-$tRNA_i^{Met}$, whereas in the presence of RqcP there is an up-shift in the ^{35}S-labeled fMet signal, which is consis-

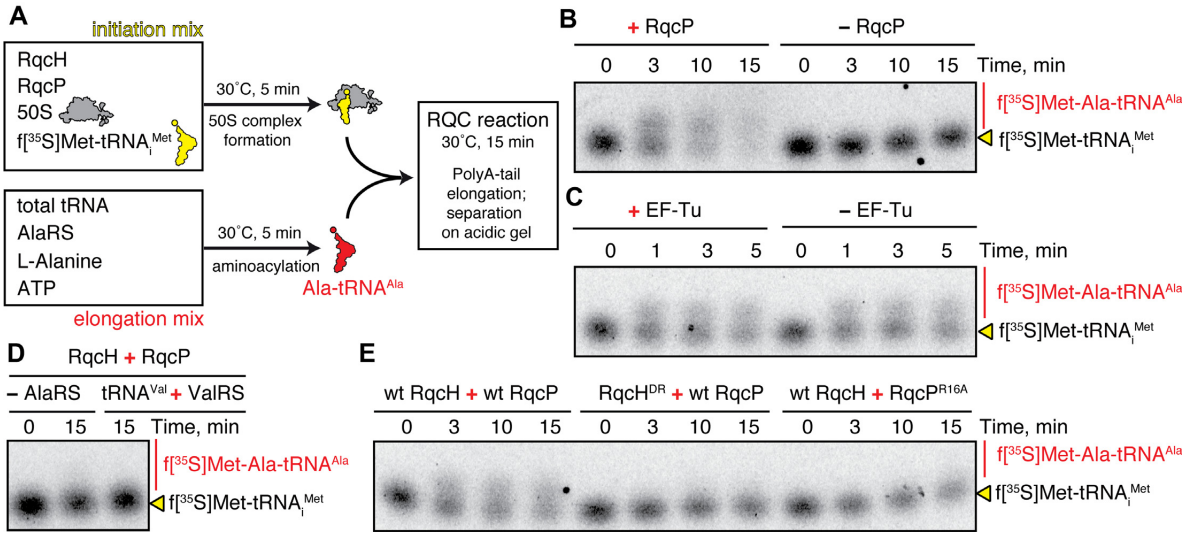

Figure 7. RqcP is a processivity factor essential for poly-Ala synthesis in a biochemically reconstituted RQC system. (**A**) Schematics of the experimental setup. Separate initiation and elongation mixtures were prepared in HEPES:Polymix buffer (7.5 Mg^{2+} pH 7.0) and incubated at 30°C for 5 min before combining. After an additional 15 minute-long incubation, tRNA species were resolved in a bis-tris gel and visualised by phosphoimaging. (**B**) Formation of Ala-$tRNA^{Ala}$ in the reconstituted RQC system is abrogated upon omission of RqcP. (**C**) Addition of canonical translation elongation factor EF-Tu and 1 mM GTP does not affect the efficiency of Ala-$tRNA^{Ala}$ synthesis. (**D**) No poly-Ala synthesis is observed either upon omission of AlaRS or in the presence of $tRNA^{Val}$, Valyl-tRNA synthetase (ValRS) and L-valine. (**E**) Neither $RqcH^{DR}$ nor $RqcP^{R16A}$ support Ala-$tRNA^{Ala}$ formation in the reconstituted RQC system.

tent with the polyalanine tailing of the fMet (Figure 7B), thus directly demonstrating the role of RqcP as an essential processivity factor for RQC elongation. No effect of the efficiency of poly-Ala synthesis was observed in the RQC reaction that was additionally supplemented with canonical translation elongation factor EF-Tu and 1 mM GTP (Figure 7C), suggesting that EF-Tu does not play a role in delivery of Ala-tRNA to the 50S subunit and that tailing proceeds independently of GTP. Moreover, no polyalanine tailing was observed when the aminoacylation mix was replaced with the presence of $tRNA^{Val}$, valyl-tRNA synthetase (ValRS), ATP and L-valine (Figure 7D), which is consistent with the strong preference of RqcH for $tRNA^{Ala}$. Similarly, no activity was detected when AlaRS was omitted (Figure 7D). Finally, our reconstituted RQC system faithfully reproduces the effects of loss-of-function substitutions in RqcH ($RqcH^{DR}$ variant compromised in $tRNA^{Ala}$ selection) and RqcP ($RqcP^{R16A}$ variant compromised in interaction with the H69 rRNA element), since no poly-alanine tailing was observed when replacing the wild-type RqcH and RqcP with these variants (Figure 7E). Collectively, our biochemical results establish that the combination of RQC factors RqcP and RqcH is both necessary and sufficient to drive polyalanine synthesis on isolated 50S subunits in the absence of canonical translation elongation factors.

CONCLUSIONS AND PERSPECTIVE

This study supports the proposed molecular mechanism of C-terminal alanine tailing mediated by the concerted action of RqcH and RqcP (Figure 1D) (42). Importantly, it also opens up several research directions for follow-up investigations. What is the significance of $tRNA^{Lys}$ enrichment in 50S RQC complexes compromised in RQC elongation due to the DR substitution in the NFACT-N domain of RqcH or loss of RqcP? It is tempting to speculate that $tRNA^{Lys}$ is enriched in these complexes due to ribosomal stalling on lysine residues triggering RQC. Indeed, a recent analysis of ribosome profiling data suggests that the presence of P-site Lys residues encoded by AAA codons are associated with a moderate slowing down of translation elongation in *E. coli* (71). However, no Lys-associated ribosomal stalling signal was detected in a *B. subtilis* study using 5Pseq (72). Therefore, while tempting, this hypothesis requires further investigation. Second is the question of a potential C-terminal-tailing processivity factor in eukaryotic RQC. Here we directly demonstrate *in vitro* that S4 homologue Hsp15-family protein RqcP is, indeed, essential to drive the poly-alanine tailing by 50S-associated RqcH/Rqc2/NEMF in a minimal bacterial system. This indicates that an analogous yet-to-be-discovered factor could be also cooperating with Rqc2/NEMF in archaea and eukaryotes. Additionally, the establishment of a reconstituted bacterial RQC system provides researchers with a powerful tool for activity-driven discovery of additional bacterial RQC factors, either by directly testing candidate factors identified through structural and genetic studies or through fractionation of cellular lysates. Currently, it is unclear which cellular factors split the stalled 70S ribosomes to generate the 50S RQC substrate and which factors terminate the RQC-mediated poly-alanine addition to release the tagged polypeptide. Our genetic experiments suggest that ribosome-splitting factor HflX (73) is not essential for RQC in live cells since we detect no synthetic growth defect upon the simultaneous deletion of *hflX* and *ssrA* (Supplementary Figure S8). A fully reconstituted biochemical RQC system could be instrumental for deconvoluting the redundancies and overlapping functions of the factors involved. Finally,

an analogous eukaryotic RQC system could be established using 60S ribosomal subunits, Rqc2/NEMF and aminoacylated tRNAs to enable activity-driven discovery of additional RQC factors.

DATA AVAILABILITY

The cryo-EM map of the RqcH^{DR}-50S complex and the associated molecular model have been deposited in the Protein Data Bank and Electron Microscopy Data Bank with the accession codes EMPIAR-10726, EMD-13017 and PDB-7OPE, respectively. The tRNA microarray data have been deposited in Gene Expression Omnibus (GEO) database under the accession number GSE174254.

SUPPLEMENTARY DATA

Supplementary Data are available at NAR Online.

ACKNOWLEDGEMENTS

We thank Michael Hall for help with cryo-EM data collection, Marcus J.O. Johansson for help with tRNA northern blotting assays, and Fujio Kawamura for providing anti-L3 primary antibodies. The electron microscopy data was collected at the Umeå Core Facility for Electron Microscopy, a node of the Cryo-EM Swedish National Facility, funded by the Knut and Alice Wallenberg, Family Erling Persson and Kempe Foundations, SciLifeLab, Stockholm University and Umeå University.

FUNDING

Swedish Research Council (Vetenskapsrådet) grants [2017-03783 to V.H and 2019-01085 to G.C.A.]; Deutsche Forschungsgemeinschaft [WI3285/8-1 to D.N.W.]; Ragnar Söderbergs Stiftelse (to V.H.); Umeå Centre for Microbial Research, UCMR (to H.T.); European Union from the European Regional Development Fund through the Centre of Excellence in Molecular Cell Engineering [2014-2020.4.01.15-0013 to V.H.]; EU Horizon 2020 program (Marie Skłodowska-Curie) [764591 to Z.I.]; Estonian Research Council [PRG335 to V.H.]; G.C.A. and V.H. groups were supported by a project grant from the Knut and Alice Wallenberg Foundation [2020-0037 to G.C.A.]; D.N.W. and V.H. groups were supported by the Deutsche Zentrum für Luft- und Raumfahrt [DLR01KI1820 to D.N.W.]; Swedish Research Council [2018-00956 to V.H.] within the RIBOTARGET consortium under the framework of JPIAMR. Funding for open access charge: Swedish Research Council (Vetenskapsrådet) [2017-03783 to V.H.].
Conflict of interest statement. None declared.

REFERENCES

1. Keiler,K.C. and Feaga,H.A. (2014) Resolving nonstop translation complexes is a matter of life or death. *J. Bacteriol.*, **196**, 2123–2130.
2. Müller,C., Crowe-McAuliffe,C. and Wilson,D.N. (2021) Ribosome rescue pathways in bacteria. *Front. Microbiol.*, **12**, 652980.
3. Sitron,C.S. and Brandman,O. (2020) Detection and degradation of stalled nascent chains via ribosome-associated quality control. *Annu. Rev. Biochem.*, **89**, 417–442.
4. Yip,M.C.J. and Shao,S. (2021) Detecting and rescuing stalled ribosomes. *Trends Biochem. Sci.*, https://doi.org/10.1016/j.tibs.2021.03.008.
5. Keiler,K.C., Waller,P.R. and Sauer,R.T. (1996) Role of a peptide tagging system in degradation of proteins synthesized from damaged messenger RNA. *Science*, **271**, 990–993.
6. Tu,G.F., Reid,G.E., Zhang,J.G., Moritz,R.L. and Simpson,R.J. (1995) C-terminal extension of truncated recombinant proteins in *Escherichia coli* with a 10Sa RNA decapeptide. *J. Biol. Chem.*, **270**, 9322–9326.
7. Komine,Y., Kitabatake,M., Yokogawa,T., Nishikawa,K. and Inokuchi,H. (1994) A tRNA-like structure is present in 10Sa RNA, a small stable RNA from *Escherichia coli*. *Proc. Natl. Acad. Sci. U.S.A.*, **91**, 9223–9227.
8. Karzai,A.W., Susskind,M.M. and Sauer,R.T. (1999) SmpB, a unique RNA-binding protein essential for the peptide-tagging activity of SsrA (tmRNA). *EMBO J.*, **18**, 3793–3799.
9. Gottesman,S., Roche,E., Zhou,Y. and Sauer,R.T. (1998) The ClpXP and ClpAP proteases degrade proteins with carboxy-terminal peptide tails added by the SsrA-tagging system. *Genes Dev.*, **12**, 1338–1347.
10. Chadani,Y., Ito,K., Kutsukake,K. and Abo,T. (2012) ArfA recruits release factor 2 to rescue stalled ribosomes by peptidyl-tRNA hydrolysis in *Escherichia coli*. *Mol. Microbiol.*, **86**, 37–50.
11. Chadani,Y., Ono,K., Kutsukake,K. and Abo,T. (2011) *Escherichia coli* YaeJ protein mediates a novel ribosome-rescue pathway distinct from SsrA- and ArfA-mediated pathways. *Mol. Microbiol.*, **80**, 772–785.
12. Gueneau de Novoa,P. and Williams,K.P. (2004) The tmRNA website: reductive evolution of tmRNA in plastids and other endosymbionts. *Nucleic Acids Res.*, **32**, D104–D108.
13. Keiler,K.C., Shapiro,L. and Williams,K.P. (2000) tmRNAs that encode proteolysis-inducing tags are found in all known bacterial genomes: A two-piece tmRNA functions in *Caulobacter*. *Proc. Natl. Acad. Sci. U.S.A.*, **97**, 7778–7783.
14. Burroughs,A.M. and Aravind,L. (2019) The origin and evolution of release factors: Implications for translation termination, ribosome rescue, and quality control pathways. *Int. J. Mol. Sci.*, **20**, 1981.
15. Goralski,T.D.P., Kirimanjeswara,G.S. and Keiler,K.C. (2018) A new mechanism for ribosome rescue can recruit RF1 or RF2 to nonstop ribosomes. *mBio*, **9**, e02436-18.
16. Shimokawa-Chiba,N., Müller,C., Fujiwara,K., Beckert,B., Ito,K., Wilson,D.N. and Chiba,S. (2019) Release factor-dependent ribosome rescue by BrfA in the Gram-positive bacterium *Bacillus subtilis*. *Nat. Commun.*, **10**, 5397.
17. Joazeiro,C.A.P. (2019) Mechanisms and functions of ribosome-associated protein quality control. *Nat. Rev. Mol. Cell Biol.*, **20**, 368–383.
18. Inada,T. (2020) Quality controls induced by aberrant translation. *Nucleic Acids Res.*, **48**, 1084–1096.
19. Brandman,O., Stewart-Ornstein,J., Wong,D., Larson,A., Williams,C.C., Li,G.W., Zhou,S., King,D., Shen,P.S., Weibezahn,J. *et al.* (2012) A ribosome-bound quality control complex triggers degradation of nascent peptides and signals translation stress. *Cell*, **151**, 1042–1054.
20. Defenouillere,Q., Yao,Y., Mouaikel,J., Namane,A., Galopier,A., Decourty,L., Doyen,A., Malabat,C., Saveanu,C., Jacquier,A. *et al.* (2013) Cdc48-associated complex bound to 60S particles is required for the clearance of aberrant translation products. *Proc. Natl. Acad. Sci. U.S.A.*, **110**, 5046–5051.
21. Kuroha,K., Zinoviev,A., Hellen,C.U.T. and Pestova,T.V. (2018) Release of ubiquitinated and Non-ubiquitinated nascent chains from stalled mammalian ribosomal complexes by ANKZF1 and Ptrh1. *Mol. Cell*, **72**, 286–302.
22. Pisareva,V.P., Skabkin,M.A., Hellen,C.U., Pestova,T.V. and Pisarev,A.V. (2011) Dissociation by Pelota, Hbs1 and ABCE1 of mammalian vacant 80S ribosomes and stalled elongation complexes. *EMBO J.*, **30**, 1804–1817.
23. Shao,S., von der Malsburg,K. and Hegde,R.S. (2013) Listerin-dependent nascent protein ubiquitination relies on ribosome subunit dissociation. *Mol. Cell*, **50**, 637–648.
24. Shoemaker,C.J. and Green,R. (2011) Kinetic analysis reveals the ordered coupling of translation termination and ribosome recycling in yeast. *Proc. Natl. Acad. Sci. U.S.A.*, **108**, E1392–E1398.

25. Tsuboi,T., Kuroha,K., Kudo,K., Makino,S., Inoue,E., Kashima,I. and Inada,T. (2012) Dom34:Hbs1 plays a general role in quality-control systems by dissociation of a stalled ribosome at the 3′ end of aberrant mRNA. *Mol. Cell*, **46**, 518–529.
26. Hashimoto,S., Sugiyama,T., Yamazaki,R., Nobuta,R. and Inada,T. (2020) Identification of a novel trigger complex that facilitates ribosome-associated quality control in mammalian cells. *Sci. Rep.*, **10**, 3422.
27. Juszkiewicz,S., Speldewinde,S.H., Wan,L., Svejstrup,J.Q. and Hegde,R.S. (2020) The ASC-1 complex disassembles collided ribosomes. *Mol. Cell*, **79**, 603–614.
28. Shen,P.S., Park,J., Qin,Y., Li,X., Parsawar,K., Larson,M.H., Cox,J., Cheng,Y., Lambowitz,A.M., Weissman,J.S. *et al.* (2015) Rqc2p and 60S ribosomal subunits mediate mRNA-independent elongation of nascent chains. *Science*, **347**, 75–78.
29. Kostova,K.K., Hickey,K.L., Osuna,B.A., Hussmann,J.A., Frost,A., Weinberg,D.E. and Weissman,J.S. (2017) CAT-tailing as a fail-safe mechanism for efficient degradation of stalled nascent polypeptides. *Science*, **357**, 414–417.
30. Yonashiro,R., Tahara,E.B., Bengtson,M.H., Khokhrina,M., Lorenz,H., Chen,K.C., Kigoshi-Tansho,Y., Savas,J.N., Yates,J.R., Kay,S.A. *et al.* (2016) The Rqc2/Tae2 subunit of the ribosome-associated quality control (RQC) complex marks ribosome-stalled nascent polypeptide chains for aggregation. *eLife*, **5**, e11794.
31. Defenouillere,Q., Zhang,E., Namane,A., Mouaikel,J., Jacquier,A. and Fromont-Racine,M. (2016) Rqc1 and Ltn1 prevent C-terminal Alanine-Threonine tail (CAT-tail)-induced protein aggregation by efficient recruitment of Cdc48 on stalled 60S subunits. *J. Biol. Chem.*, **291**, 12245–12253.
32. Sitron,C.S. and Brandman,O. (2019) CAT tails drive degradation of stalled polypeptides on and off the ribosome. *Nat. Struct. Mol. Biol.*, **26**, 450–459.
33. Thrun,A., Garzia,A., Kigoshi-Tansho,Y., Patil,P.R., Umbaugh,C.S., Dallinger,T., Liu,J., Kreger,S., Patrizi,A., Cox,G.A. *et al.* (2021) Convergence of mammalian RQC and C-end rule proteolytic pathways via alanine tailing. *Mol. Cell*, **81**, 2112–2122.
34. Udagawa,T., Seki,M., Okuyama,T., Adachi,S., Natsume,T., Noguchi,T., Matsuzawa,A. and Inada,T. (2021) Failure to degrade CAT-Tailed proteins disrupts neuronal morphogenesis and cell survival. *Cell Rep.*, **34**, 108599.
35. Li,S., Wu,Z., Tantray,I., Li,Y., Chen,S., Dong,J., Glynn,S., Vogel,H., Snyder,M. and Lu,B. (2020) Quality-control mechanisms targeting translationally stalled and C-terminally extended poly(GR) associated with ALS/FTD. *Proc. Natl. Acad. Sci. U.S.A.*, **117**, 25104–25115.
36. Burroughs,A.M. and Aravind,L. (2014) A highly conserved family of domains related to the DNA-glycosylase fold helps predict multiple novel pathways for RNA modifications. *RNA Biol.*, **11**, 360–372.
37. Singh,K.V., La Rosa,S.L., Somarajan,S.R., Roh,J.H. and Murray,B.E. (2015) The fibronectin-binding protein EfbA contributes to pathogenesis and protects against infective endocarditis caused by *Enterococcus faecalis*. *Infect. Immun.*, **83**, 4487–4494.
38. Dramsi,S., Bourdichon,F., Cabanes,D., Lecuit,M., Fsihi,H. and Cossart,P. (2004) FbpA, a novel multifunctional *Listeria monocytogenes* virulence factor. *Mol. Microbiol.*, **53**, 639–649.
39. Osanai,A., Li,S.J., Asano,K., Sashinami,H., Hu,D.L. and Nakane,A. (2013) Fibronectin-binding protein, FbpA, is the adhesin responsible for pathogenesis of *Listeria monocytogenes* infection. *Microbiol. Immunol.*, **57**, 253–262.
40. Pracht,D., Elm,C., Gerber,J., Bergmann,S., Rohde,M., Seiler,M., Kim,K.S., Jenkinson,H.F., Nau,R. and Hammerschmidt,S. (2005) PavA of *Streptococcus pneumoniae* modulates adherence, invasion, and meningeal inflammation. *Infect. Immun.*, **73**, 2680–2689.
41. Lytvynenko,I., Paternoga,H., Thrun,A., Balke,A., Muller,T.A., Chiang,C.H., Nagler,K., Tsaprailis,G., Anders,S., Bischofs,I. *et al.* (2019) Alanine tails signal proteolysis in bacterial ribosome-associated quality control. *Cell*, **178**, 76–90.
42. Crowe-McAuliffe,C., Takada,H., Murina,V., Polte,C., Kasvandik,S., Tenson,T., Ignatova,Z., Atkinson,G.C., Wilson,D.N. and Hauryliuk,V. (2021) Structural basis for bacterial ribosome-associated quality control by RqcH and RqcP. *Mol. Cell*, **81**, 115–126.
43. Shao,S., Brown,A., Santhanam,B. and Hegde,R.S. (2015) Structure and assembly pathway of the ribosome quality control complex. *Mol. Cell*, **57**, 433–444.
44. Filbeck,S., Cerullo,F., Paternoga,H., Tsaprailis,G., Joazeiro,C.A.P. and Pfeffer,S. (2021) Mimicry of canonical translation elongation underlies alanine tail synthesis in RQC. *Mol. Cell*, **81**, 104–114.
45. Katoh,K. and Standley,D.M. (2013) MAFFT multiple sequence alignment software version 7: improvements in performance and usability. *Mol. Biol. Evol.*, **30**, 772–780.
46. Waterhouse,A.M., Procter,J.B., Martin,D.M., Clamp,M. and Barton,G.J. (2009) Jalview Version 2–a multiple sequence alignment editor and analysis workbench. *Bioinformatics*, **25**, 1189–1191.
47. Takada,H., Roghanian,M., Murina,V., Dzhygyr,I., Murayama,R., Akanuma,G., Atkinson,G.C., Garcia-Pino,A. and Hauryliuk,V. (2020) The C-Terminal RRM/ACT domain is crucial for Fine-Tuning the activation of 'Long' RelA-SpoT homolog enzymes by ribosomal complexes. *Front. Microbiol.*, **11**, 277.
48. Candiano,G., Bruschi,M., Musante,L., Santucci,L., Ghiggeri,G.M., Carnemolla,B., Orecchia,P., Zardi,L. and Righetti,P.G. (2004) Blue silver: a very sensitive colloidal Coomassie G-250 staining for proteome analysis. *Electrophoresis*, **25**, 1327–1333.
49. Zivanov,J., Nakane,T., Forsberg,B.O., Kimanius,D., Hagen,W.J., Lindahl,E. and Scheres,S.H. (2018) New tools for automated high-resolution cryo-EM structure determination in RELION-3. *eLife*, **7**, e42166.
50. Zheng,S.Q., Palovcak,E., Armache,J.-P., Verba,K.A., Cheng,Y. and Agard,D.A. (2017) MotionCor2: anisotropic correction of beam-induced motion for improved cryo-electron microscopy. *Nat. Methods*, **14**, 331–332.
51. Rohou,A. and Grigorieff,N. (2015) CTFFIND4: Fast and accurate defocus estimation from electron micrographs. *J. Struct. Biol.*, **192**, 216–221.
52. Wagner,T., Merino,F., Stabrin,M., Moriya,T., Antoni,C., Apelbaum,A., Hagel,P., Sitsel,O., Raisch,T., Prumbaum,D. *et al.* (2019) SPHIRE-crYOLO is a fast and accurate fully automated particle picker for cryo-EM. *Commun. Biol.*, **2**, 218.
53. Scheres,S.H.W. (2012) RELION: Implementation of a Bayesian approach to cryo-EM structure determination. *J. Struct. Biol.*, **180**, 519–530.
54. Bai,X., Rajendra,E., Yang,G., Shi,Y. and Scheres,S.H. (2015) Sampling the conformational space of the catalytic subunit of human γ-secretase. *eLife*, **4**, e11182.
55. Scheres,S.H. and Chen,S. (2012) Prevention of overfitting in cryo-EM structure determination. *Nat. Methods*, **9**, 853–854.
56. Kucukelbir,A., Sigworth,F.J. and Tagare,H.D. (2014) Quantifying the local resolution of cryo-EM density maps. *Nat. Methods*, **11**, 63–65.
57. Pettersen,E.F., Goddard,T.D., Huang,C.C., Meng,E.C., Couch,G.S., Croll,T.I., Morris,J.H. and Ferrin,T.E. (2021) UCSF ChimeraX: Structure visualization for researchers, educators, and developers. *Protein Sci.*, **30**, 70–82.
58. Takada,H., Roghanian,M., Caballero-Montes,J., Van Nerom,K., Jimmy,S., Kudrin,P., Trebini,F., Murayama,R., Akanuma,G., Garcia-Pino,A. *et al.* (2021) Ribosome association primes the stringent factor Rel for tRNA-dependent locking in the A-site and activation of (p)ppGpp synthesis. *Nucleic Acids Res.*, **49**, 444–457.
59. Schneider,C.A., Rasband,W.S. and Eliceiri,K.W. (2012) NIH Image to ImageJ: 25 years of image analysis. *Nat. Methods*, **9**, 671–675.
60. Sebaugh,J.L. (2011) Guidelines for accurate EC_{50}/IC_{50} estimation. *Pharm. Stat.*, **10**, 128–134.
61. Polte,C., Wedemeyer,D., Oliver,K.E., Wagner,J., Bijvelds,M.J.C., Mahoney,J., de Jonge,H.R., Sorscher,E.J. and Ignatova,Z. (2019) Assessing cell-specific effects of genetic variations using tRNA microarrays. *BMC Genomics*, **20**, 549.
62. Shi,H. and Moore,P.B. (2000) The crystal structure of yeast phenylalanine tRNA at 1.93 Å resolution: a classic structure revisited. *RNA*, **6**, 1091–1105.
63. Harms,J.M., Wilson,D.N., Schluenzen,F., Connell,S.R., Stachelhaus,T., Zaborowska,Z., Spahn,C.M. and Fucini,P. (2008) Translational regulation via L11: molecular switches on the ribosome turned on and off by thiostrepton and micrococcin. *Mol. Cell*, **30**, 26–38.
64. Britton,R.A., Eichenberger,P., Gonzalez-Pastor,J.E., Fawcett,P., Monson,R., Losick,R. and Grossman,A.D. (2002) Genome-wide

analysis of the stationary-phase sigma factor (sigma-H) regulon of *Bacillus subtilis*. *J. Bacteriol.*, **184**, 4881–4890.
65. Pestka,S. (1972) Peptidyl-puromycin synthesis on polyribosomes from *Escherichia coli*. *Proc. Natl. Acad. Sci. U.S.A.*, **69**, 624–628.
66. Shimizu,Y., Kuruma,Y., Kanamori,T. and Ueda,T. (2014) The PURE system for protein production. *Methods Mol. Biol.*, **1118**, 275–284.
67. Shimizu,Y., Inoue,A., Tomari,Y., Suzuki,T., Yokogawa,T., Nishikawa,K. and Ueda,T. (2001) Cell-free translation reconstituted with purified components. *Nat. Biotechnol.*, **19**, 751–755.
68. Shetty,S., Shah,R.A., Chembazhi,U.V., Sah,S. and Varshney,U. (2017) Two highly conserved features of bacterial initiator tRNAs license them to pass through distinct checkpoints in translation initiation. *Nucleic Acids Res.*, **45**, 2040–2050.
69. Konevega,A.L., Soboleva,N.G., Makhno,V.I., Semenkov,Y.P., Wintermeyer,W., Rodnina,M.V. and Katunin,V.I. (2004) Purine bases at position 37 of tRNA stabilize codon-anticodon interaction in the ribosomal A site by stacking and Mg^{2+}-dependent interactions. *RNA*, **10**, 90–101.
70. Wohlgemuth,I., Beringer,M. and Rodnina,M.V. (2006) Rapid peptide bond formation on isolated 50S ribosomal subunits. *EMBO Rep.*, **7**, 699–703.
71. Pavlov,M.Y., Ullman,G., Ignatova,Z. and Ehrenberg,M. (2021) Estimation of peptide elongation times from ribosome profiling spectra. *Nucleic Acids Res.*, **49**, 5124–5142.
72. Huch,S., Nersisyan,L., Ropat,M., Barret,D., Wang,J., HuertaCepas,J., Wei,W., Steinmetz,L.M., Engstrand,L. and Pelechano,V. (2021) RNA degradation analysis reveals ribosome dynamics in complex microbiome samples. bioRxiv doi: https://doi.org/10.1101/2021.04.08.439066, 10 April 2021, preprint: not peer reviewed.
73. Zhang,Y., Mandava,C.S., Cao,W., Li,X., Zhang,D., Li,N., Zhang,Y., Zhang,X., Qin,Y., Mi,K. *et al.* (2015) HflX is a ribosome-splitting factor rescuing stalled ribosomes under stress conditions. *Nat. Struct. Mol. Biol.*, **22**, 906–913.
74. Tereshchenkov,A.G., Dobosz-Bartoszek,M., Osterman,I.A., Marks,J., Sergeeva,V.A., Kasatsky,P., Komarova,E.S., Stavrianidi,A.N., Rodin,I.A., Konevega,A.L. *et al.* (2018) Binding and action of amino acid analogs of chloramphenicol upon the bacterial ribosome. *J. Mol. Biol.*, **430**, 842–852.

6 Discussion

6.1 Overview

This work has addressed structural aspects of two groups of ARE-ABCFs (Sections 5.1, 5.2, 5.3) and the bacterial RQC system mediated by RqcH (Section 5.4). The ABCF proteins were found to bind in the E-site of the ribosome, as expected from the structure of EttA, the closest structurally-characterised homologue of these proteins (Chen et al., 2014). Major questions about the action of ARE-ABCFs prior to these studies were how a tRNA bound in the P-site would accommodate an extended interdomain linker reaching into the core of the LSU, and how the interdomain linker might mediate antibiotic resistance (Wilson, 2016). For bacterial RQC, relatively little was known about this process and so an exploratory approach was adopted. Previously, a low-resolution study of the yeast NEMF-family protein was the only available structural information about the RQC process in any kingdom (Shen et al., 2015), and the question of how the alternative elongation cycle proceeds without the SSU or mRNA, was the major question to be addressed.

6.2 Single-particle cryo-EM as a tool to understand translation

In current implementations, single-particle cryo-EM can be used to analyse snapshots of translation and translation-associated processes. The states to be analysed can be captured with the use of mutants (e.g. EQ_2 variants of ABCF proteins that cannot hydrolyse ATP), antibiotics or other small molecules (e.g. translocation inhibitors), or using rapid grid freezing after reaction mixing (i.e. time-resolved cryo-EM, as used to analyse translocation and termination).

Each particle used for reconstruction is noisy and classification of the particles into discrete states is an arbitrary process—especially in cases of continuous movements not defined by intermediates with strong free-energy minima. Machine-learning-driven advances in particle classification (Zhong et al., 2021; Chen and Ludtke, 2021), as well as advances in cryo-TEM to improve the signal-to-noise ratio of individual particles (Nakane et al., 2020; Yip et al., 2020), can be expected to enhance our ability to sort individual particles into finer and finer sub-states.

Although often not explicitly stated, these methods ultimately allow us to interpret a biological process as a 'movie' created by interpolating the observed snapshots, and then usually using a machine metaphor to rationalise how movements of a molecule relate to a biological process. There are fundamental limitations with this approach, in particular with relying heavily on the metaphor of a machine to describe biological processes operating under unfamiliar and sometimes counter-intuitive physical conditions (Moore, 2012; Spirin, 2002). Consequently, integrating information from biochemistry and orthogonal techniques such as smFRET is an essential complement to cryo-EM.

Although powerful, current implementations of time-resolved cryo-EM are rather crude, often involving slow reactions with manual grid making or only a single time-point that captures multiple states. This limitation is particularly important as many biological reactions are reversible. These studies therefore suffer from the fundamental limitation common to other classification-based approaches to cryo-EM in that substantial outside deduction is required to determine the order of observed states. This process may be as simple as seeing how similar individual states are to known trapped intermediates (e.g. for bacterial initiation and translocation) or using our knowledge of the fundamentals of translation (e.g. in the case of RqcH). The promise of using a series of data collections of grids prepared at different time points to distinguish between early and late states of a reaction remains rarely utilised (Fu et al., 2019).

6.3 ABCF proteins as antibiotic resistance elements

Five structures of ARE-ABCF proteins in complex with ribosomes have been presented in this work: VmlR, in complex with the *B. subtilis* ribosome (Section 5.1); LsaA, in complex with the *E. faecalis* ribosome (Section 5.2); VgaA_{LC}, in complex with the *S. aureus* ribosome (Section 5.2); VgaL (formerly Lmo0919), in complex with the *L. monocytogenes* ribosome (Section 5.2); and PoxtA, in complex with the *E. faecalis* ribosome (Section 5.3). Four of these ARE-ABCFs confer resistance to PLS_{A} antibiotics, while the fifth, PoxtA, confers resistance to phenicols and oxazolidinones. All complexes were formed utilising an EQ_2-variant ARE-ABCF, which can bind but not hydrolyse ATP. With the exception of the VmlR complex, which was reconstituted from purified components, complexes were formed by an *ex vivo* immunoprecipitation approach in the absence of relevant antibiotic. Single-particle cryo-EM was used to reconstruct structures of each complex.

As expected by analogy to the structure of EttA bound to a 70S ribosome (Chen et al., 2014), each ARE-ABCF bound in the E-site of the ribosome, with the interdomain linker extending towards the PTC. The P-tRNA was distorted to varying degrees, with ARE-ABCFs with medium-to-long interdomain linkers (i.e. VmlR, LsaA, VgaA_{LC}, and VgaL, those that confer resistance to PLS_{A} antibiotics) triggering a highly distorted conformation in which the CCA $3'$ end of tRNA was flexible, allowing the interdomain linker to bind in the PTC. By contrast, the interdomain linker of PoxtA caused a much milder distortion of the P-tRNA, leading to a modest retraction of the CCA $3'$ end from the PTC.

6.3.1 ARE-ABCF mechanism of action

Two main competing hypotheses could explain the mechanism of antibiotic resistance conferred by ARE-ABCFs. In the first, direct steric overlap between the factor and the bound antibiotic leads to a competition between the two for binding. In the second, the ARE-ABCF induces a conformational change in the ribosome that is refractory to antibiotic binding.

In the VmlR, LsaA, VgaA_{LC}, and VgaL structures, the interdomain linker extended towards the antibiotic binding site, in some cases overlapping with the antibiotics (VmlR, LsaA, and in some instances VgaA_{LC}) and in other cases not (VgaL and VgaA_{LC} for some antibiotics; Sections 5.1, 5.2). For VmlR, LsaA, VgaA_{LC}, mutagenesis of the overlapping amino acid of the interdomain linker to alanine, which was predicted to abolish the overlap, did not affect the antibiotic resistance activity of the ARE-ABCF *in vivo*.[2] This strongly implies the that mode of action for these ARE-ABCFs is indirect i.e. does not require direct interaction or overlap between the ARE-ABCF and antibiotic. A variety of distortions around the PTC was observed, making it difficult to form a general model of action for this class of proteins. Nonetheless, modulation of the 23S rRNA around nucleotide A2451 was common among all examined structures.

In the case of PoxtA, the interdomain linker is positioned far from the antibiotic binding site, precluding a direct steric mechanism of antibiotic resistance (Section 5.3). By integrating knowledge about how oxazolidinone and phenicol antibiotics bind and stall elongating ribosomes (Marks et al., 2016; Syroegin et al., 2021; Tsai et al., 2021), an indirect model involving pulling of the nascent peptide chain was proposed. In summary, the structures presented in this thesis all reveal ARE-ABCFs bound in the ribosomal E-site with variable interdomain linkers reaching towards (but often not directly contacting) the site of antibiotic binding, and triggering a distorted P-tRNA conformation in the process. In combination with mutagenesis experiments, these structures favour an indirect model of ARE-ABCF function with respect to antibiotic binding.

[2] An exception is the Phe237A variant of VmlR, which fails to confer resistance to virginiamycin M while retaining activity against the other tested antibiotics.

It is not clear why ARE-ABCFs seem to favour an indirect mechanism. One possibility is that too much direct overlap between the ARE-ABCF and antibiotic leads to competition for ribosome binding between the two, which may favour the antibiotic in some circumstances.

6.3.2 Comparison with the contemporaneous study of MsrE by Su *et al.*

During the preparation of the manuscript describing the VmlR–70S structure (Section 5.1), Su et al. (2018) reported the structure of the ARE-ABCF MsrE in complex with the 70S ribosome from *T. thermophilus*. The non-hydrolysable ATP analogue ADPNP was used to form a stable complex between MsrE and the 70S ribosome. MsrE confers resistance to macrolides, ketolides, and streptogramin Bs, and thus has a different antibiotic specificity compared to the ARE-ABCFs analysed in this thesis. Broadly, the structure of the MsrE–70S complex is in agreement with the structures presented here, with the tip of the interdomain linker overlapping slightly with the antibiotic binding site.

Su et al. (2018) predicted overlap between MsrE L242, situated at the tip of the interdomain linker, and the azithromycin binding site. Mutation of L242 to alanine mostly, but not completely, abolished the antibiotic resistance phenotype of MsrE. Additionally, mutation of the nearby residues R241 and H244—which do not overlap with the azithromycin binding site, instead interacting with the rRNA—similarly severely reduced the antibiotic resistance phenotype of MsrE. A double mutant of R241A and L242A abolished antibiotic resistance. In summary, some evidence for both a direct overlap/steric exclusion mechanism and an indirect mechanism, in which the antibiotic binding site is modulated, were presented by Su et al. (2018).

Comparison of the cryo-EM map deposited by Su et al. (2018) (EMD-6934) with other ribosomal structures indicates that the voxel size of this map is approximately 5% too large. This error is carried over to the resulting molecular model (PDB 5ZLU), likely accounting for why some rendering softwares do not detect secondary structure in some clearly helical elements. This presents challenges when interpreting the MsrE–70S structure in comparison to other models. However, as the antibiotic binding sites of interest are close to the centre of mass of the ribosome, inaccuracies in alignment stemming from this error are unlikely to substantially change interpretation of the overlap between MsrE and PLS_A, macrolide, ketolide, and streptogramin B antibiotics.

6.3.3 Identity of the translating ribosome complex bound by ARE-ABCFs

Antibiotics can inhibit translation at various stages. Toeprinting and ribosome profiling experiments indicate that PLS_As inhibit initiation, while macrolides, streptogramin Bs, phenicols, and oxazolidinones inhibit elongation (Orelle et al., 2013; Marks et al., 2016). ARE-ABCFs that confer resistance to different classes of antibiotics therefore must act on ribosomes at different stages of translation: initiation complexes for PLS_A resistance proteins, and elongation complexes stalled at specific motifs for other ARE-ABCFs.

In the work presented here, VmlR was complexed with $ErmD_L$-stalled elongating ribosomes, which are different to the expected natural substrate of 70S ribosomes stalled after initiation, with fMet-tRNA in the P-site (Section 5.1). The short nascent chain was not observed in the VmlR-bound state, which could be expected due to the high flexibility at the tRNA 3′ end. In the class of ribosomal particles without bound VmlR density corresponding to the nascent chain was observed, albeit weakly. The density is especially weak in comparison to a similar complex that has been recently reported (Beckert et al., 2021), and hydrolysis of the short nascent chain during sample preparation, allowing VmlR to bind 70S complexes with no nascent chain, therefore cannot be excluded.

Other ARE-ABCF complexes were prepared by *ex vivo* immunoprecipitation, and each consisted of an ARE-ABCF bound to an initiation complex (Sections 5.2, 5.3). For LsaA, $VgaA_{LC}$, and VgaL, such a complex represents the native complex bound in the cell. By contrast for PoxtA, a phenicol- and oxazolidinone-resistance protein, the initiation complex does not represent the native substrate (i.e. a stalled elongating ribosome) in the context of antibiosis.

As ARE-ABCFs must require a free E-site for binding, it is likely that, in the absence of antibiotics, only initiation complexes are available for binding by the expressed ARE-ABCF EQ_2 variants, which is fortuitous for LsaA, $VgaA_{LC}$, and VgaL, but unfortunate in the case PoxtA. In the case of MsrE, which confers resistance to macrolides, ketolides, and streptogramin Bs, which are elongation inhibitors, an initiation complex was used for structural analysis. No structure of an ARE-ABCF that acts on stalled elongating ribosomes (e.g. MsrE or PoxtA) in a complex with a nascent chain has been reported. Directly visualising how the nascent chain is modulated downstream of P-tRNA displacement in response to Msr and PoxtA/OptrA binding is therefore a future goal for the field of ARE-ABCF research.

As ribosome-targeting antibiotics inhibit the expression of proteins of interest, it is not trivial to form truly native complexes—i.e. ribosomes stalled with the antibiotic of interest—that can then be bound by an ARE-ABCF *in vivo*. An alternative approach would be biochemical reconstitution of complexes by mixing antibiotic-stalled ribosomes with recombinant ARE-ABCFs of interest. Preparation of the required components is not trivial, however, as structures of the base complexes have only very recently been described (Tsai et al., 2021; Syroegin et al., 2021). Endogenously tagging an ARE-ABCF, dosing cells with antibiotic, and then harvesting complexes by immunoprecipitation in the presence of a non-hydrolysable ATP analogue is another alternative. This approach would rely on the native regulation of the expression of the ARE-ABCF in response to an antibiotic to overcome inhibition of translation and bind the native substrate. However, such an approach is not guaranteed to yield sufficient material and there would be no way to assess whether ribosome complexes prepared by this method were truly stalled by an antibiotic prior to binding by the ARE-ABCF.

6.3.4 Antibiotic specificity of ARE-ABCFs

What properties determine the antibiotic specificity of a given ARE-ABCF? In the case of PLS_A-resistance ABCFs, the lack of resistance to macrolides, ketolides, and streptogramin Bs can be easily rationalised, as the interdomain linker of these proteins does not reach far enough into the LSU to modulate the antibiotic binding site of the antibiotics. Why this group of ARE-ABCFs does not confer resistance to oxazolidinones and phenicols (antibiotics with binding sites that substantially overlap with PLS_A antibiotics) is less clear. Notably, oxazolidinones and phenicols bind and stall elongating ribosomes, and therefore perhaps PLS_A-resistance ABCFs cannot productively bind to elongation complexes *in vivo*.

More difficult to rationalise is the specificity of the Msr ARE-ABCFs, which confer resistance to macrolide, ketolide, and streptogramin B antibiotics. The MsrE interdomain linker, for example, substantially overlaps with the PLS_A binding site (Su et al., 2018). Perhaps MsrE binds only elongation complexes *in vivo*, precluding the rescue of initiating ribosomes stalled by PLS_A antibiotics. Surprisingly, no evidence about whether this class of ARE-ABCFs confer resistance to oxazolidinones and phenicols—antibiotics that stall elongating ribosomes and have a binding site that substantially overlaps with the MsrE interdomain linker—has been presented (Fostier et al., 2021). This may be due to the early initial characterisation of this family, before oxazolidinones were developed, as well as the use of a chloramphenicol-resistance marker for cloning plasmids (Ross et al., 1989). Fully determining the antibiotic-resistance profile of the *Msr* genes is therefore an interesting avenue for future research.

PoxtA, which confers resistance only to oxazolidinones and phenicols, distorts the P-tRNA rather mildly compared to the other classes of ARE-ABCFs. Such a distortion is not predicted to affect binding of PLS_A antibiotics. In the case of macrolides, ketolides, and streptogramin Bs, the modest distortion of the nascent chain predicted to be induced by PoxtA binding may not propagate through to the antibiotic binding site, which is deeper in the nascent peptide exit channel. The degree of spring-like characteristic in the nascent chain is critical for the testing of this last assumption. It therefore could be interesting to solve the structure of a macrolide, ketolide, or streptogramin B-stalled complex in both the presence and absence of PoxtA and compare the conformation of the nascent chains.

6.3.5 State definition in ARE-ABCF studies

Several lines of evidence indicate that ARE-ABCFs–70S complexes described in this thesis represent the post-antibiotic-dissociation state. Firstly, in all complexes except for PoxtA, the conformation of the complex is incompatible with antibiotic binding due to movements of the PTC 23S rRNA (Sections 5.1, 5.2). Attempts to create complexes with both antibiotic and ARE have been unsuccessful (unpublished data). Finally, Su et al. (2018) found that the EQ_2 variant of MsrE can displace azithromycin in an antibiotic binding assay, lending direct biochemical support to this interpretation. The arguments above apply explicitly to the PLS_A-resistance ARE-ABCFs, and this argument has also been extended to PoxtA by analogy.

6.3.6 Role of ATP hydrolysis in ABCF function

To date, all ARE-ABCF–70S structures have been solved with either EQ_2 variants with bound ATP or the wild-type enzyme with a non-hydrolysable ATP analogue (Sections 5.1, 5.2, 5.3, and Su et al. (2018)). Our structural understanding of the role of ATP hydrolysis in the binding cycle of ARE-ABCFs is therefore limited. In a parsimonious model, ATP binding triggers the closed conformation of the ARE-ABCF NBDs and facilitates binding to the ribosome. After ATP hydrolysis, perhaps triggered by an unknown signal, and subsequent product release, the ARE-ABCF leaves the ribosome. However, Su et al. (2018) observed binding of MsrE to *T. thermophilus* ribosomes in the presence of ATP, and Boël et al. (2014) proposed a model in which EttA stably associates with 70S ribosomes in the presence of ADP. Additionally, Arb1 was observed to bind the yeast 60S with NBDs in an open conformation (Su et al., 2019). The relationship between nucleotide binding, hydrolysis, and product release and ARE-ABCF association with the ribosome therefore deserves further scrutiny, especially in the case of proteins such as PoxtA in which the structure does not *eo ipso* inform what stage of the antibiotic-dissociation cycle is observed.

One common feature of all ARE-ABCF structures to date is a poorly-resolved (and therefore likely flexible) linker region between the interdomain linker and NBD2. Opening of the NBDs, triggered for example by nucleotide hydrolysis and product release, may therefore not necessarily cause movement of the interdomain linker on the ribosome. However, models in which ATP hydrolysis drives a thrusting-like movement of the interdomain linker via the positioning of NBD1, perhaps in multiple rounds of turnover per each ribosome-binding event, may also be worth exploring.

6.3.7 Miscellaneous notes about ARE-ABCF proteins

Regulation of AREs through leader peptides has been well described (Ohki et al., 2005; Dar et al., 2016; Koberska et al., 2021). These models generally rely on a ribosome, stalled on the

leader peptide by an antibiotic, disrupting secondary to obscure a transcription termination element, and thus coupled transcription and translation. However, it has recently been argued that transcription and translation are uncoupled in *Bacillus subtilis* (Johnson et al., 2020). Current models of transcriptional regulation (or coupled transcription–translation) therefore require further scrutiny, and regulation at the level of translation, as for example observed in the Erm stallers, may also be considered (Wilson et al., 2016).

It has been reported that heterologous expression of an ARE-ABCF, LmrC, resulted in antibiotic resistance. However, upon further examination this effect was found to be mediated by a cellular stress response to protein expression, rather than the activity of LmrC itself (Dorrian et al., 2011). This example indicates that caution is warranted when interpreting results in *in vivo* overexpression experiments in the context of antibiotic resistance.

6.3.8 Summary and open questions

We now have structural information of six ARE-ABCFs with a range of antibiotic-resistance profiles, bound to the ribosome. Each structure contains either ATPs or ATP mimics in the NBDs, which are in the closed conformation. Evidence favours that this represents the post-antibiotic-release state, and that the mechanism of antibiotic release is indirect, mediated by the modulation of the antibiotic binding site by the ARE-ABCF. These structures represent a rather narrow view of the entire ARE-ABCF ribosome binding cycle. It is not clear that alternative ARE-ABCF–70S states (such as the pre-antibiotic-dissociation state, or post-nucleotide-hydrolysis state) consist of stable intermediates amenable to structural characterisation. Alternative techniques such as fluorescence assays, smFRET, or time-resolved cryo-EM may further contribute to our understanding of ARE-ABCF action.

6.4 Bacterial ribosome-associated quality control

To better understand bacterial RQC, an *ex vivo* immunoprecipitation approach of tagged RqcH was used to prepare samples for analysis by cryo-EM. The resulting reconstructions revealed an LSU with diverse RqcH and tRNA conformations (Section 5.4). The NFACT-N domain of RqcH was observed to make intimate contact with the anticodon of the tRNA in the P-site. Two additional factors, RsfS and the S4-domain protein RqcP, were additionally identified bound to the complex. RsfS had no apparent genetic interaction with the RqcH pathway, while RqcP appears to be a core factor involved in bacterial RQC. A reciprocal immunoprecipitation of tagged RqcP revealed a similar, complementary set of states. In terms of tRNA position, the suite of states observed comprise most stages of typical translation elongation, and were used to propose a model of alanine tailing on the LSU, mediated by RqcH and RqcP in the absence of the SSU or mRNA.

6.4.1 Comparison with the contemporaneous study from Filbeck *et al.*

Structural aspects of bacterial RQC were simultaneously analysed by Filbeck et al. (2021), utilising a similar sample preparation approach. The findings of the two studies are largely complementary, with the binding of RqcH and RqcP common between each structure. One critical state, consisting of tRNAs in both the A- and P- sites, as well as RqcH, was observed by Filbeck et al. (2021) but not in the work presented in this thesis (Section 5.4). Although the exact reason for this difference is unclear, it may be due to differences in sample preparation, as a high level of methanol was added to a sample used by Filbeck et al. (2021). The 3′ end of the A-site tRNA appears to be deacylated in the resulting cryo-EM map, rationalising why such a state might be stable enough for visualisation instead of immediately proceeding to peptidyl transfer.

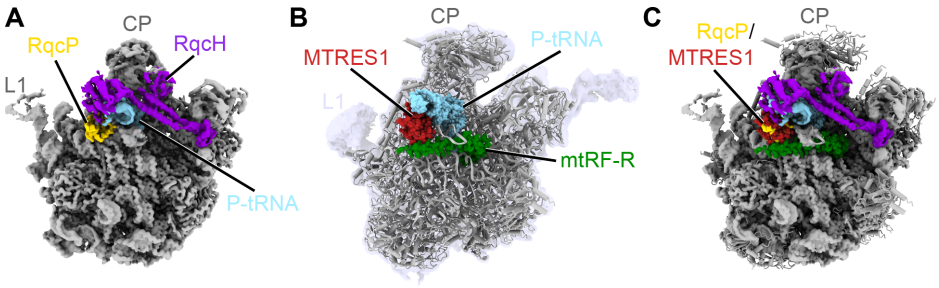

Figure 4: (A) Isosurface rendering of bacterial RQC complex state B viewed from the intersubunit interface (Section 5.4). The LSU is shown in grey, and the P-tRNA (cyan), RqcH (purple) and RqcP (yellow) are indicated. EMBD-11889. (B) Molecular model of a mitoribosome RQC complex reported by Desai et al. (2020) with the P-tRNA (cyan) MTRES1 (red), and mtRF-R (green) indicated, superimposed on an isosurface rendering of the cryo-EM density. Same view as panel A. PDB 7A5H. (C) Superimposition of structures from panels A and B, with position of RqcP (yellow) and MTRES1 (red) indicated. Figure assembled with UCSF ChimeraX (Pettersen et al., 2021).

Importantly, Filbeck et al. (2021) demonstrated involvement of RqcP in the alanine tailing reaction using a reporter construct. Subsequently, we have corroborated this observation with an *in vitro* assay (Section 5.5).

6.4.2 Comparison with the contemporaneous study from Desai *et al.*

Desai et al. (2020) examined RQC in mitochondria by genetically reducing levels of mitochondrial $tRNA^{Lys}$ and then analysing the total ribosomal fraction by cryo-EM. Diverse translational states were observed. One involved a large ribosomal subunit in complex with a peptidyl-tRNA and two additional previously uncharacterised proteins: mtRF-R and MTRES1. mtRF-R is a non-canonical class-I release factor that appeared poised to release the nascent chain. MTRES1 is an S4-domain protein that binds similarly to RqcP (Figure 4). MTRES1 was further shown to enhance the release activity of mtRF-R on *E. coli* 50S–tRNA–nascent chain complexes in an *in vitro* assay. This indicates that the binding of S4 proteins such as RqcP/MTRES1 between H69 and the P-tRNA during RQC is ancient and has been conserved even through significant evolutionary bottlenecks. It remains to be determined whether other S4-domain proteins bind analogously and whether an equivalent protein acts in cytosolic eukaryotic RQC.

6.4.3 The alanine-tailing translation cycle

In yeast, the alanine and threonine tailing reaction mediated by Rqc2p can proceed in the presence of inhibitors of eEF1A and eEF2, implying that GTP hydrolysis is not required for this process (Osuna et al., 2017). Recently, bacterial RQC has been reconstituted using an initiation complex as a starting substrate and in the absence of EF-G or EF-Tu (Section 5.5). Bacterial RQC is therefore likely to proceed in the absence of GTP hydrolysis—as can regular translation, albeit slowly (Pestka, 1968; Gavrilova et al., 1976). This naturally leads to the question of how the tRNAs proceed through the three sites on the LSU. An appealing explanation is that, between the A- and P-sites, the coiled-coil domain of RqcH may transmit Brownian motion from the mobile L7/L12 stalk base to the peptidyl-tRNA. Binding of RqcP then locks the peptidyl-tRNA in the P-site and prevents further lateral motion until peptidyl transfer (Section 5.4).

One unresolved issue in the alanine-tailing reaction is how RqcH binds and recognises $tRNA^{Ala}$ and delivers them to the 50S–tRNA–nascent chain complex. So far, structural information indicates that only the tRNA acceptor stem is recognised by RqcH, and that the $_{97}DR_{98}$ motif of the NFACT-N domain is important for this recognition (Section 5.5). This indicates that an alternative mode of binding must be necessary if RqcH specifically recognises aminoacyl-tRNA.

6.4.4 Substrates and triggers of bacterial RQC

Synthetic lethality screens imply an overlapping but not identical biological action of various ribosome rescue systems in bacteria. For example, in *E. coli ssrA* and *arfA*, but not *ssrA* and *arfB* display synthetic lethality (Chadani et al., 2010, 2011). In *B. subtilis*, a double knockout between *ssrA* and *rqcH* can be made (Lytvynenko et al., 2019). Conversely, *ssrA* has synthetic lethality with *brfA*, implying that there are certain stalling events that RqcH cannot resolve (Shimokawa-Chiba et al., 2019). It would be interesting to determine whether *rqcH* and *brfA* display synthetic lethality. In summary, genetic evidence indicates that tmRNA, alternative rescue factors, and bacterial RQC are only partially redundant, hinting at substrate specificity among these systems.

One important open question is the exact nature of the substrate for bacterial RQC. Lytvynenko et al. (2019) reported a genetic interaction between *ssrA* and *rqcH*, implying that non-stop mRNAs may become a target for bacterial RQC subsequent to an unknown splitting mechanism. This hypothesis was corroborated by the demonstration of alanine tailing on a non-stop reporter in the absence of *ssrA* and *clpP* (the protease responsible for degrading alanine-tailed proteins; Lytvynenko et al. (2019)). Additionally, in comparison to a Δ*ssrA* strain, Δ*ssrA* Δ*rqcH* cells were sensitive to the translation inhibitors erythromycin and spectinomycin and high heat (Lytvynenko et al., 2019). Notably, in *E. coli* Hsp15 is expressed in response to heat shock and strongly binds 50S–tRNA–nascent chain complexes, indicating that such complexes may be generated either directly by, or in response to, heat-shock (Korber et al., 2000). A precise definition of bacterial RQC substrates, for example using mass spectrometry or sequencing approaches, may enable further dissection of bacterial RQC *in vitro* and *in vivo*.

One candidate subunit splitting factor is HflX, which in *E. coli* causes dissociation of ribosomal subunits in response to heat stress (Zhang et al., 2015). However, in a recent study no genetic interaction between *ssrA* and *hflX* in *B. subtilis* was detected, while a strong phenotype was observed in a Δ*ssrA* Δ*rqcH* strain (Section 5.5). This indicates that bacterial RQC does not require HflX for subunit splitting.

6.4.5 Termination of the tailing reaction

In eukaryotes, it has been proposed that Pth can act on 60S– and 80S–tRNA–nascent chain complexes (Kuroha et al., 2018). Eukaryotes additionally contain specialised release factors such as Vms1 and ANKZF1 that act on RQC complexes (Verma et al., 2018). The nature of peptide release during bacterial RQC is less clear. Class-I release factor homologues of unknown function have been described in bacteria, and these proteins are good candidates for dedicated RQC release factors; however they tend to have a limited phylogenetic distribution (Baranov et al., 2006; Burroughs and Aravind, 2019).

Bacterial Pth is thought mostly to act after peptidyl-tRNA drop-off (i.e. dissociation of the peptidyl-tRNA) on short nascent chains (Heurgué-Hamard et al., 2000), although it has also been reported in one instance to act on a 24-amino-acid nascent chain (Gong et al., 2007). A single crystal structure reports the binding site of bacterial peptidyl hydrolase on deacylated tRNA (Ito et al., 2012). This site is not compatible with the currently observed 50S–tRNA–nascent chain complexes (Figure 5), indicating that a substantial change in conformation of the

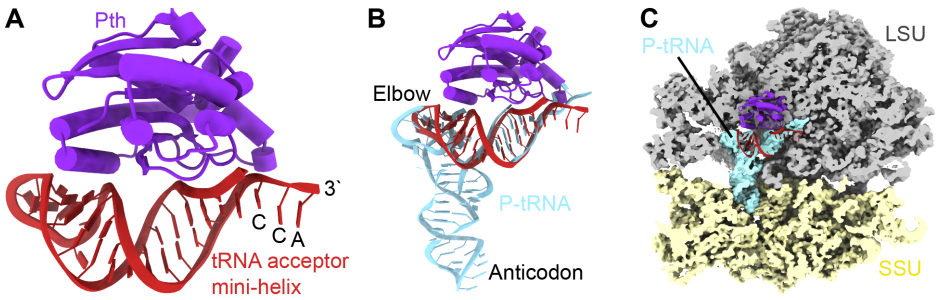

Figure 5: (A) Molecular model of Pth (purple) in complex with a minihelix mimicking the tRNA acceptor stem (red). PDB 3VJR, Ito et al. (2012). (B) Same structure as in A superimposed on a P-tRNA (from the P-tRNA-only volume in the PoxtA study, Section 5.3) (C) Structure from A superimposed with cryo-EM density of a P-tRNA–70S structure (from the PoxtA study). A cut-through is applied to the P-tRNA–70S structure only. Nearly the entirety of Pth overlaps with the LSU. Figure assembled with UCSF ChimeraX (Pettersen et al., 2021).

peptidyl-tRNA is required if it is to be a substrate of Pth on the 50S or 70S ribosome. In summary, although there are both candidate dedicated termination factors and Pth that could mediate the termination of bacterial RQC, more work is required to understand the termination of alanine tailing in bacteria.

Since bacterial *pth* is essential, much work has been performed with a *pth*(ts) temperature-sensitive mutant, and therefore a heat-shock step was used to disrupt Pth activity in the cell (Atherly and Menninger, 1972; García-Villegas et al., 1991). Mutants of many RQC-associated genes are now known to have a heat-sensitive phenotype, indicating that heat stress plays a role in the formation of abnormal translational products (Korber et al., 2000; Lytvynenko et al., 2019). Caution is therefore warranted in interpreting studies that utilise temperature-sensitive alleles with respect to bacterial RQC.

6.4.6 Summary and open questions

Bacterial alanine tailing was first described in 2019, after RqcH was discovered by homology to eukaryotic NEMF proteins (Lytvynenko et al., 2019). Consequently, although we now have multiple snapshots of the alanine tailing elongation process, our understanding of other parts of the bacterial RQC pathway is limited. In particular, what conditions trigger subunit splitting, how RqcH delivers tRNAs to the 50S–tRNA–nascent chain complex, how the process is terminated, and the relationship between the various bacterial ribosomal rescue systems remain to be determined.

6.5 Final word

Recent technical developments in single-particle cryo-EM have enabled an enhanced understanding of translation and translation-associated processes. Compared to techniques such as X-ray crystallography, relatively little sample is required for single-particle cryo-EM, allowing the use of *ex vivo* immunoprecipitation to prepare complexes for structural analysis. This facilitates the discovery of unexpected states and factors, at the cost of state definition.

This thesis presents cryo-EM structures pertaining to two such processes: ABCF-mediated dissociation of ribosome-targeting antibiotics, and RqcH- and RqcP-mediated alanine tailing on

the LSU. In both cases, some deduction was required to define the state of the cryo-EM reconstructions relative to the underlying biological processes. Ultimately these reconstructions lead to the proposals that ARE-ABCFs trigger dissociation of antibiotics indirectly, by modulating the conformation of the 23S rRNA, and how alanine tailing proceeds through a series of tRNA states that are similar to those observed in canonical translation elongation. However, many questions about each process remain to be answered. This will likely require both structural characterisation of additional states as well as complementary approaches to fully contextualise the insights gained from the molecular structures.

References

Agrawal, R. K., Sharma, M. R., Kiel, M. C., Hirokawa, G., Booth, T. M., Spahn, C. M. T., Grassucci, R. A., Kaji, A. and Frank, J. (2004). Visualization of ribosome-recycling factor on the *Escherichia coli* 70S ribosome: Functional implications. Proc. Natl. Acad. Sci. U.S.A. *101*, 8900–8905.

Akopian, D., Shen, K., Zhang, X. and Shan, S.-o. (2013). Signal recognition particle: an essential protein-targeting machine. Ann. Rev. Biochem. *82*, 693–721.

Allignet, J. and El Solh, N. (1997). Characterization of a new staphylococcal gene, *vgaB*, encoding a putative ABC transporter conferring resistance to streptogramin A and related compounds. Gene *202*, 133–138.

Allignet, J., Loncle, V. and El Solh, N. (1992). Sequence of a staphylococcal plasmid gene, *vga*, encoding a putative ATP-binding protein involved in resistance to virginiamycin A-like antibiotics. Gene *117*, 45–51.

Andersen, C. B. F., Becker, T., Blau, M., Anand, M., Halic, M., Balar, B., Mielke, T., Boesen, T., Pedersen, J. S., Spahn, C. M. T., Kinzy, T. G., Andersen, G. R. and Beckmann, R. (2006). Structure of eEF3 and the mechanism of transfer RNA release from the E-site. Nature *443*, 663–668.

Angelini, S., Deitermann, S. and Koch, H.-G. (2005). FtsY, the bacterial signal-recognition particle receptor, interacts functionally and physically with the SecYEG translocon. EMBO Rep. *6*, 476–481.

Antonelli, A., D'Andrea, M. M., Brenciani, A., Galeotti, C. L., Morroni, G., Pollini, S., Varaldo, P. E. and Rossolini, G. M. (2018). Characterization of poxtA, a novel phenicol–oxazolidinone–tetracycline resistance gene from an MRSA of clinical origin. J. Antimicrob. Chemoth. *73*, 1763–1769.

Aparicio, G., Buche, A., Méndez, C. and Salas, J. A. (1996). Characterization of the ATPase activity of the N-terminal nucleotide binding domain of an ABC transporter involved in oleandomycin secretion by *Streptomyces antibioticus*. FEMS Microbiol. Lett. *141*, 157–162.

Arenz, S., Abdelshahid, M., Sohmen, D., Payoe, R., Starosta, A. L., Berninghausen, O., Hauryliuk, V., Beckmann, R. and Wilson, D. N. (2016). The stringent factor RelA adopts an open conformation on the ribosome to stimulate ppGpp synthesis. Nucleic Acids Res. *44*, 6471–6481.

Arenz, S., Nguyen, F., Beckmann, R. and Wilson, D. N. (2015). Cryo-EM structure of the tetracycline resistance protein TetM in complex with a translating ribosome at 3.9-Å resolution. Proc. Nat. Acad. Sci. U.S.A. *112*, 5401–5406.

Artsimovitch, I., Patlan, V., Sekine, S.-i., Vassylyeva, M. N., Hosaka, T., Ochi, K., Yokoyama, S. and Vassylyev, D. G. (2004). Structural basis for transcription regulation by alarmone ppGpp. Cell *117*, 299–310.

Atherly, A. G. and Menninger, J. R. (1972). Mutant *E. coli* strain with temperature sensitive peptidyltransfer RNA hydrolase. Nature New Biol. *240*, 245–246.

Atkins, J. F., Loughran, G., Bhatt, P. R., Firth, A. E. and Baranov, P. V. (2016). Ribosomal frameshifting and transcriptional slippage: From genetic steganography and cryptography to adventitious use. Nucleic Acids Res. *44*, 7007–7078.

Atkinson, G. C., Tenson, T. and Hauryliuk, V. (2011). The RelA/SpoT Homolog (RSH) superfamily: distribution and functional evolution of ppGpp synthetases and hydrolases across the tree of life. PLOS One *6*, e23479.

Baccani, I., Antonelli, A., Di Pilato, V., Coppi, M., Di Maggio, T., Spinicci, M., Villagran, A. L., Revollo, C., Bartoloni, A. and Rossolini, G. M. (2021). Detection of poxtA2, a presumptive poxtA ancestor, in a plasmid from a linezolid-resistant *Enterococcus gallinarum* isolate. Antimicrob. Agents Chemother. *65*, e00695–21.

Ban, N., Nissen, P., Hansen, J., Moore, P. B. and Steitz, T. A. (2000). The complete atomic structure of the large ribosomal subunit at 2.4 Å resolution. Science *289*, 905–920.

Baranov, P. V., Vestergaard, B., Hamelryck, T., Gesteland, R. F., Nyborg, J. and Atkins, J. F. (2006). Diverse bacterial genomes encode an operon of two genes, one of which is an unusual class-I release factor that potentially recognizes atypical mRNA signals other than normal stop codons. Biol. Direct *1*, 28.

Barthelme, D., Dinkelaker, S., Albers, S.-V., Londei, P., Ermler, U. and Tampé, R. (2011). Ribosome recycling depends on a mechanistic link between the FeS cluster domain and a conformational switch of the twin-ATPase ABCE1. Proc. Natl. Acad. Sci. U.S.A. *108*, 3228–3233.

Barthelme, D., Scheele, U., Dinkelaker, S., Janoschka, A., Macmillan, F., Albers, S.-V., Driessen, A. J. M., Stagni, M. S., Bill, E., Meyer-Klaucke, W., Schünemann, V. and Tampé, R. (2007). Structural organization of essential iron-sulfur clusters in the evolutionarily highly conserved ATP-binding cassette protein ABCE1. J. Biol. Chem. *282*, 14598–14607.

Becker, T., Franckenberg, S., Wickles, S., Shoemaker, C. J., Anger, A. M., Armache, J.-P., Sieber, H., Ungewickell, C., Berninghausen, O., Daberkow, I., Karcher, A., Thomm, M., Hopfner, K.-P., Green, R. and Beckmann, R. (2012). Structural basis of highly conserved ribosome recycling in eukaryotes and archaea. Nature *482*, 501–506.

Beckert, B., Leroy, E. C., Sothiselvam, S., Bock, L. V., Svetlov, M. S., Graf, M., Arenz, S., Abdelshahid, M., Seip, B., Grubmüller, H., Mankin, A. S., Innis, C. A., Vázquez-Laslop, N. and Wilson, D. N. (2021). Structural and mechanistic basis for translation inhibition by macrolide and ketolide antibiotics. Nat. Commun. *12*, 4466.

Berg, B. v. d., Clemons, W. M., Collinson, I., Modis, Y., Hartmann, E., Harrison, S. C. and Rapoport, T. A. (2004). X-ray structure of a protein-conducting channel. Nature *427*, 36–44.

Bernstein, H. D., Poritz, M. A., Strub, K., Hoben, P. J., Brenner, S. and Walter, P. (1989). Model for signal sequence recognition from amino-acid sequence of 54K subunit of signal recognition particle. Nature *340*, 482–486.

Bieling, P., Beringer, M., Adio, S. and Rodnina, M. V. (2006). Peptide bond formation does not involve acid-base catalysis by ribosomal residues. Nat. Struct. Mol. Biol. *13*, 423–428.

Bishop, J., Leahy, J. and Schweet, R. (1960). FORMATION OF THE PEPTIDE CHAIN OF HEMOGLOBIN. Proc. Natl. Acad. Sci. U.S.A. *46*, 1030–1038.

Blaha, G., Stanley, R. E. and Steitz, T. A. (2009). Formation of the first peptide bond: the structure of EF-P bound to the 70S ribosome. Science *325*, 966–970.

Blanchard, S. C., Kim, H. D., Gonzalez, R. L., Puglisi, J. D. and Chu, S. (2004). tRNA dynamics on the ribosome during translation. Proc. Natl. Acad. Sci. U.S.A. *101*, 12893–12898.

Bodley, J. W., Zieve, F. J., Lin, L. and Zieve, S. T. (1969). Formation of the ribosome-G factor-GDP complex in the presence of fusidic acid. Biochem. Biophys. Res. Commun. *37*, 437–443.

Boël, G., Smith, P. C., Ning, W., Englander, M. T., Chen, B., Hashem, Y., Testa, A. J., Fischer, J. J., Wieden, H.-J., Frank, J., Gonzalez, R. L. and Hunt, J. F. (2014). The ABC-F protein EttA gates ribosome entry into the translation elongation cycle. Nat. Struct. Mol. Biol. *21*, 143–151.

Brandman, O., Stewart-Ornstein, J., Wong, D., Larson, A., Williams, C. C., Li, G.-W., Zhou, S., King, D., Shen, P. S., Weibezahn, J., Dunn, J. G., Rouskin, S., Inada, T., Frost, A. and Weissman, J. S. (2012). A ribosome-bound quality control complex triggers degradation of nascent peptides and signals translation stress. Cell *151*, 1042–1054.

Brilot, A. F., Korostelev, A. A., Ermolenko, D. N. and Grigorieff, N. (2013). Structure of the ribosome with elongation factor G trapped in the pretranslocation state. Proc. Natl. Acad. Sci. U.S.A. *110*, 20994–20999.

Brodersen, D. E., Clemons, W. M., Carter, A. P., Morgan-Warren, R. J., Wimberly, B. T. and Ramakrishnan, V. (2000). The structural basis for the action of the antibiotics tetracycline, pactamycin, and hygromycin B on the 30S ribosomal subunit. Cell *103*, 1143–1154.

Brown, A., Amunts, A., Bai, X.-C., Sugimoto, Y., Edwards, P. C., Murshudov, G., Scheres, S. H. W. and Ramakrishnan, V. (2014). Structure of the large ribosomal subunit from human mitochondria. Science *346*, 718–722.

Brown, A., Fernández, I. S., Gordiyenko, Y. and Ramakrishnan, V. (2016). Ribosome-dependent activation of stringent control. Nature *534*, 277–280.

Brown, A., Shao, S., Murray, J., Hegde, R. S. and Ramakrishnan, V. (2015). Structural basis for stop codon recognition in eukaryotes. Nature *524*, 493–496.

Brown, C. M. and Tate, W. P. (1994). Direct recognition of mRNA stop signals by *Escherichia coli* polypeptide chain release factor two. J. Biol. Chem. *269*, 33164–33170.

Burdett, V. (1986). Streptococcal tetracycline resistance mediated at the level of protein synthesis. J. Bacteriol. *165*, 564–569.

Burdett, V. (1991). Purification and characterization of Tet(M), a protein that renders ribosomes resistant to tetracycline. J. Biol. Chem. *266*, 2872–2877.

Burroughs, A. M. and Aravind, L. (2019). The origin and evolution of release factors: Implications for translation termination, ribosome rescue, and quality control pathways. Int. J. Mol. Sci. *20*, 1–24.

Capecchi, M. R. (1967). Polypeptide chain termination in vitro: isolation of a release factor. Proc. Natl. Acad. Sci. U.S.A. *58*, 1144–1151.

Capecchi, M. R. and Klein, H. A. (1969). Characterization of three proteins involved in polypeptide chain termination. Cold Spring Harb. Symp. Quant. Biol. *34*, 469–477.

Carbone, C. E., Demo, G., Madireddy, R., Svidritskiy, E. and Korostelev, A. A. (2020). ArfB can displace mRNA to rescue stalled ribosomes. Nat. Commun. *11*, 5552.

Carbone, C. E., Loveland, A. B., Gamper, H., Hou, Y.-M., Demo, G. and Korostelev, A. A. (2021). Time-resolved cryo-EM visualizes ribosomal translocation with EF-G and GTP. Preprint, doi:10.1101/2021.05.31.446434 bioRxiv.

Carter, A. P., Clemons, W. M., Brodersen, D. E., Morgan-Warren, R. J., Hartsch, T., Wimberly, B. T. and Ramakrishnan, V. (2001). Crystal structure of an initiation factor bound to the 30S ribosomal subunit. Science *291*, 498–501.

Cashel, M. and Gallant, J. (1969). Two compounds implicated in the function of the RC gene of *Escherichia coli*. Nature *221*, 838–841.

Castilho, B. A., Shanmugam, R., Silva, R. C., Ramesh, R., Himme, B. M. and Sattlegger, E. (2014). Keeping the eIF2 alpha kinase Gcn2 in check. Biochim. Biophys. Acta *1843*, 1948–1968.

Cech, T. R. (2000). The ribosome is a ribozyme. Science *289*, 878–879.

Chadani, Y., Ito, K., Kutsukake, K. and Abo, T. (2012). ArfA recruits release factor 2 to rescue stalled ribosomes by peptidyl-tRNA hydrolysis in *Escherichia coli*. Mol. Microbiol. *86*, 37–50.

Chadani, Y., Ono, K., Kutsukake, K. and Abo, T. (2011). *Escherichia coli* YaeJ protein mediates a novel ribosome-rescue pathway distinct from SsrA- and ArfA-mediated pathways. Mol. Microbiol. *80*, 772–785.

Chadani, Y., Ono, K., Ozawa, S.-I., Takahashi, Y., Takai, K., Nanamiya, H., Tozawa, Y., Kutsukake, K. and Abo, T. (2010). Ribosome rescue by *Escherichia coli* ArfA (YhdL) in the absence of trans-translation system. Mol. Microbiol. *78*, 796–808.

Chan, K.-H., Petrychenko, V., Mueller, C., Maracci, C., Holtkamp, W., Wilson, D. N., Fischer, N. and Rodnina, M. V. (2020). Mechanism of ribosome rescue by alternative ribosome-rescue factor B. Nat. Commun. *11*, 4106.

Chen, B., Boël, G., Hashem, Y., Ning, W., Fei, J., Wang, C., Gonzalez, R. L., Hunt, J. F. and Frank, J. (2014). EttA regulates translation by binding the ribosomal E site and restricting ribosome-tRNA dynamics. Nat. Struct. Mol. Biol. *21*, 152–159.

Chen, J., Lu, G., Lin, J., Davidson, A. L. and Quiocho, F. A. (2003). A tweezers-like motion of the ATP-binding cassette dimer in an ABC transport cycle. Mol. Cell *12*, 651–661.

Chen, M. and Ludtke, S. J. (2021). Deep learning-based mixed-dimensional Gaussian mixture model for characterizing variability in cryo-EM. Nat. Methods *18*, 930–936.

Chen, Y., Kaji, A., Kaji, H. and Cooperman, B. S. (2017). The kinetic mechanism of bacterial ribosome recycling. Nucleic Acids Res. *45*, 10168–10177.

Chesneau, O., Ligeret, H., Hosan-Aghaie, N., Morvan, A. and Dassa, E. (2005). Molecular analysis of resistance to streptogramin A compounds conferred by the Vga proteins of staphylococci. Antimicrob. Agents Chemother. *49*, 973–980.

Choi, J. and Puglisi, J. D. (2017). Three tRNAs on the ribosome slow translation elongation. Proc. Natl. Acad. Sci. U.S.A. *114*, 13691–13696.

Conway, T. W. and Lipmann, F. (1964). CHARACTERIZATION OF A RIBOSOME-LINKED GUANOSINE TRIPHOSPHATASE IN ESCHERICHIA COLI EXTRACTS. Proc. Natl. Acad. Sci. U.S.A. *52*, 1462–1469.

Coots, R. A., Liu, X.-M., Mao, Y., Dong, L., Zhou, J., Wan, J., Zhang, X. and Qian, S.-B. (2017). m6A facilitates eIF4F-independent mRNA translation. Mol. Cell *68*, 504–514.e7.

Cornish, P. V., Ermolenko, D. N., Noller, H. F. and Ha, T. (2008). Spontaneous intersubunit rotation in single ribosomes. Mol. Cell *30*, 578–588.

Cox, G., Thompson, G. S., Jenkins, H. T., Peske, F., Savelsbergh, A., Rodnina, M. V., Wintermeyer, W., Homans, S. W., Edwards, T. A. and O'Neill, A. J. (2012). Ribosome clearance by FusB-type proteins mediates resistance to the antibiotic fusidic acid. Proc. Natl. Acad. Sci. U.S.A. *109*, 2102–2107.

Craigen, W. J., Cook, R. G., Tate, W. P. and Caskey, C. T. (1985). Bacterial peptide chain release factors: conserved primary structure and possible frameshift regulation of release factor 2. Proc. Natl. Acad. Sci. U.S.A. *82*, 3616–3620.

Crick, F. H., Barnett, L., Brenner, S. and Watts-Tobin, R. J. (1961). General nature of the genetic code for proteins. Nature *192*, 1227–1232.

Cuzin, F., Greenberg, R. E. and Chapeville, F. (1967). Enzymatic hydrolysis of N-substituted aminoacyl-tRNA. Proc. Natl. Acad. Sci. U.S.A. *58*, 2079–2086.

Dar, D., Shamir, M., Mellin, J. R., Koutero, M., Stern-Ginossar, N., Cossart, P. and Sorek, R. (2016). Term-seq reveals abundant ribo-regulation of antibiotics resistance in bacteria. Science *352*, aad9822.

Dasmahapatra, B. and Chakraburtty, K. (1981). Purification and properties of elongation factor 3 from *Saccharomyces cerevisiae*. J. Biol. Chem. *256*, 9999–10004.

Davidson, A. L., Dassa, E., Orelle, C. and Chen, J. (2008). Structure, function, and evolution of bacterial ATP-binding cassette systems. Microbiol. Mol. Biol. Rev. *72*, 317–364.

Davidson, A. L. and Nikaido, H. (1990). Overproduction, solubilization, and reconstitution of the maltose transport system from *Escherichia coli*. J. Biol. Chem. *265*, 4254–4260.

Demo, G., Svidritskiy, E., Madireddy, R., Diaz-Avalos, R., Grant, T., Grigorieff, N., Sousa, D. and Korostelev, A. A. (2017). Mechanism of ribosome rescue by ArfA and RF2. eLife *6*, e23687.

Deng, F., Wang, H., Liao, Y., Li, J., Feßler, A. T., Michael, G. B., Schwarz, S. and Wang, Y. (2017). Detection and genetic environment of pleuromutilin-lincosamide-streptogramin A resistance genes in staphylococci isolated from pets. Front. Microbiol. *8*, 234.

Desai, N., Yang, H., Chandrasekaran, V., Kazi, R., Minczuk, M. and Ramakrishnan, V. (2020). Elongational stalling activates mitoribosome-associated quality control. Science *370*, 1105–1110.

Dibb, N. J. and Wolfe, P. B. (1986). *lep* operon proximal gene is not required for growth or secretion by *Escherichia coli*. J. Bacteriol. *166*, 83–87.

Dintzis, H. M. (1961). Assembly of the peptide chains of hemoglobin. Proc. Natl. Acad. Sci. U.S.A. *47*, 247–261.

Doerfel, L. K., Wohlgemuth, I., Kothe, C., Peske, F., Urlaub, H. and Rodnina, M. V. (2013). EF-P is essential for rapid synthesis of proteins containing consecutive proline residues. Science *339*, 85–88.

Dong, J., Lai, R., Jennings, J. L., Link, A. J. and Hinnebusch, A. G. (2005). The novel ATP-binding cassette protein ARB1 is a shuttling factor that stimulates 40S and 60S ribosome biogenesis. Mol. Cell Biol. *25*, 9859–9873.

Dorrian, J. M., Briggs, D. A., Ridley, M. L., Layfield, R. and Kerr, I. D. (2011). Induction of a stress response in *Lactococcus lactis* is associated with a resistance to ribosomally active antibiotics. FEBS J. *278*, 4015–4024.

Dunkle, J. A., Wang, L., Feldman, M. B., Pulk, A., Chen, V. B., Kapral, G. J., Noeske, J., Richardson, J. S., Blanchard, S. C. and Cate, J. H. D. (2011). Structures of the bacterial ribosome in classical and hybrid states of tRNA binding. Science *332*, 981–984.

Dutta, D., Bandyopadhyay, K., Datta, A. B., Sardesai, A. A. and Parrack, P. (2009). Properties of HflX, an enigmatic protein from *Escherichia coli*. J. Bacteriol. *191*, 2307–2314.

Duval, M., Dar, D., Carvalho, F., Rocha, E. P. C., Sorek, R. and Cossart, P. (2018). HflXr, a homolog of a ribosome-splitting factor, mediates antibiotic resistance. Proc. Natl. Acad. Sci. U.S.A. *115*, 13359–13364.

Dönhöfer, A., Franckenberg, S., Wickles, S., Berninghausen, O., Beckmann, R. and Wilson, D. N. (2012). Structural basis for TetM-mediated tetracycline resistance. Proc. Natl. Acad. Sci. U.S.A. *109*, 16900–16905.

Ero, R., Kumar, V., Su, W. and Gao, Y.-G. (2019). Ribosome protection by ABC-F proteins—Molecular mechanism and potential drug design. Protein Sci. *28*, 684–693.

FDA/Pfizer (2010). Zyvox product information. Technical report.

Feaga, H. A., Viollier, P. H. and Keiler, K. C. (2014). Release of nonstop ribosomes is essential. mBio *5*, e01916.

Filbeck, S., Cerullo, F., Paternoga, H., Tsaprailis, G., Joazeiro, C. A. P. and Pfeffer, S. (2021). Mimicry of canonical translation elongation underlies alanine tail synthesis in RQC. Mol. Cell *81*, 104–114.e6.

Fischer, N., Neumann, P., Bock, L. V., Maracci, C., Wang, Z., Paleskava, A., Konevega, A. L., Schröder, G. F., Grubmüller, H., Ficner, R., Rodnina, M. V. and Stark, H. (2016). The pathway to GTPase activation of elongation factor SelB on the ribosome. Nature *540*, 80–85.

Forchhammer, K., Leinfelder, W. and Böck, A. (1989). Identification of a novel translation factor necessary for the incorporation of selenocysteine into protein. Nature *342*, 453–456.

Fostier, C. R., Monlezun, L., Ousalem, F., Singh, S., Hunt, J. F. and Boël, G. (2021). ABC-F translation factors: from antibiotic resistance to immune response. FEBS Lett. *595*, 675–706.

Frank, J. and Agrawal, R. K. (2000). A ratchet-like inter-subunit reorganization of the ribosome during translocation. Nature *406*, 318–322.

Fu, J., Hashem, Y., Wower, I., Lei, J., Liao, H. Y., Zwieb, C., Wower, J. and Frank, J. (2010). Visualizing the transfer-messenger RNA as the ribosome resumes translation. EMBO J. *29*, 3819–3825.

Fu, Z., Indrisiunaite, G., Kaledhonkar, S., Shah, B., Sun, M., Chen, B., Grassucci, R. A., Ehrenberg, M. and Frank, J. (2019). The structural basis for release-factor activation during translation termination revealed by time-resolved cryogenic electron microscopy. Nat. Commun. *10*, 2579.

Fu, Z., Kaledhonkar, S., Borg, A., Sun, M., Chen, B., Grassucci, R. A., Ehrenberg, M. and Frank, J. (2016). Key intermediates in ribosome recycling visualized by time-resolved cryoelectron microscopy. Structure *24*, 2092–2101.

Gagnon, M. G., Lin, J. and Steitz, T. A. (2016). Elongation factor 4 remodels the A-site tRNA on the ribosome. Proc. Natl. Acad. Sci. U.S.A. *113*, 4994–4999.

Gagnon, M. G., Seetharaman, S. V., Bulkley, D. and Steitz, T. A. (2012). Structural basis for the rescue of stalled ribosomes: structure of YaeJ bound to the ribosome. Science *335*, 1370–1372.

Gao, N., Zavialov, A. V., Li, W., Sengupta, J., Valle, M., Gursky, R. P., Ehrenberg, M. and Frank, J. (2005). Mechanism for the disassembly of the posttermination complex inferred from cryo-EM studies. Mol. Cell *18*, 663–674.

García-Villegas, M. R., De La Vega, F. M., Galindo, J. M., Segura, M., Buckingham, R. H. and Guarneros, G. (1991). Peptidyl-tRNA hydrolase is involved in lambda inhibition of host protein synthesis. EMBO J. *10*, 3549–3555.

Garza-Sánchez, F., Shoji, S., Fredrick, K. and Hayes, C. S. (2009). RNase II is important for A-site mRNA cleavage during ribosome pausing. Mol. Microbiol. *73*, 882–897.

Gavrilova, L., Kostiashkina, O., Koteliansky, V., Rutkevitch, N. and Spirin, A. (1976). Factor-free ("Non-enzymic") and factor-dependent systems of translation of polyuridylic acid by *Escherichia coli* ribosomes. J. Mol. Biol. *101*, 537–552.

Gibbs, M. R. and Fredrick, K. (2018). Roles of elusive translational GTPases come to light and inform on the process of ribosome biogenesis in bacteria. Mol. Microbiol. *107*, 445–454.

Gilson, E., Nikaido, H. and Hofnung, M. (1982). Sequence of the malK gene in *E. coli* K12. Nucleic Acids Res. *10*, 7449–7458.

Glick, B. R. and Ganoza, M. C. (1975). Identification of a soluble protein that stimulates peptide bond synthesis. Proc. Natl. Acad. Sci. U.S.A. *72*, 4257–4260.

Gong, M., Cruz-Vera, L. R. and Yanofsky, C. (2007). Ribosome recycling factor and release factor 3 action rromotes TnaC-peptidyl-tRNA dropoff and relieves ribosome stalling during tryptophan induction of tna operon expression in *Escherichia coli*. J. Bacteriol. *189*, 3147–3155.

Goralski, T. D. P., Kirimanjeswara, G. S. and Keiler, K. C. (2018). A new mechanism for ribosome rescue can recruit RF1 or RF2 to nonstop ribosomes. mBio *9*, e02436–18.

Gottesman, S., Roche, E., Zhou, Y. and Sauer, R. T. (1998). The ClpXP and ClpAP proteases degrade proteins with carboxy-terminal peptide tails added by the SsrA-tagging system. Genes Dev. *12*, 1338–1347.

Gouridis, G., Hetzert, B., Kiosze-Becker, K., de Boer, M., Heinemann, H., Nürenberg-Goloub, E., Cordes, T. and Tampé, R. (2019). ABCE1 controls ribosome recycling by an asymmetric dynamic conformational equilibrium. Cell Rep. *28*, 723–734.e6.

Graf, M., Huter, P., Maracci, C., Peterek, M., Rodnina, M. V. and Wilson, D. N. (2018). Visualization of translation termination intermediates trapped by the Apidaecin 137 peptide during RF3-mediated recycling of RF1. Nat. Commun. *9*, 3053.

Greber, B. J., Boehringer, D., Leitner, A., Bieri, P., Voigts-Hoffmann, F., Erzberger, J. P., Leibundgut, M., Aebersold, R. and Ban, N. (2014). Architecture of the large subunit of the mammalian mitochondrial ribosome. Nature *505*, 515–519.

Grentzmann, G., Brechemier-Baey, D., Heurgue, V., Mora, L. and Buckingham, R. H. (1994). Localization and characterization of the gene encoding release factor RF3 in *Escherichia coli*. Proc. Natl. Acad. Sci. U.S.A. *91*, 5848–5852.

Grigoriadou, C., Marzi, S., Kirillov, S., Gualerzi, C. O. and Cooperman, B. S. (2007). A quantitative kinetic scheme for 70 S translation initiation complex formation. J. Mol. Biol. *373*, 562–572.

Guo, X., Peisker, K., Bäckbro, K., Chen, Y., Koripella, R. K., Mandava, C. S., Sanyal, S. and Selmer, M. (2012). Structure and function of FusB: an elongation factor G-binding fusidic acid resistance protein active in ribosomal translocation and recycling. Open Biol. *2*, 120016.

Guyomar, C., D'Urso, G., Chat, S., Giudice, E. and Gillet, R. (2021). Structures of tmRNA and SmpB as they transit through the ribosome. Nature Commun. *12*, 4909.

Handa, Y., Inaho, N. and Nameki, N. (2011). YaeJ is a novel ribosome-associated protein in Escherichia coli that can hydrolyze peptidyl-tRNA on stalled ribosomes. Nucleic Acids Res. *39*, 1739–1748.

Haroche, J., Allignet, J., Buchrieser, C. and El Solh, N. (2000). Characterization of a variant of *vga*(A) conferring resistance to streptogramin A and related compounds. Antimicrob. Agents Chemother. *44*, 2271–2275.

Haseltine, W. A. and Block, R. (1973). Synthesis of guanosine tetra- and pentaphosphate requires the presence of a codon-specific, uncharged transfer ribonucleic acid in the acceptor site of ribosomes. Proc. Natl. Acad. Sci. U.S.A. *70*, 1564–1568.

Hauryliuk, V., Atkinson, G. C., Murakami, K. S., Tenson, T. and Gerdes, K. (2015). Recent functional insights into the role of (p)ppGpp in bacterial physiology. Nat. Rev. Microbiol. *13*, 298–309.

Hauschild, T., Fessler, A. T., Kadlec, K., Billerbeck, C. and Schwarz, S. (2012). Detection of the novel *vga*(E) gene in methicillin-resistant *Staphylococcus aureus* CC398 isolates from cattle and poultry. J. Antimicrob. Chemoth. *67*, 503–504.

Hayes, C. S. and Sauer, R. T. (2003). Cleavage of the A site mRNA codon during ribosome pausing provides a mechanism for translational quality control. Mol. Cell *12*, 903–911.

Heuer, A., Gerovac, M., Schmidt, C., Trowitzsch, S., Preis, A., Kötter, P., Berninghausen, O., Becker, T., Beckmann, R. and Tampé, R. (2017). Structure of the 40S–ABCE1 post-splitting complex in ribosome recycling and translation initiation. Nat. Struct. Mol. Biol. *24*, 453–460.

Heurgué-Hamard, V., Dinçbas, V., Buckingham, R. H. and Ehrenberg, M. (2000). Origins of minigene-dependent growth inhibition in bacterial cells. EMBO J. *19*, 2701–2709.

Heurgué-Hamard, V., Karimi, R., Mora, L., MacDougall, J., Leboeuf, C., Grentzmann, G., Ehrenberg, M. and Buckingham, R. H. (1998). Ribosome release factor RF4 and termination factor RF3 are involved in dissociation of peptidyl-tRNA from the ribosome. EMBO J. *17*, 808–816.

Higgins, C. F., Haag, P. D., Nikaido, K., Ardeshir, F., Garcia, G. and Ames, G. F.-L. (1982). Complete nucleotide sequence and identification of membrane components of the histidine transport operon of *S. typhimurium*. Nature *298*, 723–727.

Higgins, C. F., Hiles, I. D., Salmond, G. P. C., Gill, D. R., Downie, J. A., Evans, I. J., Holland, I. B., Gray, L., Buckel, S. D., Bell, A. W. and Hermodson, M. A. (1986). A family of related ATP-binding subunits coupled to many distinct biological processes in bacteria. Nature *323*, 448–450.

Hirashima, A. and Kaji, A. (1973). Role of elongation factor G and a protein factor on the release of ribosomes from messenger ribonucleic acid. J. Biol. Chem. *248*, 7580–7587.

Hirokawa, G., Kiel, M. C., Muto, A., Selmer, M., Raj, V., Liljas, A., Igarashi, K., Kaji, H. and Kaji, A. (2002). Post-termination complex disassembly by ribosome recycling factor, a functional tRNA mimic. EMBO J. *21*, 2272–2281.

Hot, C., Berthet, N. and Chesneau, O. (2014). Characterization of *sal*(A), a novel gene responsible for lincosamide and streptogramin a resistance in *Staphylococcus sciuri*. Antimicrob. Agents Chemother. *58*, 3335–3341.

Huang, W. M., Ao, S. Z., Casjens, S., Orlandi, R., Zeikus, R., Weiss, R., Winge, D. and Fang, M. (1988). A persistent untranslated sequence within bacteriophage T4 DNA topoisomerase gene 60. Science *239*, 1005–1012.

Hudson, C. M., Lau, B. Y. and Williams, K. P. (2014). Ends of the line for tmRNA-SmpB. Front. Microbiol. *5*, 421.

Hussain, T., Llácer, J. L., Wimberly, B. T., Kieft, J. S. and Ramakrishnan, V. (2016). Large-scale movements of IF3 and tRNA during bacterial translation initiation. Cell *167*, 133–144.e13.

Huter, P., Arenz, S., Bock, L. V., Graf, M., Frister, J. O., Heuer, A., Peil, L., Starosta, A. L., Wohlgemuth, I., Peske, F., Nováček, J., Berninghausen, O., Grubmüller, H., Tenson, T., Beckmann, R., Rodnina, M. V., Vaiana, A. C. and Wilson, D. N. (2017a). Structural basis for polyproline-mediated ribosome stalling and rescue by the translation elongation factor EF-P. Mol. Cell *68*, 515–527.e6.

Huter, P., Müller, C., Beckert, B., Arenz, S., Berninghausen, O., Beckmann, R. and Wilson, D. N. (2017b). Structural basis for ArfA-RF2-mediated translation termination on mRNAs lacking stop codons. Nature *541*, 546–549.

Huxley, H. E. and Zubay, G. (1960). Electron microscope observations on the structure of microsomal particles from *Escherichia coli*. J. Mol. Biol. *2*, 10–IN8.

Imai, H., Uchiumi, T. and Kodera, N. (2020). Direct visualization of translational GTPase factor pool formed around the archaeal ribosomal P-stalk by high-speed AFM. Proc. Natl. Acad. Sci. U.S.A. *117*, 32386–32394.

Indrisiunaite, G., Pavlov, M. Y., Heurgué-Hamard, V. and Ehrenberg, M. (2015). On the pH dependence of class-1 RF-dependent termination of mRNA translation. J. Mol. Biol. *427*, 1848–1860.

Ito, K., Chadani, Y., Nakamori, K., Chiba, S., Akiyama, Y. and Abo, T. (2011). Nascentome analysis uncovers futile protein synthesis in *Escherichia coli*. PloS One *6*, e28413.

Ito, K., Murakami, R., Mochizuki, M., Qi, H., Shimizu, Y., Miura, K.-i., Ueda, T. and Uchiumi, T. (2012). Structural basis for the substrate recognition and catalysis of peptidyl-tRNA hydrolase. Nucleic Acids Res. *40*, 10521–10531.

Iwakura, N., Yokoyama, T., Quaglia, F., Mitsuoka, K., Mio, K., Shigematsu, H., Shirouzu, M., Kaji, A. and Kaji, H. (2017). Chemical and structural characterization of a model Post-Termination Complex (PoTC) for the ribosome recycling reaction: Evidence for the release of the mRNA by RRF and EF-G. PLoS One *12*, e0177972.

Jacinto-Loeza, E., Vivanco-Domínguez, S., Guarneros, G. and Hernández-Sánchez, J. (2008). Minigene-like inhibition of protein synthesis mediated by hungry codons near the start codon. Nucleic Acids Res. *36*, 4233–4241.

James, N. R., Brown, A., Gordiyenko, Y. and Ramakrishnan, V. (2016). Translational termination without a stop codon. Science *354*, 1437–1440.

Janosi, L., Shimizu, I. and Kaji, A. (1994). Ribosome recycling factor (ribosome releasing factor) is essential for bacterial growth. Proc. Natl. Acad. Sci. U.S.A. *91*, 4249–4253.

Jha, V., Roy, B., Jahagirdar, D., McNutt, Z. A., Shatoff, E. A., Boleratz, B. L., Watkins, D. E., Bundschuh, R., Basu, K., Ortega, J. and Fredrick, K. (2021). Structural basis of sequestration of the anti-Shine-Dalgarno sequence in the Bacteroidetes ribosome. Nucleic Acids Res. *49*, 547–567.

Jiang, L., Schaffitzel, C., Bingel-Erlenmeyer, R., Ban, N., Korber, P., Koning, R. I., de Geus, D. C., Plaisier, J. R. and Abrahams, J. P. (2009). Recycling of aborted ribosomal 50S subunit-nascent chain-tRNA complexes by the heat shock protein Hsp15. J. Mol. Biol. *386*, 1357–1367.

Johnson, G. E., Lalanne, J.-B., Peters, M. L. and Li, G.-W. (2020). Functionally uncoupled transcription-translation in *Bacillus subtilis*. Nature *585*, 124–128.

Johnson, Z. L. and Chen, J. (2018). ATP binding enables substrate release from Multidrug Resistance Protein 1. Cell *172*, 81–89.e10.

Jung, Y. H., Shin, E. S., Kim, O., Yoo, J. S., Lee, K. M., Yoo, J. I., Chung, G. T. and Lee, Y. S. (2010). Characterization of two newly identified genes, *vgaD* and *vatG*, conferring resistance to streptogramin A in *Enterococcus faecium*. Antimicrob. Agents Chemother. *54*, 4744–4749.

Kadlec, K. and Schwarz, S. (2009). Novel ABC transporter gene, *vga*(C), located on a multiresistance plasmid from a porcine methicillin-resistant *Staphylococcus aureus* ST398 Strain. Antimicrob. Agents Chemother. *53*, 3589–3591.

Karcher, A., Schele, A. and Hopfner, K.-P. (2008). X-ray structure of the complete ABC enzyme ABCE1 from *Pyrococcus abyssi*. J. Biol. Chem. *283*, 7962–7971.

Karimi, R., Pavlov, M. Y., Buckingham, R. H. and Ehrenberg, M. (1999). Novel roles for classical factors at the interface between translation termination and initiation. Mol. Cell *3*, 601–609.

Karpowich, N., Martsinkevich, O., Millen, L., Yuan, Y.-R., Dai, P. L., MacVey, K., Thomas, P. J. and Hunt, J. F. (2001). Crystal structures of the MJ1267 ATP binding cassette reveal an induced-fit effect at the ATPase active site of an ABC transporter. Structure *9*, 571–586.

Karray, F., Darbon, E., Oestreicher, N., Dominguez, H., Tuphile, K., Gagnat, J., Blondelet-Rouault, M. H., Gerbaud, C. and Pernodet, J. L. (2007). Organization of the biosynthetic gene cluster for the macrolide antibiotic spiramycin in *Streptomyces ambofaciens*. Microbiology *153*, 4111–4122.

Karzai, A. W., Susskind, M. M. and Sauer, R. T. (1999). SmpB, a unique RNA-binding protein essential for the peptide-tagging activity of SsrA (tmRNA). EMBO J. *18*, 3793–3799.

Kasari, V., Pochopien, A. A., Margus, T., Murina, V., Turnbull, K., Zhou, Y., Nissan, T., Graf, M., Nováček, J., Atkinson, G. C., Johansson, M. J. O., Wilson, D. N. and Hauryliuk, V. (2019). A role for the *Saccharomyces cerevisiae* ABCF protein New1 in translation termination/recycling. Nucleic Acids Res. *47*, 8807–8820.

Kater, L., Frieg, B., Berninghausen, O., Gohlke, H., Beckmann, R. and Kedrov, A. (2019). Partially inserted nascent chain unzips the lateral gate of the Sec translocon. EMBO Rep. *20*, e48191.

Kawashima, T., Berthet-Colominas, C., Wulff, M., Cusack, S. and Leberman, R. (1996). The structure of the *Escherichia coli* EF-Tu.EF-Ts complex at 2.5 Å resolution. Nature *379*, 511–518.

Keiler, K. C. and Feaga, H. A. (2014). Resolving nonstop translation complexes is a matter of life or death. J. Bacteriol. *196*, 2123–2130.

Keiler, K. C., Shapiro, L. and Williams, K. P. (2000). tmRNAs that encode proteolysis-inducing tags are found in all known bacterial genomes: A two-piece tmRNA functions in *Caulobacter*. Proc. Nat. Acad. Sci. U.S.A. *97*, 7778–7783.

Keiler, K. C., Waller, P. R. and Sauer, R. T. (1996). Role of a peptide tagging system in degradation of proteins synthesized from damaged messenger RNA. Science *271*, 990–993.

Kerr, I. D. (2004). Sequence analysis of twin ATP binding cassette proteins involved in translational control, antibiotic resistance, and ribonuclease L inhibition. Biochem. Biophys. Res. Commun. *315*, 166–173.

Kim, K. K., Min, K. and Suh, S. W. (2000). Crystal structure of the ribosome recycling factor from *Escherichia coli*. EMBO J. *19*, 2362–2370.

Kitani, S., Yamauchi, T., Fukushima, E., Kwon Lee, C., Ningsih, F., Kinoshita, H. and Nihira, T. (2010). Characterization of *varM* encoding type II ABC transporter in *Streptomyces virginiae*, a virginiamycin M1 producer. Actinomycetologica *24*, 51–57.

Koberska, M., Vesela, L., Vimberg, V., Lenart, J., Vesela, J., Kamenik, Z., Janata, J. and Balikova Novotna, G. (2021). Beyond self-resistance: ABCF ATPase LmrC Is a signal-transducing component of an antibiotic-driven signaling cascade accelerating the onset of lincomycin biosynthesis. mBio *0*, e01731–21.

Komine, Y., Kitabatake, M., Yokogawa, T., Nishikawa, K. and Inokuchi, H. (1994). A tRNA-like structure is present in 10Sa RNA, a small stable RNA from *Escherichia coli*. Proc. Natl. Acad. Sci. U.S.A. *91*, 9223–9227.

Korber, P., Stahl, J. M., Nierhaus, K. H. and Bardwell, J. C. (2000). Hsp15: a ribosome-associated heat shock protein. EMBO J. *19*, 741–748.

Korostelev, A., Trakhanov, S., Asahara, H., Laurberg, M., Lancaster, L. and Noller, H. F. (2007). Interactions and dynamics of the Shine–Dalgarno helix in the 70S ribosome. Proc. Natl. Acad. Sci. U.S.A. *104*, 16840–16843.

Koutmou, K. S., McDonald, M. E., Brunelle, J. L. and Green, R. (2014). RF3:GTP promotes rapid dissociation of the class 1 termination factor. RNA *20*, 609–620.

Kratzat, H., Mackens-Kiani, T., Ameismeier, M., Potocnjak, M., Cheng, J., Dacheux, E., Namane, A., Berninghausen, O., Herzog, F., Fromont-Racine, M., Becker, T. and Beckmann, R. (2021). A structural inventory of native ribosomal ABCE1-43S pre-initiation complexes. EMBO J. *40*, e105179.

Krishnan, A., Burroughs, A. M., Iyer, L. M. and Aravind, L. (2020). Comprehensive classification of ABC ATPases and their functional radiation in nucleoprotein dynamics and biological conflict systems. Nucleic Acids Res. *48*, 10045–10075.

Krogh, A., Larsson, B., von Heijne, G. and Sonnhammer, E. L. (2001). Predicting transmembrane protein topology with a hidden Markov model: application to complete genomes. J. Mol. Biol. *305*, 567–580.

Kummer, E., Schubert, K. N., Schoenhut, T., Scaiola, A. and Ban, N. (2021). Structural basis of translation termination, rescue, and recycling in mammalian mitochondria. Mol. Cell *81*, 2566–2582.e6.

Kurland, C. G. (1960). Molecular characterization of ribonucleic acid from *Escherichia coli* ribosomes: I. Isolation and molecular weights. J. Mol. Biol. *2*, 83–91.

Kuroha, K., Zinoviev, A., Hellen, C. U. and Pestova, T. V. (2018). Release of ubiquitinated and non-ubiquitinated nascent chains from stalled mammalian ribosomal complexes by ANKZF1 and Ptrh1. Mol. Cell *72*, 286–302.e8.

Kössel, H. and RajBhandary, U. L. (1968). Studies on polynucleotides: LXXXVI. Enzymic hydrolysis of N-acylaminoacyl-transfer RNA. J. Mol. Biol. *35*, 539–560.

Lancaster, L., Kiel, M. C., Kaji, A. and Noller, H. F. (2002). Orientation of ribosome recycling factor in the ribosome from directed hydroxyl radical probing. Cell *111*, 129–140.

Laurberg, M., Asahara, H., Korostelev, A., Zhu, J., Trakhanov, S. and Noller, H. F. (2008). Structural basis for translation termination on the 70S ribosome. Nature *454*, 852–857.

Leipe, D. D., Wolf, Y. I., Koonin, E. V. and Aravind, L. (2002). Classification and evolution of P-loop GTPases and related ATPases. J. Mol. Biol. *317*, 41–72.

Lenart, J., Vimberg, V., Vesela, L., Janata, J. and Novotna, G. B. (2015). Detailed mutational analysis of Vga(A) interdomain linker: Implication for antibiotic resistance specificity and mechanism. Antimicrob. Agents Chemother. *59*, 1360–1364.

Leroy, M., Piton, J., Gilet, L., Pellegrini, O., Proux, C., Coppée, J., Figaro, S. and Condon, C. (2017). Rae1/YacP, a new endoribonuclease involved in ribosome-dependent mRNA decay in *Bacillus subtilis*. EMBO J. *36*, 1167–1181.

Li, J., Li, B., Wendlandt, S., Schwarz, S., Wang, Y., Wu, C., Ma, Z. and Shen, J. (2014). Identification of a novel *vga*(E) gene variant that confers resistance to pleuromutilins, lincosamides and streptogramin A antibiotics in staphylococci of porcine origin. J. Antimicrob. Chemoth. *69*, 919–923.

Li, W., Atkinson, G. C., Thakor, N. S., Allas, U., Lu, C.-c., Chan, K.-Y., Tenson, T., Schulten, K., Wilson, K. S., Hauryliuk, V. and Frank, J. (2013). Mechanism of tetracycline resistance by ribosomal protection protein Tet(O). Nat. Commun. *4*, 1477.

Li, X., Hirano, R., Tagami, H. and Aiba, H. (2006). Protein tagging at rare codons is caused by tmRNA action at the 3′ end of nonstop mRNA generated in response to ribosome stalling. RNA *12*, 248–255.

Ling, C. and Ermolenko, D. N. (2016). Structural insights into ribosome translocation. Wiley Interdiscip. Rev. RNA *7*, 620–636.

Liu, H., Pan, D., Pech, M. and Cooperman, B. S. (2010). Interrupted catalysis: the EF4 (LepA) effect on back-translocation. J. Mol. Biol. *396*, 1043–1052.

Loveland, A. B., Bah, E., Madireddy, R., Zhang, Y., Brilot, A. F., Grigorieff, N. and Korostelev, A. A. (2016). Ribosome•RelA structures reveal the mechanism of stringent response activation. eLife *5*, e17029.

Loveland, A. B., Demo, G., Grigorieff, N. and Korostelev, A. A. (2017). Ensemble cryo-EM elucidates the mechanism of translation fidelity. Nature *546*, 113–117.

Loveland, A. B., Demo, G. and Korostelev, A. A. (2020). Cryo-EM of elongating ribosome with EF-Tu•GTP elucidates tRNA proofreading. Nature *584*, 640–645.

Lozano, C., Aspiroz, C., Rezusta, A., Gómez-Sanz, E., Simon, C., Gómez, P., Ortega, C., Revillo, M. J., Zarazaga, M. and Torres, C. (2012). Identification of novel vga(A)-carrying plasmids and a Tn5406-like transposon in meticillin-resistant *Staphylococcus aureus* and *Staphylococcus epidermidis* of human and animal origin. Int. J. Antimicrob. Agents *40*, 306–312.

Lytvynenko, I., Paternoga, H., Thrun, A., Balke, A., Müller, T. A., Chiang, C. H., Nagler, K., Tsaprailis, G., Anders, S., Bischofs, I., Maupin-Furlow, J. A., Spahn, C. M. and Joazeiro, C. A. (2019). Alanine tails signal proteolysis in bacterial ribosome-associated quality control. Cell *178*, 76–90.e22.

Ma, C., Kurita, D., Li, N., Chen, Y., Himeno, H. and Gao, N. (2017). Mechanistic insights into the alternative translation termination by ArfA and RF2. Nature *541*, 550–553.

Maguire, B. A., Beniaminov, A. D., Ramu, H., Mankin, A. S. and Zimmermann, R. A. (2005). A protein component at the heart of an RNA machine: the importance of protein L27 for the function of the bacterial ribosome. Mol. Cell *20*, 427–435.

Malbruny, B., Werno, A. M., Murdoch, D. R., Leclercq, R. and Cattoir, V. (2011). Cross-resistance to lincosamides, streptogramins A, and pleuromutilins due to the *lsa*(C) Gene in *Streptococcus agalactiae* UCN70. Antimicrob. Agents Chemother. *55*, 1470–1474.

Manavathu, E. K., Fernandez, C. L., Cooperman, B. S. and Taylor, D. E. (1990). Molecular studies on the mechanism of tetracycline resistance mediated by Tet(O). Antimicrob. Agents Chemother. *34*, 71–77.

Margus, T., Remm, M. and Tenson, T. (2007). Phylogenetic distribution of translational GTPases in bacteria. BMC Genom. *8*, 15.

Marks, J., Kannan, K., Roncase, E. J., Klepacki, D., Kefi, A., Orelle, C., Vázquez-Laslop, N. and Mankin, A. S. (2016). Context-specific inhibition of translation by ribosomal antibiotics targeting the peptidyl transferase center. Proc. Natl. Acad. Sci. U.S.A. *113*, 12150–12155.

Marton, M. J., Vazquez de Aldana, C. R., Qiu, H., Chakraburtty, K. and Hinnebusch, A. (1997). Evidence that GCN1 and GCN20, translational regulators of GCN4, function on elongating ribosomes in activation of eIF2α kinase GCN2. Mol. Cell Biol. *17*, 4474–4489.

Mateyak, M. K., Pupek, J. K., Garino, A. E., Knapp, M. C., Colmer, S. F., Kinzy, T. G. and Dunaway, S. (2018). Demonstration of translation elongation factor 3 activity from a non-fungal species, *Phytophthora infestans*. PLoS One *13*, e0190524.

Matsuoka, M., Jánosi, L., Endou, K. and Nakajima, Y. (1999). Cloning and sequences of inducible and constitutive macrolide resistance genes in *Staphylococcus aureus* that correspond to an ABC transporter. FEMS Microbiol. Lett. *181*, 91–100.

Meir, M., Rozenblit, A., Fliger, S., Geffen, Y. and Barkan, D. (2020). EttA is likely non-essential in *Staphylococcus aureus* persistence, fitness or resistance to antibiotics. BMC Microbiol. *20*, 288.

Menninger, J. R. (1976). Peptidyl transfer RNA dissociates during protein synthesis from ribosomes of *Escherichia coli*. J. Biol. Chem. *251*, 3392–3398.

Menninger, J. R. (1979). Accumulation of peptidyl tRNA is lethal to *Escherichia coli*. J. Bacteriol. *137*, 694–696.

Mikuni, O., Ito, K., Moffat, J., Matsumura, K., McCaughan, K., Nobukuni, T., Tate, W. and Nakamura, Y. (1994). Identification of the *prfC* gene, which encodes peptide-chain-release factor 3 of *Escherichia coli*. Proc. Natl. Acad. Sci. U.S.A. *91*, 5798–5802.

Miller, J. D., Bernstein, H. D. and Walter, P. (1994). Interaction of *E. coli* Ffh/4.5S ribonucleoprotein and FtsY mimics that of mammalian signal recognition particle and its receptor. Nature *367*, 657–659.

Milman, G., Goldstein, J., Scolnick, E. and Caskey, T. (1969). Peptide chain termination III. Stimulation of *in vitro* termination. Proc. Natl. Acad. Sci. U.S.A. *63*, 183–190.

Milón, P., Maracci, C., Filonava, L., Gualerzi, C. O. and Rodnina, M. V. (2012). Real-time assembly landscape of bacterial 30S translation initiation complex. Nat. Struct. Mol. Biol. *19*, 609–615.

Moazed, D. and Noller, H. F. (1989). Interaction of tRNA with 23S rRNA in the ribosomal A, P, and E sites. Cell *57*, 585–597.

Monro, R. E. (1967). Catalysis of peptide bond formation by 50 S ribosomal subunits from *Escherichia coli*. J. Mol. Biol. *26*, 147–151.

Moody, J. E., Millen, L. and Binns, D. (2002). Cooperative, ATP-dependent association of the nucleotide binding cassettes during the catalytic cycle of ATP-binding cassette transporters. J. Biol. Chem. *277*, 21111–21114.

Moore, P. B. (2012). How should we think about the ribosome? Ann. Rev. Biophys. *41*, 1–19.

Moore, S. D. and Sauer, R. T. (2005). Ribosome rescue: tmRNA tagging activity and capacity in *Escherichia coli*. Mol. Microbiol. *58*, 456–466.

Morse, J. C., Girodat, D., Burnett, B. J., Holm, M., Altman, R. B., Sanbonmatsu, K. Y., Wieden, H.-J. and Blanchard, S. C. (2020). Elongation factor-Tu can repetitively engage aminoacyl-tRNA within the ribosome during the proofreading stage of tRNA selection. Proc. Natl. Acad. Sci. U.S.A. *117*, 3610–3620.

Murina, V., Kasari, M., Hauryliuk, V. and Atkinson, G. C. (2018). Antibiotic resistance ABCF proteins reset the peptidyl transferase centre of the ribosome to counter translational arrest. Nucleic Acids Res. *46*, 3753–3763.

Murina, V., Kasari, M., Takada, H., Hinnu, M., Saha, C. K., Grimshaw, J. W., Seki, T., Reith, M., Putrinš, M., Tenson, T., Strahl, H., Hauryliuk, V. and Atkinson, G. C. (2019). ABCF ATPases involved in protein synthesis, ribosome assembly and antibiotic resistance: structural and functional diversification across the tree of life. J. Mol. Biol. *431*, 3568–3590.

Mustafi, M. and Weisshaar, J. C. (2018). Simultaneous binding of multiple EF-Tu copies to translating ribosomes in live *Escherichia coli*. mBio *9*.

Müller, C., Crowe-McAuliffe, C. and Wilson, D. N. (2021). Ribosome rescue pathways in bacteria. Front. Microbiol. *12*, 558.

Nakagawa, S., Niimura, Y., Miura, K. I. and Gojobori, T. (2010). Dynamic evolution of translation initiation mechanisms in prokaryotes. Proc. Natl. Acad. Sci. U.S.A. *107*, 6382–6387.

Nakamoto, J. A., Evangelista, W., Vinogradova, D. S., Konevega, A. L., Spurio, R., Fabbretti, A. and Milón, P. (2021). The dynamic cycle of bacterial translation initiation factor IF3. Nucleic Acids Res. *49*, 6958–6970.

Nakane, T., Kotecha, A., Sente, A., McMullan, G., Masiulis, S., Brown, P. M. G. E., Grigoras, I. T., Malinauskaite, L., Malinauskas, T., Miehling, J., Uchański, T., Yu, L., Karia, D., Pechnikova, E. V., de Jong, E., Keizer, J., Bischoff, M., McCormack, J., Tiemeijer, P., Hardwick, S. W., Chirgadze, D. Y., Murshudov, G., Aricescu, A. R. and Scheres, S. H. W. (2020). Single-particle cryo-EM at atomic resolution. Nature *587*, 152–156.

Neubauer, C., Gillet, R., Kelley, A. C. and Ramakrishnan, V. (2012). Decoding in the absence of a codon by tmRNA and SmpB in the ribosome. Science *335*, 1366–1369.

Nissen, P., Hansen, J., Ban, N., Moore, P. B. and Steitz, T. A. (2000). The structural basis of ribosome activity in peptide bond synthesis. Science *289*, 920–930.

Nissen, P., Kjeldgaard, M., Thirup, S., Polekhina, G., Reshetnikova, L., Clark, B. F. and Nyborg, J. (1995). Crystal structure of the ternary complex of Phe-tRNA$^{\mathrm{Phe}}$, EF-Tu, and a GTP analog. Science *270*, 1464–1472.

Noller, H. F., Hoffarth, V. and Zimniak, L. (1992). Unusual resistance of peptidyl transferase to protein extraction procedures. Science *256*, 1416–1419.

Novotna, G. and Janata, J. (2006). A new evolutionary variant of the streptogramin A resistance protein, Vga(A)$_{\mathrm{LC}}$, from *Staphylococcus haemolyticus* with shifted substrate specificity towards lincosamides. Antimicrob. Agents Chemother. *50*, 4070–4076.

Nunez-Samudio, V. and Chesneau, O. (2013). Functional interplay between the ATP binding cassette Msr(D) protein and the membrane facilitator superfamily Mef(E) transporter for macrolide resistance in *Escherichia coli*. Res. Microbiol. *164*, 226–235.

Nürenberg-Goloub, E., Heinemann, H., Gerovac, M. and Tampé, R. (2018). Ribosome recycling is coordinated by processive events in two asymmetric ATP sites of ABCE1. Life Sci. Alliance *1*.

Nürenberg-Goloub, E., Kratzat, H., Heinemann, H., Heuer, A., Kötter, P., Berninghausen, O., Becker, T., Tampé, R. and Beckmann, R. (2020). Molecular analysis of the ribosome recycling factor ABCE1 bound to the 30S post-splitting complex. EMBO J. *39*, e103788.

Ogasawara, F., Kodan, A. and Ueda, K. (2020). ABC proteins in evolution. FEBS Lett. *594*, 3876–3881.

Ogle, J. M., Brodersen, D. E., Clemons, W. M., Tarry, M. J., Carter, A. P. and Ramakrishnan, V. (2001). Recognition of cognate transfer RNA by the 30S ribosomal subunit. Science *292*, 897–902.

Ohki, R., Ohki, R., Tateno, K., Tateno, K., Okada, Y., Okada, Y., Okajima, H., Okajima, H., Asai, K., Asai, K., Sadaie, Y., Sadaie, Y., Murata, M., Murata, M., Aiso, T. and Aiso, T. (2003). A bacitracin-resistant *Bacillus subtilis* gene encodes a homologue of the membrane-spanning subunit of the *Bacillus licheniformis* ABC transporter. J. Bacteriol. *185*, 51–59.

Ohki, R., Tateno, K., Takizawa, T., Aiso, T. and Murata, M. (2005). Transcriptional termination control of a novel ABC transporter gene involved in antibiotic resistance in *Bacillus subtilis*. J. Bacteriol. *187*, 5946–5954.

Ojo, K. K., Striplin, M. J., Ulep, C. C., Close, N. S., Zittle, J., Luis, H., Bernardo, M., Leitao, J. and Roberts, M. C. (2006). *Staphylococcus* efflux *msr*(A) gene characterized in *Streptococcus*, *Enterococcus*, *Corynebacterium*, and *Pseudomonas* isolates. Antimicrob. Agents Chemother. *50*, 1089–1091.

Olano, C., Rodriguez, A. M., Méndez, C. and Salas, J. A. (1995). A second ABC transporter is involved in oleandomycin resistance and its secretion by *Streptomyces antibioticus*. Mol. Microbiol. *16*, 333–343.

Oldham, M. L. and Chen, J. (2011). Snapshots of the maltose transporter during ATP hydrolysis. Proc. Natl. Acad. Sci. U.S.A. *108*, 15152–15156.

Oldham, M. L., Khare, D., Quiocho, F. A., Davidson, A. L. and Chen, J. (2007). Crystal structure of a catalytic intermediate of the maltose transporter. Nature *450*, 515–521.

O'Neill, A. J. and Chopra, I. (2006). Molecular basis of fusB-mediated resistance to fusidic acid in *Staphylococcus aureus*. Mol. Microbiol. *59*, 664–676.

O'Neill, A. J., McLaws, F., Kahlmeter, G., Henriksen, A. S. and Chopra, I. (2007). Genetic basis of resistance to fusidic acid in staphylococci. Antimicrob. Agents Chemother. *51*, 1737–1740.

Ontiveros, C., Gerardo Valadez, J., Hernández, J. and Guarneros, G. (1997). Inhibition of Escherichia coli protein synthesis by abortive translation of phage λ minigenes. J. Mol. Biol. *269*, 167–175.

Orelle, C., Mathieu, K. and Jault, J.-M. (2019). Multidrug ABC transporters in bacteria. Res. Microbiol. *170*, 381–391.

Orelle, C., Szal, T., Klepacki, D., Shaw, K. J., Vázquez-Laslop, N. and Mankin, A. S. (2013). Identifying the targets of aminoacyl-tRNA synthetase inhibitors by primer extension inhibition. Nucleic Acids Res. *41*.

Osuna, B. A., Howard, C. J., KC, S., Frost, A. and Weinberg, D. E. (2017). In vitro analysis of RQC activities provides insights into the mechanism and function of CAT tailing. eLife *6*, e27949.

Ousalem, F., Singh, S., Chesneau, O., Hunt, J. F. and Boël, G. (2019). ABC-F proteins in mRNA translation and antibiotic resistance. Res. Microbiol. *170*, 435–447.

Palade, G. E. (1955). A small particulate component of the cytoplasm. J. Biophys. Biochem. Cyt. *1*, 59–68.

Pedersen, F. S., Lund, E. and Kjeldgaard, N. O. (1973). Codon specific, tRNA dependent in vitro synthesis of ppGpp and pppGpp. Nature New Biol. *243*, 13–15.

Peschke, U., Schmidt, H., Zhang, H.-Z. and Piepersberg, W. (1995). Molecular characterization of the lincomycin-production gene cluster of *Streptomyces lincolnensis* 78-11. Mol. Microbiol. *16*, 1137–1156.

Peske, F., Rodnina, M. V. and Wintermeyer, W. (2005). Sequence of steps in ribosome recycling as defined by kinetic analysis. Mol. Cell *18*, 403–412.

Pestka, S. (1968). Studies on the formation of transfer ribonucleic acid-ribosome complexes: III. the formation of peptide bonds by ribosomes in the absence of supernatant enzymes. J. Biol. Chem. *243*, 2810–2820.

Petrychenko, V., Peng, B.-Z., Schwarzer, A. C. d. A. P., Peske, F., Rodnina, M. V. and Fischer, N. (2021). Structural mechanism of GTPase-powered ribosome-tRNA movement. Preprint doi:10.1101/2021.06.01.446629 bioRxiv.

Pettersen, E. F., Goddard, T. D., Huang, C. C., Meng, E. C., Couch, G. S., Croll, T. I., Morris, J. H. and Ferrin, T. E. (2021). UCSF ChimeraX: Structure visualization for researchers, educators, and developers. Protein Sci. *30*, 70–82.

Pisarev, A. V., Skabkin, M. A., Pisareva, V. P., Skabkina, O. V., Rakotondrafara, A. M., Hentze, M. W., Hellen, C. U. T. and Pestova, T. V. (2010). The role of ABCE1 in eukaryotic posttermination ribosomal recycling. Mol. Cell *37*, 196–210.

Pisareva, V. P., Skabkin, M. A., Hellen, C. U. T., Pestova, T. V. and Pisarev, A. V. (2011). Dissociation by Pelota, Hbs1 and ABCE1 of mammalian vacant 80S ribosomes and stalled elongation complexes. EMBO J. *30*, 1804–1817.

Pochopien, A. A., Beckert, B., Kasvandik, S., Berninghausen, O., Beckmann, R., Tenson, T. and Wilson, D. N. (2021). Structure of Gcn1 bound to stalled and colliding 80S ribosomes. Proc. Natl. Acad. Sci. U.S.A. *118*.

Polikanov, Y. S., Steitz, T. A. and Innis, C. A. (2014). A proton wire to couple aminoacyl-tRNA accommodation and peptide bond formation on the ribosome. Nat. Struct. Mol. Biol. *21*, 787–793.

Poole, E., Brown, C. and Tate, W. (1995). The identity of the base following the stop codon determines the efficiency of *in vivo* translational termination in *Escherichia coli*. EMBO J. *14*, 151–158.

Portillo, A., Ruiz-Larrea, F., Zarazaga, M., Alonso, A., Martinez, J. L. and Torres, C. (2000). Macrolide resistance genes in *Enterococcus* spp. Antimicrob. Agents Chemother. *44*, 967–971.

Potrykus, K. and Cashel, M. (2008). (p)ppGpp: still magical? Ann. Rev. Microbiol. *62*, 35–51.

Prabhakar, A., Capece, M. C., Petrov, A., Choi, J. and Puglisi, J. D. (2017). Post-termination ribosome intermediate acts as the gateway to ribosome recycling. Cell Rep. *20*, 161–172.

Preis, A., Heuer, A., Barrio-Garcia, C., Hauser, A., Eyler, D. E., Berninghausen, O., Green, R., Becker, T. and Beckmann, R. (2014). Cryoelectron microscopic structures of eukaryotic translation termination complexes containing eRF1-eRF3 or eRF1-ABCE1. Cell Rep. *8*, 59–65.

Qin, Y., Polacek, N., Vesper, O., Staub, E., Einfeldt, E., Wilson, D. N. and Nierhaus, K. H. (2006). The highly conserved LepA Is a ribosomal elongation factor that back-translocates the ribosome. Cell *127*, 721–733.

Quentin, Y., Fichant, G. and Denizot, F. (1999). Inventory, assembly and analysis of *Bacillus subtilis* ABC transport systems. J. Mol biol. *287*, 467–484.

Rae, C. D., Gordiyenko, Y. and Ramakrishnan, V. (2019). How a circularized tmRNA moves through the ribosome. Science *363*, 740–744.

Ramrath, D. J. F., Yamamoto, H., Rother, K., Wittek, D., Pech, M., Mielke, T., Loerke, J., Scheerer, P., Ivanov, P., Teraoka, Y., Shpanchenko, O., Nierhaus, K. H. and Spahn, C. M. T. (2012). The complex of tmRNA-SmpB and EF-G on translocating ribosomes. Nature *485*, 526–529.

Ranjan, N., Pochopien, A. A., Chih-Chien Wu, C., Beckert, B., Blanchet, S., Green, R., V Rodnina, M. and Wilson, D. N. (2021). Yeast translation elongation factor eEF3 promotes late stages of tRNA translocation. EMBO J. *40*, e106449.

Rao, A. R. and Varshney, U. (2001). Specific interaction between the ribosome recycling factor and the elongation factor G from *Mycobacterium tuberculosis* mediates peptidyl-tRNA release and ribosome recycling in *Escherichia coli*. EMBO J. *20*, 2977–2986.

Reynolds, E., Ross, J. I. and Cove, J. H. (2003). *Msr*(A) and related macrolide/streptogramin resistance determinants: Incomplete transporters? Int. J. Antimicrob. Agents *22*, 228–236.

Rheinberger, H. J., Sternbach, H. and Nierhaus, K. H. (1981). Three tRNA binding sites on *Escherichia coli* ribosomes. Proc. Nat. Acad. Sci. U.S.A. *78*, 5310.

Richter, R., Rorbach, J., Pajak, A., Smith, P. M., Wessels, H. J., Huynen, M. A., Smeitink, J. A., Lightowlers, R. N. and Chrzanowska-Lightowlers, Z. M. (2010). A functional peptidyl-tRNA hydrolase, ICT1, has been recruited into the human mitochondrial ribosome. EMBO J. *29*, 1116–1125.

Roberts, M. C. (2005). Update on acquired tetracycline resistance genes. FEMS Microbiol. Lett. *245*, 195–203.

Rodnina, M. V. (2018). Translation in prokaryotes. Cold Spring Harb. Perspect. Biol. *10*, a032664.

Rodnina, M. V., Korniy, N., Klimova, M., Karki, P., Peng, B.-Z., Senyushkina, T., Belardinelli, R., Maracci, C., Wohlgemuth, I., Samatova, E. and Peske, F. (2020). Translational recoding: canonical translation mechanisms reinterpreted. Nucleic Acids Res. *48*, 1056–1067.

Ross, J. I., Eady, E. A., Cove, J. H., Cunliffe, W. J., Baumberg, S. and Wootton, J. C. (1990). Inducible erythromycin resistance in staphlyococci is encoded by a member of the ATP-binding transport super-gene family. Mol. Microbiol. *4*, 1207–1214.

Ross, J. I., Farrell, A. M., Eady, E. A., Cove, J. H. and Cunliffe, W. J. (1989). Characterisation and molecular cloning of the novel macrolide-streptogramin B resistance determinant from *Staphylococcus epidermidis*. J. Antimicrob. Chemoth. *24*, 851–862.

Rosteck, P. R., Reynolds, P. A. and Hershberger, C. L. (1991). Homology between proteins controlling *Streptomyces fradiae* tylosin resistance and ATP-binding transport. Gene *102*, 27–32.

Rudra, P., Hurst-Hess, K. R., Cotten, K. L., Partida-Miranda, A. and Ghosh, P. (2020). Mycobacterial HflX is a ribosome splitting factor that mediates antibiotic resistance. Proc. Natl. Acad. Sci. U.S.A. *117*, 629–634.

Rundlet, E. J., Holm, M., Schacherl, M., Natchiar, S. K., Altman, R. B., Spahn, C. M. T., Myasnikov, A. G. and Blanchard, S. C. (2021). Structural basis of early translocation events on the ribosome. Nature *595*, 741–745.

Sands, M. K. and Roberts, R. B. (1952). The effects of a tryptophan-histidine deficiency in a mutant of *Escherichia coli*. J. Bacteriol. *63*, 505–511.

Saraste, M., Sibbald, P. R. and Wittinghofer, A. (1990). The P-loop — a common motif in ATP- and GTP-binding proteins. Trends Biochem. Sci. *15*, 430–434.

Schaub, R. E., Poole, S. J., Garza-Sánchez, F., Benbow, S. and Hayes, C. S. (2012). Proteobacterial ArfA peptides are synthesized from non-stop messenger RNAs. J. Biol. Chem. *287*, 29765–29775.

Schmeing, T. M., Huang, K. S., Strobel, S. A. and Steitz, T. A. (2005). An induced-fit mechanism to promote peptide bond formation and exclude hydrolysis of peptidyl-tRNA. Nature *438*, 520–524.

Schwarz, S., Zhang, W., Du, X.-D., Krüger, H., Feßler, A. T., Ma, S., Zhu, Y., Wu, C., Shen, J. and Wang, Y. (2021). Mobile oxazolidinone resistance genes in Gram-positive and Gram-negative bacteria. Clin. Microbiol. Rev. *34*, e0018820.

Scolnick, E., Tompkins, R., Caskey, T. and Nirenberg, M. (1968). Release factors differing in specificity for terminator codons. Proc. Natl. Acad. Sci. U.S.A. *61*, 768–774.

Selmer, M. (1999). Crystal structure of *Thermotoga maritima* ribosome recycling factor: a tRNA mimic. Science *286*, 2349–2352.

Selmer, M., Dunham, C. M., Murphy, F. V., Weixlbaumer, A., Petry, S., Kelley, A. C., Weir, J. R. and Ramakrishnan, V. (2006). Structure of the 70S ribosome complexed with mRNA and tRNA. Science *313*, 1935–1942.

Sharkey, L. K. R., Edwards, T. A. and O'Neill, A. J. (2016). ABC-F proteins mediate antibiotic resistance through ribosomal protection. mBio *7*, e01975–15.

Sharkey, L. K. R. and O'Neill, A. J. (2018). Antibiotic resistance ABC-F proteins: bringing target protection into the limelight. ACS Infect. Dis. *4*, 239–246.

Shaw, J. J. and Green, R. (2007). Two distinct components of release factor function uncovered by nucleophile partitioning analysis. Mol. Cell *28*, 458–467.

Shen, P. S., Park, J., Qin, Y., Li, X., Parsawar, K., Larson, M. H., Cox, J., Cheng, Y., Lambowitz, A. M., Weissman, J. S., Brandman, O. and Frost, A. (2015). Rqc2p and 60S ribosomal subunits mediate mRNA-independent elongation of nascent chains. Science *374*, 74–78.

Shimizu, Y. (2012). ArfA recruits RF2 into stalled ribosomes. J. Mol. Biol. *423*, 624–631.

Shimokawa-Chiba, N., Müller, C., Fujiwara, K., Beckert, B., Ito, K., Wilson, D. N. and Chiba, S. (2019). Release factor-dependent ribosome rescue by BrfA in the Gram-positive bacterium *Bacillus subtilis*. Nat. Commun. *10*, 5397.

Shine, J. and Dalgarno, L. (1974). The 3'-terminal sequence of *Escherichia coli* 16S ribosomal RNA: complementarity to nonsense triplets and ribosome binding sites. Proc. Natl. Acad. Sci. U.S.A. *71*, 1342–1346.

Shoemaker, C. J. and Green, R. (2011). Kinetic analysis reveals the ordered coupling of translation termination and ribosome recycling in yeast. Proc. Natl. Acad. Sci. U.S.A. *108*, E1392–E1398.

Shultzaberger, R. K., Bucheimer, R. E., Rudd, K. E. and Schneider, T. D. (2001). Anatomy of *Escherichia coli* ribosome binding sites. J. Mol. Biol. *313*, 215–228.

Sievers, A., Beringer, M., Rodnina, M. V. and Wolfenden, R. (2004). The ribosome as an entropy trap. Proc. Natl. Acad. Sci. U.S.A. *101*, 7897–7901.

Singh, K. V., Malathum, K. and Murray, B. E. (2001). Disruption of an *Enterococcus faecium* species-specific gene, a homologue of acquired macrolide resistance genes of staphylococci, is associated with an increase in macrolide susceptibility. Antimicrob. Agents Chemother. *45*, 263–266.

Singh, K. V., Weinstock, G. M. and Murray, B. E. (2002). An *Enterococcus faecalis* ABC homologue (Lsa) is required for the resistance of this species to clindamycin and quinupristin-dalfopristin. Antimicrob. Agents Chemother. *46*, 1845–1850.

Singh, N. S., Ahmad, R., Sangeetha, R. and Varshney, U. (2008). Recycling of ribosomal complexes stalled at the step of elongation in *Escherichia coli*. J. Mol. Biol. *380*, 451–464.

Skogerson, L. and Wakatama, E. (1976). A ribosome-dependent GTPase from yeast distinct from elongation factor 2. Proc. Natl. Acad. Sci. U.S.A. *73*, 73–76.

Spahn, C. M., Blaha, G., Agrawal, R. K., Penczek, P., Grassucci, R. A., Trieber, C. A., Connell, S. R., Taylor, D. E., Nierhaus, K. H. and Frank, J. (2001). Localization of the ribosomal protection protein Tet(O) on the ribosome and the mechanism of tetracycline resistance. Mol. Cell *7*, 1037–1045.

Spirin, A. S. (2002). Ribosome as a molecular machine. FEBS Letters *514*, 2–10.

Sprink, T., Ramrath, D. J., Yamamoto, H., Yamamoto, K., Loerke, J., Ismer, J., Hildebrand, P. W., Scheerer, P., Bürger, J., Mielke, T. and Spahn, C. M. (2016). Structures of ribosome-bound initiation factor 2 reveal the mechanism of subunit association. Sci. Adv. *2*, 1–7.

Staker, B. L., Korber, P., Bardwell, J. C. and Saper, M. A. (2000). Structure of Hsp15 reveals a novel RNA-binding motif. EMBO J. *19*, 749–757.

Stent, G. S. and Brenner, S. (1961). A genetic locus for the regulation of ribonucleic acid synthesis. Proc. Natl. Acad. Sci. U.S.A. *47*, 2005–2014.

Su, T., Izawa, T., Thoms, M., Yamashita, Y., Cheng, J., Berninghausen, O., Hartl, F. U., Inada, T., Neupert, W. and Beckmann, R. (2019). Structure and function of Vms1 and Arb1 in RQC and mitochondrial proteome homeostasis. Nature *570*, 538–542.

Su, W., Kumar, V., Ding, Y., Ero, R., Serra, A., Lee, B. S. T., Wong, A. S. W., Shi, J., Sze, S. K., Yang, L. and Gao, Y.-G. (2018). Ribosome protection by antibiotic resistance ATP-binding cassette protein. Proc. Nat. Acad. Sci. U.S.A. *115*, 5157–5162.

Sunohara, T., Jojima, K., Tagami, H., Inada, T. and Aiba, H. (2004). Ribosome stalling during translation elongation induces cleavage of mRNA being translated in *Escherichia coli*. J. Biol. Chem. *279*, 15368–15375.

Svidritskiy, E., Demo, G., Loveland, A. B., Xu, C. and Korostelev, A. A. (2019). Extensive ribosome and RF2 rearrangements during translation termination. eLife *8*, e46850.

Syroegin, E. A., Flemmich, L., Klepacki, D., Vazquez-Laslop, N., Micura, R. and Polikanov, Y. S. (2021). Structural basis for the context-specific action of classic peptidyl transferase inhibitors. Preprint doi:10.1101/2021.06.17.448903 bioRxiv.

Takanami, M. and Okamoto, T. (1963). Interaction of ribosomes and synthetic polyribonucleotides. J. Mol. Biol. *7*, 323–333.

Tanaka, N., Kinoshita, T. and Masukawa, H. (1968). Mechanism of protein synthesis inhibition by fusidic acid and related antibiotics. Biochem. Biophys. Res. Commun. *30*, 278–283.

Taniuchi, S., Miyake, M., Tsugawa, K., Oyadomari, M. and Oyadomari, S. (2016). Integrated stress response of vertebrates is regulated by four eIF2α kinases. Sci. Rep. *6*, 32886.

Tenson, T., Herrera, J. V., Kloss, P., Guarneros, G. and Mankin, A. S. (1999). Inhibition of translation and cell growth by minigene expression. J. Bacteriol. *181*, 1617–1622.

Tenson, T., Lovmar, M. and Ehrenberg, M. (2003). The mechanism of action of macrolides, lincosamides and streptogramin B reveals the nascent peptide exit path in the ribosome. J. Mol biol. *330*, 1005–1014.

Tereshchenkov, A. G., Dobosz-Bartoszek, M., Osterman, I. A., Marks, J., Sergeeva, V. A., Kasatsky, P., Komarova, E. S., Stavrianidi, A. N., Rodin, I. A., Konevega, A. L., Sergiev, P. V., Sumbatyan, N. V., Mankin, A. S., Bogdanov, A. A. and Polikanov, Y. S. (2018). Binding and action of amino acid analogs of chloramphenicol upon the bacterial ribosome. J. Mol. Biol. *430*, 842–852.

Thomas, C. and Tampé, R. (2020). Structural and mechanistic principles of ABC transporters. Ann. Rev. Biochem. *89*, 605–636.

Thomas, E. N., Kim, K. Q., McHugh, E. P., Marcinkiewicz, T. and Zaher, H. S. (2020). Alkylative damage of mRNA leads to ribosome stalling and rescue by trans translation in bacteria. eLife *9*, e61984.

Tomlinson, J. H., Thompson, G. S., Kalverda, A. P., Zhuravleva, A. and O'Neill, A. J. (2016). A target-protection mechanism of antibiotic resistance at atomic resolution: insights into FusB-type fusidic acid resistance. Sci. Rep. *6*, 19524.

Trieber, C. A., Burkhardt, N., Nierhaus, K. H. and Taylor, D. E. (1998). Ribosomal protection from tetracycline mediated by Tet(O): Tet(O) interaction with ribosomes is GTP-dependent. Biol. Chem. *379*, 847–855.

Trobro, S. and Åqvist, J. (2007). A model for how ribosomal release factors induce peptidyl-tRNA cleavage in termination of protein synthesis. Mol. Cell *27*, 758–766.

Tsai, K., Stojković, V., Lee, D. J., Young, I. D., Szal, T., Vazquez-Laslop, N., Mankin, A. S., Fraser, J. S. and Fujimori, D. G. (2021). Structural basis for context-specific inhibition of translation by oxazolidinone antibiotics. Preprint doi:10.1101/2021.08.10.455846 bioRxiv.

Tu, G. F., Reid, G. E., Zhang, J. G., Moritz, R. L. and Simpson, R. J. (1995). C-terminal extension of truncated recombinant proteins in *Escherichia coli* with a 10Sa RNA decapeptide. J. Biol. Chem. *270*, 9322–9326.

Tyzack, J. K., Wang, X., Belsham, G. J. and Proud, C. G. (2000). ABC50 interacts with eukaryotic initiation factor 2 and associates with the ribosome in an ATP-dependent manner. J. Biol. Chem. *275*, 34131–34139.

Udagawa, T., Seki, M., Okuyama, T., Adachi, S., Natsume, T., Noguchi, T., Matsuzawa, A. and Inada, T. (2021). Failure to degrade CAT-tailed proteins disrupts neuronal morphogenesis and cell survival. Cell Rep. *34*, 108599.

Ude, S., Lassak, J., Starosta, A. L., Kraxenberger, T., Wilson, D. N. and Jung, K. (2013). Translation elongation factor EF-P alleviates ribosome stalling at polyproline stretches. Science *339*, 82–85.

Uritani, M. and Miyazaki, M. (1988). Characterization of the ATPase and GTPase activities of Elongation Factor 3 (EF-3) purified from yeasts. J. Biol. Chem. *103*, 522–530.

Ushida, C., Himeno, H., Watanabe, T. and Muto, A. (1994). tRNA-like structures in 10Sa RNAs of *Mycoplasma capricolum* and *Bacillus subtilis*. Nucleic Acids Res. *22*, 3392–3396.

Vazquez de Aldana, C. R., Marton, M. J. and Hinnebusch, A. G. (1995). GCN20, a novel ATP binding cassette protein, and GCN1 reside in a complex that mediates activation of the eIF-2α kinase GCN2 in amino acid-starved cells. EMBO J. *14*, 3184–99.

Verma, M., Choi, J., Cottrell, K. A., Lavagnino, Z., Thomas, E. N., Pavlovic-Djuranovic, S., Szczesny, P., Piston, D. W., Zaher, H. S., Puglisi, J. D. and Djuranovic, S. (2019). A short translational ramp determines the efficiency of protein synthesis. Nat. Commun. *10*, 5774.

Verma, R., Reichermeier, K. M., Burroughs, A. M., Oania, R. S., Reitsma, J. M., Aravind, L. and Deshaies, R. J. (2018). Vms1 and ANKZF1 peptidyl-tRNA hydrolases release nascent chains from stalled ribosomes. Nature *557*, 446–451.

Vivanco-Domínguez, S., Bueno-Martínez, J., León-Avila, G., Iwakura, N., Kaji, A., Kaji, H. and Guarneros, G. (2012). Protein synthesis factors (RF1, RF2, RF3, RRF, and tmRNA) and peptidyl-tRNA hydrolase rescue stalled ribosomes at sense codons. J. Mol. Biol. *417*, 425–439.

Voorhees, R. M., Schmeing, T. M., Kelley, A. C. and Ramakrishnan, V. (2010). The mechanism for activation of GTP hydrolysis on the ribosome. Science *330*, 835–838.

Walker, J. E., Saraste, M., Runswick, M. J. and Gay, N. J. (1982). Distantly related sequences in the alpha- and beta-subunits of ATP synthase, myosin, kinases and other ATP-requiring enzymes and a common nucleotide binding fold. EMBO J. *1*, 945–951.

Wang, Y., Lv, Y., Cai, J., Schwarz, S., Cui, L., Hu, Z., Zhang, R., Li, J., Zhao, Q., He, T., Wang, D., Wang, Z., Shen, Y., Li, Y., Feßler, A. T., Wu, C., Yu, H., Deng, X., Xia, X. and Shen, J. (2015). A novel gene, optrA, that confers transferable resistance to oxazolidinones and phenicols and its presence in *Enterococcus faecalis* and *Enterococcus faecium* of human and animal origin. J. Antimicrob. Chemoth. *70*, 2182–2190.

Watanabe, Y., Nakamura, Y. and Ito, K. (2010). A novel class of bacterial translation factor RF3 mutations suggests specific structural domains for premature peptidyl-tRNA drop-off. FEBS Lett. *584*, 790–794.

Watson, J. D. (1963). Involvement of RNA in the synthesis of proteins. Science *140*, 17–26.

Weis, F., Bron, P., Giudice, E., Rolland, J.-P., Thomas, D., Felden, B. and Gillet, R. (2010). tmRNA-SmpB: a journey to the centre of the bacterial ribosome. EMBO J. *29*, 3810–3818.

Wendlandt, S., Lozano, C., Kadlec, K., Gómez-Sanz, E., Zarazaga, M., Torres, C. and Schwarz, S. (2013). The enterococcal ABC transporter gene *lsa*(E) confers combined resistance to lincosamides, pleuromutilins and streptogramin A antibiotics in methicillin-susceptible and methicillinresistant *Staphylococcus aureus*. J. Antimicrob. Chemoth. *68*, 473–475.

Werner, G., Hildebrandt, B., Witte, W., Murray, B. E. and Singh, K. V. (2001). The newly described msrC gene is not equally distributed among all isolates of *Enterococcus faecium*. Antimicrob. Agents Chemother. *45*, 3672–3673.

Wilson, D. N. (2014). Ribosome-targeting antibiotics and mechanisms of bacterial resistance. Nat. Rev. Microbiol. *12*, 35–48.

Wilson, D. N. (2016). The ABC of ribosome-related antibiotic resistance. mBio *7*, 16–18.

Wilson, D. N., Arenz, S. and Beckmann, R. (2016). Translation regulation via nascent polypeptide-mediated ribosome stalling. Curr. Opin. Struct. Biol. *37*, 123–133.

Wilson, D. N., Hauryliuk, V., Atkinson, G. C. and O'Neill, A. J. (2020). Target protection as a key antibiotic resistance mechanism. Nat. Rev. Microbiol. *18*, 637–648.

Wilson, D. N., Schluenzen, F., Harms, J. M., Yoshida, T., Ohkubo, T., Albrecht, R., Buerger, J., Kobayashi, Y. and Fucini, P. (2005). X-ray crystallography study on ribosome recycling: the mechanism of binding and action of RRF on the 50S ribosomal subunit. EMBO J. *24*, 251–260.

Wohlgemuth, I., Pohl, C., Mittelstaet, J., Konevega, A. L. and Rodnina, M. V. (2011). Evolutionary optimization of speed and accuracy of decoding on the ribosome. Philos. Trans. R. Soc. Lond., B, Biol. Sci. *366*, 2979–2986.

Wurtmann, E. J. and Wolin, S. L. (2009). RNA under attack: cellular handling of RNA damage. Crit. Rev. Biochem. Mol. biol. *44*, 34–49.

Yip, K. M., Fischer, N., Paknia, E., Chari, A. and Stark, H. (2020). Atomic-resolution protein structure determination by cryo-EM. Nature *587*, 157–161.

Zaher, H. S. and Green, R. (2011). A primary role for release factor 3 in quality control during translation elongation in *Escherichia coli*. Cell *147*, 396–408.

Zavialov, A. V., Hauryliuk, V. V. and Ehrenberg, M. (2005). Splitting of the posttermination ribosome into subunits by the concerted action of RRF and EF-G. Mol. Cell *18*, 675–686.

Zeng, F., Chen, Y., Remis, J., Shekhar, M., Phillips, J. C., Tajkhorshid, E. and Jin, H. (2017). Structural basis of co-translational quality control by ArfA and RF2 bound to ribosome. Nature *541*, 554–557.

Zhang, Y., Mandava, C. S., Cao, W., Li, X., Zhang, D., Li, N., Zhang, Y., Zhang, X., Qin, Y., Mi, K., Lei, J., Sanyal, S. and Gao, N. (2015). HflX is a ribosome-splitting factor rescuing stalled ribosomes under stress conditions. Nat. Struct. Mol. Biol. *22*, 906–913.

Zhong, E. D., Bepler, T., Berger, B. and Davis, J. H. (2021). CryoDRGN: reconstruction of heterogeneous cryo-EM structures using neural networks. Nature Methods *18*, 176–185.

7 Appendix

7.1 Auflistung der verwendeten Gefahrenstoffe

Gefahrstoff	H- und P-Sätze
2-mercaptoethanol	H: 301+331, 310, 315, 317, 318, 361d, 373, 410 P: 201, 262, 280, 301+310+330, 302+352+310, 305+351+338+310 
Imidazol	H: 360D, 302, 314 P: 201, 280, 301+330+331, 305+351+338, 308+310 

7.2 Structure of the VmlR ABCF protein in complex with the 70S ribosome, supplementary material

PNAS
www.pnas.org

Supplementary Information for

Structural basis for antibiotic resistance mediated by the *Bacillus subtilis* ABCF ATPase VmlR

Caillan Crowe-McAuliffe, Michael Graf, Paul Huter, Hiraku Takada, Maha Abdelshahid, Jiří Nováček, Victoriia Murina, Gemma C. Atkinson, Vasili Hauryliuk, Daniel N. Wilson

Daniel N. Wilson
Email: Daniel.Wilson@chemie.uni-hamburg.de

This PDF file includes:

MATERIALS AND METHODS

Protein expression and purification

VmlR-EQ$_2$ in pET21b was synthesized by Eurofins. The resulting sequence encoded for a protein identical to GenBank record WP_003234144.1, except for the presence of an N-terminal hexahistidine tag and with glutamates 129 and 432 mutated to glutamines. *E. coli* BL21 (DE3) was used for protein expression. An 800 mL culture was grown at 37°C to OD_{600} ~0.5, and protein expression was induced 1 mM IPTG for 5 h at 22°C. Cells were harvested at 8,000 × *g* for 10 min at 4°C. All subsequent steps were performed at 4°C or on ice. The pellet was washed with 50 mM sodium-phosphate (pH 8.0), 300 mM NaCl, and stored at −80°C. The pellet was thawed and resuspended in 30 mL buffer A (20 mM HEPES/KOH [pH 7.8], 200 mM NH_4Ac, 10 mM $Mg(OAc)_2$, 5 mM 2-mercaptoethanol) with 300 mM NaCl, protease inhibitor cocktail (Complete ultra EDTA-free, Roche), and 0.2 µL DNase I (Thermo). Cells were lysed with three passages through an EmulsiFlex-C3 cell homogeniser (AVESTIN, Inc, Ottawa, Canada) and the lysate was centrifuged at 15,000 × *g* for 10 min. Tween 20 was added to a concentration of 0.01% and the supernatant was applied to 0.5 mL pre-washed cobalt resin (TALON, Clontech). After binding for 90 min with gentle agitation, the resin was washed with 150 mL wash buffer (buffer A with 300 mM NaCl, 10 mM imidazole, and 5 mM 2-mercaptoethanol). Protein was eluted in 1 mL fractions with buffer A with 300 mM imidazole. Elution fractions 1-4 were centrifuged at 21,000 × *g* for 10 min, the supernatants pooled, and the resulting fraction purified by gel filtration over a HiPrep 16/600 75 pg column (GE Healthcare). The buffer used for gel filtration was buffer A supplemented with 0.5 mM EDTA. Elution fractions were centrifuged at 21,000 × *g* for 10 min, concentrated in a centrifugal concentrator (Ultra 4, 10 kDa MWCO, Amicon) and aliquots of the supernatant were snap-frozen in liquid N_2 and stored at -80°C.

Generation and purification of ErmDL-SRC

The ErmDL-SRC was generated based on the disome approach, as previously described (1, 2). The *2XermDL* construct contained a T7 promoter followed by a strong ribosome binding site (RBS) spaced by 7 nucleotides (nts) to the ATG start codon of the first *ermDL* cistron. A linker of 22 nts separated the stop codon of the first *ermDL* cistron and the start codon of the second *ermDL* cistron. The linker also comprised the strong RBS 7 nts upstream of the ATG start codon of the second *ermDL* cistron, enabling initiation of translation independent from the first *ermDL* cistron. With the exception of an R8K mutation, each *ermDL* cistron encoded amino acids 1-14 corresponding to the ErmDL leader peptide (Entry code P62188) present on the macrolide resistance plasmid pE194. The complete sequence of *2XermDL* construct is: 5′-*TAATACGACTCACTATAGGG*AGTTTTATAA**GGAGG**AAAAAATATGACACACTC
AATGAGA**CTT**AAGTTCCCAACTTTGAACCAGTAAAGTTTTATAA**GGAGG**AAA
AAATATGACACACTCAATGAGA**CTT**AAGTTCCCAACTTTGAACCAGTAA-3′
(T7 promoter, italics; RBS, bold; ErmDL ORF, shaded grey with CTT codon in P-site of stalled ribosome shown in bold; annealing site for complementary DNA oligonucleotide, underlined).

In vitro translation of the *ermDL* construct was performed using purified *Bacillus subtilis* 70S and the PURExpress delta ribosome Kit (NEB). Translation reactions were

analyzed on sucrose density gradients (10-55% sucrose in buffer containing 50 mM HEPES-KOH, pH 7.4, 100 mM KOAc, 25 mM $Mg(OAc)_2$, 6 mM β-mercaptoethanol, 100 μM telithromycin and 1x Complete EDTA-free Protease Inhibitor cocktail (Roche)) by centrifugation at 154,693 × *g* (SW-40 Ti, Beckman Coulter) for 3 h at 4°C. For ErmDL-SRC purification, disome fractions were collected using a Gradient Station (Biocomp) with an Econo UV Monitor (Biorad) and a FC203B Fraction Collector (Gilson). Purified ErmDL-SRC disomes were concentrated by centrifugation at 88,760 × *g* for 4 h at 4°C (TLA120.2 rotor, Beckman Coulter). To obtain monosomes of the ErmDL-SRC, a short DNA oligonucleotide (5′-ttcctccttataaaact-3′, Metabion) was annealed to the linker between the *ermDL* cistrons, generating a DNA-RNA hybrid that could be cleaved by RNase H (NEB) treatment in buffer A at 25°C for 1 h. After cleavage of the disomes, ErmDL-SRC monosomes were again purified and concentrated by centrifugation at 88,760 × *g* for 4 h at 4°C (TLA120.2 rotor, Beckman Coulter).

Grid preparation

Samples containing 2.5 pmol ErmDL-SRC, 12.5 pmol VmlR-EQ_2, 100 μM ATP, 10 μM telithromycin were prepared in 20 μL of buffer B (20 mM HEPES/KOH [pH 7.8], 100 mM NH_4Ac, 10 mM $Mg(OAc)_2$, 5 mM 2-mercaptoethanol). N-dodecyl β-D-maltoside was added to a final concentration of 0.1 % (v/v). (The final reaction contained 0.035% DMSO from the telithromycin stock). Reactions were incubated for 15 min at 22°C and then held at 4°C as samples were applied to 2 nm precoated Quantifoil R3/3 holey-carbon-supported grids and vitrified using a Vitrobot Mark IV (FEI, Netherlands).

Data collection and Processing

Images were collected with a Titan Krios TEM equipped with a Falcon III direct electron detector (FEI, Netherlands) at 300 kV using a pixel size of 1.061 Å and an under-defocus range of −0.8 to −1.6 μm. Micrographs were recorded as 39 frames, each with a dose of 1.425 $e^-/Å^2$. Micrographs were aligned and dose-weighted with MotionCor2 (3) and the CTF of every micrograph was determined using GCTF (4). Template-free particle picking was performed using Gautomatch (http://www.mrc-lmb.cam.ac.uk/kzhang/) resulting in 286,701 particles. Manual inspection of thrice-decimated particle after 2D classification resulted in 159,722 particles that were further used for 3D-refinement using an *E. coli* ribosome filtered to 70 Å as an initial reference. The resulting volume was used as a reference for 3D classification yielding four different classes. The class containing VmlR and P-tRNA was subjected to focused sorting, using a spherical mask encompassing the P- and E-sites. Volumes of interest were then refined using undecimated particles. Final reconstructions were corrected for the modulation transfer function and sharpened by applying a negative B-factor estimated by RELION-2.1 (5). The average resolution of reconstructions was determined using the "gold-standard" criterion (FSC = 0.143) (6). ResMap was used for local resolution estimation (7). The final volumes were locally filtered using SPHIRE (8).

Modelling

A homology model of VmlR was created using the deposited structure of ABCF protein EttA (PDB ID 3J5S) (9) as a template for SWISS-MODELLER (10). The homology model was fitted into density with UCSF Chimera (11) using the command 'fit in map',

and manually adjusted with Coot (12). The well-resolved ARD helices could be modelled *de novo*, while residues 486–547 of the CTE of VmlR were modelled as polyalanine. The model of the *B. subtilis* 70S ribosome was derived from PDB ID 3J9W (13). For the less well resolved L1 protein, a homology model was created based on the *E. coli* L1 protein (PDB ID 5AFI) (14) using SWISS-MODELLER (10). The resulting model was rigid body fitted into the cryo-EM density using UCSF Chimera (11). ATP molecules and the *E. coli* Leu-tRNA were obtained from PDB ID 6BHU (15) and PDB ID 4WSM (16), respectively, and subjected to refinement as necessary. The atomic coordinates were refined using phenix.real_space refine (17) with restraints obtained by phenix.secondary_structure_restraints (17). Statistics for the model were obtained using Molprobity (18).

Figure preparation

Figures showing atomic models and electron densities were generated using either UCSF Chimera (11) or PyMol Molecular Graphic Systems (Schrödinger) and assembled with Adobe Illustrator. Growth curves were prepared with Igor Pro.

Construction of *B. subtilis* strains

Strain VHB5 [*trpC2* Δ*vmlR*] was constructed using the marker-free deletion technique (19) with wild type *B. subtilis* strain 168. First, three linear ≈500 nt-long DNA fragments were amplified by PCR using genomic DNA as a template: one located upstream of the *vmlR* ORF (primers VmlR-A-F and VmlR-A-R; see **Table S2** for sequences), one downstream of the *vmlR* ORF (primers VmlR-B-F and VmlR-B-R) and one within the *vmlR* ORF (primers VmlR-C-F and VmlR-C-R). Second, the TMO310 *mazF* cassette was amplified by PCR using primers chpA-R and pAPNC-F. The cassette contains i) the *mazF* toxin ORF under the control of an IPTG-inducible promoter (P_{spac}), ii) the *lacI* ORF for expression of Lac repressor controlling the P_{spac}, and iii) the spectinomycin resistance marker (*spc*). All four PCR products described above were used simultaneously as the template for PCR amplification using primers VmlR-A-F and VmlR-C-R. The resultant long PCR fragment was used to transform the *B. subtilis* strain 168. *vmlR* deletion mutants were selected by spectinomycin resistance, followed by a second selection step on IPTG plates to identify marker-less *vmlR* deletion mutants lacking the *mazF* toxin ORF, yielding the VHB5 strain.

To construct the VHB44 [trpC2 Δ*vmlR thrC::*$P_{hyspnak}$*-vmlR kmR*] strain untagged VmlR under the control of an IPTG-inducible P*hy-spank* promotor, a PCR product encoding *vmlR* was PCR-amplified from the VHp62 plasmid (pAPNC-*vmlR-HTF*) using the primers PhyvmlR_F and PhyvmlR_R. The second PCR fragment encoding a kanamycin-resistance marker, a polylinker downstream of the P*hy-spank* promoter and the *lac* repressor ORF – all inserted in the middle of the *thrC* gene – was PCR-amplified from pHT009 plasmid using primers pHT002_F and pHT002_R. The two fragments were ligated using the NEBuilder HiFi DNA Assembly master mix (New England BioLabs, Ipswich, MA) yielding the pHT009-*vmlR* plasmid which was used to transform the VHB5 [*trpC2* Δ*vmlR*] strain. Selection for kanamycin resistance yielded the desired VHB44 strain.

A QuikChange Multi Site-Directed Mutagenesis Kit (Agilent Technologies) was used to mutate the *vmlR* gene expressed from the pHT009-*vmlR* plasmid. Sequences of

the primers used to generate plasmids pHT009-*vmlRF237A* (F237A), pHT009-*vmlRF237V* (F237V), and pHT009-*vmlRΔCTE* (491STOPx2) are provided in the **Table S2**. To generate pHT009-*vmlRΔCTE,* two consecutive stop codons (TGATAA) were introduced after codon 491 (GAA). VHB5 [*trpC2* Δ*vmlR*] strain was transformed with the plasmids listed above yielding upon selection for kanamycin resistance strains [*trpC2* Δ*vmlR thrC::*$P_{hyspnak}$*-vmlRF237A kmR*], VHB89 [*trpC2* Δ*vmlR thrC::*$P_{hyspnak}$*-vmlRF237V kmR*], and VHB88 [*trpC2* Δ*vmlR thrC::*$P_{hyspnak}$*-vmlRΔCTE kmR*].

Antibiotic sensitivity testing

B. subtilis strains were pre-grown on LB plates either supplemented with 1 mM IPTG (VHB44 strain) or lacking the inducer (wt 168 and VHB5 strains) overnight at 30˚C. Fresh individual colonies were used to inoculate filtered LB medium in the presence and absence of 1 mM IPTG, and OD_{600} adjusted to 0.01. The cultures were seeded on a 100-well honeycomb plate (Oy Growth Curves AB Ltd, Helsinki, Finland), and plates incubated in a Bioscreen C (Labsystems, Helsinki, Finland) at 37°C with continuous medium shaking. After 90 min ($OD_{600} \approx 0.1$), antibiotics were added and growth was followed for an additional 6 hours.

Sequence alignments

To compare the sequence of the ARD domain among VmlR orthologs and other ABCF AREs, we generated a multiple sequence alignment using MAFFT v7.164b (20). VmlR-like proteins in the ARE2 family of ABCFs were retrieved from the ABCF database (21); VgaALC, LsaA, SalA, MsrE and OptrA were downloaded from The Comprehensive Antibiotic Resistance Database (CARD) (22), and EttA from Uniprot (23).

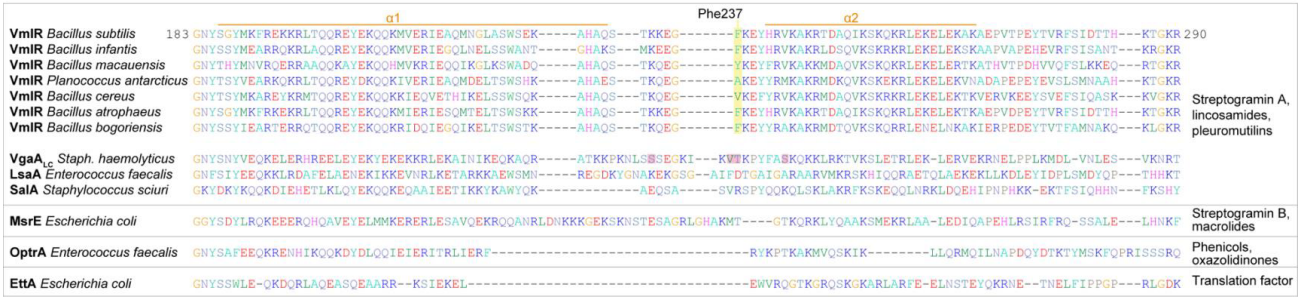

Figure S1. Sequence alignment of selected ARE-ABCF proteins. VmlR, a selection of uncharacterized proteins closely related to vmlR, as well as other AREs with known specificities, were aligned with MAFFT as described in the methods. A portion of an alignment spanning the interdomain linker region was selected for analysis. Helices α1 and α2 and Phe237 from *Bacillus subtilis* VmlR are indicated. Accession identifiers for sequences from top to bottom: *Bacillus subtilis* VmlR (Uniprot P39115), *Bacillus infantis NRRL B-14911* (NCBI YP_008607708.1), *Bacillus macauensis ZFHKF-1* (NCBI WP_007203347.1), *Planococcus antarcticus DSM 14505* (NCBI WP_006828374.1), *Bacillus cereus m1293* (NCBI WP_000675965.1), *Bacillus atrophaeus 1942* (NCBI YP_003971957.1), *Bacillus bogoriensis ATCC BAA-922* (NCBI WP_026673438.1), VgaALC [*Staphylococcus haemolyticus*] (CARD gb|ABH10964.1), MsrE [*Escherichia coli*] (CARD gb|YP_724476.1), LsaA [*Enterococcus faecalis*] (CARD gb|AAT46077.1), SalA [*Staphylococcus sciuri subsp. sciuri*] (CARD gb|AGN74946), OptrA [*Enterococcus faecalis*] (CARD gb|AKA86814)

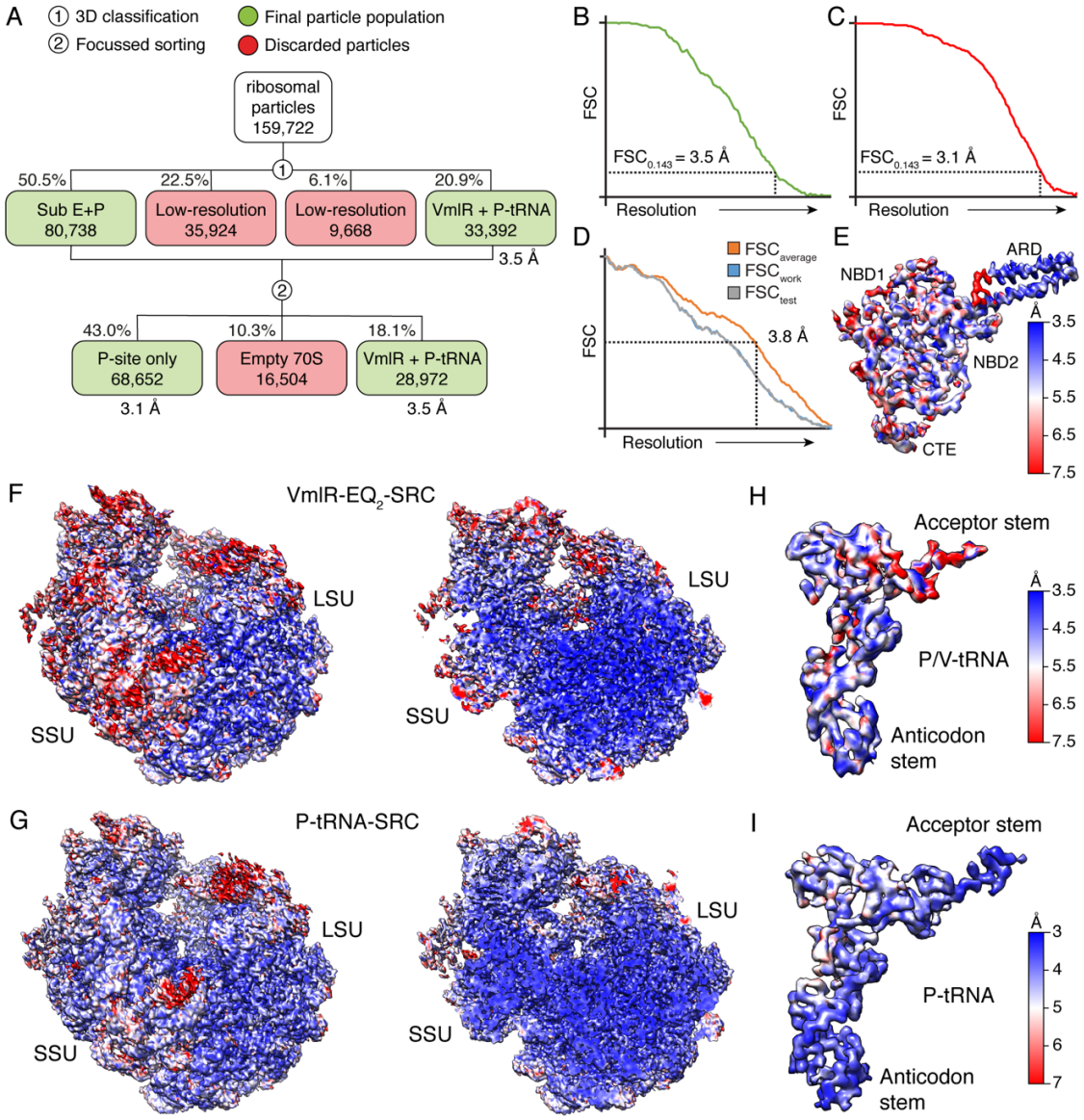

Figure S2. Processing of the cryo-EM data of VmlR-ribosome complex. (**A**) Following 2D classification, 159,722 ribosomal particles were subjected to 3D classification, sorting the particles into four distinct classes, with one defined population containing VmlR and P/V-tRNA (20.9%, 33,392 particles), a population with sub-stoichiometric P-tRNA and two poorly resolved subpopulations that were discarded (red). Focused sorting was implemented yielding three classes, one bearing P-tRNA only (60.2%, 68,652 particles), one vacant 70S class (14.5%, 16,504 particles) and a defined population containing VmlR and P/V-tRNA (25.4%, 28,972 particles). (**B-C**) Fourier Shell Correlation ($FSC_{0.143}$; green) of the (**B**) VmlR-SRC (green) and (**C**) P-tRNA-SRC (red), with the resolution at FSC=0.143 indicated with a dashed line (**D**) $FSC_{average}$ (orange) and self and cross-validated correlations FSC_{work} (red) and FSC_{test} (green), respectively, shown for VmlR-70S complex. (**E**) Isolated density of VmlR from the cryo-EM map of the VmlR-ribosome complex colored according to local resolution. (**F**) Overview and (**G**) transverse section of the cryo-EM map of the VmlR-SRC colored

according to local resolution. (**H-I**) Isolated density of (**H**) P/V-tRNA from the VmlR-SRC and (**I**) P-tRNA from the P-tRNA-SRC colored according to local resolution. (**A**) Following 2D classification, 159,722 ribosomal particles were subjected to 3D classification, sorting the particles into four distinct classes, with one defined population containing VmlR and P/V-tRNA (20.9%, 33,392 particles), a population with sub-stoichiometric P-tRNA and two poorly resolved subpopulations that were discarded (red). Focused sorting was implemented yielding three classes, one bearing P-tRNA only (60.2%, 68,652 particles), one vacant 70S class (14.5%, 16,504 particles) and a defined population containing VmlR and P/V-tRNA (25.4%, 28,972 particles). (**B-C**) Fourier Shell Correlation ($FSC_{0.143}$; green) of the (**B**) VmlR-SRC (green) and (**C**) P-tRNA-SRC (red), with the resolution at FSC=0.143 indicated with a dashed line (**D**) $FSC_{average}$ (orange) and self and cross-validated correlations FSC_{work} (red) and FSC_{test} (green), respectively, shown for VmlR-70S complex. (**E**) Isolated density of VmlR from the cryo-EM map of the VmlR-ribosome complex colored according to local resolution. (**F**) Overview and (**G**) transverse section of the cryo-EM map of the VmlR-SRC colored according to local resolution. (**H-I**) Isolated density of (**H**) P/V-tRNA from the VmlR-SRC and (**I**) P-tRNA from the P-tRNA-SRC colored according to local resolution.

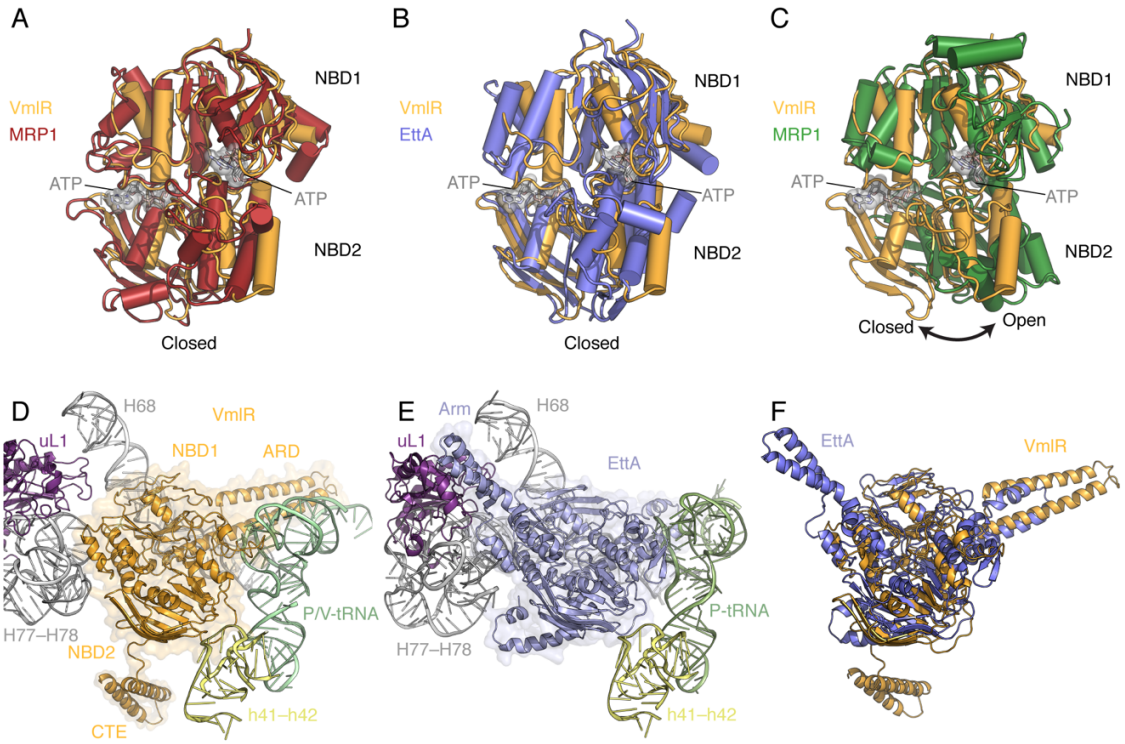

Figure S3. Conformation of the VmlR NBDs with respect to other ABC proteins. (**A-C**) Alignment (based on NBD1) of the closed conformation ABC domains of VmlR (orange) with (**A**) the closed conformations of multi-drug transporter MRP1 (red, PDB ID 6BHU) (15), (**B**) EttA (blue, PDB ID 3J5S) (9) as well as (**C**) the open conformation observed for ABCE1 (green, PDB ID 5LL6) (24). (**D-F**) Comparison of the binding site of VmlR (**D**) and EttA (**E**) on the ribosome. (F) Superimposition of ribosome-bound VmlR (orange) and EttA (blue) from (**D**) and (**E**), respectively.

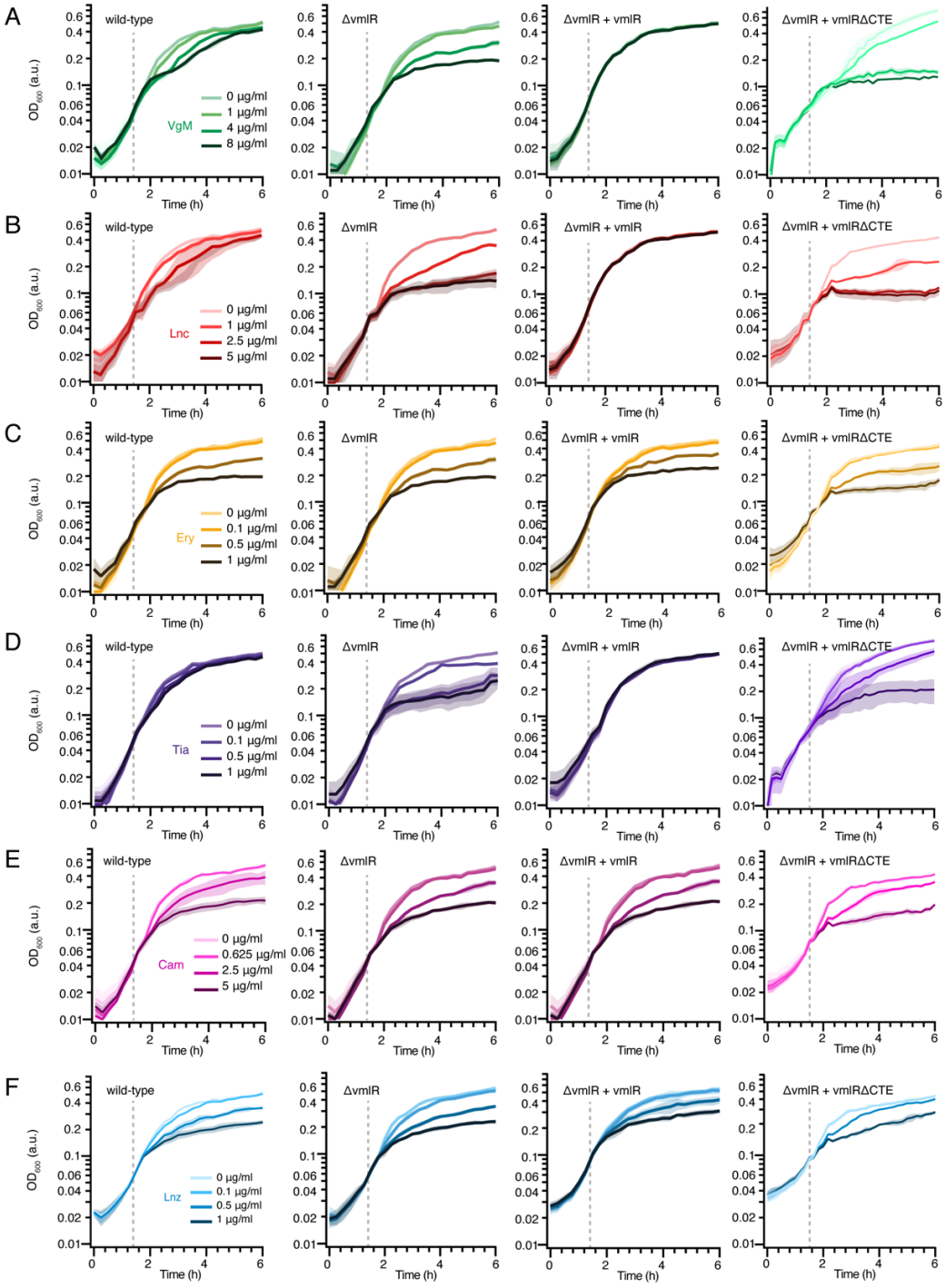

Figure S4. Antibiotic resistance conferred by VmlR and VmlRΔCTE *in vivo*. (**A-F**) Growth curves of wild-type *B. subtilis*, *vmlR*-knockout (Δ*vmlR*) alone, and complemented by wildtype VmlR (Δ*vmlR* + *vmlR*) VmlR-ΔCTE grown in the presence of increasing concentrations of (**A**) virginiamycin M1 (VgM), (**B**) lincomycin (Lnc), (**C**) erythromycin (Ery), (**D**) tiamulin (Tia), (**E**) chloramphenicol (Cam) and (**F**) linezolid (Lnz). Cells were diluted to an OD_{600} value of 0.01 and grown in LB (with IPTG for the

complemented cells) at 37°C with shaking. After 90 minutes antibiotics were added at the indicated concentrations (dashed line) and growth was measured for a further 6 h.

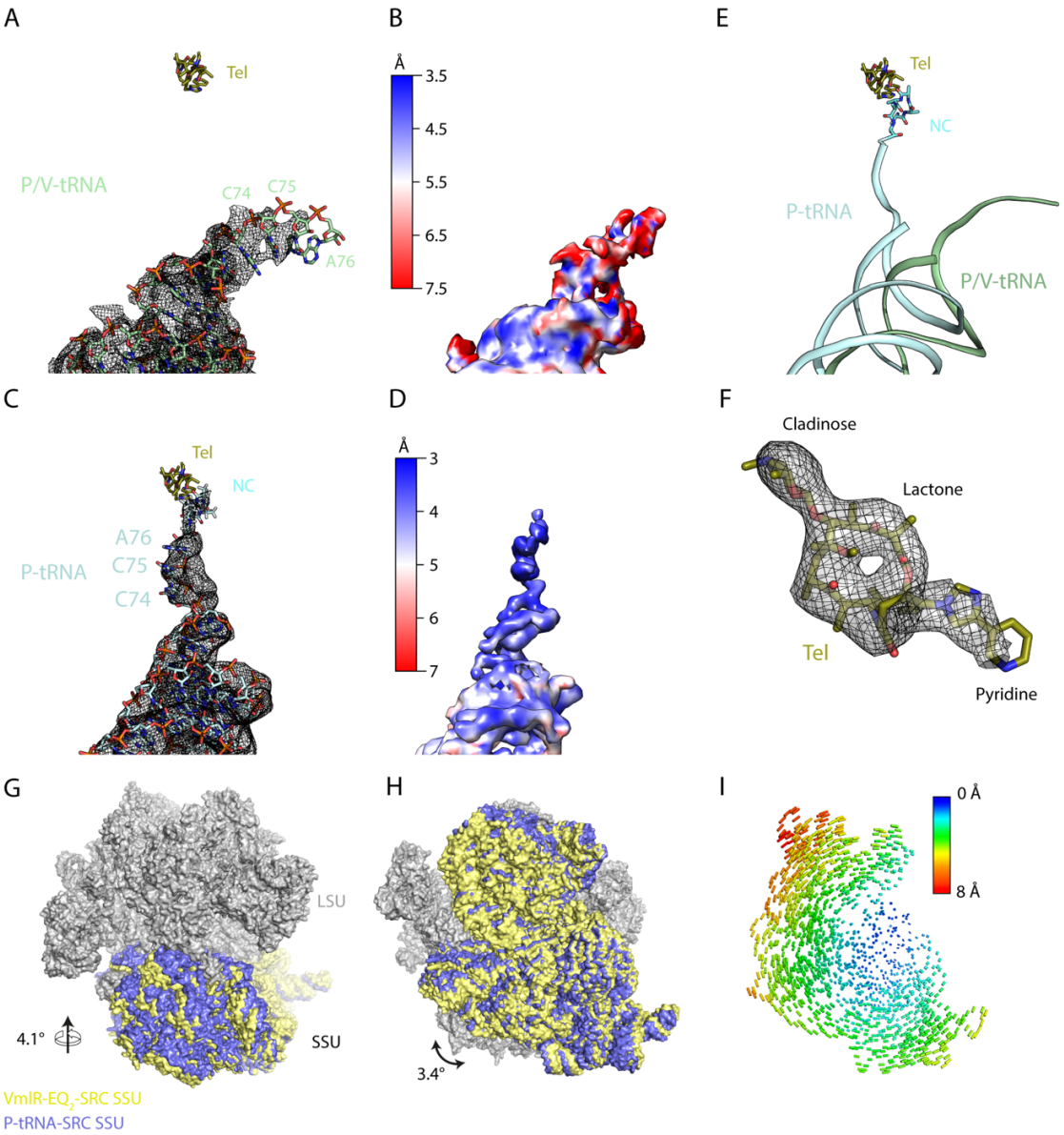

Figure S5. VmlR induces a P/V-site tRNA and subunit rotation. (**A**) Isolated cryo-EM electron density (grey mesh) for the P/V-tRNA (model in green sticks) from the VmlR-EQ_2-SRC. (**B**) Isolated cryo-EM electron density for the P/V-tRNA, as in (A), but coloured according to local resolution. (**C**) Isolated cryo-EM electron density (grey mesh) for the P-tRNA (model in cyan sticks) and ErmDL nascent chain (NC model in cyan sticks) from the P-tRNA-SRC. (**D**) Isolated cryo-EM electron density for the P-tRNA, as in (**C**), but colored according to local resolution. (**E**) Superimposition of P/V-tRNA (green ribbon) and ErmBL nascent chain (cyan) with P-tRNA (cyan ribbon). In (**A-E**), the binding site of telithromycin (Tel) is shown for reference. (**F**) Isolated cryo-EM electron density (grey mesh) for telithromycin (Tel, khaki sticks) from the P-tRNA-SRC, with cladinose, lactone ring and pyridine heterocycle indicated. (**G-H**) Alignment based on the LSU (grey) of the structures of the VmlR-EQ2-SRC (SSU, yellow) and P-tRNA-SRC (blue) revealing a (**G**) 4.1° swivel of the SSU head and (**H**) 3.4° rotation of the SSU

body. (**I**) Illustration of movement of the SSU between the VmlR-EQ2-SRC and P-tRNA-SRC. The length and color of the lines correspond to the degree of movement between each phosphate group in of the SSU between the VmlR-EQ2-SRC and P-tRNA-SRC structures. The view is the same as in (**H**).

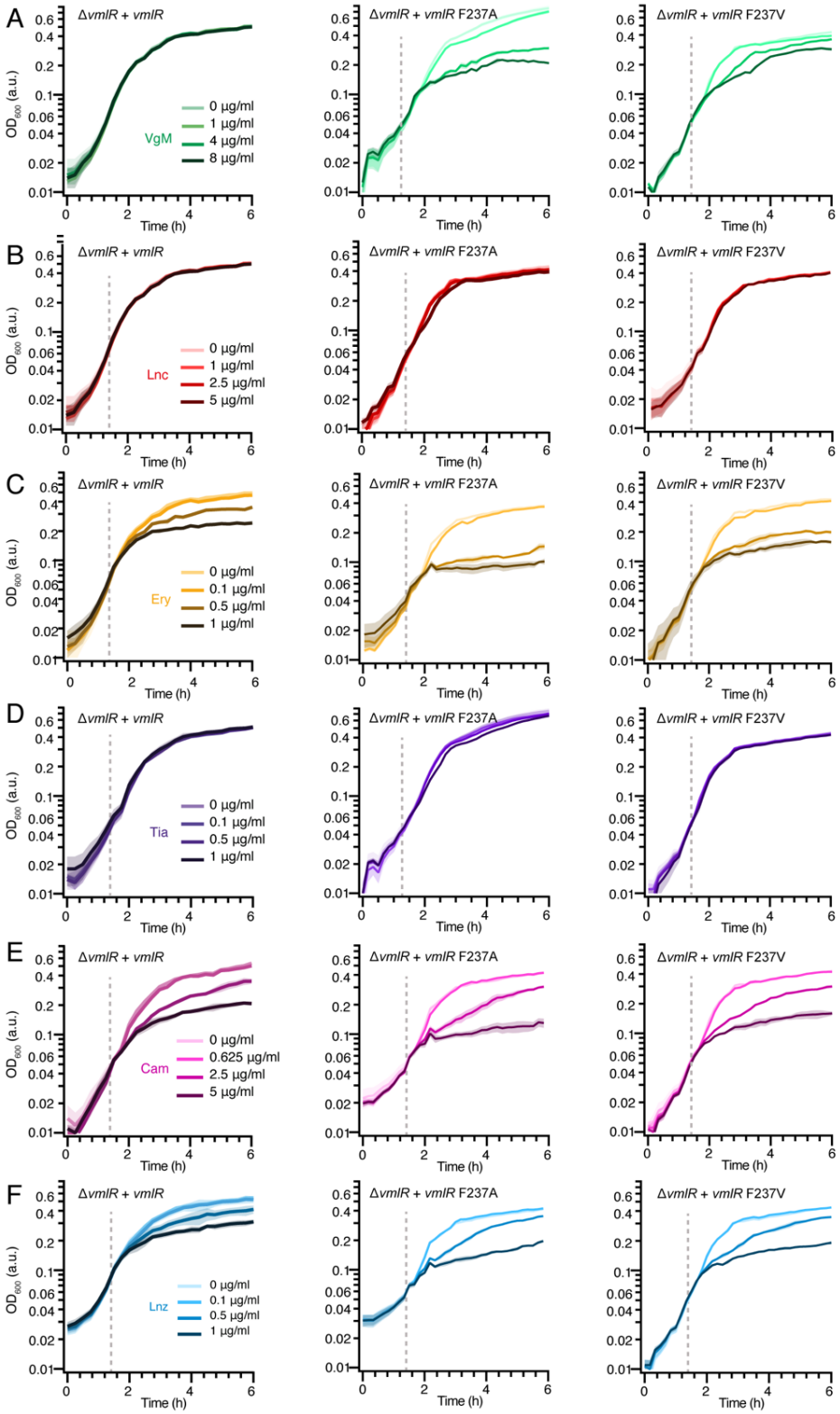

Figure S6. Antibiotic resistance conferred by VmlR variants *in vivo*. (**A-F**) Growth curves of *vmlR*-knockout (Δ*vmlR*) complemented by wildtype VmlR (Δ*vmlR* + *vmlR*, same panels as in Figure S4), or VmlR variants VmlR-F237A or VmlR-F237V grown in

the presence of increasing concentrations of (**A**) virginiamycin M1 (VgM), (**B**) lincomycin (Lnc), (**C**) erythromycin (Ery), (**D**) tiamulin (Tia), (**E**) chloramphenicol (Cam) and (**F**) linezolid (Lnz). Cells were diluted to an OD_{600} value of 0.01 and grown in LB (with IPTG for the complemented cells) at 37°C with shaking. After 90 minutes antibiotics were added at the indicated concentrations (dashed line) and growth was measured for a further 6 h.

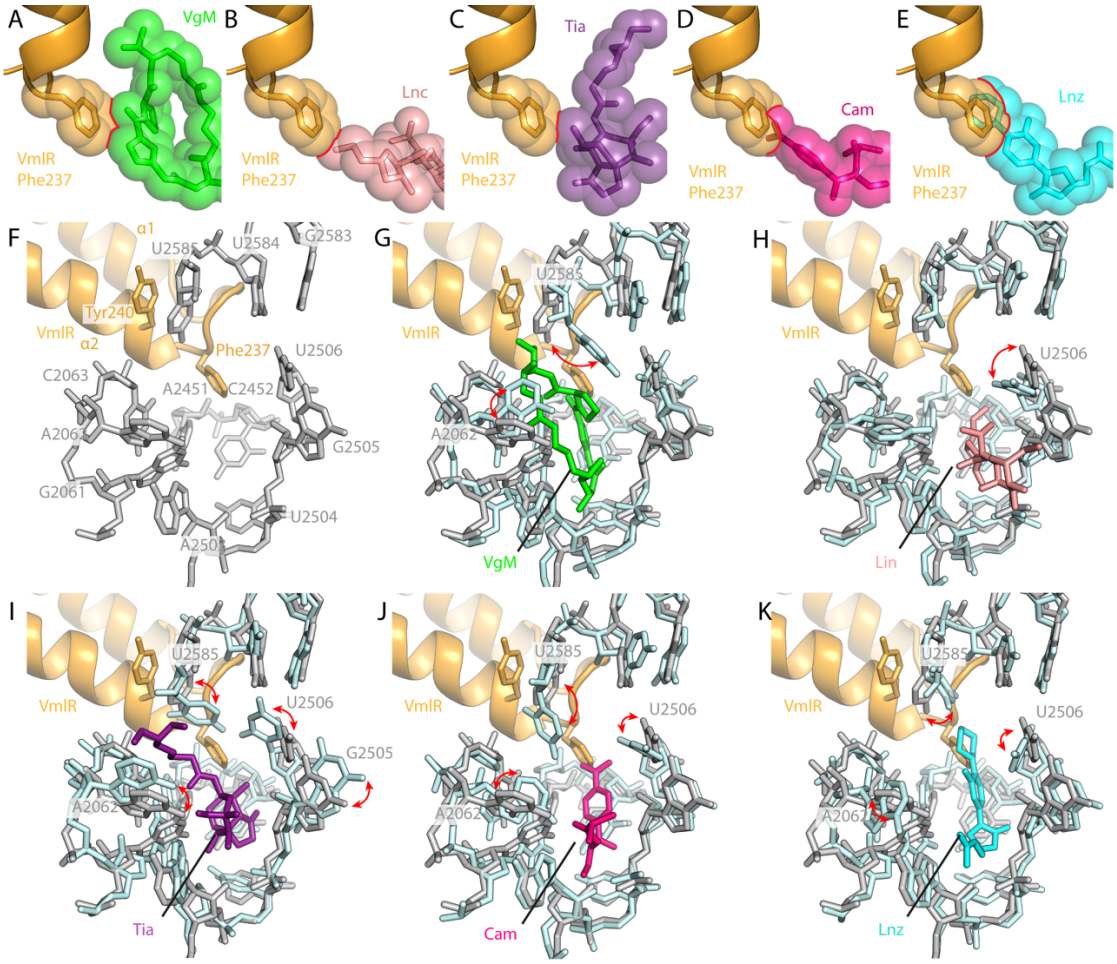

Figure S7. Conformation of the PTC in the presence of VmlR and antibiotics. (**A-E**) Zoom showing steric clash between Phe237 of VmlR with (**A**) virginiamycin M (VgM, green), (**B**) lincomycin (Lnc, salmon), (**C**) tiamulin (Tia, purple), (**D**) chloramphenicol (Cam, pink) and (**E**) linezolid (Lnz, cyan). (**F**) The conformation of selected 23S rRNA nucleotides (grey sticks) at the PTC in the presence of VmlR (orange). Tyr240 within the ARD of VmlR stacks upon U2585. (**G-K**) Superimposition of (**F**) with 23S rRNA nucleotides (cyan) that comprise the binding site of (**G**) virginiamycin M (VgM, green, PDB ID 1YIT) (25), (**H**) lincomycin (Lin, pink, PDB ID 5HKV) (26) and (**I**) tiamulin (Tia, purple, PDB ID 1XBP) (27), (**J**) chloramphenicol (Cam, pink, PDB ID 4V7U) (28), and (**K**) linezolid (Lnz, cyan, PDB ID 3DLL) (29). Conformational differences of 23S rRNA nucleotides between VmlR and antibiotic structures are highlighted with red arrows. Note that for (B) lincomycin (Lin, pink, PDB ID 5HKV) (26), the nucleobase of U2585 is not present in the model.

Table S1. Cryo-EM data collection, refinement and validation statistics

	VmlR-SRC (EMD ID EMD-0177, PDB 6HA8)	P-tRNA-SRC (EMD ID EMD-0176, PDB 6HA1)
Data collection		
Microscope	FEI Titan Krios	FEI Titan Krios
Camera	Falcon III	Falcon III
Magnification	131,951	131,951
Voltage (kV)	300	300
Electron dose (e^{-}/Å^2)	55.5	55.5
Defocus range (μm)	-0.8 to -1.6	-0.8 to -1.6
Pixel size (Å)	1.061	1.061
Initial particles (no.)	159,722	159,722
Final particles (no.)	33,392	68,652
Model composition		
Nonhydrogen atoms	146,414	140,834
Protein residues	6,053	5,300
RNA bases	4,610	4,622
Refinement		
Average resolution (Å)	3.5	3.1
Map CC (around atoms)	0.77	0.79
Map CC (whole unit cell)	0.75	0.79
Map sharpening *B* factor (Å^2)	-88.20	-88.14
R.m.s. deviations		
Bond lengths (Å)	0.010	0.007
Bond angles (°)	1.3	1.1
Validation		
MolProbity score	1.96 (100th percentile for structures 3.50Å ± 0.25Å)	1.92 (100th percentile for structures 3.10Å ± 0.25Å)
Clashscore	7.68 (80th percentile for structures ≥ 3Å)	7.12 (98th percentile for structures ≥ 2.85Å)
Poor rotamers (%)	0.87%	0.90%
Ramachandran plot		
Favored (%)	90.36 %	90.67 %
Allowed (%)	9.15 %	8.77 %
Disallowed (%)	0.49 %	0.56 %

Table S2. Primers used for construction of *B. subtilis* strains

VmlR-A-F	CATATGAAATACCGCAAAACAAG
VmlR-A-R	CAATGCCGCTTGAACTTTCTCCC-CCATATCCCTCGCTTTAAAGGGAG
VmlR-B-F	GGGAGAAAGTTCAAGCGGCATTG
VmlR-B-R	GCTTGAGTCAATTCCGCTGTCGCATAACGTCAGGAACTTGGACG
VmlR-C-F	CAAAATTAACGTACTGATTGGGTAGGATCCGCGGCTTGAGGATCAGACGCT GATTG
VmlR-C-R	CTGTCCCAGAATGATGTTCAGTAATG
chpA-R	CGCGGATCCTACCCAATCAGTACGTTAATTTTG
pAPNC-F	CGACAGCGGAATTGACTCAAGC
PhyvmlR_F	CGGATAACAATTAAGCTTAGTCGACGAAGGAGAGAGCGATAATGGCCGGC AAAGAGATCGTAACA
PhyvmlR_R	GTTTCCACCGAATTAGCTTGCATGCTTAGTCTTTTTTGTCTTGATGATCCAGC TCTTTTATTC
pHT002_R	GTCGACTAAGCTTAATTGTTATCCGCTCACAATTACACACATTATGCC
pHT002_F	GCATGCAAGCTAATTCGGTGGAAACGAGGTCATC
F237A	CTCAATCGACGAAAAAGGAAGGGGCTAAAGAATATCACCGGGTAAAAG
F237V	TCGACGAAAAAGGAAGGGGTTAAAGAATATCACCGGG
491STOPx2	CAGTTAAACGACGTTCCTTCAGAATGATAAGAGCGGGAGGAGC

References

1. Arenz S, *et al.* (2014) Drug sensing by the ribosome induces translational arrest via active site perturbation. *Mol Cell* 56(3):446-452.
2. Arenz S, *et al.* (2014) Molecular basis for erythromycin-dependent ribosome stalling during translation of the ErmBL leader peptide. *Nat Commun* 5:3501.
3. Zheng SQ, *et al.* (2017) MotionCor2: anisotropic correction of beam-induced motion for improved cryo-electron microscopy. *Nat Methods* 14(4):331-332.
4. Zhang K (2016) Gctf: Real-time CTF determination and correction. *J Struct Biol* 193(1):1-12.
5. Kimanius D, Forsberg BO, Scheres SH, & Lindahl E (2016) Accelerated cryo-EM structure determination with parallelisation using GPUs in RELION-2. *Elife* 5.
6. Scheres SH & Chen S (2012) Prevention of overfitting in cryo-EM structure determination. *Nat Methods* 9(9):853-854.
7. Kucukelbir A, Sigworth FJ, & Tagare HD (2014) Quantifying the local resolution of cryo-EM density maps. *Nat Methods* 11(1):63-65.
8. Moriya T, *et al.* (2017) High-resolution single particle analysis from electron cryo-microscopy images using SPHIRE. *J Vis Exp* (123).
9. Chen B, *et al.* (2014) EttA regulates translation by binding the ribosomal E site and restricting ribosome-tRNA dynamics. *Nat Struct Mol Biol* 21(2):152-159.
10. Bienert S, *et al.* (2017) The SWISS-MODEL Repository—new features and functionality. *Nucleic Acids Res* 45(D1):D313-D319.
11. Pettersen EF, *et al.* (2004) UCSF Chimera - A visualization system for exploratory research and analysis. *J Comput Chem* 25(13):1605-1612.
12. Emsley P & Cowtan K (2004) Coot: Model-building tools for molecular graphics. *Acta Crystallographica Section D - Biological Crystallography* 60:2126-2132.
13. Sohmen D, *et al.* (2015) Structure of the *Bacillus subtilis* 70S ribosome reveals the basis for species-specific stalling. *Nat Commun* 6:6941.
14. Fischer N, *et al.* (2015) Structure of the *E. coli* ribosome-EF-Tu complex at <3 Å resolution by C-corrected cryo-EM. *Nature* 520(7548):567-570.
15. Johnson ZL & Chen J (2018) ATP binding enables substrate release from Multidrug Resistance Protein 1. *Cell* 172(1-2):81-89 e10.
16. Rozov A, Demeshkina N, Westhof E, Yusupov M, & Yusupova G (2015) Structural insights into the translational infidelity mechanism. *Nat Commun* 6:7251.
17. Adams PD, *et al.* (2010) PHENIX: a comprehensive Python-based system for macromolecular structure solution. *Acta Crystallogr D Biol Crystallogr* 66(Pt 2):213-221.
18. Chen VB, *et al.* (2010) MolProbity: all-atom structure validation for macromolecular crystallography. *Acta Crystallogr D Biol Crystallogr* 66(Pt 1):12-21.
19. Morimoto T, Ara K, Ozaki K, & Ogasawara N (2011) A simple method for introducing marker-free deletions in the *Bacillus subtilis* genome. *Methods Mol Biol* 765:345-358.

20. Katoh K & Standley DM (2013) MAFFT multiple sequence alignment software version 7: improvements in performance and usability. *Mol Biol Evol* 30(4):772-780.
21. Murina V, Kasari M, Reith M, Hauryliuk V, & Atkinson GC (2017) ABCF ATPases involved in protein synthesis, ribosome assembly and antibiotic resistance: structural and functional diversification across the tree of life. *bioRvix*: 10.1101/220046. Posted November 16, 2017.
22. Jia B*, et al.* (2017) CARD 2017: expansion and model-centric curation of the comprehensive antibiotic resistance database. *Nucleic Acids Res*:gkw1004.
23. Consortium U (2018) UniProt: the universal protein knowledgebase. *Nucleic Acids Res* 45(5):2699.
24. Karcher A, Schele A, & Hopfner KP (2008) X-ray structure of the complete ABC enzyme ABCE1 from *Pyrococcus abyssi*. *J Biol Chem* 283(12):7962-7971.
25. Tu D, Blaha G, Moore P, & Steitz T (2005) Structures of MLS_BK antibiotics bound to mutated large ribosomal subunits provide a structural explanation for resistance. *Cell* 121(2):257-270.
26. Matzov D*, et al.* (2017) Structural insights of lincosamides targeting the ribosome of *Staphylococcus aureus*. *Nucleic Acids Res* 45(17):10284-10292.
27. Schlunzen F, Pyetan E, Fucini P, Yonath A, & Harms J (2004) Inhibition of peptide bond formation by pleuromutilins: the structure of the 50S ribosomal subunit from *Deinococcus radiodurans* in complex with tiamulin. *Mol Microbiol* 54(5):1287-1294.
28. Dunkle JA, Xiong L, Mankin AS, & Cate JH (2010) Structures of the *Escherichia coli* ribosome with antibiotics bound near the peptidyl transferase center explain spectra of drug action. *Proc Natl Acad Sci U S A* 107(40):17152-17157.
29. Wilson DN*, et al.* (2008) The oxazolidinone antibiotics perturb the ribosomal peptidyl-transferase center and effect tRNA positioning. *Proc Natl Acad Sci U S A* 105(36):13339-13344.

7.3 Structures of the LsaA, $VgaA_{LC}$, and VgaL ABCF protein in complex with the 70S ribosome, supplementary material

SUPPLEMENTARY DATA FOR

Structural basis of ABCF-mediated resistance to pleuromutilin, lincosamide, and streptogramin A antibiotics in Gram-positive pathogens

Caillan Crowe-McAuliffe[1,#], Victoriia Murina[2,3,#], Kathryn Jane Turnbull[2,3], Marje Kasari[4] Merianne Mohamad[5], Christine Polte[1], Hiraku Takada[2,3], Karolis Vaitkevicius[2,3], Jörgen Johansson[2,3], Zoya Ignatova[1], Gemma C. Atkinson[2], Alex J. O'Neill[5], Vasili Hauryliuk[2,3,4,6,*], Daniel N. Wilson[1,*]

[1] Institute for Biochemistry and Molecular Biology, University of Hamburg, Martin-Luther-King-Platz 6, 20146 Hamburg, Germany.

[2] Department of Molecular Biology, Umeå University, 90187 Umeå, Sweden.

[3] Laboratory for Molecular Infection Medicine Sweden (MIMS), Umeå University, 90187 Umeå, Sweden.

[4] University of Tartu, Institute of Technology, 50411 Tartu, Estonia.

[5] Astbury Centre for Structural Molecular Biology, School of Molecular & Cellular Biology, Faculty of Biological Sciences, University of Leeds, Leeds LS2 9JT, UK.

[6] Department of Experimental Medical Science, Lund University, 221 00 Lund, Sweden.

[#] These authors contributed equally.

*Correspondence to: Daniel.Wilson@chemie.uni-hamburg.de, vasili.hauryliuk@med.lu.se.

Supplementary Figures

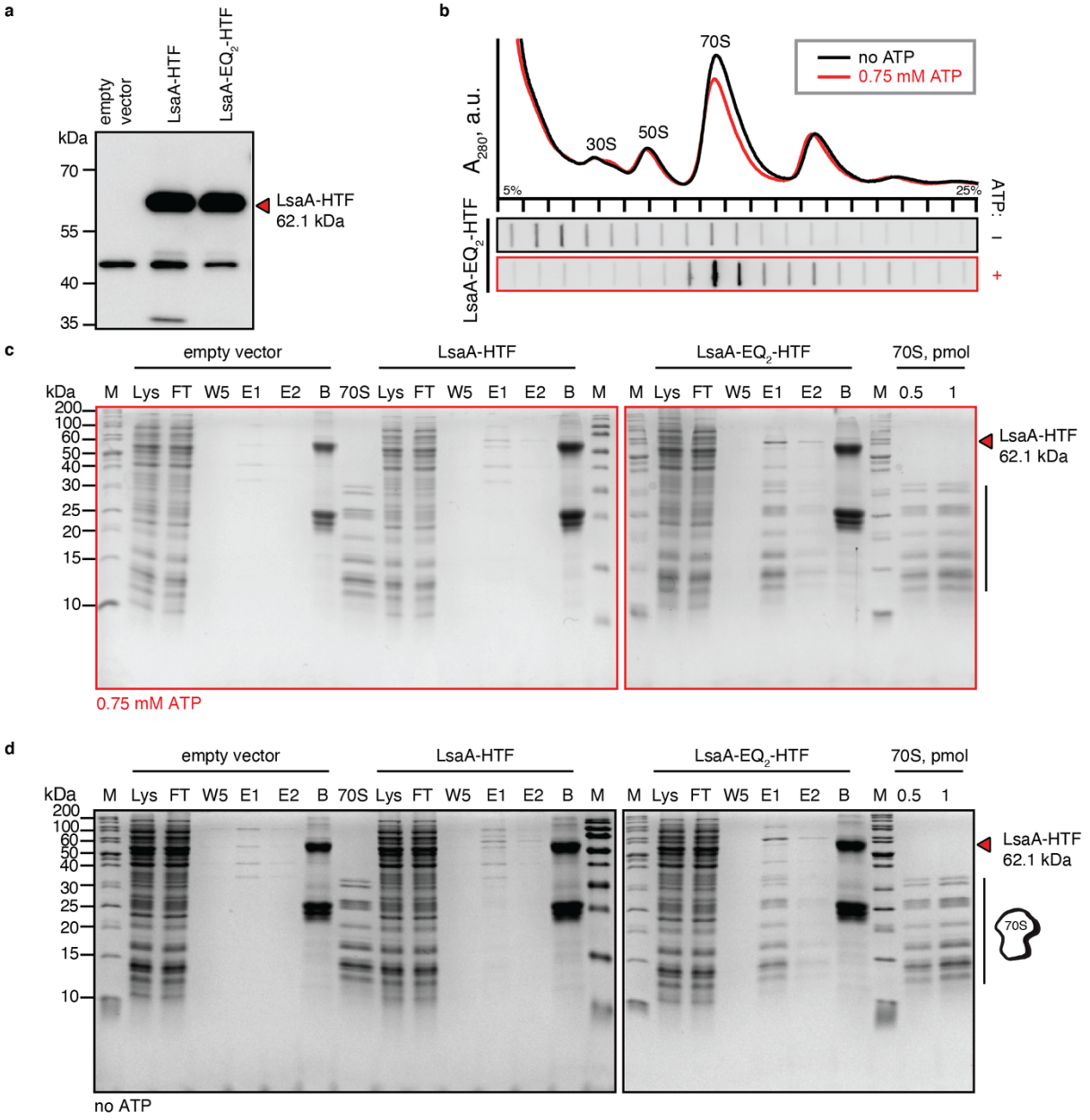

Figure S1. Characterization of *E. faecalis* LsaA interactions with ribosomes and preparation of samples for cryo-EM. a, b Polysome profiles and immunoblot analyses of C-terminally His_6-TEV-$FLAG_3$-tagged (HTF) ATPase-deficient (EQ_2) LsaA-EQ_2 ectopically expressed in Δ*lsaA E. faecalis* TX5332. **a** Specificity of α-$FLAG_3$ detection assessed by probing whole-lysate samples resolved on SDS-PAGE. The immunoprecipitation was repeated at least once. **b** Sucrose gradient centrifugation followed by slot-plot detection. Experiments were performed both in the presence or absence of 0.75 mM ATP in gradients. **c, d** Affinity purification of wild-type and EQ_2 *E. faecalis* LsaA-HTF ectopically expressed in TX5332 *E. faecalis*. Pull-down experiments were performed either in the presence **c** or absence **d** of 0.75 mM ATP using clarified lysates of *E. faecalis* either transformed with empty pCIE vector (background control), expressing *E. faecalis* LsaA-HTF (VHp100) or

expressing *E. faecalis* LsaA-EQ_2-HTF (VHp149). Samples: M: molecular weight marker; Lys: 2 µL of clarified lysate, FT: 2 µL of flow-through; W5: 10 µL of last wash before specific elution; E1: 10 µL of the first elution with $FLAG_3$ peptide; E2: 10 µL of the second elution with $FLAG_3$ peptide; B: 10 µL of SDS-treated post-elution anti-FLAG beads; 70S: purified *E. faecalis* 70S ribosomes. The samples were resolved on 15% SDS-PAGE gel. The 0.75 mM ATP *E. faecalis* LsaA-EQ_2-HTF pulldown sample was used for further cryo-EM and tRNA array analysis. Source data are provided as a Source Data file.

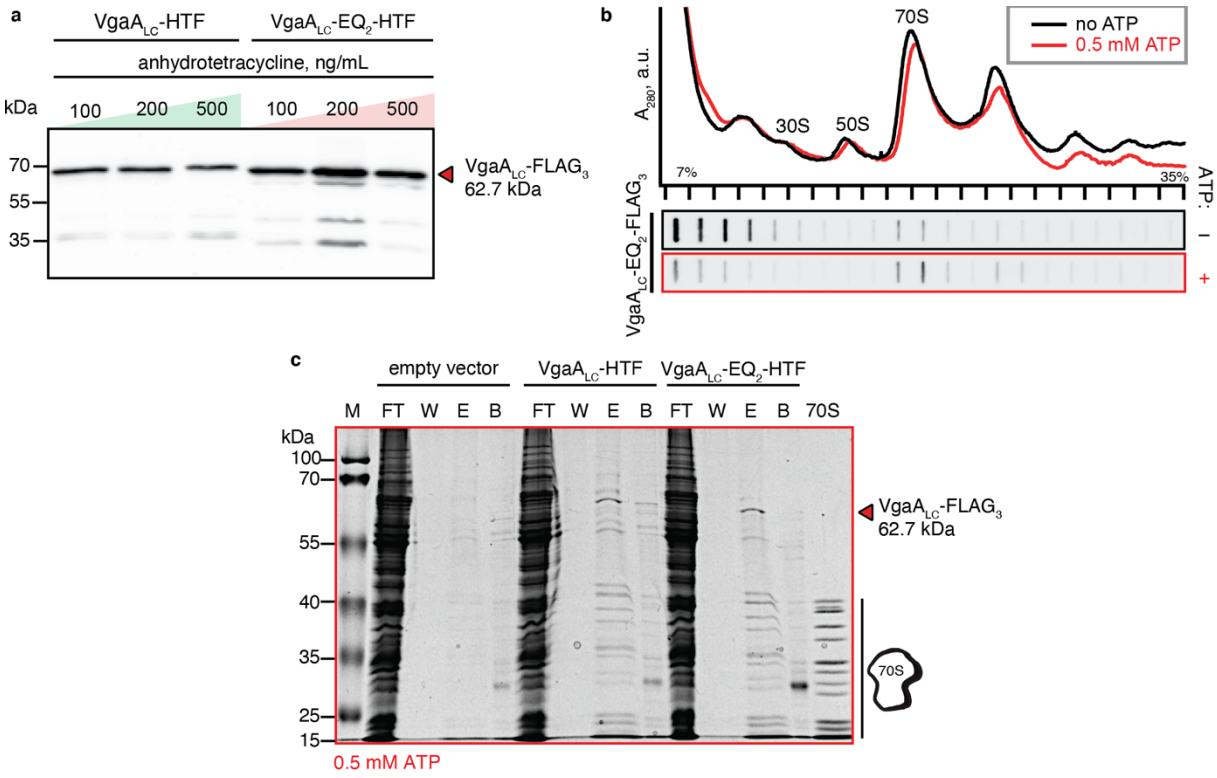

Figure S2. Characterization of *S. haemolyticus* VgaA$_{LC}$ interactions with ribosomes and preparation of samples for cryo-EM reconstructions. a Specificity of α-FLAG$_3$ detection assessed by probing whole-lysate samples resolved on SDS-PAGE. The immunoprecipitation was repeated at least once. **b** Polysome profiles and immunoblot analyses of FLAG$_3$-tagged *S. haemolyticus* VgaA$_{LC}$-EQ$_2$ ectopically expressed in wild-type SH-1000 *S. aureus*. Experiments were performed both in the presence or absence of 0.5 mM ATP in gradients **c** Affinity purification of wild-type and EQ$_2$ *S. haemolyticus* VgaA$_{LC}$-FLAG$_3$ ectopically expressed in SH-1000 *S. aureus*. Immunoprecipitations were performed in the presence of 0.5 mM ATP and the samples were resolved on a 15% polyacrylamide gel by SDS-PAGE. Samples: M: 2 µL of molecular weight marker; FT: 2 µL of flow-through, W: 10 µL of last wash before specific elution; E: 10 µL of elution with FLAG$_3$ peptide; B: 2 µL of SDS-treated post-elution anti-FLAG beads; 70S: 1 pmol of purified *S. aureus* 70S ribosomes. The 0.5 mM ATP *S. haemolyticus* VgaA$_{LC}$-EQ$_2$-HTF pulldown sample was used for cryo-EM reconstructions. Source data are provided as a Source Data file.

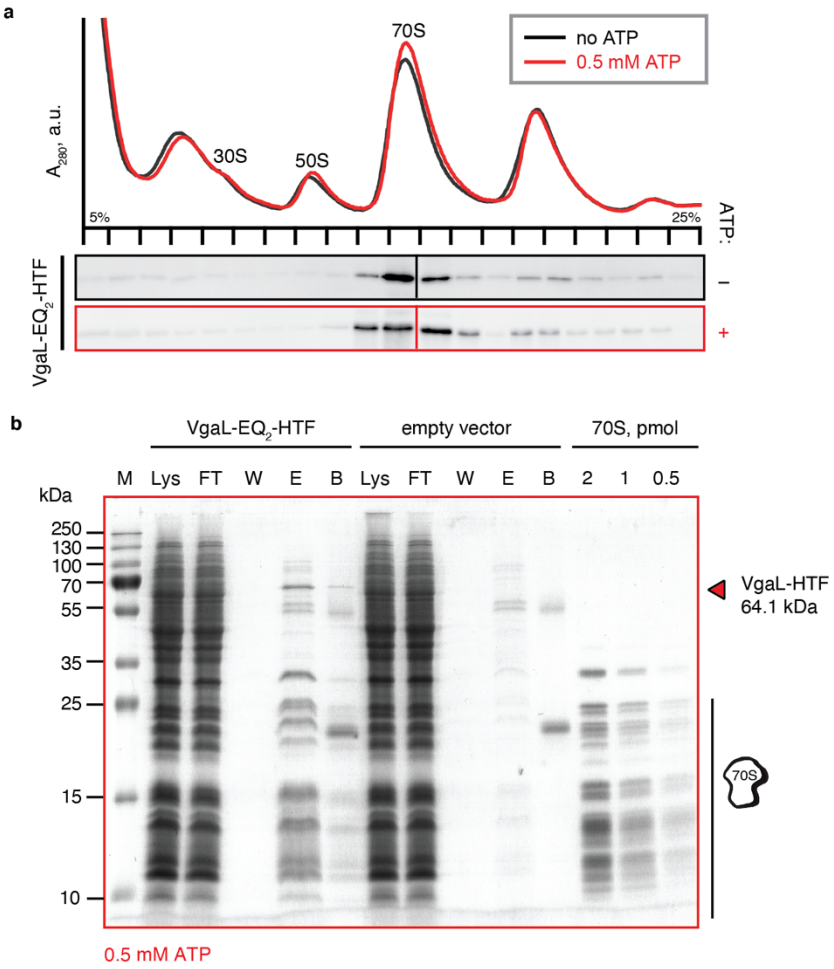

Supplementary Figure 3. Characterization of *L. monocytogenes* VgaL (Lmo0919) interactions with ribosomes and preparation of samples for cryo-EM reconstructions. (**a**) Polysome profiles and immunoblot analyses of HTF-tagged *L. monocytogenes* VgaL-EQ_2 (Lmo0919-EQ_2) ectopically expressed in wild-type EGD-e *L. monocytogenes*. Experiments were performed both in the presence or absence of 0.5 mM ATP in gradients. Note that all the samples derive from the same experiment and that gels and blots were processed in parallel. The immunoprecipitation was repeated at least once. (**b**) Affinity purification of *L. monocytogenes* VgaL-EQ_2 ectopically expressed in EGD-e *L. monocytogenes*. Pull-down experiments were performed in the presence of 0.5 mM ATP using clarified lysates of *L. monocytogenes* transformed with empty integrative pIMK3 vector (background control), expressing VgaL-HTF (VHp692) or expressing VgaL-EQ_2-HTF (VHp149). Samples: M: 2 µL of molecular weight marker; FT: 2 µL of flow-through; W: 10 µL of last wash before specific elution; E: 10 µL of elution with $FLAG_3$ peptide; B: 2 µL of SDS-treated post-elution anti-FLAG beads; 70S: purified *B. subtilis* 70S ribosomes, the samples were resolved on 15 % SDS-PAGE gel. The 0.5 mM ATP *L. monocytogenes* VgaL-EQ_2-HTF pulldown sample was used for cryo-EM reconstructions. Source data are provided as a Source Data file.

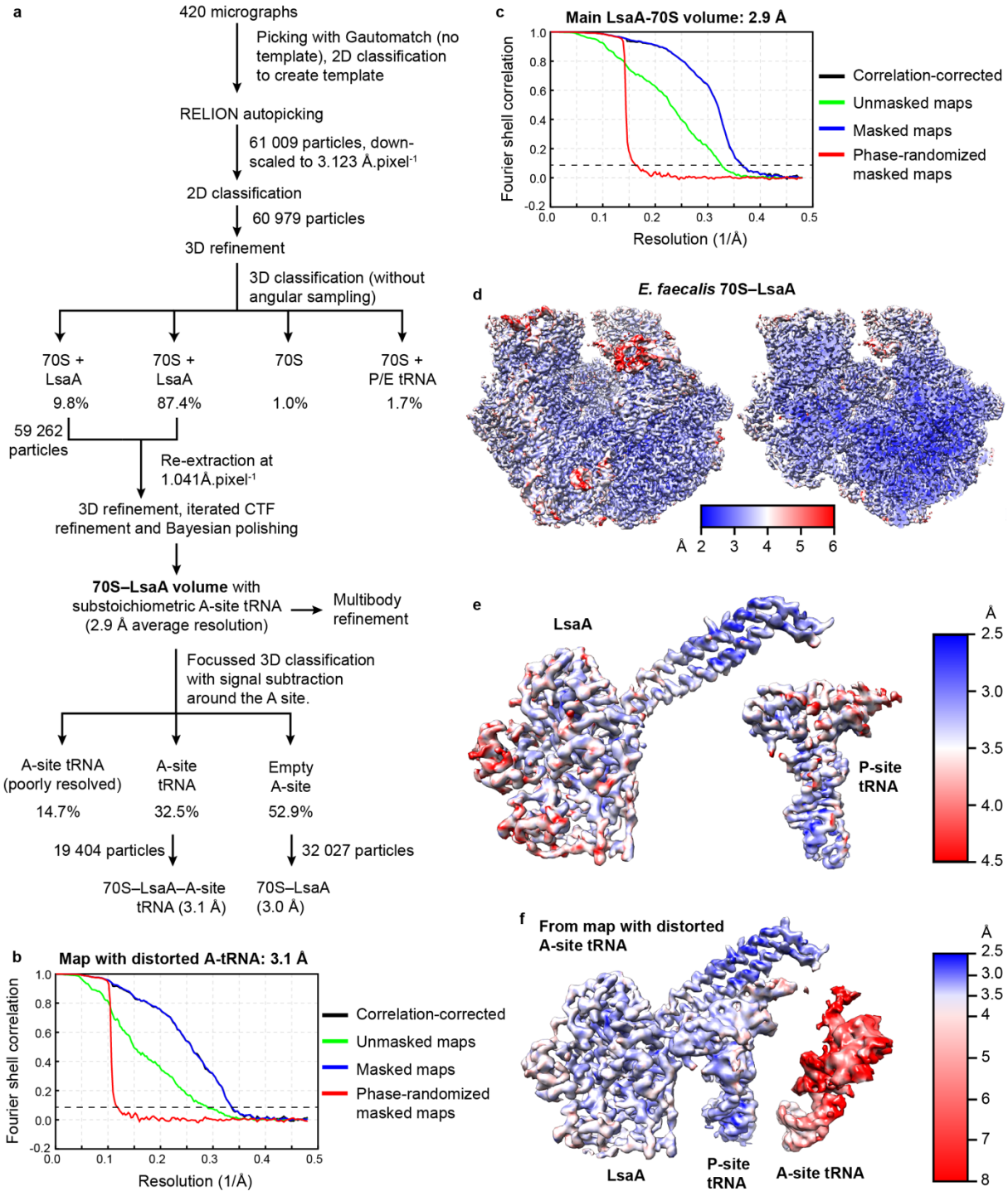

Supplementary Figure 4. Processing of the cryo-EM data of LsaA-70S complex. a Processing scheme for the LsaA-70S complex, yielding two subpopulations of LsaA-70S complexes with and without A-site tRNA. **b,c** Fourier Shell Correlation (FSC) curves of the LsaA-70S **b** with A-tRNA and **c** without A-tRNA with a dashed line at 0.143 indicating average resolutions of 3.1 Å and 2.9 Å, respectively. **d** Overview (left) and transverse section (right) of the cryo-EM map of the LsaA-70S (without A-tRNA) coloured according to local resolution. **e** Isolated density of LsaA (left) and P-site tRNA (right) from **d**. **f** Isolated density of LsaA, P-site and A-site tRNA from the LsaA-70S map (with A-tRNA) coloured according to local resolution.

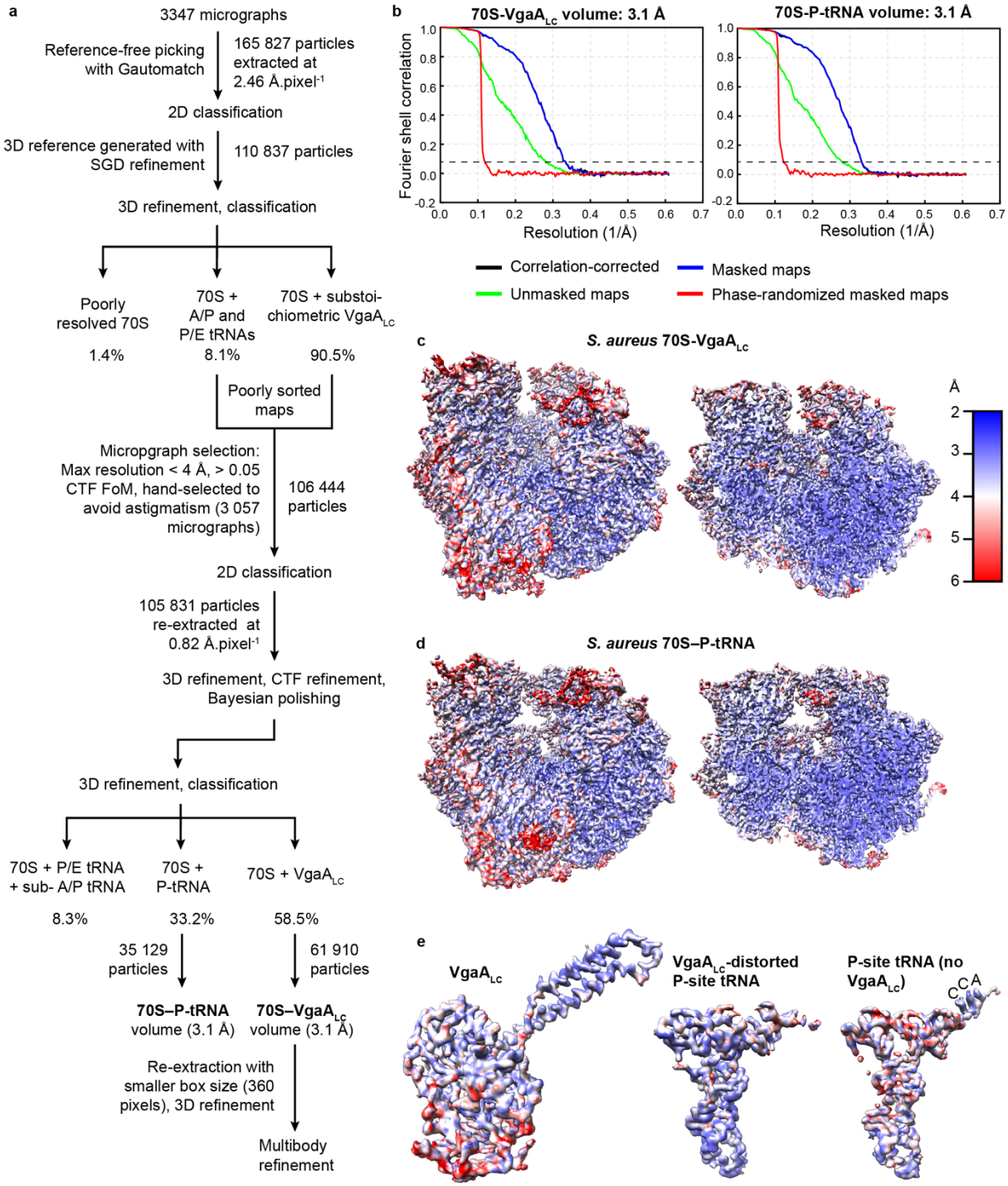

Supplementary Figure 5. Processing of the cryo-EM data of VgaA$_{LC}$-70S complex. (**A**) Processing scheme for the LsaA-70S complex, yielding a VgaA$_{LC}$-70S and 70S-P-tRNA complex without VgaA$_{LC}$. (**B**) Fourier Shell Correlation (FSC) curves of the VgaA$_{LC}$-70S and 70S-P-tRNA complexes with a dashed line at 0.143 indicating average resolutions of 3.1 Å. (**C, D**) Overview (left) and transverse section (right) of the cryo-EM map of the (**C**) VgaA$_{LC}$-70S and (**D**) 70S-P-tRNA complexes coloured according to local resolution. (**E**) Isolated density of VgaA$_{LC}$ (left) and P-site tRNA (right) from the VgaA$_{LC}$-70S complex, and the P-site-tRNA from the 70S–P-tRNA complex, coloured according to local resolution.

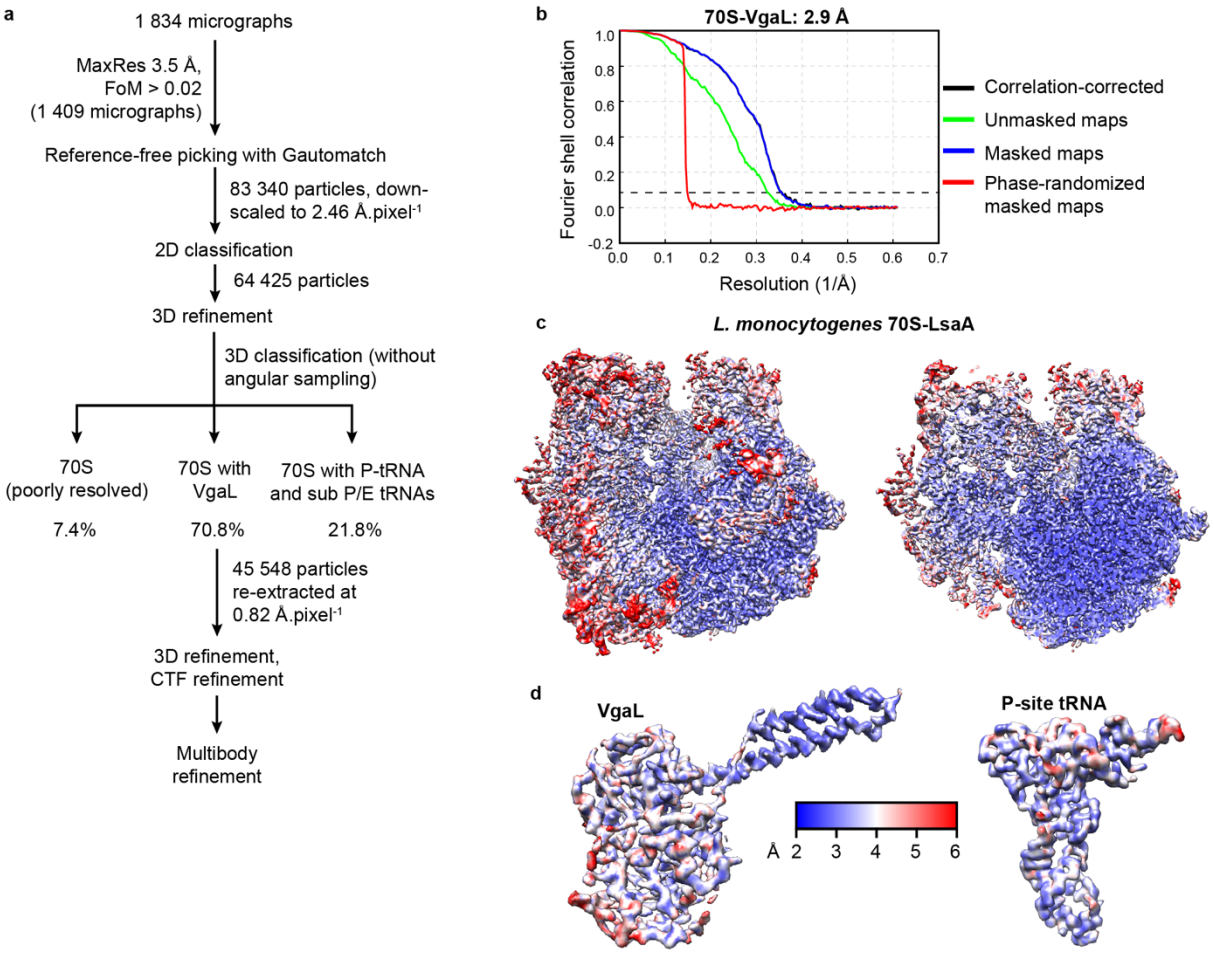

Supplementary Figure 6. Processing of the cryo-EM data of VgaL-70S complex. (**A**) Processing scheme for the VgaL-70S complex. (**B**) Fourier Shell Correlation (FSC) curves of the VgaL-70S complex with a dashed line at 0.143 indicating average resolutions of 2.9 Å. (**C**) Overview (left) and transverse section (right) of the cryo-EM map of the VgaL-70S complex coloured according to local resolution. (**D**) Isolated density of VgaL (left) and P-site tRNA (right) from the VgaL-70S complex coloured according to local resolution.

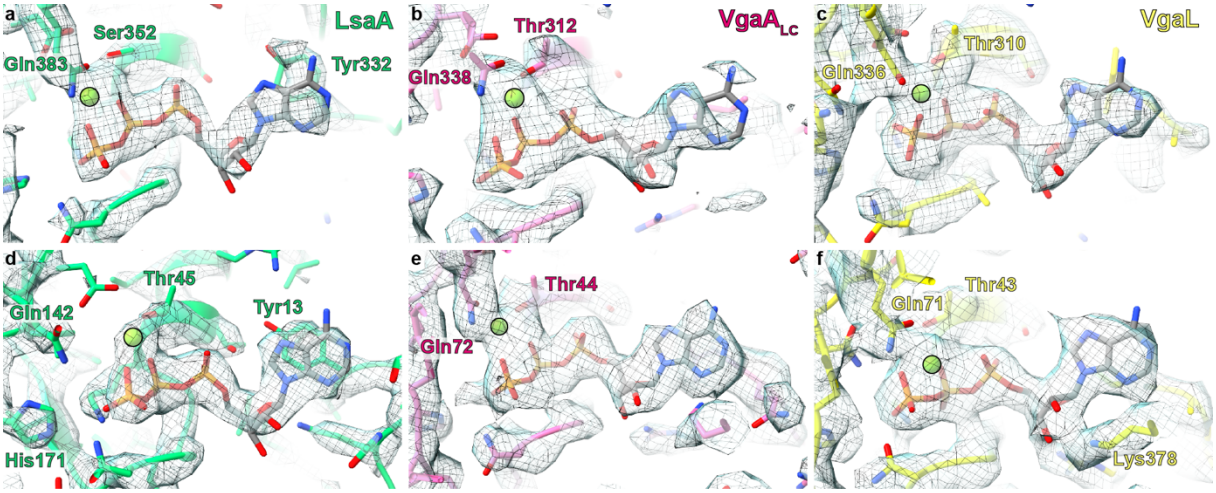

Supplementary Figure 7. ATP in the ARE-bound 70S structures. Model and density surrounding the outermost ATP (site 1) bound by LsaA (**a**), VgaA$_{LC}$ (**b**), and VgaL (**c**) viewed from the direction of the signature sequence of NBD2 (not shown). A black outline highlights a putative magnesium ion. **d–f**, as for **a–c** except for the innermost nucleotide-binding site (site 1) viewed from the direction of the signature sequence of NBD1 (not shown). Density from post-processed maps is shown.

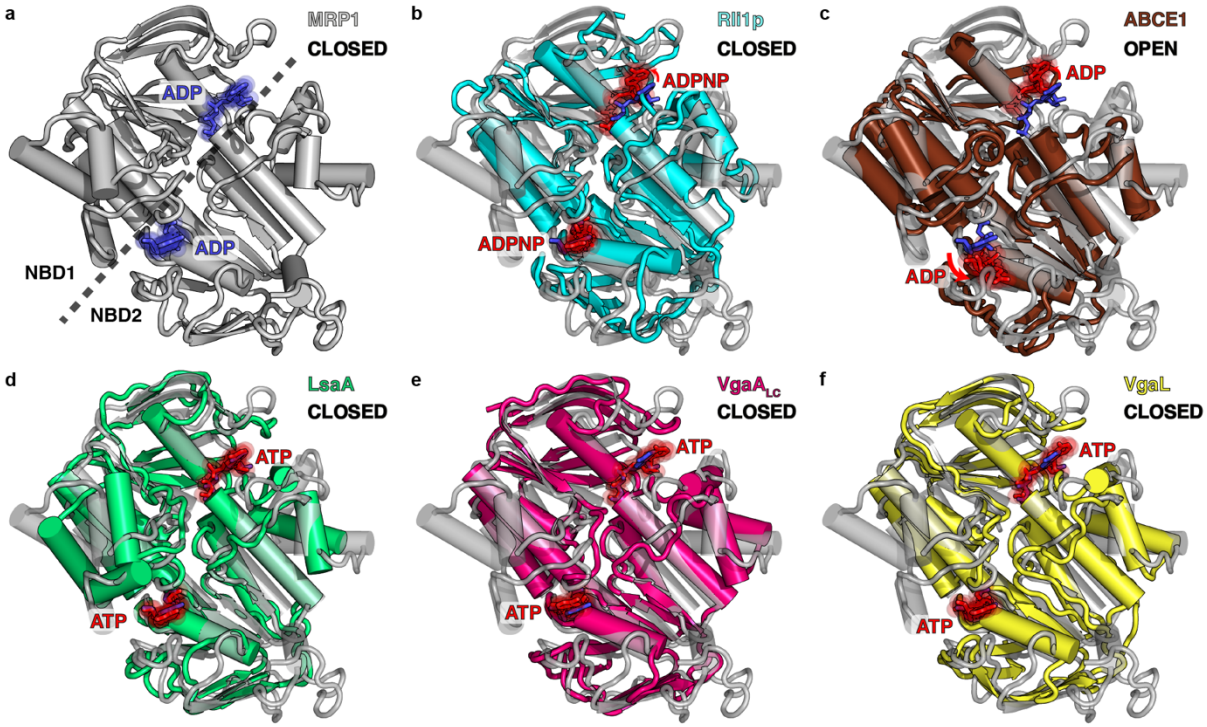

Supplementary Figure 8. LsaA, $VgaA_{LC}$ and VgaL NBDs exhibit a closed conformation. **a** The closed conformation of the multidrug transporter MRP1 (grey) with bound ADP molecules (blue, PDB 6BHU)[1]. **b,c** Alignment (based on NBD1) and superimposition of the closed conformation of MRP1 from **a** with the ABC domains of **b** Rli1p (cyan) in closed conformation with bound ADPNP (red, PDB 5LL6)[2], **c** ABCE1 (brown) in open conformation with bound ADP (red, PDB 3J15)[3], and with **d–f** closed ARE-ABCF NBD conformations with bound ATP (red) for **d** LsaA (green), **e** $VgaA_{LC}$ (magenta) and **f** VgaL (yellow).

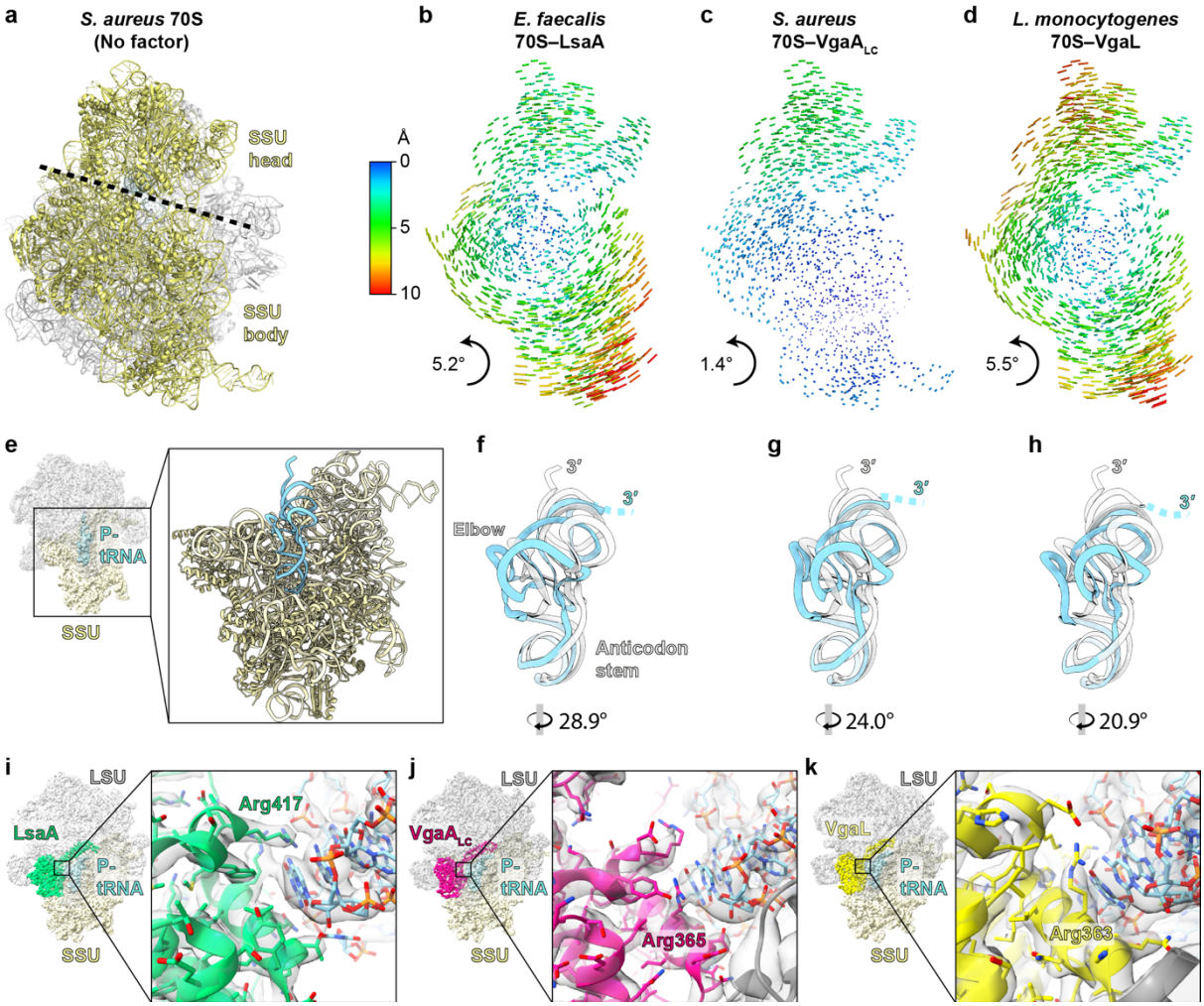

Supplementary Figure 9. Small subunit and P-tRNA rotation in the ARE-bound 70S structures. a *S. aureus* 70S ribosome with P-tRNA and no ARE viewed from the small subunit-solvent interface. **b–d** comparison of the small subunit in the non-rotated state (shown in **a**) and the small subunit from the ARE-bound structures. Movements between residues are represented as lines coloured according to the distance moved. **b**, *E. faecalis* LsaA-70S; **c**, *S. aureus* VgaA$_{LC}$-70S; **d**, *L. monocytogenes* VgaL-70S. **e** overview of *S. aureus* 70S ribosome with P-tRNA with inset showing position of P-tRNA on the small subunit. **f–h** the canonical, non-rotated P-tRNA from **e** (light grey) compared with P-tRNAs from ARE-bound structures (blue), with the rotation quantified below. **f**, *E. faecalis* LsaA-70S; **g**, *S. aureus* VgaA$_{LC}$-70S; **h**, *L. monocytogenes* VgaL-70S. A dashed line represents the likely path of the 3' CCA end, which is not included in the models, for the tRNAs from the ARE-bound 70S structures. **i–k**, overviews with insets showing the site of interaction between each ARE and the P-tRNA elbow. **i**, *E. faecalis* LsaA-70S; **j**, *S. aureus* VgaA$_{LC}$-70S; **k**, *L. monocytogenes* VgaL-70S.

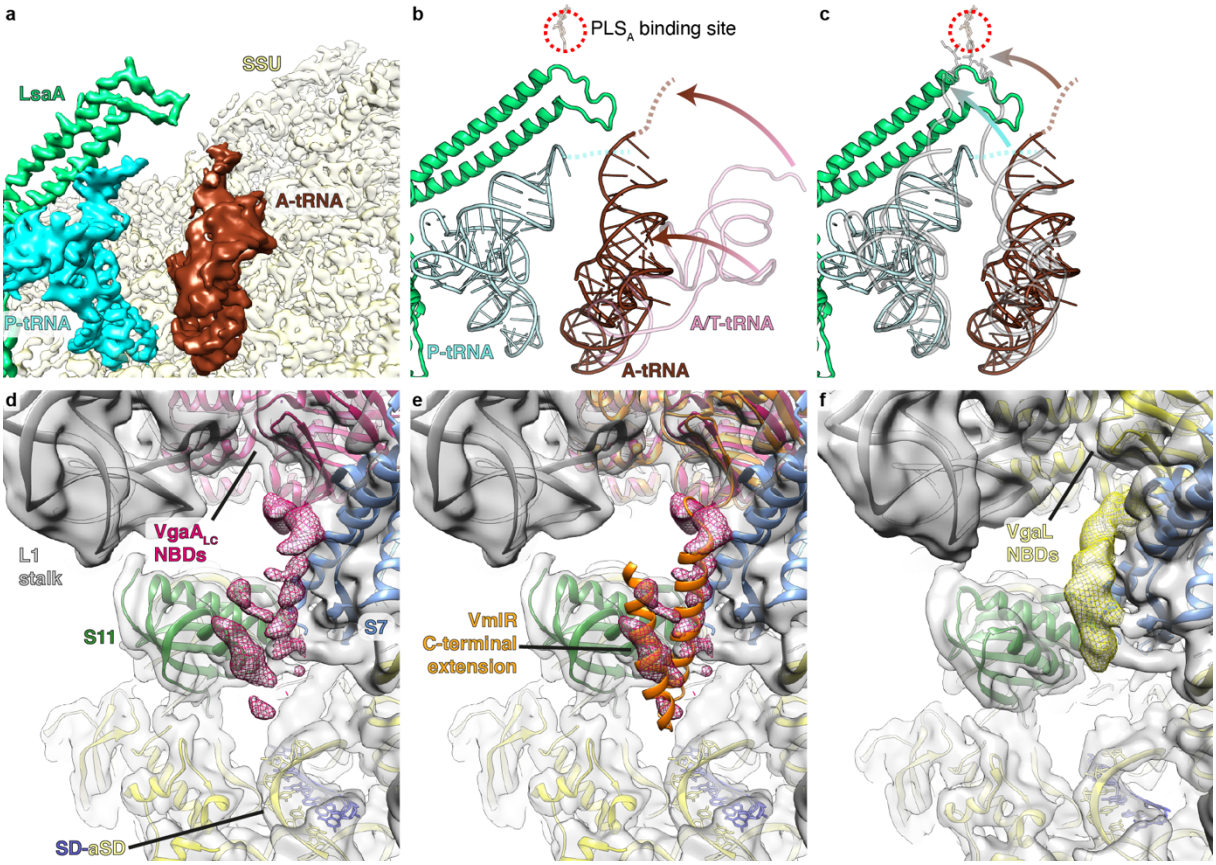

Supplementary Figure 10. Presence of A-site tRNA in the LsaA-70S complex. a Cryo-EM map density for LsaA (green), P-site tRNA (cyan) and A-site tRNA (brown) in the LsaA-70S complex with A-site tRNA. Density for small subunit (yellow) is shown for reference. Density for the large subunit is not shown. **b** The same view as A, except with molecular models. The brown dashed line indicates a likely path for the 3′ CCA end of the distorted A-tRNA. A pre-accommodation A/T tRNA (pink, PDB 4V5L)[4] is superimposed. The position of the lincomycin binding site (red dotted circle) is shown for comparison (PDB 5HKV)[5]. **c** Similar to **b** except with classical accommodated A- and P-site tRNAs from pre-attack state superimposed (both grey, PDB 1VY4)[6]. **d–f** Cryo-EM map (grey) with molecular model for **e–f** VgaA$_{LC}$-70S complex, and (**f**) VgaL-70S complex, showing density for L1 stalk (grey) on the large subunit, and ribosomal proteins S7 (blue), S11 (green) as well as the SD–anti-SD helix on the small subunit (yellow). In **d** and **e**, density for the C-terminal extension (CTE) of VgaA$_{LC}$ (magenta mesh) is fragmented, and in **e** fitted with the model of the CTE from VmlR (orange, PDB 6HA8)[7] based on alignment of the NBDs. In **f**, density for the C-terminal extension (CTE) of VgaL (yellow mesh) also reaches between the S7–S11 cleft and is consistent with an α-helical conformation, but appears to be distinct from VmlR and VgaA$_{LC}$ and could not be modelled at this resolution.

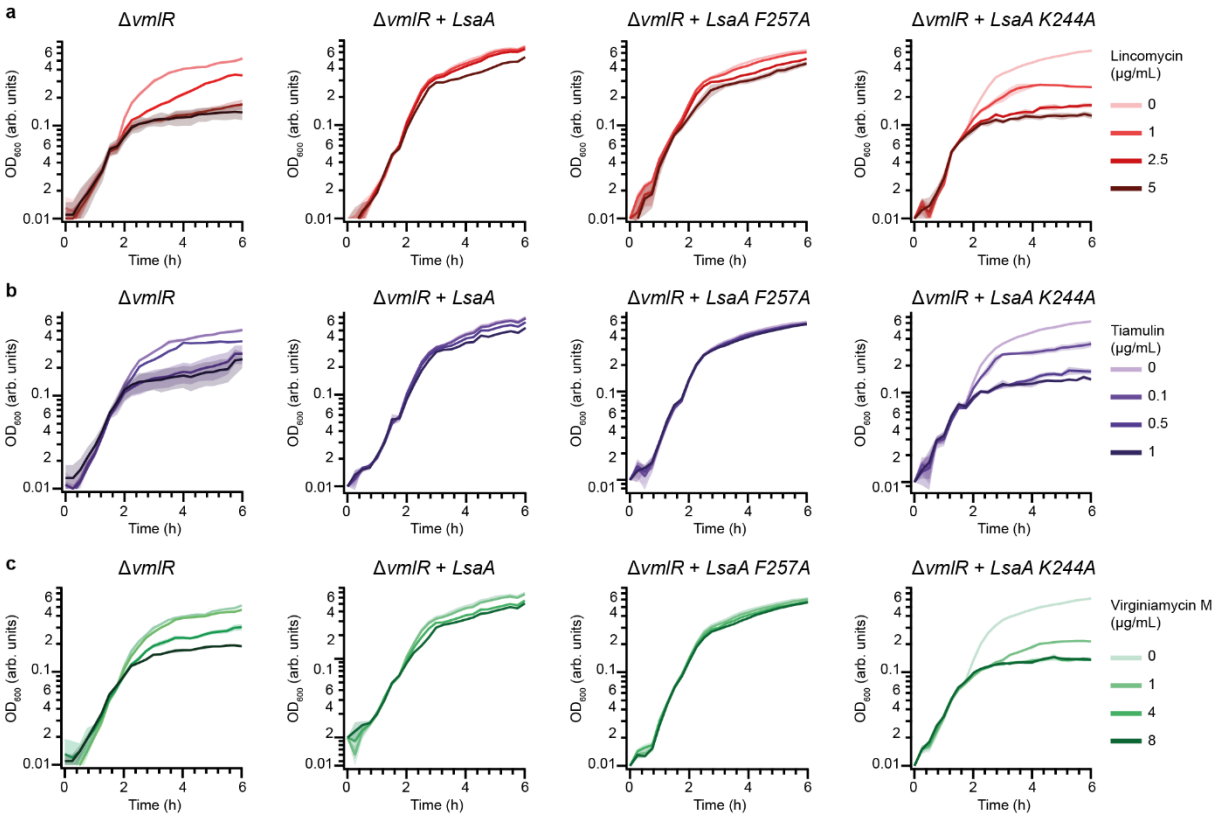

Supplementary Figure 11. Effect of amino acid substitutions in ARD on antibiotic resistance in LsaA. Growth of *B. subtilis* Δ*vmlR* expressing the indicated LsaA variants over time in the presence of lincomycin **a**, tiamulin **b**, and virginiamycin M **c**. *B. subtilis* strains (VHB109, 168 and 169) were grown in LB media with 1 mM IPTG at 37 °C with medium shaking. At the 90 minutes time point (OD_{600} ≈ 0.1) antibiotics were added to the final concentrations as indicated on the figure. The mean is shown as a line with the SD of three biological replicates is indicated with pale shading. The leftmost panels, showing susceptibility to the antibiotics in the base Δ*vmlR* strain, are the same as used in Crowe-McAuliffe *et al.*, 2018[7]. Source data are provided as a Source Data file.

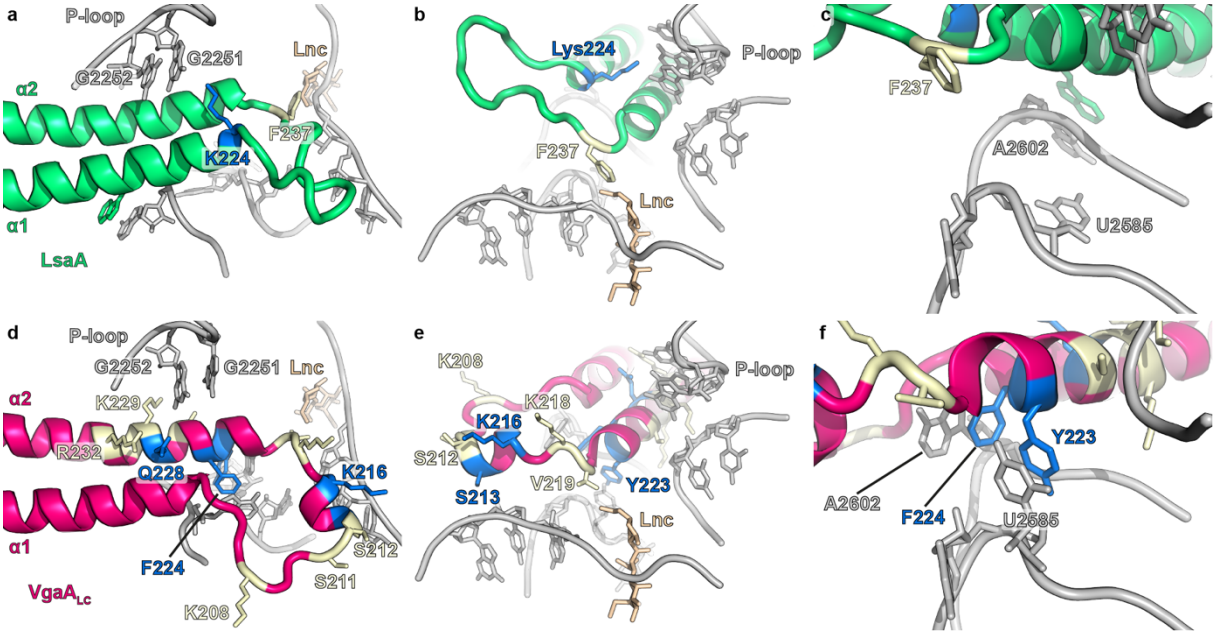

Supplementary Figure 12. Visualisation of tested mutations in $VgaA_{LC}$ and LsaA. Residues in blue reduced antibiotic resistance when mutated to alanine, and residues in yellow did not affect antibiotic resistance when mutated to alanine. **a–c**, three views of the LsaA ARD with selected *E. faecalis* 23S 23S rRNA nucleotides shown. **d–f**, three views of the $VgaA_{LC}$ ARD with selected *S. aureus* 23S 23S rRNA nucleotides shown. See also Tables S1 and S2.

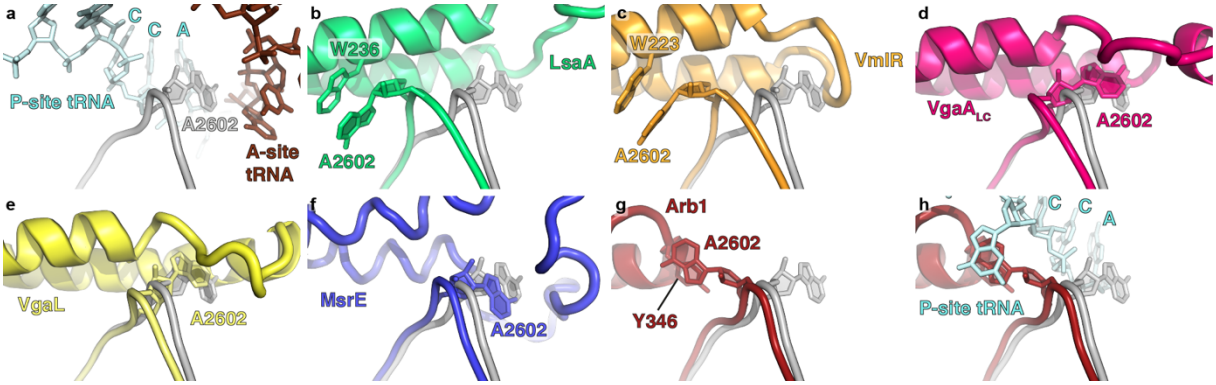

Supplementary Figure 13. Comparison of A2602 position between ribosomes with and without bound AREs. a A2602 with accommodated A- and P-site tRNAs in the 'pre-attack' state (PDB 1VY4)[6] **b** Conformation of A2602 with bound LsaA with 23S rRNA from **a**. **c–g** Similar to **b**, except for VmlR (PDB 6HA8)[7], VgaA$_{LC}$, VgaL, MsrE (PDB 5ZLU)[8], and Arb1 (PDB 6R84)[9].

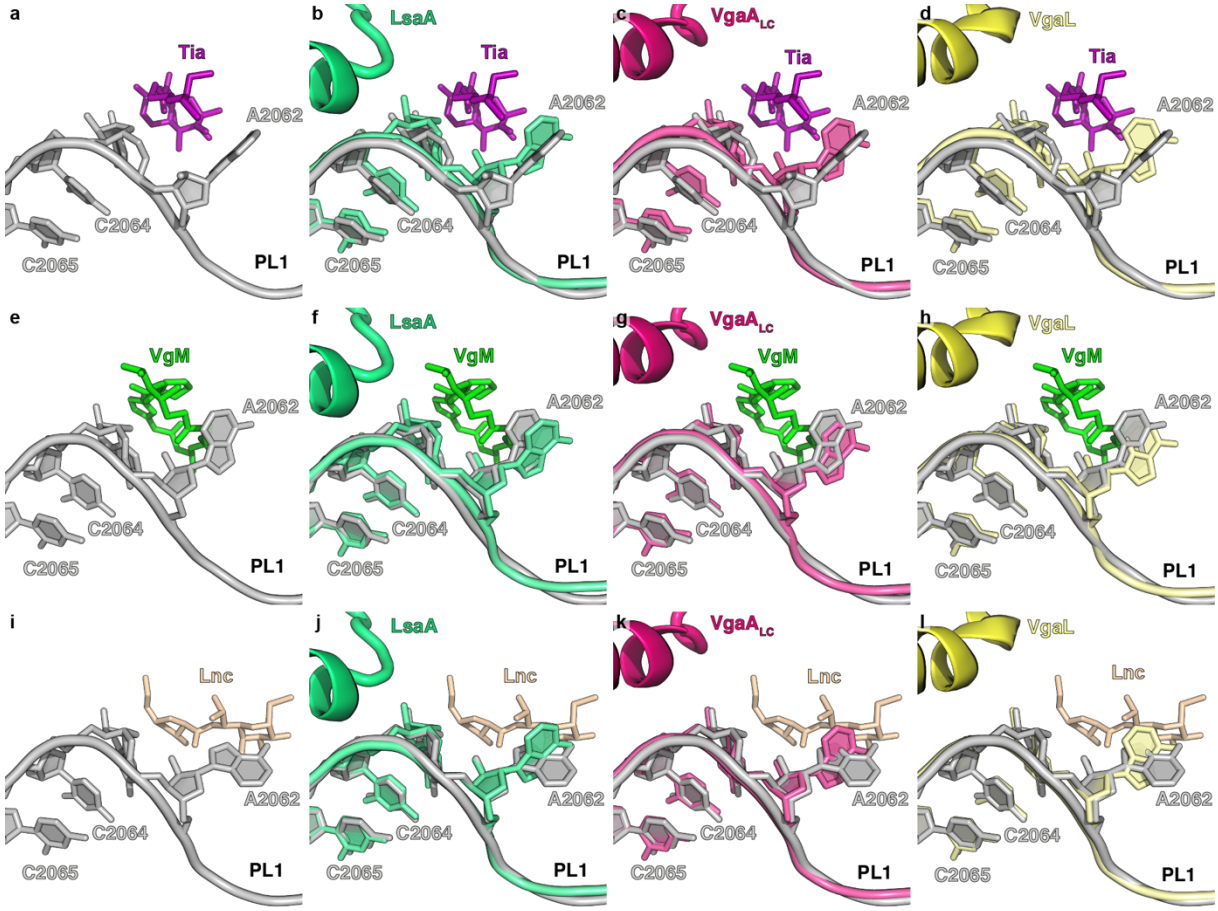

Supplementary Figure 14. PTC loop 1 in the presence of PLS$_A$ antibiotics and AREs. a–d The conformation of selected nucleotides from PL1 at the PLS$_A$ binding site in the presence of tiamulin (Tia, purple, PDB 1XBP)[10] and LsaA (**b**, green nucleotides), VgaA$_{LC}$ (**c**, pink nucleotides), and VgaL (**d**, yellow nucleotides) **e–h** Same as **a–d** but with virginiamycin M (VgM, green, PDB 4U25)[11] instead of tiamulin. **i–l** as for **a–d** but with lincomycin (Lnc, tan, PDB 5HKV)[5] instead of tiamulin.

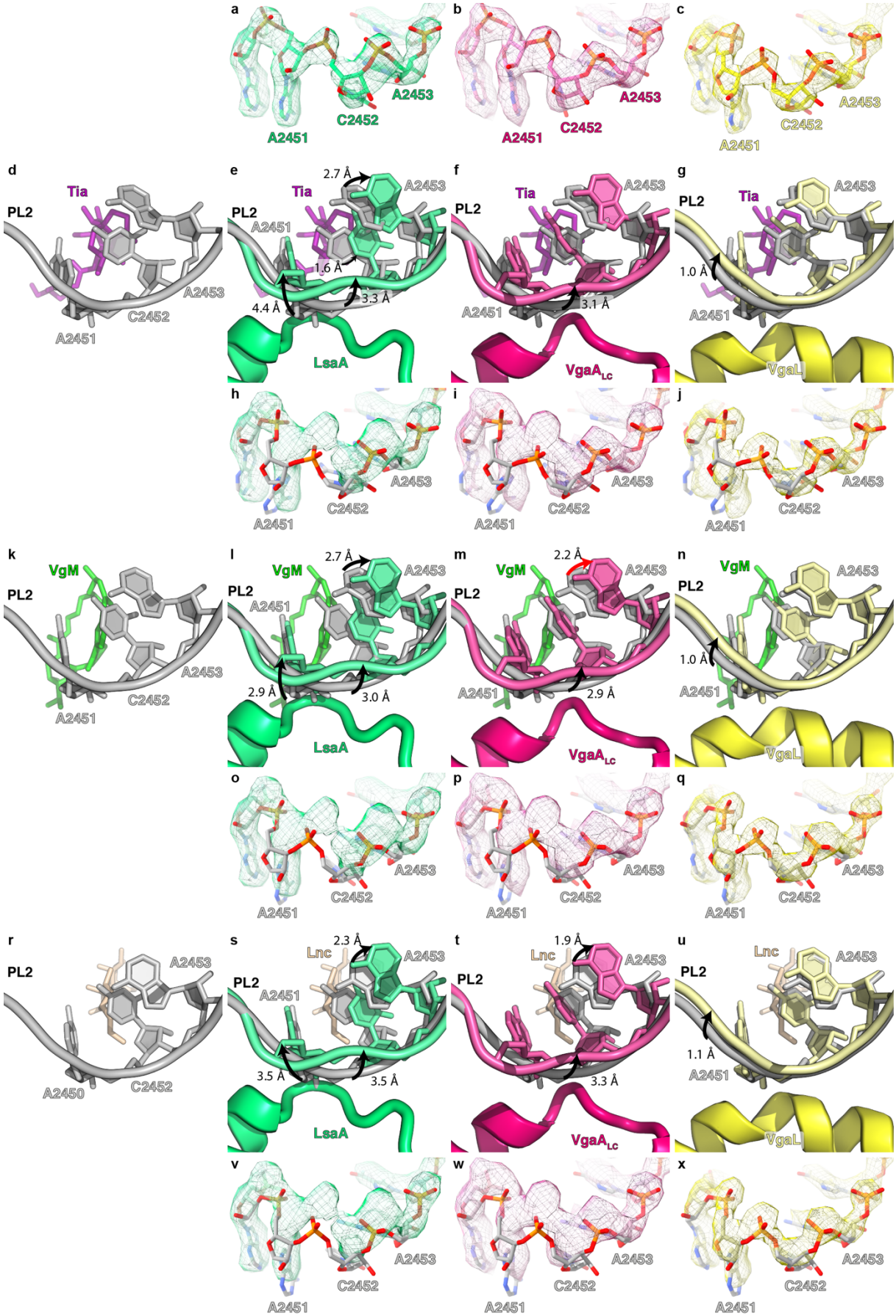
a
A2453
C2452
A2451
b
A2453
C2452
A2451
c
A2453
C2452
A2451
d
Tia
PL2
A2453
C2452
A2451
e
2.7 Å
Tia
A2453
PL2
A2451
1.6 Å
4.4 Å
3.3 Å
LsaA
f
Tia
A2453
PL2
A2451
3.1 Å
VgaALc
g
PL2
Tia
A2453
1.0 Å
A2451
VgaL
h
A2453
C2452
A2451
i
A2453
C2452
A2451
j
A2453
C2452
A2451
k
VgM
PL2
A2453
C2452
A2451
l
2.7 Å
VgM
A2453
PL2
A2451
2.9 Å
3.0 Å
LsaA
m
2.2 Å
VgM
A2453
PL2
A2451
2.9 Å
VgaALc
n
VgM
A2453
PL2
1.0 Å
A2451
VgaL
o
A2453
C2452
A2451
p
A2453
C2452
A2451
q
A2453
C2452
A2451
r
PL2
A2453
A2450
C2452
s
2.3 Å
Lnc
A2453
PL2
A2451
3.5 Å
3.5 Å
LsaA
t
1.9 Å
Lnc
A2453
PL2
3.3 Å
VgaALc
u
Lnc
A2453
PL2
1.1 Å
A2451
VgaL
v
A2453
C2452
A2451
w
A2453
C2452
A2451
x
A2453
C2452
A2451

Supplementary Figure 15. PTC loop 2 in the presence of PLS_A antibiotics and AREs. a–c Density and model of selected nucleotides from PL2 in the ARE-bound form. **d–g** Selected nucleotides from PL2 at the PLS_A binding site in the presence of tiamulin (Tia, purple, PDB 1XBP)[10] and LsaA (**e**, green nucleotides), $VgaA_{LC}$ (**f**, pink nucleotides), and VgaL (**g**, yellow nucleotides). **h–j** Density of selected nucleotides from PL2 in the ARE-bound form (same as **a–c**) with model from the tiamulin-bound state superimposed. **k–n** Selected nucleotides from PL2 at the PLS_A binding site in the presence of virginiamycin M (VgM, green, PDB 4U25)[11] and LsaA (**l**, green nucleotides), $VgaA_{LC}$ (**m**, pink nucleotides), and VgaL (**n**, yellow nucleotides). **o–q** Density of selected nucleotides from PL2 in the ARE-bound form (same as **a–c**) with model from the virginiamycin M-bound state superimposed. **r–u** Selected nucleotides from PL2 at the PLS_A binding site in the presence of lincomycin (Lnc, tan, PDB 5HKV)[5] and LsaA (**s**, green nucleotides), $VgaA_{LC}$ (**t**, pink nucleotides), and VgaL (**u**, yellow nucleotides). **v–x** Density of selected nucleotides from PL2 in the ARE-bound form (same as **a–c**) with model from the lincomycin-bound state superimposed.

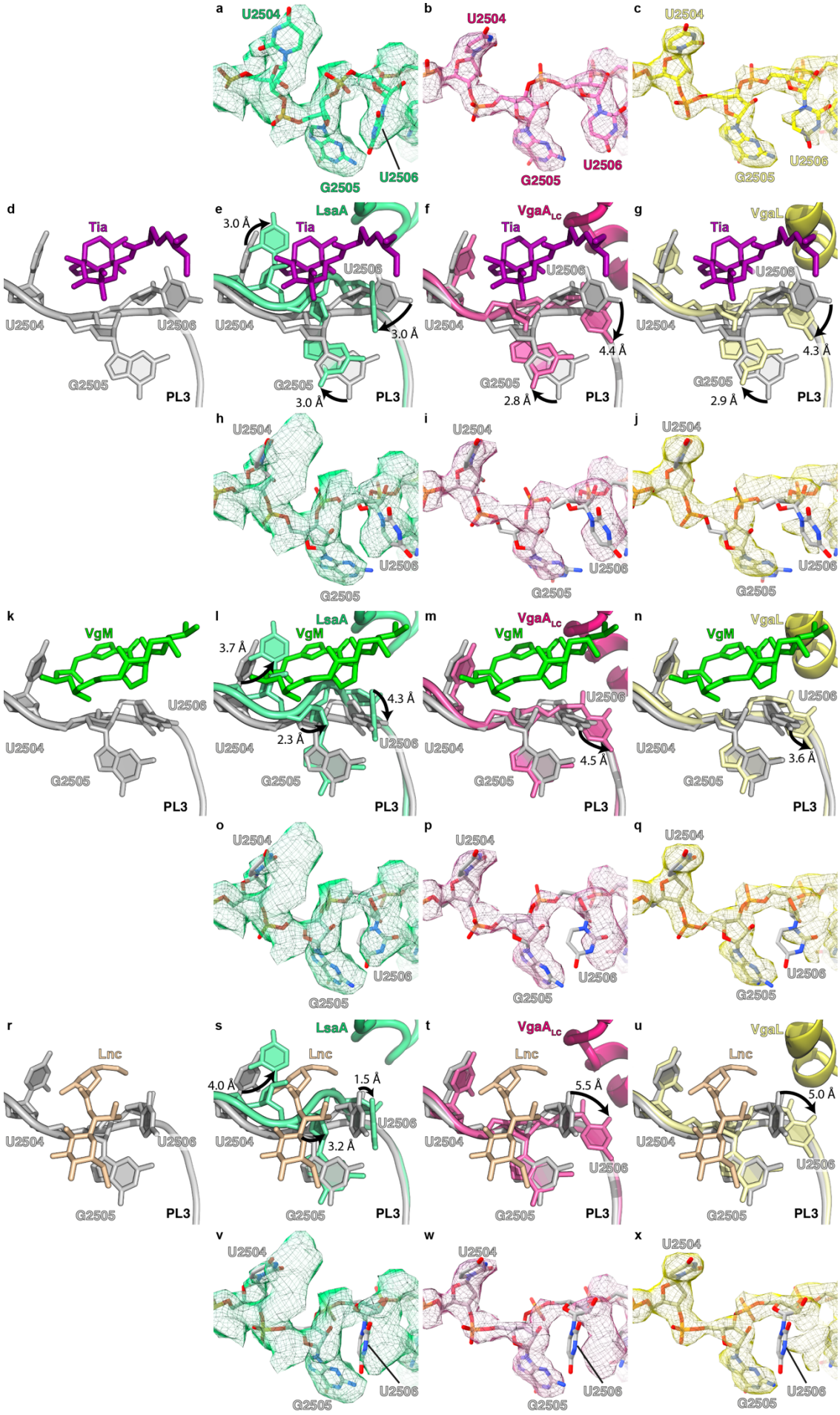
a
U2504
G2505
U2506
b
U2504
U2506
G2505
c
U2504
U2506
G2505
d
Tia
U2504
U2506
G2505
PL3
e
LsaA
Tia
3.0 Å
U2506
U2504
3.0 Å
G2505
3.0 Å
PL3
f
VgaA$_{LC}$
Tia
U2506
U2504
4.4 Å
G2505
2.8 Å
PL3
g
VgaL
Tia
U2506
U2504
4.3 Å
G2505
2.9 Å
PL3
h
U2504
U2506
G2505
i
U2504
U2506
G2505
j
U2504
U2506
G2505
k
VgM
U2506
U2504
G2505
PL3
l
LsaA
VgM
3.7 Å
4.3 Å
2.3 Å
U2504
U2506
G2505
PL3
m
VgaA$_{LC}$
VgM
U2506
U2504
4.5 Å
G2505
PL3
n
VgaL
VgM
U2506
U2504
3.6 Å
G2505
PL3
o
U2504
U2506
G2505
p
U2504
U2506
G2505
q
U2504
U2506
G2505
r
Lnc
U2504
U2506
G2505
PL3
s
LsaA
Lnc
4.0 Å
1.5 Å
U2506
U2504
3.2 Å
G2505
PL3
t
VgaA$_{LC}$
Lnc
5.5 Å
U2504
U2506
G2505
PL3
u
VgaL
Lnc
5.0 Å
U2504
U2506
G2505
PL3
v
U2504
U2506
G2505
w
U2504
U2506
G2505
x
U2504
U2506
G2505

Supplementary Figure 16. PTC loop 3 in the presence of PLS_A antibiotics and AREs. a–c Density and model of selected nucleotides from PL3 in the ARE-bound form. **d–g** Selected nucleotides from PL3 at the PLS_A binding site in the presence of tiamulin (Tia, purple, PDB 1XBP)[10] and LsaA (**e**, green nucleotides), $VgaA_{LC}$ (**f**, pink nucleotides), and VgaL (**g**, yellow nucleotides). **h–j** Density of selected nucleotides from PL3 in the ARE-bound form (same as **a–c**) with model from the tiamulin-bound state superimposed. **k–n** Selected nucleotides from PL3 at the PLS_A binding site in the presence of virginiamycin M (VgM, green, PDB 4U25)[11] and LsaA (**l**, green nucleotides), $VgaA_{LC}$ (**m**, pink nucleotides), and VgaL (**n**, yellow nucleotides). **o–q** Density of selected nucleotides from PL3 in the ARE-bound form (same as **a–c**) with model from the virginiamycin M-bound state superimposed. **r–u** Selected nucleotides from PL3 at the PLS_A binding site in the presence of lincomycin (Lnc, tan, PDB 5HKV)[5] and LsaA (**s**, green nucleotides), $VgaA_{LC}$ (**t**, pink nucleotides), and VgaL (**u**, yellow nucleotides). **v–x** Density of selected nucleotides from PL3 in the ARE-bound form (same as **a–c**) with model from the lincomycin-bound state superimposed.

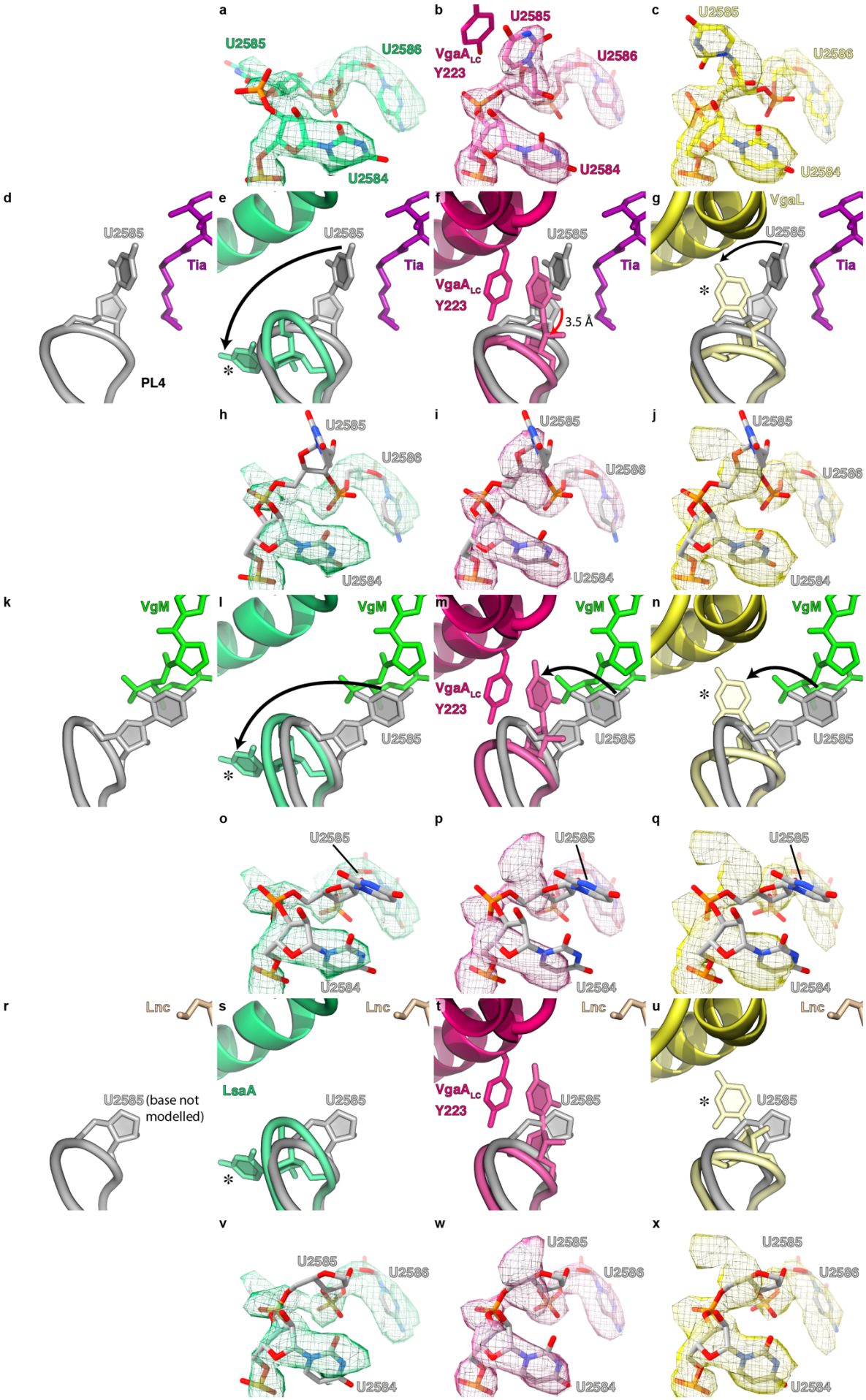
a
U2585
U2586
U2584
b
U2585
VgaA$_{LC}$
Y223
U2586
U2584
c
U2585
U2586
U2584
d
U2585
Tia
PL4
e
U2585
Tia
*
f
U2585
VgaA$_{LC}$
Y223
Tia
3.5 Å
g
VgaL
U2585
Tia
*
h
U2585
U2586
U2584
i
U2585
U2586
U2584
j
U2585
U2586
U2584
k
VgM
l
VgM
U2585
*
m
VgM
VgaA$_{LC}$
Y223
U2585
n
VgM
*
U2585
o
U2585
U2584
p
U2585
U2584
q
U2585
U2584
r
Lnc
U2585 (base not modelled)
s
Lnc
LsaA
U2585
*
t
Lnc
VgaA$_{LC}$
Y223
U2585
u
Lnc
*
U2585
v
U2585
U2586
U2584
w
U2585
U2586
U2584
x
U2585
U2586
U2584

Supplementary Figure 17. PTC loop 4 in the presence of PLS_A antibiotics and AREs. a–c Density and model of selected nucleotides from PL3 in the ARE-bound form. **d–g** Selected nucleotides from PL4 at the PLS_A binding site in the presence of tiamulin (Tia, purple, PDB 1XBP)[10] and LsaA (**e**, green nucleotides), $VgaA_{LC}$ (**f**, pink nucleotides), and VgaL (**g**, yellow nucleotides). **h–j** Density of selected nucleotides from PL4 in the ARE-bound form (same as **a–c**) with model from the tiamulin-bound state superimposed. **k–n** Selected nucleotides from PL4 at the PLS_A binding site in the presence of virginiamycin M (VgM, green, PDB 4U25)[11] and LsaA (**l**, green nucleotides), $VgaA_{LC}$ (**m**, pink nucleotides), and VgaL (**n**, yellow nucleotides). **o–q** Density of selected nucleotides from PL4 in the ARE-bound form (same as **a–c**) with model from the virginiamycin M-bound state superimposed. **r–u** Selected nucleotides from PL4 at the PLS_A binding site in the presence of lincomycin (Lnc, tan, PDB 5HKV)[5] and LsaA (**s**, green nucleotides), $VgaA_{LC}$ (**t**, pink nucleotides), and VgaL (**u**, yellow nucleotides). **v–x** Density of selected nucleotides from PL4 in the ARE-bound form (same as **a–c**) with model from the lincomycin-bound state superimposed.

Table S1. Minimum inhibitory concentrations (MICs) of ribosome-targeting antibiotics against *E. faecalis* expressing LsaA. 5 x 10^5 CFU/mL (OD_{600} approximately 0.0005) of either *E. faecalis* OG1RF, Δ*lsaA* (*lsa::Kan*) strain TX5332 transformed with empty $pCIE_{spec}$ plasmid, or with $pCIE_{spec}$ derivative for expression of LsaA was used to inoculate BHI media supplemented with 2 mg/mL kanamycin to prevent *lsa* revertants, 0.1 mg/mL spectinomycin to maintain the $pCIE_{spec}$ plasmid, 100 ng/mL of cCF10 peptide to induce expression of LsaA as well as increasing concentrations of antibiotics. After 16–20 hours at 37 °C without shaking, the presence or absence of bacterial growth was scored by eye. The MIC values that exceed the empty vector control by at least 4-fold are shown in bold.

		MIC, µg/mL			
antibiotic class	antibiotic	*E. faecalis* OG1RF	*E. faecalis* TX5332 $pCIE_{spec}$	*E. faecalis* TX5332 $pCIE_{spec}$ *lsaA*	*E. faecalis* TX5332 pCIE *lsaA-HTF*
phenicols	chloramphenicol	2-4	2-4	2-4	
	thiamphenicol	4	4	4	
	florfenicol	1	1-2	1-2	
oxazolidinones	linezolid	1	1	1	1
macrolides	erythromycin	1	0.5-1	0.5	0.5
	azithromycin	1-2	0.5-1	0.5-1	
	leucomycin	0.5-1	0.5	0.5-1	
lincosamides	lincomycin	**32**	0.125	**16-32**	**8-16**
	clindamycin	**16-32**	0.0156	**16**	**4-8**
pleuromutilins	tiamulin	**128**	0.0625	**128**	**32-64**
	retapamulin	**>64**	0.0156	**>64**	
streptogramins	virginiamycin M1	**>64**	4	**>128**	
	virginiamycin S1	8	8	8	
tetracyclines	tetracycline	0.5	0.25	0.25	

Table S2. Minimum inhibitory concentrations (MICs) of ribosome-targeting antibiotics against *S. aureus* expressing VgaA$_{LC}$ *S. aureus* strain SH1000, harbouring empty vector pRMC2 or pRMC2 expressing wild-type *vgaA$_{LC}$* or its mutants. The MIC values that exceed the empty vector control by at least 4-fold are shown in bold.

	MIC, µg/mL				
Construct (mutation)	lincomycin	clindamycin	tiamulin	retapamulin	virginiamycin M1
pRMC2	0.5	0.06	0.5	0.06	2
pRMC2: *vgaA$_{LC}$*	**16**	**2**	**8**	**4**	4
pRMC2: *vgaA$_{LC}$* (K_{208}A)	**16**	**2**	**16**	**8**	4
pRMC2:*vgaA$_{LC}$* (S_{211}A)	**16**	**2**	**16**	**4**	4
pRMC2:*vgaA$_{LC}$* (S_{212}A)	**8**	**2**	**16**	**8**	4
pRMC2:*vgaA$_{LC}$* (S_{213}A)	**2**	0.125	1	0.125	1
pRMC2:*vgaA$_{LC}$* (K_{216}A)	**8**	**0.5**	**4**	**1**	4
pRMC:*vgaA$_{LC}$* (K_{218}A)	**16**	**1**	**16**	**4**	4
pRMC2:*vgaA$_{LC}$* (V_{219}A)	**16**	**1**	**16**	**8**	2
pRMC2:*vgaA$_{LC}$* (Y_{223}A)	**2**	0.125	1	0.125	1
pRMC2:*vgaA$_{LC}$* (F_{224}A)	0.5	0.06	0.25	0.06	1
pRMC2:*vgaA$_{LC}$* (S_{226}A)	**16**	**2**	**16**	**8**	4
pRMC2:*vgaA$_{LC}$* (K_{227}A)	**4**	**0.25**	1	0.125	2
pRMC2:*vgaA$_{LC}$* (Q_{228}A)	**8**	**2**	**8**	**2**	2
pRMC2:*vgaA$_{LC}$* (K_{229}A)	**16**	**2**	**8**	**4**	4
pRMC2:*vgaA$_{LC}$* (K_{230}A)	**16**	**2**	**8**	**4**	4
pRMC2:*vgaA$_{LC}$* (R_{232}A)	**16**	**2**	**8**	**2**	4

Table S3. Minimum inhibitory concentrations (MICs) of ribosome-targeting antibiotics against *L. monocytogenes* EGD-e expressing VgaL (Lmo0919). 5 x 10^5 CFU/mL (approximately OD_{600} 0.0003) of *L. monocytogenes EGDe*, Δ*lmo0919* (markerless) strain with integrated empty pIMK3 plasmid, or with pIMK3 encoding VgaL or VgaL-HTF was used to inoculate BHI media supplemented with 50 µg/mL kanamycin to maintain the integrative pIMK3 plasmid, 1 mM IPTG to induce expression of VgaL as well as increasing concentrations of antibiotics. After 16–20 hours at 37 °C without shaking, the presence or absence of bacterial growth was scored by eye. The MIC values that exceed the empty vector control lacking chromosomal *lmo0919* are shown in bold.

		MIC, µg/mL			
antibiotic class	antibiotic	*L. monocytogenes* EGDe::pIMK3	*L. monocytogenes* EGDe::Δ*lmo0919* pIMK3	*L. monocytogenes* EGDe::Δ*lmo0919* pIMK3 *vgaL*	*L. monocytogenes* EGDe::Δ*lmo0919* pIMK3 *vgaL-HTF*
phenicols	chloramphenicol	4	4	4	4
oxazolidinones	linezolid	1	1	1	
macrolides	erythromycin	< 0.125	< 0.125	< 0.125	< 0.125
lincosamides	lincomycin	**2**	0.5	**4**	**4**
pleuromutilins	tiamulin	**16-32**	0.125	**32**	**16-32**
streptogramins	virginiamycin M1	**32**	4-8	**64**	**32**
	virginiamycin S1	1	1	1	1
tetracyclines	tetracycline	0.25	0.25	0.25	0.25

Table S4. Cryo-EM data collection, modelling and refinement statistics.

	LsaA-70S (EMDB-12331) (PDB 7NHK)	$VgaA_{LC}$-70S (EMDB-12332) (PDB 7NHL)	*S. aureus* 70S (EMDB-12333) (PDB 7NHM)	VgaL-70S (EMDB-12334) (PDB 7NHN)
Data collection and processing				
Magnification	130 000	165 000	165 000	165 000
Voltage (kV)	300	300	300	300
Electron exposure (e^{-}/Å^2)	38.0	26.3	26.3	28.28
Defocus range (μm)	−0.7–2.2	−0.7–1.9	−0.7–1.9	−0.8–2.0
Pixel size (Å)	1.041	0.82	0.82	0.82
Symmetry imposed	None	None	None	None
Initial particle images (no.)	61 009	165 827	165 827	83 340
Final particle images (no.)	59 262	35 129	61 910	45 548
Map resolution (Å)	2.9	3.1	3.1	2.9
FSC threshold	0.143	0.143	0.143	0.143
Refinement				
Map sharpening *B* factor (Å^2)	−35.42	−62.31	−56.43	−68.16
Model composition				
Non-hydrogen atoms	146 171	145 988	140 264	144 398
Protein residues	5 938	5 839	5 388	5 715
RNA residues	4 623	4 647	4 554	4 617
R.m.s. deviations				
Bond lengths (Å)	0.007	0.012	0.012	0.012
Bond angles (°)	0.895	1.095	1.113	1.108
Validation				
MolProbity score	1.51	1.67	1.58	1.53
Clashscore	3.03	3.42	2.94	3.12
Poor rotamers (%)	0.04	0.10	0.13	0.00
Ramachandran plot				
Favored (%)	93.64	90.47	91.85	93.42
Allowed (%)	6.36	9.53	8.13	6.58
Disallowed (%)	0.0	0.0	0.02	0.0

Table S5. Strains and Plasmids used in this study. Plasmid and strain construction is described in detail in supplemental text. *Denotes a plasmid constructed by the PEP facility at Umeå University.

Strain	Description	Source
L. monocytogenes EGDe	Wild-type serotype 1/2a strain	Glaser *et al.*, 2001[12]
L. monocytogenes EGDe::pIMK3	EGDe with empty pIMK3 plasmid containing P_{help} promoter integrated at $tRNA^{Arg}$ locus	This work
L. monocytogenes EGDe::pIMK3*lmo0919*^{HTF}	EGDe with VgaL-HTF overexpressed from the P_{help} promoter integrated at $tRNA^{Arg}$ locus	This work
L. monocytogenes EGDe::pIMK3*lmo0919*$^{EQ2\text{-}HTF}$	EGDe with VgaL EQ2-HTF overexpressed from the P_{help} promoter integrated at $tRNA^{Arg}$ locus	This work
L. monocytogenes EGDe::Δ*lmo0919*	EGDe harboring a *lmo0919* marker less deletion lacking VgaL	This work
L. monocytogenes EGDe::Δ*lmo0919*::pIMK3	EGDe::Δ*lmo0919* with empty pIMK3 plasmid containing P_{help} promoter integrated at $tRNA^{Arg}$ locus	This work
L. monocytogenes EGDe::Δ*lmo0919*::pIMK3*lmo0919*	EGDe::Δ*lmo0919* with VgaL overexpressed from the P_{help} promoter integrated at $tRNA^{Arg}$ locus	This work
L. monocytogenes EGDe::Δ*lmo0919*::pIMK3*lmo0919*^{HTF}	EGDe::Δ*lmo0919* with VgaL-HTF overexpressed from the P_{help} promoter integrated at $tRNA^{Arg}$ locus	This work
L. monocytogenes EGDe:: Δ*lmo0919*::pIMK3*lmo0919*$^{HFT\text{-}EQ2}$	EGDe::Δ*lmo0919* with VgaL-EQ2-HTF overexpressed from the P_{help} promoter integrated at $tRNA^{Arg}$ locus	This work
E. faecalis OG1RF	Rif^r Fus^r; WT *E. faecalis*	Singh *et al.*, 2002[13]
E. faecalis TX5332	Rif^r Fus^r Kan^r; *lsa* gene disruption mutant (OG1RF *lsa*::pTEX4577)	Davis *et al.*, 2001[14]
S. aureus SH1000	Functional *rsbU*$^+$ derivative of *S. aureus* 8325-4	O'Neill, 2001, and Horsburgh *et al.*, 2002 [15, 16]
E. coli S17.1	*E. coli* strain used for conjugative plasmid transfer to *L. monocytogenes*	Simon *et al.*, 1983[17]

Plasmid	Description	Reference
pIMK3	Kan^r; Listerial tRNA^{Arg} locus specific integrative vector for high-level IPTG-induced protein expression from the P_{help} promoter	Monk *et al.,* 2008[18]
pMAD	Amp^r, Ery^r; *lacZ*; thermosensitive shuttle vector used for allelic exchange in *L. monocytogenes*	Arnaud *et al.*, 2004[19]
pHT009	Amp^r, Km^r; thrC locus specific integrative vector for high-level IPTG-induced protein expression from the $P_{hy\text{-}spnak}$ promoter	Crowe-McAuliffe *et al.*, 2018[7]
VHp689	pMAD Δ*lmo0919*	This work
VHp690	pIMK3:*lmo0919*	This work
VHp692	pIMK3:*lmo0919-HTF*	This work
VHp693	pIMK3:*lmo0919-EQ2-HTF*	This work
pTX5333	Cm^r; *E. faecalis-E. coli* shuttle plasmid expressing LsaA from native promoter	Singh *et al.*, 2002[13]
pCIE	Cm^r; *E. faecalis-E. coli* shuttle plasmid for cCF10 induced expression of proteins	Weaver *et al.*, 2017[20]
VHp100	pCIE:*lsaA-HTF*	This work*
VHp149	pCIE:*lsaA-EQ2-HTF*	This work*
VHp369	pHT009-*lsaA*	This work
VHp426	pCIE, Sc^r; Cm^r gene swapped to spectinomycin resistance (Sc^r) gene	This work*
VHp431	VHp426:*lsa*	This work*
VHp526	pHT009-*lsaA*K244A	This work
VHp526	pHT009-*lsaA*K244A	This work
pRMC2	Amp^r, Cm^r; *E. coli - S. aureus* shuttle plasmid for tetracycline-regulable expression of proteins in the latter host.	Corrigan *et al.*, 2009[21]
pRMC2:*vgaA-FLAG$_3$*	pRMC2 expressing C-terminally FLAG$_3$ tagged VgaA$_{LC}$	This work
pRMC2:*vgaA-EQ2-FLAG$_3$*	pRMC2 expressing C-terminally FLAG$_3$ tagged VgaA$_{LC}$-E$_{105}$Q, E$_{410}$Q	This work
pRMC2:*vgaA$_{LC}$*	pRMC2 expressing wild-type VgaA$_{LC}$	This work
pRMC2:*vgaA$_{LC}$* (K$_{208}$A)	pRMC2 expressing VgaA$_{LC}$ ^{K208A}	This work
pRMC2:*vgaA$_{LC}$* (S$_{211}$A)	pRMC2 expressing VgaA$_{LC}$ ^{S211A}	This work
pRMC2:*vgaA$_{LC}$* (S$_{212}$A)	pRMC2 expressing VgaA$_{LC}$ ^{S212A}	This work
pRMC2:*vgaA$_{LC}$* (S$_{213}$A)	pRMC2 expressing VgaA$_{LC}$ ^{S213A}	This work
pRMC2:*vgaA$_{LC}$* (K$_{216}$A)	pRMC2 expressing VgaA$_{LC}$ ^{K216A}	This work
pRMC2:*vgaA$_{LC}$* (K$_{218}$A)	pRMC2 expressing VgaA$_{LC}$ ^{K218A}	This work
pRMC2:*vgaA$_{LC}$* (V$_{219}$A)	pRMC2 expressing VgaA$_{LC}$ ^{V219A}	This work
pRMC2:*vgaA$_{LC}$* (Y$_{223}$A)	pRMC2 expressing VgaA$_{LC}$ ^{Y223A}	This work
pRMC2:*vgaA$_{LC}$* (F$_{224}$A)	pRMC2 expressing VgaA$_{LC}$ ^{F224A}	This work
pRMC2:*vgaA$_{LC}$* (S$_{226}$A)	pRMC2 expressing VgaA$_{LC}$ ^{S226A}	This work
pRMC2:*vgaA$_{LC}$* (K$_{227}$A)	pRMC2 expressing VgaA$_{LC}$ ^{K227A}	This work
pRMC2:*vgaA$_{LC}$* (Q$_{228}$A)	pRMC2 expressing VgaA$_{LC}$ ^{Q228A}	This work

pRMC2:*vgaA*$_{LC}$ ($K_{229}A$)	pRMC2 expressing $VgaA_{LC}^{K229A}$	This work
pRMC2:*vgaA*$_{LC}$ ($K_{230}A$)	pRMC2 expressing $VgaA_{LC}^{K230A}$	This work
pRMC2:*vgaA*$_{LC}$ ($A_{232}A$)	pRMC2 expressing $VgaA_{LC}^{A232A}$	This work

Table S6 Primers used in this study.

Name	Sequence
$vgaA_{LC}$-F	GGTGGTGGTACCAGGATGAGGAAATATGAAAA
$vgaA_{LC}$-R	GGTGGTGAATTCGGTAATTTATTTATCTAAATTTCTT
VHKT12	CCCCCCATGGCATCTACAATCGAAATAAATC
VHKT13	GGGGCTGCAGTTAGCCTTTGTCATCGTC
VHKT14	AGACAGCAATTTAGTGGCGGCCATCATCATCATC
VHKT15	ATGATGATGGCCGCCACTAAATTGCTGTCTTTTTG
VKT35	GGGGGGATCCATCACTAGCCGAATCCAAAC
VKT36	GGGGGAATTCAAAAAATAACCTCCTGAATATTTTCAGAG
VHKT37	GGGGGAATTCAAAAAATAACCTCCTGAATATTTTCAGAG
VHKT38	GGGGCCATGGCGTGCTGTACGGTATGC
VHKT39	GGGGCTGCAGTTAACTAAATTGCTGTCTTTTTG
VHT123	CATTATCGCTCTCTCCTTCGTCGACTAAGCTAATTG
VHT125	TAAGCATGCAAGCTAATTCGGTGGAAACGAGG
VHT127	CGACGAAGGAGAGAGCGATAATGTCGAAAATTGAACTAAAACAACTATC
VHT128	CACCGAATTAGCTTGCATGCTTATGATTTCAAGACAATTTTTTTATCTGTTA
VHT264	AGCAGACCAACCAACAAGCAATCTTGATGTCG
VHT265	TGGTTGGTTGATCAAGAATCAAGAAATTGGCGT
VHT266	TCTTGATCAACCAACCAACTATTTGGATATCTACGCAATGGAA
VHT267	TTGTTGGTTGGTCTGCTAGGAGAACACTTGGATTTTGGCGCA
VHP303	GCATCACCTTCACGGTTCATCGACCATTCCGCT
VHP304	GTACGGCAACGCTAAGGAAAAAGGGAGCGGGGCGA
VHP305	CAATCGCCCCGCTCCCTTTTTCCTTAGCGT
VHP306	CGGATACAGGAGCCATTGGTGCCCGGGCA

Supplementary References

1. Johnson ZL, Chen J. ATP binding enables substrate release from Multidrug Resistance Protein 1. *Cell* **172**, 81-89 (2018).

2. Heuer A*, et al.* Structure of the 40S–ABCE1 post-splitting complex in ribosome recycling and translation initiation. *Nat Struct Mol Biol* **24**, 453-460 (2017).

3. Becker T*, et al.* Structural basis of highly conserved ribosome recycling in eukaryotes and archaea. *Nature* **482**, 501-506 (2012).

4. Voorhees RM, Schmeing TM, Kelley AC, Ramakrishnan V. The mechanism for activation of GTP hydrolysis on the ribosome. *Science* **330**, 835-838 (2010).

5. Matzov D*, et al.* Structural insights of lincosamides targeting the ribosome of *Staphylococcus aureus*. *Nucleic Acids Res* **45**, 10284-10292 (2017).

6. Polikanov YS, Steitz TA, Innis CA. A proton wire to couple aminoacyl-tRNA accommodation and peptide-bond formation on the ribosome. *Nat Struct Mol Biol* **21**, 787-793 (2014).

7. Crowe-McAuliffe C*, et al.* Structural basis for antibiotic resistance mediated by the *Bacillus subtilis* ABCF ATPase VmlR. *Proc Natl Acad Sci U S A* **115**, 8978-8983 (2018).

8. Su W*, et al.* Ribosome protection by antibiotic resistance ATP-binding cassette protein. *Proc Natl Acad Sci U S A* **115**, 5157-5162 (2018).

9. Su T*, et al.* Structure and function of Vms1 and Arb1 in RQC and mitochondrial proteome homeostasis. *Nature* **570**, 538-542 (2019).

10. Schlünzen F, Pyetan E, Fucini P, Yonath A, Harms JM. Inhibition of peptide bond formation by pleuromutilins: the structure of the 50S ribosomal subunit from *Deinococcus radiodurans* in complex with tiamulin. *Mol Microbiol* **54**, 1287-1294 (2004).

11. Noeske J, Huang J, Olivier NB, Giacobbe RA, Zambrowski M, Cate JH. Synergy of streptogramin antibiotics occurs independently of their effects on translation. *Antimicrob Agents Chemother* **58**, 5269-5279 (2014).

12. Glaser P*, et al.* Comparative genomics of *Listeria* species. *Science* **294**, 849-852 (2001).

13. Singh KV, Weinstock GM, Murray BE. An Enterococcus faecalis ABC homologue (Lsa) is required for the resistance of this species to clindamycin and quinupristin-dalfopristin. *Antimicrob Agents Chemother* **46**, 1845-1850 (2002).

14. Davis Dv*, et al. Enterococcus faecalis* multi-drug resistance transporters: application for antibiotic discovery. *J Mol Microbiol Biotechnol* **3**, 179-184 (2001).

15. O'Neill A. *Staphylococcus aureus* SH1000 and 8325-4: comparative genome sequences of key laboratory strains in staphylococcal research. *Lett Appl Microbiol* **51**, 358-361 (2010).

16. Horsburgh MJ, Aish JL, White IJ, Shaw L, Lithgow JK, Foster SJ. σB modulates virulence determinant expression and stress resistance: characterization of a functional *rsbU* strain derived from *Staphylococcus aureus* 8325-4. *J Bacteriol* **184**, 5457-5467 (2002).

17. Simon R, Priefer U, Pühler A. A broad host range mobilization system for *in vivo* genetic engineering: transposon mutagenesis in Gram negative bacteria. *Bio/technology* **1**, 784-791 (1983).

18. Monk IR, Gahan CG, Hill C. Tools for functional postgenomic analysis of *Listeria monocytogenes*. *Appl Environ Microbiol* **74**, 3921-3934 (2008).

19. Arnaud M, Chastanet A, Débarbouillé M. New vector for efficient allelic replacement in naturally nontransformable, low-GC-content, gram-positive bacteria. *Appl Environ Microbiol* **70**, 6887-6891 (2004).

20. Weaver KE*, et al.* Examination of *Enterococcus faecalis* toxin-antitoxin system toxin Fst function utilizing a pheromone-inducible expression vector with tight repression and broad dynamic range. *J Bacteriol* **199**, e00065-00017 (2017).

21. Corrigan RM, Foster TJ. An improved tetracycline-inducible expression vector for *Staphylococcus aureus*. *Plasmid* **61**, 126-129 (2009).

7.4 Structure of the PoxtA ABCF protein in complex with the 70S ribosome, supplementary material

Supplementary Tables

Table S1. Broth microdilution (BMD) and gradient (GRAD) MIC testing of multidrug-resistant ST872 *E. faecium* 9-F-6.

	MIC, μg/mL		
	EUCAST breakpoints	**BMD**	**GRAD**
Ampicillin	S≤4 R> 8	**>32**	**>256**
Amoxicillin	S≤4 R> 8	**>32**	ND
Imipenem	S≤0,001 R> 4	**>16**	ND
Ciprofloxacin	S≤4 R> 4	**>16**	ND
Levofloxacin	S≤4 R> 4	**>16**	ND
Gentamicin	HLGR >128	**>256**	**>1024**
Streptomycin	HLSR > 512	**>1024**	ND
Teicoplanin	S≤2 R> 2	**>8**	**128**
Vancomycin	S≤4 R> 4	**>16**	**>256**
Clindamycin	NA	ND	>256
Quinupristin/Dalfopristin	S≤1 R>4	4	ND
Tigecycline	S≤0.25 R>0.25	0.12	ND
Linezolid	S≤4 R> 4	**8**	**16**
Chloramphenicol	NA	ND	16

MICs above the clinical break points, i.e. classifying the strain as resistant (R) are in bold, MICs below the break point, i.e. classifying the strain as susceptible (S) are in regular font. HLGR and HLSR stands for high-level gentamicin and streptomycin resistance. Note that BMD-based MICs overrule GRAD test MICs. ND stands for not determined, NA stands for not applicable.

Table S2. Cryo-EM data collection, modelling and refinement statistics.

	Combined 70S	State I	State II	State III	State IV
Data collection					
Magnification (×)	165 000	165 000	165 000	165 000	165 000
Electron fluence ($e^-/Å^2$)	30.255	30.255	30.255	30.255	30.255
Defocus range (μm)	−0.5 to −1.5	−0.5 to −1.5	−0.5 to −1.5	−0.5 to −1.5	−0.5 to −1.5
Pixel size (Å)	0.82	0.82	0.82	0.82	0.82
Initial particles	203 321	203 321	203 321	203 321	203 321
Final particles	112 877	29 581	29 875	23 806	18 512
Average resolution (Å) (FSC threshold 0.143)	2.4	2.9	3.0	2.9	3.1
Model composition					
Atoms	151 224	147 584	147 584	149 091	139 841
Protein residues	6 097	6 097	6 097	6 097	5 337
RNA bases	4 625	4 625	4 625	4697	4 549
Refinement					
Map CC around atoms	0.80	0.71	0.69	0.73	0.72
Map CC whole unit cell	0.80	0.70	0.69	0.71	0.70
Map sharpening B factor ($Å^2$)	−46	−55	−59	−58	−59
R.M.S. deviations					
Bond lengths (Å)	0.007	0.007	0.004	0.005	0.004
Bond angles (°)	1.041	0.861	0.677	0.743	0.500
Validation					
MolProbity score	1.76	1.95	1.90	1.81	1.48
Clash score	4.38	6.11	6.76	6.06	5.98
Poor rotamers (%)	2.88	3.58	3.19	2.80	1.12
Ramachandran statistics					
Favoured (%)	96.82	96.78	97.25	97.25	97.44
Outlier (%)	0.08	0.07	0.03	0.05	0.06

Table S3. Strains and plasmids used in this study.

Abbreviations used: spec – spectinomycin, RBS – ribosome binding site, cm – chloramphenicol, HTF - His_6-TEV-$FLAG_3$, ARD – antibiotic resistance domain. NA stands for not applicable.

Strain or Plasmid	VH lab database number	Description	Reference
E. faecium 9-F-6	N.A.	Multidrug-resistant clinical isolate	(Sivertsen et al., 2018)
E. faecalis TX5332 Δ*lsaA* (*lsa*::Kan)	N.A.	Rif^r Fus^r Kan^r; *lsa* gene disruption mutant (OG1RF *lsa*::pTEX4577))	(Singh et al., 2002)
$pCIE_{spec}$	VHp426	pCIE, $Spec^r$; Cm^r gene swapped to spectinomycin resistance ($Spec^r$) gene	(Crowe-McAuliffe et al., 2021)
$pCIE_{spec}$:*poxtA-AOUC-0915*-HTF	VHp553	$pCIE_{spec}$ with optimized RBS expressing PoxtA AOUC-0915 with C-terminal His_6-TEV-$FLAG_3$ tag	This work
$pCIE_{spec}$:*poxtA-AOUC-0915*-EQ_2-HTF	VHp609	$pCIE_{spec}$ with optimized RBS expressing PoxtA AOUC-0915 with C-terminal His_6-TEV-$FLAG_3$ tag and $E_{184}Q$ and $E_{471}Q$ mutations	This work
$pCIE_{spec}$:*lsaA*	VHp431	$pCIE_{spec}$ with optimized RBS expressing LsaA	(Crowe-McAuliffe et al., 2021)
$pCIE_{spec}$:*optrA-ST16*	VHp432	$pCIE_{spec}$ with optimized RBS expressing OptrA ST16	This work
$pCIE_{spec}$:*optrA-E35048*	VHp506	$pCIE_{spec}$ with optimized RBS expressing OptrA-E35048	This work
$pCIE_{spec}$:*poxtA-EF9F6*	VHp504	$pCIE_{spec}$ with optimized RBS expressing PoxtA EF9F6	This work
$pCIE_{spec}$:*poxtA-AOU-0915*	VHp507	$pCIE_{spec}$ with optimized RBS expressing PoxtA AOUC-0915	This work
$pCIE_{Cam}$:*optrA-ST16-HTF*	VHp223	$pCIE_{Cam}$ with optimized RBS expressing OptrA ST16 with C-terminal His_6-TEV-$FLAG_3$ tag	This work
$pCIE_{Cam}$:*optrA-ST16-E470Q-HTF*	VHp294	$pCIE_{Cam}$ with optimized RBS expressing OptrA ST16 with C-terminal His_6-TEV-$FLAG_3$ tag and $E_{470}Q$ substitution	This work
$pCIE_{Cam}$:*optrA-ST16-EQ_2-HTF*	VHp295	$pCIE_{Cam}$ with optimized RBS expressing OptrA ST16 with C-terminal His_6-TEV-$FLAG_3$ tag and $E_{190}Q$ and $E_{470}Q$ substitutions	This work

Supplementary Figures

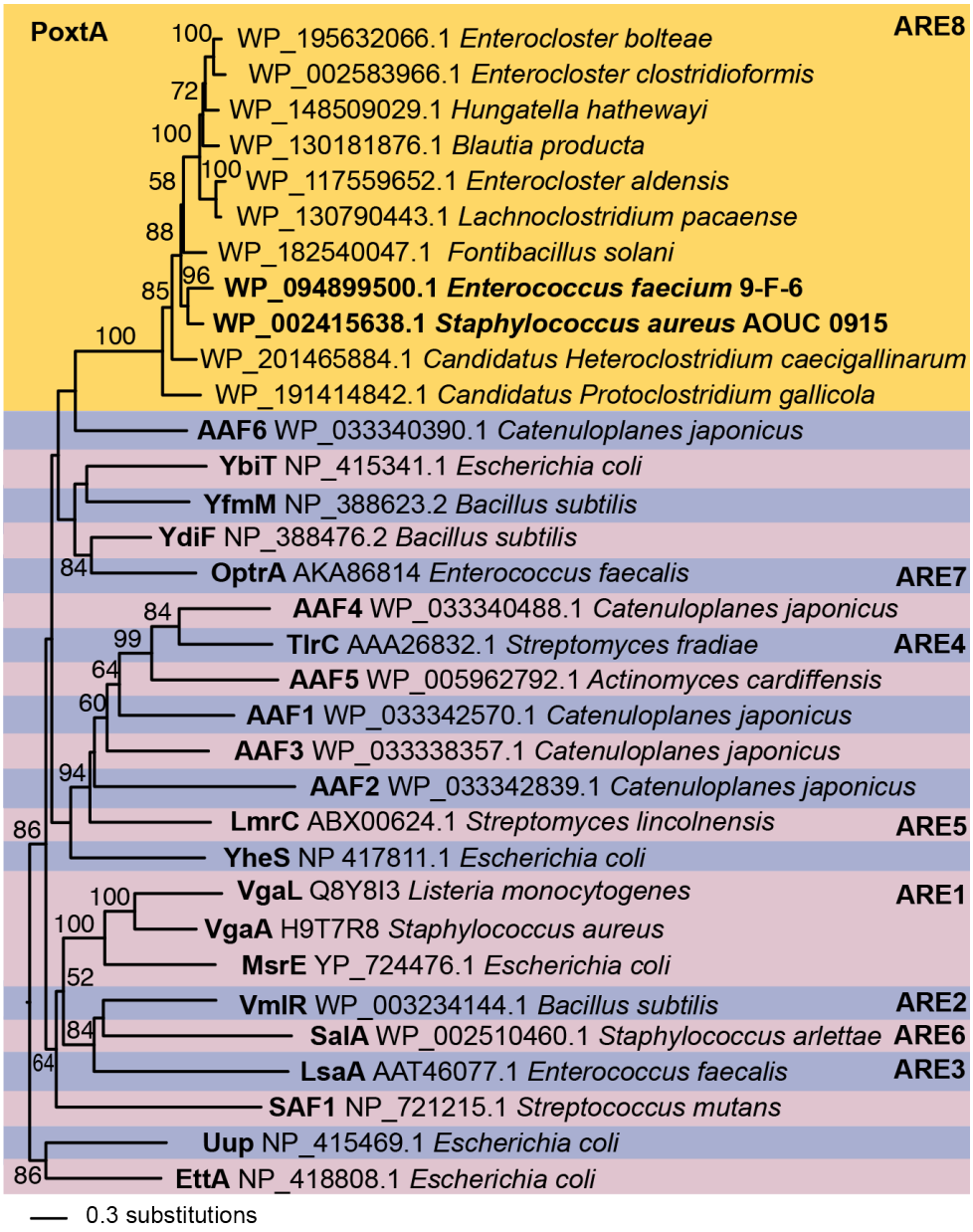

Fig. S1. ARE-ABCF phylogeny with a focus on PoxtA. The tree is a maximum likelihood phylogeny of selected ABCF representatives. Numbers on branches correspond to IQ-Tree ultra-fast bootstrap support in percentages (Minh et al., 2020), and branch length is proportional to the number of substitutions as per the scale bar in the lower left. The ARE8 subfamily comprising PoxtA-like proteins has 100% support, but its relationship with other subfamilies is unresolved. OptrA is most closely related to the YdiF subfamily of mostly vertically inherited and presumably housekeeping ABCF (84% bootstrap support). This suggests that the similar resistance spectrum of OptrA and PoxtA is a case of convergent evolution.

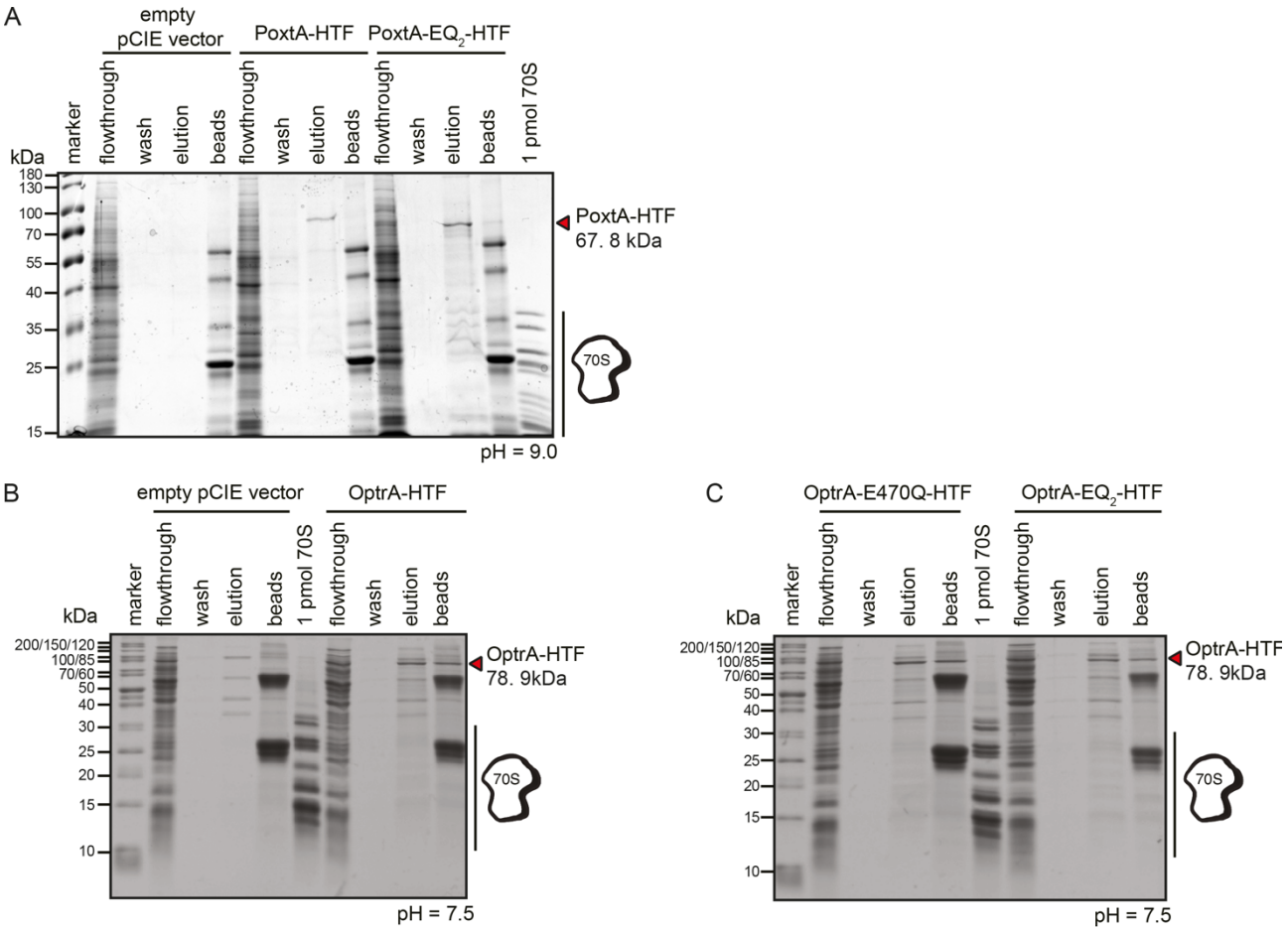

Fig. S2. Characterization of PoxtA-E9F6 interactions with ribosomes and preparation of samples for cryo-EM reconstructions. (*A*) Affinity purification of PoxtA-EQ_2-HTF ectopically expressed in *E. faecalis* Δ*lsaA* (*lsa*::Kan) strain TX5332. Pull-down experiments were performed in the presence of 0.5 mM ATP using clarified lysates of *E. faecalis* either transformed with empty integrative $pCIE_{spec}$ vector (background control), or either expressing PoxtA-HTF or PoxtA-EQ_2-HTF. Samples: marker: 2 µL of molecular weight marker; flowthrough: 2 µL of flowthrough; wash: 10 µL of last wash before specific elution; elution: 10 µL of elution with $FLAG_3$ peptide at pH 9.0; beads: 2 µL of SDS-treated post-elution anti-FLAG beads; 70S: purified *E. faecalis* 70S ribosomes, the samples were resolved on 12 % SDS-PAGE gel. (*B, C*) Affinity purification attempts with wild-type, EQ_2 and EQ_1 (E470Q) *E. faecalis* OptrA-ST16-HTF ectopically expressed in TX5332 *E. faecalis*. Pull-down experiments were performed in the presence of 0.75 mM ATP at pH 7.5 using clarified lysates of *E. faecalis* either transformed with *E. faecalis* OptrA-ST16-HTF (VHp223) or expressing either *E. faecalis* OptrA-ST16-E470Q-HTF (VHp294) or OptrA-ST16-EQ_2-HTF (VHp295). Samples: marker: molecular weight marker; lysate: 2 µL of clarified lysate, flowthrough: 2 µL of flow-through; wash: 10 µL of last wash before specific elution; elution: 10 µL of the elution with $FLAG_3$ peptide; B: 10 µL of SDS-treated post-elution anti-FLAG beads; 70S: purified *E. faecalis* 70S ribosomes. The samples were resolved on 15% SDS-PAGE gel.

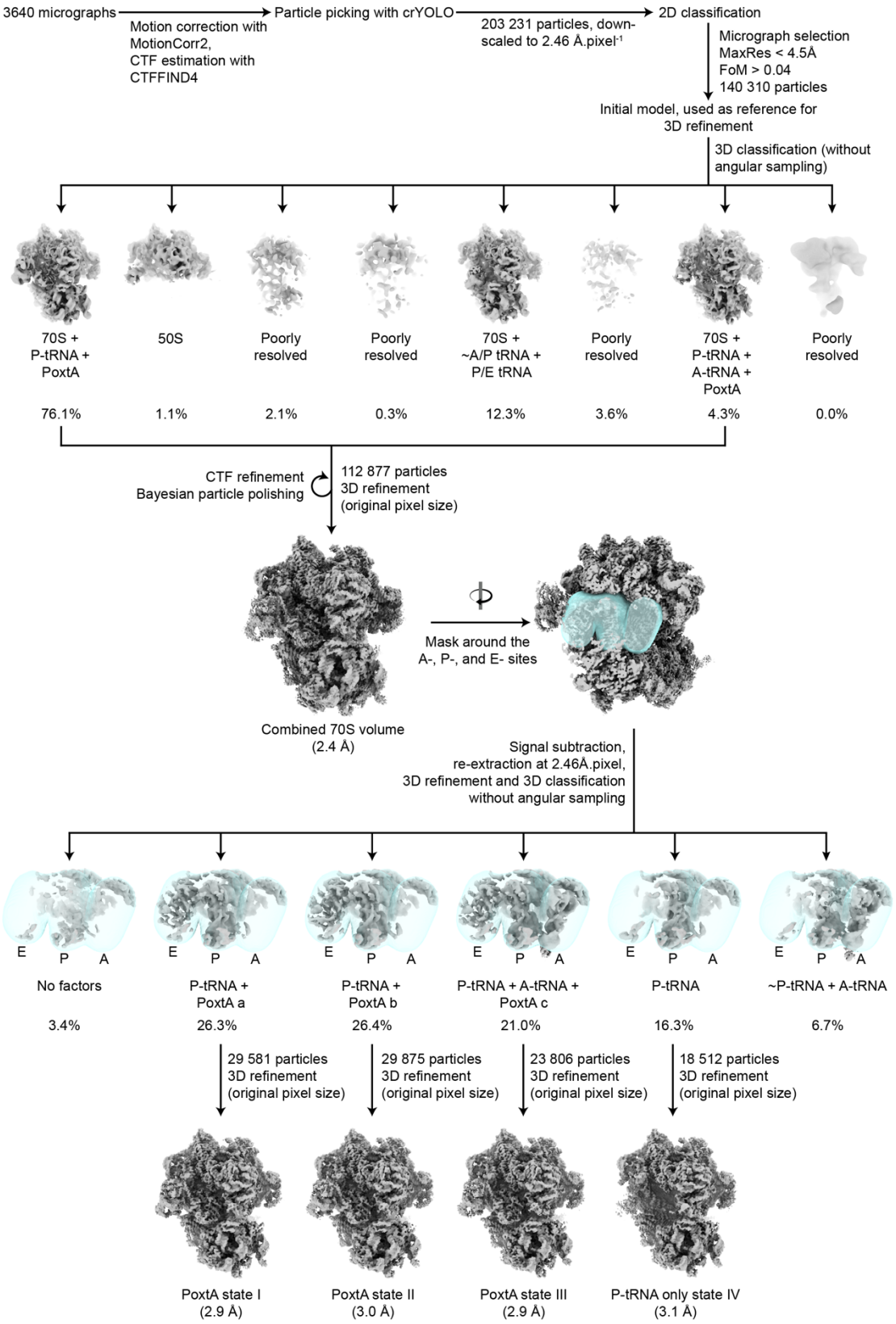

Fig. S3 Processing scheme for the PoxtA-70S complex. See also Methods for details.

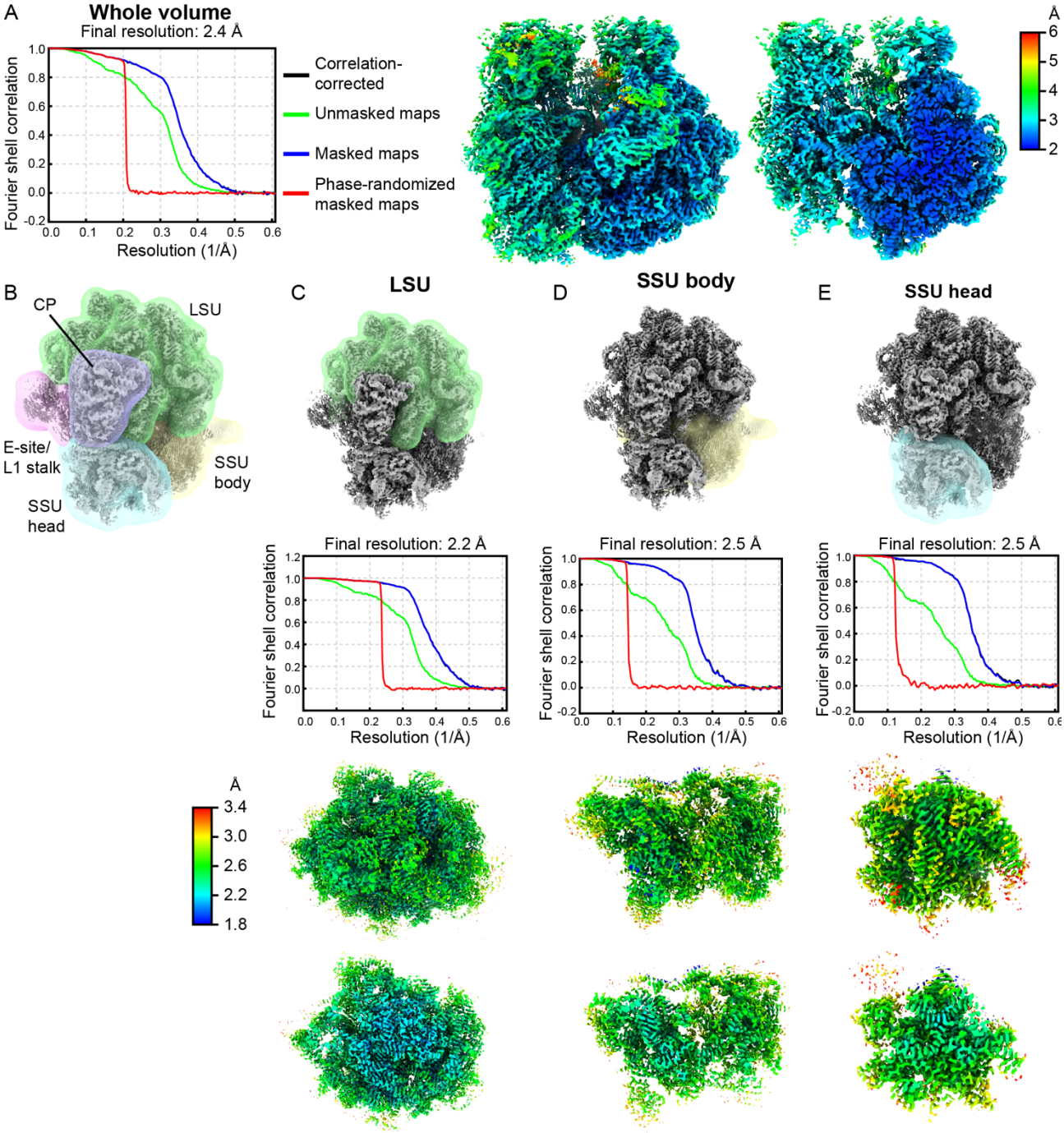

Fig. S4 Local resolutions and multibody refinements for the combined 70S volume. (*A*) FSC curve and local resolution images for the combined 70S volume. (*B*) Overview of masks used for multibody refinement (*C–E*) masks relative to whole 70S (top row), FSC curves (second row), and density coloured according to local resolution (bottom two rows) for (*C*) the LSU core, (*D*) the SSU body, and (*E*) the SSU head.

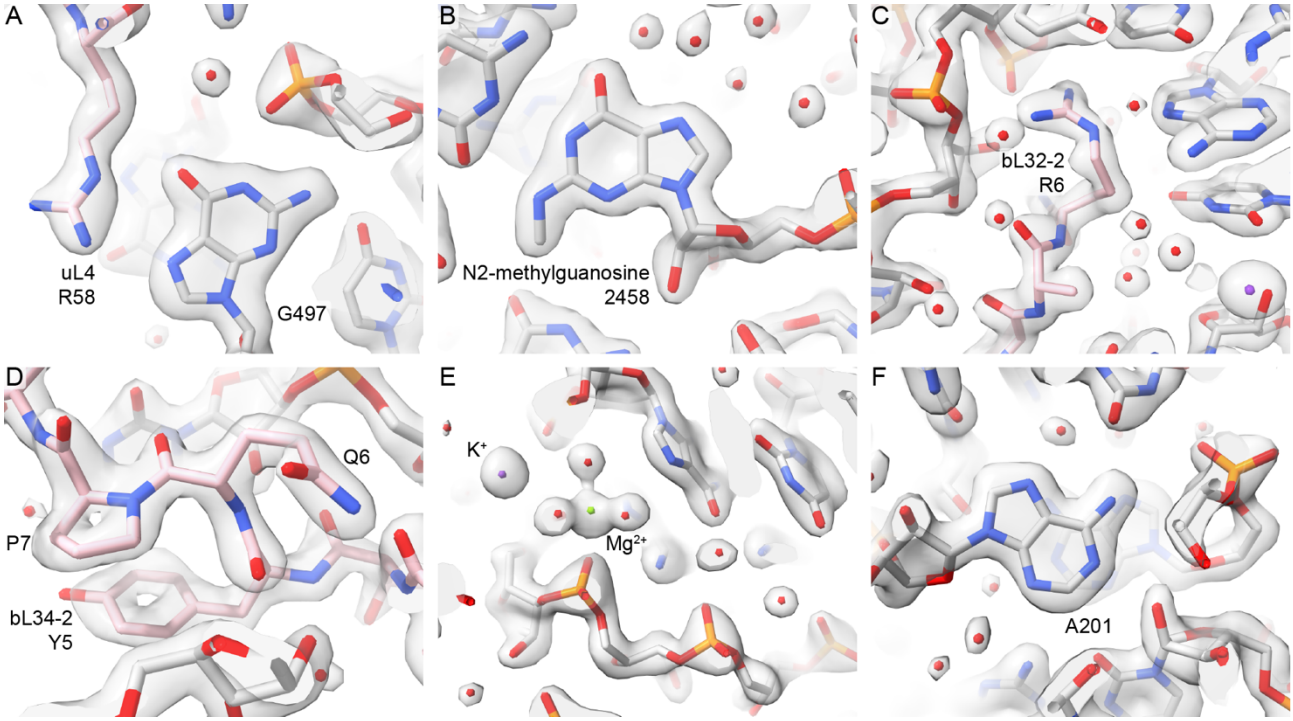

Fig. S5 Selected density images from the high-resolution LSU core. Modelled water molecules are colored red, magnesium green, and potassium purple.

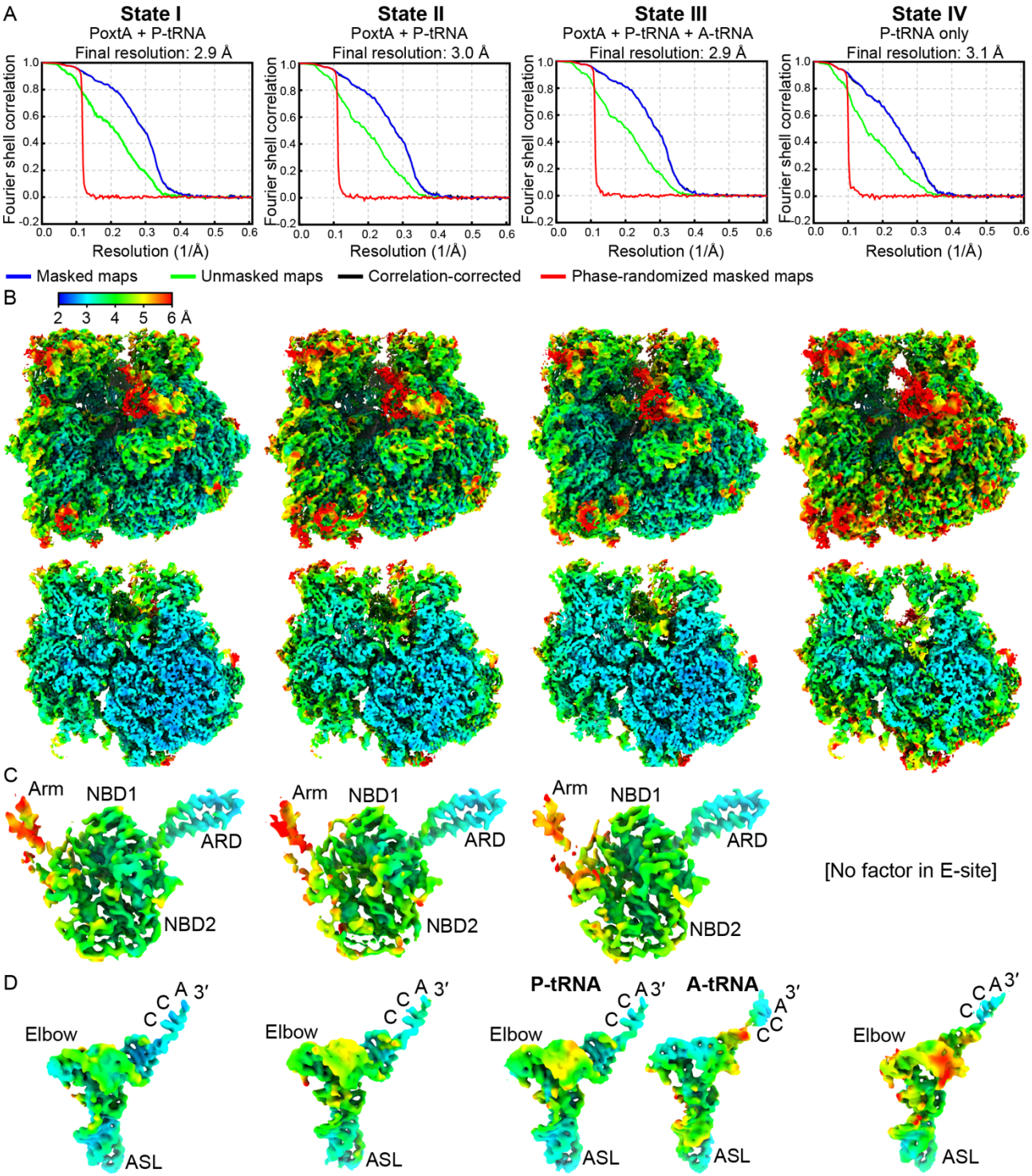

Fig. S6 FSC curves and density coloured by local resolution for states I-IV. (*A*) FSC curves. (*B*) density coloured by local resolution for whole volumes with cut-throughs (bottom row). (*C*) Isolated density for isolated PoxtA coloured by local resolution. (*D*) Isolated density for isolated tRNAs coloured by local resolution.

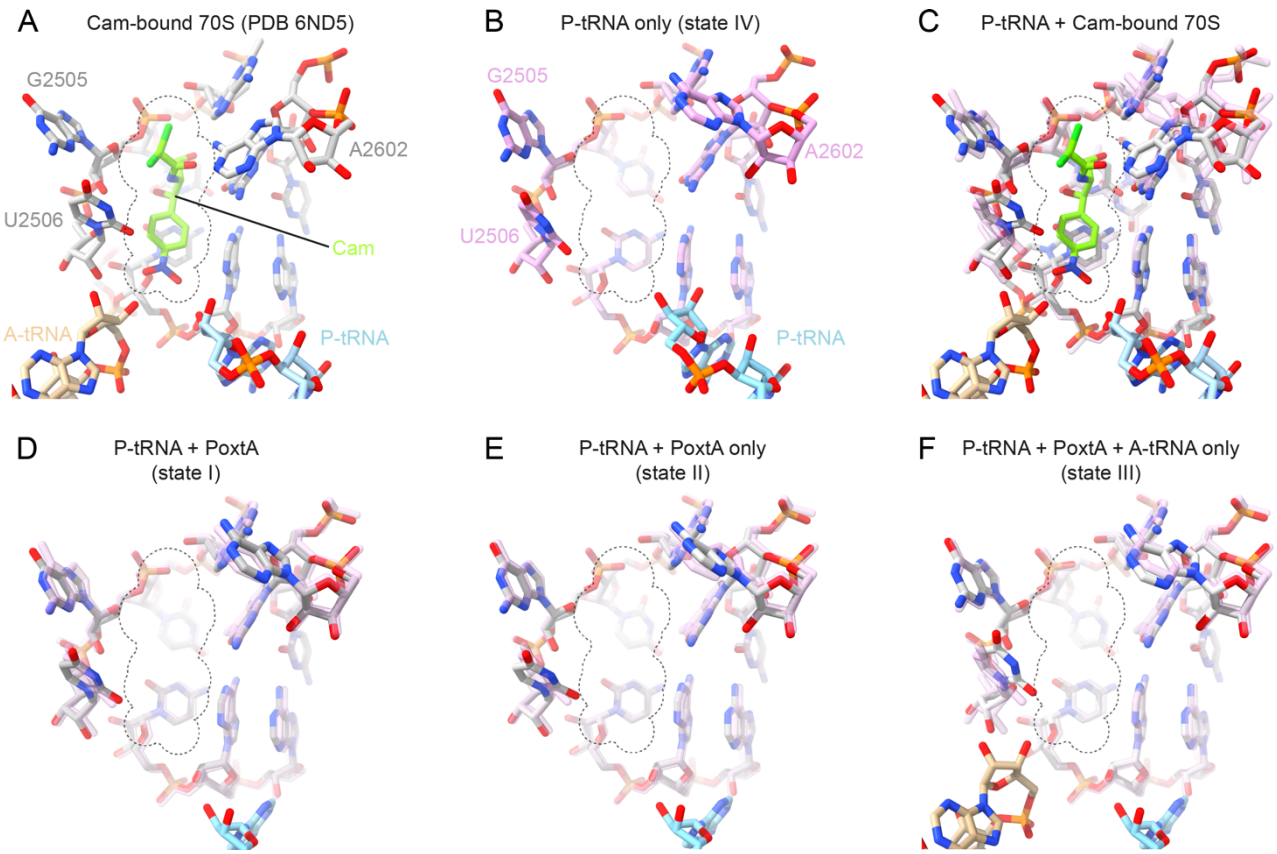

Fig. S7 Effects of PoxtA binding on the 23S rRNA chloramphenicol binding site. (*A*) Chloramphenicol (cam, green, PDB ID 6ND5, (Svetlov et al., 2019)) bound to 23S rRNA (grey). Dotted lines indicate the extent of a space-filling model of chloramphenicol. A-tRNA (tan) and P-tRNA (light blue) are also shown). (*B*) Same view as (A) but for the P-tRNA-only bound volume (state IV). 23S rRNA is shown in pink. (*C*) Same as panel A but with P-tRNA-only (state IV) 23S rRNA superimposed (transparent pink). (*D–F*) As for *C*, but comparing the P-tRNA-only (state IV) 23S rRNA with PoxtA bound states I–III. The chloramphenicol outline is shown for reference.

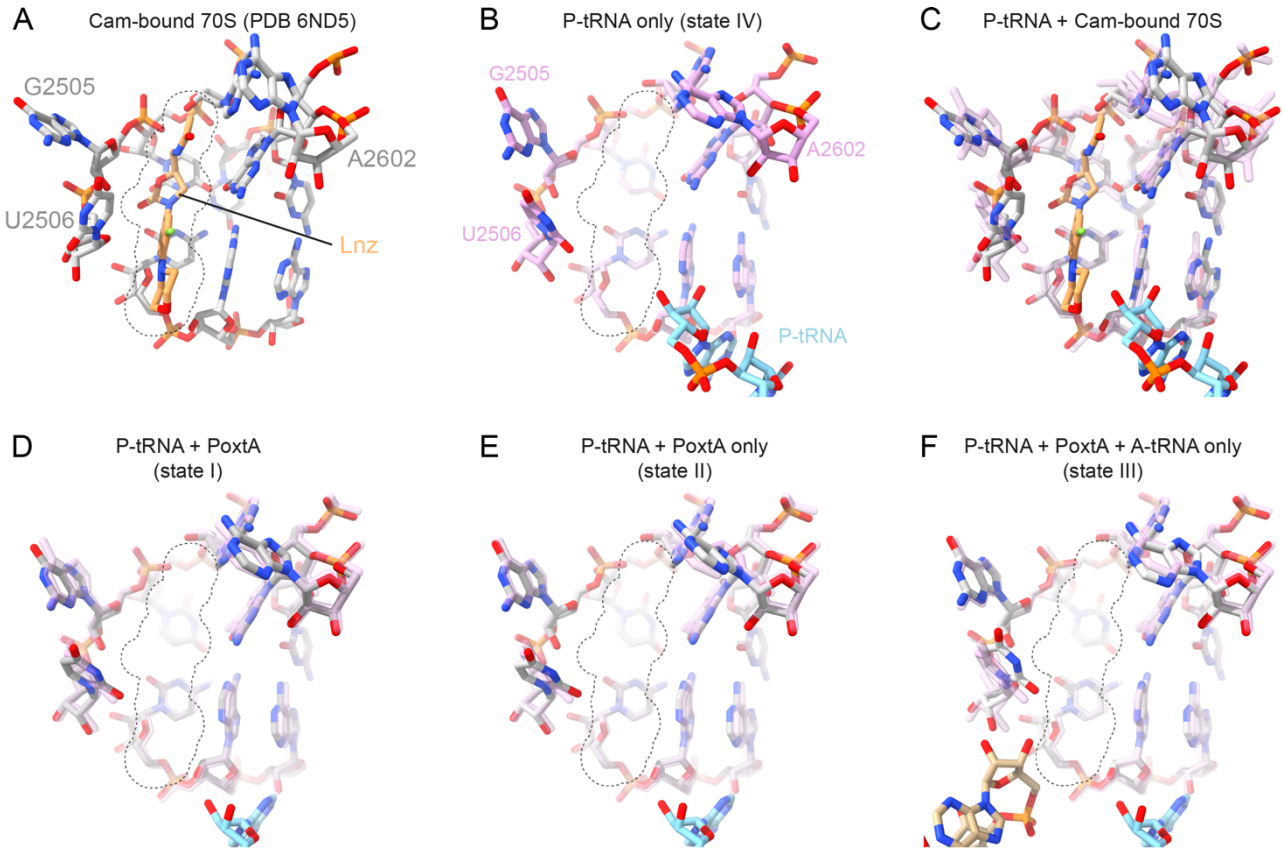

Fig. S8 Effects of PoxtA binding on the 23S rRNA linezolid binding site. (*A*) Linezolid (Lnz, light orange, PDB ID 3DLL, (Wilson et al., 2008)) bound to 23S rRNA (grey). Dotted lines indicate the extent of a space-filling model of linezolid. A-tRNA (tan) and P-tRNA (light blue) are also shown). (*B*) Same view as (*A*) but for the P-tRNA-only bound volume (state IV). 23S rRNA is shown in pink. (*C*) Same as panel A but with P-tRNA-only (state IV) 23S rRNA superimposed (transparent pink). (*D–F*) As for *C*, but comparing the P-tRNA-only (state IV) 23S rRNA with PoxtA bound states I–III. The linezolid outline is shown for reference.

7.5 Structures of bacterial RQC elongation complexes, supplementary material

Please cite this article in press as: Crowe-McAuliffe et al., Structural Basis for Bacterial Ribosome-Associated Quality Control by RqcH and RqcP, Molecular Cell (2020), https://doi.org/10.1016/j.molcel.2020.11.002

CellPress

STAR★METHODS

KEY RESOURCES TABLE

REAGENT or RESOURCE	SOURCE	IDENTIFIER
Antibodies		
Anti-FLAG M2 primary antibodies (1:10000)	Sigma-Aldrich	Cat#F1804; RRID: AB_262044
Anti-mouse-HRP secondary antibodies (1:10000)	Rockland	Cat#610-103-040; RRID: AB_2614833
Goat anti-rabbit IgG-HRP secondary antibodies (1:10000)	Sigma-Aldrich	Cat#A0545; RRID: AB_257896
Anti-L3 primary antibody (1:20000)	Fujio Kawamura	N/A
Bacterial and Virus Strains		
Escherichia coli DH5α	ThermoFischer	Cat#18265017
For *B. subtilis* strains see Table S3	This manuscript	N/A
Chemicals, Peptides, and Recombinant Proteins		
Anti-FLAG M2 Affinity Gel	Sigma-Aldrich	Cat#A2220-25ML; RRID:AB_10063035
Poly FLAG Peptide lyophilized powder	Bimake	Cat#B23112
Phusion High-Fidelity PCR Master Mix with HF Buffer	ThermoFischer	Cat#F531L
Lysobacter enzymogenes Lys-C	Fujifilm Wako Pure Chemicals	Cat#129-02541
Dimethylated Sus scrofa trypsin	Sigma Aldrich	Cat#T6567
WesternBright Quantum	Advansta	Cat#K-12042-D10
cOmplete EDTA-free Protease Inhibitor Cocktail	Roche	Cat#4693132001
Deposited Data		
Micrograph frames from RqcH-IP collections	Umeå Core Facility for Electron Microscopy	EMPIAR: 10540
Micrograph frames from YabO-IP collection	Umeå Core Facility for Electron Microscopy	EMPIAR: 10541
Cryo-EM map for RqcH IP State A	This manuscript	EMDB: EMD-11890
Cryo-EM map for RqcH IP State B	This manuscript	EMDB: EMD-11889
Cryo-EM map for RqcH IP State B multibody	This manuscript	EMDB: EMD-11891
Cryo-EM map for RqcH IP State B*	This manuscript	EMDB: EMD-11915
Cryo-EM map for RqcH IP State C	This manuscript	EMDB: EMD-11913
Cryo-EM map for RqcH IP State D	This manuscript	EMDB: EMD-11914
Cryo-EM map for RqcP/YabO IP State B	This manuscript	EMDB: EMD-11919
Cryo-EM map for RqcP/YabO IP State D	This manuscript	EMDB: EMD-11918
Cryo-EM map for RqcP/YabO IP State E	This manuscript	EMDB: EMD-11916
Cryo-EM map for RqcP/YabO IP 50S-RsfS	This manuscript	EMDB: EMD-11920
Cryo-EM map for RqcP/YabO IP 50S-SRP	This manuscript	EMDB: EMD-11917
Molecular model of RqcH IP State A	This manuscript	PDB: 7AS9
Molecular model of RqcH IP State B	This manuscript	PDB: 7AS8
Molecular model of RqcH IP State B multibody	This manuscript	PDB: 7ASA
Data from tRNA microarray	This manuscript	GEO: GSE15259
Raw data from SDS-PAGE and Western immunoblots	This manuscript	https://doi.org/10.17632/27ynjm3f2f.1
Data related to mass spectrometry	This manuscript	PRIDE: PXD019364
Oligonucleotides		
For primers used for cloning of *B. subtilis* mutants see Table S3	This manuscript	N/A
For primers used for cloning of vectors see Table S3	This manuscript	N/A

(*Continued on next page*)

Please cite this article in press as: Crowe-McAuliffe et al., Structural Basis for Bacterial Ribosome-Associated Quality Control by RqcH and RqcP, Molecular Cell (2020), https://doi.org/10.1016/j.molcel.2020.11.002

Continued

REAGENT or RESOURCE	SOURCE	IDENTIFIER
5′ pC dG dC dA dC dT dG dC dT dT X dT dT dG dC dA dG dT dG dC dG dT dG dG dN (X = dT with fluorophore Cy3)	Microsynth	N/A
5′ pC dG dC dA dC dT dG dC dT dT X dT dT dG dC dA dG dT dG dC dG dT dG dG dN (X = dT with fluorophore CAtto647)	Microsynth	N/A
Recombinant DNA		
For *B. subtilis* vectors see Table S3	This manuscript	N/A
Software and Algorithms		
Relion 3.1	Zivanov et al., 2018	RRID:SCR_016274
MotionCor2	Zheng et al., 2017	RRID:SCR_016499
Gctf	Zhang, 2016	RRID:SCR_016500
crYOLO	Wagner et al., 2019	RRID:SCR_018392
SPHIRE	Moriya et al., 2017	RRID:SCR_018391
ResMap	Kucukelbir et al., 2014	http://resmap.sourceforge.net/
SWISS-MODEL	Waterhouse et al., 2018	RRID:SCR_018123
PSI-PRED	Buchan and Jones, 2019	http://bioinf.cs.ucl.ac.uk/psipred/
DALI	Holm, 2019	RRID:SCR_013433
Coot	Emsley et al., 2010	RRID:SCR_014222
ISOLDE	Croll, 2018	https://isolde.cimr.cam.ac.uk/
Phenix	Liebschner et al., 2019	RRID:SCR_014224
MolProbity	Williams et al., 2018	RRID:SCR_014226
PyMOL	Schrödinger	RRID:SCR_000305
UCSF Chimera	Pettersen et al., 2004	RRID:SCR_004097
UCSF ChimeraX	Goddard et al., 2018	RRID:SCR_015872
Inkscape	Inkscape's Contributors	RRID:SCR_014479
GenePix Pro7	Molecular Devices	https://www.moleculardevices.com
MaxQuant (version 1.6.1.0)	Tyanova et al., 2016	RRID:SCR_014485
MaxLFQ algorithm	Tyanova et al., 2016	https://www.maxquant.org/
MAFFT	Katoh et al., 2005	RRID:SCR_011811
TrimAL	Capella-Gutiérrez et al., 2009	RRID:SCR_017334
RaxML	Stamatakis, 2014	RRID:SCR_006086
Other		
FastPrep-24 classic	MP Biomedicals	https://www.mpbio.com
Biocomp Gradient Station	BioComp Instruments	http://www.biocompinstruments.com
Trans-Blot Turbo 0.2 μm Midi Nitrocellulose Transfer Pack	Bio-Rad	Cat#1704159
ImageQuant LAS 4000	GE Healthcare	https://www.cytivalifesciences.com/country-selection?originalItemPath=%2f
0.1 mm Zirconium beads	BioSpec	Cat#11079101z
Micro Bio-Spin Columns columns	Bio-Rad	Cat#7326204
Vitrobot	ThermoFisher	https://www.thermofisher.com/us/en/home.html
300 kV Titan Krios	ThermoFisher	https://www.thermofisher.com/us/en/home.html
K2 Summit camera	Gatan	https://www.gatan.com
Quantifoil 2/1 Cu 300	Quantifoil	https://www.quantifoil.com/
Quantifoil 2/2 Cu 300	Quantifoil	https://www.quantifoil.com/
GenePix 4300A scanner	Molecular Devices	https://www.moleculardevices.com
Ultimate 3000 RSLCnano system	Dionex	Cat#ULTIM3000RSLCNANO

(*Continued on next page*)

Please cite this article in press as: Crowe-McAuliffe et al., Structural Basis for Bacterial Ribosome-Associated Quality Control by RqcH and RqcP, Molecular Cell (2020), https://doi.org/10.1016/j.molcel.2020.11.002

Continued

REAGENT or RESOURCE	SOURCE	IDENTIFIER
0.3 × 5 mm trap-column	Dionex	Cat#163589
50 cm × 75 μm emitter-column	New Objective	Cat#FS360-75-8-N-5-C50
Quadrupole-orbitrap Q Exactive Plus	ThermoFisher	Cat#IQLAAEGAAPFALGMBDK

RESOURCE AVAILABILITY

Lead Contact

Further information and requests for resources and reagents should be directed to and will be fulfilled by the Lead Contact, Daniel N. Wilson (daniel.wilson@chemie.uni-hamburg.de).

Materials Availability

All unique/stable reagents generated in this study are available from the Lead Contact without restriction.

Data and Code Availability

Cryo-EM raw images for the RqcH and RqcP/YabO IPs have been deposited to EMPIAR with the accession numbers EMPIAR-10540 and EMPIAR-10541, respectively. Cryo-EM maps and molecular models have been deposited in the EMDB or PDB with the primary accession codes: RqcH IP State A, EMD-11890 and PDB ID 7AS9; RqcH IP State B, EMD-11889 and PDB ID 7AS8; RqcH IP State B RqcH-focused multibody refinement, EMD-11891 and PDB ID 7ASA. Cryo-EM maps have also been deposited in the EMDB for RqcH IP State B* (EMD-11915), State C (EMD-11913) and State D (EMD-11914), as well as for the and RqcP/YabO IP States B (EMD-11919), State D (EMD-11918), State E (EMD-11916), 50S-RsfS (EMD-11920) and 50S-SRP (EMD-11917). For mass spectrometry, raw files along with MaxQuant identification and quantification outputs have been deposited to the ProteomeXchange Consortium via the PRIDE partner repository with the dataset identifier PXD019364. Data from tRNA microarray analysis have been deposited in Gene Expression Omnibus (GEO) database under accession GSE152592. Scripts for analyzing microarray data are available upon request to Z.I.

EXPERIMENTAL MODEL AND SUBJECT DETAILS

Bacterial strains

B. subtilis and *E. coli* strains (Crowe-McAuliffe et al., 2018; Guérout-Fleury et al., 1995, 1996; Horinouchi and Weisblum, 1982; Murina et al., 2019; Takada et al., 2014) used in this study are listed in Table S3. All *B. subtilis* strains used were derivatives of the wild-type 168 strain.

METHOD DETAILS

DNA and plasmids

Plasmids as well as DNA oligonucleotides used in this study are listed in Table S3. All *B. subtilis* strains used were derivatives of the wild-type 168 strain. Mutant strains were constructed by transformation with plasmids or DNA fragments (the latter were generated by recombinant PCR, combining 3 or 4 smaller PCR fragments) and relied upon *in vivo* recombination, followed by selection for antibiotic resistance. The plasmids carried engineered *B. subtilis* genes of interest flanked by sequences corresponding to the integration target loci. PCR fragments and plasmids used in the study, as well as the schematics of their generation, are provided in Table S3. Plasmids and PCR fragments were constructed by standard cloning methods including PCR, Phusion Site-Directed Mutagenesis (Thermo Fisher Scientific) and Gibson assembly (NEB).

Sucrose gradient fractionation and western blotting

Sucrose gradient fractionation and western blotting were carried out as described earlier (Takada et al., 2020), with minor modifications. *B. subtilis* strains were pre-grown on Luria Broth (LB) plates overnight at 30°C. Fresh individual colonies were used to inoculate 200 mL LB cultures. The cultures were grown until OD_{600} of 0.8 at 37°C and the cells were collected by centrifugation at 8,000 rpm for 5 minutes in JLA-16.25 rotor (Beckman Coulter), dissolved in 0.5 mL of HEPES:Polymix buffer, 5 mM $Mg(OAc)_2$ (Takada et al., 2020) supplemented with 2 mM PMSF. Cells were lysed using FastPrep homogenizer (MP Biomedicals) by four 20 s pulses at speed 6.0 mp/sec with chilling on ice for 3 minutes between the cycles and the resultant lysates were clarified by ultracentrifugation at 14,800 rpm for 20 minutes in F241.5P rotor using Microfuge 22R centrifuge (Beckman Coulter). 10 A_{260} units of each extract were loaded onto 10%–35% (w/v) sucrose density gradients in Polymix buffer, 5 mM $Mg(OAc)_2$. Gradients were resolved at 36,000 rpm for 3 hours at 4°C in SW41 rotor (Beckman). Both separation and fractionation of gradients used a Biocomp Gradient Station (BioComp Instruments) with A_{280} as a readout.

Please cite this article in press as: Crowe-McAuliffe et al., Structural Basis for Bacterial Ribosome-Associated Quality Control by RqcH and RqcP, Molecular Cell (2020), https://doi.org/10.1016/j.molcel.2020.11.002

For western blotting, 0.5 mL fractions were supplemented with 1.5 mL of 99.5% ethanol, and precipitated overnight at –20°C. After centrifugation at 14,800 rpm for 30 minutes at 4°C the supernatants were discarded and the samples were dried. The pellets were resuspended in 40 μL of 2x SDS loading buffer (100 mM Tris-HCl pH 6.8, 4% SDS (w/v) 0.02% Bromophenol blue, 20% glycerol (w/v) 4% β-mercaptoethanol), resolved on the 12% SDS-PAGE and transferred to nitrocellulose membrane (Trans-Blot Turbo Midi Nitrocellulose Transfer Pack, Bio-Rad, 0.2 μm pore size) using Trans-Blot Turbo Transfer Starter System (Bio-Rad) (10 minutes, 2.5A, 25V). Membranes were blocked for one hour in PBS-T (1 × PBS, 0.05% Tween-20) with 5% w/v non-fat dry milk at room temperature. RqcH-$FLAG_3$ was detected using anti-Flag M2 primary (Sigma-Aldrich, F1804; 1:10,000 dilution) antibodies combined with anti-mouse-HRP secondary (Rockland; 610-103-040; 1:10,000 dilution) antibodies. Ribosomal protein L3 was detected using anti-L3 primary antibodies (a gift from Fujio Kawamura; 1:20,000 dilution) combined with goat anti-rabbit IgG-HRP secondary antibodies (Sigma-Aldrich, A0545; 1:10,000 dilution). ECL detection was performed using WesternBright™ Quantum (K-12042-D10, Advansta) western blotting substrate and ImageQuant LAS 4000 (GE Healthcare) imaging system.

Growth assays

B. subtilis 168 wild-type and deletion strains were pre-grown on LB plates overnight at 30°C. Fresh individual colonies were used to inoculate liquid LB medium cultures (OD_{600} adjusted to 0.01) at 37°C. Log phase cultures (OD_{600} of about 0.4) diluted to OD_{600} = 0.1 were used to prepare 10- to 10^5-fold serial dilutions which were then spotted onto LB agar plates (with or without 1 mM isopropyl-β-D-thiogalactoside [IPTG]). The plates were scored after 18 hours incubation at either 37°C or 49°C.

Immunoprecipitation of $FLAG_3$-tagged proteins

Strains expressing $FLAG_3$-tagged proteins were pre-grown on LB plates overnight at 30°C. Fresh individual colonies were used for inoculation and grown in LB medium. 3 × 1 L cultures were grown at 37°C to OD_{600} = 0.8. Cells were collected by centrifugation (8 000 rpm for 10 min at 4°C, JLA-16.25 Beckman Coulter rotor), pellets frozen in liquid nitrogen and stored at –80°C. Cell pellets were resuspended in 8 mL of cell opening buffer (95 mM KCl, 5 mM NH_4Cl, 20 mM HEPES (pH = 7.5), 1 mM DTT, 15 mM $Mg(OAc)_2$, 0.5 mM $CaCl_2$, 8 mM putrescine, 1 mM spermidine, 1 tablet of cOmplete EDTA-free Protease Inhibitor Cocktail (Roche) per 50 mL of buffer) and disrupted using FastPrep homogenizer (MP Biomedicals) with 0.1 mm Zirconium beads (Techtum) in 6 cycles by 20 s with 3 minute chill on ice. Cell debris was removed by centrifugation at 14,800 rpm for 20 minutes 4°C in F241.5P rotor using 149 Microfuge 22R centrifuge (Beckman Coulter). The supernatant was combined with 100 μL of ANTI-FLAG M2 Affinity Gel (Sigma) pre-equilibrated in cell opening buffer, and incubated for 1.5 hours at 4°C on a turning wheel (Fisherbrand Multi-Purpose Tube Rotators). The samples were loaded on Micro Bio-Spin Columns columns (Bio-Rad) pre-equilibrated in cell opening buffer, and washed 10 times with 1 mL of cell opening buffer by gravity flow. RqcH- $FLAG_3$ was eluted by addition of 200 μL opening buffer containing 0.1 mg/mL poly-FLAG peptide (Biotool, Bimake) for 45 min on a turning wheel. All incubations, washes and elutions were performed at 4°C. The eluted sample was collected by centrifugation at 2000 rpm for 1 minutes 4°C in a F241.5P rotor using a 149 Microfuge 22R centrifuge (Beckman Coulter). One aliquot of the eluted sample was resolved on SDS-PAGE, the other was blotted on cryo-EM grids, and the remaining sample was used for mass spectrometry and tRNA-array analyses. For SDS-PAGE analyses, 20 μL aliquots of samples (flowthrough, washes and elutions) were mixed with 5 μL of 5x SDS loading buffer and heated at 95°C for 15 minutes. The beads remaining in the column were washed twice with 1 mL of cell opening buffer and resuspended in 100 μL of 1x SDS loading buffer. Denatured samples were loaded on 12% SDS-PAGE. SDS-gels were stained by ''Blue-Silver'' Coomassie Staining (Candiano et al., 2004) and washed with water for 6 hours or overnight before imaging with LAS4000 (GE Healthcare).

Preparation and imaging of cryo-EM grids

Eluted pull-down samples were kept on ice and loaded on grids within two hours after preparation without freezing. The concentration of ribosomes in the samples was estimated from SDS-PAGE gels by comparison of ribosomal band intensities in eluted samples with the bands from loaded ribosomes with known concentration. The concentration of ribosomes in elution of RqcH-$FLAG_3$ and YabO-$FLAG_3$ was about 20 nM and 100 nM, respectively. Vitrobot (FEI) blotting was performed at 100% humidity, 4°C, 5 s blot time, 1 s wait time and 0 s drain time; the resultant sample was vitrified by plunge-freezing in liquid ethane. Grids were imaged on a Titan Krios (FEI) operated at 300 kV at a nominal magnification of 165 000 × and a pixel size of 0.82 Å with a Gatan K2 Summit camera with a 5 s exposure and 20 frames using the EPU software. For RqcH-$FLAG_3$ pull-downs, two datasets were collected on Quantifoil 2/1 Cu 300 and Quantifoil 2/2 Cu 300 grids with defocus range of −0.7 to −1.9 μm and electron fluence of 28.3 $e^-/Å^2$. The YabO-$FLAG_3$ dataset was collected on a carbon-coated Quantifoil 2/2 Cu 300 grid with defocus range of −0.4 to −1.9 μm and electron fluence of 27.4 $e^-/Å^2$.

Cryo-EM data processing

Processing was performed with Relion 3.1 unless otherwise stated (Zivanov et al., 2018). Movies were aligned with MotionCor2 with 5 × 5 patches (Zheng et al., 2017) and the CTF was estimated with Gctf (Zhang, 2016). Particles were picked with crYOLO using the provided general model (Wagner et al., 2019), and initially extracted with a box size of 140 pixels, pixel size of 2.46 Å. 3D classifications were performed without angular sampling. For focused classification with partial signal subtraction, the volume eraser and vop commands in UCSF Chimera were used to create starting volumes for masks. For high-resolution refinements, particles were re-extracted in a box of 420 × 420 pixels with a pixel size of 0.82 Å. For CTF refinement, anisotropic magnification, higher order

Please cite this article in press as: Crowe-McAuliffe et al., Structural Basis for Bacterial Ribosome-Associated Quality Control by RqcH and RqcP, Molecular Cell (2020), https://doi.org/10.1016/j.molcel.2020.11.002

aberrations, and per-particle defocus and astigmatism were refined. Volumes were locally filtered with SPHIRE (Moriya et al., 2017), and local resolution was estimated with RELION or ResMap (Kucukelbir et al., 2014). The pixel size of the final maps was estimated by comparison to existing structures using UCSF Chimera. Resolutions were estimated with RELION using the 'gold standard' criterion (Scheres and Chen, 2012).

For the RqcH IP sample, 725,554 particles were initially picked from 6,730 micrographs (selected from 7,177 initial micrograph movies) from two separate data collections. After 2D classification, 724,098 particles were selected for further processing. An initial model was made *de novo* using the RELION 3D initial model tool, and this was low-pass filtered to 60 Å and used as a reference for a 3D refinement of all particles selected after 2D classification. 3D classification with eight classes was then performed without alignment. The two classes from this classification that contained 50S, RqcH and tRNA, but no extra density toward the edge of the volume (643,616 particles or 88.9% of the starting particles) were selected for further subsorting. 3D refinement was repeated, a generous soft mask encompassing the A-, P- and E-sites was used for partial signal subtraction, and 3D classification was performed with eight classes, T = 200 and the resolution of the expectation step limited to 10 Å. Two classes (totalling 13.9% of the particles) contained RqcH and an A/P-tRNA, with the class among these that had the most interpretable density for the RqcH NFACT-N and HhH domains was selected for further subsorting. Partial signal subtraction around the A- and P-sites was followed by 3D classification with four classes, T = 200, and the resolution of the expectation step limited to 10 Å. The class with the most interpretable density for the RqcH NFACT-N and HhH domains (totalling 10,703 particles or 24.3% of the total particles) was selected for 3D refinement and designated State A. Three classes (totalling 51.5% of the particles) contained RqcH and P-site tRNA. The class with the most interpretable density (containing 74,210 particles) was chosen for further refinement and the resulting volume designated State B. A class with particularly poorly resolved RqcH NFACT-N and HhH domains (containing 110,597 particles) was designated State B*. The third class resembled state B with the RqcH NFACT-N and HhH domains modestly shifted away from the P-site tRNA ASL. A class with 6.1% of particles (39,077 total) contained an E-site tRNA, and was designated State C. A class containing 28.4% of particles (182,833 total) contained P-site tRNA and YabO, but no RqcH, and was designated State D. The resolution of this volume was enhanced by CTF refinement. The final remaining class, containing 10.3% of particles, contained density corresponding to the RqcH CC-M, but not the NFACT-N or HhH, domains.

For the YabO IP sample, 592,872 particles were initially picked from 5,242 micrographs (selected from 5,614 initial micrograph movies). After 2D classification, 579,606 particles were selected for further processing. State D from the RqcH IP processing was low-pass filtered to 60 Å and used as a reference for 3D refinement prior to 3D classification with eight classes and no angular sampling. Four classes comprising 98.3% of particles (569,758 total) were recognizably 50S and were selected for further processing. 3D refinement was repeated, a generous mask around the A-, P- and E-sites was used for partial signal subtraction, and 3D classification was performed with eight classes, T = 200 and the resolution of the expectation step limited to 10 Å. Four of the resulting classes, comprising 31.1% of starting particles (317,968 total) resembled State D and were refined further, including CTF refinement. One class comprising 9.3% of particles (53,124 total) resembled State B, and another with 8.0% (45,313 particles) and which contained P-site tRNA, E-site tRNA and YabO was designated State E. The remaining two classes consisted of an apparent 50S with no ligand (12.8%) or with poorly resolved RqcH (14.1%) and were not refined further. For RsfS-focused classification, a soft mask around RsfS was used for partial signal subtraction, and 3D classification was performed with four classes, T = 50 and the resolution of the expectation step limited to 10 Å. For exit-tunnel-focused classification, a soft mask around the edge of the exit tunnel was used for partial signal subtraction, and 3D classification was performed with six classes and T = 20.

Starting models for the 60S subunit were taken from PDB entries 6HA1 and 6HA8, as well as 4V9F for the uL11/H44 stalk base (Crowe-McAuliffe et al., 2018; Gabdulkhakov et al., 2013). For RqcH and YabO, SWISS-MODEL (Waterhouse et al., 2018) was used to generate homology models using the following templates: RqcH NFACT-N, 6PON (Manne et al., 2019); RqcH HhH, 3DOA and 6PON; RqcH CC and NFACT-R domains, 5H3W (Musyoki et al., 2016); YabO, 1DM9 (Staker et al., 2000). PDB entries 5H3X and 3J92 were additionally used to help with modeling RqcH (Musyoki et al., 2016; Shao et al., 2015). PDB entry 1EHZ was used as a template for modeling *B. subtilis* alanine tRNA-TGC-1-1 (Shi and Moore, 2000).

Models were initially fitted with UCSF Chimera (Pettersen et al., 2004) or aligned with Pymol (Schrödinger; https://pymol.org/2/), and manually adjusted with Coot (Emsley et al., 2010) and ISOLDE (Croll, 2018). The initial RqcH model was built using the volume from multibody refinement, and individual domains from this model were then placed in the other maps with minor adjustments. Serine 2 was chosen as the starting amino acid because a peptide lacking the initiator methionine was the most abundant in mass spectrometry (Table S1). The linker regions between the NFACT-N and HhH domains (residues 174–178), as well as between the CC-M and NFACT-R domains (residues 434–445), were poorly resolved and therefore not included in the final model. The NFACT-R domain was particularly poorly resolved and was therefore modeled as poly-alanine only. For the 50S ribosomal subunit, the uL1 stalk and tip of the ASF were flexible and were not included in the final models. The YabO model was built initially into the State B volume. Phenix was used for refinement (Liebschner et al., 2019), and models were assessed using MolProbity (Williams et al., 2018). States A and B were refined against locally filtered volumes. The RqcH-focused State B multibody refinement was refined against a volume that had been sharpened using the RELION post-pro-

Please cite this article in press as: Crowe-McAuliffe et al., Structural Basis for Bacterial Ribosome-Associated Quality Control by RqcH and RqcP, Molecular Cell (2020), https://doi.org/10.1016/j.molcel.2020.11.002

cessing procedure with automatic b-factor estimation. For the state C model shown in Figure 5, individual chains (individual domains for RqcH) from state A or state B were placed by rigid-body fitting in ChimeraX. The E-tRNA was the same as the A/P tRNA in state A.

tRNA microarrays

tRNA microarrays were performed similarly to as previously described (Beckert et al., 2018). The RqcH-50S-bound tRNA (i.e., in the immunoprecipitated RqcH-$FLAG_3$ aliquots) was compared on the same arrays to the total *B. subtilis* tRNA. A detailed protocol is published on protocols.io (https://dx.doi.org/10.17504/protocols.io.hfcb3iw). For deacylation lysate and immunoprecipitated samples were incubated with 125 mM Tris-HCl, pH = 9.0, 0.1 M EDTA, 0.5% (w/v) SDS at room temperature for 45 minutes, before neutralisation with an equal volume of 1 M NaOAc, pH = 5.5. RNA was extracted twice with 5:1 acidic phenol:chloroform, precipitated with ethanol, and resuspended in ddH_2O. Using the unique invariant single stranded 3′-NCCA-ends of intact tRNA a Cy3-labeled RNA/DNA and CAtto647-labeled RNA/DNA hybrid oligonucleotide was ligated to the tRNA extracted from the RqcH-50S samples and total *B. subtilis* tRNA, respectively. Labeled RNA was purified by phenol:chloroform extraction and ligation efficiency verified on denaturing 10% SDS-PAGE. Labeled tRNA samples were loaded on a microarray containing 24 replicates of full-length tDNA probes recognizing 36 *B. subtilis* tRNA isoacceptors and hybridized for 16 h at 60°C. Fluorescence signals of microarrays were recorded with a GenePix 4200A scanner (Molecular Devices) and statistically analyzed with in-house scripts with Python version 3.7.0. Data have been deposited in Gene Expression Omnibus (GEO) database under accession GSE152592.

Proteomics sample preparation and LC/MS/MS analysis

Proteins were precipitated with 10% (w/v) trichloroacetic acid overnight at 4°C, pelleted at 17,000 g 4°C and washed twice with cold 90% (v/v) acetone. Precipitated proteins were solubilized in 7 M urea, 2 M thiourea, 100 mM ammonium bicarbonate (ABC) buffer, reduced with 5 mM dithiothreitol for 30 min at room temperature (RT) and alkylated with 20 mM chloroacetamide in the dark. Predigestion with 1:50 (enzyme to protein ratio) *Lysobacter enzymogenes* Lys-C (Fujifilm Wako Pure Chemical) was carried out for 4 hours at RT. Next, the solution was diluted five times with 100 mM ABC buffer and a further digestion with 1:50 dimethylated *Sus scrofa* trypsin (Sigma Aldrich) was carried out overnight at RT. Samples were then acidified with trifluoroacetic acid (TFA) added to 1.0% (v/v), and desalted on in-house made C18 SPE tips. Purified peptides were reconstituted in 0.5% TFA (v/v) for nano-LC/MS/MS.

Peptides were injected to an Ultimate 3000 RSLCnano system (Dionex) using a 0.3 × 5 mm trap-column (5 μm C18 particles, Dionex) and an in-house packed (3 μm C18 particles, Dr Maisch) analytical 50 cm × 75 μm emitter-column (New Objective). Peptides were eluted at 250 nL/min with an 8%–40% (2 h) A to B gradient (buffer A: 0.1% (v/v) formic acid; buffer B: 80% (v/v) acetonitrile + 0.1% (v/v) formic acid) to a quadrupole-orbitrap Q Exactive Plus (Thermo Fisher Scientific) MS/MS via a nano-electrospray source (positive mode, spray voltage of 2.5 kV). The MS was operated with a top-5 data-dependent acquisition strategy. Briefly, one 350-1,400 m/z MS scan at a resolution setting of R = 70,000 was followed by higher-energy collisional dissociation fragmentation (normalized collision energy of 26) of the 5 most intense ions (z: +2 to +6) at R = 17,500. MS and MS/MS ion target values were 3,000,000 and 50,000 ions with 50 and 100 ms injection times, respectively. Dynamic exclusion was limited to 40 s.

MS raw files were processed with the MaxQuant software package (version 1.6.1.0) (Tyanova et al., 2016). Methionine oxidation, protein N-terminal acetylation, protein N-terminal methionine formylation and removal of up to 4 N-terminal amino acids were set as potential variable modifications, while cysteine carbamidomethylation was defined as a fixed modification. Identification was performed against the UniProt (https://www.uniprot.org) database (*B. subtilis* wild-type strain 168, 4 271 protein sequences) using the tryptic digestion rule (i.e., cleavages after lysine and arginine without proline restriction). Only identifications with at least 1 peptide $\geq$ 7 amino acids long (with up to 2 missed cleavages) were accepted. Label-free intensity normalization with the MaxLFQ algorithm (Cox et al., 2014) was also applied. Protein and LFQ ratio count (i.e., number of quantified peptides for reporting a protein intensity) was set to 1. iBAQ feature of MaxQuant was enabled. This normalizes protein intensities by the number of theoretically observable peptides and enables rough intra-sample estimation of protein abundance. Peptide-spectrum match, peptide and protein false discovery rate was kept below 1% using a target-decoy approach (Elias and Gygi, 2007). All other parameters were default.

The mass spectrometry raw files along with MaxQuant identification and quantification outputs (txt folder) have been deposited to the ProteomeXchange Consortium (Vizcaíno et al., 2014) via the PRIDE partner repository with the dataset identifier PXD019364.

Alignment and phylogenetic analysis

For the sequence alignment and secondary structure assignment in Figure 3D, YabO from State B and Hsp15 from PDB 1DM9 were aligned by structure with the DALI server (Holm, 2019; Staker et al., 2000) and DSSP was used to annotate secondary structural elements. For the C-terminal extension of Hsp15, no structural information is available and PSIPRED was used to predict secondary structure (Buchan and Jones, 2019).

YabO and RqcH sequences were retrieved from the NCBI protein database, using accession numbers from the COG 2014 database (Galperin et al., 2015). The YabO/Hsp15/RluA group belongs to COG1188 (411 sequences), and RqcH to COG1293 (357 sequences). Sequences were aligned using MAFFT- L-INS-I v6.861b (Katoh et al., 2005), including curation to remove 55 ambiguously-alignable sequences in the case of COG1293 and 29 RluA sequences (more distant relatives of YabO/Hsp15 but also carrying the S4 RNA binding domain) in the case of COG1188. Representative YabO/Hsp15 sequences were selected for phylogenetic

Please cite this article in press as: Crowe-McAuliffe et al., Structural Basis for Bacterial Ribosome-Associated Quality Control by RqcH and RqcP, Molecular Cell (2020), https://doi.org/10.1016/j.molcel.2020.11.002

analysis for Figure 3D to sample broadly across protein diversity and taxonomic distributions. After trimming the alignment to remove columns with < 50% gaps with TrimAL v1.4 (Capella-Gutiérrez et al., 2009), phylogenetic analysis was carried out with RaxML v 8.2.12 (Stamatakis, 2014) on the Cipres Science Gateway (Miller et al., 2015) with 100 bootstrap replicates and the LG model of substitution.

Figure preparation

Figures were prepared using UCSF ChimeraX (Goddard et al., 2018) and Inkscape (https://inkscape.org/).

QUANTIFICATION AND STATISTICAL ANALYSIS

Cryo-EM data analysis

RELION uses a 'molecular smoothness' prior within a regularized likelihood optimization framework when refining single-particle cryo-EM data (Scheres, 2012). The 'gold standard' FSC approach is used to prevent overfitting (Scheres and Chen, 2012).

7.6 Structure of the RqcH^{DR}-variant complex, supplementary material

SUPPLEMENTARY ONLINE MATERIALS

for

RqcH and RqcP catalyze processive poly-alanine synthesis in a reconstituted ribosome-associated quality control system

Hiraku Takada[1,2,3,*], Caillan Crowe-McAuliffe[4], Christine Polte[4], Zhanna Yu. Sidorova[5,6], Victoriia Murina[2,3], Gemma C. Atkinson[8], Andrey L. Konevega[5,7,8], Zoya Ignatova[4], Daniel N. Wilson[4,*], Vasili Hauryliuk[2,3,9,10,*]

[1] Faculty of Life Sciences, Kyoto Sangyo University, Kamigamo, Motoyama, Kita-ku, Kyoto 603-8555, Japan

[2] Department of Molecular Biology, Umeå University, 90187 Umeå, Sweden

[3] Laboratory for Molecular Infection Medicine Sweden (MIMS), Umeå University, 90187 Umeå, Sweden

[4] Institute for Biochemistry and Molecular Biology, University of Hamburg, 20146 Hamburg, Germany

[5] Petersburg Nuclear Physics Institute named by B.P. Konstantinov of National Research Centre "Kurchatov Institute", 188300 Gatchina, Russia

[6] Russian Research Institute of Hematology and Transfusiology of FMBA, 191024 Saint Petersburg, Russia

[7] Peter the Great St. Petersburg Polytechnic University, 195251 Saint Petersburg, Russia

[8] National Research Centre "Kurchatov Institute", 123182 Moscow, Russia

[9] Department of Experimental Medical Science, Lund University, 221 00 Lund, Sweden

[10] University of Tartu, Institute of Technology, 50411 Tartu, Estonia

Supplementary methods

Preparation of B. subtilis *and* E. coli *tRNAs*

B. subtilis *total tRNA*. Total transfer RNA from wild-type 168 *B. subtilis* was isolated as follows. *B. subtilis* was grown in 2xLB to early stationary phase, 70 g of cells were collected by centrifugation, resuspended in 200 mL H_2O, combined with an equal volume of phenol and stirred for 1 hour. After centrifugation at 4000 g for 30 minutes the aqueous phase was taken, and the organic phase was re-extracted twice. The aqueous phase combined and mixed with 1/10 of volume 20% potassium acetate, and nucleic acids were precipitated with 2 volumes of ethanol. The pellet was resuspended in 100 mL of water, and after the NaCl concentration was brought to 1 M, the mixture was stirred for 1 hour at 4 °C. The debris was removed by centrifugation (1 hour at 10,000-15,000 g) and discarded, while the supernatant was taken and precipitated with ethanol. The resultant pellet was resuspended in 100 mL of 0.3 M sodium acetate pH 7.0, and re-extracted with 0.4 volume isopropanol. The supernatant was mixed with 0.6 volumes cold isopropanol, the RNA collected by centrifugation (1 hour at 4,000 g) and the RNA pellet was resuspended in 100 mL of buffer A (0.2 M NaCl, 50 mM NaAc, 10 mM $MgCl_2$, pH 4.5-5.0). The resultant solution was loaded onto a Q-Toyopearl column pre-equilibrated in the same buffer. After the column was washed with 2 volumes of buffer A, the tRNA was eluted with buffer B (1.0 M NaCl, 50 mM NaAc, 10 mM $MgCl_2$, pH 4.5-5.0), the pH adjusted to pH 8.5, tRNA was deacylated by incubation at 37 °C for 40 minutes at and precipitated by ethanol. The pellet was dissolved in 10 mL of ddH_2O and the tRNA quality as assessed by analytical by HPLC chromatography on Lichrospher RP18 250-4 column in 5-15% gradient of ethanol in buffer A.

B. subtilis $tRNA^{Ala}$ *and* $tRNA^{Lys}$. Individual tRNA species were prepared as per (1) with minor modifications. Briefly, total *B. subtilis* tRNA was aminoacylated with for 30 minutes at 37 °C using either recombinant *B. subtilis* Ala-RS or *E. coli* Lys-RS (30 µg of aa-RS per 1 mL of reaction mixture; 50 mM Tris HCl pH 7.5, 70 mM NH_4Cl, 30 mM KCl, 7 mM $MgCl_2$, 2 mM DTT, 3mM ATP, 0.5 mM of amino acid). Elongation factor Tu (EF-Tu) was preincubated for 15 minutes with 1 mM GTP, 3 mM PEP, 10 µg/mL pyruvate kinase in buffer C (50 mM Tris HCl pH 7.5, 70 mM NH_4Cl, 30 mM KCl, 7 mM $MgCl_2$) to convert EF-Tu from GDP- to GTP-bound form. Aminoacylated tRNA was supplemented with two-fold excess of EF-Tu-GTP to form a ternary complex (aa-tRNA–EF-Tu–GTP) for 5 min at 37 °C, and then placed on ice. The ternary complex was loaded on 1 mL column Protino@NI-IDA (MAcherey Nagel), the column washed with 3 volumes of buffer C (50 mM Tris HCl pH 7.5, 70 mM NH_4Cl, 30 mM KCl, 7 mM $MgCl_2$), and the ternary complex was eluted with 3 volumes of buffer D (25 mM Tris HCl pH 7.5, 50 mM KCl, 10 mM $MgCl_2$, 2.5% glycerol, 300 mM imidazole). The eluted ternary complex was dissociated by addition of potassium acetate (pH 5.0) to final concentration of 0.2 M, aminoacylated

tRNA was phenol-extracted and precipitated with ethanol. The tRNA pellet was dissolved in ddH_2O, deacylated as described above, re-precipitated, re-dissolved in 0.1 mL of ddH_2O and stored at –80 °C.

E. coli *f[^{35}S]Met-tRNA$_i^{Met}$*. f[^{35}S]Met-tRNA$_i^{Met}$ was produced from *E. coli* tRNA$_i^{Met}$ as described previously (2).

Protein expression and purification

B. subtilis *alanyl-tRNA synthetase*, *N-terminally His$_6$-tagged AlaS* (VHp772, pET24d-His$_6$-AlaRS). The protein was overexpressed in freshly transformed *E. coli* BL21 DE3 Rosetta (Novagen). Fresh transformants were inoculated to a final OD_{600} of 0.05 in the LB medium (2000 mL) supplemented with 100 µg/mL kanamycin. The cultures were grown at 37 °C until an OD_{600} of 0.5, induced with 1 mM IPTG (final concentration) and grown for additional 1.5 hours at 30 °C. The cells were harvested by centrifugation and resuspended in binding buffer (1000 mM NH_4Cl, 10 mM $MgCl_2$, 10 mM imidazole, 10% glycerol, 8 mM β-mercaptoethanol, 25 mM HEPES:KOH pH 7.5) supplemented with 0.1 mM PMSF and 1 U/mL of DNase I. Cells were lysed by one passage through a high-pressure cell disrupter (Stansted Fluid Power, 150 MPa), cell debris was removed by centrifugation (25,000 rpm for 40 min, JA-25.50 Beckman Coulter rotor) and clarified lysate was taken for protein purification. Clarified cell lysate was filtered through a 0.2 µm syringe filter and loaded onto a 5 mL HisTrap HP column pre-equilibrated in binding buffer. The column was washed with 5 CV of binding buffer, and the protein was eluted with a linear gradient (6 CV, 0-100% elution buffer) of elution buffer (1000 mM NH_4Cl, 10 mM $MgCl_2$, 500 mM imidazole, 10% glycerol, 8 mM β-mercaptoethanol, 25 mM HEPES:KOH pH 7.5). Fractions most enriched in His$_6$-AlaS (≈30-45% elution buffer) were pooled, totalling approximately 8 mL. The sample was diluted 4 times with dilution buffer (5 mM $MgCl_2$, 10% glycerol, 1 mM β-mercaptoethanol, 25 mM Tris-HCl pH 7.5) and loaded on HiPrep Q XL 16/10 column pre-equilibrated with binding buffer (150 mM NaCl, 5 mM $MgCl_2$, 10% glycerol, 1 mM β-mercaptoethanol, 25 mM Tris-HCl pH 7.5) and the protein was eluted with a linear gradient (3 CV, 0-100% elution buffer) of elution buffer (1000 mM NaCl, 5 mM $MgCl_2$, 10% glycerol, 1 mM β-mercaptoethanol, 25 mM Tris-HCl pH 7.5). Fractions most enriched in His$_6$-AlaS (≈65-75% elution buffer) were pooled, totalling approximately 8 mL. The fractions containing His$_6$-AlaS were pooled and applied on HiPrep 10/26 desalting column (GE Healthcare) pre-equilibrated with storage buffer (300 mM KCl, 15 mM $MgCl_2$, 10% glycerol, 1 mM β-mercaptoethanol, 25 mM HEPES:KOH pH 7.5). The fractions containing His$_6$-AlaS were collected and concentrated in an Amicon Ultra (Millipore) centrifugal filter device (cut-off 50 kDa). Protein preparations were aliquoted, frozen in liquid nitrogen.

Saccharomyces cerevisiae valyl-tRNA synthetase, His_6-tagged. The protein was overexpressed and purified as described earlier (3), the aminoacylation activity towards *E. coli* $tRNA^{Val}$ was demonstrated in the original report.

B. subtilis *EF-Tu, C-terminally His_6-tagged* (VHp733, pET24d-tufA-TEV-His_6). The protein was overexpressed in freshly transformed *E. coli* BL21 DE3 Rosetta (Novagen). Fresh transformants were inoculated to a final OD_{600} of 0.05 in the LB medium (800 mL) supplemented with 100 µg/mL kanamycin. The cultures were grown at 37 °C until an OD_{600} of 0.5, induced with 1 mM IPTG (final concentration) and grown for additional 1.5 hours at 30 °C. The cells were harvested by centrifugation and resuspended in binding buffer (500 mM NaCl, 5 mM $MgCl_2$, 10 mM imidazole, 10% glycerol, 25 µM GDP, 1 mM β-mercaptoethanol, 25 mM Tris-HCl pH 7.5) supplemented with 0.1 mM PMSF and 1 U/mL of DNase I. Cells were lysed by one passage through a high-pressure cell disrupter (Stansted Fluid Power, 150 MPa), cell debris was removed by centrifugation (25,000 rpm for 40 min, JA-25.50 Beckman Coulter rotor) and clarified lysate was taken for protein purification. Clarified cell lysate was filtered through a 0.2 µm syringe filter and loaded onto a 5 mL HisTrap HP column pre-equilibrated in binding buffer. The column was washed with 5 CV of wash buffer (1000 mM NaCl, 5 mM $MgCl_2$, 10 mM imidazole, 10% glycerol, 25 µM GDP, 1 mM β-mercaptoethanol, 25 mM Tris-HCl pH 7.5), and the protein was eluted with a linear gradient (6 CV, 0-100% elution buffer) of elution buffer (500 mM NaCl, 5 mM $MgCl_2$,500 mM imidazole, 10% glycerol, 25 µM GDP, 1 mM β-mercaptoethanol, 25 mM Tris-HCl pH 7.5). Fractions most enriched in EF-Tu-His_6 (≈35-65% elution buffer) were pooled, totalling approximately 8 mL. The sample was diluted 4 times with dilution buffer (5 mM $MgCl_2$, 10% glycerol, 25 µM GDP, 1 mM β-mercaptoethanol, 25 mM Tris-HCl pH 7.5) and loaded on HiPrep Q XL 16/10 column pre-equilibrated with binding buffer (150 mM NaCl, 5 mM $MgCl_2$, 10% glycerol, 25 µM GDP, 1 mM β-mercaptoethanol, 25 mM Tris-HCl pH 7.5) and the protein was eluted with a linear gradient (3 CV, 0-100% elution buffer) of elution buffer (1000 mM NaCl, 5 mM $MgCl_2$, 10% glycerol, 25 µM GDP, 1 mM β-mercaptoethanol, 25 mM Tris-HCl pH 7.5). Fractions most enriched in EF-Tu-His_6 (≈55-75% elution buffer) were pooled, totalling approximately 12 mL. The fractions containing EF-Tu-His_6 were pooled and applied on HiPrep 10/26 desalting column (GE Healthcare) pre-equilibrated with storage buffer (400 mM KCl, 5 mM $MgCl_2$, 10% glycerol, 25 µM GDP, 1 mM β-mercaptoethanol, 50 mM HEPES:KOH pH 8). The fractions containing EF-Tu-His_6 were collected and concentrated in an Amicon Ultra (Millipore) centrifugal filter device (cut-off 30 kDa). Protein preparations were aliquoted, frozen in liquid nitrogen.

B. subtilis *RqcH, C-terminally HTF-tagged, wild-type* (VHp982, pET24d-rqcH-HTF) *and DR variant (D97A R98A)* (VHp983, pET24d-rqcHDR-HTF). Both proteins were overexpressed in freshly transformed *E. coli*

BL21 DE3 Rosetta (Novagen). Fresh transformants were inoculated to a final OD_{600} of 0.05 in the LB medium (800 mL) supplemented with 100 µg/mL kanamycin. The cultures were grown at 37 °C until an OD_{600} of 0.5, induced with 1 mM IPTG (final concentration) and grown for additional 1.5 hours at 30 °C. The cells were harvested by centrifugation and resuspended in binding buffer (400 mM NaCl, 5 mM MgC_{l2}, 20 mM imidazole, 10% glycerol, 4 mM β-mercaptoethanol, 25 mM HEPES:KOH pH 8) supplemented with 0.1 mM PMSF and 1 U/mL of DNase I. Cells were lysed by one passage through a high-pressure cell disrupter (Stansted Fluid Power, 150 MPa), cell debris was removed by centrifugation (25,000 rpm for 40 min, JA-25.50 Beckman Coulter rotor) and clarified lysate was taken for protein purification. Clarified cell lysate was filtered through a 0.2 µm syringe filter and loaded onto a 5 mL HisTrap HP column pre-equilibrated in binding buffer. The column was washed with 5 CV of wash buffer (2000 mM NaCl, 5 mM $MgCl_2$, 20 mM imidazole, 10% glycerol, 4 mM β-mercaptoethanol, 25 mM HEPES:KOH pH 8), and the protein was eluted with a linear gradient (6 CV, 0-100% elution buffer) of elution buffer (400 mM NaCl, 5 mM $MgCl_2$,500 mM imidazole, 10% glycerol, 4 mM β-mercaptoethanol, 25 mM HEPES:KOH pH8). Fractions most enriched in RqcH-HTF (≈30-50% elution buffer) were pooled, totalling approximately 5 mL. The sample was loaded on a HiLoad 16/600 Superdex 200 pg column pre-equilibrated with Gel filtration buffer (2000 mM NaCl, 5 mM $MgCl_2$, 10% glycerol, 4 mM β-mercaptoethanol, 25 mM HEPES:KOH pH 8). The fractions containing RqcH-HTF were pooled and applied onto a HiPrep 10/26 desalting column (GE Healthcare) pre-equilibrated with storage buffer (720 mM KCl, 5 mM $MgCl_2$, 50 mM arginine, 50 mM glutamic acid, 10% glycerol, 4 mM β-mercaptoethanol, 25 mM HEPES:KOH pH 8). The fractions containing RqcH-HTF were collected and concentrated in an Amicon Ultra (Millipore) centrifugal filter device (cut-off 50 kDa). Protein preparations were aliquoted, frozen in liquid nitrogen.

B. subtilis *RqcP, wild-type* (VHp734, pET24d-rqcP-TEV-His_6) *and R16A variant* (VHp735, pET24d-rqcPR16A-TEV-His_6). C-terminally His_6-tagged protein was expressed in freshly transformed *E. coli* BL21 DE3 Rosetta (Novagen). Fresh transformants were inoculated to a final OD_{600} of 0.05 in the LB medium (800 mL) supplemented with 100 µg/mL kanamycin. The cultures were grown at 37 °C until an OD_{600} of 0.5, induced with 1 mM IPTG (final concentration) and grown for additional 1.5 hours at 30 °C. The cells were harvested by centrifugation and resuspended in binding buffer (500 mM NaCl, 5 mM $MgCl_2$, 20 mM imidazole, 10% glycerol, 1 mM β-mercaptoethanol, 25 mM HEPES:KOH pH 7.5) supplemented with 0.1 mM PMSF and 1 U/mL of DNase I. Cells were lysed by one passage through a high-pressure cell disrupter (Stansted Fluid Power, 150 MPa), cell debris was removed by centrifugation (25,000 rpm for 40 min, JA-25.50 Beckman Coulter rotor) and clarified lysate was taken for protein purification. Clarified cell lysate was filtered through a 0.2 µm syringe filter and loaded onto a 5 mL HisTrap HP column pre-equilibrated in binding buffer. The column was washed with 5 CV of wash buffer (2000

mM NaCl, 5 mM $MgCl_2$, 20 mM imidazole, 10% glycerol, 1 mM β-mercaptoethanol, 25 mM HEPES:KOH pH 7.5), and the protein was eluted with a linear gradient (6 CV, 0-100% elution buffer) of elution buffer (500 mM NaCl, 5 mM $MgCl_2$,500 mM imidazole, 10% glycerol, 4 mM β-mercaptoethanol, 25 mM HEPES:KOH pH7.5). Fractions most enriched in RqcP-TEV-His_6 (≈45-65% elution buffer) were pooled, totalling approximately 6 mL. The sample was diluted 3 times with dilution buffer (5 mM $MgCl_2$, 10% glycerol, 1 mM β-mercaptoethanol, 25 mM Tris-HCl pH 7.5) and loaded on HiPrep Q XL 16/10 column pre-equilibrated with binding buffer (150 mM NaCl, 5 mM $MgCl_2$, 10% glycerol, 1 mM β-mercaptoethanol, 25 mM Tris-HCl pH 7.5) and the protein was eluted with a linear gradient (3 CV, 0-100% elution buffer) of elution buffer (1000 mM NaCl, 5 mM $MgCl_2$, 10% glycerol, 1 mM β-mercaptoethanol, 25 mM Tris-HCl pH 7.5). Fractions most enriched in RqcP-TEV-His_6 were pooled, totalling approximately 12 mL, and applied on HiPrep 10/26 desalting column (GE Healthcare) pre-equilibrated with cleavage buffer (400 mM KCl, 5 mM $MgCl_2$, 10% glycerol, 4 mM β-mercaptoethanol, 25 mM HEPES:KOH pH 7.5). To cleave off the His_6 tag, 10 µg of His_6-Tev protease per 1 mg of RqcP were added and the reaction mixture was incubated at 10 °C for ≈14 hours. After the His_6 tag was cleaved off, the protein was passed through 5 mL HisTrap HP column pre-equilibrated with storage buffer (500 mM KCl, 5 mM $MgCl_2$, 10% glycerol, 1 mM β-mercaptoethanol, 25 mM HEPES:KOH pH 7.5). Fractions containing RqcP in the flow-through were collected and concentrated in an Amicon Ultra (Millipore) centrifugal filter device (cut-off 10 kDa). Protein preparations were aliquoted, frozen in liquid nitrogen.

Supplementary Table 1. **Reference table for *B. subtilis* tRNAs array data.**
$tRNA^{Met}CAUi$ – initiator $tRNA_i^{Met}$ and $tRNA^{Met}CAUe$ – elongator $tRNA^{Met}$.

Array probe designation	Recognised tRNA isoacceptor[a] (copy number)	Amino acid & codon(s) recognised by the tRNA	Anticodon of the tDNA array probes[b]
Ala-IGC	$tRNA^{Ala}GGC$ (1)	Ala-GCC/U	A/GGC
Ala-A/C/UGC	$tRNA^{Ala}UGC$ (3)	Ala-GCA/G/U	A/C/TGC
Arg-ICG	$tRNA^{Arg}ACG$ (2)	Arg-CGC/U/A	T/A/GCG
Arg-C/UCG	$tRNA^{Arg}CCG$ (1)	Arg-CGG	CCG
Arg-CCU	$tRNA^{Arg}CCU$ (1)	Arg-AGG	CCT
Arg-UCU	$tRNA^{Arg}UCU$ (2)	Arg-AGA	TCT
Asn-GUU	$tRNA^{Asn}GUU$ (3)	Asn-AAC/U	A/GTT
Asp-GUC	$tRNA^{Asp}GUC$ (4)	Asp-GAC/U	A/GTC
Cys-G/ACA	$tRNA^{Cys}GCA$ (1)	Cys-UGC/U	A/GCA
Gln-C/UUG	$tRNA^{Gln}UUG$ (4)	Gln-CAA/G	C/TTG
Glu-UUC	$tRNA^{Glu}UUC$ (6)	Glu-GAA/G	C/TTC
Gly-GCC	$tRNA^{Gly}GCC$ (2)	Gly-GGC/U	A/GCC
Gly-UCC	$tRNA^{Gly}UCC$ (3)	Gly-GGA/G/U	A/C/TCC
His-GUG	$tRNA^{His}GUG$ (2)	His-CAC/U	A/GTG
Ile-IAU	$tRNA^{Ile}GAU$ (3) $tRNA^{Ile}CAU$ (1)	Ile-AUC/U Ile-AUA	A/GAT TAT
Leu-CAA	$tRNA^{Leu}CAA$ (1)	UUG	CAA
Leu-CAG	$tRNA^{Leu}CAG$ (1)	CUG	CAG
Leu-A/GAG	$tRNA^{Leu}GAG$ (1)	CUC/U	A/GAG
Leu-UAA1	$tRNA^{Leu}UAA$ (2)	UUA/G	C/TAA
Leu-UAA2	$tRNA^{Leu}UAG$ (1)	CUA/G	C/TAG
Lys-UUU	$tRNA^{Lys}UUU$ (3)	AAA/G	TTT
Met-CAU1	$tRNA^{Met}CAUi$ (3)	Meti-AUG	CAT
Met-CAU2	$tRNA^{Met}CAUe$ (1)	Met-AUG	CAT
Met-CAU3	$tRNA^{Met}CAUe$ (1)	Met-AUG	CAT
Phe-GAA	$tRNA^{Phe}GAA$ (3)	Phe-UUC/U	A/GAA
Pro-A/G/C/UGG	$tRNA^{Pro}UGG$ (1)	Pro-CCA/G/U	A/C/TGG
Ser-GCU	$tRNA^{Ser}GCU$ (2)	Ser-AGC/U	A/GCT
Ser-GGA	$tRNA^{Ser}GGA$ (1)	Ser-UCC/U	A/GGA
Ser-A/C/UGA	$tRNA^{Ser}UGA$ (2)	Ser-UCA/G/U	A/C/TGA
Thr-CGU Thr-A/GGU Thr-UGU	$tRNA^{Thr}UGU$ (3)	Thr-ACG Thr-ACC/U Thr-ACA/G/U	CGT A/GGT A/C/TGT
Trp-CCA	$tRNA^{Trp}CCA$ (1)	Trp-UGG	CCA
Tyr-GUA	$tRNA^{Tyr}GUA$ (2)	Tyr-UAC/U	A/GTA
Val-mAC	$tRNA^{Val}GAC$ (1)	Val-GUC/U	A/GAC
Val-UAC	$tRNA^{Val}UAC$ (3)	Val-GUA/G/U	A/C/TAC

[a]Source: GtRNAdb (http://gtrnadb.ucsc.edu/) (4). Genomic copy number is included in parentheses.
[b]The anticodon designates the anticodon(s) implicated in the design of the complementary tDNA probes.

Supplementary Table 2. Strains and plasmids used in this work.

The table is provided as a separate Excel file.

Supplementary Table 3. Cryo-EM collection, refinement, and validation statistics.

	$RqcH^{DR}$-50S
Data collection and processing	
Magnification	165 000
Voltage (kV)	300
Electron exposure (e^{-}/Å^2)	34.8
Defocus range (μm)	−0.8–2.0.
Pixel size (Å)	0.82
Symmetry imposed	None
Initial particle images (no.)	145 631
Final particle images (no.)	16 700
Map resolution (Å)	3.2
FSC threshold	0.143
Refinement	
Map sharpening *B* factor (Å^2)	−75.814
Cross-correlation (volume)	0.80
Model composition	
Non-hydrogen atoms	93 862
Protein residues	3 818
RNA bases	2 996
R.m.s. deviations	
Bond lengths (Å)	0.011
Bond angles (°)	1.109
Validation	
MolProbity score	1.75
Clashscore	4.79
Poor rotamers (%)	0.23
Ramachandran plot	
Favored (%)	91.61
Allowed (%)	8.20
Disallowed (%)	0.19

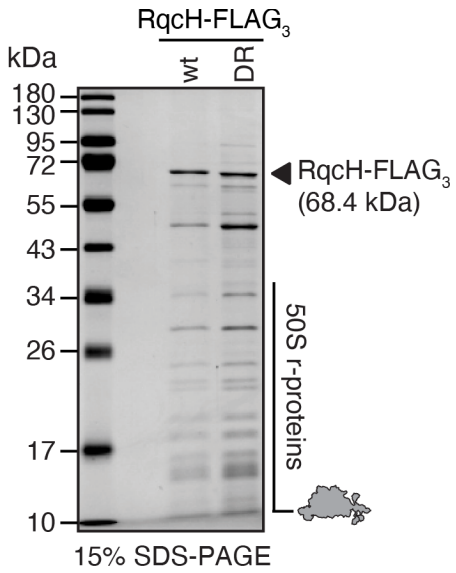

Supplementary Figure 1. Immunoprecipitation of RqcH^{DR}-FLAG$_3$-50S RQC complexes, related to Figure 4.

10 µL of co-IP samples eluted with poly-FLAG peptide and 10 µL of molecular marker were resolved on a 15% SDS-PAGE.

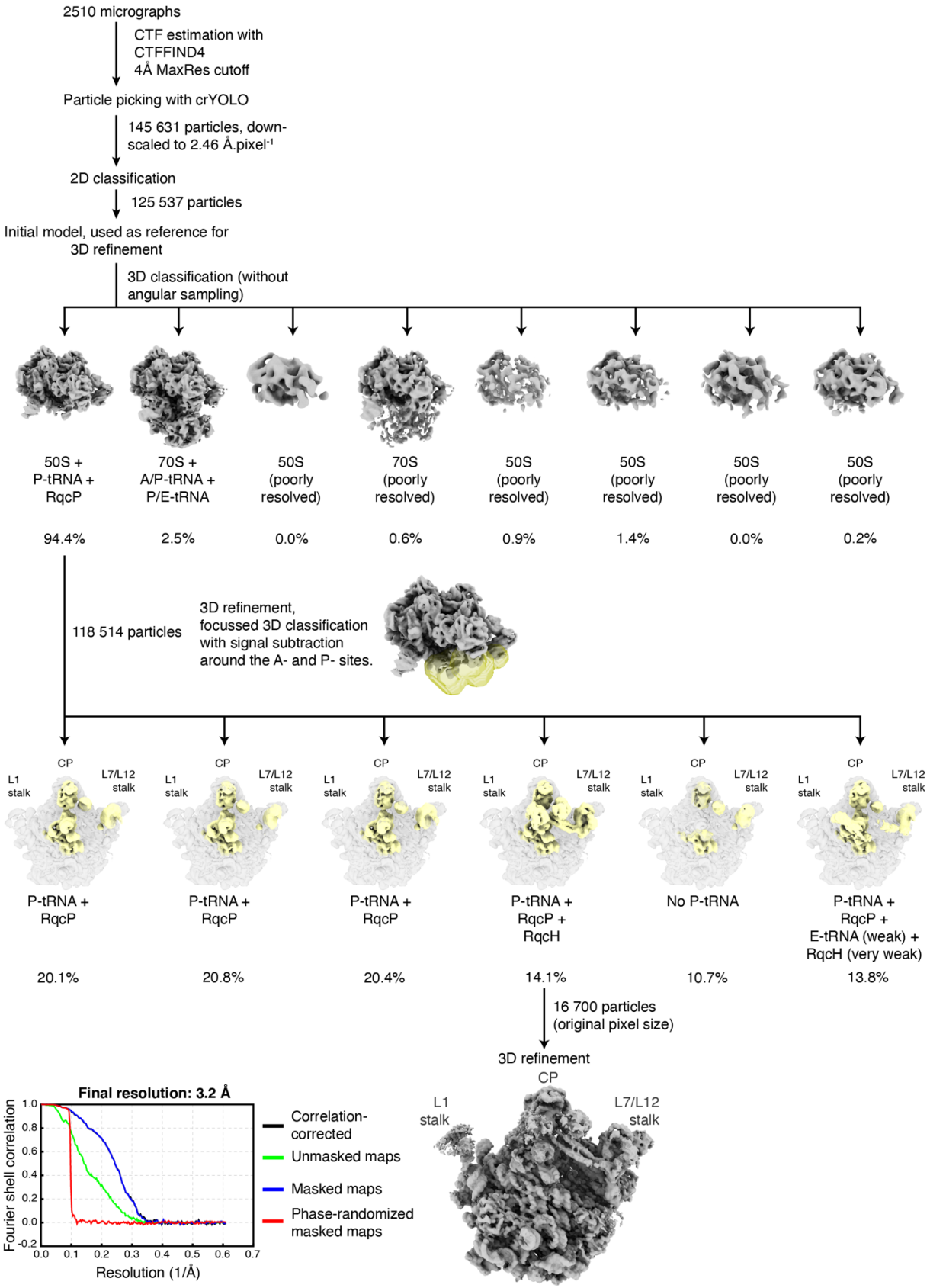

Supplementary Figure 2. Processing of cryo-EM data from RqcH^{DR}–FLAG$_3$ immunoprecipitation sample, related to Figure 4.

Processing scheme of RqcH^{DR} IP micrographs and FSC curve generated by RELION (5). Refer to methods for additional details.

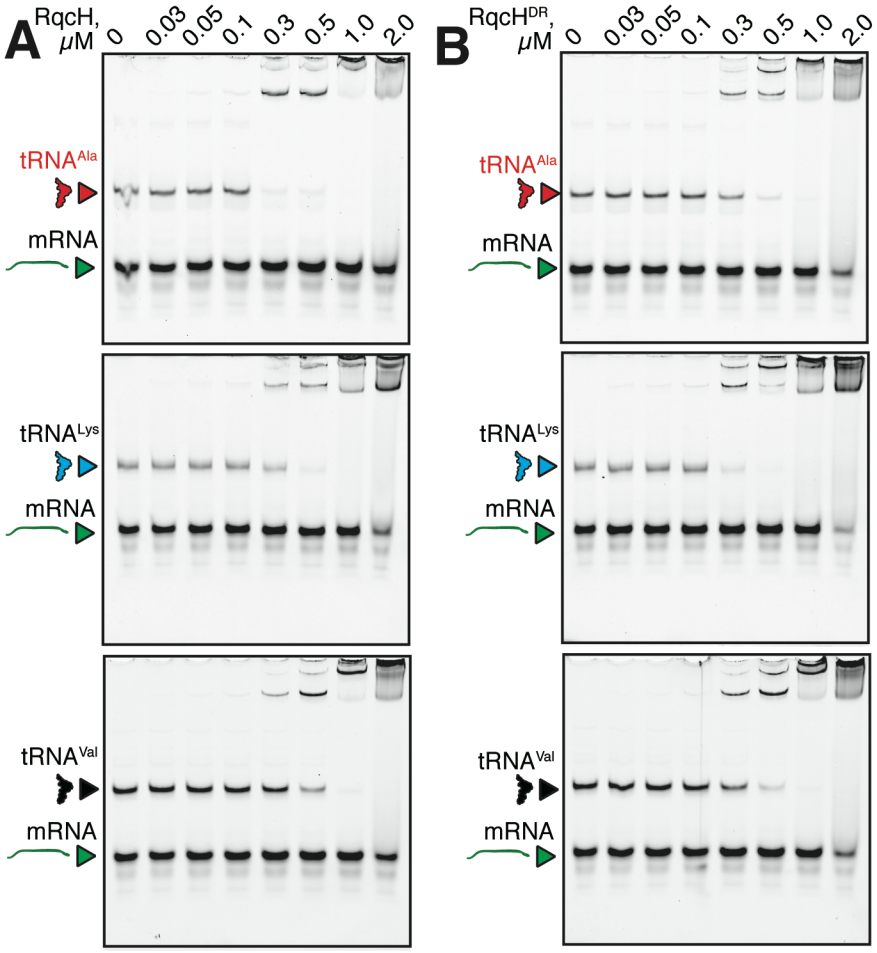

Supplementary Figure 3. Representative full-size EMSA gels, related to Figure 2.
Complex formation between 0.1 μM tRNA (either *E. coli* $tRNA^{Val}$ or *B. subtilis* $tRNA^{Lys}$ or *B. subtilis* $tRNA^{Ala}$) and increasing concentrations of *B. subtilis* RqcH-HTF (either wild-type or DR-substituted, D97A R98A) was monitored by EMSA. All experiments were performed in the presence of 1 μM of competing synthetic model mRNA(MVF) RNA oligonucleotide (5′-GGCAAGGAGGAGAUAAGAAUGGUUUUCUAAUA-3′). Gels were stained by SYBR Gold (Life Technologies) nucleic acid stain for 30 minutes.

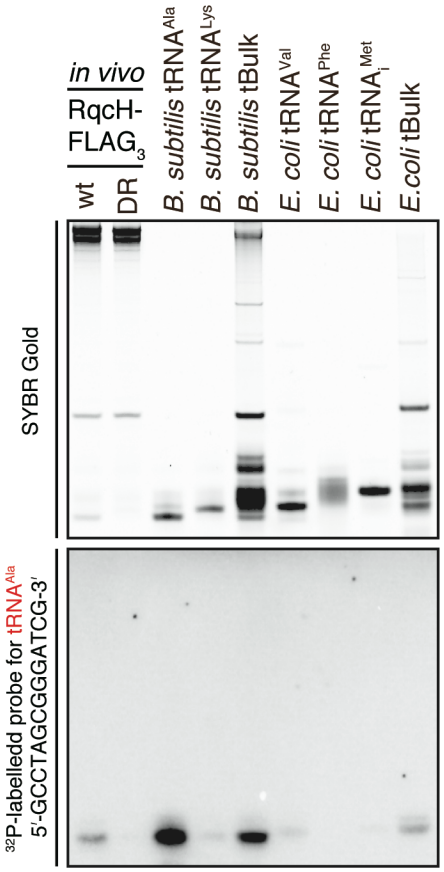

Supplementary Figure 4. Specificity of *B. subtilis* tRNA^{Ala} detection by Northern blotting, related to Figures 2 and 3.

RNA from co-IP samples (150 ng per lane), individual *B. subtilis* or *E. coli* tRNA species (1.5 pmol per lane) or either *B. subtilis* or *E. coli* total tRNA (9 pmol per lane) were resolved on 8M urea 8% polyacrylamide gels and either stained with SYBR Gold (Life Technologies) nucleic acid stain (top) and probed through Northern blotting using ^{32}P-labeled tRNA^{Ala} probe (bottom).

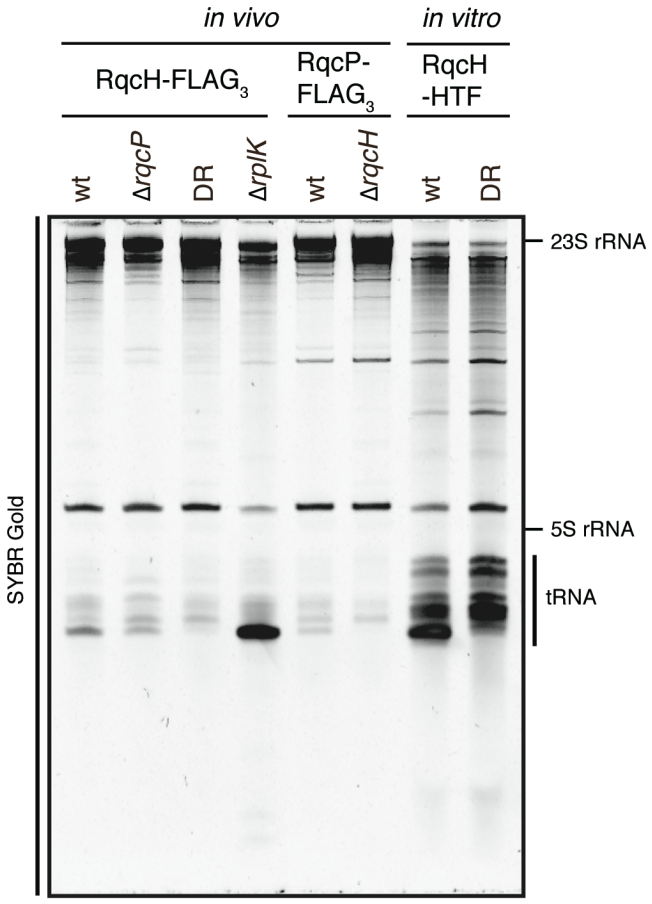

Supplementary Figure 5. SYBR Gold staining analysis of 50S RQC complexes isolated through co-IP of either RqcH-FLAG$_3$ or RqcP-FLAG$_3$ directly from lysed *B. subtilis*, related to Figures 3 and 5.
RNA from co-IP samples (150 ng per lane) were resolved on 8M urea 8% polyacrylamide gel and stained with SYBR Gold (Life Technologies) nucleic acid stain.

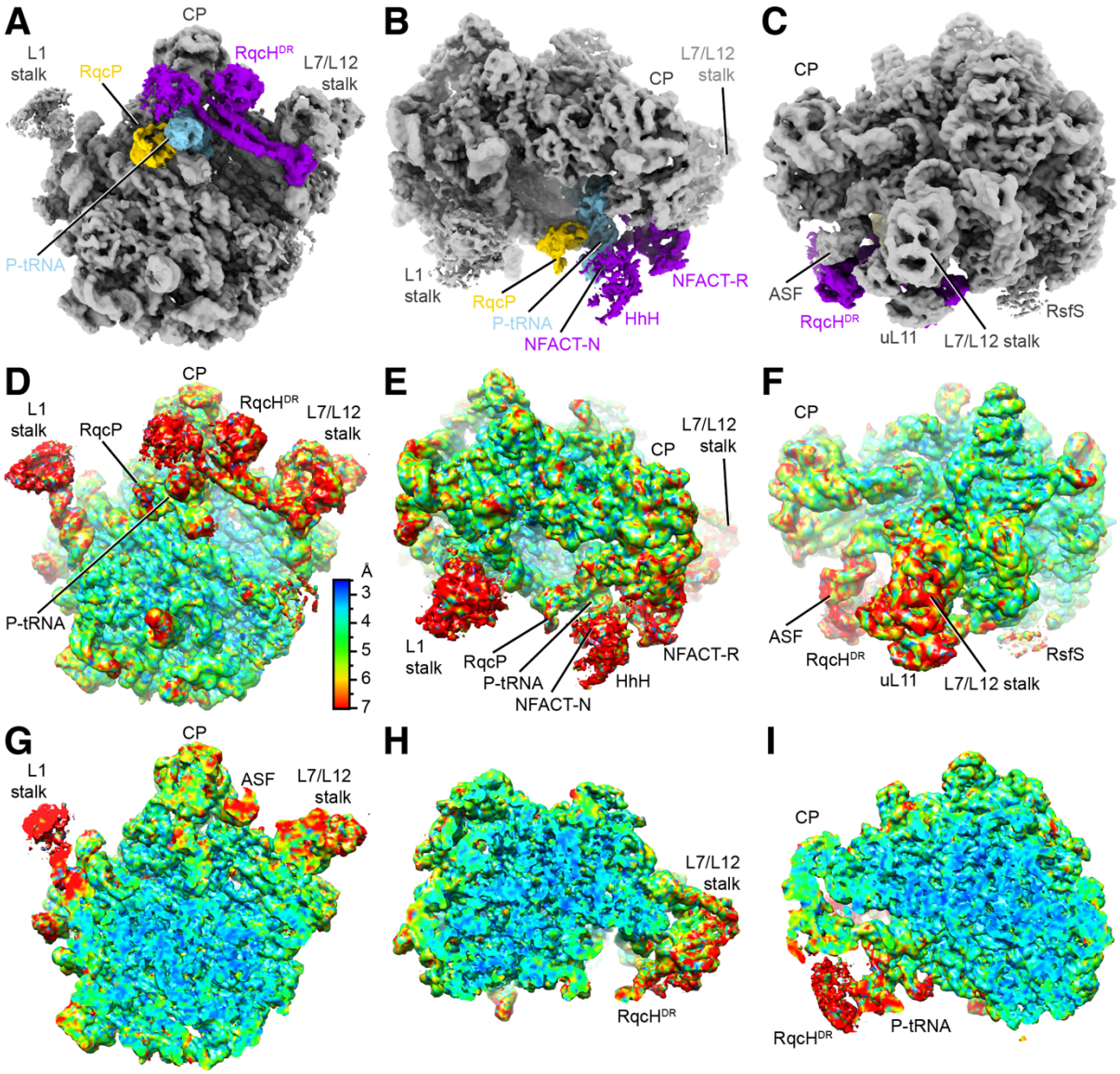

Supplementary Figure 6. Density features and local resolution of cryo-EM maps from RqcH^{DR}–FLAG$_3$ immunoprecipitation, related to Figure 4.

(**A**) Crown view of RqcH^{DR} bound to the 50S-P-tRNA-RqcP RQC complex. (**B, C**) Alternative views of **A**. (**D–I**) The same views as in **A–C** except coloured by local resolution. Either whole views (**D–F**) or cut-throughs (**G–I**) are shown.

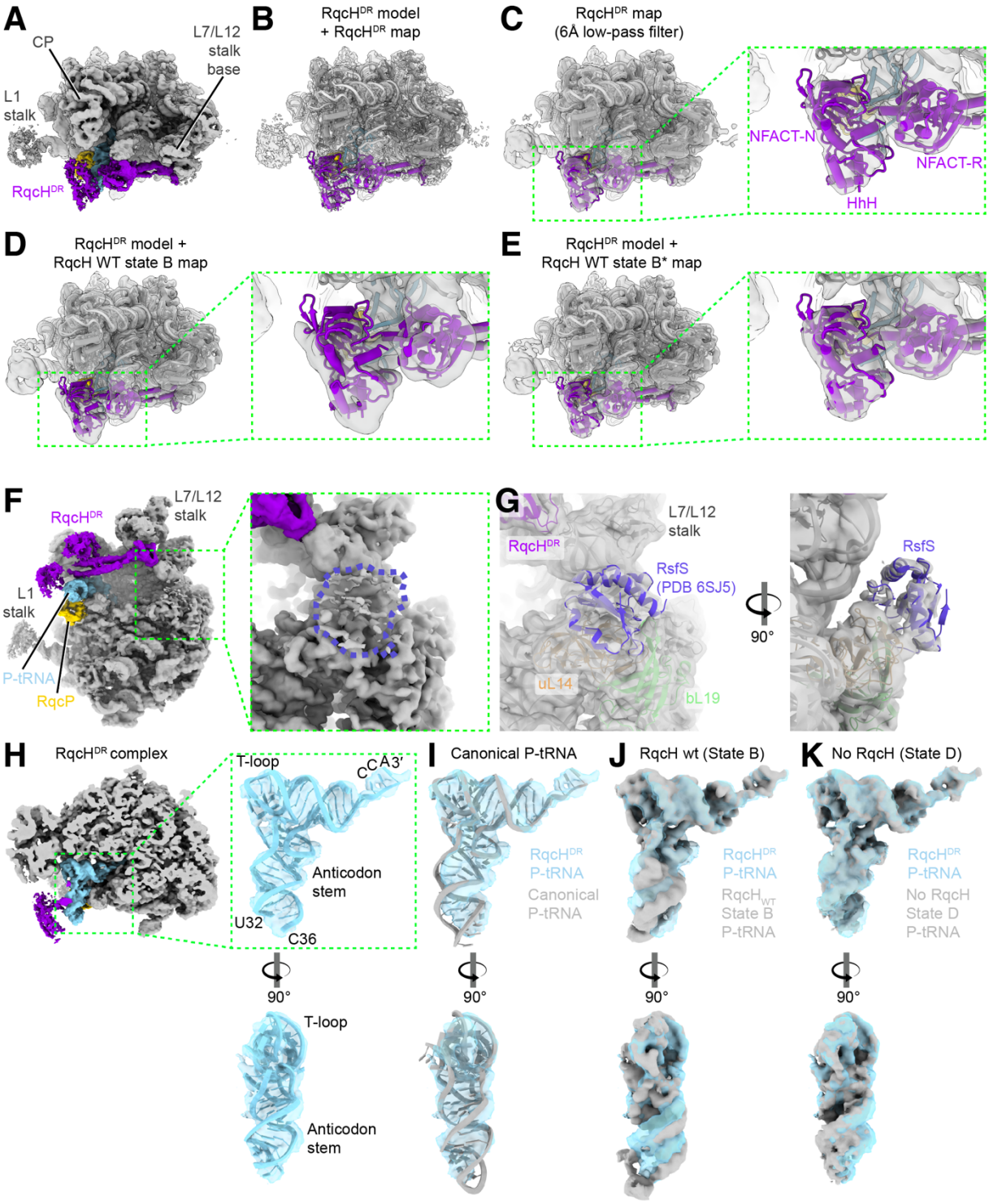

Supplementary Figure 7. Comparison of RqcH^{DR} and wild-type RqcH cryo-EM volumes, related to Figure 4.

(**A**) Overview of RqcH^{DR} bound to the 50S-P-tRNA-RqcP RQC complex. (**B**) as in A except fitted models are shown in a transparent map. (**C**) As in B, except with a 6 Å low-pass filtered map. Inset, right, is a close view of the RqcH globular domains. (**D**) The RqcH^{DR} model compared with the RqcH wild-type state B map low-pass filtered to 6 Å (EMD-11889). . (**E**) The RqcH^{DR} model compared to the wild-type RqcH state B* map low-pass filtered to 6 Å (EMD-11915). (**F**) Overview of the RqcH^{DR} complex with emphasis on the RsfS binding site (blue dashed outline in inset). (**G**) Two views of the crystal structure of *S. aureus* RsfS (PDB 6SJ5 (6)) fitted into the RqcH^{DR} complex map. (**H**) View of the P-tRNA bound to the RqcH^{DR} complex. Inset shows P-tRNA density and model. (**I–K**). Same as the inset in **H** except

RqcH^{DR}-bound tRNA (cyan density) is compared to either canonical P-tRNA (**I**, PDB 6CFJ (7)), state B tRNA from the wild-type RqcH structure (PDB 7AS8, **J**), or state D tRNA from a 50S–P-tRNA–RqcP complex but no RqcH (EMD-11914, **K**).

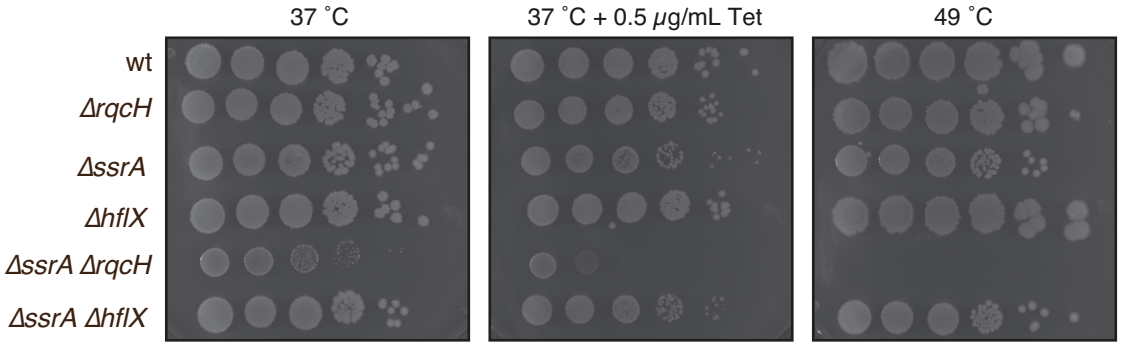

Supplementary Figure 8. HflX is does not play an essential role in RQC.
No synthetic growth defect was observed upon simultaneous *ssrA* and *hflX* deletion. The Δ*ssrA* Δ*rqcH* and Δ*ssrA* Δ*hflX* strains were used positive and specificity controls, respectively. 10-fold serial dilutions were spotted onto LB agar plates and incubated for 18 hours at 37 °C (left), 49 °C (right) or 37 °C in the presence 0.5 µg/mL tetracycline (Tet, middle).

Supplementary references:

1. Rezgui, V.A., Tyagi, K., Ranjan, N., Konevega, A.L., Mittelstaet, J., Rodnina, M.V., Peter, M. and Pedrioli, P.G. (2013) tRNA tKUUU, tQUUG, and tEUUC wobble position modifications fine-tune protein translation by promoting ribosome A-site binding. *Proc Natl Acad Sci U S A*, **110**, 12289-12294.
2. Murina, V., Kasari, M., Hauryliuk, V. and Atkinson, G.C. (2018) Antibiotic resistance ABCF proteins reset the peptidyl transferase centre of the ribosome to counter translational arrest. *Nucleic Acids Res*, **46**, 3753-3763.
3. Takada, H., Roghanian, M., Caballero-Montes, J., Van Nerom, K., Jimmy, S., Kudrin, P., Trebini, F., Murayama, R., Akanuma, G., Garcia-Pino, A. *et al.* (2021) Ribosome association primes the stringent factor Rel for tRNA-dependent locking in the A-site and activation of (p)ppGpp synthesis. *Nucleic Acids Res*, **49**, 444-457.
4. Chan, P.P. and Lowe, T.M. (2016) GtRNAdb 2.0: an expanded database of transfer RNA genes identified in complete and draft genomes. *Nucleic Acids Res*, **44**, D184-189.
5. Zivanov, J., Nakane, T., Forsberg, B.O., Kimanius, D., Hagen, W.J., Lindahl, E. and Scheres, S.H. (2018) New tools for automated high-resolution cryo-EM structure determination in RELION-3. *elife*, **7**, e42166.
6. Khusainov, I., Fatkhullin, B., Pellegrino, S., Bikmullin, A., Liu, W.T., Gabdulkhakov, A., Shebel, A.A., Golubev, A., Zeyer, D., Trachtmann, N. *et al.* (2020) Mechanism of ribosome shutdown by RsfS in *Staphylococcus aureus* revealed by integrative structural biology approach. *Nat Commun*, **11**, 1656.
7. Tereshchenkov, A.G., Dobosz-Bartoszek, M., Osterman, I.A., Marks, J., Sergeeva, V.A., Kasatsky, P., Komarova, E.S., Stavrianidi, A.N., Rodin, I.A., Konevega, A.L. *et al.* (2018) Binding and Action of Amino Acid Analogs of Chloramphenicol upon the Bacterial Ribosome. *J Mol Biol*, **430**, 842-852.

8 Acknowledgements

I would firstly like to thank my supervisor, Prof. Daniel N. Wilson for the opportunity to do work towards a PhD in his laboratory, for providing so many interesting projects, and much astute advice along the way. And for making sure to keep things fun. Other members of the lab gave invaluable advice and camaraderie along the way, and I would especially like to thank Michael and Paul for the guidance and atmosphere they provided when I first arrived. Maxi, Maha, Aga, Bertand, Claudia, Karo, Katrin, Timm, Max, and Helge and many others also deserve mentioning. Thank you also especially to Timm for the German-language suggestions to the Zusammenfassung at the beginning of this document, as well as Danny for administrative help over the years.

Much of the work presented in this thesis was performed in collaboration with other groups. Special thanks are given to the lab of Prof. Vasili Hauryliuk, which used microbiology to prepare samples for cryo-EM and test hypotheses generated by the structures—especially Hiraku and Victoriia—and for the discussion along the way. Also Prof. Zoya Ignatova, who with Christine Polte analysed tRNAs by microarray. I would also like to thank the groups of Dr Gemma C. Atkinson and Dr Vicent Pelechano, as well as Dr Michael Hall and Dr Jiří Nováček for cryo-EM data collection. The work described in this thesis would not be possible without all of you!

Finally, I would like to thank Anne for her tolerance over the last year or so, and the Sekar Kenanga gamelan group for their friendliness and for providing a non-work-related outlet for creative energy over the last few years.

9 Eidesstattliche Versicherung

Hiermit versichere ich an Eides statt, die vorliegende Dissertation selbst verfasst und keine anderen als die angegebenen Hilfsmittel benutzt zu haben. Die eingereichte schriftliche Fassung entspricht der auf dem elektronischen Speichermedium. Ich versichere, dass diese Dissertation nicht in einem früheren Promotionsverfahren eingereicht wurde.

Caillan Crowe-McAuliffe
September 29, 2021